**Universidade do Minho**
Escola de Engenharia

Graça de Fátima Moreira de Vasconcelos

# Experimental investigations on the mechanics of stone masonry: Characterization of granites and behavior of ancient masonry shear walls

# Investigação experimental na mecânica da alvenaria de pedra: Caracterização de granitos e comportamento de paredes antigas de alvenaria de pedra

2005

**Universidade do Minho**
Escola de Engenharia

Graça de Fátima Moreira de Vasconcelos

# Experimental investigations on the mechanics of stone masonry: Characterization of granites and behavior of ancient masonry shear walls

# Investigação experimental na mecânica da alvenaria de pedra: Caracterização de granitos e comportamento de paredes antigas de alvenaria de pedra

Tese de Doutoramento em Engenharia Civil

Trabalho efectuado sob a orientação do
**Professor Doutor Paulo José Brandão Barbosa Lourenço**

2005

# ACKNOWLEDGEMENTS

The present work was carried out at the Department of Civil Engineering of the University of Minho and was supervised by Prof. Paulo Lourenço, to whom I express my gratitude for having made this work possible by the support and valuable suggestions.

I would like to express my thanks to Prof. Carlos Alves and Prof. Jorge Pamplona of Department of Earth Sciences of the University of Minho by their availability and profitable suggestions.

I am grateful to Prof. Manuel Costa of Department of Physics of University of Minho for making the using of the 3D topographic inspection system possible.

To all laboratory technicians of the Laboratory of Civil Engineering of University of Minho and especially to António Matos, Marco Jorge and José Gonçalves, I would like to express my gratitude for technical suggestions and friendship.

To the company Augusto Ferreira & Filhos and very especially to mr. Emídio I express my gratitude for the essential help in the construction of the walls.

I would like to thank to the companies ArtCanter and Granicampos all interest in providing the materials in time.

I would like to thank to all colleagues of the Department of Civil Engineering and the other Phd students. In particular, I thank to Sena Cruz, to Luís Neves the availability and to Daniel Oliveira the reading and profitable discussions.

Besides the valuable technical help, I am grateful to Carlos Palha for the encouragement and the companionship along this work.

Finally, I wish to express my gratitude to all my family but in particular to my parents and my sister for their love and endless support.

# ABSTRACT

The work presented in this thesis was developed at the Department of Civil Engineering of University of Minho. This work is eminently experimental and intends to be a valuable contribution to a better insight on the mechanics of stone masonry.

In order to improve the knowledge on the mechanical properties of granite, the constitutive behavior of distinct granite types under tensile and compressive loading was successfully obtained through a set of experimental tests associated to suitable displacement control. Afterwards, elastic and fracture properties were derived and statistical correlations among these parameters were obtained. The selection of different types of granitic rocks made possible the analysis of the influence of some microstructural aspects, such as grain size and internal texture on the large range of elastic and fracture properties. Other aspects that can explain the variation of the tensile and compressive engineering properties, like weathering state, moisture content and physical properties were also investigated. The possibility of predicting the mechanical and physical properties of the granites by simple and economical nondestructive techniques, such as the ultrasonic pulse velocity (UPV) and the Schmidt hammer rebound number (N) was studied. A set of statistical correlations between the elastic and strength properties and the experimental data obtained through nondestructive techniques were defined. Moreover, a discussion of the factors (moisture content, weathering state and internal texture) that possibly induce variations on the velocity measurements and on the rebound number was performed.

The characterization of the composite behavior of masonry materials used in the construction of the stone masonry walls was carried out by means of a set of direct shear tests conducted on dry and mortared masonry joints and of uniaxial compressive tests conducted on masonry prisms. Besides the shear and compressive strength properties, results of the influence of the bond material on the overall compressive behavior were presented.

The analysis of the mechanical shear behavior of granitic masonry walls, considered representative of ancient masonry constructions, was carried out based on the experimental results of twenty-four static cyclic tests. The influence of the masonry bond and the axial load levels was analyzed by considering different masonry bonds and distinct levels of axial load. The analysis of the lateral cyclic performance of stone masonry walls was based on the results of the failure patterns and the force-displacement histeresis loops. From this information, it was possible to carry out a comparative analysis of the distinct types of walls in terms of ductility, nonlinear deformability and energy dissipation capacity. In addition, the lateral resistance was assessed by using simplified formulations for prediction of the shear strength of masonry walls under combined axial and shear loads.

# RESUMO

O trabalho apresentado nesta tese foi desenvolvido no departamento de Engenharia Civil da Universidade do Minho. Este trabalho é eminentemente experimental e pretende ser uma contribuição para uma melhor compreensão do comportamento mecânico da alvenaria de pedra.

Com o objectivo de melhorar o conhecimento das propriedades do granito, o comportamento constitutivo de diferentes tipos de granito foi obtido com sucesso através de um conjunto de ensaios experimentais realizados em controlo de deslocamento e com selecção da variável de controlo adequada. Os resultados destes ensaios permitiram determinar as propriedades elásticas e os parâmetros de fractura, obtendo-se posteriormente um conjunto de correlações estatísticas entre os mesmos que possibilitou uma melhor clarificação da gama de variação das propriedades. A selecção de diferentes tipos de granito permitiu a análise da influência de alguns aspectos micro-estruturais, como por exemplo a dimensão do grão e textura interna na diversidade das propriedades elásticas e de fractura. Foram também considerados aspectos como estado de alteração, humidade e propriedades físicas. A possibilidade de estimar as propriedades dos granitos através de técnicas não destrutivas económicas e de simples utilização foi analisada com base em medições da velocidade de propagação dos ultrassons e os valores de recuo de martelo de Schimdt. Para o efeito, foi estabelecido um conjunto de correlações estatísticas entre o módulo de elasticidade e a resistência à tracção e compressão e os valores obtidos nos ensaios não destrutivos. Adicionalmente, foram estudados os factores que potencialmente podem afectar as medidas dos ensaios não destrutivos, nomeadamente humidade, estado de alteração e anisotropia.

A caracterização do comportamento compósito dos materiais usados na construção das paredes de alvenaria de pedra foi realizada através de um conjunto de ensaio de corte directo realizados em juntas de alvenaria seca e argamassada e de um conjunto de ensaios de compressão uniaxial conduzidos em prismas de alvenaria. Para além das propriedades resistentes de corte e compressão, foram também apresentados os resultados da influência do tipo de material das juntas no comportamento global à compressão.

A análise do comportamento mecânico das paredes de alvenaria de granito, consideradas representativas de estruturas antigas de alvenaria, foi efectuada com base nos resultados experimentais de vinte e quatro ensaios estáticos cíclicos. A influência do aparelho e do nível de esforço axial foi analisada através da consideração de diferentes tipos de aparelho e pela variação do nível de esforço axial. A análise do desempenho cíclico das paredes de alvenaria foi realizada a partir da informação combinada dos modos de rotura e dos diagramas força-deslocamento. Através desta informação foi possível estabelecer uma análise comparativa entre os diferentes tipos de paredes em termos de ductilidade, capacidade de deformação não linear e capacidade para dissipar energia durante o carregamento cíclico. Além disso, os valores da resistência lateral obtidos experimentalmente foram comparados com os valores obtidos por aplicação de métodos analíticos simplificados.

# RESUMO

O trabalho apresentado nesta tese foi desenvolvido no departamento de Engenharia Civil da Universidade do Minho. Este trabalho é eminentemente experimental e pretende ser uma contribuição para uma melhor compreensão do comportamento mecânico da alvenaria de pedra.

Com o objectivo de melhorar o conhecimento das propriedades do granito, o comportamento constitutivo de diferentes tipos de granito foi obtido com sucesso através de um conjunto de ensaios experimentais realizados em controlo de deslocamento e com selecção da variável de controlo adequada. Os resultados destes ensaios permitiram determinar as propriedades elásticas e os parâmetros de fractura, obtendo-se posteriormente um conjunto de correlações estatísticas entre os mesmos que possibilitou uma melhor clarificação da gama de variação das propriedades. A selecção de diferentes tipos de granito permitiu a análise da influência de alguns aspectos micro-estruturais, como por exemplo a dimensão do grão e textura interna na diversidade das propriedades elásticas e de fractura. Foram também considerados aspectos como estado de alteração, humidade e propriedades físicas. A possibilidade de estimar as propriedades dos granitos através de técnicas não destrutivas económicas e de simples utilização foi analisada com base em medições da velocidade de propagação dos ultrassons e os valores de recuo de martelo de Schimdt. Para o efeito, foi estabelecido um conjunto de correlações estatísticas entre o módulo de elasticidade e a resistência à tracção e compressão e os valores obtidos nos ensaios não destrutivos. Adicionalmente, foram estudados os factores que potencialmente podem afectar as medidas dos ensaios não destrutivos, nomeadamente humidade, estado de alteração e anisotropia.

A caracterização do comportamento compósito dos materiais usados na construção das paredes de alvenaria de pedra foi realizada através de um conjunto de ensaio de corte directo realizados em juntas de alvenaria seca e argamassada e de um conjunto de ensaios de compressão uniaxial conduzidos em prismas de alvenaria. Para além das propriedades resistentes de corte e compressão, foram também apresentados os resultados da influência do tipo de material das juntas no comportamento global à compressão.

A análise do comportamento mecânico das paredes de alvenaria de granito, consideradas representativas de estruturas antigas de alvenaria, foi efectuada com base nos resultados experimentais de vinte e quatro ensaios estáticos cíclicos. A influência do aparelho e do nível de esforço axial foi analisada através da consideração de diferentes tipos de aparelho e pela variação do nível de esforço axial. A análise do desempenho cíclico das paredes de alvenaria foi realizada a partir da informação combinada dos modos de rotura e dos diagramas força-deslocamento. Através desta informação foi possível estabelecer uma análise comparativa entre os diferentes tipos de paredes em termos de ductilidade, capacidade de deformação não linear e capacidade para dissipar energia durante o carregamento cíclico. Além disso, os valores da resistência lateral obtidos experimentalmente foram comparados com os valores obtidos por aplicação de métodos analíticos simplificados.

CONTENTS

# 1. INTRODUCTION

Masonry is the oldest building material that survived until today, being used all over the world and being present in the most impressive historical structures as an evidence of spirit of enterprise of ancient cultures. In the last decades materials like steel and concrete have been replacing masonry as a structural material. This situation is particularly remarkable in Portugal, where almost all new buildings are constructed using reinforced concrete, which appears to be particularly practical and economical. In the recent past, masonry has been mostly used as a non-structural material, as an infill of reinforced concrete frames. This situation increased the research and the development of design rules for reinforced concrete structures but also led to insufficient knowledge about masonry and no national masonry code.

Nevertheless, Portugal is rich of monumental buildings and there is a considerable amount of existing residential masonry buildings in rural areas. Conservation, rehabilitation and strengthening of the built heritage and protection of human lives are clear demands of modern societies. This requires identification of deficiencies of existing structures and appropriate intervention techniques.

Since the early stages of the civilization, stone masonry assumed a major role in the construction of masonry buildings due to the wide availability of stone as a natural resource and the simplicity of laying stone pieces above each other. Only after the widespread of large public buildings carried out by Greeks, Romans and, later, by the Gothic builders at the Middle Age, and the development of the means of transportation, there was the need of selecting dimensioned natural stone and of creating quarries. The Romans used usually rubble stones for the foundations and dimensioned natural stone, as ashlar units, for walls and decorative functions.

Walls are fundamental structural elements in masonry buildings. They can be understood mainly as a compressive element providing the appropriate support to vaults, domes and arches, but also, when correctly constructed and connected, as the major structural element able to face in-plane actions from wind and seismic events. Severe damage was found in recent seismic extreme events on unreinforced masonry walls, leading to the idea that plain masonry is unsuitable for resisting lateral loads and is exclusively dependent on the workmanship. Nevertheless, masonry walls are also the main reason for the stability of the remaining building stock surviving such extreme events.

Even if much information has been gathered about the behavior of stone masonry walls under cyclic loadings from past seismic events, few experimental investigations have been carried out. In regions of moderate and high seismicity, as in the South of Europe, existing buildings are often made of various stone materials and structural typologies, meaning that research on stone masonry walls still appears to be of great significance and a true challenge. This leads to the need of a better insight on the mechanics of stone masonry as a composite material, which constitutes the main goal of this thesis.

## 1.1 Walls through history – an overview

The first stone masonry contructions were the shelters. In this type of masonry, the stones were not dimensioned (rubble stones) and were gathered in the vicinity of the construction.

Due to the simple technical tools, the walls were the result of laying stone units above each other. The interaction between the stones was achieved through the rough contact surfaces, assuring the global stability of the wall by the development of frictional mechanisms.

In the Greek architecture, the walls were considered ornamental objects and not structural elements (Villalba, 1996). Therefore, the execution of walls was carried out taking into account the most perfect techniques, usually without mortar and with marble ashlars contacted by perfectly smooth surfaces, in order to prevent irregularities leading to failure of the edges. The walls could be single leaf or double interconnected leaves. The connection of the stone units was made using steel clamps, or stone pieces placed at the lateral faces. According to Mark (1995), the connection of the stones was related to the prevention of settlements of the foundations or due to the seismic action. However, the steel connection could lead to the tensile failure of the stones in case of expansion provided by corrosion.

The magnificence of the Roman Empire was the basis of the consistent development of constructive systems originally from the tradition of the ancient Hellenic culture, which was particularly noticeable in the beginning of the Empire. The enlargement of the Empire led to the urgent development of infrastructures, namely bridges and ports, but also constructions of local importance such as aqueducts, temples, and residential buildings. The major technological improvement was achieved by the pozzolan concrete invention as the combination of pozzolana as the binder and lime stone or bricks as the aggregate, leading to the mortared walls, *opus caementum*. With the mortar, also the concept of adhesion appeared, which was unknown for the Greeks. This type of masonry was used as the infill material of thick walls, composed by two external leaves, typical of the Roman architecture. The external leaves can be constructed with different bond such as *opus incertum* and the *opus reticulatum* (Adam, 1996). The motivation for the construction of solid and thick masonry walls was the introduction of the arches, already known by the Greeks, but almost non-existent in the Greek architecture, as well as vaults and domes used to overcome great spans. Examples of the new architectural typology are the Domus Aurea building or the Roman Pantheon. According to recent studies (Mark, 1995), this dome works as a set of arches that transmit the large horizontal thrust to the extremely thick cylindrical wall of a total thickness of 6.0m. Another original characteristic of the Roman constructive system is due to the diagonal thrusts associated to the curved shape of the roofs. Lateral transversal thick walls are needed in order to equilibrate the horizontal thrust originated by the vaults.

The typology of the Roman walls was maintained in the first Byzantine constructions, since the techniques, masons and architects were directly imported from Rome. Due to the absence of pozzolana, the middle leaf exhibited poor mechanical characteristics, which led to the increase of the thickness of the external leaves. The most used bond of the external leaves was the *opus mixtum*, alternating coarses of brickwork with stone, see Figure 1.1a. In addition, Byzantine walls are often the combination of bricks with thick mortar joints. There are cases in which the mortar joints are higher than the brick thickness, which is attributed to the difficulty to obtain the bricks. Although doubts can be raised about the mechanical performance of the masonry, several important and impressive buildings were constructed this way, as is the case of the Hagia Sophia, see Figure 1.1b.

(a) (b)

Figure 1.1 – Example of a Byzantine construction; (a) *opus mixtum*; (b) Hagia Sophia

The early medieval architecture is still influenced by the Roman architecture, although in a considerable distinct environment, with different techniques and distinct economical possibilities and needs. The typology of the walls was similar to the Roman. The external leaves were generally composed by stonework, reused ashlar, pillaged bricks or stucco (Mark, 1995). In the absence of pozzolan concrete, the rubble cores were composed by lime mortar with varying qualities.

The development of the Romanesque construction begins in a rural environment with scarce technical knowledge. The constructions were mostly defensive or communitarian buildings. The architectural Romanesque typology was typically rectangular in plan, with timber roofs and short spans. Due to the low lateral thrusts, the walls could be single leaf of reduced thickness. However, due to the need of common fire protection, the roofs were progressively constructed as cannon masonry vaults. The cannon vaults behave as a set of parallel semicircular arches that transmit a uniform lateral thrust to the support walls (Fitchen, 1995; Heyman, 1999). The lateral thrust led to the construction of thick walls without openings or with small openings, frequently strengthened by means of buttresses or salient piers. The most used masonry bond for the external leafs was a variation of the *opus emplectum* with small and irregular stone units roughly cut. Local materials and simple tools were usually used, given the limited workmanship and means of transportation. Generally, the material of the internal leaf was poor due the low quality of the mortar, consisting frequently of clay combined with rubble stone. For the intersection of the walls at the corners, the ashlars were often used.

The Gothic constructive system, whose beginning is identified with the Abbey of St. Denis, is the result of the rigorous application of the constructive principals originated in the Romanesque together with an evolution for more complex and rational shapes of the structural elements (Viollet-le-Duc, 1996). In fact, some late Romanesque churches exhibit particular features attributed to the Gothic architecture. An example of the transition from the Romanesque for the Gothic is the church of Vézelay, where the crossed vaults were generated by means of semicircular arches, illustrating lack of knowledge of the Romanesque builders (Viollet-le-Duc, 1996). In the Gothic architecture, the semicircular arches and the cannon vaults are replaced by ogival arches and crossed and groined vaults, which appear to be much more versatile and able to adapt to the space by adjusting their shape. The structural consequence of the new typology was the reduction of the lateral thrusts and, therefore, of the wall thickness. The decrease of the wall thickness was thus attributed to the construction of

large and ribbed vaults, whose lateral thrust was conducted directly to the piers, buttresses and flying arches, see Figure 1.2. Although the thickness of the walls was lower, the typical typology of Romanesque walls was maintained, as an association of two external and a middle leaf (Froidevaux, 1985). However, in opposition to the Romanesque walls, the available tools allowed to make the external leaves composed by stonework with large and extremely well cut ashlar stone units, leading to the reduction of the internal leaf. Therefore, the Gothic walls were almost practically executed of ashlar masonry with large openings.

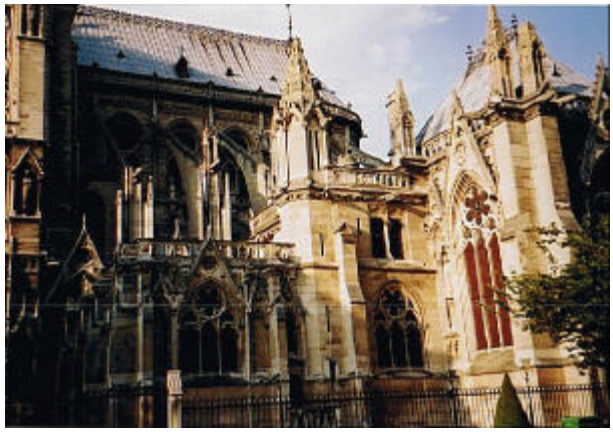

Figure 1.2 – Example of a Gothic cathedral; Notre-Dame de Paris

The Renaissance architecture develops from the empirical knowledge that architects gained about the structural stability of the buildings, partly acquired from the study of the Roman constructive systems. According to Mark (1995), the Renaissance architects knowledge about the stability of walls was considerable. As an example, they recommended the reduction of the wall thickness with height, providing a sufficiently wide base to prevent overturning. Besides, they recognized the need to select stone for external leaves based on its capacity to resist weathering and its strength, recommending that stone must be oriented with its bedding planes parallel to the ground in order to avoid splitting due to compressive loads. The Renaissance architecture represented a change to medieval construction system, being again highlighted the arched shapes already known, as the Byzantine domes and the semicircular arches. This movement started in Italy, where the Gothic architecture had a minor influence. The best example of the Renaissance architecture is the St. Peter's Basilica in Rome. In opposition to the Gothic walls, the Renaissance walls were built as replicas of the massive walls found in the Roman Empire. The Gothic ashlar masonry progressively gave place to the irregular masonry due to time constraints and economy of workmanship required by massive construction. In Italy, the stone masonry was often replaced by brick masonry due its low cost. Usually weak mortars were used and the structural elements were rendered with lime mortar, as a consequence of the rubble masonry bond.

After the Renaissance and during a period of almost three hundred years, based on the concern of saving material and space, the thickness of the walls was progressively decreased up to a minimum value that guarantees its stability. The walls were usually made of irregular masonry, not necessarily of stone, and there was a concern to increase the strength of the walls by selecting stones of regular dimensions and providing their leveling. The corners and openings were considered as particular points where a more regular masonry was needed.

In Portugal, the influence of the Roman Empire is noticed by Roman villages that appear as the result of excavations. In addition, some Roman stone bridges still subsist. The more characteristic Romanesque constructions are the churches and monasteries with small openings and the stone bridges. Although the Gothic architecture in Portugal does not reach the splendor of the Gothic architecture in France or England, there are several castles and cathedrals that are considered part of this architectonic movement (Dias, 1994). The stone was the most used material on masonry walls built up to the 20$^{th}$ century, whichever the architectonic movement. Figure 1.3 shows examples of the combination of stonework and rubble masonry, as well as the details of the critical points as corners and openings, where ashlars of large dimension are usually adopted.

Figure 1.3 – Examples of stone masonry with distinct bonds in Portugal

## 1.2 Objectives

Due to the scarce information on the mechanics of stone masonry structures, the present work aims at contributing to enlarge experimental data concerning its behavior under cyclic loadings. Being masonry a composite material, composed by units and mortar, its behavior necessarily depends on the mechanical properties of the components and on the masonry bond (arrangement of the stones). These aspects are considered using granitic stone from Portugal. In order to fully characterize the Portuguese granite, a comprehensive testing program was set-up using destructive and non-destructive testing. The latter is of much relevance, as the collection of samples from existing buildings is expensive and, often, not possible. Therefore, the three main objectives of the present experimental work are:

- Mechanical characterization of Portuguese granites under tension and compression with the aim of obtaining their complete behavior, enabling the determination of the elastic, strength and fracture properties.
- Evaluation of simple nondestructive tests, namely the ultrasonic pulse velocity and surface hardness, as potential tools for prediction of the mechanical properties.
- Analysis of the performance of masonry granitic shear walls under cyclic loading, using bonds representative of ancient structures.

The final goal of the present work is to provide useful information for the mechanics of existing stone masonry buildings, allowing the assessment of sophisticated nonlinear analysis models and the safety assessment of case studies. Moreover, the experience gathered on the mechanics of the masonry walls submitted to in-plane loading can be of great advantage in

the decision process related to the strengthening possibilities of ancient structures to face the seismic action.

## 1.3 Outline of the thesis

Besides this introductory chapter, the thesis is divided in six additional chapters and seven annexes.

Chapter 2 presents a comprehensive experimental program in order to evaluate the tensile behavior of granites by means of a set of direct tensile tests through a suitable displacement control. Variation of the tensile engineering properties based on textural aspects related to the internal structure associated to planar anisotropy (foliation and quarry planes), weathering state, moisture content and variation of the physical properties are analyzed. Besides providing ample data about the tensile behavior of granite, the experimental results enable the attainment of useful statistical correlations between strength and fracture properties. Furthermore, a detailed qualitative and quantitative analysis by means of an automated system of 3D topographical inspection of the fracture path is addressed in order to investigate the influence of roughness on the fracture energy. A complete overview of the stress-displacement diagrams is provided in Appendix A. Besides, aspects of the characterization of the roughness of the fracture surfaces are discussed in Appendix B and Appendix C.

Chapter 3 deals with the characterization of the compressive behavior of the granitic lithotypes, including the definition of the complete stress-strain diagrams by means of appropriate circumferential displacement feedback control. From the complete stress-strain diagrams, the elastic and fracture properties are obtained. The initiation and propagation of the microcracking stress levels and the Poisson's ratio are parameters used in the characterization the pre-peak fracture behavior. The different factors influencing the variation of tensile behavior of the distinct types of granite are also analyzed in compression. The dependence of the elastic and fracture compressive properties on the physical properties, as well as the relation between tensile and compressive parameters are investigated based on statistical correlations. A complete overview of the complete stress-strain diagrams is provided in Appendix D.

Chapter 4 addresses the possibility of predicting the mechanical properties of granite by simple and economical nondestructive techniques such as the ultrasonic pulse velocity (UPV) and the surface hardness measured by Schmidt hammer rebound number (N). For this purpose, results of measurements of the ultrasonic pulse velocity using distinct natural frequency of the transducers carried out on both tensile and compressive specimens are presented. Schmidt hammer rebound number is obtained in cubic specimens. The discussion of the factors that induce variations on the velocity measurements and on the rebound number is carried out. The information obtained from non-destructive techniques (NDT) and the mechanical and physical parameters obtained in Chapters 2 and 3 is combined in order to define statistical correlations that validate the usage of the selected NDT. Additional information of the experimental values of the ultrasonic pulse velocity and Schmidt hammer rebound number obtained in tensile and compressive specimens is given in Appendix E.

Chapter 5 presents the experimental characterization of the materials (granite and mortar) and masonry assemblages for use in the construction of masonry shear walls. Mechanical parameters of granite (compressive and tensile strength) and mortar (compressive strength)

are provided. The shear behavior of dry and mortared joints is characterized by means of monotonic shear tests, and the shear strength parameters of bed joints, friction coefficient and cohesion are obtained. Shear cyclic tests are also performed in dry masonry joints. The compressive strength of dry and irregular mortared masonry is obtained by means of uniaxial compressive tests conducted on masonry prisms. The influence of the joint material on the compressive behavior of masonry is discussed. Detailed information of the shear stress-shear displacement diagrams obtained in direct cyclic shear tests, as well as full information of the stress-strain diagrams obtained in masonry compressive specimens is presented in Appendix F.

In Chapter 6, experimental results of the cyclic tests conducted on twenty-four experimental masonry stone walls under combined vertical and horizontal loading are presented. Three distinct pre-compression levels and three distinct masonry bonds are considered (dry masonry walls, irregular mortared walls and rubble masonry walls). The experimental characterization focuses on the definition of the failure modes and on the force-lateral displacement hysteresis diagrams. Afterwards, the gathered experimental data is analyzed in the scope of seismic performance based on parameters of ductility and nonlinear deformation capacity represented by acceptable lateral drifts. Finally, the experimental lateral strength is assessed by simplified analytical models. Detailed information about the force-displacement histeresis diagrams are indicated in Appendix G.

Finally, in Chapter 7, an extended summary and the main conclusions that results from the present research are pointed out. Moreover, suggestions for future work are also given.

# 2. EXPERIMENTAL INVESTIGATION OF GRANITES UNDER UNIAXIAL TENSILE LOADING

## 2.1 Introduction

Although granitic rocks have been widely investigated in rock mechanics, there is a significant lack of information about the complete tensile fracture behavior. Rock failure in tension results from the propagation of one or more cracks and thus can be studied under the fracture mechanics domain.

The tensile behavior of granitic rocks, similarly to concrete and other quasi-brittle materials that have a disordered internal structure, can be well described by the cohesive crack model proposed initially by Hillerborg *et al.* (1976). Although with some limitations, the cohesive crack model has been widely used as the fundamental model that describes the nonlinear fracture mechanics of quasi-brittle materials, (Bažant, 2002, Carpinteri *et al.*, 1997, Carpinteri *et al.*, 2003, Elices *et al.*, 2002, Guinea, 1995). According to this model and due to cracking localization, which is a characteristic of fracture process of quasi-brittle materials, the tensile behavior is characterized by two constitutive laws associated to different zones of the material during the loading process, see Figure 2.1. The elastic-plastic stress-strain relationship of Figure 2.1a is valid until the peak load is reached. The stress-crack opening displacement relationship of Figure 2.1b describes the strain softening behavior at the fracture process zone, after peak. The cohesive stress-opening displacement diagram is characterized by the gradual decrease of stress from its maximum value to zero value, corresponding to the increase of the distance between the two lips of the crack from zero to the critical opening, $w_c$. The softening diagram assumes a fundamental role in the description of the fracture process and is characterized by the tensile strength, $f_t$, and the fracture energy, $G_f$, which is given by the area under the softening diagram, see Figure 2.1b.

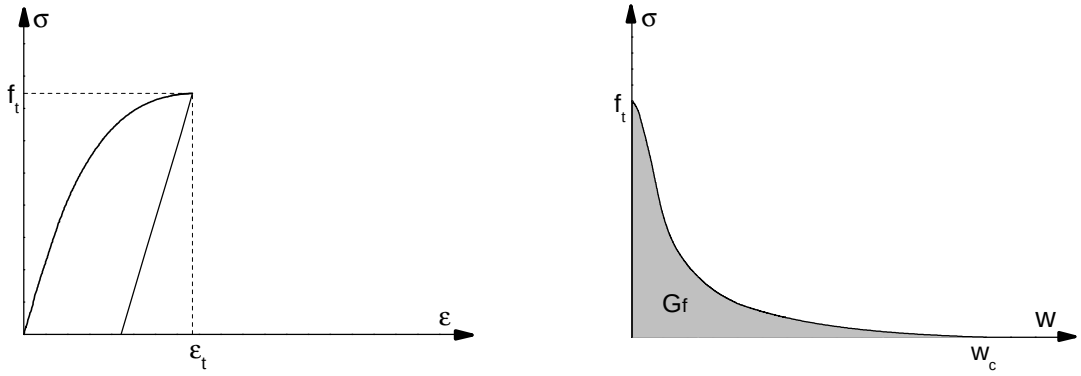


(a) (b)

Figure 2.1 – General cohesive model (Elices *et al.*, 2002); (a) elastic stress-strain diagram; (b) stress-crack opening displacement diagram

There are several experimental methods that have been used to measure the fracture properties (tensile strength, fracture energy and the critical crack opening) that allow the definition of constitutive laws of the material, namely direct tensile tests, and indirect tensile tests as the tree-point load test and the Brazilian splitting test. Although the tensile failure of structural rock elements results from a load combination and a multiplicity of factors, meaning that the direct tension is not the only cause of tensile cracking, direct tensile tests

seems to be the most appropriate test to characterize the basic failure mechanism (mode I) of quasi-brittle materials. This test is defined by Van Mier and Van Vliet (2002) as the reference method to follow. Therefore, direct tensile tests are the experimental method adopted in this work for the characterization of the tensile behavior of granites. The main reason of finding scarce or even no results from direct tensile tests on rocks in the literature can be attributed to the difficulties that are involved in the execution of this type of tests, having indirect tests been usually preferred.

Concerning direct tensile tests, different issues related to the specimens and the test procedures have been discussed in the past. In particular, the attachment of the specimens to the steel platens, and the alignment of the specimen in order to avoid secondary flexure are key aspects. Besides, the testing equipment, the control method and the location of the LVDTs are other factors that have to be taken into account when stable softening behavior of quasi-brittle materials, like rock granites, is required, (Van Mier and Van Vliet, 2002; Van Mier and Shi, 2002; Meda, 2003). In order to reach reliable experimental results, another relevant issue is the need of obtaining representative volumes of material. Although the tensile strength and fracture energy are considered intrinsic properties of the material, it is well known that fracture properties are size and scale dependent. Experimental direct tensile tests conducted in dog-bone shaped specimens performed by Carpinteri and Ferro (1994), in a scale range 1:16, and more recently by Van Vliet and Van Mier (2000) in a scale range 1:36, revealed that tensile strength increases with specimen size whereas fracture energy presents higher values for larger structures.

Apart from size effects induced by structural effects, like boundary conditions, and by the shape of the specimens that can lead to stress and strain gradients (Van Vliet and Van Mier, 1999), the variation on the fracture properties can be explained by the heterogeneity of the material. Size effect models such as size effect law (SEL) proposed by Bazant (1984) and in the last decade the multifractal scaling law (MFSL) introduced by Carpinteri and Ferro (1994), Carpinteri *et al.* (1995), Carpinteri *et al.* (2002), were developed so that the experimental results can be extrapolated to real structures.

In short, the challenge of obtaining mode I fracture properties by direct tensile tests consists of reducing the structural effects and of obtaining parameters exclusively determined by the material microstructure features. Despite the difficulties identified for direct tensile tests, it should be noted that serious limitations are also present in indirect tensile tests.

The present work represents a step forward in the knowledge about the tensile fracture behavior of the distinct granitic rocks. The accomplishment of this goal is based on the experimental study of the complete tensile behavior through the execution of a set of direct tensile tests, from which it is possible to determine the tensile fracture parameters. Before presenting the tensile mechanical characterization, a brief description of the different types of granite is presented. Besides, the physical characterization with the determination of density and porosity is also pointed out. The selection of different types of granitic rocks allows that microstructural aspects can be analyzed. Textural aspects related to planar anisotropy (preferential alignment of minerals, orientation of the quarry planes) are taken into consideration. In spite of the absence of an extensive petrographic characterization of the granites, the influence of the mineral composition and the grain size of minerals based on a simplified petrographical characterization is carried out. Other aspects that can explain the variation of the tensile engineering properties, such as the weathering state or moisture

content, as well as the variation of the physical properties, are also considered. Finally, more detailed qualitative and quantitative analysis of the fracture path is addressed in order to evaluate the surfaces roughness influence on the fracture energy values. In order to achieve this goal, the inspection of the fracture surfaces of the specimens is performed by means of an automated system of 3D topographical inspection.

## 2.2 Brief description of the material used in the experimental program

Granite is the most used stone in the construction of ancient buildings located in the North of Portugal, either in monumental or vernacular architecture. A wide range of granitic rocks is present in masonry constructions, depending on their petrographic features, such as grain size and internal structure. Therefore, the mechanical characterization of only one type of granite would be rather limitative. In addition, the weathering processes, to which granites are subjected through years, lead to changes on the mechanical properties that require characterization. The granites adopted in the present work were mostly collected from the Northern region of Portugal. The location of the quarries and the designation of the corresponding granite are shown in Figure 2.2.

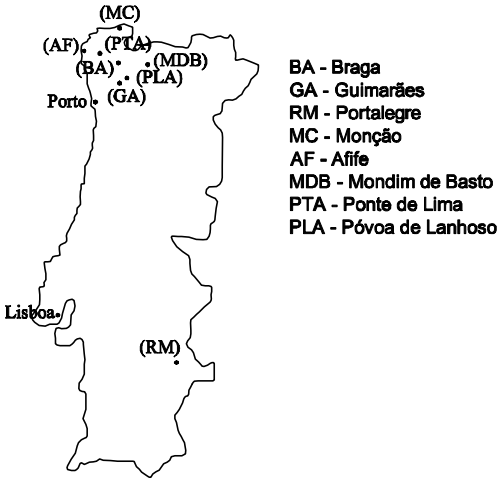


Figure 2.2 – Localization of the quarries and designation of the granites

The selection of the granitic types was based on the mineralogical composition and grain size, aiming at providing a comprehensive sample of the Portuguese granites. In addition to these criteria, the presence of preferential orientation planes and weathering condition were also taken into account. In fact, the natural orientation planes of granitic rocks or preferred orientation of minerals (foliation) can be relevant for further analysis of the variation of the mechanical properties (Prikryl, 2001). Three orthogonal planes can be identified with rock splitting planes (quarry planes) defined as planes of preferred rupture. The rift plane is the plane corresponding to the easiest splitting in the quarry being easily recognized by the quarryman since it is further associated to the plane of easiest finishing.

A brief description of the adopted different lithotypes is indicated in Table 2.1. The more weathered types of the same granite facies are distinguished with an asterisk (*). Additionally, the loading directions considered in the experimental program are also indicated. The orientation of the rift plane was marked with the help of a quarryman and, when visible in the macroscopic scale, the foliation plane, defined from the preferential orientation of the grains, was also marked. In case of the granite is assumed homogeneous

(random orientation of minerals), only the direction parallel to the rift plane was considered (granites BA, GA, GA*, RM, MC). If the granite presented visible foliation, the perpendicular and parallel directions to the foliation plane were considered (AF, MDB, MDBD*, PTA). In granites PLA and PLA*, the preferred orientation of feldspar phenocrystals (flow structure) is subparallel to the rift plane and, consequently, two loading directions (parallel and perpendicular to the rift plane) were considered. As the more weathered granite PTA* does not show clear visible foliation, directions parallel and perpendicular to the rift plane were considered.

Table 2.1 – Brief description of the selected granites and directions considered in the mechanical tests

| Granite designation | Petrologic description | Loading directions |
|---|---|---|
| BA | Fine to medium-grained porphyritic biotite granite | Parallel to the rift plane |
| GA, GA* | Fine to medium-grained, with porphyritic trend, two mica granite | Parallel to the rift plane |
| RM | Medium-grained biotite granite | Parallel to the rift plane |
| MC | Coarse-grained porphyritic biotite granite | Parallel to the rift plane |
| AF | Fine to medium-grained two mica granite | Parallel and perpendicular to the foliation plane |
| MDB, MDB* | Fine to medium-grained two mica granite | Parallel and perpendicular to the foliation plane |
| PTA, PTA* | Fine to medium-grained two mica granite | Parallel and perpendicular to the foliation/rift plane |
| PLA, PLA* | Medium to coarse-grained porphyritic biotite granite | Parallel and perpendicular to the rift plane |

Although a detailed microscopic analysis of the granites (modal mineralogical composition, internal structures, microcracks and microdefects) was not carried out, some particular features may be highlighted through observations with polarizing stereoscopic microscope and with the polarizing microscope (5X objective) of thin sections. The difference of the grain size among distinct types of granite is displayed in Figure 2.3 and Figure 2.4. As can be observed, granite BA and GA have the smallest grain size, whereas granite MC exhibits the largest grain size, followed by the granite PLA.

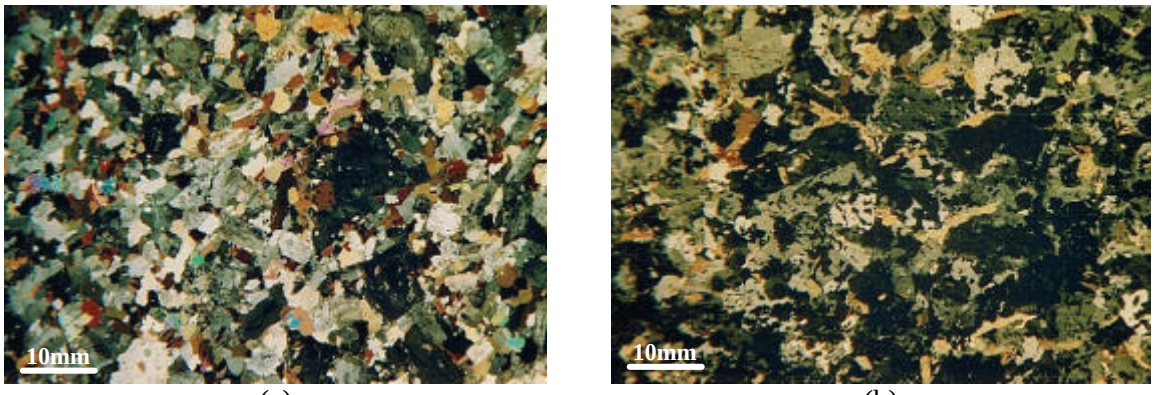


(a) (b)

Figure 2.3 – Comparison of the grain size among distinct types of granite - polarizing stereoscopic microscope (crossed polarizers); (a) granite BA; (b) granite GA

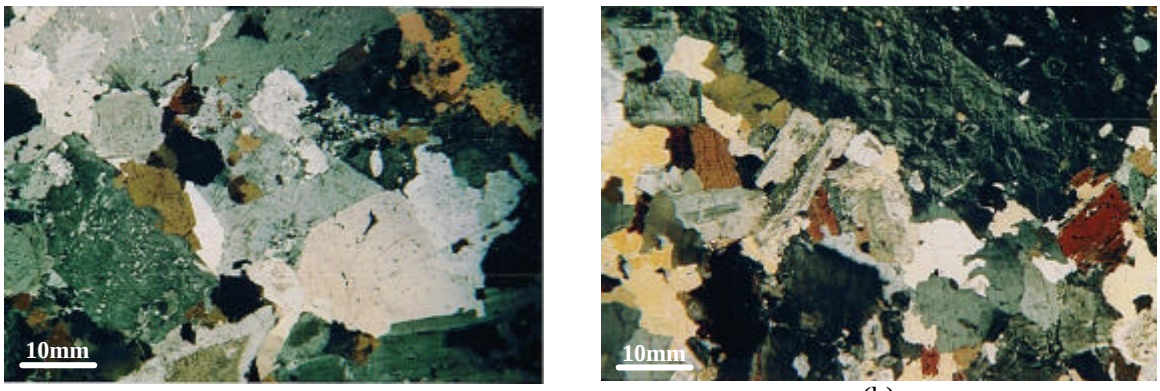


(a) (b)

Figure 2.4 – Comparison of the grain size among distinct types of granite - polarizing stereoscopic microscope (crossed polarizers); (a) granite MC; (b) granite PLA

As referred, the evaluation of the existence of a preferential alignment of the minerals was evaluated at the macroscopic level. The alignment of the muscovite sections (MU) in granite AF is also shown in Figure 2.5 from observation with polarizing stereoscopic microscope (crossed polarizers) in granite AF.

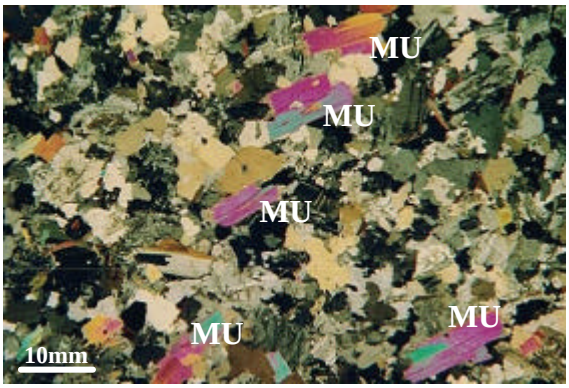


Figure 2.5 – Preferential alignment of muscovite sections in granite AF (polarizing stereoscopic microscope (crossed polarizers). MU: muscovite

With respect to granite PLA, pre-existing almost parallel microcracking was detected in the thin sections perpendicular to the rift plane, as can be seen in Figure 2.6a (no relevant microcracking was observed in the thin sections parallel to the rift plane). This feature differentiates this type of granite in relation to the other granites. Figure 2.6b shows transgranular microcracking crossing plagioclase (PL) and quartz (QZ) sections in granite PLA (thin section perpendicular to the rift plane).

The weathered state of granite MDB* that is clearly visible macroscopically, either through the alteration of the original color and rough surface, is showed clearly in Figure 2.7, where observations with the polarizing microscope are displayed. Figure 2.7a shows the intense weathering of a plagioclase section. Figure 2.7b presents intergranular microcracks between quartz sections and between quartz and plagioclase sections filled with supergenic iron compounds.

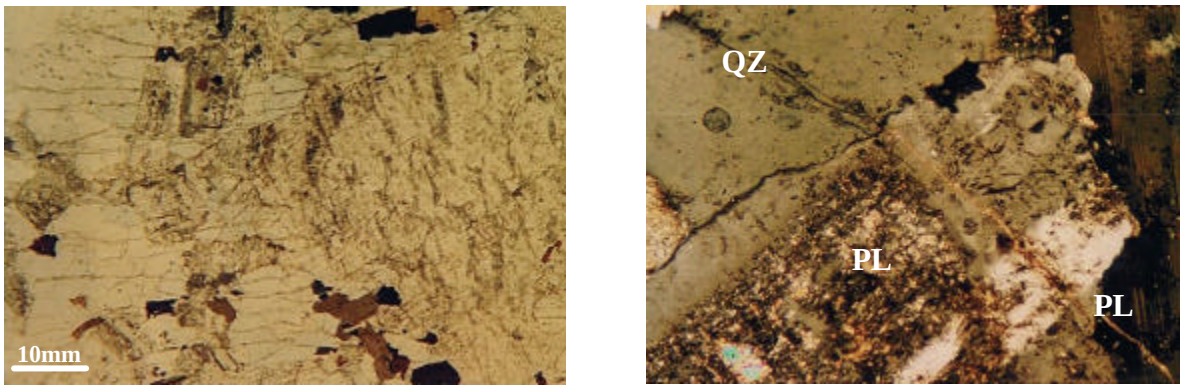


(a) (b)

Figure 2.6 – Observation of existing microcracking in granite PLA in a thin section perpendicular to the rift plane; (a) polarizing stereoscopic microscope (parallel polarizers); (b) polarizing microscope (5X objective, crossed polarizers). QZ: quartz; PL: plagioclase

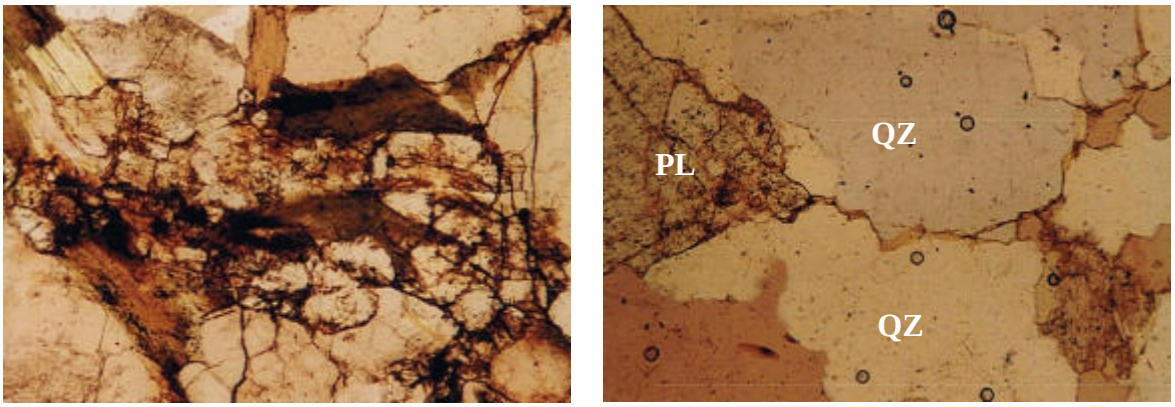


(a) (b)

Figure 2.7 – Observation through polarizing microscope (5X objective, parallel polarizers) of the granite MDB*; (a) intense weathering of a plagioclase section; (b) intergranular microcrack between quartz(QZ)-quartz and quartz-plagioclase(PL) sections

## 2.3 Brief physical characterization of the granites

The knowledge of the physical properties of rocks like porosity and density allows a better understanding of the variations on the mechanical properties of rocks. According to ISRM suggested methods (1981a), physical characterization can give additional information about the mechanical properties.

The physical properties of the granites, including porosity, saturated density and dry density, were determined in accordance with the procedures given in ISRM suggested methods (1981a). In order to use representative samples of rock masses and taking into account the average dimension of the grains, cubic specimens of size approximately 15x15x15cm3 were used in the porosity test. Additionally, the porosity tests were repeated to all specimens tested under tension. The samples were saturated by water immersion in a vacuum of less than 800Pa for a period of two hours and its saturated-surface-dry mass $M_{sat}$ is determined. The grain mass, $M_s$, is defined as the equilibrium mass of the sample after oven drying at a temperature of 105ºC. The volume of the specimen, $V$, is calculated by the Archimedes principle as:

$$V = \frac{M_{sat} - M_{sub}}{r_w} \tag{2.1}$$

where $M_{sub}$ is the saturated-submerged mass and $r_w$ the water density. The pore volume, $V_v$, is calculated as:

$$V_v = \frac{M_{sat} - M_s}{r_w} \tag{2.2}$$

The values of porosity, $n$, dry density, $r_d$, and saturated density, $r_{sat}$, were obtained as follows:

$$n = \frac{V_v}{V} \times 100 \tag{2.3}$$

$$r_d = \frac{M_s}{V} \tag{2.4}$$

$$r_{sat} = \frac{M_s + V_v r_w}{V} \tag{2.5}$$

where $V$ is the total volume of the material. The average values of the porosity, dry density and bulk density obtained in the reference cubic specimens, as well as the corresponding coefficients of variation are shown in Table 2.2.

Table 2.2 – Average values of the mechanical properties for all granites. Coefficient of variation is inside brackets (%)

| Granite | Porosity (%) | Dry density (kg/m$^3$) | Saturated density (kg/m$^3$) |
|---|---|---|---|
| BA | 0.51 (12.9) | 2560.9 (0.08) | 2606.2 (0.07) |
| GA | 0.47 (6.1) | 2660.1 (0.030) | 2664.7 (0.027) |
| GA* | 3.56 (2.6) | 2578.9 (0.068) | 2614.3 (0.037) |
| RM | 0.74 (9.6) | 2625.7 (0.14) | 2633.7 (0.11) |
| MC | 0.87 (4.3) | 2642.4 (0.07) | 2651.1 (0.07) |
| AF | 3.16 (3.2) | 2567.7 (0.16) | 2598.4 (0.14) |
| MDB | 5.06 (7.5) | 2524.2 (0.35) | 2574.9 (0.21) |
| MDB* | 7.24 (3.4) | 2466.4 (0.12) | 2538.8 (0.061) |
| PTA | 1.17 (2.8) | 2652.4 (0.12) | 2664.1 (0.055) |
| PTA* | 5.02 (7.6) | 2546.0 (0.24) | 2597.9 (0.29) |
| PLA | 0.84 (5.8) | 2662.8 (0.18) | 2671.2 (0.19) |
| PLA* | 1.55 (7.7) | 2645.6 (0.27) | 2661.1 (0.24) |

In general, fresh granites or less weathered granites (BA, GA, RM, MC, PTA, PLA), exhibit low values of porosity, being lower than 1.2%. The weathered granites present considerable higher values. Note the high porosity values of the weathered granites MDB* (7.24%) and PTA* (5.02%), which is denoted macroscopically by the changing of the color and the rough surface. Although granite MDB is considered a less weathered granite because of its white color, the value of porosity is remarkable high (5.06%). According to Goodman (1989), the porosity of igneous rocks tends to increase up to 20% or more as the weathering degree increases. It is still observed that the density of the granites decreases as the porosity

increases. The values of the porosity present some scatter, in opposite to density whose average values have associated remarkable low coefficient of variation.

## 2.4 Geometry, shape of specimens, equipment and test procedure

As addressed above, the testing equipment is absolutely essential when softening stable behavior is required, and the tests must be carried out in closed-loop control. As the main goal of this work is the characterization of the fracture behavior, which requires complete stress-displacement diagrams of the granites, the direct tensile tests were performed by using a CS7400S servo-controlled universal testing machine with fixed end platens, see Figure 2.8a. This equipment has a load cell connected to the vertical actuator with a maximum capacity of 22 kN, being particularly fit for small specimens.

It is well known that the shape of the softening branch depends on the boundary conditions and consequently the fracture energy values can be affected, see Figure 2.8b. In case of pin-ended boundary conditions, the specimens are free to rotate when the onset of the macrocrack takes place and no additional restraint is introduced. In case of fixed end platens, the eccentricity originated by the crack opening has to be balanced by the introduction of bending moments that contributes to the generation of multiple cracks. This behavior influences to certain extent the softening behavior, where a horizontal plateau is possible to occur when a second macrocrack opens. The higher cracking density found in case of fixed boundary conditions leads generally to larger values of fracture energy relatively to the ones achieved in uniaxial tension tests conducted using pin-ended platens (Van Vliet, 2000; Van Mier *et al.*,1996). Despite the effects just described, it is stressed that all experiments in different types of granites regarding the present testing program were performed under the same boundary conditions, which allows further comparative analysis of the results obtained.

The size of the specimens was defined taking into consideration the restrictions of the testing equipment and the limitations for manufacturing the stone specimens. Due to the maximum distance between the platens, prismatic specimens of 80mm height, 50mm length and 40mm width were considered (Ramos, 2001). Such dimensions are less favorable in case of coarse-grained granites and of granites with porphyritic texture, since larger representative material volume would be required.

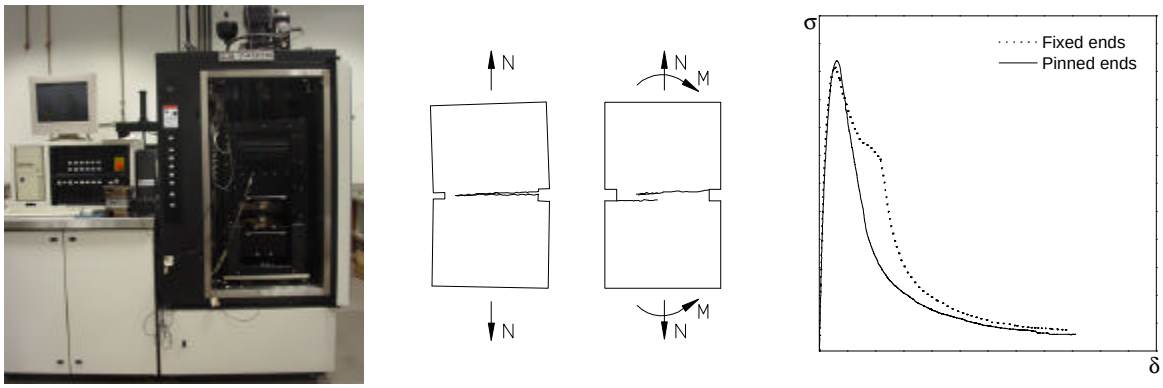


(a) (b) (c)

Figure 2.8 – Influence of boundary conditions; (a) Servo-controlled universal testing machine; (b) pin-ended vs. clamped boundary (c) effect on the softening shape, Van Vliet (2002)

The microstructure of rock materials, which exhibits variations in the grain sizes, grain shapes and interface properties, and possible preexistent microcracks and flaws, represent the main cause of the size and scale effects (Van Mier and Van Vliet, 2002; Van Mier and Van Vliet, 2003; Hudson, 1998). The ISRM (1981b) recommendations indicate that, for cylindrical specimens in direct tension, the height to diameter ratio should be between 2.5 and 3.0 and the diameter should be related to the size of the maximum grain in rock by a ratio of, at least, 10:1. If for granite specimens with fine to medium grain size the latter condition is followed here, for specimens with coarse grains the adopted dimensions for the specimens are insufficient. To overcome this limitation, a higher number of specimens were tested, so that the effect of the scatter in the results are reduced and the average values are representative of the macroscopic properties, especially in the case of granites PLA and PLA*.

The adoption of a constant cross section for the specimens leads to uncertainty about the localization of the microcraks, which represents the usual supplementary difficulty for the control method of this type of tests. Since the control system allows only one Linear Variable Displacement Transducer (LVDT) as displacement control, it was decided to introduce, by means a diamond sawing machine, two lateral notches with a depth of 5mm at mid height of the specimen in order to localize the fracture surface, see Figure 2.9a.

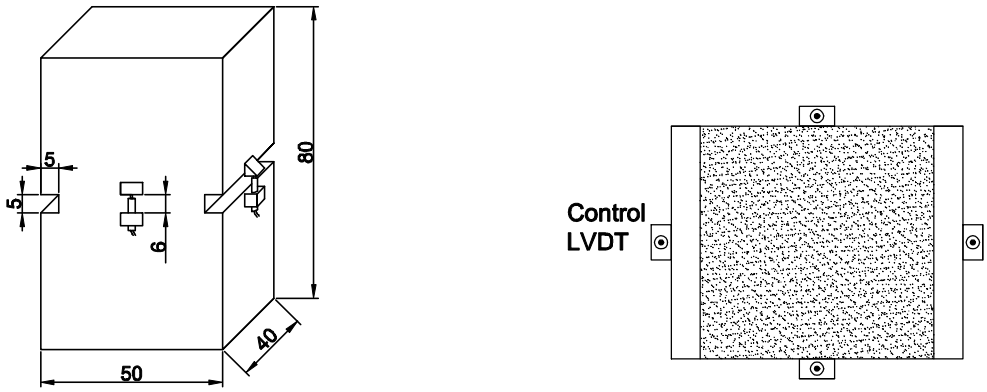


(a) (b)

Figure 2.9 – Geometry of the specimens; (a) dimensions of the specimens and location of the LVDTs; (b) definition of the control LVDT

Notched specimens allow a suitable displacement control of the test through one of the four LVDTs located in the sides. Besides providing easy control of deformation, absolutely necessary to obtain stable softening failures, the notches have other advantage (Akita *et al.*, 2003): elimination of multiple cracking and corresponding localization of the macrocrack. The use of this simple shape specimen allows straightforward observation and instrumentation of the macrocrack, which is a key issue when limited reading channels are available. However, some limitations are associated with notched specimens, namely, the localization of the fracture zone is not compatible with the weakest zone of the material (Wittman *et al.*, 1994), and the stress and deformation distribution is no longer uniform, with important stress and strain gradients occurring near the notch tips (Van Vliet and Van Mier, 1999). These limitations influence the ultimate load and induce additional structural size effects.The disposition adopted for the LVDTs, shown in Figure 2.9b, allows capturing the three-dimensional effects associated to the fracture process in direct tension. The improvement of the controlled cracking propagation during fracture process is made by fixing the minimum distance measured by the LVDTs to about 6mm, see Figure 2.9a. This

procedure leads to the minimization of the elastic energy within the measuring length of the control LVDT, and, therefore, prevents any possible snap-back behavior (Van Mier and Van Vliet, 2002; Vonk, 1993).

After preparation of the specimen ends, glue conditions were enhanced by making a series of superficial slots with a sawing machine, see Figure 2.10a. Then, the specimens were carefully fixed to the steel platens through the application of an epoxy resin (DEVCOM), in such a way that eccentricities were minimized. The complete testing setup is shown in Figure 2.10b

(a) (b)

Figure 2.10 – Materials and equipment; (a) final shape of the specimens after preparation; (b) attachment of the specimen to the steel platens

A set of preliminary tests was carried out to assess a suitable control test velocity to obtain the softening branch of the material and to prevent abrupt failures. Due to the brittle behavior of granite, direct tensile tests had to be conducted using low values of velocity, which varied between 0.08μm/s and 0.5μm/s, according to brittleness of the material. The deformation history is composed by a single ramp with constant rate, meaning that the duration of each test ranged from 15 to 30 minutes.

Most quasi-brittle materials, including granites, are weakened by the addition of water. According to the ASTM D2936 (1995) and ISRM (1981b) suggested methods, the moisture content of the material should be recorded and it is advisable to perform the tests in dry and saturated (100% humidity) conditions. In this work, due to difficulties of gluing saturated specimens, only MDB* granite was tested under saturated conditions for assessing the influence of moisture conditions. All other specimens were tested in oven dry conditions.

## 2.5 Experimental results

The complete stress-displacement diagram that characterizes the tensile behavior of all tests is the result of the average displacement measured by the four LVDTs placed in the sides of the specimen. The normal stress is calculated as the ratio between the applied vertical load and the initial cross section measured in the notched zone. For fresh stiff granites, such as granites BA, GA and PLA, a few abrupt failures have occurred immediately after the peak load. In this case, there was no possibility of obtaining the stable fracture process and only the properties that define the pre-peak behavior could be determined. Table 2.3 shows the success rate of experiments for all tests, which is rather high. Some tests were not successful due to failures that occurred outside the notched zone, mainly in granites MC, PLA, PLA* and GA*.

Table 2.3 – Number of samples and successful tests for all granite types

| Granite | Samples | Successful | Granite | Samples | Successful |
|---|---|---|---|---|---|
| BA | 15 | 9 | MDB* // foliation | 17 | 14 |
| GA | 20 | 17 | PTA ⊥ foliation | 16 | 15 |
| GA* | 18 | 14 | PTA // foliation | 15 | 15 |
| RM | 15 | 15 | PTA* ⊥ rift plan | 18 | 18 |
| MC | 19 | 15 | PTA* // rift plan | 14 | 14 |
| AF ⊥ foliation | 15 | 15 | PLA ⊥ rift plan | 18 | 15 |
| AF // foliation | 17 | 17 | PLA // rift plan | 16 | 14 |
| MDB ⊥ foliation | 16 | 15 | PLA* ⊥ rift plan | 16 | 14 |
| MDB // foliation | 16 | 16 | PLA* // rift plan | 19 | 16 |
| MDB* ⊥ foliation | 16 | 16 | | | |

### 2.5.1 *Characterization of the macrocracking process*

The general shape of the complete stress-displacement diagrams is essentially composed by four stages. The linear stretch is associated with the linear behavior of the material, whereas the stable microcracking process is reflected by a nonlinear stretch before the peak stress is reached. After this point, macrocracking propagation is established and increasing of the crack opening can be observed with naked eye. This macroscopic fracture process is associated with the steep negative stretch in the softening branch, with a slope that depends essentially on the type of granite. Finally, a stress-transfer mechanism, due the bridging effect, is responsible for the long tail of the softening branch, see Figure 2.11.

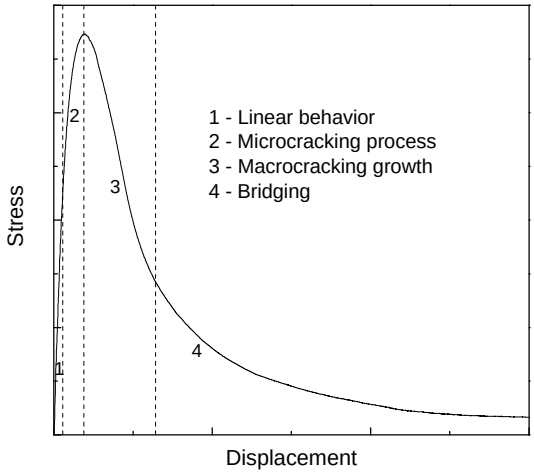


Figure 2.11 – Evolution of the fracture process in a typical stress-displacement diagram

The tensile fracture is also a process inherently three-dimensional. This fact is confirmed by the different values obtained from the four LVDTs placed in the specimen, as given in Figure 2.12-2.14. There are mainly three distinct stages that can be identified in the diagram of displacements versus time, as it is shown in Figure 2.12b. Until the peak load is reached, and during the process of stable microcracking, although with different values, the evolution of the displacements is linear. After the onset of macrocracking and localization of the tensile fracture surface, a nonlinear evolution with sudden increase of the displacements is found. Figure 2.12-2.14 shows three typical evolutions of measured displacements corresponding to macrocrack opening, which seems to be a function of the material characteristics. Stiff materials have usually associated either differential deformations measured by the LVDTs

located at the opposite unnotched sides of the specimen or a very sudden increase of the deformations at the localization of the macrocrack. For Figure 2.12a, LVDT 1 records negative displacements (side is in compression due to notch closure) at the same time that LVDT2, placed in the opposite side, is in tension.

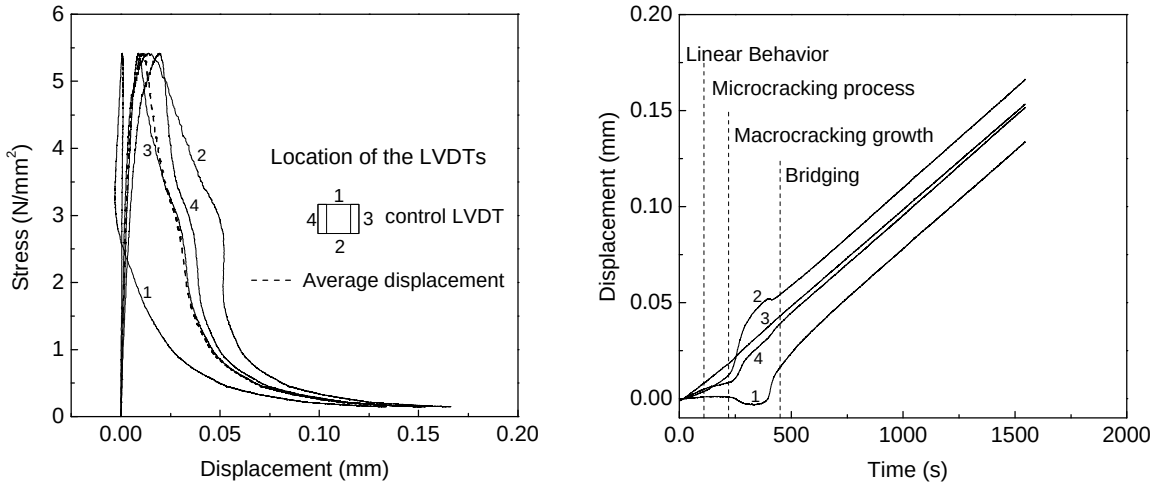


(a) (b)

Figure 2.12 – Typical evolution of measured displacements placed in the fracture zone for granite GA; (a) displacement measured at each LVDT vs. stress; (b) evolution of the displacements measured at the LVDTs with time

The waggling effect exhibited by the displacements plotted separately can be caused by the fixed loading platens, see alsoVan Mier *et al.* (1996). The sudden increase in displacements that is observed in some specimens, see Figure 2.13b, seems to be related to the swift breaking of the connections in the material reflected by the abrupt decrease of the load bearing capacity of the specimen.

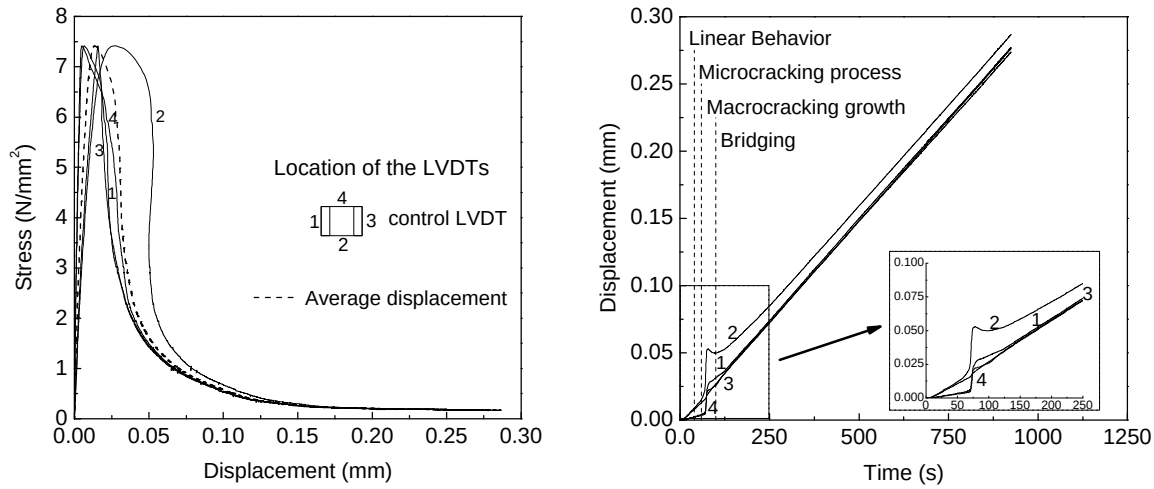


(a) (b)

Figure 2.13 – Typical evolution of measured displacements placed in the fracture zone for granite PLA in the direction parallel to the rift plane; (a) displacement measured at each LVDT vs. stress; (b) evolution of the displacements measured at the LVDTs with time

This also means that the onset of the macrocrack comes from different sides of the specimen, and not only from the ones with notches, which confirms the three-dimensional process

associated to the tensile fracture. It should be underlined that this behavior is characteristic of the fresh granites BA, GA, PLA, PTA, MC and RM.

The characteristic macrocracking growth on granites like GA*, MDB, MDB*, PTA*, is also marked by nonlinear evolution of the deformations but in a clear distinct process. In fact, from Figure 2.14, it can be observed that the increase in displacements measured by the different LVDTs is much smoother, which suggests that the failure of the connections between the matrix and the minerals and between mineral interfaces is more ductile.

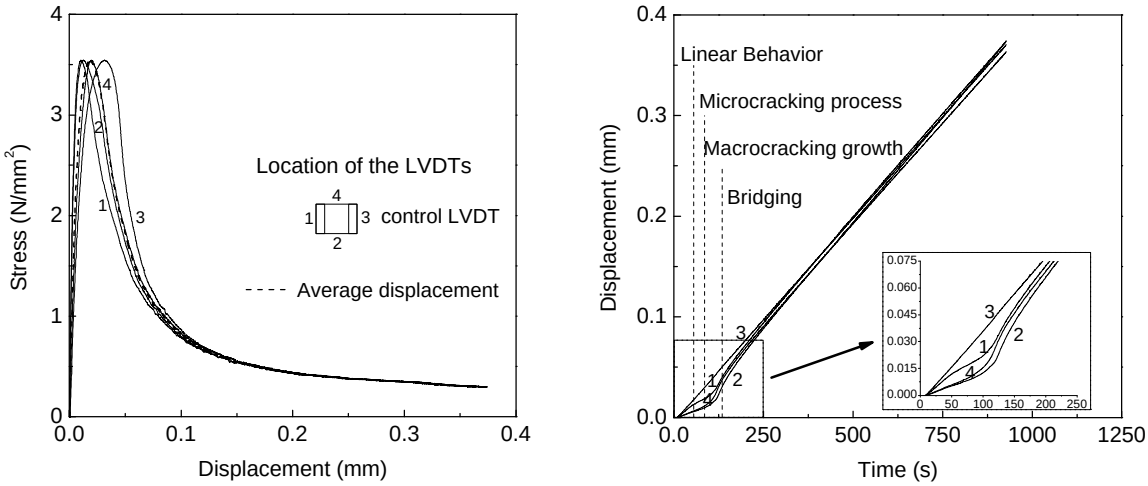


Figure 2.14 – Typical evolution of measured displacements placed in the fracture zone for granite GA*; (a) displacement measured at each LVDT vs. stress; (b) evolution of the displacements measured at the LVDTs with time

In the different cases addressed above, after localization of the macrocrack, the descending branch is determined by bridging stresses corresponding to the stress transfer between the two lips of the crack and with a shape essentially related to the microstructure of the granites. At this stage, the increasing of the macrocrack opening is approximately uniform. This fact is confirmed by the linear growth of all displacements at the same rate, and equal to the displacement defined for the control LVDT.

Finally, it is important to stress that despite the fixed loading platens used in all the experiments, distinct behavior was identified for the granites and, consequently, the different shapes of the stress-displacement diagrams should be analyzed and related to the different material properties.

### 2.5.2 *Complete stress-displacement diagrams and mechanical properties*

The distinct tensile behavior of granites can be easily identified by the different shape of the complete stress-displacement diagrams. The slope of the initial stretch, the slope of the softening branch and the length of the tail of the complete diagrams are some aspects that should be taken into consideration when a comparative analysis of the different granite lithotypes behavior is carried out. An elucidative example is shown in Figure 2.15. By comparing the complete diagrams obtained for the granites BA and AF, it can be observed that granite BA exhibits higher initial stiffness, a steeper softening branch and lower length of the bridging tail. Therefore, large difference in the elastic and fracture properties should be expected for both granites.

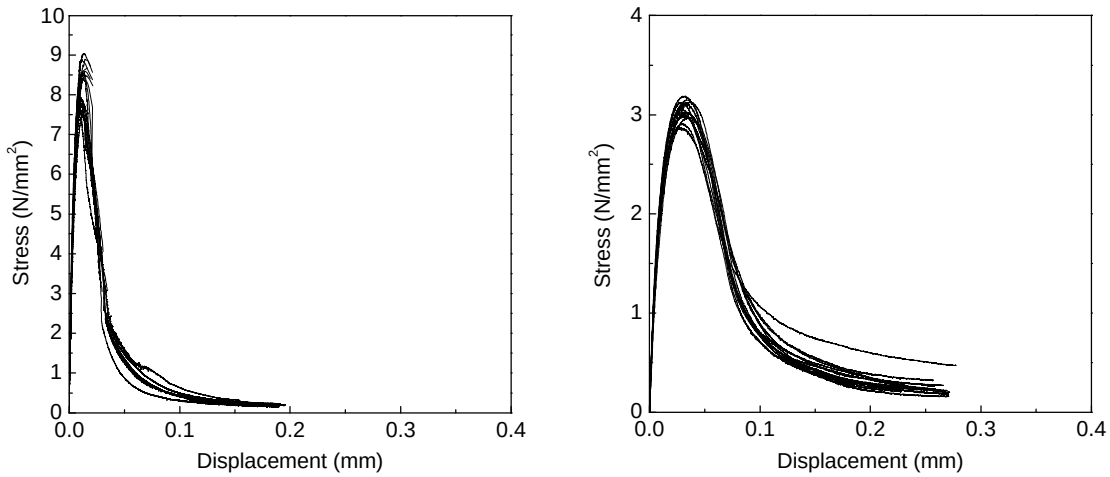


Figure 2.15 – Complete stress-displacement diagrams: (a) granite BA; (b) granite AF in the direction parallel to the foliation plane

The pre-peak behavior is quantitatively characterized by means of the value of initial stiffness, $k_0$, the displacement at the peak strength, $d_{ft}$, and the nonlinear deformation until the ultimate load, $d_{nl}$, see Figure 2.16a. The initial stiffness is calculated as the slope of the linear adjustment to the stress-strain relationship, since zero value up to around 20% of the peak stress, by means of the least-square method. These values have to be considered carefully and are merely qualitative. If on one hand, the rectangular notches lead to important stress gradients that change the stress distribution along the measured zone (Van Pluijm, 1999), on the other hand, the measuring length is small comparatively to the total height of the specimens. The latter limitation is essentially related to the heterogeneity of the material. Therefore, the obtained values are only of use for comparative analysis. For information about the elastic properties of the granites the reader is referred to Chapter 3. The nonlinear deformation until peak load, $d_{nl}$, is calculated as the difference between the mean value of the displacement recorded by the LVDTs and the linear displacement, see Figure 2.16a. The linear displacement is calculated from the initial stiffness according to the expression:

$$d_e = \frac{s\,A}{k_0}, \tag{2.6}$$

where $s$ and $A$ represent respectively the stress and the area of the cross section of the notched specimen.

The fracture properties, the tensile strength $f_t$, the fracture energy $G_f$, and the critical crack opening, $w_c$, are used in order to characterize the softening diagram. The fracture energy is identified with the work that is carried out for complete separation of the two faces of the macrocrack, per unit of area. For the calculation of the fracture energy, the procedure suggested by Van Vliet (2000) is adopted, see Figure 2.16b. The average stress-crack opening diagram is obtained after correction of the elastic energy correspondent to the pre-peak behavior. It is not possible to determine the exact crack opening for which the stress value transferred becomes zero, due to long tail exhibited by the softening branch of the stress-opening crack. Therefore, the value of the fracture energy is calculated as the result of the sum of two quantities, being one quantity measured and the other quantity estimated. The measured value of fracture energy, $G_{f,meas}$, is directly computed as the area under the stress-

crack opening diagram up to 0.15 of the peak strength. The estimated value, $G_{f,est}$, is calculated as the area under the linear curve obtained by linear adjustment of the original diagram below $0.15f_t$, through the least-square method. This procedure allows not only the calculation of the fracture energy but also the critical crack opening, $w_c$, which constitutes another fundamental property of the softening diagram.

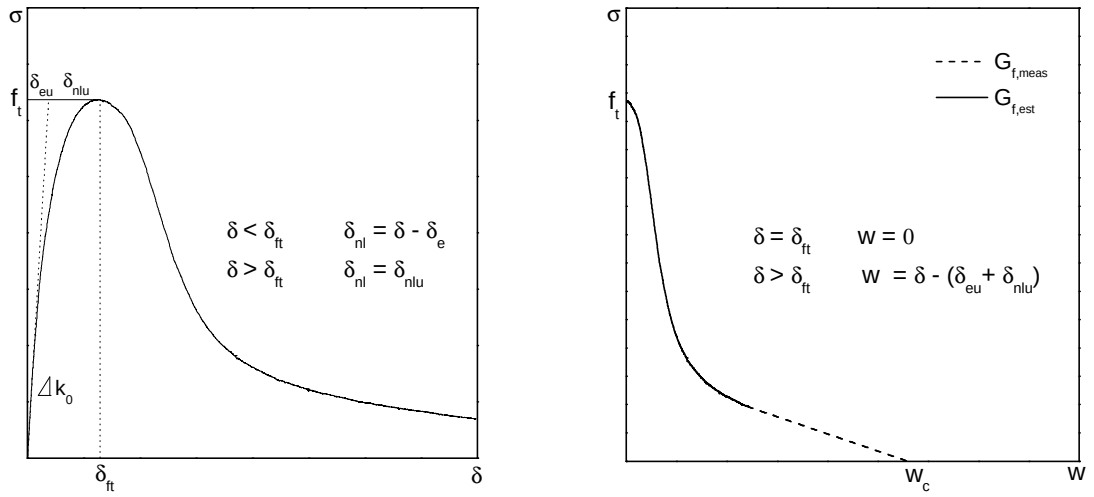


Figure 2.16 – Computing the pre and post-peak properties; (a) definition of initial stiffness, $k_0$, displacement at peak load, $d_{ft}$, and nonlinear deformation until peak load, $d_{nl}$; (b) procedure to calculate the fracture energy, $G_f$, (Van Vliet, 2000)

A general overview of parameters that characterize the complete behavior of the granites and the correspondent coefficient of variation (inside brackets) is shown in Table 2.4. These values are the result of averaging the parameters concerning all diagrams for each type of granite. Full details of the experimental results are given in Appendix A.

The granites exhibit large range of variation for the linear and fracture parameters as a result of different characteristic shapes of the complete stress-displacement diagrams. The statistical analysis indicates moderate values of the coefficient of variation (CV) for the tensile strength. Higher values of the coefficient of variation are associated with the fracture parameters, fracture energy and critical crack opening. This scatter can be visualized, to certain extent, by the set of softening diagrams correspondent to each type of granite, see Figure 2.17. The shaded area represents the interval of variation for the stress between the lower and upper envelops defined from the set of stress-displacement diagrams. The gray band is narrow in the pre-peak regime and is considerable enlarged in the softening portion of the diagrams. This means that higher scatter may be expected for the properties that characterize the post-peak behavior. Table 2.4 shows also that the magnitude of the coefficient of variation for the initial stiffness is also lower than the values regarding the critical crack opening. From its definition, the higher values obtained for the coefficient of variation related to the fracture energy can be seen as the result of the scatter associated to the tensile strength and the critical opening.

In spite of the moderate specimen size for the coarse grained granites PLA, PLA* and MC, the comparative analysis with the other granites, in terms of the coefficient of variation referring to the fracture properties, reveals that no significant increase in scattering was found for this type of granites. Therefore, this result validates the values of the fracture parameters obtained for the medium to coarse-grained granites.

Table 2.4 – Average values of the mechanical properties for all granites. Coefficient of variation is inside brackets (%)

| Granite | $k_0$ (N/mm$^2$) | $d_{ft}$ (mm) | $f_t$ (N/mm$^2$) | $G_f$ (N/mm) | $w_c$ (mm) |
|---|---|---|---|---|---|
| BA | 13413 (10.4) | 0.0123 (16.1) | 8.08 (11.4) | 0.181 (14.4) | 0.087 (27.8) |
| GA | 12550 (8.8) | 0.0110 (19.5) | 6.01 (11.1) | 0.148 (17.7) | 0.097 (28.2) |
| GA* | 3182 (13.7) | 0.0192 (15.1) | 3.52 (12.3) | 0.200 (19.4) | 0.281 (32.1) |
| RM | 5989 (14.4) | 0.0157 (9.8) | 4.51 (9.3) | 0.153 (19.7) | 0.136 (32.2) |
| MC | 7461 (12.0) | 0.0145 (20.0) | 5.23 (6.3) | 0.222 (20.4) | 0.165 (30.2) |
| AF ⊥ foliation | 1372 (14.7) | 0.0334 (5.3) | 2.34 (11.5) | 0.179 (17.3) | 0.363 (26.4) |
| AF // foliation | 1987 (11.6) | 0.0315 (8.1) | 3.04 (3.0) | 0.203 (11.1) | 0.280 (29.1) |
| MDB ⊥ foliation | 1312 (14.2) | 0.0362 (14.9) | 2.36 (5.4) | 0.258 (16.8) | 0.484 (31.6) |
| MDB // foliation | 1188 (10.6) | 0.0390 (8.5) | 2.20 (4.9) | 0.250 (16.9) | 0.533 (23.8) |
| MDB* ⊥ foliation | 901 (14.9) | 0.0412 (9.2) | 1.83 (4.3) | 0.270 (18.6) | 0.702 (21.0) |
| MDB* // foliation | 1083 (9.9) | 0.0350 (10.9) | 1.97 (5.3) | 0.249 (14.1) | 0.527 (16.0) |
| PTA ⊥ foliation | 3432 (9.7) | 0.0236 (20.7) | 4.15 (14.1) | 0.185 (20.2) | 0.188 (28.9) |
| PTA // foliation | 4979 (12.4) | 0.0205 (18.0) | 4.90 (15.6) | 0.210 (13.5) | 0.178 (22.5) |
| PTA* ⊥ rift plan | 620 (26.6) | 0.0496 (18.2) | 1.56 (11.3) | 0.234 (21.0) | 0.715 (20.9) |
| PTA* // rift plan | 1069 (14.9) | 0.0420 (10.3) | 2.12 (4.1) | 0.255 (14.8) | 0.560 (20.9) |
| PLA ⊥ rift plan | 3081 (15.4) | 0.0157 (15.4) | 2.79 (10.5) | 0.145 (20.6) | 0.246 (28.5) |
| PLA // rift plan | 7619 (9.4) | 0.0154 (23.1) | 6.31 (13.2) | 0.266 (25.0) | 0.170 (34.0) |
| PLA* ⊥ rift plan | 1754 (19.8) | 0.0234 (20.7) | 1.91 (11.1) | 0.162 (20.4) | 0.422 (12.1) |
| PLA* // rift plan | 3749 (12.0) | 0.0220 (14.3) | 3.86 (5.1) | 0.250 (11.9) | 0.265 (25.1) |

The large range of variation on the fracture properties obtained for the granites suggests that it will be convenient to perform a more detailed study of the general shape of the complete stress-displacement diagrams. Therefore, relations between the different mechanical parameters are investigated next.

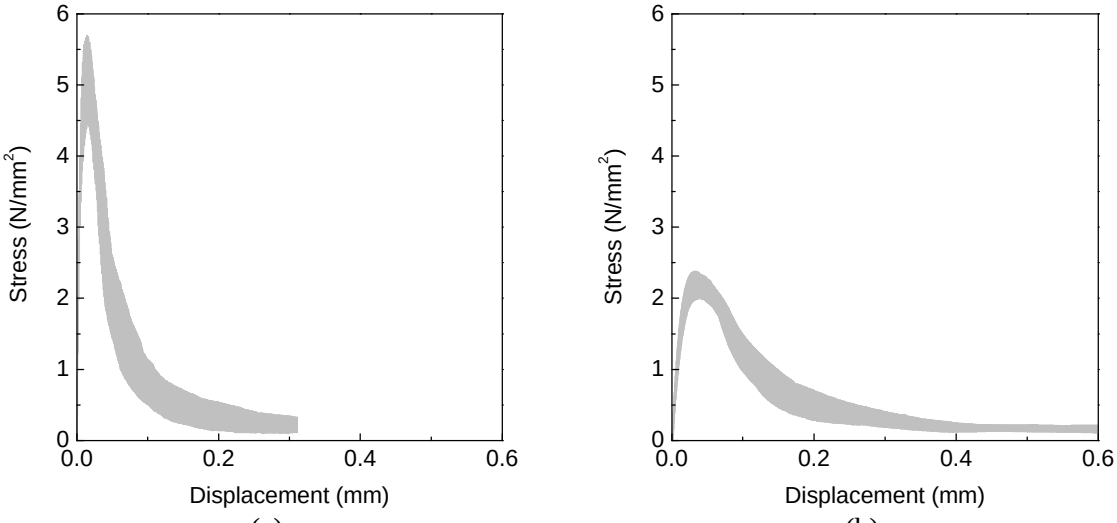


Figure 2.17 – Example of scatter in the stress-displacement diagrams; (a) granite MC; (b) granite MDB in the direction parallel to the foliation

### 2.5.3 *Correlations between mechanical parameters*

The dependence of tensile strength on initial stiffness, ultimate deformation at the peak stress, fracture energy and ultimate critical opening is analyzed next. Additionally, some remarks are made concerning the pre-peak and post-peak regimes. For a better understanding of the pre-

peak behavior, representative correlations are given between nonlinear pre-peak deformation, and the initial stiffness and tensile strength. Besides the fracture energy and the critical crack opening, a brittle index parameter is used as an additional characterization of the shape of the descending branch of the stress-displacement diagrams. The statistical correlations found are defined on the basis of all results obtained from the tensile tests carried out considering all types of granites. Besides, it must be stressed that all correlations are dimensional.

As can be seen in Figure 2.18, a significant nonlinear correlation ($r^2$ = 0.92) between tensile strength and the initial stiffness was found. Therefore, in general, higher values of tensile strength are associated with stiffer granites.

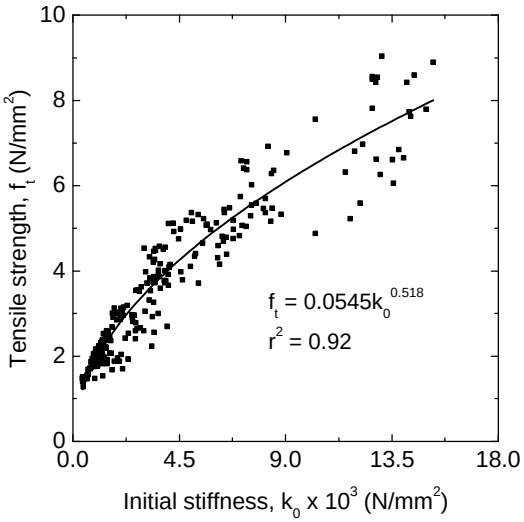


Figure 2.18 – Relations between fracture parameters; initial stiffness vs. tensile strength

The tensile strength varies nonlinearly with the corresponding deformation. Accordingly, the increase on the deformation at peak stress is associated with a decrease on the tensile strength value, see Figure 2.19a. Similar trend was obtained between the deformation at ultimate load and the initial stiffness, see Figure 2.19b.

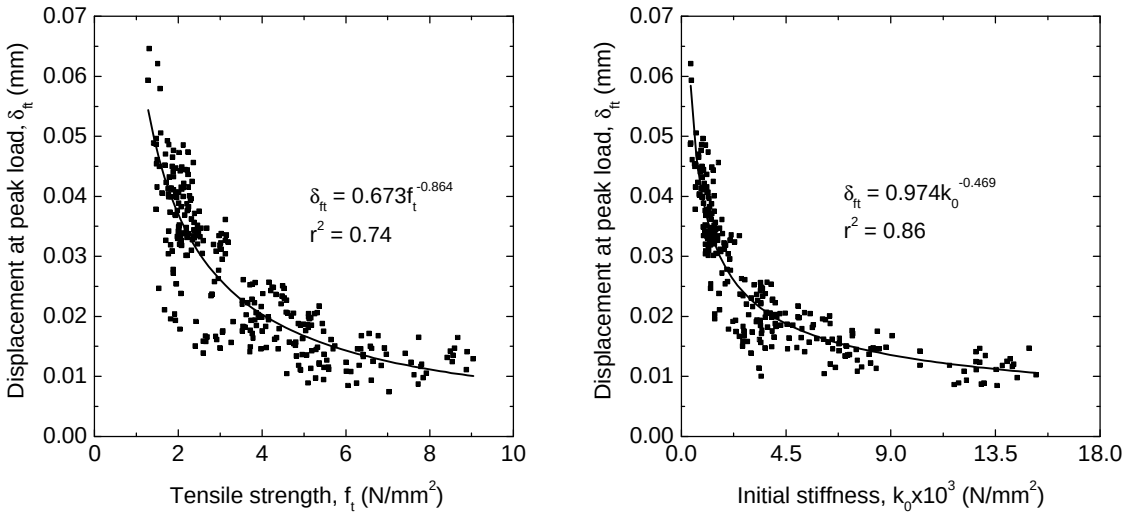


(a) (b)

Figure 2.19 – Relationship between pre-peak properties; (a) tensile strength vs. deformation at peak load; (b) initial stiffness vs. deformation at peak load

The deformation at peak stress decreases nonlinearly with the increase of the initial stiffness. This nonlinear relationship expresses, to certain extent, the nonlinear pre-peak behavior of granites associated to the microcracking process, since the deformation at ultimate load is the outcome of the sum of the linear deformation and the nonlinear pre-peak deformation.

The analysis of the ascending branch of the complete shape of the stress-displacement diagrams reveals clearly that granites exhibit markedly nonlinear behavior before the peak stress is reached, as can be seen from Figure 2.20, in which a small portion of the pre-peak diagram is highlighted. The complete stress-displacement diagrams are referring to materials with very different initial stiffness and strength levels, granite BA and PTA*. For both extreme cases, the development of nonlinear displacement, which indicates the onset of the microcracking process, takes place for very low stress levels (around 30% of the peak value).

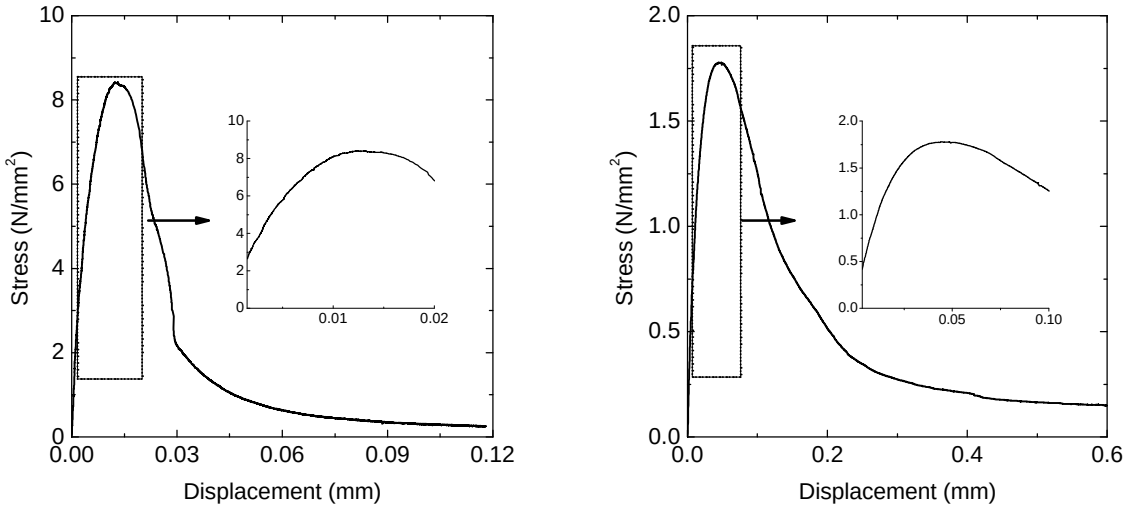


Figure 2.20 – Nonlinear pre-peak behavior; (a) granite BA; (b) granite PTA*

A linear correlation ($r^2$ = 0.97) between the total displacement at peak load, $d_{ft}$, and the nonlinear peak displacement, $d_{nl}$, is indicated in Figure 2.21.

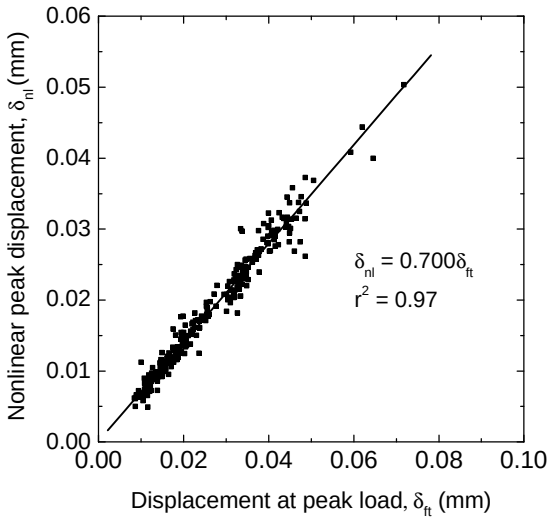


Figure 2.21 – Statistical correlation between nonlinear and total peak deformation at peak stress

It is possible to conclude that the nonlinear displacement at peak represent around 70% of the total displacement. This confirms the role of the microcracking process in granitic rocks under tensile load and the onset of the microcracking from early stages of deformation. This means also that the values of the deformation at the peak load are widely induced by the pre-peak nonlinear behavior of the material.

As already reported in literature (Prado and Van Mier, 2003), the microcracking process of concrete depends significantly on the density of the aggregates, as well as on its stiffness. Figure 2.22a shows the relation between the initial stiffness of the material, $k_0$, and the correspondent nonlinear peak deformation, $d_{nl}$. Also for granites, the nonlinear extent of the microcracking process depends highly on the stiffness of the material and consequently on its components. Stiff granites exhibit much lower nonlinear deformations until peak load.

The nonlinear pre-peak behavior can be attributed directly to the microstructure of the granites. Although the tests have been performed on assumed intact natural rock blocks, in fact, at the microstructure level it is obvious that flaws or small internal microcracks can intrinsically affect the behavior under a given stress state. The microcracks can exist in the grain boundaries, within the mineral (intragranular microcraks), and both at boundaries and through the minerals (intergranular cracks). According to Griffith's theory (Twiss and Moores, 1992), the microcraking progress under applied load origins from existing microcraks or defects and, consequently, the degree of degradation of the material stiffness is a function of the preexisting microcracking density.

In spite of the large scatter in the results and a small coefficient of correlation ($r^2 = 0.69$), the nonlinear correlation found between nonlinear peak deformation and tensile strength allows to conclude that, for strong granites, lower values of nonlinear pre-peak deformations were obtained, see Figure 2.22b.

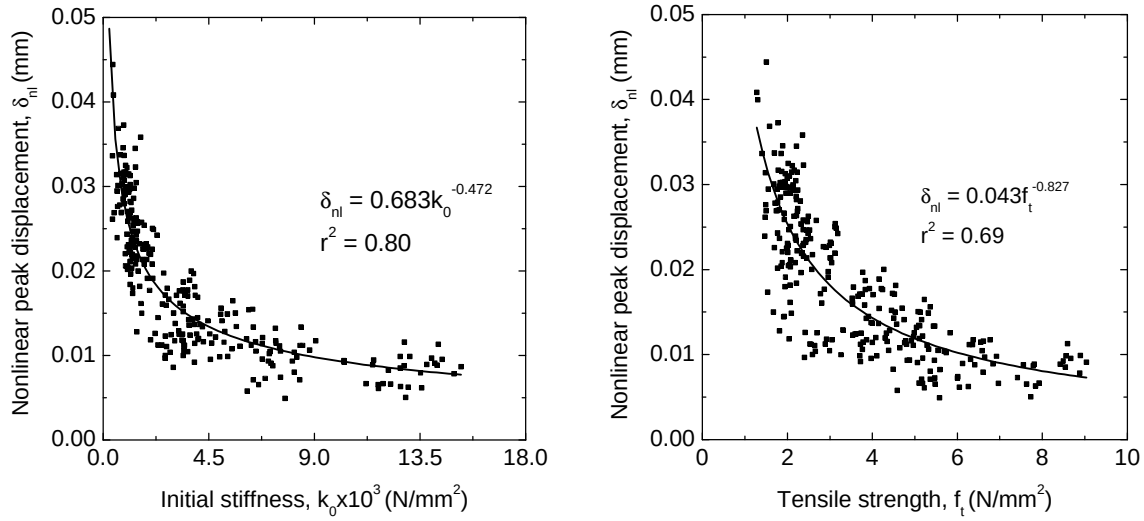


Figure 2.22 – Initial stiffness vs. nonlinear peak displacement; (b) tensile strength vs. nonlinear peak deformation

The properties used to analyze the shape of the descending branch of the stress-displacement diagrams are the tensile strength, $f_t$, the fracture energy, $G_f$, the critical crack opening, $w_c$, and, in addition, the ductility index, $d_u$. Chiaia *et al.* (1998) defines the ductility index as the ratio $G_f/f_t$, which represents the fracture energy normalized by the tensile strength. This parameter

allows to characterize the brittleness of granites and is directly related to the shape of the descending portion of the stress-displacement diagram. Increasing values of ductility index mean lower brittleness of the granites.

The complete information of the average values of the ductility index calculated for all granites is given in Table 2.5. The coefficient of variation (inside brackets) presents moderately high values. Similarly to the other post-peak properties, no significant differences are detected in values of the coefficient of variation with respect to the coarse-grained granites, PLA and PLA*, comparatively to values obtained for fine to medium granites. As aforementioned, all parameters concerning the post-peak behavior shows higher scatter. This can also be explained by the way that failure process mobilizes the heterogeneous microstructure of the material with its defects, voids and preexistent microcracking.

Figure 2.23 shows three different representative stress-displacement diagrams of granites GA, GA* and PTA*, and the corresponding ductility index. It can be seen that for low ductility indexes the post-peak diagram drops off steeply whereas for higher ductility indexes the softening branch is much smoother. Moreover, the tail of the descending part of the complete stress-displacement diagrams presents considerable larger length for more ductile granites.

Table 2.5 – Average values of the ductility index

| Granite | $d_u$ (mm) |
|---|---|
| BA | 0.023 (14.7) |
| GA | 0.025 (22.0) |
| GM | 0.058 (23.2) |
| RM | 0.033 (14.1) |
| MC | 0.043 (21.0) |
| AF ⊥ foliation | 0.077 (19.1) |
| AF // foliation | 0.067 (19.8) |
| MDB ⊥ foliation | 0.111 (17.5) |
| MDB // foliation | 0.113 (17.8) |
| MDB* ⊥ foliation | 0.147 (15.7) |
| MDB* // foliation | 0.126 (12.1) |
| PTA ⊥ foliation | 0.044 (21.7) |
| PTA // foliation | 0.042 (12.0) |
| PTA* ⊥ rift plan | 0.151 (19.4) |
| PTA* // rift plan | 0.124 (13.6) |
| PLA ⊥ rift plan | 0.053 (25.0) |
| PLA // rift plan | 0.040 (24.6) |
| PLA* ⊥ rift plan | 0.085 (18.5) |
| PLA* // rift plan | 0.065 (13.5) |

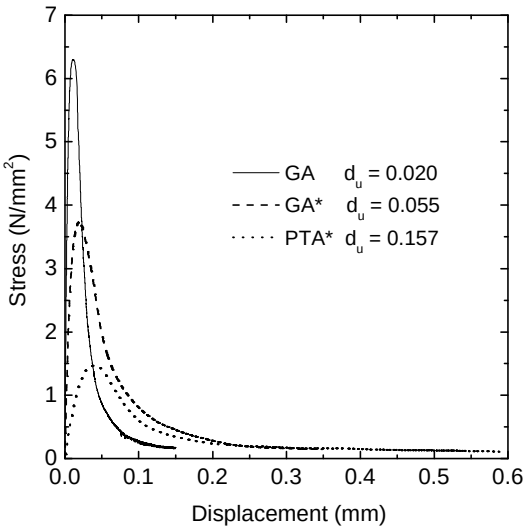


Figure 2.23 – Stress-displacement diagrams and correspondent ductility index

The dependence of the critical crack opening on the deformation at peak load and on the tensile strength is evaluated through the statistical correlations shown in Figure 2.24. A positive linear correlation was found between crack opening and the deformation at peak load, see Figure 2.24a.

As expected, this means that higher crack openings are associated to granites that also exhibit large deformation at ultimate load. Figure 2.24b indicates that a significant nonlinear correlation was found between the crack opening and the tensile strength. High strength granites exhibit low crack openings and, as a consequence, show a reduction on deformation capacity.

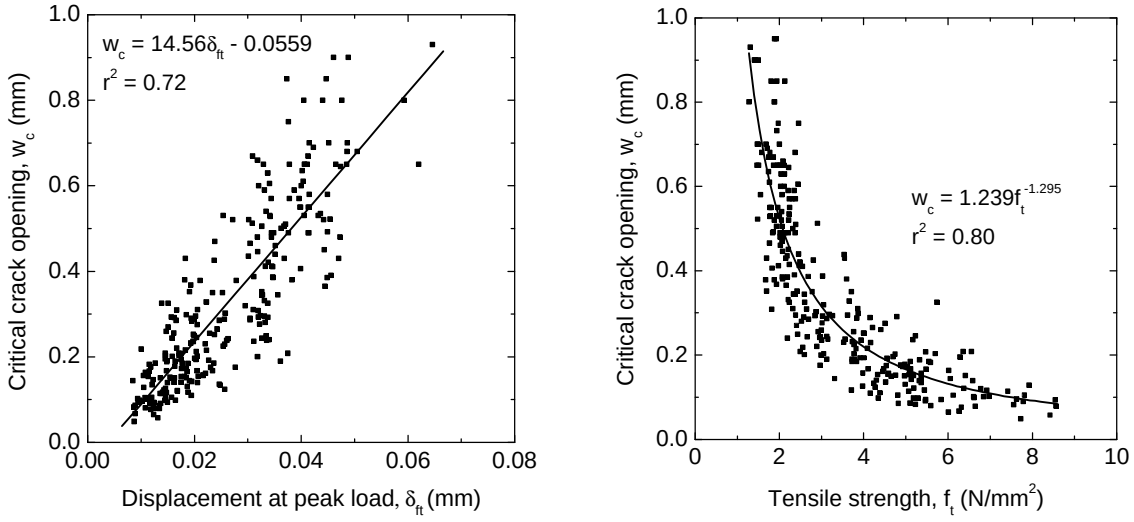


(a) (b)

Figure 2.24 – Relationships between fracture parameters; (a) deformation at ultimate load vs. critical crack opening; (b) tensile strength vs. critical crack opening

Although the critical crack opening seems to increase when fracture energy exhibits higher levels, no strong correlation was found between both parameters, see Figure 2.25a. Furthermore, as can be seen in Figure 2.25b, no correlation was found between the fracture energy and the tensile strength.

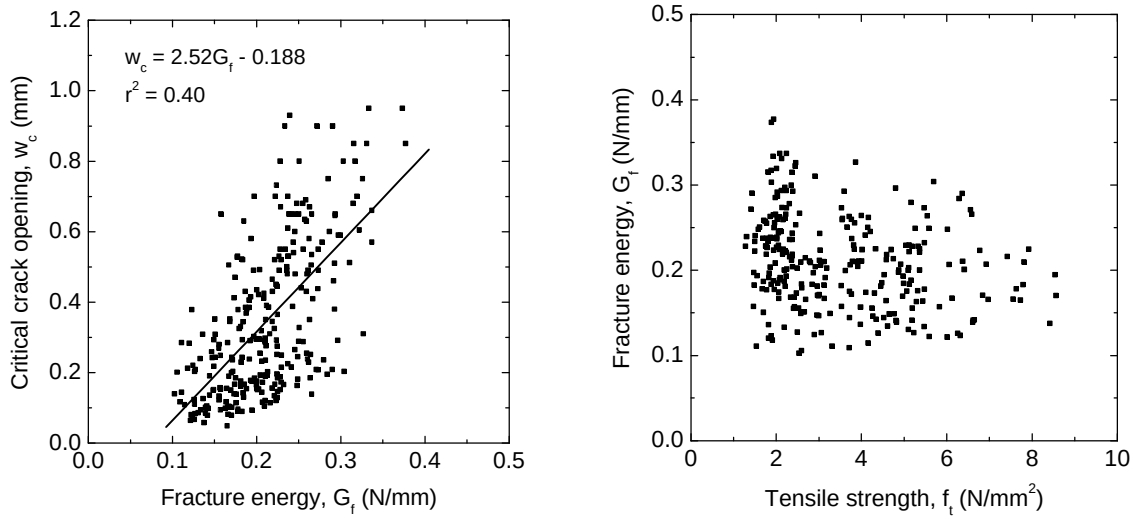


(a) (b)

Figure 2.25 – Relationships between fracture parameters; (a) fracture energy vs. critical crack opening; (b) tensile strength vs. fracture energy

The ductility index decreases with increasing tensile strength, which is confirmed by the nonlinear fitting to the experimental results obtained for all granites, see Figure 2.26a. As the tensile strength increases, the ductility presents a continuous and progressive reduction up to very low values. It can be concluded that high strength granites are more brittle, with steeper softening branches of the stress-displacements diagrams. The correlation between the ductility index and the fracture energy is not very significant, since a high level of scattering is recorded, which leads to a low value for the coefficient of correlation ($r^2$ = 0.44), see Figure 2.26b.

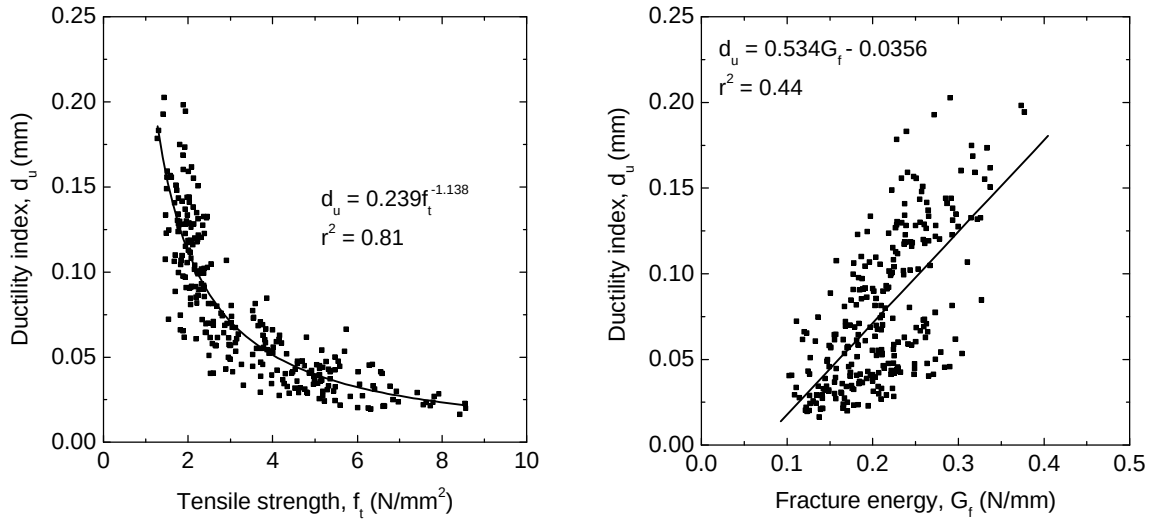


Figure 2.26 – Relationships between fracture parameters; (a) tensile strength vs. ductility index; (b) fracture energy vs. ductility index

Moreover, the ductility is directly connected with the critical crack opening. High ductile materials exhibit a long tail in the descending branch and therefore high values of the critical crack opening are expected. This assumption is largely confirmed by the linear correlation between the two parameters displayed in Figure 2.27. The critical crack opening is therefore a measure of the ductility of the material, similarly to the ductility index, as confirmed by Figure 2.24b and Figure 2.26a.

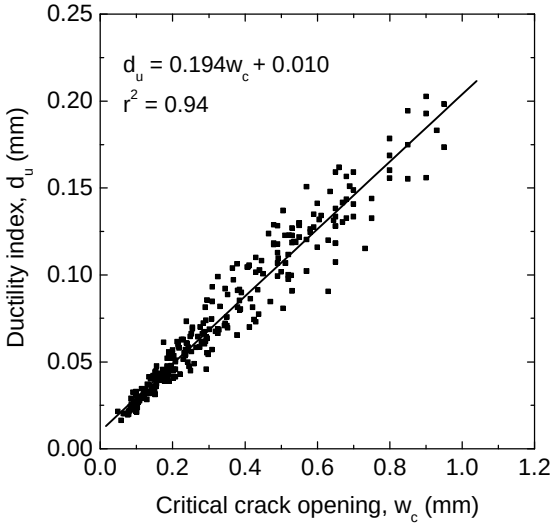


Figure 2.27 – Relationship critical crack opening and ductility index

Although the quantitative analysis of the fracture parameters has been performed in order to improve the knowledge about the fracture process of granites, more careful assessment of the main reasons that should be on the basis for the wide range of values exhibited by the fracture properties is needed. Thus, a detailed discussion of the aspects that might influence the characteristic parameters of the complete behavior of granites is performed in the following section.

## 2.6 Factors that influence fracture properties

Granitic rocks include a wide range of lithotypes as a function of their petrographical characteristics, namely, mineralogical composition, texture (size and shape of the grains), fabric and weathering state. Studies have been carried out in order to gain a better understanding on the influence of microstructural aspects in the mechanical properties. In particular, textural characteristics such as size and shape of grains contribute to the strength variation of granitic rocks (Tugrul and Zarif, 1999; Prikryl, 2001). The work carried out by Mendes *et al.* (1966), in terms of mineralogical composition, as well as the texture characterization of granitic rocks, has also revealed that good correlation exists between petrographical characteristics and mechanical properties.

In next sections, the results found for the granites in terms of complete stress-displacement diagram and fracture parameters are analyzed taking into consideration the textural characteristics, such as internal texture related to planar anisotropy (planar foliation, flow structures and rift plane), mineralogical composition and grain size. The moisture content and the weathering state, which must be taken into account when visual sign of meteorization is detected, are other important aspects. The dependence of the tensile parameters on the physical properties, namely porosity and density, is also analyzed.

### 2.6.1 *Internal structure - evaluation of the anisotropy degree*

It has been pointed out (Tugrul and Zarif, 1999; Åkesson *et al.*, 2003) that the fabric, related to the arrangement and preferential orientation of minerals, represents a textural aspect that, in general, contributes to the variation of mechanical properties, including the strength. If some granitic rocks, by its random texture, are likely to have isotropic properties, a more careful analysis is needed when visual evidence of heterogeneities and preferential orientations of the minerals are detected. The latter assumptions, which were identified on some granitic lithotypes under study, led to the necessity of conducting direct tensile tests according to different loading directions. In the present section, considerations concerning the distinct directional character of the fracture parameters resulting from the analysis of the complete tensile behavior for the granites AF, PLA, PLA*, PTA, PTA*, MDB and MDB* are performed.

By comparing the values of the fracture parameters, displayed in Table 2.4, as well as the complete shape of the stress-displacement diagrams of granite PLA and PLA*, which were obtained for the directions parallel and perpendicular to the rift plane, see Figure 2.28 and Figure 2.29, it is possible to verify that the tensile behavior is clearly dependent on the direction of the applied load. In fact, for this granite, the deformational and strength parameters assume remarkably higher values when the direction of loading is parallel to the rift plane, in comparison to the ones obtained for the perpendicular direction. According to Takemura *et al.* (2003), the orientation of preexisting microcracks can play an important role in the anisotropy exhibited by granites. When coarse grains, like feldspar phenocrystals, are present, it is possible that grain boundary microcracks develop around the crystals and induce such distinct properties according to the loading direction. However, to confirm this possibility, a more careful analysis of the microstructures would be needed. Despite the higher values of the fracture energy found for the direction parallel to the rift plane, the ductility parameter and, therefore, the critical crack opening present larger values for the perpendicular direction. This observation is in agreement with the softening shape of the

stress-displacement diagram, because, in case of loading parallel to rift plane (subparallel to the flow structures), the slope of the descending branch is much steeper.

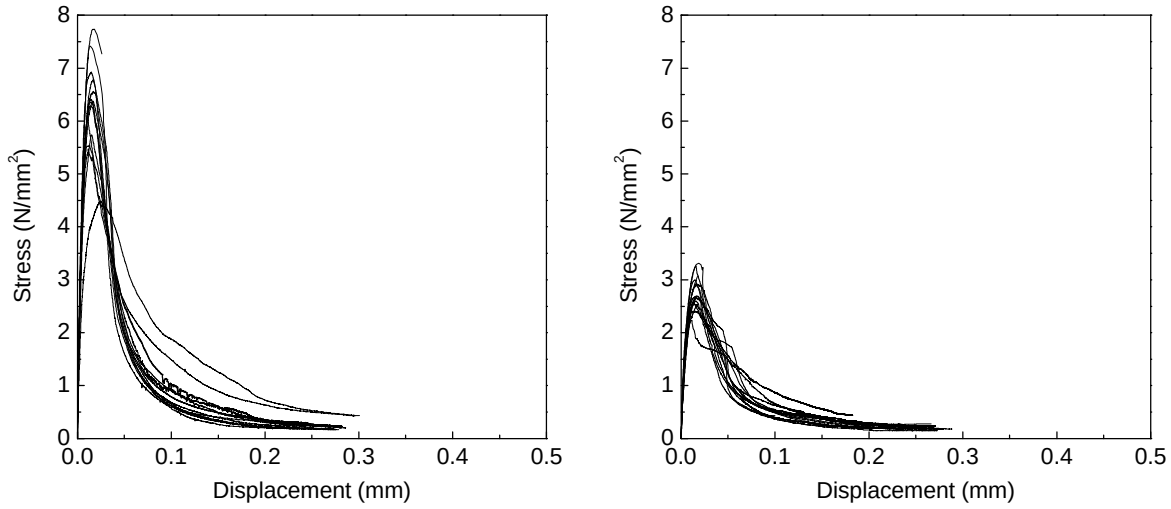


Figure 2.28 – Stress-displacement diagrams for granite PLA; (a) direction parallel to the rift plane; (b) direction perpendicular to the rift plane

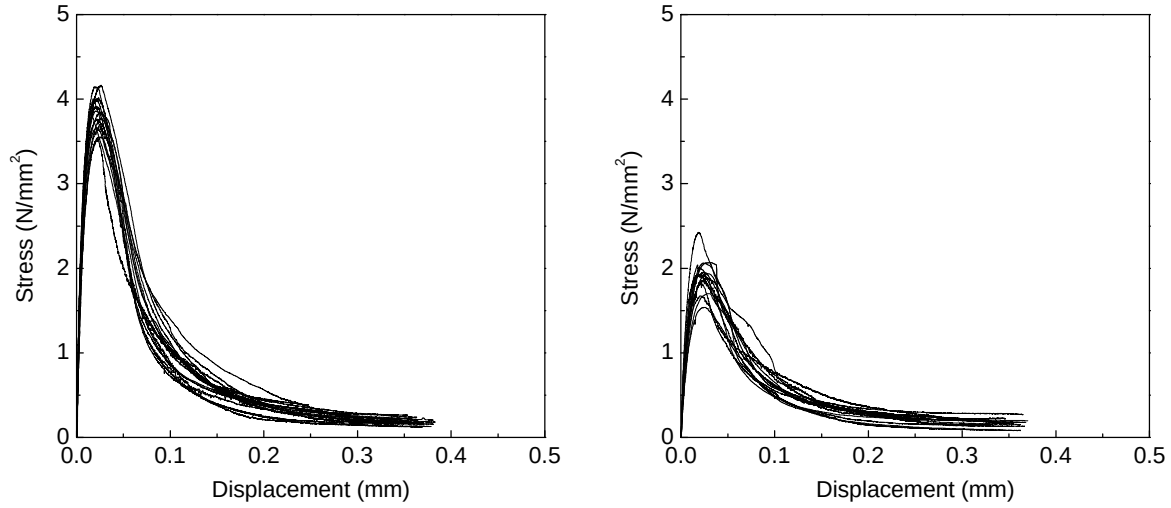


Figure 2.29 – Stress-displacement diagrams for granite PLA*; (a) direction parallel to the rift plane; (b) direction perpendicular to the rift plane

The differences in terms of the shape of stress-displacement diagram observed in foliated granites, like PTA, MDB, MDB* and AF, are much less severe, see Figure 2.30 and Figure 2.31. It is possible, however, to recognize that apart from the granite MDB, which exhibits rather close values in both directions, the values of the tensile strength are higher when the load is applied in the direction parallel to the foliation. In general, it is also observed that the descending softening branch presents a slightly longer tail, and thus a large crack opening, for the perpendicular direction to the foliation.

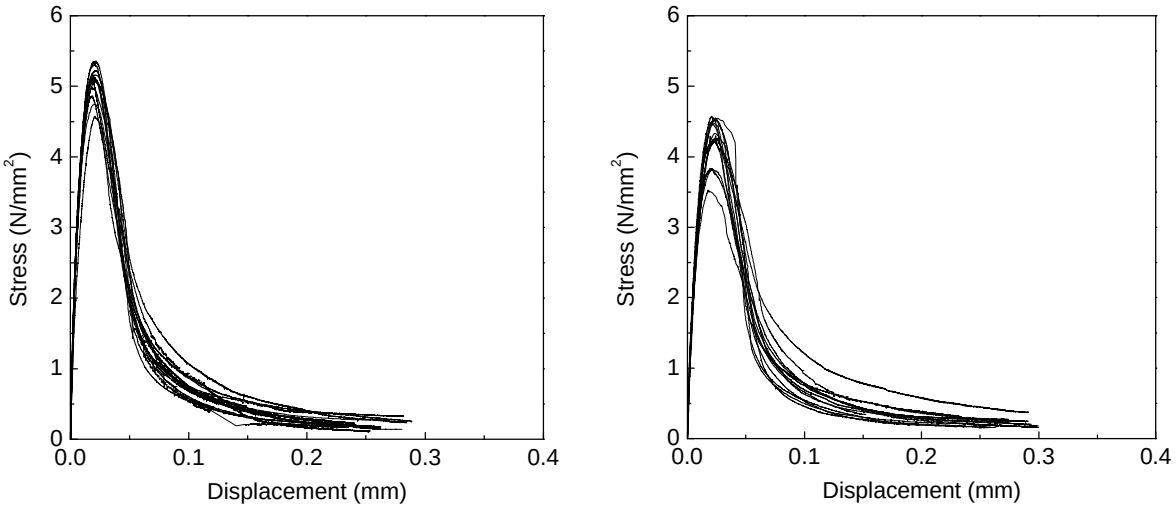


Figure 2.30 – Stress-displacement diagrams for granite PTA; (a) direction parallel to the foliation plane; (b) direction perpendicular to the foliation plane

A relevant note should be made regarding the values of the ductility. The linear correlation expected between the ductility index and the fracture energy of the granites seems to be disturbed by the tensile strength anisotropy exhibited by the granites under study, and specially by the granites PLA and PLA*, as addressed previously in Section 2.3.3. Usually, the granites present more brittle behavior in the direction parallel to foliation or rift plane, identified by higher values of the tensile strength and lower values of the ductility index.

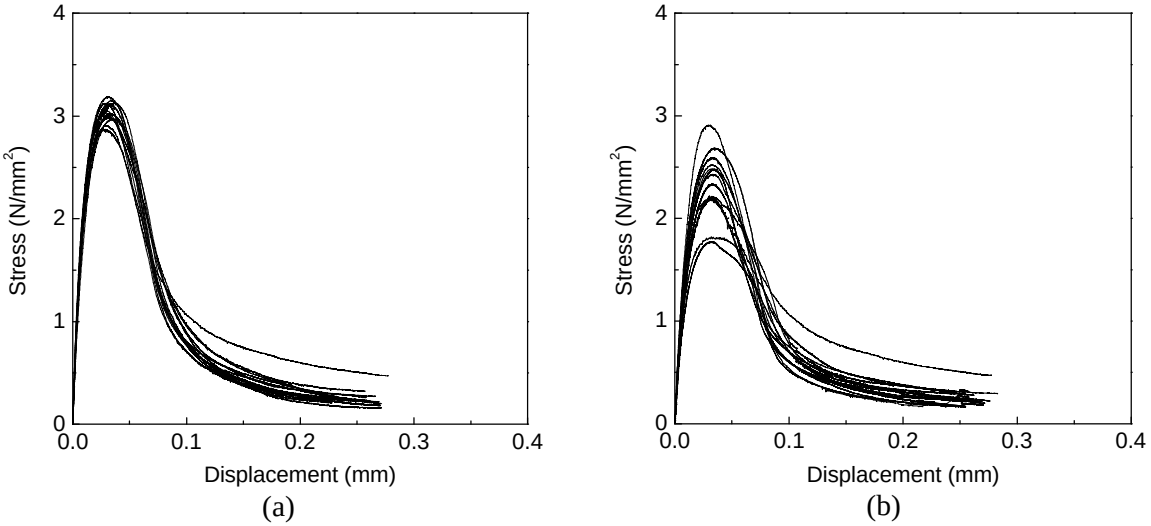


Figure 2.31 – Stress-displacement diagrams for granite AF; (a) Parallel direction to the foliation plane; (b) perpendicular plane to the foliation plane

For a better understanding of the differences found on the tensile behavior of granites, the anisotropy was calculated as a ratio between the values of the fracture parameters obtained for the parallel and the perpendicular direction of loading. The values of the anisotropy shown in Table 2.6 were calculated based on the values of the fracture properties presented in Table 2.4.

Table 2.6 – Degree of anisotropy concerning the fracture parameters

| Granite | $k_0$ | $f_t$ | $G_f$ | $w_c$ | $d_u$ |
|---|---|---|---|---|---|
| AF // foliation<br>AF ⊥ foliation | 1.45 | 1.30 | 1.13 | 0.77 | 0.87 |
| MDB // foliation<br>MDB ⊥ foliation | 0.91 | 0.93 | 0.97 | 1.10 | 1.02 |
| MDB* // foliation<br>MDB* ⊥ foliation | 1.20 | 1.08 | 1.08 | 0.75 | 0.86 |
| PTA // foliation<br>PTA ⊥ foliation | 1.45 | 1.18 | 1.14 | 0.95 | 0.95 |
| PTA* // rift plane<br>PTA* ⊥ rift plane | 1.72 | 1.36 | 1.09 | 0.78 | 0.82 |
| PLA // rift plane<br>PLA ⊥ rift plane | 2.47 | 2.26 | 1.83 | 0.69 | 0.75 |
| PLA* // rift plane<br>PLA* ⊥ rift plane | 2.13 | 2.02 | 1.54 | 0.63 | 0.76 |

The analysis of the values indicates that according to the statements mentioned before, all granites under study exhibit a certain degree of anisotropy regarding the deformation, fracture parameters and ductility index. Granites MDB and MDB* exhibit the lowest anisotropy regarding strength and fracture energy. Medium to high values of anisotropy were found for granites AF, PTA and PTA*. The considerable high values of the anisotropy obtained in the granites PLA and PLA* confirms the differences detected on the complete shape of stress-displacement diagrams.

If the main reason that contributes to the measured anisotropy in granites PTA and AF can be attributed to the foliation, for granites PLA, PLA* and PTA*, the anisotropy can be related to the orientation of the quarry planes (rift plane). Although the granites PLA and PLA* do not exhibit clear foliation, the flow structure of the coarse grained feldspar phenocrystals (that appear to be subparallel to the rift plane) determines the tensile behavior of this type of granite. The higher values of the anisotropy achieved for deformation, the critical opening and ductility index for the granite MDB*, when compared to fresh granite MDB, and the similar behavior of other weathered granites, indicate that the anisotropy can be also generated by additional directional microcracking.

### 2.6.2 *Physical properties*

The evaluation of the physical properties of granites can be a simple and practical method of evaluating the quality of rocks. Different studies revealed that mechanical properties, such as compressive strength or elastic modulus, are dependent on the porosity and density (Tugrul and Zarif, 1999; Prikryl, 2001; Tugrul, 2004). This is not only valid among rocks with distinct weathering state but also for fresh rocks, even if the correlations are characterized by a large scatter (Goodman, 1989). The dependence of the tensile fracture parameters on the physical properties, namely porosity and density, are herein investigated through statistical correlations obtained by the least-squares fit method. It is noted that granites exhibit a clear grouping for specific intervals of the porosity and the large scatter within each group often found can be related to the directional character exhibited for some granites.

Figure 2.32a and Figure 2.32b indicate that there is a reasonable correlation between the porosity and the pre-peak properties, namely the initial stiffness, $k_0$, and the nonlinear peak displacement, $d_{nl}$. However, the scatter found for the nonlinear peak displacement is particularly remarkable for granites with high porosity (AF, ADB, MDB*, PTA*). These relationships allow to conclude about the dependence of stiffness characteristics and deformational behavior on the physical properties. A trend for peak displacement increase with porosity increase is verified. Porosity plays also an important role in the variation of the initial stiffness of the granites. The initial stiffness presents high values for granites BA ($n$ = 0.51%), GA ($n$ = 0.47%) with low porosity, moderate values for granite PLA ($n$ = 0.84%), MC ($n$ = 0.87%), and RM ($n$ = 0.74%) and progressively decreasing values as the porosity assumes rather high values, which occurs in granite MDB* ($n$ = 7.2%).

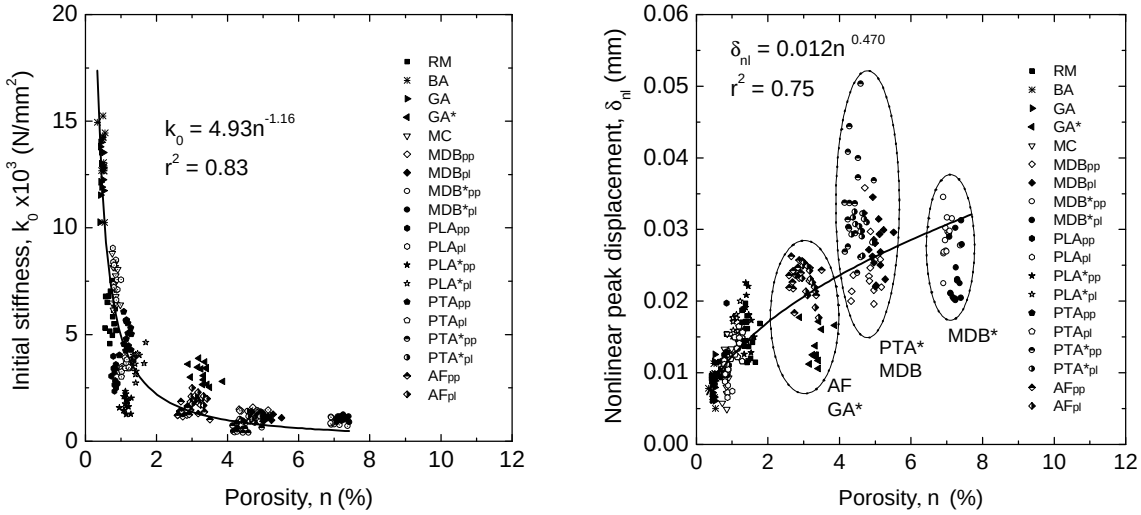


Figure 2.32 – Relationships between porosity and mechanical parameters; (a) porosity vs. initial stiffness; (b) porosity vs. peak nonlinear displacement

The evolution of the tensile strength and mode I fracture energy with porosity is shown in Figure 2.33.

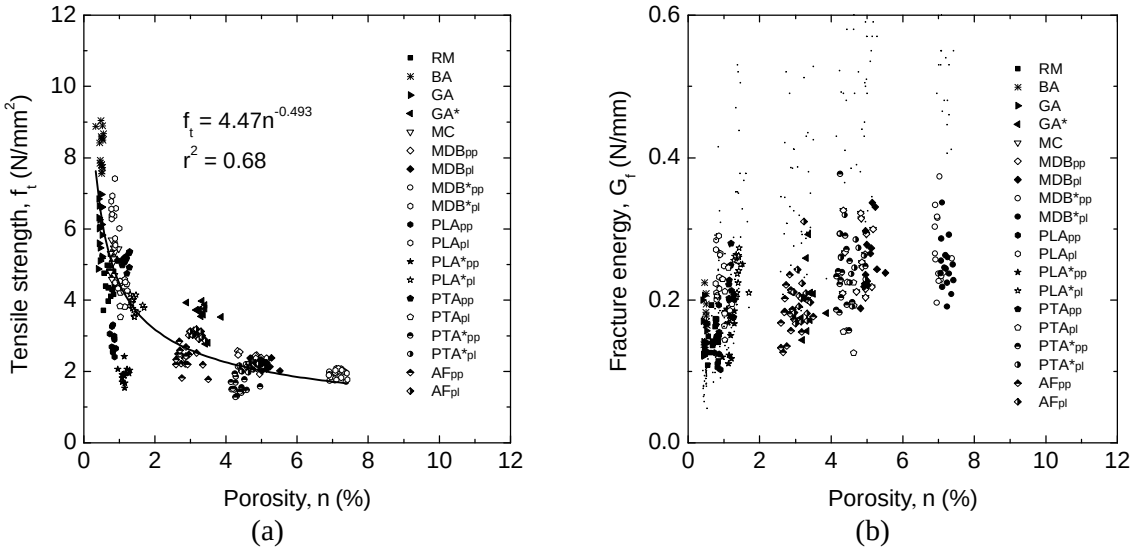


Figure 2.33 – Relationships between porosity and mechanical parameters; (a) porosity vs. tensile strength; (b) porosity vs. fracture energy

Although with larger scatter, analogous trend was found between the tensile strength and the porosity. More porous granites have generally lower strength. With regard to the fracture energy, no significant correlation was found with the porosity. However, in spite of the significant scatter shown in Figure 2.33b, there seems to be some trend for the fracture energy increase with the porosity.

The nonlinear correlations attained between the ductility index, $d_u$, and critical crack opening, $w_c$, with the porosity, indicate that this physical property influences the ductility behavior of the material, see Figure 2.34. The ultimate deformation capacity of the granites under study increases as the porosity increases. For example, granites AF ($n$ = 3.2%) and GA*($n$ = 3.6%) present similar values of ductility and critical crack opening, whereas granites PLA, MC and RM have much lower porosity. This fact can be related to internal structure of the granites. In effect, AF and GA* are fine to medium-grained granites whereas granites PLA, MC and RM are coarse-grained granites.

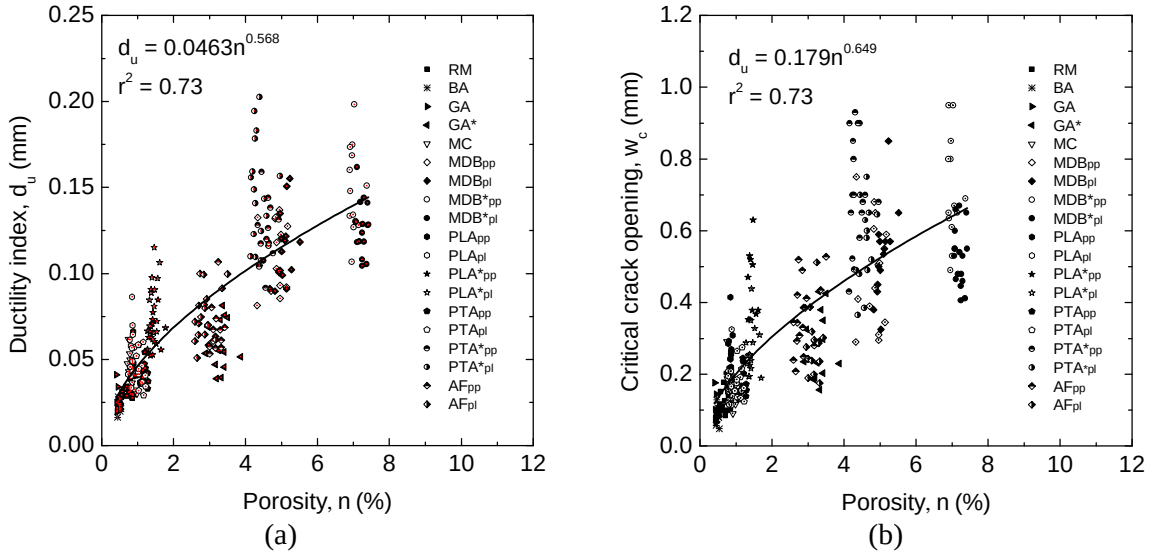


Figure 2.34 – Relationships between porosity and mechanical parameters; (a) porosity vs. ductility index; (b) porosity vs. critical crack opening

The analysis of Figure 2.35 up to Figure 2.37, where the relation between the density and some mechanical properties is displayed, demonstrates that despite considerable scatter, there are some trends between these characteristics.

Thus, the stiffness of the granites seems to increases with density and higher values of the tensile strength are associated with more dense granites, see Figure 2.35. Regarding the peak tensile behavior, it can be observed from Figure 2.36 that the nonlinear peak displacement decreases linearly with the density. Finally, the linear correlations obtained between the ductility index and the critical crack opening with the density indicate that the post-peak deformation decreases with the density increase, see Figure 2.37. High-density granites exhibit, therefore, more brittle behavior.

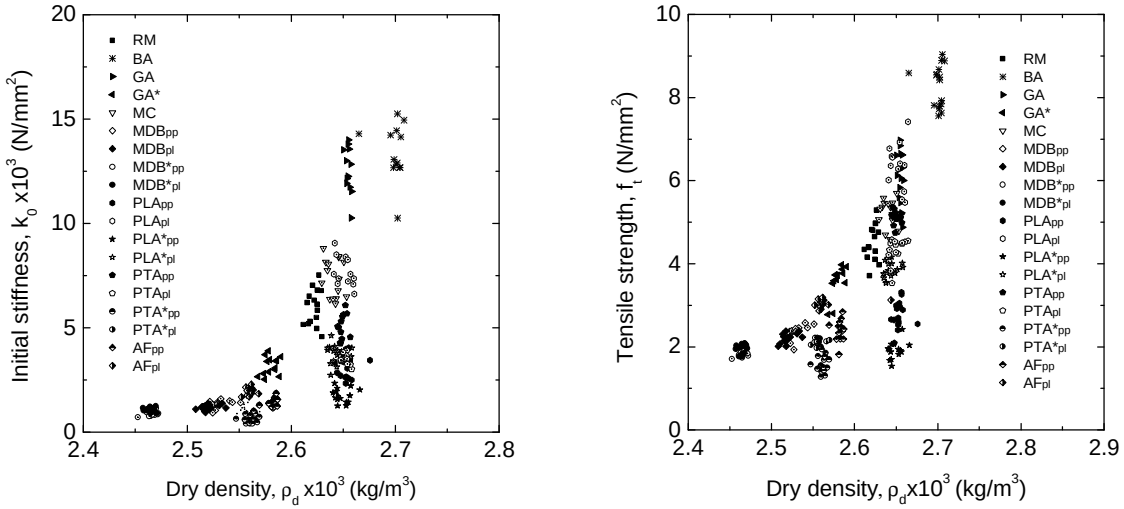


(a) (b)

Figure 2.35 – Relationships between density and mechanical parameters; (a) dry density vs. initial stiffness; (b) dry density vs. tensile strength

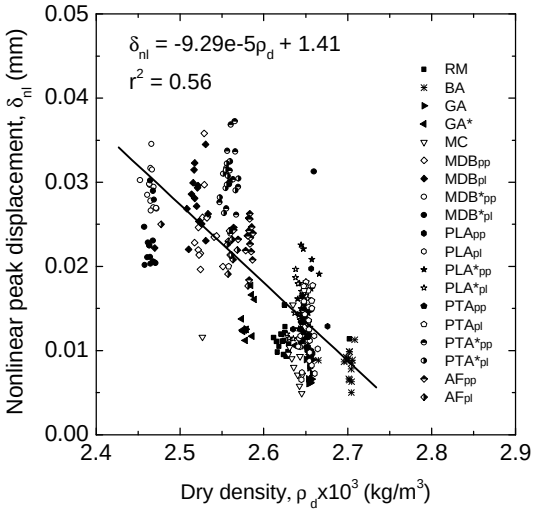


Figure 2.36 – Relationship between dry density and nonlinear peak displacement

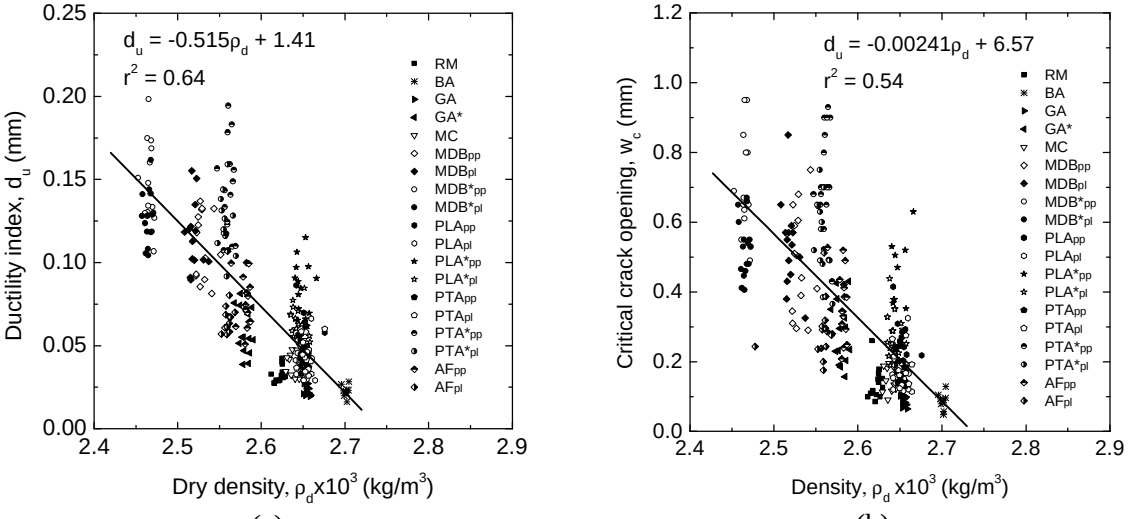


(a) (b)

Figure 2.37 – Relationships between density and mechanical parameters; (a) dry density vs. ductility index; (b) dry density vs. critical crack opening

### 2.6.3 *Weathering conditions*

The influence of the weathering state on the tensile behavior of the studied granitic rocks is analyzed on the basis of the complete stress-displacement diagrams from the direct tensile tests, which were conducted on fresh and weathered granite. The differences detected on the tensile behavior between fresh and weathered granites are also quantitatively analyzed on the basis of the fracture parameters.

Figure 2.38 to Figure 2.40 display the complete tensile behavior of granites GA, GA*, PTA, PTA* and MDB, MDB* respectively. In general, it was found that clear distinct pre and post-peak tensile behavior when fresh or less weathered granites (MDB) and weathered granites of the same lithotype are compared.

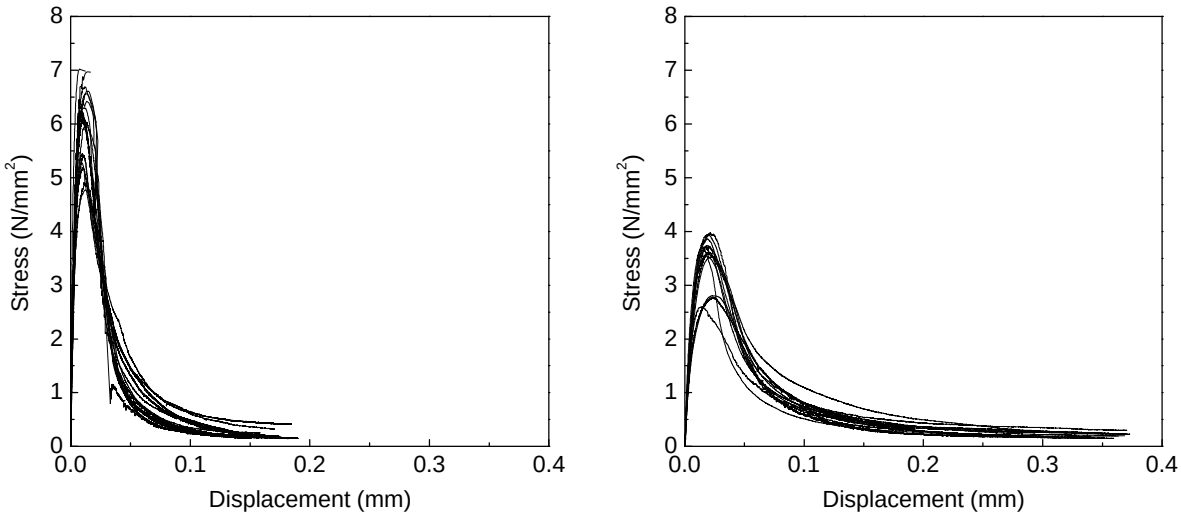


Figure 2.38 – Stress-displacement diagrams; (a) granite GA; (b) granite GA*

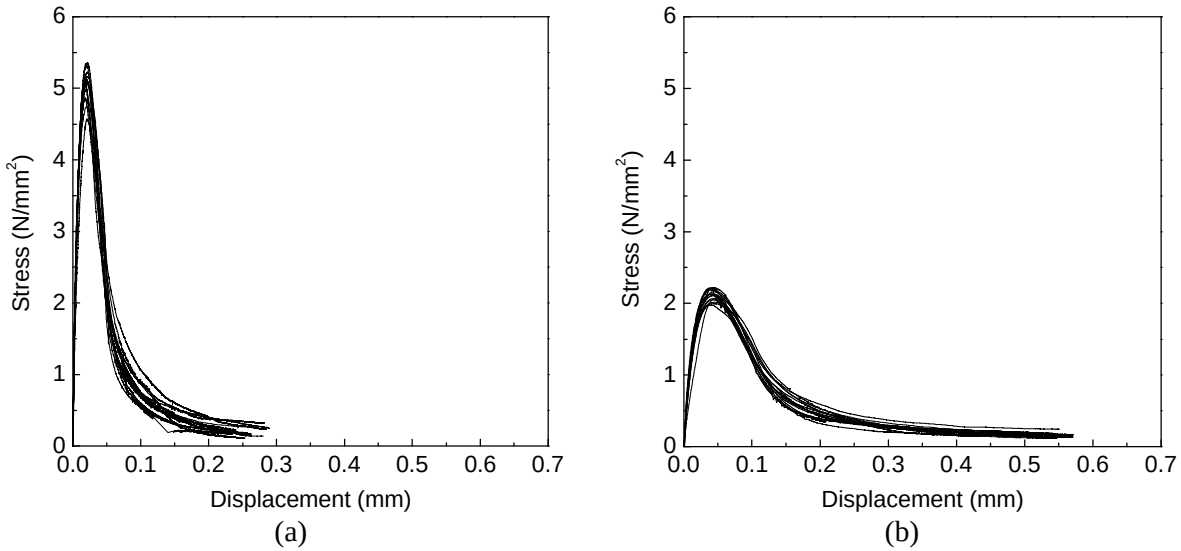


Figure 2.39 – Stress-displacement diagrams; (a) granite PTA in direction parallel to foliation; (b) granite PTA* in direction parallel to the rift plane

The fresh granite presents considerable higher values of the tensile strength. The load carrying capacity decrease, immediately after the peak load is reached, is abrupt and can be directly identified by the steep post-peak branch of the stress-displacement diagrams. On the

contrary, in case of weathered granites, the softening branch is much smoother. This means that the unloading of the material at the macrocrack zone is made with a larger amount of deformation and, consequently, higher values of ductility can be expected.

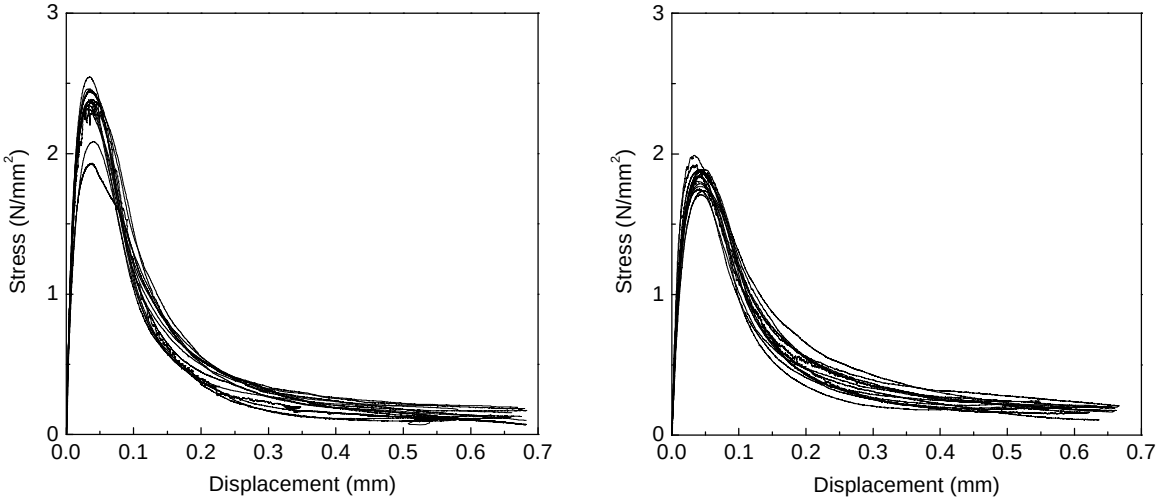


Figure 2.40 – Stress-displacement diagrams; (a) granite MDB in direction perpendicular to the foliation; (b) granite MDB* in direction perpendicular to the foliation

The pre-peak behavior also exhibits clear differences. Fresh granites present high values of the initial stiffness and the development of the nonlinear displacements up to peak load is always much less pronounced, in comparison to weathered granites, see Figure 2.41. Although the onset of nonlinear displacements takes place for low values of loading, close to the maximum tensile stress the growth rate is rather noticeable. This nonlinear displacement increase assumes major significance for weathered granites and, particularly, for granites with high values of porosity (MDB, MDB* and PTA*). The development of the inelastic deformation appears to be asymptotic, which can be directly connected to a preexisting network of microfissures that can also explain such high values of the porosity found for these weathered granites (Rodrigues, 1982).

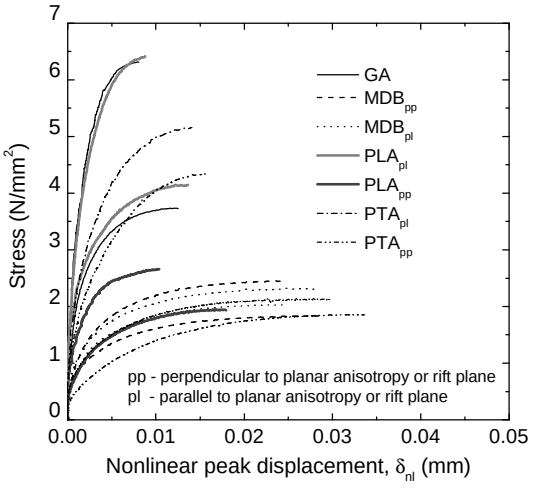


Figure 2.41 – Development of the nonlinear displacement up to ultimate load

The strength and initial stiffness differences between fresh/less weathered and weathered granites are shown in Figure 2.42 for all granites. In general, values of strength and stiffness are much higher for fresh granites. The weathering process of granites, besides changing the mineralogical composition (increase of clay component), also leads to the development of microfractures and, consequently, to the loss of stiffness and strength. The stiffness associated to fresh granites is related to high material density, as well as to low values of the porosity. In these cases, a lower amount of pores and voids are present in the material microstructure. Similar results were pointed out by Gupta and Rao (2000) and by Tugrul (2004) for the strength and deformational behavior of several types of rocks, including granites, under compression and tensile loading.

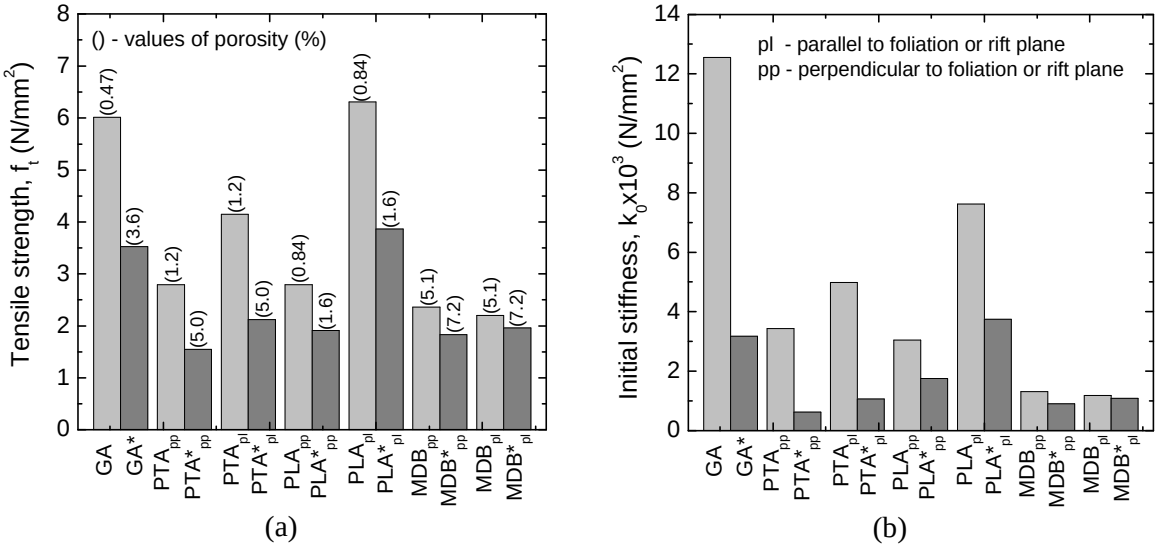


Figure 2.42 – Comparison of tensile properties between fresh/less weathered and weathered granites; (a) tensile strength; (b) initial stiffness

Furthermore, some considerations have to be made about the post-peak behavior of fresh and weathered granites. As already mentioned, the macrocracking propagation of fresh/less weathered granites is associated with steeper descending branch of the post-peak stress-displacement diagram. This suggests that, despite the higher value of the tensile strength, lower values of the energy consumed in the fracturing process of fresh granites. These assumptions can be confirmed by comparing the average values of the fracture energy as well as of the ductility index, see Figure 2.43.

According to Zhang (2002), the tensile strength is strongly correlated with the mode I fracture toughness that measures the ability of resisting to the propagation of the crack tip during the fracture process of rocks. The good correspondence is related to the analogous mechanism of failure. Generally, toughness of rocks increases linearly with strength, which means that hard rocks, with higher mineral strength and strong bond mineral interface, to which high values of density and less amount of voids are associated, offer more resistance against crack formation. This behavior can explain the fact that, for high tensile strength rocks, less amount of energy is consumed in the fracture process because more brittle failures occur.

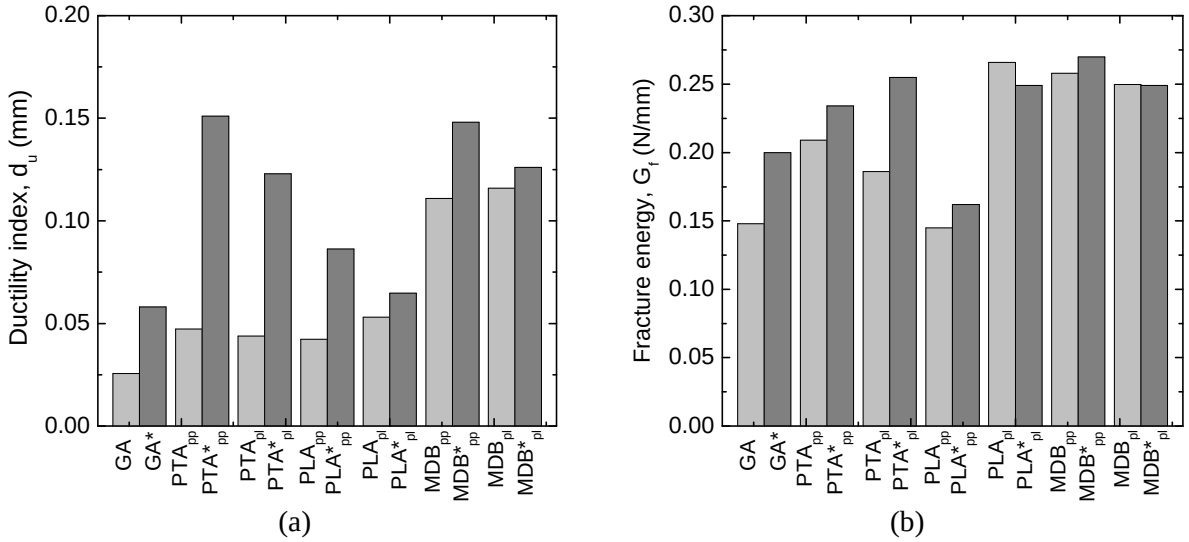


Figure 2.43 – Comparison of tensile properties between fresh/less weathered and weathered granites; (a) ductility index; (b) fracture energy

A remarkable difference on the ductility index is found between fresh/less weathered and weathered granites. The high ductility of weathered granites is associated with a remarkable deformation level, which is intrinsically connected with the long tail of the softening part of the stress-displacement diagram. Therefore, higher values of the critical opening are also found for weathered granites, see Figure 2.44.

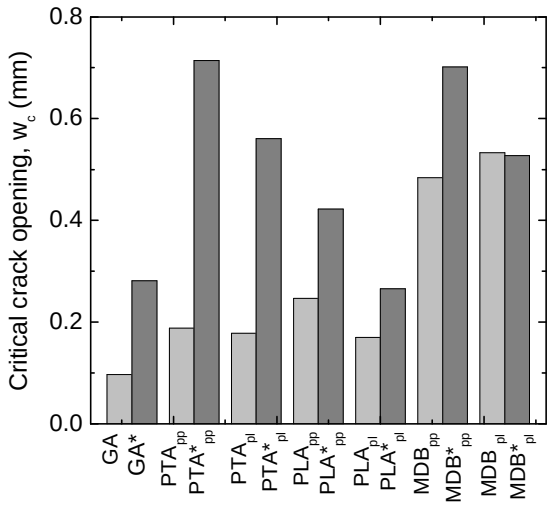


Figure 2.44 – Comparison of the critical crack opening between fresh/less weathered and weathered granites

The continuous crack-stress transfer between the two halves of the specimen, after the macrocrack is completely established, is achieved through the crack-face bridges that still connect the two halves. Although the toughening bridging mechanism is present in every granite types, it is more pronounced in case of weathered granites. The main reason that leads to such behavior can be associated, on one hand, to the high number of small particles with different stiffness, and on the other hand, to the decrease of the grain boundary strength. If in granites with coarse grain size, the bridging mechanism can occur by the formation of multiple macrocracks around the coarse grains like feldspar mineral (granites MC, PLA and PLA*), in more homogeneous granites like PTA*, MDB* or AF, the bridging mechanism can

develop around the stiffer particles that act as branches. This behavior is rather significant in case of weathered granites, see Figure 2.45. In general, this stress-transfer or bridging mechanism is responsible, to a large extent, for the softening behavior found for other quasi-brittle materials like concrete and sandstone (Vervuurt *et al.*, 1996; Bentz *et al.*, 1995).

(a) (b) (c)

Figure 2.45 – Aspect of the fracture surfaces and bridging behavior; (a) granite MDB*; (b) granite AF in the direction parallel to foliation; (c) granite PTA* in the direction parallel to rift plane

It is also noticed that particularly on weathered granites such as GA* and PLA*, some failures have occurred out of the notched zone according to very well defined planes. This fact confirms the major role played by the fissuring, induced by weathering effects, on the tensile fracture of granites, see Figure 2.46. Similar tensile fracture took place on some specimens from granites with porphiritic internal texture, namely, granites PLA and MC, essentially due to pre-existing cleavages of the feldspar minerals. Note that in crystalline rocks such as the granites, intragranular cracks are easier to occur in some of the weaker minerals, namely feldspar and biotite (Eberhardt *et al.*, 1999b; Takemura *et al.*, 2003).

Figure 2.46 – Failure modes outside the notched zone for weathered granites

Finally, it is stressed that apart from the anisotropy exhibited by some granites, the weathering conditions, which result in the weakness of the internal structure reflected by the increase on the porosity levels, explain the differences recorded in fracture parameters regarding the granites with the same petrographical characteristics.

### 2.6.4 *Petrography - mineralogical characteristics and grain size*

According to various researchers, the mechanical characteristics of granites such as strength and deformability are affected by textural aspects like size and shape of grains. As reported by Brace (1961), the strength of rocks is greater for fine-grained rocks. More recently, some

studies have revealed that grain size is the primary factor controlling the strength of granitic rocks (Tugrul and Zarif, 1999), with good correlation between compressive strength and the grain size. The fact that compressive strength increases as the grain size decreases has also been pointed out by Prikryl (2001).

A detailed petrographic description of the granites including grain size and mineralogical composition is outside the scope of the present work. Therefore, on the basis of the simplified petrographic description, it was decided to classify the fresh granites (values of porosity lower than 1.5%) in groups according to its dominant mineral, as well as the general grain size. The description of the defined groups and the corresponding selected granites is shown on Table 2.7.

Table 2.7 – Definition of groups for fresh granites

| Group | Granite |
|---|---|
| Biotite granites | BA, MC, RM, PLA |
| Two mina granites | PTA, GA |
| Fine to medium grained | PTA, GA, BA |
| Medium to coarse grained | MC, RM, PLA |

Figure 2.47a shows the mean values of the tensile strength and initial stiffness calculated for fine to medium and medium to coarse-grained granites. The grain size seems to influence the tensile strength and stiffness of the granites. Fine to medium-grained granites exhibit high values of tensile strength and are considerably stiffer than medium to coarse granites. This finding is in agreement with the results reported in the literature (Eberhardt *et al.*, 1999b; Tugrul and Zarif, 1999). In crystalline rocks, like granites, it is usual that the onset of the microcracking occurs at the weakest connection located at the grain boundaries. Longer grain boundaries associated to large size grains provide large number of weak planes that leads to the decrease on strength. The differences are not so evident with relation to the fracture energy, but there is a tendency for the coarser granites to consume higher energy than the fine to medium granites during the fracture process, see Figure 2.47b. The medium to coarse-grained granites are also the materials that exhibit higher values of ductility, see Figure 2.47b. The same tendency has been pointed out for concrete with distinct aggregate size (Tadesmir *et al.*, 1999; Yan *et al.*, 2001).

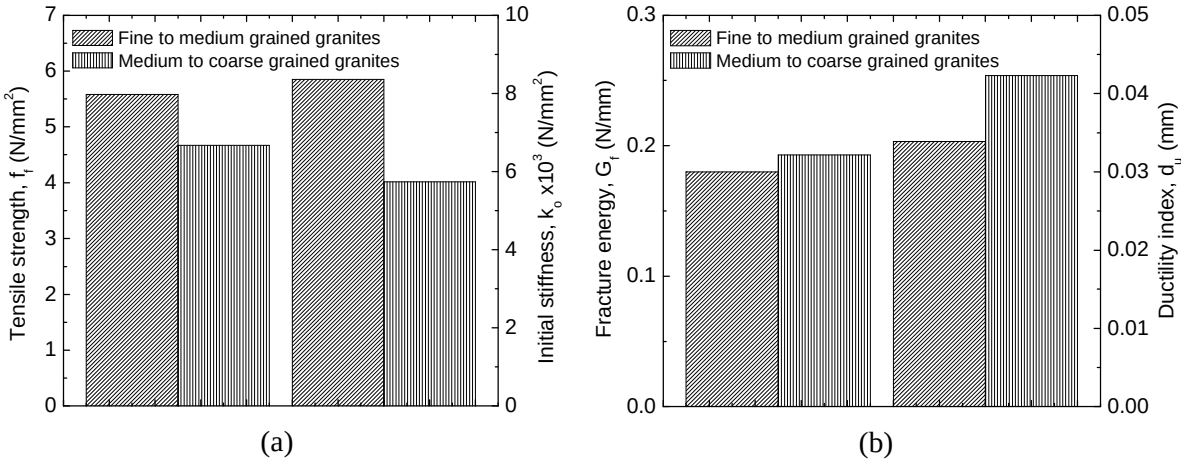


Figure 2.47 – Mechanical properties for the groups; (a) tensile strength and initial stiffness; (b) fracture energy and ductility index

As expected, higher values of the critical opening are found in medium to coarse-grained granites, which represents an additional indicator that ductility is influenced by the grain size, see Figure 2.48a. It should be also mentioned that porosity seems to be dependent on the grain size. As can be observed in the graphic of Figure 2.48a, porosity presents increasing values on medium to coarse-grained granites. The higher values of porosity on coarse-grained granites may be explained by the larger amount of microfissures on the grain interfaces. Finally, Figure 2.48b shows the values of the tensile strength for biotite granites and for the two mica granites. In spite of granite BA presenting clearly higher values than the two mica granites, other biotite granites, such as MC, RM and PLA, exhibit values rather close to the granites PTA and GA. The fact that MC, RM and PLA are coarse-grained and present high feldspar content, justifies such tensile strength reduction. As indicated by Tugrul and Zarif (1999), the abundance of easily cleavable minerals, such as feldspar, can lead to a strength reduction. Moreover, granite GA presents a very low value of porosity, which contributes to the increase of its tensile strength.

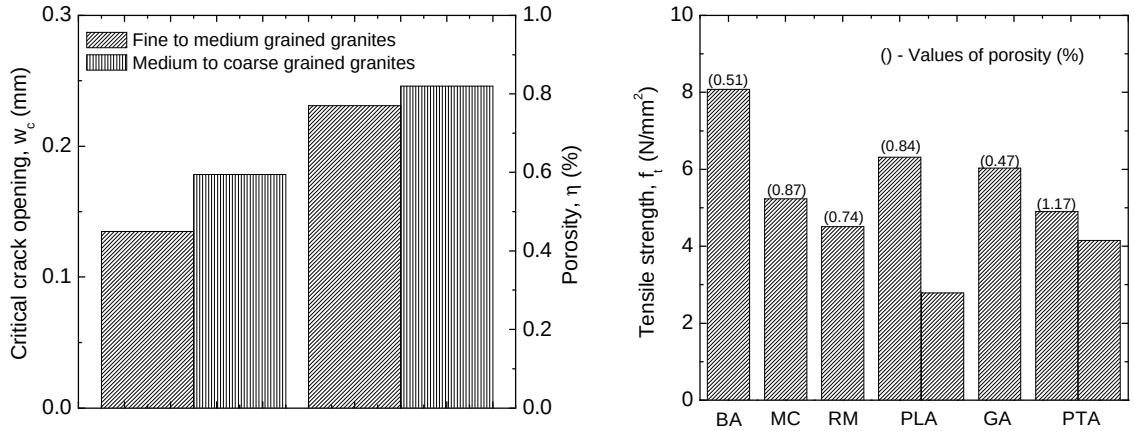


(a) (b)

Figure 2.48 – Physical and mechanical properties for the groups of granites; (a) influence of the grain size on the critical crack opening and on the porosity; (b) evaluation of the tensile strength for biotite granites and two mica granites

The higher values of the fracture energy can be interpreted by the large tortuosity of the fracture path induced by the grain boundary failures. In effect, in case of coarse-grained granites, the post-peak stress-transfer mechanism is usually established from the interface grain bridging. This mechanism is particularly evidenced in coarse-grained granites with large feldspar phenocrystals, such as in granites MC and PLA. Figure 2.49 displays some examples of failures where the fracture path follows the grain interfaces.

To sum up, in view of the other important aspects discussed above that contributes to the variation of the mechanical properties, it should be stressed that, for the granites under study, the mineralogic composition will not be the most important factor that explains the variation of the mechanical properties. For fresh granites, aspects related to the anisotropy, porosity level and the grain size seem to be more relevant.

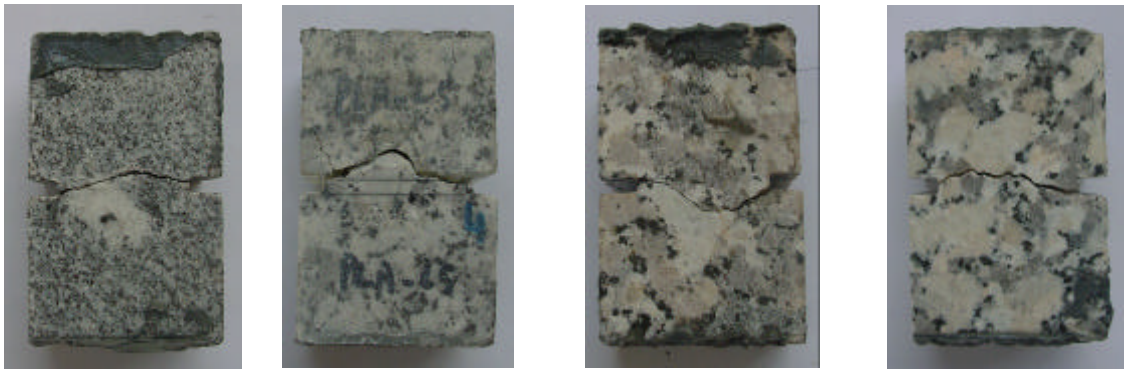

(a) (b) (c) (d)

Figure 2.49 – View of the fracture profiles; (a) granite BA; (b) granite PLA; (c), (d) granite MC

### 2.6.5 *Moisture content*

The mechanical behavior of rocks is substantially affected by the presence of water. The decrease of strength on saturated rocks can be attributed, on one hand, to the chemical deterioration of the cement binder and, on the other hand, to the increase of the pore and fissure water pressure (Goodman, 1989).

In the present work, only the granite MDB* is considered under two different moisture content, namely oven dry and saturated conditions. The main reason for this concerns the difficulty to conduct direct tensile tests under saturated conditions. When granites are saturated, there is no sufficient adhesion between the material and the glue that is needed to clamp the specimens to the steel platens. The results shown here address the direction perpendicular to the foliation plane, see Figure 2.50.

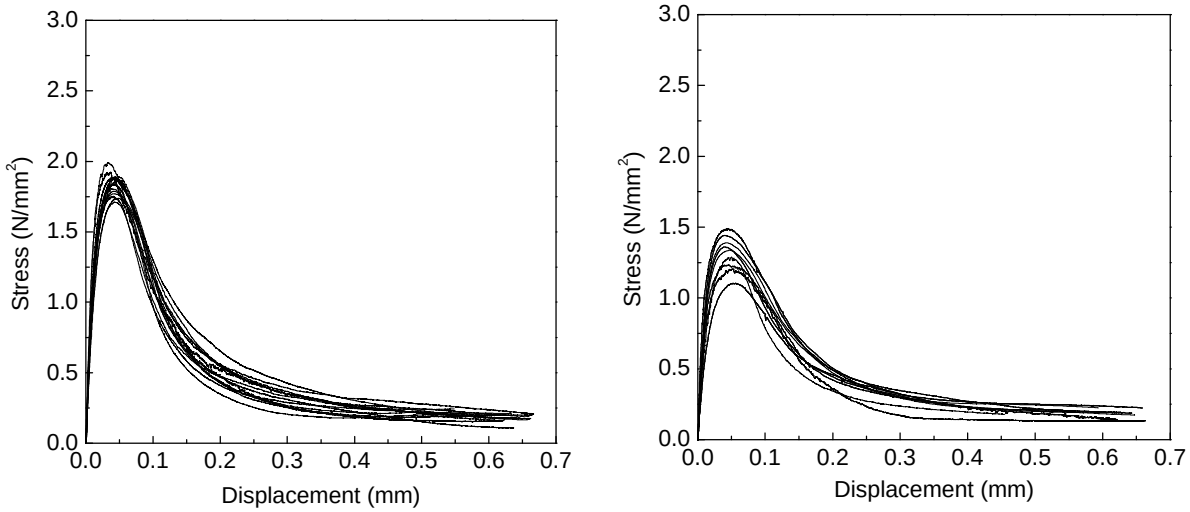


(a) (b)

Figure 2.50 – Stress-deformation diagram for granite MDB*; (a) dry conditions; (b) saturated conditions

By comparing the stress-displacement diagrams of granite MBD, it can be observed that moisture content influences clearly the tensile strength. In addition to a higher scatter, the average value of the tensile strength exhibits a decrease from 1.81N/mm$^2$ (dry specimens) up to 1.33N/mm$^2$ (saturated specimens), which corresponds to a decrease of about 36% from the oven dry specimens. Similar behavior was recorded for the initial modulus of elasticity, with a decrease of 32%. Regarding the fracture energy no significant differences were identified

between dry and saturated conditions. The reduction found is in agreement with the results indicated by Vasarhelyi (2003) for sandstones and by Feng *et al.* (2001) for granites. However, in the latter case, the decrease on the compressive strength of granites was only of about 24%.

A more detailed investigation of the influence of the moisture content on the mechanical behavior is needed in order to assess the differences between granites with distinct levels of porosity. In Chapter 3, more detailed results will be presented regarding the behavior of granites under uniaxial compression for saturated conditions.

## 2.7 Characterization of the fracture surfaces

In the tensile fracture, the transition process between micro and macrocracking states depends, on one hand, on the external applied load and, on the other hand, on the characteristics of the microstructure of the materials. In natural rocks, like granite, to which different petrographic characteristics are attributed, different interfacial mineral strengths and arrangements are expected to influence the macrocracking growth and, thus, the fracture properties, strength and fracture energy. The tensile fracture of granites with coarse grained internal structure and longer interfaces between the minerals that act as the weakest link and from which the onset of the microcracking takes place, generally leads to higher tortuosity of the fracture surfaces. In case of fine-grained granites with high strength cement matrix, the fracture surface tends to develop through minerals and smoother surfaces are achieved. Similar behavior is found in concrete where the tortuosity of the fractures surfaces is governed essentially by two aspects: the differential strength between aggregates and the cement-based matrix, and the different aggregate size. When the strength of the aggregates is higher than the cement matrix, the failure takes place in the interfaces around the inclusions. The opposite happens when the strength of the matrix prevails and cracking progress occurs through the aggregates leading to a more plane fracture surfaces and, therefore, to more brittle behavior. The increment of the aggregate size also increases the roughness of the fractures surfaces and the ductility (Sabir *et al.*, 1997; Tadesmir *et al.*, 1999; Rao and Prasad, 2002).

In general, artificial objects exhibit a smoothly curvilinear shape and can be analyzed by the Euclidean geometry. On the contrary, due to its rough nature and irregular geometry, natural objects, like mountains, clouds and even fractures, belong to a different spatial domain, the fractal geometry. It is largely accepted that the fracture surfaces of the heterogeneous quasi-brittle materials like rocks, concrete and ceramics, by its intrinsic internal disorder due to different constituent minerals or aggregates, pores, microcraks and interfaces, are well described by fractal geometry (Chiaia *et al.*, 1998; Bobji *et al.*, 1999; Saouma and Barton, 1994; Carpinteri and Chiaia, 1995; Wang and Diamond, 2001). The fractal structures are characterized by its similarity under different length scales, i.e., they appear identical to any degree of magnification. This property implies that any two subsequent points of the surface are not completely uncorrelated, being the degree of correlation measured by the fractal dimension $D$. It should be mentioned that the higher heterogeneity and tortuosity of the fracture surface is characterized by higher values of fractal dimension.

Some recent studies have indicated that as far as fracture energy is concerned the fracture path plays a major role. Although a clear or a strong correlation between fractal dimension and fracture energy has not been found, some micro-structural aspects of the fracture surfaces could be explained by different fractal dimension values (Chiaia *et al.*, 1998; Chiaia *et al.*,

1997; Addison *et al.*, 1999). The fractal character of the fracture energy is highlighted by Yan *et al.* (2001), which pointed out a linear positive correlation between the fractal dimension and the fracture energy, meaning that a higher amount of energy is needed for the development of the fracture process on more complex surfaces. In addition to this statement, it was found that fractal dimension depends on the aggregate size: fractal dimension increases with the increase of the maximum aggregate size. Issa *et al.* (2003) found a positive linear correlation between fractal dimension and fracture toughness measured over 100 wedge-splitting specimens cast with four different maximum aggregate sizes. In addition, the dependence of the roughness surface on the fractal dimension was also evidenced, as a rougher surface corresponds to a higher fractal dimension.

In this study, an investigation is carried out aiming at finding a correlation for granites, between roughness of the fracture surface and characteristic mechanical properties of the fracture process. In addition, a study on the variation of roughness parameters as function of petrographical characteristics, such as the weathering state and the internal structure, with preferred mineral orientation is also performed. To attain such aim, a 3D topographical inspection system is used to capture fracture surface texture profiles at various locations of the surface. Afterwards, the statistical characterization of the fracture surfaces is carried out in terms of classical quantities used in the characterization of the topography of surfaces, average roughness and root-mean square roughness (RMS). Finally, correlations between fracture surface parameters and mechanical fracture parameters are discussed.

### 2.7.1 *Qualitative analysis of the fracture surfaces*

The first assumption that the fracture energy is related to the fracture path comes from the observation of the fracture surfaces obtained for both loading directions, regarding e.g. granites PLA and PLA* and, see Figure 2.51. For this type of granite a much more tortuous fracture surface is observed in the direction parallel to the rift plane of the applied load, when compared with the rather flat surface obtained in the perpendicular direction. The internal structure with the directional arrangement of the coarse feldspar phenocrystals is the reason for such different behavior.


Figure 2.51 – Fracture surfaces; (a) granite PLA loaded in the direction parallel to the rift plane; (b) granite PLA loaded in the direction perpendicular to the rift plane; (c) granite PLA* loaded in the direction parallel to the rift plane; (d) granite PLA* loaded in the direction perpendicular to the rift plane

It should be mentioned that the location of the notches in the specimens that were used in the mechanical characterization imposes that fracture plane occurs almost perpendicular to the

applied load. This fact implies that a different fracture features occurs for both loading directions regarding the preferential alignment of the coarse feldspar phenocrystals. As it was referred before, the feldspar becomes visible predominantly at the subparallel direction to the rift plan. This means that the fracture of this mineral according to its direction of alignment leads to a much more tortuous surface, which implies as requirement a higher amount of energy to produce and develop the fracture process, see Figure 2.52. When the direction of loading is perpendicular to the rift plane, the splitting of the two half becomes easier considering that the cleavage of this mineral according to its preferred orientation occurs with less absorption of energy.

Figure 2.52 – Fracture profiles for granites PLA and PLA* in the parallel direction to the rift plane

Although the foliation degree exhibited by some granitic rocks (associated to the particular alignment of the biotite and muscovite minerals) is not extremely remarkable, differences are found on roughness of the respective fracture surfaces. Furthermore, in weathered granites, as the mineral interfaces becomes weaker, it is reasonable that the fracture growth occurs along these, leading to more tortuous fracture surfaces and, thus, higher values of the fracture roughness should be found.

### 2.7.2 *Inspection of the fracture surface - equipment and procedure*

The inspection of the fracture surfaces of the specimens was performed by means of an automated system of 3D topographical inspection of rough surfaces developed at the Laboratory of Microtopography of the Physics Department of University of Minho (Costa, 1996; Costa and Pinho, 2001).

The system is based on an active optical triangulation method with mechanical sample scanning, see Figure 2.53. This microtop system uses, in its usual configuration, a geometry with oblique incidence and normal observation. In order to cope with the requirements presented by the particular type of granite samples, characterized by relatively large depths up to several millimeters with steep relief structures, the geometry was changed to normal incidence with oblique observation at low angles, so that the shadowing can be reduced. A high depth of field microscope objective was used in the observation lever of the system.

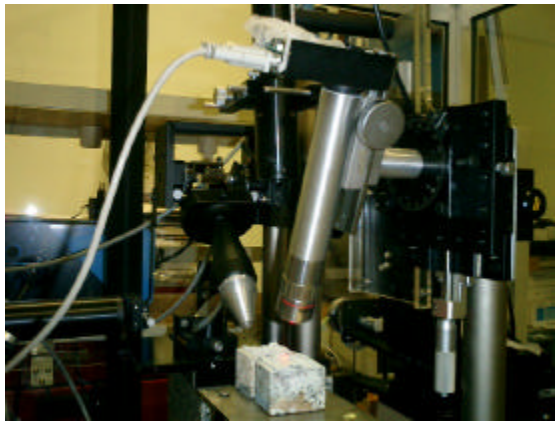

Figure 2.53 – 3D surface inspection system

The surface inspection was made on one of the cracked halves of six to height specimens, per granite type, see Figure 2.54a. In order to facilitate the incidence of the laser and the measurements of the height differences at each scanned point, a white coat was applied on the fracture surfaces of the specimens to be measured, see Figure 2.54a.

(a)

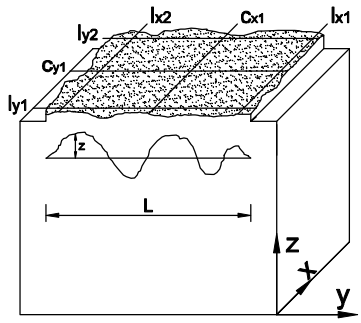


(b)

Figure 2.54 – Specimens and definition of the coordinate system for acquisition; (a) preparation of the specimens for inspection; (b) definition of the acquired profiles

According to Figure 2.54b, three profiles were taken in each direction of the fracture surface, being two of them lateral and the one central. The profile points were recorded every 10μm along the path with a resolution of 0.3μm in height. As the surface parameters are scale dependent (Avdelidis *et al.*, 2004; Fardin *et al.*, 2004), the measurement length of the profiles should be the same for all specimens, so that the results are comparable.

### 2.7.3 *Roughness profile analysis*

The first step of the fracture surface characterization is based on the determination of the standard amplitude parameters related to entire profiles. The average roughness, $r_a$, and the root-mean square roughness (RMS), $r_q$, are given by the following expressions (Whitehouse, 1994):

$$r_a = \frac{1}{L}\int_0^L |z(x)|\, dx \tag{2.7}$$

$$r_q = \sqrt{\frac{1}{L}\int_0^L z^2(x)dx}\,, \tag{2.8}$$

where $z$ ($x$) is the center-line profile and $L$ is the length of the projected profile, see Figure 2.54b. The mean values of these parameters were computed taking into account the values obtained for the six profiles defined for each specimen. The average roughness parameters for each granite type were then obtained as the average of the measured specimens.

The roughness parameters for the total profile calculated according to eqs. (2.7, 2.8), designated by $P_a$ and $P_q$, are well correlated. As displayed in Figure 2.55, the mean-root square roughness, $P_q$, presents systematically higher values than the mean roughness, $P_a$. The obtained linear relation is in agreement with results indicated by Guinea *et al.* (2002) in the characterization of fracture surfaces of concrete.

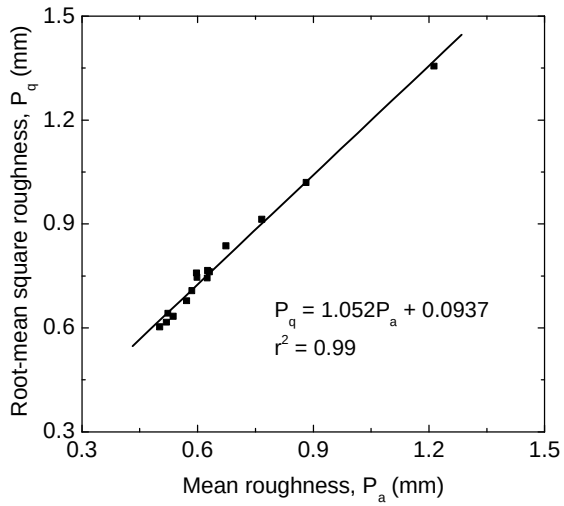


Figure 2.55 – Relation between total root-mean square (RMS), $P_q$, and the average total roughness, $P_a$

Figure 2.56a gives the relation between the average total roughness $P_a$ and the fracture energy. The results for the complete set of lithotypes is somewhat scattered. However, it is clear that the three granites MC, PLA* and PLA deviate from a general trend. In particular, the value of the average roughness obtained for granite MC is abnormally high, when comparing with the other granites. The reason for this is the coarse feldspar phenocrystals, that seems to present some degree of cleavage, as well as the clusters of quartz that are randomly spread on the fracture surface. Very high values of the roughness are also found for the granites PLA and PLA* in the parallel direction to the rift plane. If these values are excluded of the data, a reasonable linear correlation is achieved for the other granite results, see Figure 2.56b.

The surface profile texture can be understood as a composition of structures with different ranges of irregularities and irregularities distribution, or a range of frequency components. The high frequency short wavelength components, corresponding to the finest irregularities on a surface, are repeated with low spacing and are identified as the roughness or microroughness (Costa, 1996). The low frequencies or long wave components correspond to smooth changes in the profile and represent the longer spatial wavelength features of the surface, being associated with the waviness or macroroughness, (Costa, 1996). Although often both regimes are considered together in the characterization of the texture of the

surfaces, it is advisable to separate them, since each regime can be associated to different mechanism.

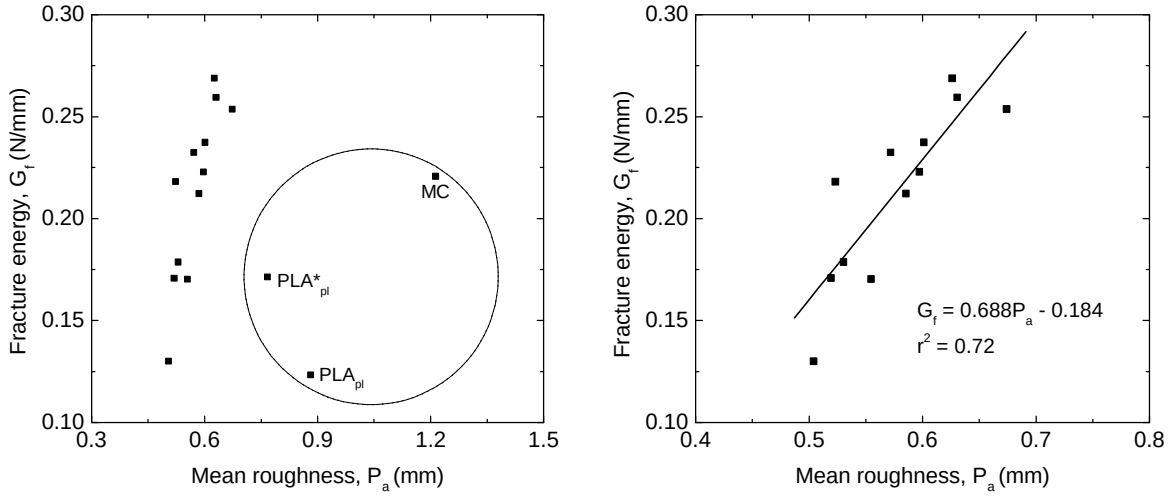


Figure 2.56 – Relation between mean roughness, $P_a$, and fracture energy, $G_f$: (a) full set of tests; (b) selected samples, without granites MC and PLA

Figure 2.57 illustrates a typical surface profile, with the waviness and the roughness regimes presented separately. It can be seen that the waviness assumes an important role in the final geometry of the texture profile and to some extent commands its relief. Obviously, the sum of the waviness and the roughness yields to the texture profile.

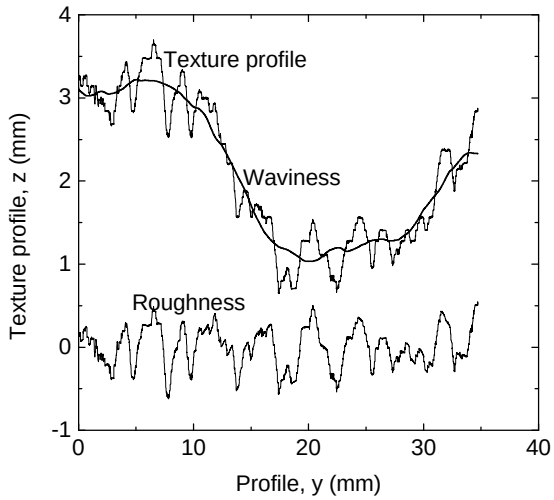


Figure 2.57 – Surface texture profile and the different roughness regimes: waviness and roughness

The identification of these distinct roughness regimes on the texture profiles obtained for the granite specimens leads to the need of clarification of the mechanisms that may lead to it. In addition, it is important to understand how the different components of the texture profile are correlated with the variation in the fracture parameters such as the fracture energy. The definition of the appropriate frequency components in order to set apart the waviness from roughness implies filtering of the texture profile. The description of the adopted filtering procedure for the texture profiles is given in Appendix B.

### 2.7.4 *Texture parameters*

After filtering the original texture profiles, the amplitude parameters regarding the waviness, $W_a$ and $W_q$, and the roughness, $R_a$ and $R_q$, were calculated according to eqs. (2.7, 2.8) applied to the appropriate waviness and roughness profiles. The mean values of these parameters as well as the coefficients of variation inside brackets (%) corresponding to the granite types are shown in Table 2.8. For all granites the values of the average roughness, $R_a$, is lower than the values of the root mean square of the roughness, $R_q$, which is characteristic of rough surfaces. The values of the average surface waviness are always substantially higher than the values obtained for the roughness. This indicates that the longer space wavelength features assume an important contribution to the total texture profile surface.

Table 2.8 – Mean values of the roughness parameters

| Granite | $R_a$ (mm) | $R_q$ (mm) | $W_a$ (mm) | $W_q$ (mm) |
|---|---|---|---|---|
| BA | 0.179 (13.0) | 0.236 (14.1) | 0.547 (28.0) | 0.630 (26.0) |
| GA | 0.159 (15.6) | 0.207 (14.1) | 0.415 (23.1) | 0.494 (23.3) |
| GA* | 0.190 (7.1) | 0.252 (11.0) | 0.535 (22.4) | 0.537 (22.3) |
| RM | Not measured | Not measured | Not measured | Not measured |
| MC | 0.243 (18.7) | 0.323 (20.3) | 1.105 (21.8) | 1.235 (18.7) |
| AF ⊥ foliation | Not measured | Not measured | Not measured | Not measured |
| AF // foliation | 0.170 (10.4) | 0.235 (12.2) | 0.416 (22.2) | 0.495(21.7) |
| MDB ⊥ foliation | 0.232 (9.7) | 0.309 (9.2) | 0.595 (20.1) | 0.701 (20.1) |
| MDB // foliation | 0.204 (6.4) | 0.273 (7.4) | 0.516 (21.3) | 0.605 (20.1) |
| MDB* ⊥ foliation | Not measured | Not measured | Not measured | Not measured |
| MDB* // foliation | Not measured | Not measured | Not measured | Not measured |
| PTA // foliation | 0.157 (11.4) | 0.202 (11.5) | 0.507 (19.1) | 0.593 (18.8) |
| PTA ⊥ foliation | 0.165 (6.0) | 0.216 (7.5) | 0.429 (33.6) | 0.504 (33.4) |
| PTA* ⊥ rift plan | 0.209 (20.7) | 0.284 (14.6) | 0.483 (19.9) | 0.557 (17.8) |
| PTA* // rift plan | 0.198 (10.9) | 0.261 (14.5) | 0.519 (13.7) | 0.601 (12.8) |
| PLA ⊥ rift plan | 0.155 (14.4) | 0.221 (13.5) | 0.477 (24.7) | 0.555 (23.1) |
| PLA // rift plan | 0.212 (10.9) | 0.272 (16.5) | 0.733 (22.1) | 0.859 (20.4) |
| PLA* ⊥ rift plan | 0.176 (8.6) | 0.235 (9.3) | 0.515 (16.5) | 0.608 (15.4) |
| PLA* // rift plan | 0.244 (9.8) | 0.322 (10.4) | 0.622 (14.9) | 0.728 (15.6) |

#### 2.7.4.1 Analysis of the influence of weathering and grain size on the texture parameters

The analysis of the mean values of the roughness, $R_a$ and $R_q$, regarding the fresh and weathered granites, namely GA, GA*, PTA, PTA*, PLA and PLA*, indicates that weathered granites present always higher values, see Figure 2.58a. This fact can be explained by the alteration of the internal microstructure activated by the weathering effects. In fact, weathering not only affects the strength of the minerals, but also leads to the appearance of pores and voids that result in significant increase on the porosity. It is understandable, therefore, that if the macrocrack develops around weakest mineral boundaries, a more tortuous fracture surface is obtained and higher values of the roughness parameters are found. This seems to indicate that the variation in the roughness parameters can explain with more accuracy the structural changes in the microstructure of the weathered granites. However, the difference detected in the roughness parameters between fresh and weathered granites is not followed by the waviness parameters. The mean values of $W_a$ and $W_q$ are higher for granite GA* than for granite GA, but the same trend does not occur for the granites PLA and PTA. This seems to indicate that the roughness parameters are more important than the waviness

parameters for the fracture energy and the effect of weathering, due to weakness of the material, can reduce the amplitude of the crack.

A simplified grain size mineral analysis can be performed on the basis of the groups considered in Section 2.6.4. Thus, the medium to coarse granites exhibit larger values of roughness parameters (around 20% higher), $R_a$ and $R_q$, and waviness parameters (around 35% higher), $W_a$ and $W_q$, in comparison with fine to medium grained granites, see Figure 2.58b. Therefore, the increase of the grain size of the granites implies a marked increase on all the calculated roughness parameters.

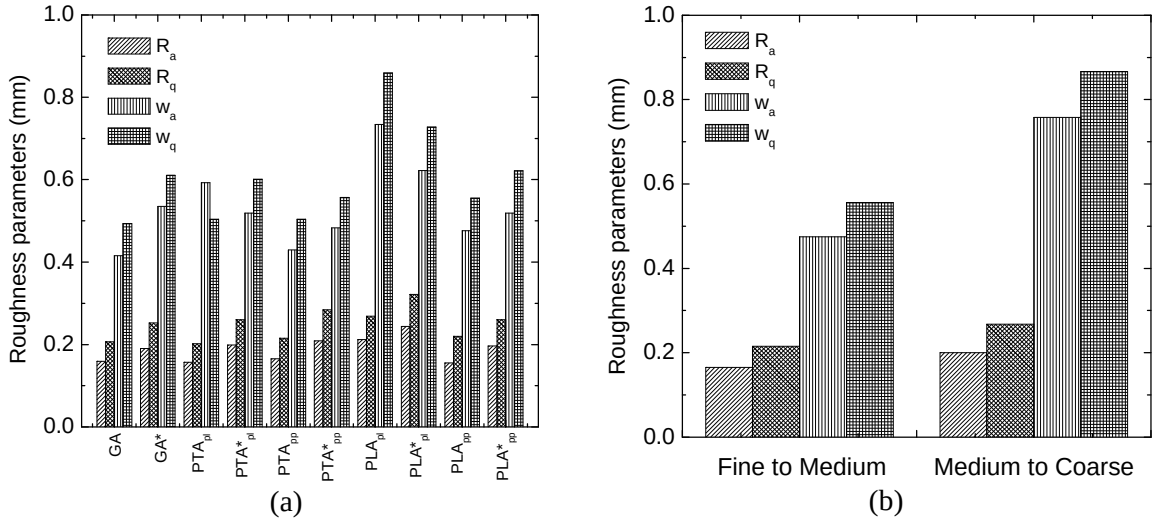


Figure 2.58 – Roughness parameters; (a) fresh vs. weathered granites; (b) effect of the grain size

The difference obtained for the roughness parameters between the two groups of granites is explained by the intrinsic microstructure of medium to coarse granites. In effect, the failure occurs in the interfacial zone of the different minerals, with higher surface contact, or through the minerals, with larger grain size. In both cases, the texture surface always presents higher tortuosity. It is noted that part of the coarse grained granites, such as PLA and MC, have a porphyritic texture, which takes a major relevance on the fracture surface parameters, see Figure 2.59.

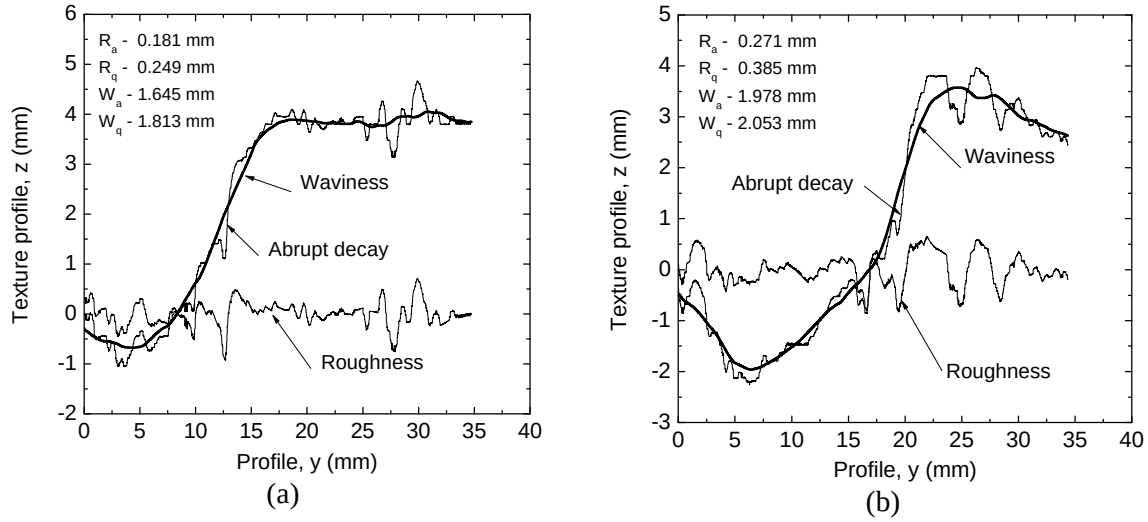


Figure 2.59 – Examples of surface texture profiles; (a) granite PLA*; (b) granite MC

The characteristic orientation from the cleavage of the feldspar phenocrystals of these granites leads to the increase of the roughness and waviness parameters. As the cleavages are local, its influence seems to be more importance in the waviness profile and consequently in the waviness parameters. This aspect confirms the major role of the waviness texture on the total profile in case of the granites PLA, PLA* and MC. In Figure 2.60, some examples of cleavages in the feldspar phenocrystals are shown.

By comparing the values of the waviness, $W_a$, and the total roughness, $P_a$, obtained for the granite PLA tested in the parallel direction to the rift plane and specially for the granite MC, it can be seen that the total profile is markedly characterized by the long wave components.

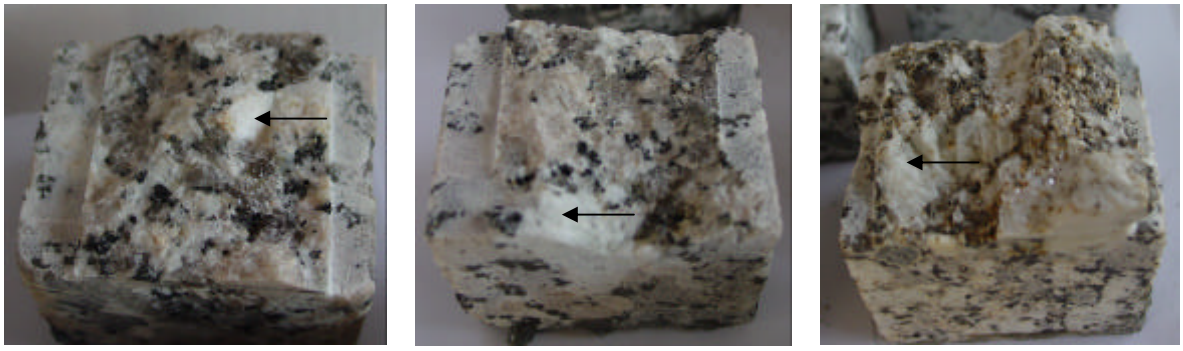

Figure 2.60 – View of some fracture surfaces with identification of fracture cleavage of feldspar mineral

2.7.4.2 Analysis of the influence of the internal structure on the texture parameters

The values of the roughness parameters, $R_a$ and $R_q$, depend on the direction of the surface fracture propagation. For granites MDB and PTA*, the roughness presents lower values when the fracture surface develops in the parallel direction to the perceptible foliation plan. The interval of variation is, however, relatively small between 5 and 10%, see Table 2.8 and Figure 2.58a. This feature seems to be in disagreement with the expected theoretical flat surface in the parallel plane to the foliation due to the natural alignment of the mica minerals. As the foliation plan can act as a large flaw, which induces the onset of the microcracking, the fracture surface should be approximately flat when the applied load is perpendicular to the foliation. This aspect would be fully verified if the foliation plan is clearly defined, which is the case of fresh PTA granite. Indeed, the degree of planar foliation exhibited by MDB and PTA* granites is not penetrative and consequently it will not be very significant. This can be the reason for the unexpected higher values of the roughness parameters achieved for the perpendicular fracture surfaces. Note, however, that in case of granites PTA and PTA*, the values of the waviness present higher values in the parallel direction to the foliation/rift planes.

A more clear structural deviation on the texture parameters was found for the PLA and PLA* granites. All roughness parameters depend substantially on the direction as fracture surface propagates, see Figure 2.58a. Both roughness and the waviness parameters exhibit higher values in the parallel direction to the rift plane. This fact numerically confirms the visual evidence that more tortuous fracture surfaces are generated in the perpendicular direction to the rift plan. Similarly to the anisotropy exhibited in terms of the fracture parameters, this material also presents large anisotropy regarding the roughness parameters.

The mechanical behavior of this type of granite seems to be essentially governed by the structural arrangement of the feldspar phenocrystals and by its interfacial bond with the other minerals.

2.7.4.3 Dependence of the fracture parameters on the surface texture parameters

The mean values of the fracture energy were plotted against the mean values of the roughness and the waviness. Figure 2.61a shows that there is a linear correlation between the fracture energy and the mean values of the roughness, $R_a$. The energy consumed in the crack opening process depends on the tortuosity of the fracture path that is essentially related to the finest features of the fracture surface texture. The increase of the microroughness means the increase of the consumed energy. This finding is in agreement with other results reported in literature (Sabir and Asili, 1997; Saouma and Barton, 1994; Yan *et al.*, 2001; Issa *et al.*, 2003; Santos and Rodrigues, 2003). Nevertheless, it should be stressed that in the present work the fracture surfaces characterization is performed only based on the statistical average roughness. Note that the fractal dimension is also a measure of the tortuosity of the fracture surfaces and is essentially related to the high frequency components of the surface profiles.

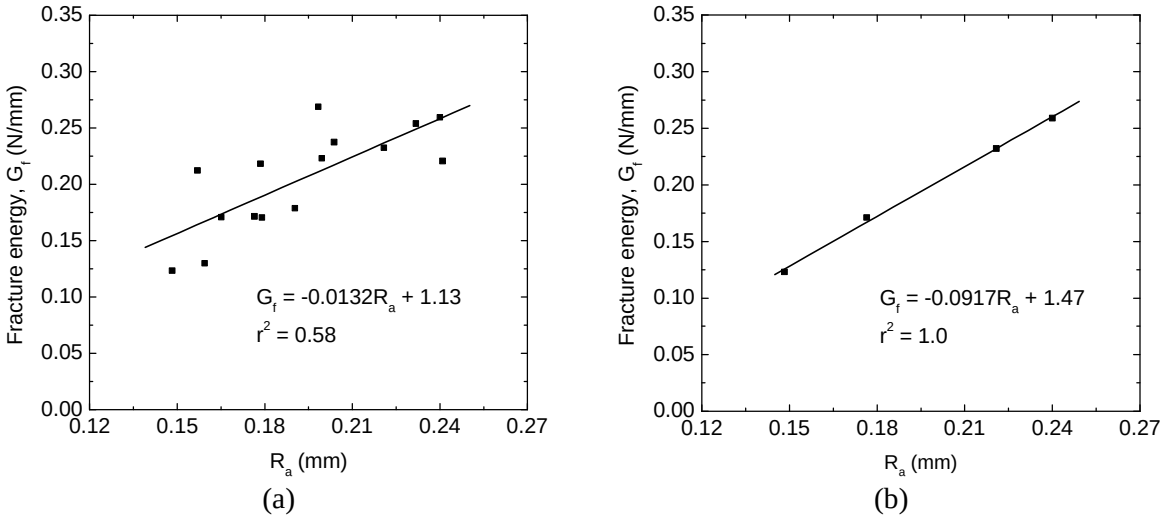


Figure 2.61 – Relation between texture properties and fracture parameters; (a) roughness vs. fracture energy; (b) roughness vs. fracture energy for granites PLA and PLA*

When the analysis is restricted to the granites PLA and PLA*, whose simple visual inspection of the fracture surfaces led to the present investigation, the linear fit is excellent, see Figure 2.61b. This relation confirms numerically the qualitative assumption that the fracture energy is largely influenced by the internal structure of this heterogeneous type of granite.

Figure 2.62a shows that no correlation was found between waviness parameter and the fracture energy. However, if the values of the waviness obtained for the granites MC and PLA in the direction parallel to the rift plane are excluded, a trend for the values of fracture energy increase with the increase of the waviness is verified. This trend is much less significant than the relation found for the mean roughness, $R_a$. Furthermore, the relation between the texture parameters and the tension strength was also analyzed. From Figure 2.62b, it can be observed that no correlation was found between the tensile strength and the roughness parameters. A similar conclusion was achieved as far as the critical crack opening

is concerned. The high anisotropy exhibited by the granites PLA and PLA* can be pointed out as one reason that will disturb any possible relation.

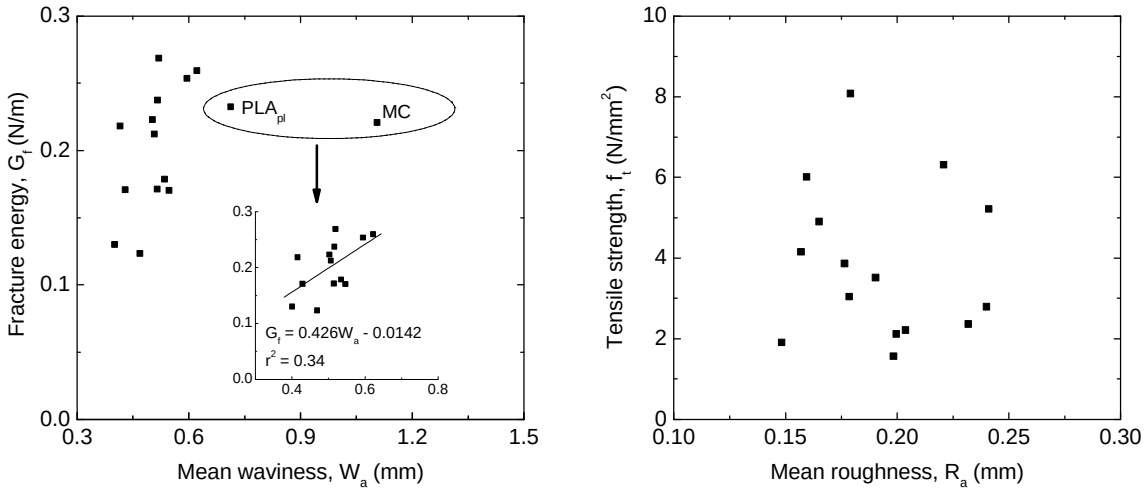


(a) (b)

Figure 2.62 – Relation between texture properties and fracture parameters; (a) average waviness vs. fracture energy; (b) average roughness vs. tensile strength

The aspects that can be on the basis of different roughness features of the fracture surface are accordingly discussed in Appendix C.

To sum up, the performed analysis indicated that the fracture energy can be roughly predicted or estimated from the roughness of the fracture surface through the expression given in Figure 2.61a, but no information can, however, be obtained about the roughness parameter $R_a$ and $R_q$ from the knowledge of the tensile strength.

## 2.8 Concluding remarks

A comprehensive mechanical characterization of different granites with different petrographic characteristics was carried out using direct tensile tests. The influence of different factors on the tensile behavior of granites was evaluated, namely the shape and grain size, the internal structure, including the planar foliation and heterogeneity, the weathering state and the moisture content.

From the results, the following aspects can be highlighted:

- Attainment of the complete stress-displacement diagrams for all granites was possible through the use of a suitable testing equipment and control system. This allowed the determination of the fracture parameters, i.e. tensile strength, $f_t$, fracture energy, $G_f$, and critical crack opening, $w_c$.
- A set of statistical correlations between the fracture parameters was established, which allows a better understanding of the pre-peak and post-peak shape of the stress-displacement diagrams.
- Noticeable distinct stress-displacement diagrams and therefore different fracture parameters were achieved as a function of the internal structure (planar foliation and lineation, flow structure and orientation of the quarry planes). Low, medium and high degrees of anisotropy with relation to the fracture parameters were obtained.

- In general, higher strength and stiffer granites are attributed to fine to medium grained granites, whereas higher values of fracture energy and ductility occur with medium to coarse granites.
- A clear reduction of strength and pre-peak deformation characteristics occur for weathered granites, in comparison with fresh granites. However, larger fracture energy and higher ductility are features of weathered granites.
- A clear reduction of the tensile strength was also found for saturated conditions, in comparison with oven dry granites.

In order to evaluate the roughness of the fracture surfaces, a three-dimensional inspection was performed by means of a 3D topographic inspection system, which enabled the definition of the texture profiles. The characterization of the fracture surfaces was performed on the basis of the classical parameters, mean and mean square roughness. A filtering procedure was applied to the total profiles so that the micro (roughness) and macro features (waviness) of the fracture surface could be highlighted. A significant achievement of this task was the proposed correlation between roughness and fracture energy.

# 3. EXPERIMENTAL INVESTIGATION OF GRANITES UNDER UNIAXIAL COMPRESSIVE LOADING

## 3.1 Introduction

In general, concrete structures and rock masses are mainly subjected to compressive loading. This observation was on the basis of several theoretical, numerical and experimental studies performed during decades in order to clarify the fracture mechanisms that better describe the compressive behavior of these materials. The pioneer work in the scope of fracture mechanics was carried out by Griffith (1920) (initially used to explain the differences found between the theoretical and experimental tensile strength of brittle materials), which postulated that brittle fracture initiated through tensile stress concentrations at the tips of small, thin cracks randomly distributed in the isotropic material. According to Lajtai *et al*. (1990), the Griffith theory or at least the basic assumption that fracture starts from flaws is fundamental to all investigations in quasi-brittle fracture. Several other studies have followed in order to obtain a better insight on the fracture behavior of brittle materials regarding the mechanisms of crack initiation, crack interaction, propagation and coalescence (Kranz, 1979; Lajtai *et al*., 1990; Wang and Shrive, 1995; Carpinteri *et al*., 1996; Bobet and Einstein, 1998; Tang and Kou, 1998; Eberhardt *et al*., 1998; Li and Lajtai, 1998; Li *et al*., 1998). An issue commonly accepted in the fracture process under uniaxial compression is that nucleation, growth, interaction and coalescence of microcraks leads to macroscopic failure of rocks. Besides, in general, the fracture forming under uniaxial compression conditions, before attaining the peak load, is a tensile fracture. Therefore, the propagation of fracture occurs in the direction parallel to the maximum principal stress. It should be stressed that several experimental studies have been carried out recently in order to characterize the microcracking process of granites under compression (Lajtai, 1998; Eberhardt *et al*., 1999a; Seo *et al*., 2002). The stress levels from which the microcracking initiates, as well as its propagation and interaction, were accurately defined. In addition, it was stated that intragranular and interfacial grain interfaces are the sources of initiation and propagation of microcracking.

Although some experimental studies have been carried out on strain localization detection in concrete and rocks (Vonk, 1993; Haied *et al*., 2000; Bésuelle *et al*., 2000), and apart from the extensive experimental characterization of concrete under multiaxial loading conditions carried out by Van Mier (1984), few information on the experimental characterization on the softening behavior of rocks, namely granites, is available in literature. The obtainment of the complete stress-strain diagrams that comprise the ascending and the softening behavior is practically non-existent in case of granites, namely high strength granites. The lack of information about the softening behavior of this type of material is due to several aspects. On one hand, the softening characterization under compression of plain or reinforced concrete has received the main attention from the Civil Engineering research community due to the role taken in new structures. On the other hand, the obtainment of the softening behavior of very brittle materials like high strength concrete or hard rocks is still a challenge due to difficulties related to the testing equipment and testing control technique that have to be used to achieve a stable fracture process (Jansen *et al*., 1995; Jansen and Shah, 1997; Hudson and Harrison, 1998; Fairshurst and Hudson, 1999). According to these authors, high strength granites, which exhibit snap-back behavior, are classified as class II and low strength granites are classified as class I. This classification gives an idea of the brittleness of the material.

Some other aspects, related to the shape and size of the specimens, and to the boundary conditions have to be carefully taken into account so that reliable results can be achieved (Kotsovos, 1983; Torrenti *et al*., 1993)

The main goal of the present research is the definition of the complete stress-strain diagrams of granites. For this purpose, a campaign of uniaxial compression tests was carried out on selected granite lithotypes. To accomplish this, a specific device was designed so that circunferential displacement control can be used. The elastic properties, namely modulus of elasticity and Poisson's ratio, are derived from the pre-peak diagrams. For all granites, the characterization of the pre-peak fracture process is analyzed by means of the values of the crack initiation stress and of the crack damage stress. Moreover, strain localization and softening characterization of granites are evaluated through the descending branch and post-peak diagrams. Values of the pre and post-peak fracture energies are obtained and represent an additional measure of the compression fracture process.

The factors that affect the tensile behavior of granites (see Chapter 2), such as planar anisotropy (foliation, flow structures and rift plane), weathering effects and, to lower degree, the mineralogic composition are also analyzed in compression. The relation between the elastic and fracture properties in compression and the physical properties, measured in compressive specimens, is investigated through a set of statistical correlations based on the experimental data.

It should be stressed that the significance of this study is the gathering of experimental data required as input data in advanced nonlinear numerical analysis of structural members of ancient structures where the granite plays the central role, together with full characterization of Portuguese lithotypes.

## 3.2 Geometry, specimens, equipment and test procedure

Some changes had to be made to the specifications described in the ISRM suggested methods (1981c) and in ASTM D2938 (1986) standard to obtain the complete stress-strain curve in compression and the modulus of elasticity (Young's modulus). Nevertheless, the shape and geometry of the specimens, the preparation of the specimens, measurement devices and test procedures were defined according to these international standards. A more detailed description of the experimental program is performed next.

### 3.2.1 *Geometry and shape of the specimens*

The specimens to be tested under uniaxial compression were prepared in accordance with ISRM suggested methods (1981c) and ASTM D2938 (1986) standard. According to the recommendations, the test specimens shall be right circular cylinders having a height to diameter ratio between 2.0 and 3.0 and a diameter of not less than approximately 50mm. In addition, the diameter shall be at least 10 or 20 times the largest grain in the rock microstructure. The restriction for the height to diameter ratio is related to the influence of the boundary effects. The restraint to the lateral expansion of the specimen conferred by the boundary platens leads to changes in the stress field around the ends of the specimen with the presence of compression lateral forces, which can significantly influence the compression strength. This effect is particularly noticeable when squat specimens are used in the compression tests. The reduction or even the vanishing of this effect occurs when a perfect uniaxial uniform stress field can be established in the central zone of the specimen, which is

accomplished for the dimensions aforementioned. The size effect originated by the lateral restraint due to the boundary conditions on the compressive strength was early detected and empirical relations for the compression strength as a function of height to diameter ratio were presented, see Hudson and Harrison (1998). Hawkes and Mellor (1970) presented curves for several types of rocks, including granites, from where it is possible to conclude that only for the above mentioned height to diameter ratios the compression strength is independent of the size.

Besides the shape effects, some recent experimental and theoretical studies have revealed that quasi-brittle materials that exhibit softening behavior, like concrete and rock, present size effect under compressive loads due to localization of the cracking path similarly to what occurs in tensile tests (Van Mier, 1984; Vonk, 1993; Bazant and Xiang, 1997; Pan *et al*., 2002). Besides, size effects can be attributed to the fact that specimens of larger size contain a higher amount of microcracks and thus larger likelihood of existence of severe flaws, which acts as the weakest link, leading to the reduction of the compression strength (Hudson and Harrison, 1998; Leal Gomes, 2000).

In spite of the size effects not being addressed here, it is important to refer that due to the limitations of the vertical loading actuator existing at the laboratory, a diameter of 75mm was adopted for all specimens. The length to diameter ratio was slightly higher than 2.0. If, in general, such dimensions are clearly sufficient to be in agreement with the above recommendations, for coarse-grained granites that exhibit porphyritic internal texture, the diameter is smaller than 10 times the largest grain.

In the preparation of the specimens, special care was taken to ensure parallel ends and perpendicular to the longitudinal axis. In addition, the specimen ends were suitably ground so that a smooth surface could be obtained. The diameter was calculated as the average value of three measures carried out at mid height and close to the top and the bottom of the specimen. The height was obtained as the average value of four measures carried out at points separated by an angle of 90º.

In order to assure the same moisture conditions for all granites, the specimens were oven dried and placed in environment laboratory conditions. Following the IRSM recommendations (1981) and repeating the procedure used for the direct tensile tests, some types of granites were also tested under saturated conditions in order to evaluate the strength and stiffness variations induced by the moisture content. The samples were saturated by water immersion in a vacuum of less than 800Pa for a period of two hours.

### 3.2.2 *Test equipment and control system*

As mentioned above, the main goal of the present compression tests campaign is the characterization of the full compressive behavior of all types of granites. From the stress-strain diagrams, it will be possible to derive the pre-peak behavior, as well as the post-peak descending branch features of the compressive behavior of the granites.

The testing equipment and the control system represent the major factors for a successful compression test conducted on stiff rocks, like granites. The stiffness of the testing machine, including loading platens, hydraulic system and the frame plays the central role, when the behavior beyond the peak load is required. Nevertheless, the systematic acquisition of the complete stress-strain diagram for rocks was only possible by introducing servo-controlled

machines, where the closed-loop control is available, as achieved firstly in the 1960s, see Hudson and Harrison (1998).

Moreover, the choice of the internal variable that makes the controlled failure process in uniaxial compression possible is not straightforward. Generally, in uniaxial compression tests, three feedback variables can be selected, namely the compressive uniaxial load, the uniaxial vertical displacement and the circumferential or lateral displacement. Due to the explosive failures originated by the axial load control, this control technique should be avoided and the displacement control is preferred. The vertical displacement is appropriate to obtain the softening behavior of soft rocks or soils but, for stiff rocks like high strength granites, this type of feedback control leads also to uncontrolled compressive failures. This behavior results from the fact that the axial strain does not increase monotonically and hence can not be used as the feedback signal. From the characteristic compressive behavior of rocks or concrete, which is marked by lateral expansion, it is clear that the lateral or circumferential displacement monotonically increases. Therefore, it can be taken as the most appropriate and sensitive feedback control to obtain the descending branch of the compressive behavior of brittle rocks and to avoid snap-back behavior. It should be noticed that similar post-peak snap-back behavior is found in high strength concrete. The alternative lateral feedback signal has been largely studied and it has been indicated as the standard feedback signal in uniaxial compression tests of high strength concrete (Jansen *et al*. 1995; Jansen *et al*., 1997; Van Mier *et al*., 1997; Van Mier *et al*., 2000).

In the present work, a set of uniaxial compression tests were carried out in a very stiff frame connected with an appropriate closed-loop control system, see Figure 3.1, at the Structural Laboratory of University of Minho.

Figure 3.1 – Testing equipment

As among the granites to be tested, some of them, are expected to be high strength granites, the internal variable selected as feedback signal was the lateral displacement. In the absence of a circumferential extensometer, a special device was design to measure the lateral deformations, see Figure 3.2. This device is composed by a central ring that is attached locally to the specimen by means of three steel screws. The expansion of the ring is made possible by the lateral spring. The couple of rods attached to the central ring can move freely, when the lateral displacement of the specimen increases, since they are connected through an

axis. The control LVDT is placed at the end of one of the rods and is able to measure the deviation between both rods during the compression test.

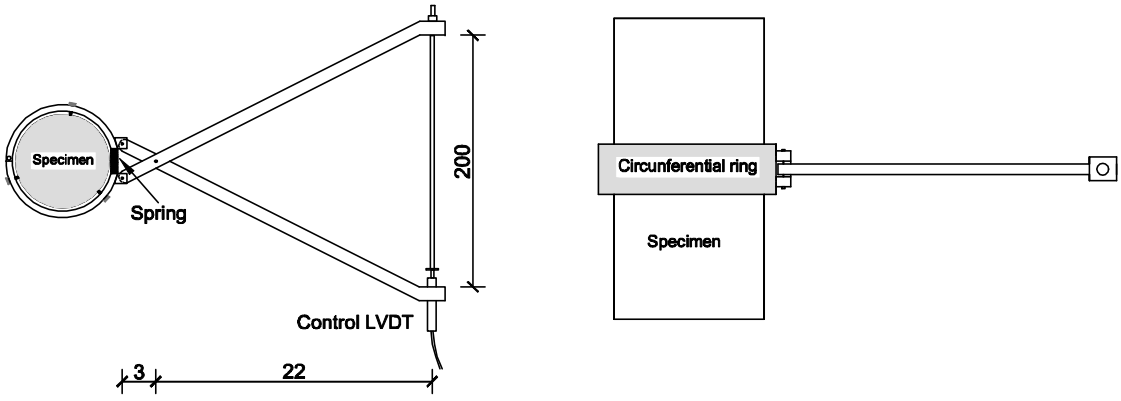


Figure 3.2 – Control equipment; (a) plan view; (b) elevation view

Besides the possibility of testing the specimens by means of the lateral displacement, the device allows the amplification of the actual diametric displacement by a factor of seven, which means that if the programmed velocity of the control LVDT is 2μm/s, the correspondent lateral increment measured in the specimen is approximately 0.3μm/s. Additionally, this low velocity improves the stable progress of failure, with increasing localization of the damage due to axial compression and hence the attainment of the post-peak behavior of the granites.

The boundary conditions are known to influence significantly the post-peak behavior of quasi-brittle materials under uniaxial compression. According to Kotsovos (1983), the slope of the descending branch depends on the restraint degree between the platen and the specimen, see Figure 3.3. The uniaxial compressive stress increases with the increase of the restraint whereas the softening branch becomes smoother.

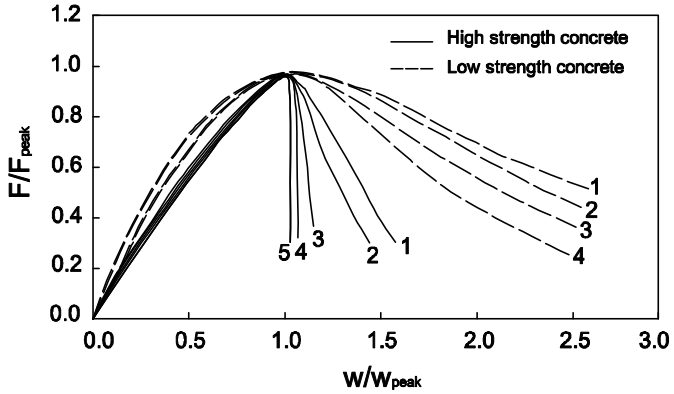


Figure 3.3 – Effect of the lateral boundary restraint on softening of concrete. The restraint decreases as the number in figure decreases (after Kotsovos, 1983)

In order to reduce the friction coefficient between the specimen and the steel platens, two sheets of Teflon with a thickness of 100μm were placed at the interfaces between the specimen and the steel platens. To improve its performance a small amount of grease was placed between the sheets.

The steel platens have a diameter of 80mm and are 50mm thickness. The surfaces in contact with the specimen were ground and mechanically treated, so that, perfect flatness could be obtained. Etched circles were made at the contact interface to facilitate the centering of the specimen. The upper platen has a spherical seat with a radius approximately equal to the specimen, which allows the initial alignment accommodation of the specimen and thus the centering and alignment of the applied load, Figure 3.4a.

### 3.2.3 *Measurements and test procedure*

The axial measurements were carried out by means of three LVDTs located between the lower and upper platens according to the disposition indicated in Figure 3.4b. These LVDTs have a linear field of 20mm with a resolution of 0.05%. In order to obtain the Young's modulus, $E$, and the Poisson's ratio, $\nu$, two vertical and two lateral strain gauges were glued to the specimen, placed 180º apart at mid height of three specimens in each series, as shown in Figure 3.4c. Even if some of the granites under study present porphyritic texture, the length adopted for the extensometers was always about 60mm, which represents 40% of the axial dimension.

Before starting of the compressive tests, the special device designed to measure the lateral displacements was attached to the specimens so that the position of the control LVDT remains horizontal during the test. Simultaneouly, the specimen was suitably aligned and centered with the steel platen. In order to obtain a better adjustment between the specimen and the steel platens and between the upper loading platen and the spherically seated steel platen, a preload was applied in force control. The adopted test procedure was composed by two phases. In the first phase, so that the lateral LVTD could measure clear horizontal displacements, the specimen was loaded in load control up to a force of 80kN. It should be noticed that, for low levels of stress, the lateral displacement increment is relatively slow which would be a limitation if the compression test was controlled by horizontal displacement. Subsequently, the control was switched to displacement control by means of the horizontal LVDT at a rate of 2μm/s which corresponds to a rate of the lateral displacement of the specimen of about 0.3μm/s. This procedure was followed in all types of granite.

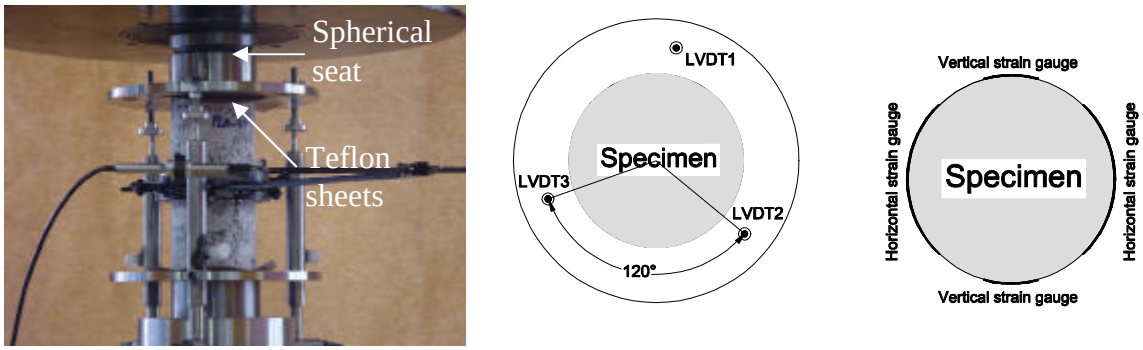


(a) (b) (c)

Figure 3.4 – (a) test setup; (b) location of the LVDTs; (c) location of strain gauges

## 3.3 Experimental results

The complete stress-strain diagrams that characterize the compressive behavior of all granites is the result of averaging the displacement recorded by the three LVDTs placed 120º apart

between the upper and lower steel platens. The normal stress is calculated as the ratio between the applied vertical load and the initial cross section. The normal strain is obtained by dividing the changing in measured axial length by the initial length of the specimen. When strain gauges are attached to the specimens, the lateral and axial strains are the outcome of averaging the two strains measured by the strain gauges placed in the horizontal and the vertical directions respectively. From the axial strain, $e_a$, and lateral strain, $e_l$, the volumetric strain, $e_v$, which is a measure of the changing on the volume of the specimen ($DV/V$), is obtained from the following expression:

$$e_v = e_a + 2e_l \tag{3.1}$$

The total number of specimens tested under uniaxial compression is summarized in Table 3.1. The number of specimens tested under saturated conditions is indicated inside brackets. The distinct number of specimens is related to the variable dimensions of the original stone blocks since they had different dimensions.

Table 3.1 – Number of samples tested for all granite types. The number of saturated specimens is indicated inside brackets

| Granite | Samples | Granite | Samples |
|---|---|---|---|
| BA | 9 | MDB* // foliation | 8 |
| GA | 9 | PTA ⊥ foliation | 7 |
| GA* | 8 (3) | PTA // foliation | 7 |
| RM | 8 | PTA* // rift plan | 13 (5) |
| MC | 8 | PTA* ⊥ rift plan | 7 |
| AF ⊥ foliation | 8 (3) | PLA ⊥ rift plan | 8 |
| AF // foliation | 8 | PLA // rift plan | 6 |
| MDB ⊥ foliation | 8 (3) | PLA* ⊥ rift plan | 7 (4) |
| MDB // foliation | 9 (4) | PLA* // rift plan | 8 (3) |
| MDB* ⊥ foliation | 7 | | |

As a small pre-load of 20kN had to be applied before starting the compression test, the stress-strain diagrams presented here do not include this initial branch. In terms of compressive strength, the final value obtained for each specimen results by adding the pre-load to the maximum value recorded during the test.

### 3.3.1 *Pre-peak behavior and validation of the control procedure*

This section aims at describing the typical pre-peak behavior of the granites. Besides, the assessment of the experimental control procedure is also discussed.

The main stages that describe the complete deformational behavior up to peak load of cylindrical rock specimens under uniaxial compression, namely granites, are indicated in the stress-lateral strain and in the stress-uniaxial strain diagrams, in conjunction with the evolution diagram of the volumetric strain with the axial stress, see Figure 3.5. The different deformational mechanisms that characterize the compressive pre-peak behavior are revealed by the changes in the shape of these diagrams. Certain stress levels allow the description of the microprocesses and the onset of the macrofracture mechanisms that take part of the failure process of granites under compression. In general, the uniaxial compressive behavior of granites is composed by the following phases: (a) microcracking and pore closure; (b) linear elastic deformation; (c) crack initiation and stable crack growth; (d) crack damage and

unstable crack growth; (e) post-peak behavior. Microcracking and pore closure occurs during the initial stages of loading up to the stress level, $f_{cc}$, when pre-existing microcracks or pore space are oriented at an angle to the applied load close. This phase is characterized by a nonlinear behavior of the stress-axial strain diagram with increasing stiffness. After the closure of the pre-existing microcracks, rocks exhibit linear elastic behavior. A linear branch of both axial and lateral stress-strain diagrams is observed, which is associated with recoverable strains. The onset of the microcraking corresponding to the stress level $f_{ci}$ is followed by the nonlinear increase on the lateral strain, as well as by the nonlinearity of the volumetric strain. This is the result of the development of the microcraks in axial direction. Many previous studies demonstrated that microcraks induced during uniaxial tests are mainly tensile cracks (Lajtai *et al*., 1990; Moore and Lockner, 1995; Prikryl *et al*., 2003). The shape of the stress-axial strain is not sensitive to this deformational mechanism. This is essentially due to the fact that the compressive stress-parallel cracks do not change the axial stiffness (Li and Lajtai, 1998; Lajtai, 1998). Therefore, the stretch of the stress-strain diagram is still linear and the axial strains are almost fully recoverable. At this stage, the microcrack propagation is considered stable since it can be stopped if the applied load is removed. The unstable microcracking occurs for the crack damage stress level, $f_{cd}$, and is associated to the point of reversal in the total volumetric strain diagram ($V_r$). This point is connected to the maximum compaction of the specimen and to the onset of dilation since the increase on volume generated by the cracking process is larger than the standard volumetric decrease due to the axial load. For this stage, a rapid and significant increase on the lateral strains is observed, as a result of the volume increase. The microcracking spreading is no longer independent, the local stress fields begin to interact and the microcraks previously formed tend to coalesce. After the peak load is reached, the material becomes weaker and the strain is concentrated in the weaker elements (strain localization) which constitute the damaged zone. The issue of post-peak behavior is of particular relevance and is addressed in the next section.

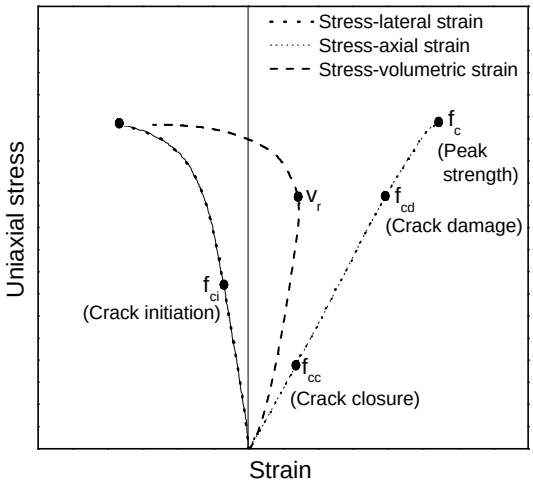


Figure 3.5 – Evolution of the fracture process in a typical stress-displacement diagram up to peak load (Eberhardt *et al*., 1999a)

The simple observation of selected stress-volumetric strain diagrams, displayed in Figure 3.6 for distinct types of granites, indicates that clear different deformational behavior occurs. Consequently variable mechanical properties should be associated with them. The stress levels at which initiation and propagation of the microcracking and the onset of the dilation

takes place seem to depend on the type of the granite. For a better insight into the compressive behavior up to peak load, parameters like the slope of the stress-axial strain, $E$, and the ratio between lateral and axial stiffness, $n$, will be calculated. In addition to these parameters, the values of the different stress levels ($f_{ci}$ and $f_{cd}$ ) corresponding to different stages of cracking development will be also discussed.

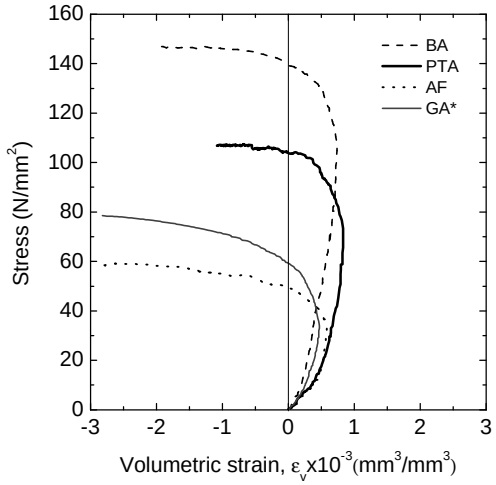


Figure 3.6 – Examples of stress-strain diagrams for different types of granite

It should be noted that the initial upward concave part of the stress-strain diagram is not only a characteristic of the material but also reflects a structural effect. It can be reduced if internal measurement, like strain gauges or LVDTs directly connected to the specimen surface, are used (Korinets and Alehossein, 2002). This can be assessed by comparison of the initial stretch of the stress-strain diagram displayed in Figure 3.7.

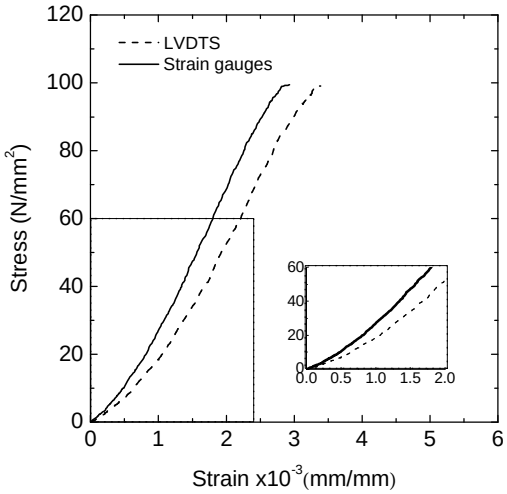


Figure 3.7 – Effect of the measurement system in the initial upward concave of the stress-strain diagram

Figure 3.8 shows the stress-strain diagrams obtained for granite PTA* in parallel direction to the rift plane using vertical and lateral displacement control. As it can be observed, in spite of this granite being low strength, a lack of information about the behavior in the post-peak regime is obtained due to premature uncontrolled failure. Besides, both values of peak

strength and stiffness are inside the interval of variation achieved when lateral displacement control was selected.

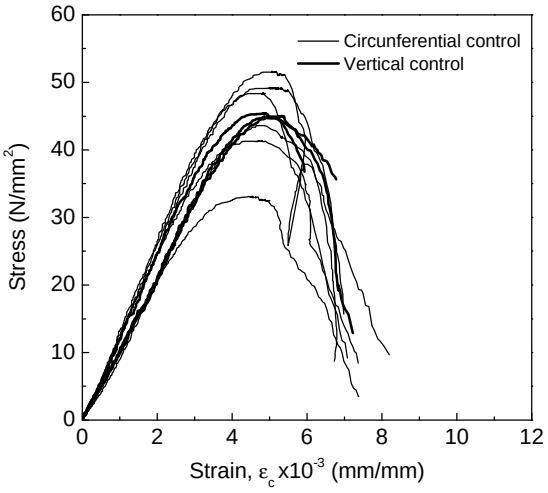


Figure 3.8 – Stress-strain diagrams of granite PTA* obtained with distinct variable control

In addition, two specimens of granites GA and granite BA were tested under two different type of control. After the crack initiation stress has been calculated based on two tests, a third specimen of each granite was loaded up to this stress level under force control. Subsequently, the results of the axial stress-axial strain and axial stress-lateral strain diagrams were compared with the results obtained with lateral displacement control, see Figure 3.9. Practically, no differences were found between stress-axial and stress-lateral strain given by the extensometers previously attached to the specimen. These results make valid the procedure of conducting compression tests with the adopted lateral displacement control through the device that was previously described.

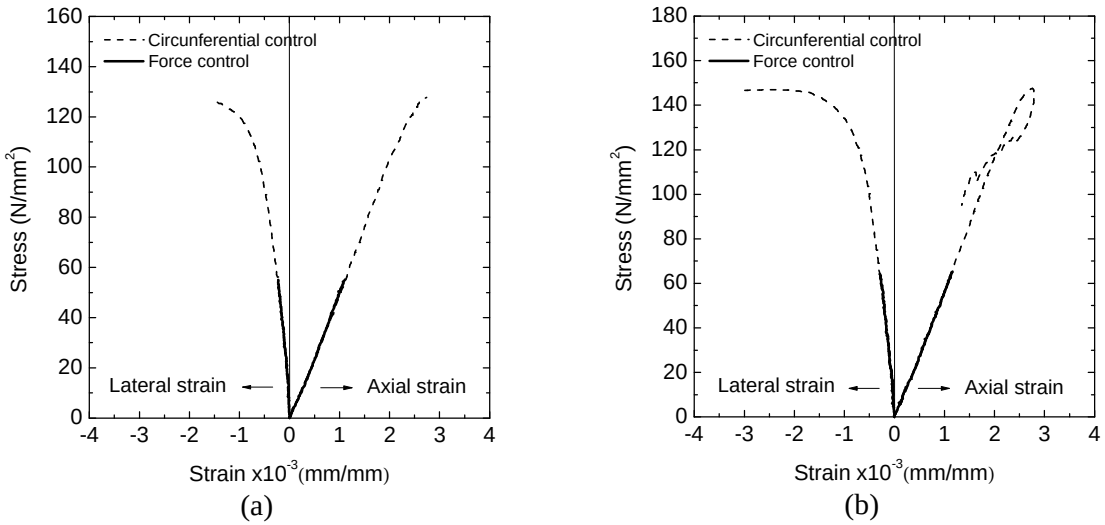


Figure 3.9 – Comparison of the initial stretch of the stress-strain diagrams obtained in force and lateral displacement control; (a) granite GA; (b) granite BA

The normalized vertical displacement versus normalized lateral displacement for granites MC (high strength) and MDB (Low strength) is displayed in Figure 3.10. As it can be observed, the lateral displacement has always increasing values for both granites. However, the vertical displacements for granite MC exhibit decreasing values (snap-back behavior) after the

maximum value has been achieved (corresponding to the peak stress) and then returns to an increasing trend. On the contrary, granite MDB presents increasing values as the lateral displacement increases. This evolution justifies the need of using the lateral displacement control, especially in the case of high strength granites such as MC.

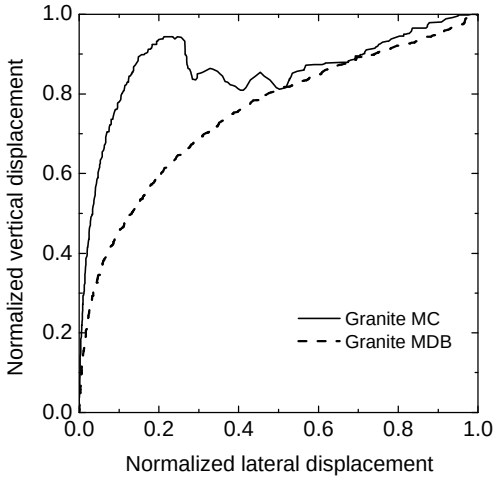


Figure 3.10 – Relation between normalized lateral and normalized vertical displacements for granites MC and MDB

### 3.3.2 *Post-peak behavior*

After the peak load is reached, the compressive behavior is characterized by macrocracking growth as strain localization occurs. Macrocracks result from coalescence of the microfractures developed until the peak load is reached. At this stage, the tensile or the shear fractures are fully formed and are visible with naked eye. The strain localization and the growth of the crack length are followed by a significant load carrying capacity decrease of the material. The shape of the softening branch is highly dependent on the type of granite. Be aware that, although the post-peak softening diagram is highly dependent on the boundary conditions (degree of restraint) and on the specimen size (Kotsovos, 1983; Vonk, 1993; Torrenti *et al.*, 1993; Tang *et al.*, 2000b; Zisopoulos *et al.*, 2000), in the present study the same boundary conditions were used for all granites. This allows further comparison of the results. As far as the post-peak behavior is concerned, the slope of the softening branch plays the major role in the evaluation of the brittleness of a material. The analysis of typical complete stress-strain diagrams, displayed in Figure 3.11, shows that depending on the type of granite, softening branch presents distinct negative slopes, being in some of them even positive (snap-back). In case of granite PTA, after localization, the stress-strain diagram drops off abruptly, whereas in case of granite PTA* the shape of the descending branch is significantly smoother. The former descending shape is more characteristic of medium to high strength granites (PTA, PLA, PLA*), while the latter is associated to low to medium strength granites (MDB, MDB*, PTA*, AF). For high strength granites (BA, GA, GA*, RM, MC), the compressive brittle behavior results in simultaneous decrease of the stress and the strain (snap-back behavior), see Figure 3.12a. Sometimes, the specimen fails suddenly just after reaching its maximum strength. Another usual feature of the shape of the softening diagram for high strength granites is presented in Figure 3.12b. The opening of the macrocrack and the resulting phased process of localization leads to the discontinuous shape of the softening branch. This is characterized by a set of successive abrupt losses (unloading of the material) and recoveries of the loading capacity. In the macrocracking progress, the

increase of the loading capacity is associated with the recovery of the stress transfer mechanism between both sides of the macrocrack, which is provided by the grain interlocking. This compressive behavior is also characteristic of high strength concrete and has been reported in several works (Jansen *et al*., 1995). According to Pan *et al*. (2002), the snap-back behavior is the result the localized failure under uniaxial compression but this remains open for discussion. Full details of the complete stress-strain diagrams for all granites are given in Appendix D.

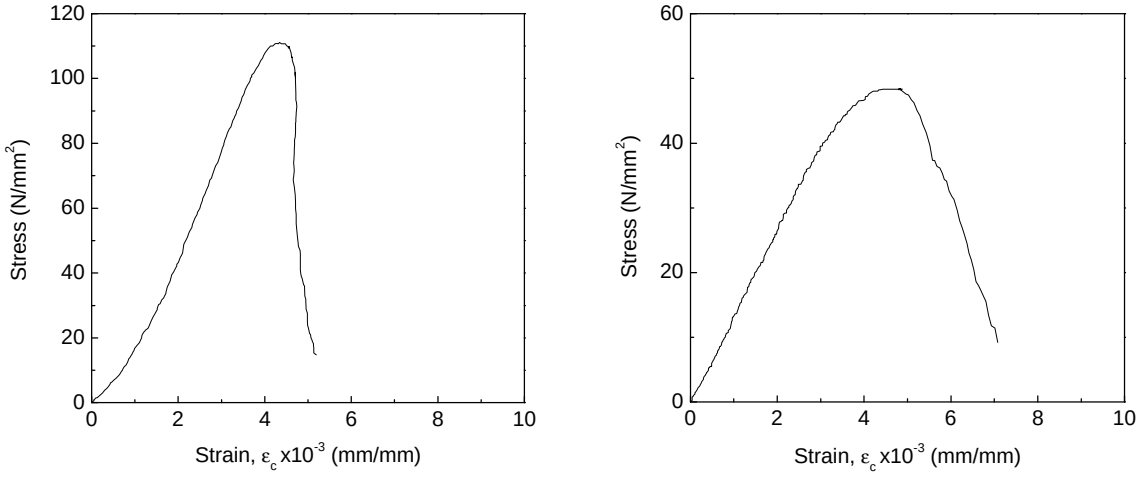


Figure 3.11 – Typical smooth stress-strain diagrams; (a) granite PTA; (b) granite PTA*

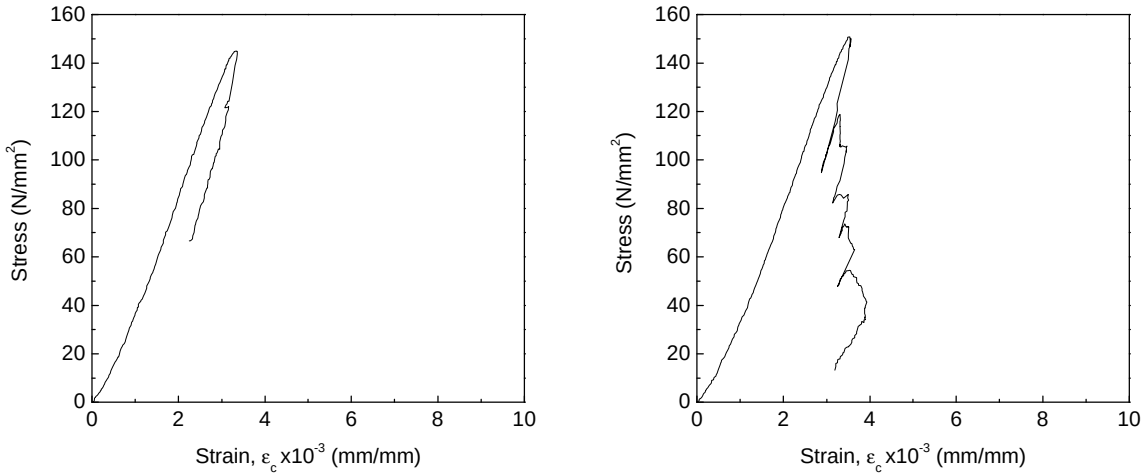


Figure 3.12 – Typical snap-back or non-smooth stress-strain diagrams; (a) granite MC; (b) granite RM

It should be noticed that the evolution of the descending branch of the stress-strain diagrams reveals the development of the macrocracking process and strain localization. This is directly connected with the internal structure of the material, namely with the grain boundary strength. For low to medium strength granites the breakage of internal bonding connections and the preferential shear strain localization should involve higher dissipation of energy relatively to the high strength granites that breaks in a brittle manner due the strong bond boundary grains. The preferential tensile macrocracking localization characteristic of high strength granites may be associated to lower amount of dissipated energy during the softening process. A more

detailed and comparative analysis of the final crack patterns resulting from the crack and strain localization in compression tests for all granites is performed later in the text. The distinct shape of pre-peak and softening branches found for the different types of granites reflects necessarily the internal structure (arrangement of minerals and interface bond strengths). Similarly to what was found on the tensile behavior of the granites analyzed in Chapter 2, a wide range for the compressive mechanical properties is expected. These aspects will be discussed in detail in the next sections.

### 3.3.3 *Mechanical properties*

#### 3.3.3.1 Modulus of elasticity, Poisson's ratio and compressive strength

The pre-peak behavior of rocks is essentially characterized by means of the modulus of elasticity, *E*, and the Poisson's ratio, *n*. The Obtainment of these parameters appears to be difficult since stress-axial or stress-lateral strain diagrams do not exhibit fully linear behavior in any stress interval. The ASTM 2938 standard (1986), ISRM suggested methods (1981c) and Fairhurst and Hudson (1999) indicate three distinct methods to calculate the Young's modulus, *E*, namely the tangent, the average and the secant Young's modulus, calculated at certain stress levels, which means that they depend on the stress level. The Poisson's ratio is calculated from the knowledge of the modulus of elasticity according to the following expression:

$$n = -E \,/\, (\text{slope of lateral stress - strain diagram}) \tag{3.2}$$

The analysis of the stress-strain diagrams obtained for the granites allows to verify that, on one hand, it is possible to identify a quasi-linear stretch in the stress-axial strain diagram after reaching the crack closure stress, $f_{cc}$, and, on the other hand, the lateral stress-strain diagram exhibits nonlinearity, which complicates the determination of the Poisson's ratio. This fact rises the question about which stress level should be considered to accept that the material still has linear behavior. It should be stressed that the Poisson's ratio, as an elastic property, has to be calculated for elastic conditions, which occur for stress levels lower than the microcracking stress, $f_{ci}$. From Figure 3.13, where the value of the Poisson's ratio (obtained from expression (4.2)) is indicated for three distinct stress levels (0.3, 0.5 and 0.7 $f_c$), it can be observed that its maximum theoretical value of 0.5 is exceeded in some of the granites.

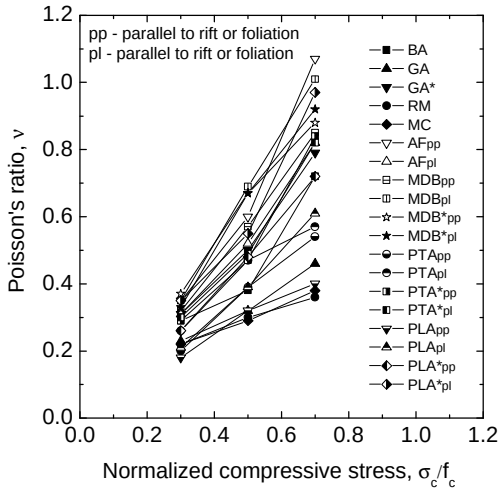


Figure 3.13 – Evaluation of the Poisson's ratio for distinct levels of compressive stress

This necessarily means that the lateral stress-lateral diagram is highly affected by the material damage due to axial microcracking. In this work, the elastic properties, *E* and *v*, are calculated according to the procedure proposed by Lajtai (1998). The diagrams of evolution of the axial and lateral stiffness with the axial stress are obtained by the first order derivative of polynomial functions adjusted to experimental data composed by the stress-axial and stress-lateral strain diagrams defined up to peak stress, see Figure 3.14. The coefficient of determination, $r^2$, obtained for the nonlinear fitting was always rather close to 1.0. From the diagrams similar to the ones shown in Figure 3.14, a relatively constant stiffness interval was identified after the crack closure stress. The reference values of the axial and lateral stiffness are the result of averaging the axial and lateral stiffness within this interval. The modulus of elasticity, *E*, is associated to the axial stiffness and the ratio between the axial and lateral stiffness is the Poisson's ratio, *n*. It should be noticed that almost always the determination of the Poisson's ratio falls within the ($f_{cc}$-$f_{ci}$) interval.

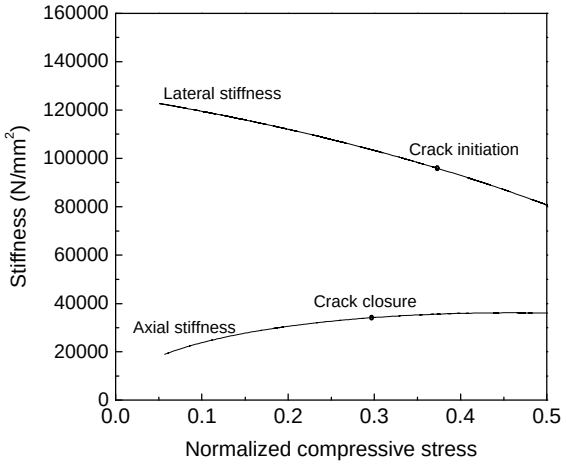


Figure 3.14 – Evolution of the axial and lateral stiffness with normalized compressive stress

The elastic parameters and the compressive strength that characterize the pre-peak behavior of the granites and the corresponding coefficient of variation (inside brackets) are summarized in Table 3.2. The elastic parameters for each specimen are the outcome of averaging the measurements carried out by two axial and two lateral strain gauges attached to three specimens, whereas the values of the compressive stress are the result of averaging the results of the compressive tests conducted on the number of specimens indicated in Table 3.1.

The values that were found for the elastic properties and specially for the modulus of elasticity lie on a large interval. The minimum (11062 N/mm$^2$) and the maximum (63794N/mm$^2$) values for the modulus of elasticity were obtained for the granites MDB* and MC, respectively. By averaging the results concerning all granites, a mean value of 34572 N/mm$^2$ is attained. Regarding the Poisson's ratio the values are in the interval (0.19-0.35) with a mean value of 0.28. The compressive strength shows the same tendency and exhibits a large range of variation (26.0-159.8 N/mm$^2$). The values of the coefficient of variation are, in general, quite low for the modulus of elasticity and the compressive strength. Higher scatter was found for the Poisson's ratio in granites PLA* and MDB*. However, note that the values of the elastic properties are the result of three measurements and, thus, are only indicative. In the ASTM D2938 standard (1986) and in the suggested methods (1981c), a minimum of five specimens is recommended. The values proposed for the modulus of

elasticity with the tangent modulus obtained for $0.5f_c$, as indicated in the ASTM D2938 standard (1986) were found to be practically coincident.

The modulus of elasticity obtained from the displacements measured by the platen-to-platen LVDTs, $E^*$, is lower than the modulus of elasticity calculated based on strains measured by the strain gauges. Similarly to the definition of the modulus of elasticity, $E$, the modulus of elasticity, $E^*$, is also the averaging of the first order derivatives of a representative polynomial function fitted to the stress-axial strain diagram in the interval where the derivatives appear approximately constant. The difference between both values of the modulus of elasticity is, on average, only 12% but reaches more significant values in granite MDB* (29.3%) and in granite PTA* (28.7%), see Table 3.2. The same finding was reported by Jansen *et al*. (1995), Jansen and Shah (1997) and by Oliveira (2003). The difference is attributed to fact that the displacement measured by the LVDTs not only includes the deformation of the samples but also the deformation of the interfaces between the platens and the specimen, as well as the deformation associated to the material (Teflon) introduced at the specimen ends in order to minimize the boundary effects by reducing the friction between the platens and the sample. This means that the modulus of elasticity calculated from the strain gauges measurements is more reliable.

Table 3.2 – Mean values of the elastic properties and the compressive strength for the granites; coefficient of variation (%) is indicated inside brackets

| Granite | $E$ (N/mm$^2$) | $E^*$ (N/mm$^2$) | $n$ | $f_c$ (N/mm$^2$) |
|---|---|---|---|---|
| BA | 59939 (5.2) | 53043 (5.2) | 0.29 (2.0) | 148.5 (4.8) |
| GA | 52244 (2.3) | 45353 (3.3) | 0.23 (13.1) | 135.7 (5.0) |
| GA* | 35088 (3.3) | 30461 (8.1) | 0.30 (17.1) | 89.5 (2.5) |
| RM | 58926 (1.8) | 52516 (1.8) | 0.22 (6.5) | 159.8 (2.5) |
| MC | 63794 (5.6) | 52181 (4.3) | 0.24 (8.3) | 146.7 (2.8) |
| AF⊥ foliation plan | 15748 (7.2) | 11760 (4.4) | 0.34 (7.9) | 66.7 (7.8) |
| AF // foliation | 18954 (6.9) | 11910 (11.8) | 0.31 (17.1) | 68.9 (5.6) |
| MDB ⊥ foliation | 15886 (13.5) | 14145 (7.5) | 0.29 (7.4) | 49.7 (5.2) |
| MDB // foliation | 11600 (4.2) | 9649 (2.3) | 0.31 (3.0) | 44.8 (2.8) |
| MDB* ⊥ foliation | 11028 (12.0) | 7795 (5.7) | 0.29 (10.2) | 35.2 (3.4) |
| MDB* // foliation | 12243 (13.6) | 10292 (2.8) | 0.32 (22.1) | 26.0 (7.1) |
| PTA ⊥ foliation | 40526 (3.1) | 35237 (7.7) | 0.21 (21.1) | 119.1 (3.1) |
| PTA // foliation | 41504 (1.6) | 36065 (5.9) | 0.23 (2.6) | 109.1 (7.3) |
| PTA* ⊥ rift plan | 15008 (7.1) | 10700 (7.9) | 0.28 (5.8) | 60.4 (4.8) |
| PTA* // rift plan | 18168 (3.3) | 12705 (9.6) | 0.26 (15.4) | 50.2 (11.1) |
| PLA ⊥ rift plan | 53737 (2.8) | 43230 (2.6) | 0.19 (13.2) | 147.0 (2.6) |
| PLA // rift plan | 58180 (2.6) | 48602 (2.6) | 0.22 (1.1) | 125.2 (6.1) |
| PLA* ⊥ rift plan | 28981 (1.6) | 25403 (8.3) | 0.32 (13.6) | 88.5 (4.2) |
| PLA* // rift plan | 41607 (7.6) | 31222 (3.9) | 0.35 (30.4) | 76.9 (3.2) |

$E^*$ – value of the modulus of elasticity obtained from the LVDTs measurements

$E$ – value of the modulus of elasticity obtained from the strain gauges measurements

For a better understanding of the microcracking process in the granites under study, the values of the stress markers that indicate the microcracking initiation and the onset of the inelastic deformation ($f_{ci}$) and the onset of the dilatancy ($f_{cd}$) are also evaluated. As indicated above (Figure 3.5), the crack damage stress, $f_{cd}$, is associated to the reversal point of the stress-volumetric diagram (point associated to maximum decrease on the volume or

maximum compaction of the specimen). The crack initiation stress, $f_{ci}$, corresponds to the point of the stress-lateral strain diagram and the stress-volumetric strain from which the onset of the nonlinearity is verified. This point is obtained by linear fitting of the stress-lateral and stress-volumetric strain, (Lajtai *et al*., 1990; Hatzor and Palchick, 1997; Yuan and Harrison, 2004), see Figure 3.15. As reported by Eberhardt *et al*. (1999a), these damage stages can be more accurately determined using simultaneously the analysis of the stress-strain data and the acoustic emission event (AE event).

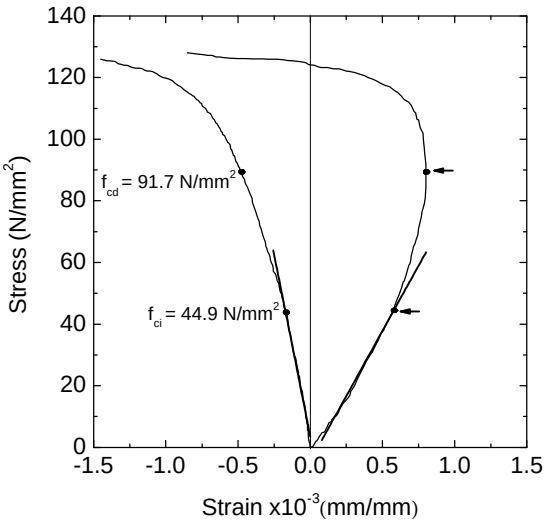


Figure 3.15 – Typical definition of the crack initiation stress, $f_{ci}$, and the onset of unstable cracking, $f_{cd}$, for granite GA

The values of the stress levels that better describe the deformational pre-peak behavior and the corresponding variation on volume are listed in Table 3.3. In general, the onset of the microcracking occurs at low stress levels. For low to medium strength granites the values of $f_{ci}$ are lower than $0.3f_c$ and for high strength granites the values lies on the interval $0.3\text{-}0.4f_c$. The latter range is also indicated by other authors (Farmer, 1983; Eberhardt *et al*., 1999a).

This finding is, to a large extent in agreement with the results presented in Chapter 2 concerning the tensile behavior of granites, in which a pre-peak inelastic behavior detected at early stages of loading was pointed out. In effect, the microcracking plays a major role in the compressive behavior of granites. This is the main reason by which significant increasing values of the Poisson's ratio are recorded during the loading process. The process of fracture at early loading stage has also been reported for concrete (Bascoul, 1996; Choi and Shah, 1998).

For the granites under study, the acceleration of the microcracking growth is observed also for low levels of crack damage stress, $f_{cd}$. Only for high strength granites (MC, RM, GA and BA), the values of the crack damage stress are close to the values reported by Eberhardt *et al*. (1999) for Lac du Bonnet granite ($0.7\text{-}0.8f_c$). In case of low to medium strength granites the onset of dilatancy (increase in volume) occurs even for stress levels close but lower than $0.5f_c$ (GA*, AF, MDB, MDB*). The variation of the crack damage stress between one-half to two thirds of the peak strength of the rock was reported by Yuan and Harrison (2004).

Table 3.3 – Average values of the stress markers, $f_{ci}$ and $f_{cd}$, and the corresponding axial strains

| Granite | $e_{ci}$ (mm/m) | $f_{ci}$ (N/mm$^2$) | $e_{cd}$ (mm/m) | $f_{cd}$ (N/mm$^2$) |
|---|---|---|---|---|
| BA | 0. 469 | 55.1 (0.36$f_c$) | 0. 6813 | 102.2 (0.66 $f_c$) |
| GA | 0. 562 | 50.0 (0.37$f_c$) | 0. 8974 | 96.2 (0.71 $f_c$) |
| GA* | 0. 401 | 25.1 (0.28$f_c$) | 0. 5467 | 43.2 (0.49 $f_c$) |
| RM | 0. 649 | 52.4 (0.33$f_c$) | 1.060 | 123.3 (0.78 $f_c$) |
| MC | 0. 678 | 58.5 (0.39 $f_c$) | 1.039 | 120.9 (0.81 $f_c$) |
| AF ⊥ foliation plan | 0. 675 | 17.5 (0.26 $f_c$) | 0. 9007 | 29.1 (0.43 $f_c$) |
| AF // foliation | 0. 431 | 15.8 (0.23 $f_c$) | 0. 7334 | 30.1 (0.44 $f_c$) |
| MDB ⊥ foliation | 0. 367 | 14.5 (0.30 $f_c$) | 0. 4819 | 21.8 (0.45 $f_c$) |
| MDB // foliation | 0. 373 | 11.8 (0.26 $f_c$) | 0. 4931 | 17.8 (0.40 $f_c$) |
| MDB* ⊥ foliation | 0. 289 | 9.7 (0.27 $f_c$) | 0. 3866 | 15.2 (0.43 $f_c$) |
| MDB* // foliation | 0. 157 | 6.8 (0.27 $f_c$) | 0. 1850 | 10.7 (0.43 $f_c$) |
| PTA ⊥ foliation | 1.127 | 30.1 (0.25 $f_c$) | 1.370 | 75.4 (0.63 $f_c$) |
| PTA // foliation | 0. 555 | 27.0 (0.24 $f_c$) | 0. 7910 | 58.3 (0.53 $f_c$) |
| PTA* ⊥ rift plan | 0. 572 | 14.1 (0.24 $f_c$) | 0. 9532 | 31.4 (0.53 $f_c$) |
| PTA* // rift plan | 0. 316 | 14.7 (0.29 $f_c$) | 0. 5131 | 26.6 (0.52 $f_c$) |
| PLA ⊥ rift plan | 1.070 | 45.1 (0.31 $f_c$) | 1.906 | 113.3 (0.77 $f_c$) |
| PLA // rift plan | 0.628 | 40.8 (0.33 $f_c$) | 0.8435 | 85.9 (0.70 $f_c$) |
| PLA* ⊥ rift plan | 0. 793 | 26.3 (0.30 $f_c$) | 1.046 | 48.5 (0.55 $f_c$) |
| PLA* // rift plan | 0. 267 | 19.7 (0.26 $f_c$) | 0.3379 | 37.8 (0.49 $f_c$) |

When the crack damage stress is lower than 0.5$f_c$, the Poisson's ratio is already higher than its theoretical value of 0.5, see Figure 3.16. The dilatancy process has always associated values of the Poisson's ratio higher than 0.5, which means that it takes an important role in the evaluation of the pre-peak fracture process (Li *et al*., 1998; Choi and Shah, 1998). Therefore, the pre-peak damage can also be evaluated by means of the Poisson's ratio. This fact stresses the deformational behavior of granites corresponding to crack damage characterized by the development and coalescence of the microstructural damage with preferential alignment parallel to the axial stress. In addition, it is observed a clear tendency for the Poisson's ratio to decrease as the normalized crack damage stress increases, meaning that that there is a tendency for high strength granites to exhibit lower values of the Poisson's ratio.

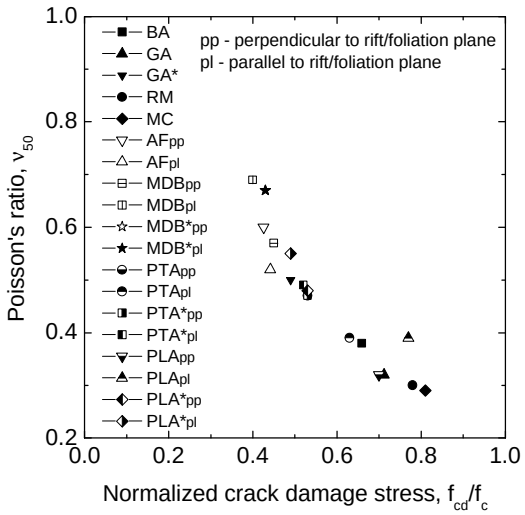


Figure 3.16 – Relation between of the Poisson's ratio obtained at 50% of the compressive strength and the normalized crack damage stress for the distinct types of granites

### 3.3.3.2 Fracture energy

As reported by several authors, the compressive loading process of quasi-brittle materials, like rock and concrete, leads to localization of macrocracks when peak stress is attained (Van Mier, 1984; Torrenti *et al.*, 1993; Vonk, 1993; Markeset and Hillerborg, 1995; Lee and William, 1997; Jansen and Shah, 1997; Watanabe *et al.*, 2004). Localization prior to the peak stress and early in the dilatancy history was identified by Haied *et al*. (2003) in sandstones and in concrete by Shah and Sankar (1987). With respect to the present campaign of compression tests, localization always occurred after peak loaded is attained, because no signs of perceptible cracking were detected before peak load. Indication of the onset of the localization consists in the detachment of very small particles when decreasing of load carrying capacity is recorded. Examples of failure patterns that illustrate strain localization are displayed in Figure 3.17. Although some spread splitting vertical cracks are visible in most specimens, a clear macrocrack localized in a generalized shear band is often present.

Figure 3.17 – Examples of failed specimens

According to the compressive damage crack model (CDZ) (Markset and Hillerborg, 1995), it is accepted that the failure takes place within a damage zone of limited length ($L_d$), see Figure 3.18.

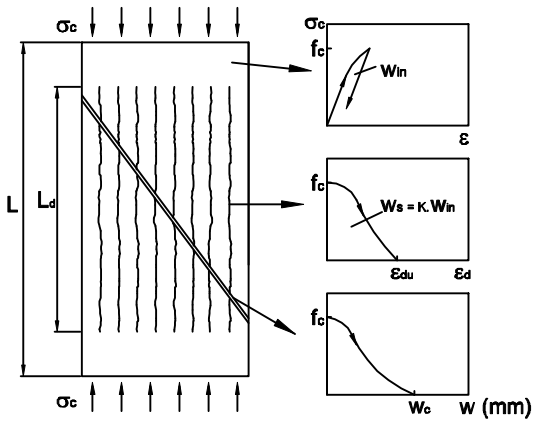


Figure 3.18 – Ilustration of the CZD model of a specimen loaded in uniaxial compression (Markset and Hillerborg, 1995)

Until the peak stress is reached, the stress-strain diagram describes the compressive behavior of the continuum bulk rock, both elastic and inelastic zone corresponding to the formation of predominantly longitudinal microcracks. Immediately after peak is reached and strain localization occurs, the material outside the damage zone unloads. The area described by this loading path is the pre-peak fracture energy, which is associated to the microcracking

initiation and propagation, see the top diagram in Figure 3.18. The post-peak diagram describes the deformation at the damage zone that includes the deformation related to the formation and coalescence of distributed longitudinal cracks ($e_d$), and the deformation at localized zone ($w$), see center and bottom diagrams, respectively. The latter component of deformation represents the vertical component of the displacement in the shear band. For a specimen with length $L$, the total average strain, $e_m$, is given by:

$$e_m = e + e_d \frac{L_d}{L} + \frac{w}{L} \tag{3.3}$$

The total energy, $W$, dissipated by cracks per unit of volume, is obtained as the sum of the energy consumed by the different failure modes within the fracture process zone and the energy consumed by microcracking in the bulk:

$$W = W_{in} + W_s \frac{L_d}{L} + G\frac{1}{L} \tag{4.4}$$

where $W_{in}$, $W_s$, $G$ are respectively the energy consumed in the ascending branch of the stress-strain diagram, the energy consumed in the longitudinal cracks after the maximum stress and G is the energy consumed during localization. The total post-peak fracture energy dissipated in the damage zone is, thus, the sum of the energy dissipated as the result of coalescence of microfractures initiated before peak and the fracture energy consumed in the localized fracture zone. As is indicated in Figure 3.18, this energy is calculated as the area under the corresponding diagrams. According to Markset and Hillerborg (1995), the absorbed energy in the longitudinal cracks is assumed to be proportional to the mode I fracture energy $G_f$.

The procedure used here for the determination of the post-peak fracture energy is similar to the one indicated by Jansen and Shah (1997). In order to take into account the localization and the consequent unloading of the undamaged continuum, the inelastic displacement is calculated by subtraction of the inelastic pre-peak displacement to the total displacement. The stress ratio $f/f_c$ up to which the softening diagram is considered was fixed in 0.33. The pre and post-peak fracture energies, $G_{cpre}$ and $G_{cpost}$ respectively, are obtained by integrating the pre and post-peak diagrams, as is indicated in Figure 3.19.

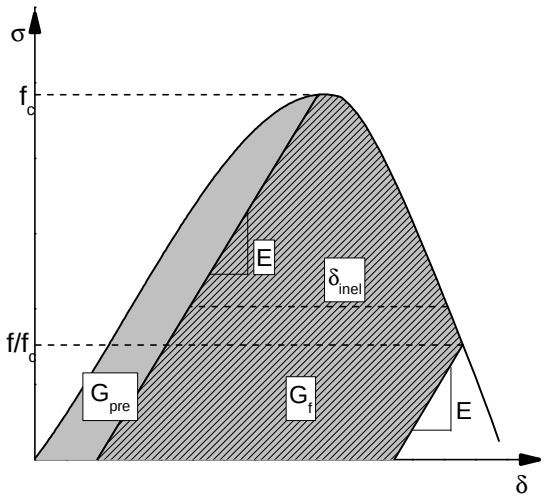


Figure 3.19 – Procedure used for determination of the pre-peak and post-peak fracture energies and definition of inelastic displacement, $d_{inel}$ (Jansen and Shah, 1997)

The pre-peak fracture energy corresponds to the amount of energy dissipated during the microcracking process before the maximum load is attained. In addition, in order to get a better insight about the ductility behavior of granites under compression, the pre and post-peak normalized fracture energies with respect to the compressive stress, $G_{cpre}/f_c$ and $G_{cpost}/f_c$, were also calculated. This quantity has been termed as "ductility index" in Chapter 2 and will be used also in this Chapter.

The mean values of the pre and post-peak fracture energies, $G_{cpre}$ and $G_{cpost}$, and the corresponding normalized values (ductility indexes), $d_{upre}$ ($G_{cpre}/f_c$) and $d_{upost}$ ($G_{cpost}/f_c$), are shown in Table 3.4. The corresponding coefficient of variation is also indicated (inside brackets). It is observed that moderate values of the coefficient of variation were generally found. This fact underlines the reliability of these parameters in the fracture characterization in compression. Both values of pre-peak and post-peak fracture energy depend largely on the type of granite and, therefore, exhibit large range of variation. The values of pre-peak energy lie on the interval (3.2-10.4N/mm), whereas the values of the dissipated energy in the macroscopic fracture are between 11.8 for granite MDB* and 49.1N/mm for granite PTA*. In addition, the values of the ductility index are between 0.224mm (high strength granite) and 0.874 mm (low strength granite). In general, high strength granites have low ductility index values, meaning that the behavior is more brittle.

Table 3.4 – Mean values of the fracture energy; coefficient of variation (%) is indicated inside brackets

| Granite | $G_{cpre}$ (N/mm) | $d_{upre}$ (mm) | $G_{cpost}$ (N/mm) | $d_{upost}$ (mm) |
|---|---|---|---|---|
| BA | 7.1 (21.1) | 0.053 (15.0) | 45.3 (8.3) | 0.316 (14.3) |
| GA | 7.9 (15.6) | 0.064 (13.8) | 43.3 (8.2) | 0.318 (7.9) |
| GA* | 8.5 (26.0) | 0.101 (26.6) | 31.3 (8.2) | 0.368 (7.4) |
| RM | 5.1 (20.6) | 0.033 (20.9) | 42.1 (14.4) | 0.277 (12.6) |
| MC | 3.7 (33.4) | 0.026 (32.0) | 39.6 (4.6) | 0.279 (4.6) |
| AF ⊥ foliation | 10.4 (9.6) | 0.173 (13.7) | 47.8 (9.5) | 0.792 (9.6) |
| AF // foliation | 8.2 (11.0) | 0.126 (8.9) | 37.3 (9.3) | 0.574 (9.5) |
| MDB ⊥ foliation | 6.9 (9.4) | 0.152 (6.0) | 22.3 (23.4) | 0.494 (19.6) |
| MDB // foliation | 8.3 (15.2) | 0.210 (14.2) | 30.3 (8.2) | 0.764 (5.8) |
| MDB* ⊥ foliation | 4.6 (15.0) | 0.155 (12.7) | 17.2 (8.0) | 0.570 (6.3) |
| MDB* // foliation | 3.2 (10.1) | 0.147 (8.3) | 11.8 (14.0) | 0.549 (14.8) |
| PTA ⊥ foliation | 8.1 (28.1) | 0.071 (27.4) | 45.5 (6.1) | 0.403 (7.5) |
| PTA // foliation | 7.1 (16.4) | 0.068 (15.8) | 44.4 (24.6) | 0.414 (24.9) |
| PTA* ⊥ rift plan | 11.8 (9.2) | 0.211 (9.7) | 49.1 (3.2) | 0.874 (6.5) |
| PTA* // rift plan | 7.3 (17.4) | 0.167 (16.4) | 28.0 (17.5) | 0.638 (10.2) |
| PLA ⊥ rift plan | 8.0 (16.8) | 0.057 (16.7) | 31.7 (20.7) | 0.224 (21.3) |
| PLA // rift plan | 4.2 (22.9) | 0.034 (20.3) | 32.8 (10.0) | 0.265 (11.9) |
| PLA* ⊥ rift plan | 7.4 (5.3) | 0.096 (12.3) | 35.7 (2.8) | 0.463 (4.1) |
| PLA* // rift plan | 4.6 (26.4) | 0.065 (24.6) | 24.2 (15.6) | 0.340 (10.8) |

### 3.3.4 *Correlations between mechanical properties*

In view of the range of variation of the elastic and inelastic parameters that describes the pre and post-peak compressive behavior of granites, a quantitative analysis is performed based on statistical correlations between the mechanical parameters. Note that the pre-peak parameters

like the Young's modulus and the Poisson's ratio, as well as the stress markers, $f_{ci}$ and $f_{cd}$, are referring to three specimens tested for each type of granite.

The general trend that stiffer granites have associated high compressive strengths is shown in Figure 3.20, through the significant linear positive correlation ($r^2$ = 0.89) found for both properties. This means that the modulus of elasticity can be estimated from the compressive strength. The value achieved for the relation between these two parameters is close to the values indicated by Goodman (1989) for other type of granites. This good correlation reflects the intrinsic microstructure and suggests that the combination of high stiff minerals and high stiff grain interfaces, which is on the basis of the stiffness of granites, leads to an increase of strength. A linear trend was also reported by Palchick (1999) for sandstones.

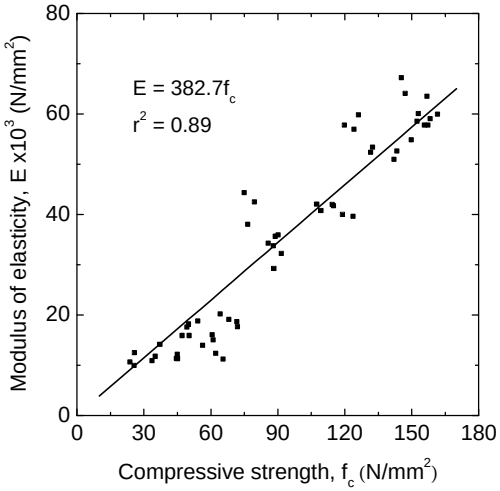


Figure 3.20 – Relationship between compressive strength and modulus of elasticity

Both the crack initiation stress, $f_{ci}$, and the crack damage stress, $f_{cd}$, are well correlated with the compressive strength and modulus of elasticity of the granites, $f_c$, and, thus, it can be estimated with some accuracy from these parameters, see Figure 3.21 and Figure 3.22. A significant nonlinear positive correlation was found between the compressive strength and the other stress markers ($r^2$ = 0.94 for $f_c$ vs. $f_{ci}$ and $r^2$ = 0.96 for $f_c$ vs. $f_{cd}$).

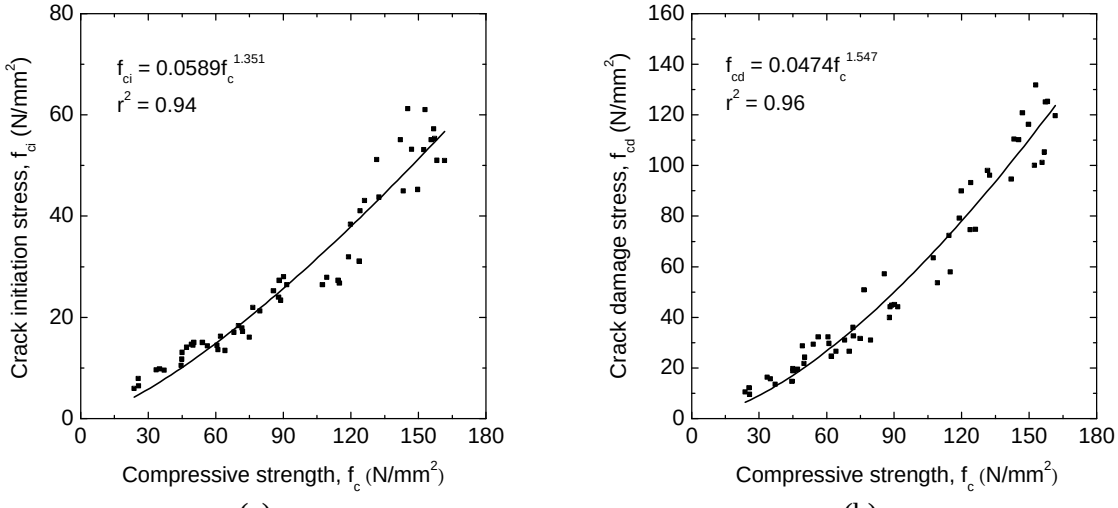


Figure 3.21 – Relationship between distinct stress levels: (a) compressive strength vs. crack initiation stress; (b) compressive strength vs. crack damage stress

If a linear function is fitted to the experimental data, the value of the crack initiation stress will be given by the expression ($f_{ci} = 0.32f_c$, $r^2 = 0.90$). This value is generally suggested for the onset of the nonlinear behavior of concrete Van Mier (1984). For the crack damage stress the relationship will be ($f_{cd} = 0.66f_c$, $r^2 = 0.88$). It should be stressed that these correlations are useful for practice when there is no strain gauges available and, thus, no measurements of the lateral strains are possible. In Figure 3.22, it is observed that a linear correlation was achieved between the stress markers and the modulus of elasticity. The increase on the stiffness of the granites means the increase on the stress to which the onset of the nonlinear pre-peak behavior is recorded. Palchick and Hatzor (2002) pointed out also a nonlinear positive correlation between the modulus of elasticity and the crack damage stress.

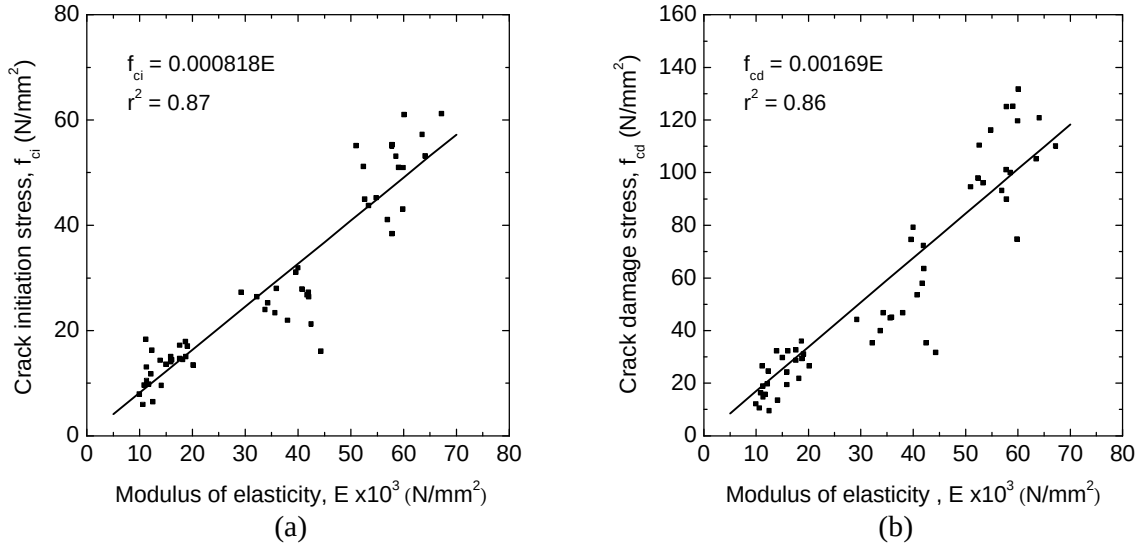


Figure 3.22 – Relationship between stress markers and modulus of elasticity: (a) modulus of elasticity vs. crack initiation stress; (b) modulus of elasticity vs. crack damage stress

In spite of the scatter, Figure 3.23 shows that there is a clear tendency for the dilatant behavior to occur at late stress levels, as both compressive strength and the modulus of elasticity increase.

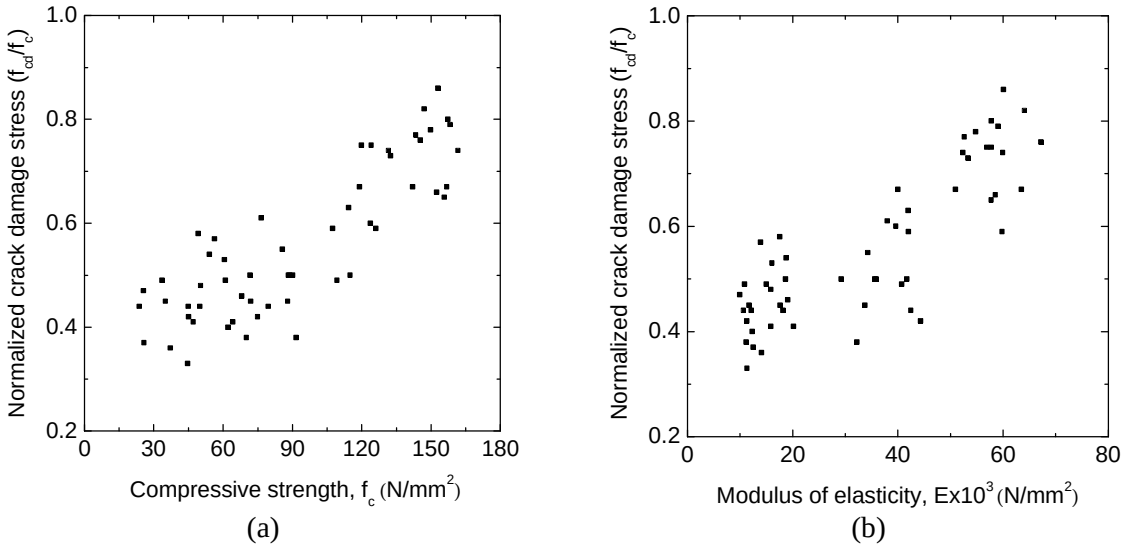


Figure 3.23 – Relationship between normalized crack damage stress and: (a) compressive strength; (b) modulus of elasticity

It is observed that additional insight of the dependence of the onset of the dilatancy behavior on the compressive strength and the modulus of elasticity is attained if one considers the normalized value of the crack damage stress using the peak stress.

Figure 3.24 shows that both stress markers are strongly correlated, which is confirmed by the significant linear positive correlation ($r^2$ = 0.93) found between both properties. This means that the onset of dilation is directly related to the microcracking process.

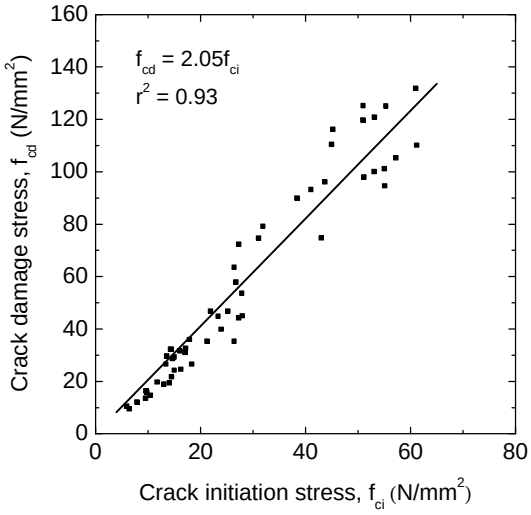


Figure 3.24 – Relationship between crack initiation stress and crack damage stress

Regarding the softening behavior of granites some merely indicative trends can be proposed between fracture energy and compressive strength. The nonlinear correlation found between the compressive strength and the post-peak fracture energy indicates that the fracture energy increases as the compressive strength increases, see Figure 3.25a. However, this tendency should be used very carefully due the large scatter. The compressive strength seems to act as a measure of the brittleness of granites, which is confirmed by the tendency shown in Figure 3.25b.

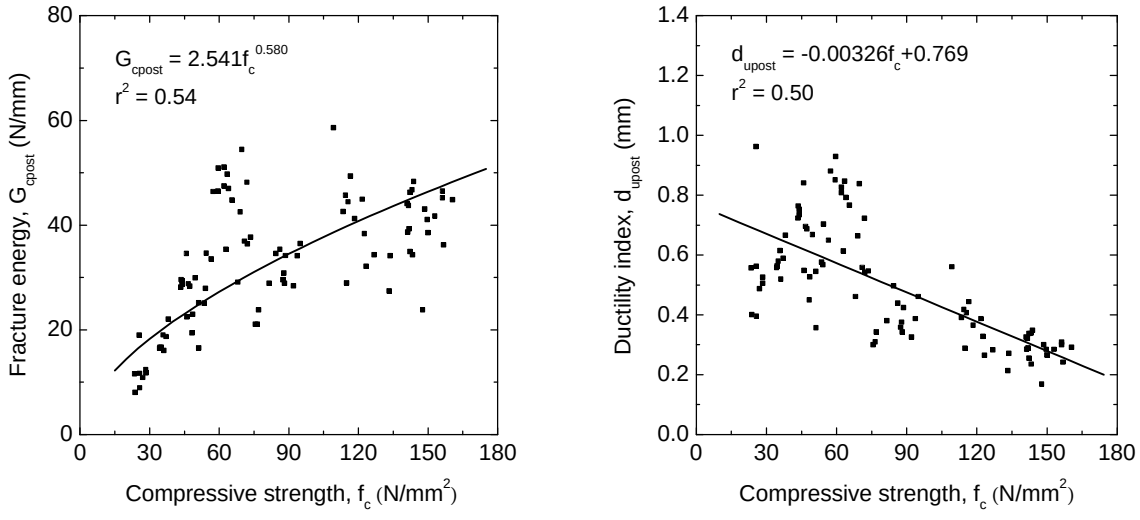


(a) (b)

Figure 3.25 – Relationship between compressive strength and: (a) post-peak fracture energy: (b) ductility index

The ductility of granites decreases as the compressive strength increases. The scatter that was achieved for both trends is, to great extent, influenced by the values found for the granite AF and PTA*. Although no correlation was found between the compressive strength and the pre-peak fracture energy, as can be observed in Figure 3.26a, a negative correlation was obtained for the normalized pre-peak fracture energy, $d_{upre}$, regarding the compressive strength. The nonlinear pre-peak behavior is, thus, more significant in case of low strength granites. This is in agreement with the low values obtained for the crack initiation stress and for the crack damage stress achieved in low strength granites. The values of the ductility of granites can be roughly estimated from the values of the normalized pre-peak fracture energy, through the expression indicated in Figure 3.26b. In spite of the scatter, a reasonable linear correlation was attained between pre and post-peak normalized fracture energies.

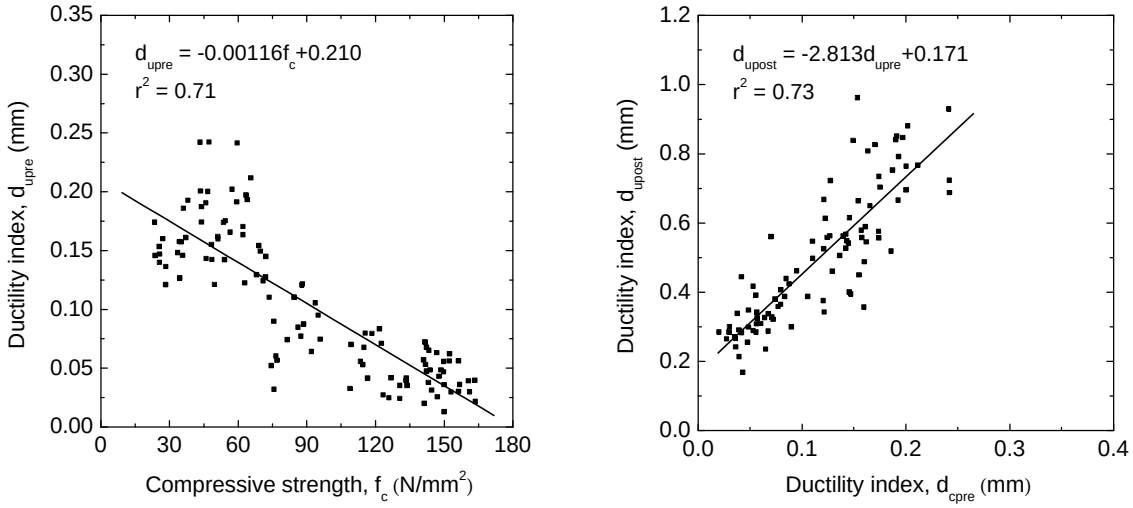


(a) (b)

Figure 3.26 – Relationship between fracture parameters; (a) compressive strength vs. ductility index; (b) normalized pre-peak energy vs. normalized post-peak energy

### 3.3.5 *Correlations between tensile and compressive properties*

The dominant mechanism of brittle fracture in compression is basically mode I cracking, the same as in tension. Previous studies have suggested that pre-peak microcracks in compression are tensile cracks that nucleate from pre-existing flaws and propagate predominantly as mode I fracture (Lajtai *et al*., 1990; Carpinteri *et al*., 1997; Wang and Shrive, 1995). This is the basis of the pre-peak dilatant behavior exhibited by granites. According to Carpinteri *et al*. (1997), the strain localization in a shear band is only the result the lateral restraint induced by the boundary conditions. Therefore, it is expected that both tensile and compressive strength are correlated (Zhang, 2002).

In the present work, this possibility is investigated by fitting a statistical correlation to the experimental data obtained in this Chapter and the results pointed out in Chapter 3. The average values of the compressive and tensile strength were considered. The expected correlation between tensile and compressive strength is shown in Figure 3.27a. The statistical correlation is not very significant, which can be attributed to the anisotropy and inhomogeneity exhibited by granites. If the linear correlation is obtained without the values of highly anisotropic granites PLA and PLA* in the direction perpendicular to the rift plane, the relation between tensile strength and compressive strength would be given by $f_t = 0.0416 f_c$

($r^2$ = 0.73). This means that compressive strength is roughly 24 times higher than tensile strength, which is close to the values indicated by Goodman (1989) for distinct types of rocks, including granites. Similar finding was pointed out by Tugrul and Zarif (1999). Since the values of the elastic stiffness calculated in the tensile tests were solely indicative, a new correlation is proposed between the tensile strength and the modulus of elasticity, see Figure 3.27b. In general, higher values of elastic stiffness are associated to higher values of the tensile strength. Similarly to the former correlation, this one is also disturbed by the tensile strength anisotropy. If one consider the data without the obtained values of granites PLA and PLA* in the direction perpendicular to the rift plane, a significant linear correlation would be proposed: $f_t = 0.000858E + 0.884$, ($r^2 = 0.83$).

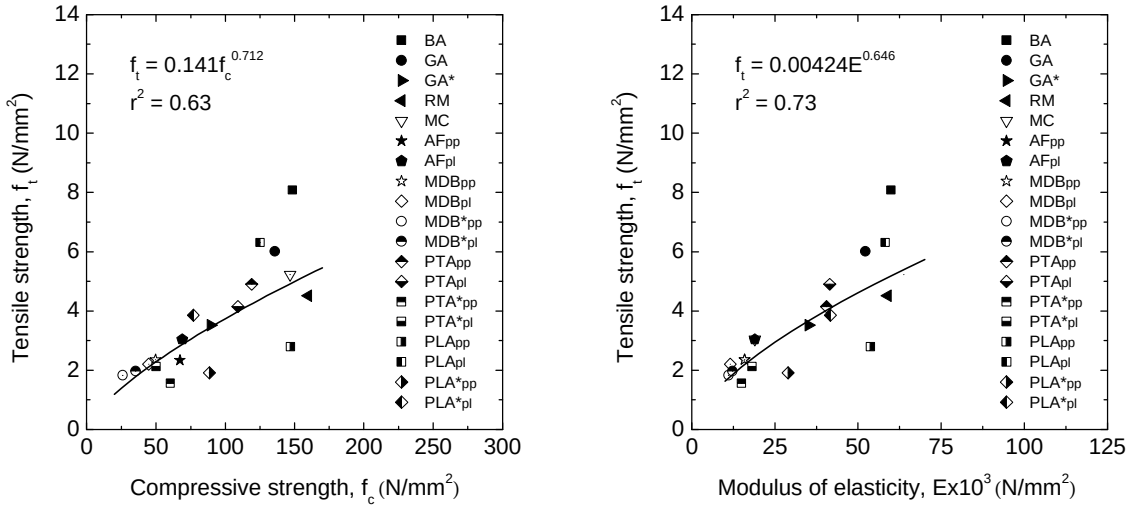


Figure 3.27 – Relationship between: (a) compressive strength and tensile strength; (b) modulus of elasticity and tensile strength

The ductility index corresponding to the mode I tensile fracture can also be estimated based on the compressive strength and on the modulus of elasticity. As can be observed in Figure 3.28, reasonable nonlinear negative correlations were found to exist between compressive strength and modulus of elasticity with the mode I ductility.

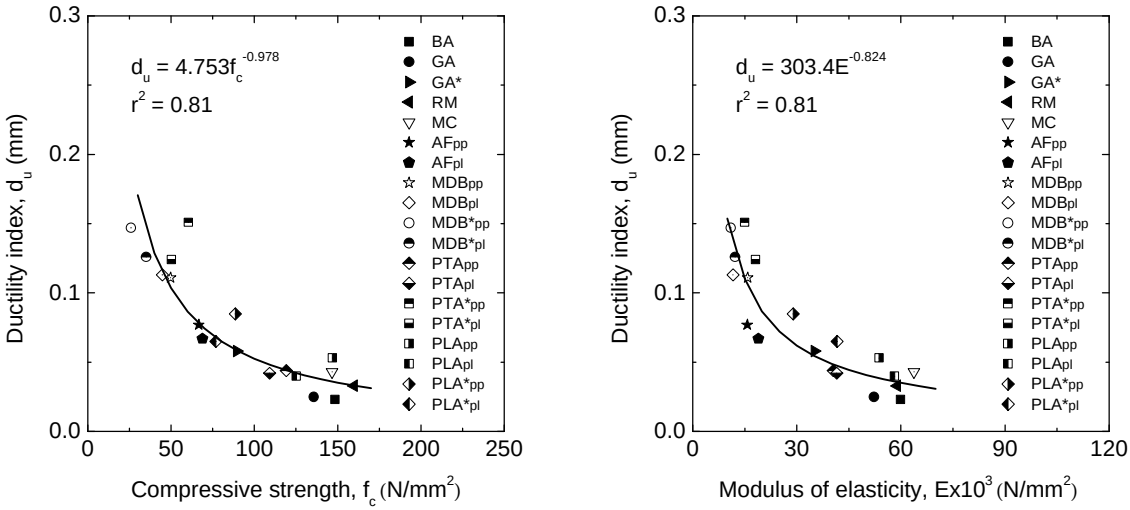


(a) (b)

Figure 3.28 – Relationship between mode I ductility index and: (a) compressive strength; (b) modulus of elasticity

The ductility index decreases as the modulus of elasticity and the compressive strength increase behaving the granites in a more brittle manner. This means that compressive strength and modulus of elasticity are also reasonable measures of the mode I ductility of the material.

Finally, from the trends achieved between the pre and post-peak normalized fracture energy and the mode I ductility show in Figure 3.29, it is possible to observe a similar tendency for pre and post-peak ductility in compression to increase as the mode I ductility increases. The trend obtained for the compressive pre-peak normalized fracture energy is particularly relevant ($r^2$ = 0.75). This seems to confirm that the pre-peak compressive fracture process is, in fact, predominantly characterized by mode I facture, corresponding to the opening of microcracks in the direction parallel to the applied load. In addition, the proportionality between the energy consumed in the opening of the longitudinal cracks during compressive fracture process and the mode I fracture energy appears to be confirmed by this linear correlation.

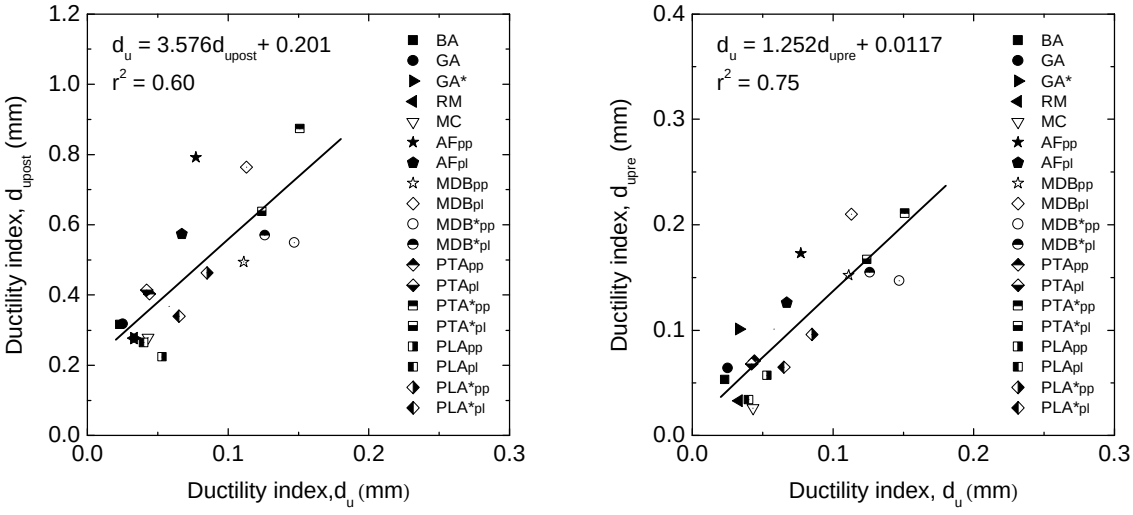


(a) (b)

Figure 3.29 – Relationship between compressive and mode I fracture energy; (a) mode I ductility index vs. normalized pre-peak fracture energy; (b) mode I ductility index vs. normalized post-peak fracture energy

## 3.4 Microstructural influence on the mechanical parameters

This section presents an analysis of the microstructural aspects that influence the variation of the compressive mechanical properties among the granites under study. Aspects like the internal structure, weathering state and moisture content, which explain the features of distinct tensile behavior of granites (Chapter 2), are also expected to influence its compressive behavior. To a brief overview of the motivations that induced this analysis, the reader is referred to Chapter 2.

### 3.4.1 *Internal structure*

From a preliminary comparative analysis of the shape of the complete stress-strain diagrams and a quantitative comparative analysis of the elastic and fracture parameters properties previously indicated in Table 3.2 and Table 3.3, a dependence of the compressive behavior on the direction of the applied load is detected. From Figure 3.30 to Figure 3.32, where the complete stress-strain diagrams of the granites PLA, PLA* and PTA are displayed, distinct

pre-peak deformational and strength features can be pointed out for both directions of the applied load.

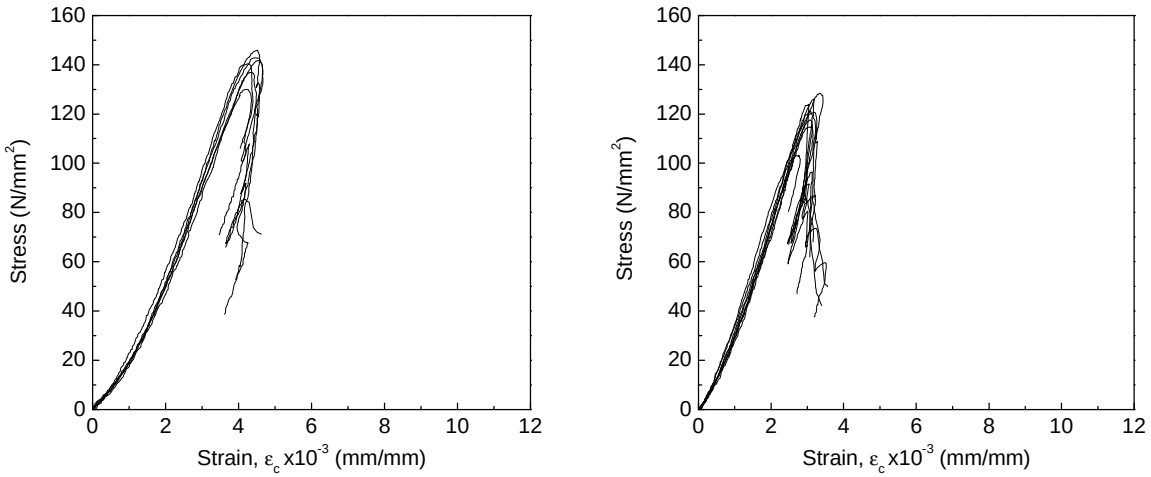


Figure 3.30 – Stress-strain diagrams for granite PLA; (a) direction perpendicular to the rift plane; (b) direction parallel to the rift plane

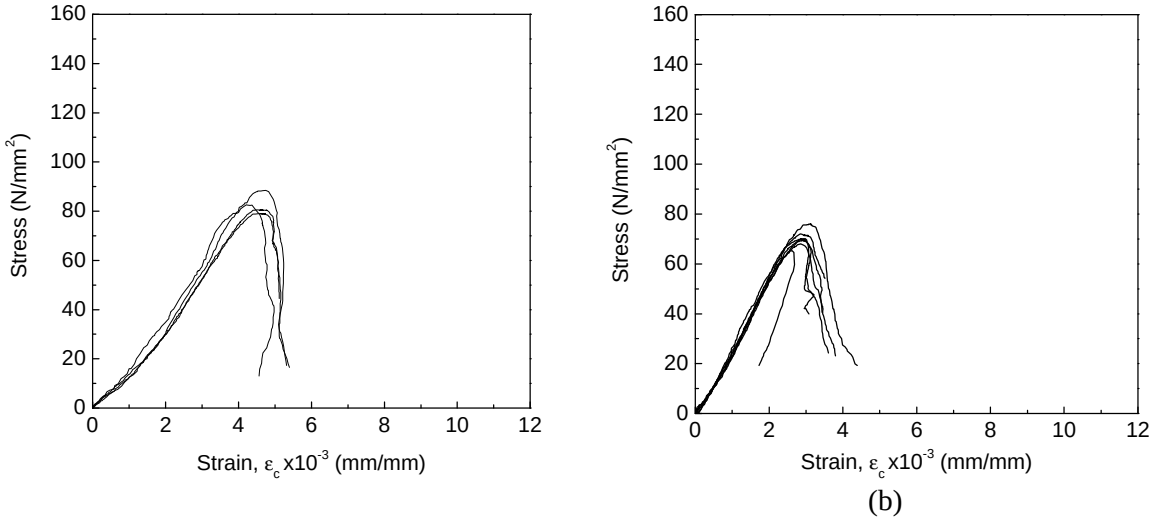


Figure 3.31– Stress-strain diagrams for granite PLA*; (a) direction perpendicular to the rift plane; (b) direction parallel to the rift plane

Granites PLA and PTA exhibit higher compressive strength in the direction perpendicular to the planar anisotropy, which appears to be in disagreement with which was found for the direct tensile load. This fact can be explained by the internal structure related, essentially, to the preferential alignment of minerals, and by the way it is mobilized during the fracture process under uniaxial unconfined compression. In the compressive fracture process of these granites the mode I cracking is the predominant fracture mechanism, which is largely confirmed by the parallel or subparallel direction of the main macrocrack relatively to the applied load. Although in other scale in terms of tensile strains, when the direction of the applied load is parallel to the rift of foliation planes, the tensile strains are mostly perpendicular to the planar anisotropy. The same case occurs in the direct tensile tests when the applied load is in the direction perpendicular to the rift or foliation planes. Similar results

were found in granites PTA*, MDB and MDB*, where the compressive strength presents higher value for the direction perpendicular to the rift plane and the foliation plane, respectively. For granite AF the compressive strength seem almost independent on the loading direction.

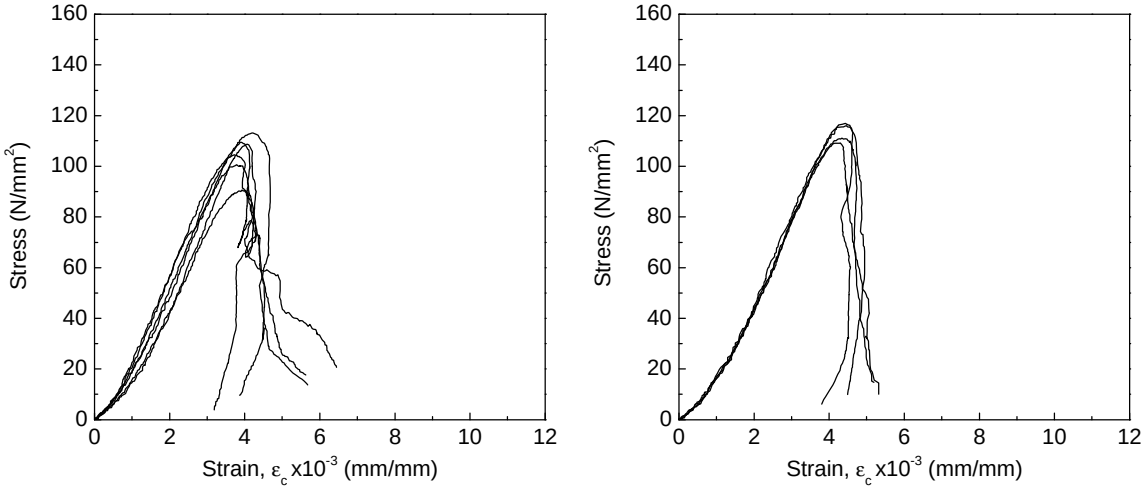


Figure 3.32 – Stress-strain diagrams for granite PTA (a) direction parallel to the foliation plane; (b) direction perpendicular to the foliation plane

As referred in literature (Prikryl, 2001; Åkesson *et al.*, 2003), when a preferred orientation of the feldspar phenocrystals (flow structure) or a foliation plane is clearly defined as predominant internal structure of granites, they can act as a weakness plane, which contributes to the decrease of the compressive strength in the parallel direction to such planar anisotropy. The role that the anisotropic internal texture plays in the mechanical strength of the granites under study becomes clear due to the major influence in the statistical correlation expected between tensile and compressive strength. Anisotropy leads to results opposed to the general trend, in which larger compressive strength is associated to larger tensile strength. This effect is particularly remarkable in granites PLA, PLA* and PTA.

With respect to the elastic properties, in general, the granites exhibit higher axial stiffness in the directions parallel to the rift or to the foliation planes. This seems to indicate that both oriented feldspar phenocrystals and biotite increase the stiffness of the material. This assumption is confirmed when a comparative analysis of the Poisson's ratio is performed in granites PLA, PLA*, PTA and PTA*. In these cases, smaller values of the Poisson's ratio were obtained in the direction perpendicular to the rift or foliation planes.

The analysis of the ascending branch of the stress-strain diagrams for the granites PLA, PLA* and PTA, indicates that the extent of the initial upward concave is more pronounced when the granite is loaded in the perpendicular direction to the rift or foliation planes. The crack closure process is, therefore, more significant when the planar anisotropy is oriented in the perpendicular direction to the applied load. This anisotropic behavior appears thus to be the result of a larger amount of pre-existing open microcraks preferred oriented according to the foliation or the rift plane (parallel or subparallel to the flow structure). At this stage, the compressive behavior is not only affected by the solid skeleton but also by the open microcracks. Similar anisotropic behavior was recorded by Takemura *et al*. (2003). Some other recent studies have been suggested that the rock splitting planes and the consequent

induced anisotropy are normally associated to a preferred orientation of pre-existing microcracks (Chen *et al*., 1999).

The values of the crack damage stress, $f_{cd}$, and the corresponding maximum compaction (maximum decrease of volume), $e_{cd}$, are displayed in Figure 3.33. By comparing the values obtained for these parameters it can be observed that the onset of the dilatancy and the corresponding decrease of the volume are dependent on the direction of the applied load. In granites PLA, PLA*, PTA and PTA*, the values of the crack damage stress exhibit higher levels and simultaneously higher values of volume decrease in the direction perpendicular to the planar anisotropy.

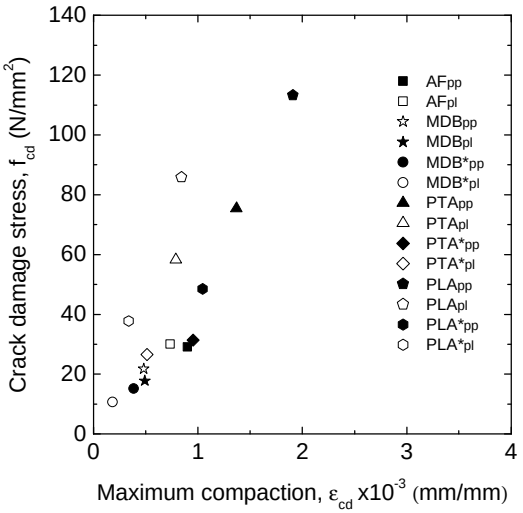


Figure 3.33 – Mean values of the crack damage stress and the corresponding maximum compaction for the directions perpendicular and parallel to the rift or foliation planes.

It has been common to accept that in crystalline rocks, grain boundaries can function as potential Griffith's cracks (Twiss and Moores, 1992). They act as stress concentrators and thus as crack starters (Lajtai *et al*., 1990; Hatzor and Palchick, 1997; Seo *et al*., 2002). Assuming that most of the initial cracks are aligned with the feldspar megacrystals, they are parallel or subparallel at a given angle to the applied load when the rift or foliation planes are considered. This orientation represents exactly the most critical orientation, so that tensile stresses can develop near the crack tips and new cracks develop in a stable manner according the maximum principal stress. This can be the reason why dilatancy starts at lower stress levels for the rift or foliation planes, leading simultaneously to lower strengths. On the other hand, with respect to the deformation, if the maximum compaction is subtracted by the value of variation of volume corresponding to the onset of the microcracking (Table 3.5), it is found that microcracking processes involve higher nonlinear decrease in volume in the direction perpendicular to the rift or foliation planes.

With respect to the energy dissipated in the compressive fracture process, the qualitative analysis of the complete stress-strain diagrams appears to indicate that a steeper drop of the descending branch occurs for the perpendicular direction to the rift or foliation planes. However, this does not hold as a rule, since in granites AF, PLA and PTA* the values of the ductility are considerably higher in the direction perpendicular to the foliation or the rift plane. On the other hand, apart from the granites MDB, all other granites present higher values of dissipated energy and ductility index in the pre-peak fracture process when uniaxial

load is applied in the perpendicular direction to the planar anisotropy. This fact seems to be directly related to the fact that a large part of the nonlinear variation on the bulk volume occurs when the applied load is perpendicular to the planar anisotropy.

The values of the quantitative degree of anisotropy concerning the elastic and fracture properties are shown in Table 3.6. These values were calculated from the mean values of the elastic and fracture properties summarized in Table 3.2 and in Table 3.3. Although all the granites exhibit a certain degree of anisotropy (low to medium), granites PLA and PLA* present significant lower values than the ones obtained in direct tension, see Chapter 2. Nevertheless, it is clear that planar anisotropy influences considerably both elastic and fracture properties.

Table 3.6 – Degree of anisotropy concerning elastic and fracture parameters

| Granite | $E$ | $n$ | $f_c$ | $f_{cd}$ | $f_{ci}$ | $G_{cpost}$ | $d_{upost}$ |
|---|---|---|---|---|---|---|---|
| AF // foliation<br>AF ⊥ foliation | 1.61 | 0.91 | 1.03 | 1.13 | 0.90 | 0.78 | 0.72 |
| MDB // foliation<br>MDB ⊥ foliation | 0.73 | 1.07 | 0.90 | 0.97 | 0.81 | 1.35 | 1.15 |
| MDB* // foliation<br>MDB* ⊥ foliation | 1.11 | 1.10 | 0.74 | 0.70 | 0.70 | 0.69 | 0.96 |
| PTA // foliation<br>PTA ⊥ foliation | 1.02 | 1.10 | 0.92 | 1.14 | 0.90 | 0.98 | 1.03 |
| PTA* // rift plane<br>PTA* ⊥ rift plane | 1.21 | 0.93 | 0.83 | 1.09 | 1.04 | 0.57 | 0.73 |
| PLA // rift plane<br>PLA ⊥ rift plane | 1.08 | 1.15 | 0.85 | 1.83 | 0.90 | 1.03 | 1.18 |
| PLA* // rift plane<br>PLA* ⊥ rift plane | 1.43 | 0.91 | 0.87 | 1.54 | 0.75 | 0.68 | 0.73 |

### 3.4.2 *Physical properties*

The dependence of the compressive mechanical properties on the physical properties of rocks have been reported by several authors (Goodman, 1989; Hatzor and Palchick, 1997; Tugrul and Zarif, 2000; Palchick and Hatzor, 2002; Palchick and Hatzor, 2004). The assessment of this relation is also investigated in case of granites under study, using a set of statistical correlations between mechanical and physical properties. The porosity and density were obtained for each compressive specimen following the same procedures indicated in Chapter 2.

The dependence of the compressive strength on the physical properties, namely porosity, $n$, and dry density, $r_d$, is confirmed by the relations displayed in Figure 3.34. A nonlinear correlation was found between the compressive strength and the porosity ($r^2$ = 0.87). The compressive strength decreases as the porosity increases. In addition, a tendency for the compressive strength increase as density increase is indicated by the nonlinear correlation shown in Figure 3.34b. The main reason that explains this effect is related to the increase on the number of pores, voids and microcracks as the result of the lower strength of the grain boundaries. These features lead to the weakness of the resistant matrix since these defects act as stress concentrators and, thus, the local strength should govern the global compressive behavior. In the same way, the modulus of elasticity presents high values for dense and low

porosity granites and decreases as the porosity increases and density decreases, see Figure 3.35. The stiffness of rocks depends, on one hand, on the stiffness of the rock forming minerals and, on the other hand, on the cohesion of the grain boundaries. An observation should be made, however, concerning values of the compressive strength and stiffness obtained in granite GA*. They are much higher than expected and contribute to increase the scatter. Nevertheless, these correlations are better than the ones obtained in Chapter 3, referring to the tensile behavior. This can be explained by the higher anisotropy exhibited by the granites under tension, and by the fact there are no directional differences regarding porosity or density. The analysis between the physical properties and Poisson's ratio reveals that no correlation was possible.

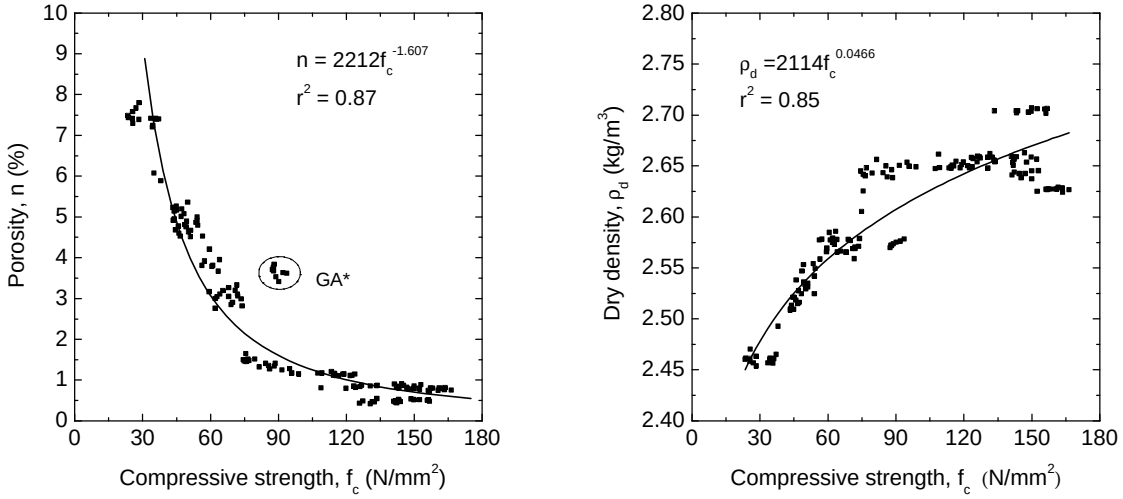


(a) (b)

Figure 3.34 – Relation between compressive strength and physical properties; (a) compressive strength vs. porosity; (b) compressive strength vs. dry density

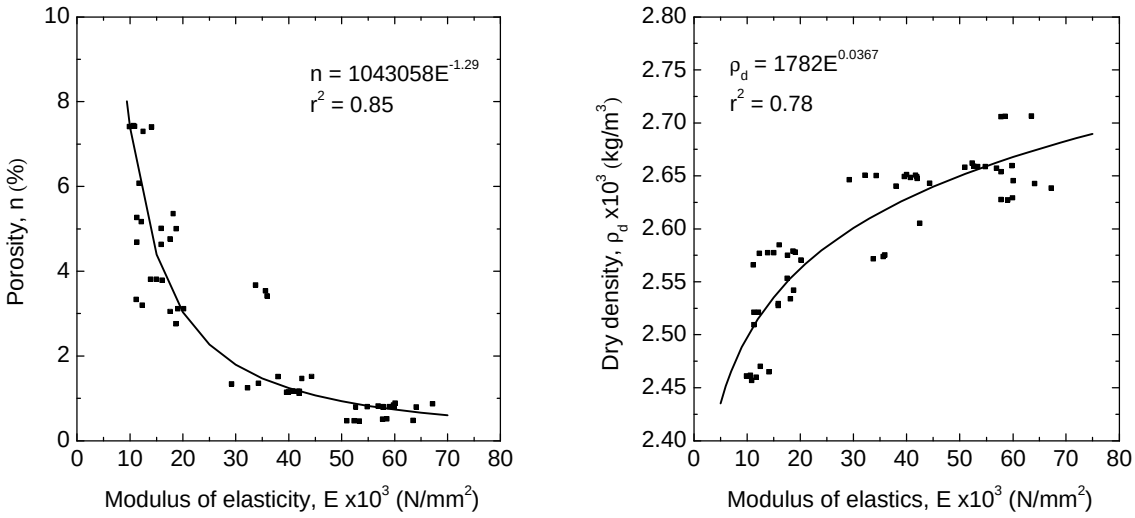


Figure 3.35 – Relation between modulus of elasticity and physical properties; (a) modulus of elasticity vs. porosity; (b) modulus of elasticity vs. dry density

The relations between stress markers and the porosity are indicated in Figure 3.36. Significant nonlinear correlations were found between initial crack stress ($r^2$ = 0.88) and crack damage stress ($r^2$ = 0.86) with porosity. The stress for which crack initiation and crack damage takes place is directly connected to the porosity, and decreases as the porosity increases. Since the

stress markers characterize the fracture process that occurs until the compressive strength is reached, the porosity takes a crucial role in the initiation and propagation of the pre-peak microcracking network. This confirms the role of pores function as stress concentrators. Similar results were pointed out by Hatzor and Palchick (1997) and Palchick and Hatzor (2002) in dolomites and limestones. According to these authors, the initial cracks in porous rocks were found to be the union of several crystal faces properly aligned with the maximum principal stress.

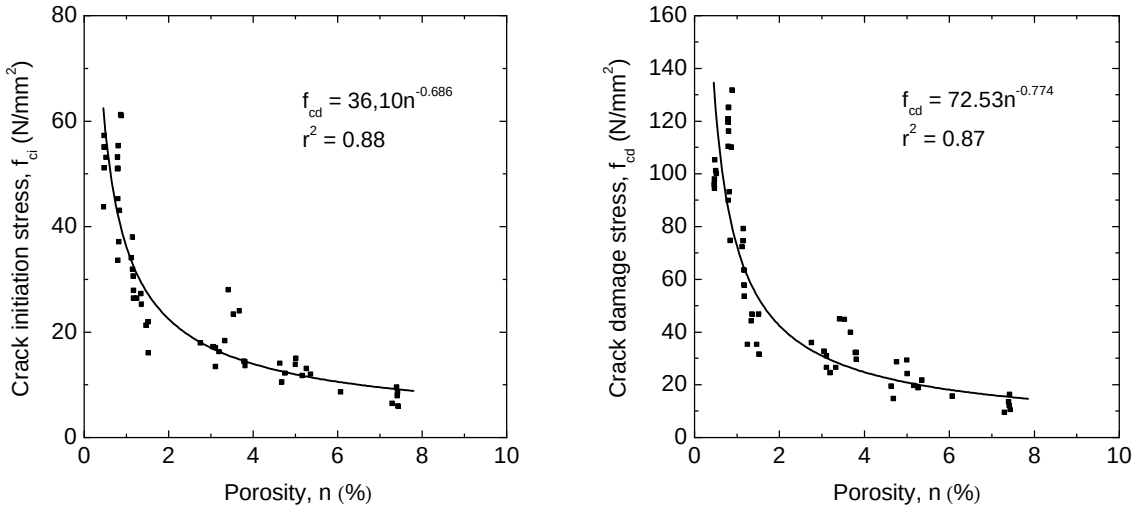


Figure 3.36 – Relation between stress markers and porosity; (a) porosity vs. crack initial stress; (b) porosity vs. crack damage stress

Although no clear relation between pre and post-peak fracture energy and porosity was found, it is possible to observe some relation between the normalized values, $d_{upre}$ and $d_{upost}$, see Figure 3.37.

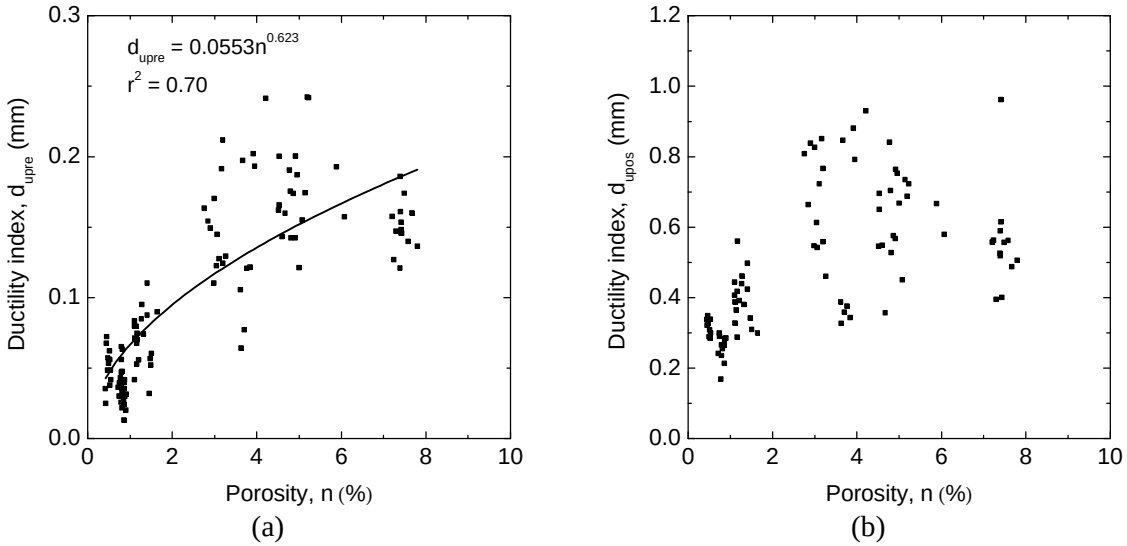


Figure 3.37 – Relation between porosity fracture properties; a) porosity vs. ductility index, $d_{upre}$; (b) porosity vs. ductility index, $d_{upost}$

In Figure 3.37a, a positive nonlinear correlation ($r^2 = 0.70$) is shown, between the normalized pre-peak fracture energy and porosity. This seems to indicate that in more porous granites, the

microcracking process, as well as its interaction and propagation, involve higher amount of energy. This is possibly the result of the higher level of dilatancy due to high crack densities and, therefore, large nonlinear variation of volume is associated to the coalescence of microcracks. Despite the high scatter, there seems to be a tendency for the normalized post-peak fracture energy to increase as the porosity increases, which means that, at least to certain extent, the porosity gives an indication of the ductility of the material. This result is in agreement with the trend observed in Chapter 2 concerning the mode I ductility index.

### 3.4.3 *Weathering state*

The evaluation of the influence of the weathering effects on the compressive behavior of granites is established from the qualitative analysis of the complete stress-strain diagrams and from the comparative study of the elastic and fracture parameters. The complete stress-strain diagrams for the fresh granites GA, PTA, MDB and the corresponding weathered granite, GA*, PTA* and MDB* are displayed from Figure 3.38 to Figure 3.40.

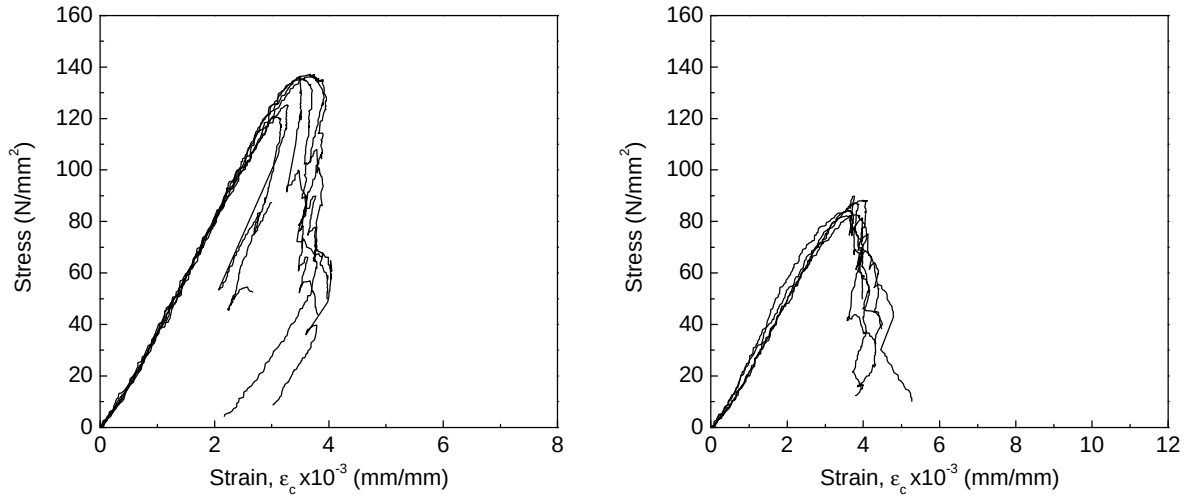


Figure 3.38 – Stress-strain diagrams; (a) granite GA; (b) granite GA*

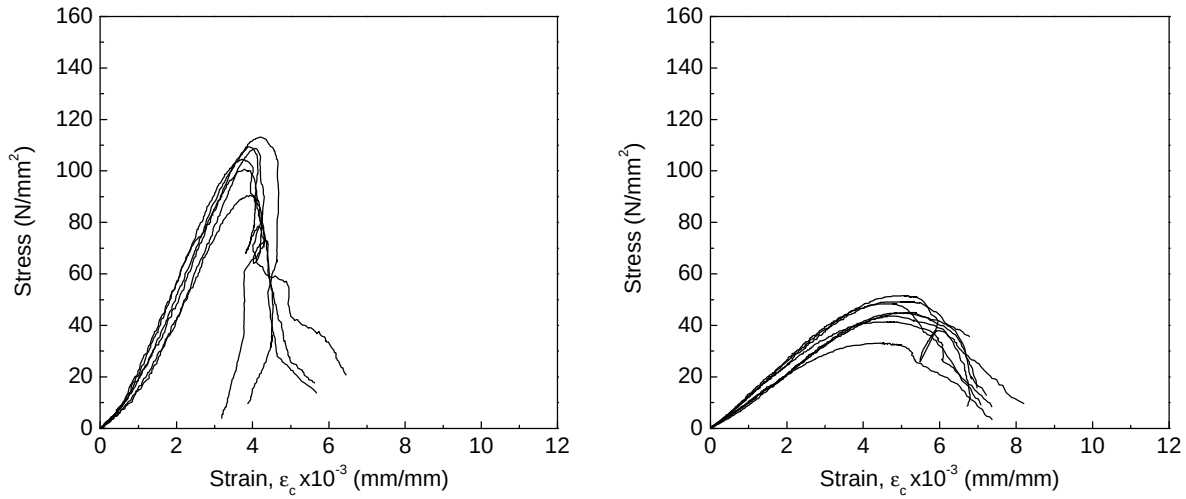


Figure 3.39 – Stress-strain diagrams; (a) granite PTA in direction parallel to foliation plane; (b) granite PTA* in direction parallel to rift plane

The shape of these diagrams shows clearly that significant distinct pre and post-peak compressive behavior is addressed for fresh and weathered granites. Besides the higher values of the compressive strength, the slope of the ascending branch of the stress-strain diagrams is considerably higher in fresh granites, in comparison with the slope exhibited by weathered granites. Moreover, the deformation capacity until peak load is attained is significantly larger in weathered granites. In terms of post-peak behavior it is noticeable that the fresh granites exhibit very brittle response, associated to a steep and often discontinuous softening branch, whereas for weathered granites the descending branch is mostly continuous and smooth. The remarkable difference of the post-peak behavior seems to be the result of a distinct mechanism of macrocracking localization. In effect, in fresh granites the main macrocrack that result from the localization is parallel or sub-parallel to the axial load. In weathered granites the localization occurs predominantly in a shear band. Note that granite MDB is less weathered than MDB*, but its high porosity is similar to the granite PTA*, which leads to the smooth post-peak branch, as shown in Figure 3.40a.

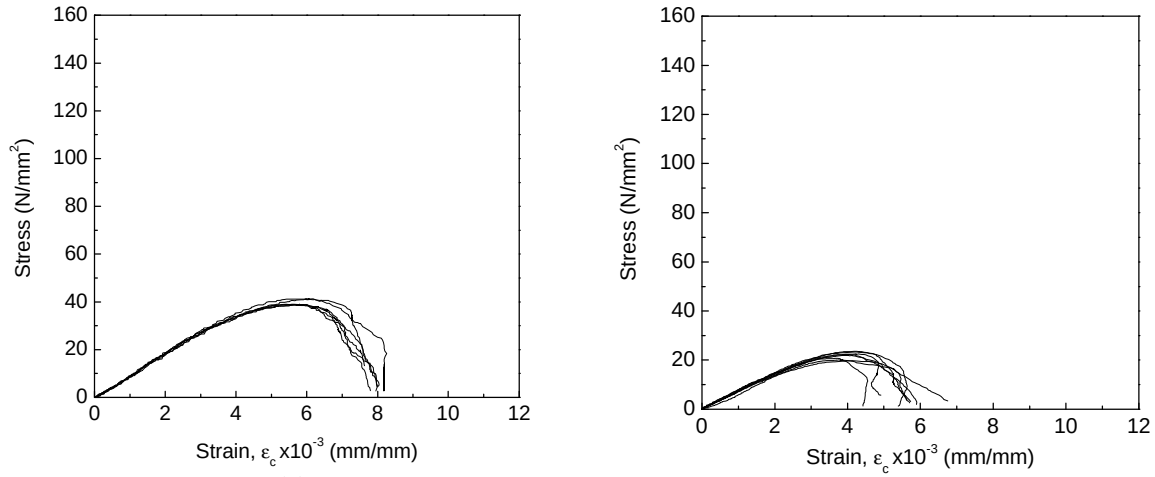


Figure 3.40 – Stress-strain diagrams; (a) granite MDB in direction parallel to foliation plane; (b) granite MDB* in direction parallel to foliation

The ultimate deformation is considerable higher in weathered granites, which appears as an outcome of a more ductile behavior of the material. By comparing the mean values of the elastic parameters that characterize the pre-peak behavior of the granites, modulus of elasticity, *E*, and Poisson's ratio, *n*, see Figure 3.41, it is clear that much higher values of the modulus of elasticity are associated to fresh granites. The main reasons that contribute for the decrease upon weathering are related to the lower stiffness of the rock forming minerals as a result of their alteration, as well as to progressive weakness of the bond interface stiffness. On the other hand, higher values of the Poisson's ratio were obtained for weathered granites. The increase on the porosity that characterizes the weathered granites reflects the change on the granite skeleton with the increase of pores, voids and free stress microfissures, which are expected to occur at the grain boundaries. Thus, the increase in the Poisson's ratio of the weathered granites can be attributed to the decrease on the grain boundary strength.

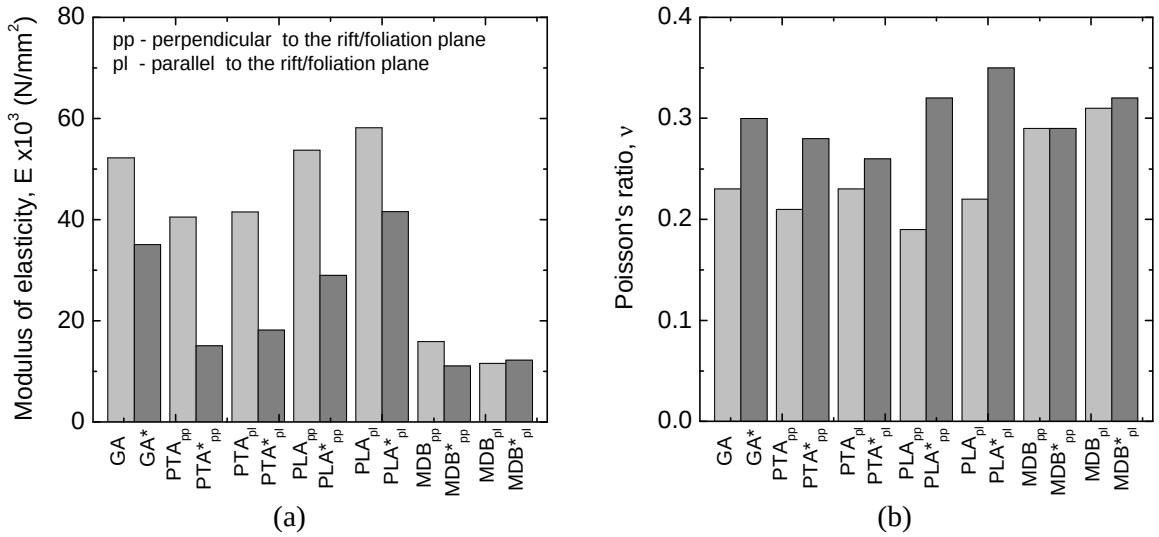


(a) (b)

Figure 3.41 – Comparison of the mean values of the elastic parameters between fresh/less weathered granites and weathered granites; (a) modulus of elasticity; (b) Poisson's ratio

The analysis of the mean values of the compressive strength reveals that fresh granites present high compressive strength, while, in general, weathered granites exhibit low strength, see Figure 3.42.

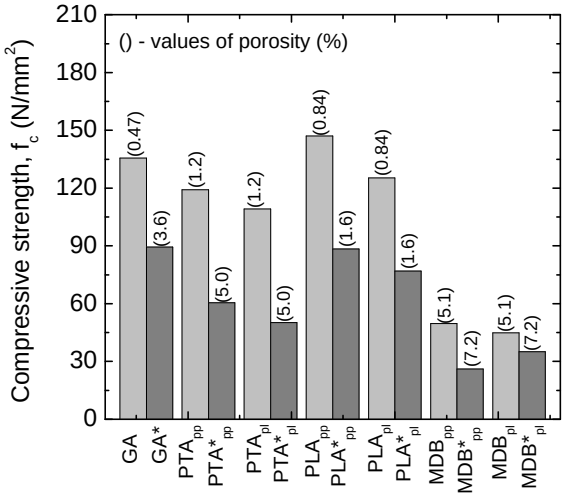


Figure 3.42 – Comparison of the compressive strength between fresh /less weathered and weathered granites

The decrease in the compressive strength for weathered granites reaches considerable values, ranging between 47.6% and 54.0% of the less weathered strength, respectively for granites MDB* (direction perpendicular to foliation) and PTA* (direction parallel to foliation). Note also the remarkable lowering of the compressive strength of granites MDB and MDB*, with high porosity, with respect to the other granites. On one hand, the same rock forming minerals that are present in both fresh and weathered undergoes stiffness and strength changes due to weathering effects and, on the other hand, the heterogeneity degree is remarkably higher in case of weathered granites as the result of new pre-existing cracks. From numerical simulations, Tang *et al*. (2000a) and Chen *et al*. (2002) found that the heterogeneity plays an important role in the deformation and strength characteristics of rocks. Besides higher values of strength, more homogeneous specimens were found to deform more

linearly prior to the peak stress. In more heterogeneous materials, the strength of the materials is essentially ruled by the local strength of potential stress concentrators like pores, voids and grain boundaries. This finding is in agreement with the decrease on the tensile strength pointed out in Chapter 2 as well as with results reported elsewhere (Gupta and Rao, 2000; Tugrul, 2004).

The quantitative comparative analysis of the pre-peak fracture process features between fresh and weathered granites is performed through the evaluation of the stress markers, crack initiation stress, $f_{ci}$, and crack damage stress, $f_{cd}$. These properties characterize, to a certain extent, the shape of the stress-lateral and stress-volumetric strain diagrams, see Figure 3.43. The onset of microcracking was found to occur earlier for weathered granites, being the difference more significant for granites GA, PLA and PTA in the direction perpendicular to the foliation. A similar trend was observed for the crack damage stress. The onset of dilatancy takes place for remarkably higher stress levels in case of fresh granites comparatively to weathered granites. In weathered granites, the propagation and interaction of microcracking occurs for low stresses, roughly at $0.5f_c$. In granites GA*, MDB and MDB* the stress levels found for $f_{cd}$ are even lower than $0.5f_c$.

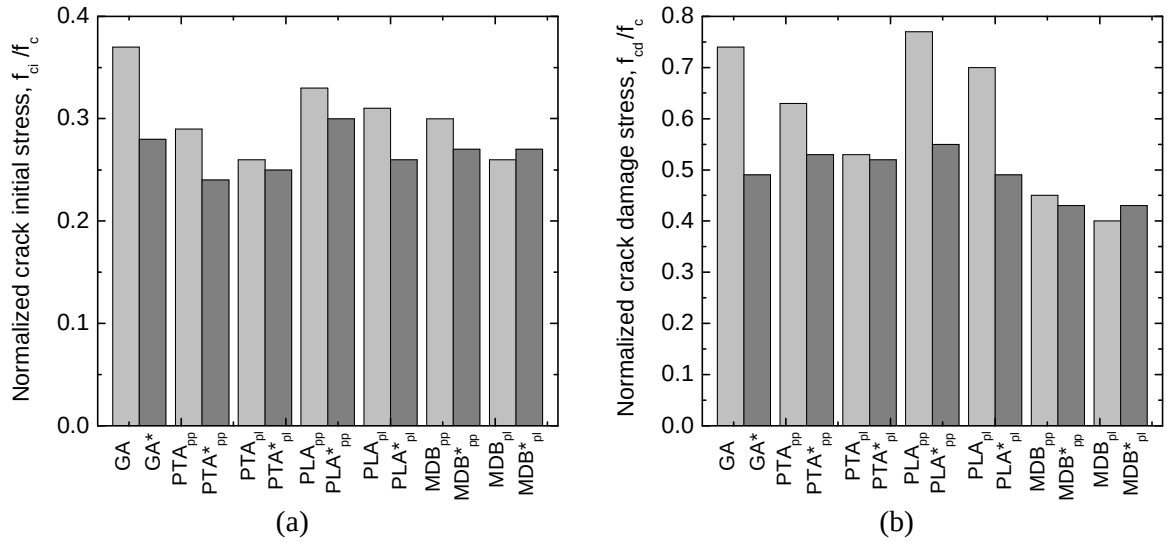


Figure 3.43 – Comparison of the compressive stress markers between fresh/less weathered and weathered granites; (a) normalized crack initiation stress; (b) normalized crack damage stress

Since porosity in weathered granites is significantly higher than in fresh granites, it is acceptable that a higher number of pores acting as stress concentrators and crack initiators are present. This means that larger a amount of microcracks grow from the pores and voids, which is revealed by the higher level of nonlinearity in the stretch of the stress-volumetric diagram prior the crack damage threshold, see Figure 3.44a. On the other hand, the microfracture growth and its interaction and coalescence involve a remarkably high variation of volume in weathered granites. This is the outcome of large lateral deformations shown in the stress-lateral deformation diagram. The distinct pre-peak fracture process between fresh and weathered granites is also confirmed by the evolution of the Poisson's ratio with the stress level, Figure 3.44b.

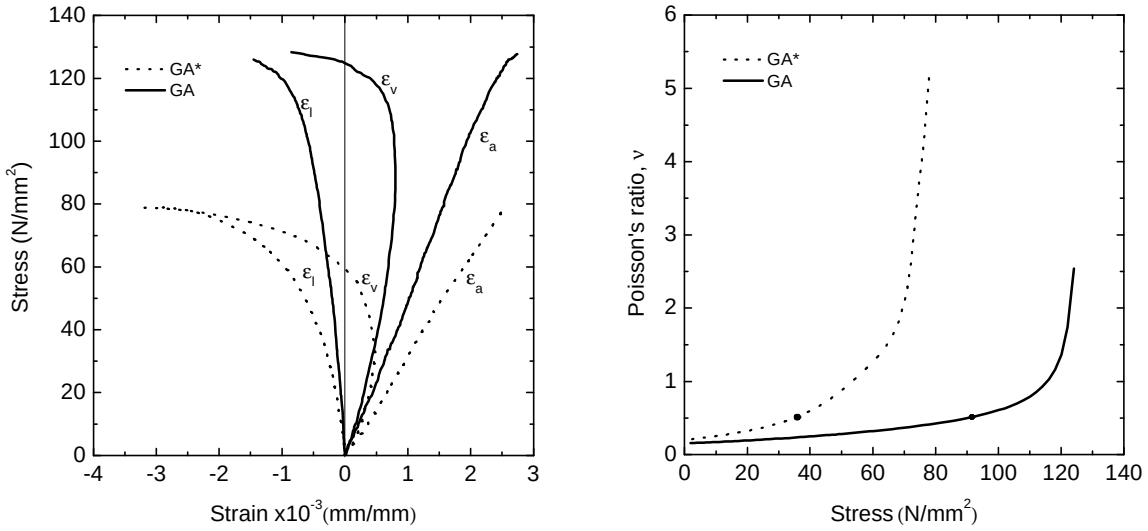


Figure 3.44 – Comparison of the pre-peak fracture process between granites GA and GA*; (a) stress-strain diagrams; (b) evolution of the Poisson's ratio with axial stress

For granite GA, the Poisson's ratio exhibits roughly constant values up to a stress of 45N/mm$^2$ and progressively increases until attain a stress of 95N/mm$^2$, achieving its maximum theoretical value of 0.5. This stress level fits the onset of the dilation for $0.73f_c$. In granite GA*, the nonlinear evolution of the Poisson's ratio starts at significant lower stress level ($0.25f_c$), reaches its maximum value at approximately $0.5f_c$ and then increases continuously.

The energy dissipated in the pre and post peak fracture process and the corresponding normalized values are displayed in Figure 3.45 and in Figure 3.46, respectively.

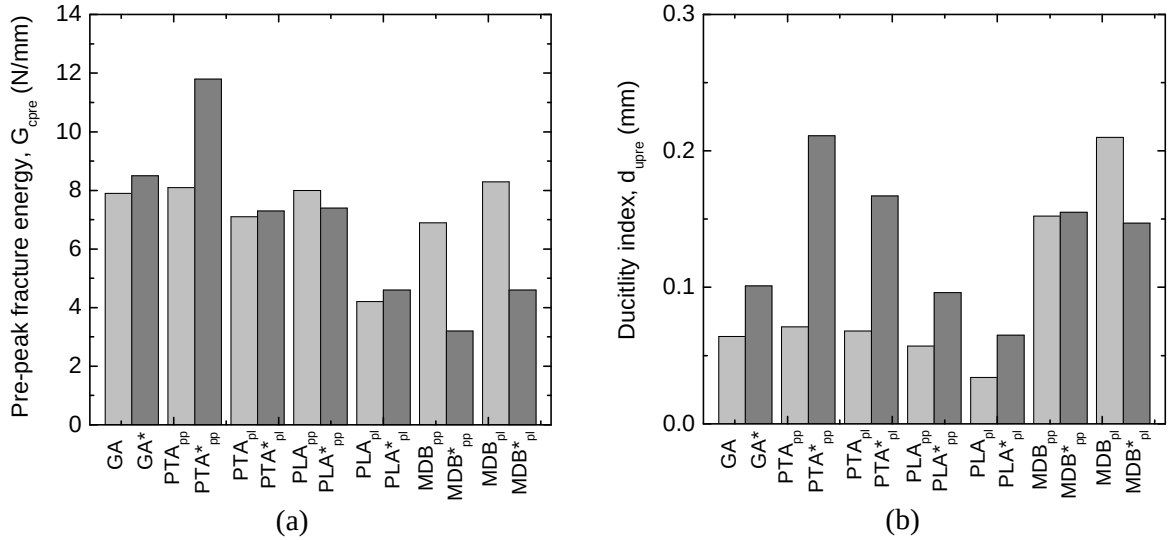


Figure 3.45 – Comparison of the pre-peak behavior between fresh/less weathered and weathered granites; (a) fracture energy; (b) ductility index

Large values of fracture energy are found in weathered granite PTA* in the direction perpendicular to foliation, but decreasing values are found in granite MDB* with respect to granite MDB. In the other cases, the fracture energy shows small variations being considered approximately constant. In opposite, apart from granite PTA* (direction perpendicular to

foliation), the fracture energy dissipated in the post peak regime is higher in fresh/less weathered granites in relation to weathered granites. On the other hand, more significant differences are observed when the ductility index is compared. Apart from granite MDB* (direction parallel to foliation), all other weathered granites exhibit higher ductility than fresh granites, which is valid for the pre and post peak regimes. This is mainly attributed to the significant decrease of the compressive strength of weathered granites.

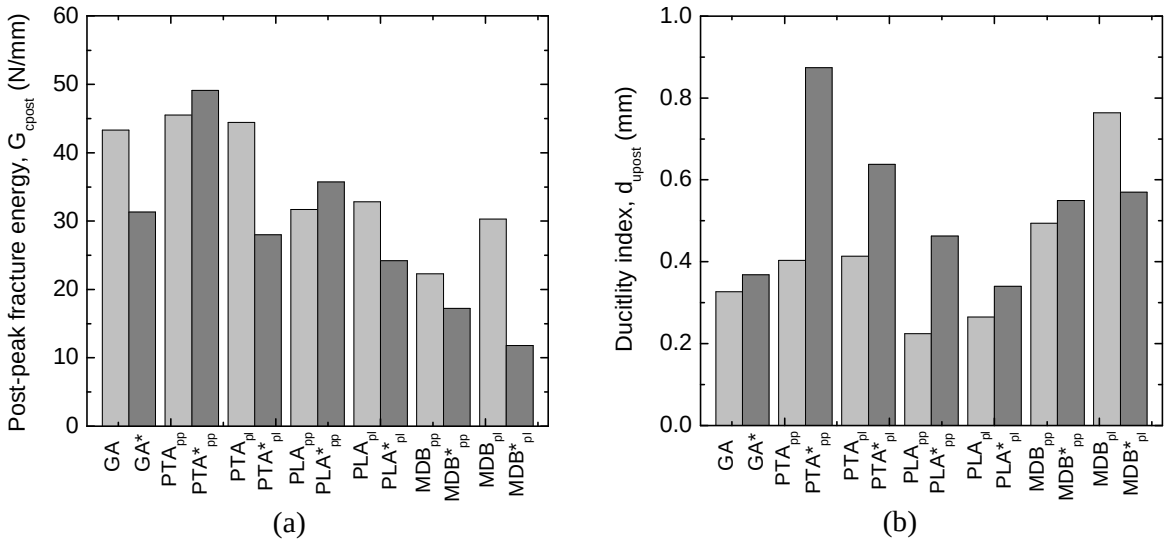


(a) (b)

Figure 3.46 – Comparison of the post-peak behavior between fresh/less weathered and weathered granites; (a) fracture energy; (b) ductility index

To a certain extent, the increase in the ductility index can be explained by the weakness of the grain boundaries that govern the fracture process, leading to more tortuous paths, see Figure 3.47. This trend is not observed for granite MDB*. Although granite MDB is considered a less weathered granite, as stressed in Chapter2, its porosity is remarkable and, in fact, MDB and MDB* indicate two granites with different degrees of alteration.

Figure 3.47– Fracture path for weathered granite PLA*

### 3.4.4 *Mineralogical composition*

In order to evaluate the influence of the mineralogical composition in the compressive behavior of granites, a procedure analogous to the one used in the characterization of the tensile behavior is followed. Thus, to perform the analysis of the role that the mineralogical composition plays on the compressive parameters, a distinction between biotite granites (BA,

MC, RM, PLA) and two mica granites (PTA, GA) is considered. Regarding the grain size, the granites PTA, GA and BA are considered fine to medium-grained, while granites MC, RM, PLA are medium to coarse-grained. Note that only fresh granites were taken into account so that unreliable conclusions could be avoided. The distinction of the elastic properties and the normalized stress markers regarding the compressive strength between biotite and two mica granite is displayed in Figure 3.48a and Figure 3.48b respectively. Biotite granites exhibit higher values of axial stiffness and slightly higher values of the Poisson's ratio than two mica granites. Besides, the stress levels from which cracking initiation and propagation take place are higher in case of biotite granites. This indicates that pre-peak nonlinear behavior is more severe for two mica granites. This appears to be also confirmed by the higher values of pre-peak fracture energy exhibited by two mica granites, see Figure 3.49a. Similarly, biotite granites exhibit higher brittleness in the post-peak regime since lower values of fracture energy and ductility index are associated to them, see Figure 3.49b.

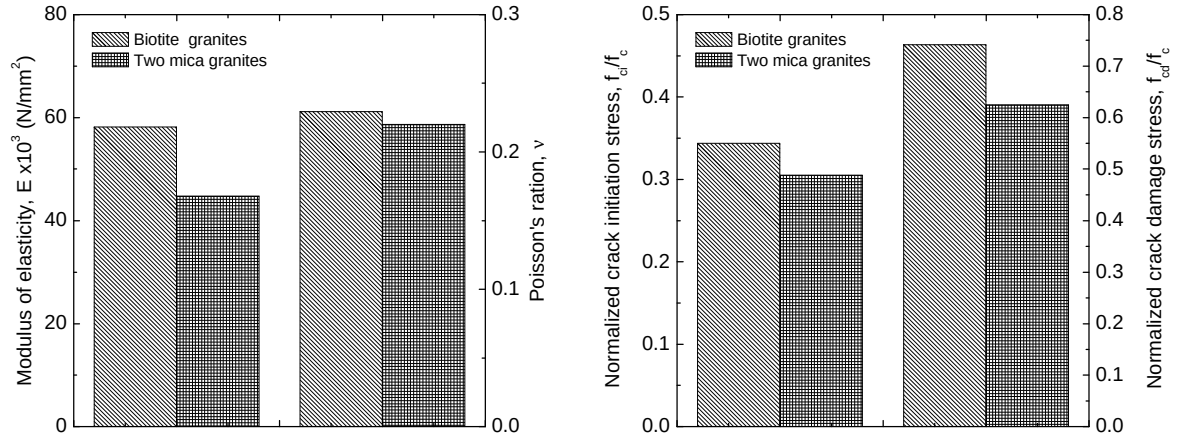


Figure 3.48 – Mechanical properties for biotite and two mica granites; (a) modulus of elasticity and Poisson's ratio; (b) normalized stress markers

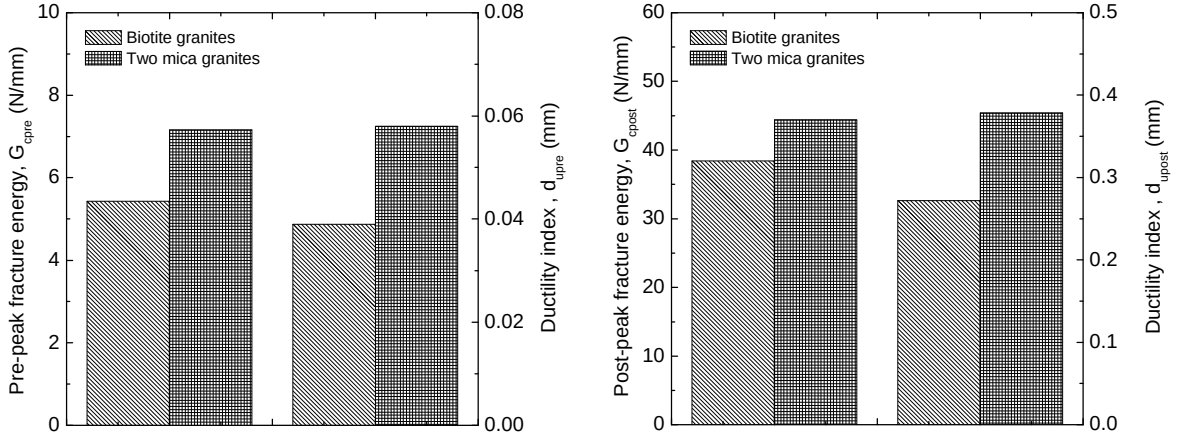


Figure 3.49 – Mechanical properties for biotite and two mica granites; (a) pre-peak fracture energy and ductility index, $d_{upre}$; (b) post-peak fracture energy and ductility index, $d_{upost}$

From the analysis of Figure 3.50, where the compressive strength in shown, it can be seen that, in general, biotite granites exhibit higher values relatively to two mica granites. Note

that, apart from granite BA, biotite granites are medium to coarse-grained granites. Coarse-grained granites are expected to have lower strength due to possible larger grain boundaries and intergranular cracks that may act as weakness paths and promote the development of secondary cracks (Eberhardt *et al*., 1999b). According to Hatzor and Palchick (1997), if grain boundaries are assumed as initial flaws, a longer initial crack corresponds to a higher stress intensity factor and thus, the lower the ultimate stress that leads to failure. In the present case, this seems not to be the main reason that determines the compressive strength. The strength of the rock forming minerals, the stiffness and strength of the grain boundary should be the basis of the higher compressive strength found for these granites. However, it should be mentioned that the compressive strength found for granites MC and RM is higher than expected, if the values of the tensile strength would serve the reference.

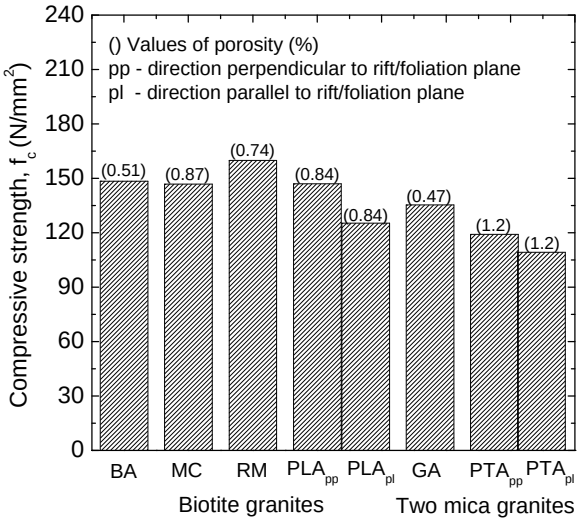


Figure 3.50– Compressive strength for biotite and two mica granites

### 3.4.5 *Moisture Content*

As reported in literature (Goodman, 1989; Hawkins, 1998; Gupta and Rao, 2000; Feng *et al*., 2001), the mechanical properties of rocks, namely compressive strength and modulus of elasticity, are affected by the moisture content. The results of tensile tests shown in Chapter 2 indicated that the tensile strength is significantly reduced in saturated conditions. In order to obtain a better insight on the influence of water saturation on the compressive behavior of granites, twenty-five compression tests were performed on six types of granites. From the stress-strain diagrams, it is possible to obtain compressive parameters, namely compressive strength, stiffness and fracture energy and to compare the new values with the values obtained in specimens tested under dry conditions.

The qualitative analysis of the complete stress-strain diagrams obtained for dry and saturated specimens are shown in Figure 3.51 and Figure 3.52. These indicate that a significant decrease on the compressive strength is recorded in saturated specimens, with respect to dry specimens. Furthermore, under saturated conditions the material exhibits lower deformation capacity at peak load. On the other hand, the saturated specimens show a slightly more ductile behavior since the slope of the descending branch appear to be steeper in case of dry specimens. In spite of less specimens tested under saturated conditions, the complete stress-stain diagrams seem to exhibit lower scatter both in the pre and post-peak regimes.

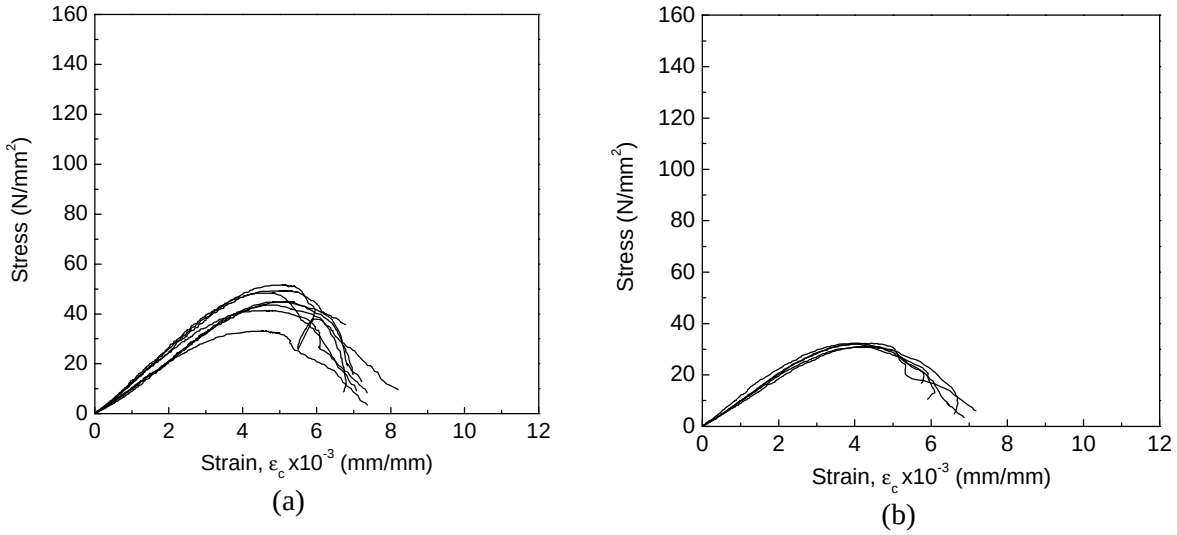


Figure 3.51 – Stress-strain diagrams of granite PTA* in the direction parallel to the rift plane; (a) dry specimens; (b) saturated specimens

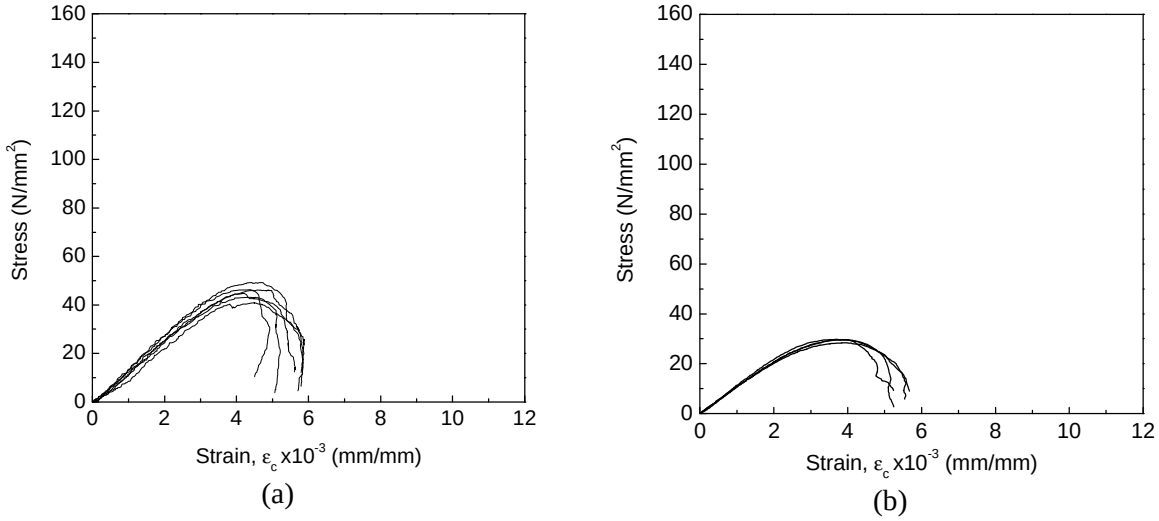


Figure 3.52 – Stress-strain diagrams of granite MDB in the direction perpendicular to the foliation; (a) dry specimens; (b) saturated specimens

The average values of the compressive parameters obtained under saturated conditions are summarized in Table 3.7. The ratio of the compressive parameters obtained under saturated conditions with respect to the ones obtained in dry conditions is indicated inside brackets. In quantitative terms, the wet specimens undergo a reduction in strength ranging between 27.0% and 42.3% of the dry compressive strength. Similar decreasing trend is recorded in the axial stiffness that exhibits differences between 16 and 36%. These results are in agreement with others reported in literature (Gupta and Rao, 2000; Feng *et al*., 2001). Hawkins (1998) reported losses in compressive strength ranging between 8% and 59%. The lower stiffness and strength attributed to the saturated specimens can be explained by the changing of stone skeleton due to water filling of pores and voids. The solid grain interaction is reduced due to lower grain to grain contact (Gupta and Rao, 2000). On the other hand, water pressure in pores should increase stress concentrations and, thus, lead to earlier fracture. This fact is also pointed out as the reason by which the peak load is attained with lower deformation. The fracture energy involved in the pre-peak microcracking in saturated conditions is always

lower than in dry conditions. If the normalized value of the pre-peak fracture energy with respect to the compressive strength is taken into account, it can be verified that its decrease is particularly significant in case of granite PLA*. Although with lower porosity, this granite is believed to possess higher amount of microfissures that should bound the microcracking process under saturated conditions.

Regarding the post-peak behavior, the fracture energy exhibits systematically lower values in saturated specimens, which seems to be essentially the outcome of a reduction on the compressive strength. By comparing the mean values of the ductility index for both moisture contents, the higher ductility suggested by the shape of the softening branch of the stress-strain diagrams is effectively confirmed for granites GA*, PTA* and MDB* in the direction perpendicular to foliation. The elastic anisotropy found in dry specimens (MDB and PLA*) is maintained in saturated specimens. If, on one hand, the characteristics of deformation until peak load follows the anisotropic tendency found in dry specimens, on the other hand, the anisotropy strength recorded in granite PLA* is almost vanished in saturated specimens. With respect to post-peak behavior, the anisotropy achieved for the fracture properties, namely in granites MDB and PLA*, fracture energy and ductility index, is also kept in saturated specimens. Although values of the crack damage stress were not calculated, a reduction on the stress level that marks the onset of propagation of microcracking is expected in case of saturated granites (Lajtai, 1998).

Table 3.7 – Average values of the elastic and compressive fracture parameters for saturated conditions

| Granite | $f_c^{wet}$ (N/mm$^2$) | $E^{*wet}$ (N/mm$^2$) | $G_{cpre}^{wet}$ (N/mm) | $G_{cpost}^{wet}$ (N/mm) | $d_{upost}^{wet}$ (mm) |
|---|---|---|---|---|---|
| GA* | 65.1 (0.73$f_c$) | 25218 (0.83$E$) | 5.4 (0.65$G_{cpre}$) | 23.6 (0.78$G_{cpost}$) | 0.389 (1.11$d_{upost}$) |
| AF // foliation | 47.9 (0.70$f_c$) | 12252 (0.78$E$) | 3.6 (0.56$G_{cpre}$) | 23.1 (0.62$G_{cpost}$) | 0.518 (0.90$d_{upost}$) |
| MDB ⊥ foliation | 33.9 (0.68$f_c$) | 11006 (0.78$E$) | 4.4 (0.64$G_{cpre}$) | 16.0 (0.72$G_{cpost}$) | 0.545 (1.10$d_{upost}$) |
| MDB // foliation | 30.9 (0.69$f_c$) | 7768 (0.81$E$) | 5.7 (0.70$G_{cpre}$) | 18.9 (0.63$G_{cpost}$) | 0.717 (0.96$d_{upost}$) |
| PTA* // rift plan | 36.3 (0.72$f_c$) | 10727 (0.84$E$) | 5.1 (0.69$G_{cpre}$) | 24.4 (0.87$G_{cpost}$) | 0.774 (1.21$d_{upost}$) |
| PLA* ⊥ rift plan | 51.0 (0.58$f_c$) | 16369 (0.64$E$) | 2.9 (0.69$G_{cpre}$) | 21.0 (0.60$G_{cpost}$) | 0.457 (1.00$d_{upost}$) |
| PLA* // rift plan | 52.0 (0.68$f_c$) | 25509 (0.84$E$) | 2.2 (0.61$G_{cpre}$) | 14.2 (0.60$G_{cpost}$) | 0.303 (0.92$d_{upost}$) |

### 3.4.6 *Evaluation of the crack patterns*

It has been widely recognized that microcracks initiated and propagated in the fracture process before the peak stress is reached are predominantly tensile cracks and develop in the direction parallel to the applied loading (Kranz, 1979; Moore and Lockner, 1995; Seo *et al*., 2002; Zhang, 2002). Lajtai *et al*. (1990) refers that shear fractures do not form before failure and represent a post-failure phenomenon. According to Carpinteri *et al*. (1997), in uniaxial tests the macroscopic cracks essentially starts parallel to the direction to the axial loading. This is explained by the heterogeneity due to pre-existing microcracks, pores and voids that are considered as stress producers in compression.

Concerned the post-peak behavior, the higher complexity of the failure patterns is associated to the possible combination of mode I, II and mode III cracking. Some authors outlined that macroscopic failure modes such as conical, pyramidal or wedge cracking pattern are believed to occur due to boundary restraint of the loading platens (Carpinteri *et al*., 1997). The

influence of the boundary conditions on the failure modes was also reported by Tang *et al*. (2000b) through numerical simulations.

As already mentioned, strain localization and formation of visible macrocracks is a characteristic of the failure patterns found for all granites under study and is the result of softening behavior, see Figure 3.53a. The evaluation of the post mortem failures of the tested specimens reveals that in most cases, the macrocrack appears in the parallel or subparallel direction to the applied loading. This typical crack patterns is more common in high strength granites such as granite BA, MC, RM and GA, see Figure 3.53b. On average, macrocracking develops at an angle lower than 10º from the axial longitudinal axis of the specimen. It should be noticed that Teflon sheets were placed between the steel platens and the specimen so that lateral displacement could occur with almost not restrictions. This procedure avoided the confinement and the induced localization in a pronounced shear band.

(a) (b)

Figure 3.53 – Failure patterns; (a) strain localization; (b) splitting failure paths

Holzhausen and Johnson (1979) pointed out that the insertion of the Teflon could produce additional tension at the specimen ends leading to splitting of the specimen. However, this possibility seems unlikely since more curved failure pattern occurs in porous low strength granites, especially granites like MDB, MDB*, PTA*, PLA*and AF. In these cases it is usual that a macrocrack localizes within a shear band, see Figure 3.54, with a shear band exhibiting inclination up to 25º from the direction of loading.

Figure 3.54 – Failure patterns of granite MDB

If one compares the failure patterns between fresh and weathered granites, fresh granites fail in a tensile mode, whereas weathered granites localize in a shear band. Some examples of failure patterns of fresh (PTA, RM, BA, AG), and weathered granites (MDB*, MDB, AF,

GA*, PTA*) are shown in Figure 3.55. This can be associated to the existence of microcracks aligned according a preferential plane, as pointed out by Gupta and Rao (2000).

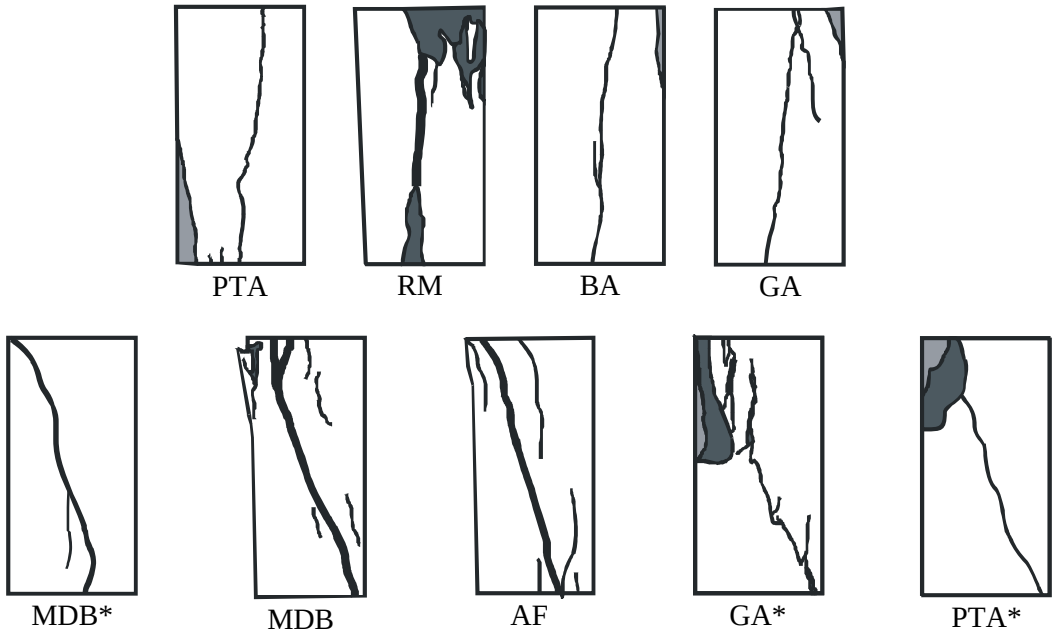


Figure 3.55 – Examples of failure patterns

In granite PLA and PLA* it is common that a high number of small splitting cracks occur through feldspar crystals, which can be attributed to cleavages of this rock forming mineral. Besides, the granite PLA exhibit rather low values for the fracture energy. This can also contribute for the presence of large splitting crack densities, see Figure 3.56.

Figure 3.56 – Splitting crack densities in granite PLA and PLA*

## 3.5 Concluding remarks

In order to characterize the uniaxial compressive behavior of distinct granitic lithotypes, a campaign of uniaxial tests was carried out at University of Minho. The circumferential displacement feedback control used in the compression tests of granites appears to be the sole control technique to obtain the complete stress-strain diagrams. The use of this technique is particularly valuable is case of high strength granites. From the complete stress-strain diagrams, the elastic properties, the modulus of elasticity and the Poisson's ratio were derived. The initiation and the propagation of the microcracking and the onset of the dilatancy

were the parameters used to characterize the pre-peak fracture behavior. In addition to these parameters, the energy dissipated in the continuum bulk was also evaluated. The post-peak behavior was characterized by the fracture parameters, namely, compressive strength, fracture energy and ductility index.

Comprehensive correlations between compressive mechanical and physical parameters were obtained. Among them, the relations between modulus of elasticity and compressive strength ($E = 382.7f_c$, $r^2 = 0.89$), and compressive strength and porosity ($n = 2212f_c^{-1.607}$, $r^2 = 0.87$) are highlighted. It is shown that compressive strength and modulus of elasticity can be a measure of the brittleness of granites, which is shown by the correlations between mode I ductility index and compressive strength ($d_u = 4.753f_c$, $r^2 = 0.81$) and modulus of elasticity ($d_u = 303.4E^{-0.0824}$, $r^2 = 0.81$). Is spite of anisotropy exhibited by granites, indicative correlations between tensile and compressive parameters, namely between tensile and compressive strengths ($f_t = 0.141f_c^{0.712}$, $r^2 = 0.63$), and between modulus of elasticity and tensile strength ($f_t = 0.00424E^{0.646}$, $r^2 = 0.73$), are possible. The pre-peak fracture process was found to be well estimated from the compressive strength, being the crack initiation stress and crack damage stress given by the correlations $f_{ci} = 0.0589f_c^{1.351}$, $r^2 = 0.94$ and $f_{cd} = 0.0474f_c^{1.547}$, $r^2 = 0.96$, respectively. Only a rough nonlinear correlation was found between the post-peak fracture energy and the compressive strength, $G_{cpost} = 2.541f_c^{0.580}$, $r^2 = 0.54$).

The analysis of the compressive parameters shows that the granites considered possess a wide range of variation of the elastic and fracture parameters. This variation is explained by microstructural aspects such as the internal texture, weathering state and moisture content and, to minor extent, the by mineralogy:

- It was found that similarly to the tensile behavior, the rock easiest splitting plane (rift plane) and the foliation plane are sources of anisotropy concerning the compressive parameters. In general, all granites exhibit medium to low anisotropy.

- The pre and post-peak compressive behavior are highly affected by the weathering state of granites. The compressive strength, as well as the modulus of elasticity undergoes remarkable decrease for weathered granites, while the Poisson's ratio presents higher values. This behavior reflects the structural alterations in the bulk material that is generally associated to increase of porosity. Physical properties, namely, the porosity and density play obviously an important role in the compressive behavior of granites.

- Although no influence of the grain size is recorded, the simplified mineralogical grouping indicated that biotite granites exhibit generally higher compressive strength and modulus of elasticity than two mica granites.

- It was shown that the moisture content plays an important role in the compressive parameters. Granites under saturated conditions present lower stiffness, lower deformation at peak stress and lower strength.

Finally, regarding the crack patterns, axial or subaxial failures are characteristic of low porosity granites. More porous granites, including weathered granites, fail with a shear band.

# 4. NDT – CORRELATIONS WITH PHYSICAL AND MECHANICAL PROPERTIES OF GRANITES

## 4.1 Introduction

One of the major challenges in the scope of rehabilitation and repair of existing structures is the inspection, which includes the detection of the damaged zones, cracking and defects, and mechanical characterization of materials. This preliminary work is generally carried out not only based on experimental investigation on the laboratory but also by means of in situ nondestructive methods. Sophisticated non destructive techniques have been developed and improved throughout the years and are applied to various types of structures in distinct fields, namely masonry structures. One example of such techniques is the ground probe radar, which appear to be a powerful tool in the detection of voids and structural irregularities such as inclusions, moisture content and in the identification of the cross section of ancient multiple leaf masonry walls (Binda *et al*., 1998). Another example are sonic tests, probably the most widely used non destructive method in the inspection of masonry structures. This method allows the evaluation of the morphology of the masonry walls, detection of voids and flaws, crack damage patterns and assessment of the weathering state of materials. By using appropriate tomography techniques, it is possible to reconstruct the evolution of the sonic data, which provides general information about the damage in the structure and material characteristics, mainly as far the crack damage is concerned or even changes on the material in terms of density and porosity (Schuller *et al*., 1997). These tests are mainly used in structural identification, whereas other, easy, simple, flexible and economical tests such as the ultrasonic pulse velocity and Schmidt hammer tests are essentially suitable in the characterization of elastic and strength properties of structural materials.

The ultrasonic pulse velocity testing is reported by several authors (Hassan *et al*., 1995; Sack and Olson, 1995) as a useful and reliable non destructive tool of assessing the mechanical characteristics of concrete from existing structures, such as, the modulus of elasticity and the compressive strength. These parameters can be subsequently used in the safety evaluation of the whole structure. In the field of rock structures, the ultrasonic pulse velocity has also been suggested as a useful method for a preliminary estimation of elastic and strength properties. This aim has been accomplished by means of empirical correlations between the ultrasonic pulse velocity and the compressive strength and modulus of elasticity (Uchida *et al*., 1999; Kahraman, 2001; and Yasar and Erdogan, 2004a). However, its applicability can be much more enlarged. Saka and Uchikawa (1995) described an ultrasonic technique to evaluate closed cracks in a material. It has also been widely used to study concrete behavior at early stages, namely in the analysis of the concrete microstructure development (Reinhardt *et al*., 2000; Kolluru *et al*., 2002; Akkaya *et al*., 2003; Lin *et al*., 2003). When associated to tomography, it can give good qualitative information on the changes on material properties as well as on its microcracking state (Popovics, 2003; Grinzato *et al*., 2004; Meglis *et al*., 2005). Kahraman (2002) has studied the influence of the fracture roughness of granites on the ultrasonic pulse velocity and pointed out a reliable nonlinear correlation between both parameters. Although acoustic emission plays the major role in the evaluation of the crack damage in concrete and especially in rocks under uniaxial compression (Farmer, 1983; Eberhardt *et al*., 1999a; Pettitt and King, 2004), ultrasonic pulse velocity was recently found to provide quite good indication about the damage in concrete. Nogueira and William (2001)

showed also the possibility of estimating the damage of concrete under uniaxial compressive loading through the ultrasonic pulse velocity. Similar result was obtained by Mirmiram and Wei (2001) in the uniaxial behavior of concrete-filled FRP tubes used as columns. The Schmidt hammer was initially developed and used for concrete but extensive application of it has been performed as a preliminary estimation of the stone strength (Karpuz and Pasamehmetoglu, 1997; Katz *et al.*, 2000).

The main goal of the present study consists in the attainment of empirical correlations between the ultrasonic pulse velocity (UPV) and the Schmidt hammer rebound number (N) with the mechanical properties that describe the tensile and compressive behavior. Correlations with physical properties, porosity and density, are also analyzed. Besides, a discussion of the factors that influence variations on the velocity measurements and on the rebound number is also carried out. The influencing factors such as, moisture content, weathering state and material anisotropy are highlighted.

The major significance of the proposed statistical correlations using simple nondestructive techniques consists in the possibility of estimating the mechanical properties of similar granitic lithotypes existing in ancient masonry structures, particularly in the Northern region of Portugal. This can be of great value in a preliminary phase of the diagnosis and inspection of the structural and material condition, particularly in cases in which the possibility of sampling material cores is reduced.

## 4.2 Geometry, shape of specimens, test equipment and test procedure

### 4.2.1 *Ultrasonic pulse velocity (UPV)*

As mentioned above, the main goal of using the ultrasonic pulse velocity (UPV) as a non destructive technique, in the scope of the present work, is to evaluate the elastic and strength properties of the granites under study. This implies that measurements of these mechanical properties and the ultrasonic pulse velocity should be made in the same specimens. Thus, before tensile and compressive tests have been undertaken, the ultrasonic pulse velocity was measured in the tensile and compressive specimens. However, the technical limitations that have been discussed in the previous Chapters regarding the dimensions of the test specimens, particularly in case of tensile tests, raise some doubts about the reliability of the ultrasonic pulse velocity test results. In fact, according to ISRM (1981d), and other standards like ASTM D2845 (1995) and BS188: Part 203 (1986), the ultrasonic pulse velocity is influenced by the shape and size of the specimens. The natural resonance frequency of the transducers, the minimum lateral dimension and the grain size of the rock are interrelated factors that affect the test results. The wavelength, $l$, corresponding to the dominant frequency of the pulse train in the rock is approximately connected to the natural resonance frequency of the transducer, *f*, and the pulse velocity, *v*, by the expression:

$$l \approx \frac{v}{f} \tag{4.1}$$

The minimum lateral dimension of the cross section, *D*, shall be at least five times the wavelength of the compression wave, so that, true dilational wave velocity is measured:

$$D \geq 5l \tag{4.2}$$

In addition, to reduce the scatter and to improve the reception of the signal at the receiving transducer, the wavelength, $l$, shall be at least three times the average grain size, $d$:

$$l \geq 3d \tag{4.3}$$

The combination of the above equations yields the following relationship for the minimum lateral dimension (ASTM D2845, 1995):

$$D \geq 5\left(\frac{v}{f}\right) \geq 5d \tag{4.4}$$

Since the pulse propagation velocity and the average grain size of the material are intrinsic properties, the values of the minimum lateral dimension and the natural resonance frequency of the transducers shall be suitably selected so that accurate measurements of the ultrasonic pulse velocity can be obtained.

The dimensions of the cylindrical compressive specimens (D = 75mm, L = 150mm) are satisfactory to attain reliable results, but the dimensions of the specimens used in the tensile tests seem to be too small (D = 40mm, L = 80mm) in case of medium to coarse grained granites, MC, PLA, PLA* and RM. In order to overcome this limitation, the ultrasonic pulse velocity measurements were also made in cubic specimens (150x150x150mm) used in the porosity tests, see Figure 4.1. Subsequently, a comparison of the results obtained among the distinct shape and size specimens will be performed.

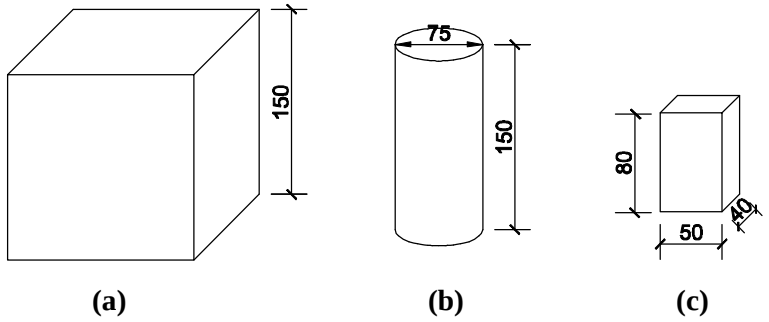


Figure 4.1 – Geometry of the distinct specimens (dimensions are in mm); (a) cubic specimens; (b) cylindrical specimens; (c) prismatic specimens

Since moisture content of the tests specimen is expected to affect the ultrasonic pulse velocity measurements, two extreme moisture conditions were considered, namely oven dried and saturated specimens. It is advisable that the surface area under each transducer is sufficiently plane and parallel within 0.005mm/mm of the lateral dimension.

The ultrasonic pulse measurements were carried out by using the TICO equipment, see Figure 4.2 composed by a central pulse generator unit with a measuring range of approximately 15 to 6550μs, with a resolution of 0.1μs, a pulse rate of 3/s and a voltage pulse of 1kV. Piezoelectric transducers of natural resonance frequency of 54kHz and 150kHz were used in the measurements. The main reason for using distinct frequencies was the small lateral dimension of the tensile specimens, in which only the transducers of natural resonance frequency of 150kHz could be used. In fact, the diameter of the transducers of 54kHz is unsuitable for these specimens and large wavelength is associated to them can even be higher than the pulse travel distance. For concrete, suggestions about the natural frequency of the

transducers as a function of the path length and the minimum lateral dimension are provided by BS1881: Part 203 (1986).

Figure 4.2 – Testing equipment

The ultrasonic pulse velocity was obtained by direct transmission, where the transmitter and the receiver transducers are located directly opposite to each other on parallel surfaces, see Figure 4.3a. This means that longitudinal pulses were propagating in the normal direction to the surface, where the transducers were placed and going through the material directly from the transmitter to the receiver. This measurement arrangement is considered to be the most accurate among other possibilities, as shown in Figure 4.3b,c, since maximum energy of the pulse is transmitted and received (Malhotra and Carino, 1991). Semi-direct and indirect measurement methods must be applied when two parallel surfaces are not available.

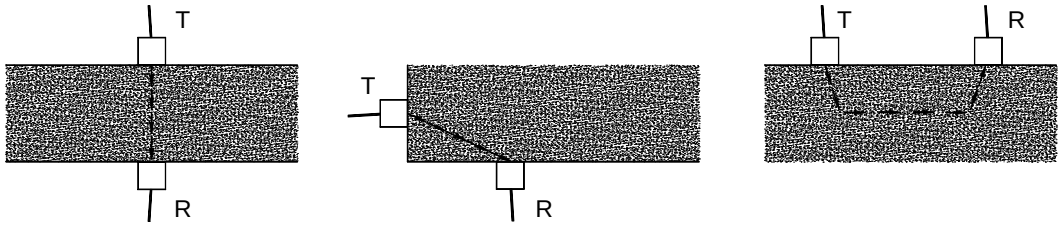


Figure 4.3 – Distinct types of ultrasonic pulse velocity measurements; (a) direct transmission; (b) semi-direct transmission; (c) indirect transmission

In order to ensure a perfect alignment of the transducers' center, their position was carefully marked. In order to reduce the influence of possible voids between the material and the transducers, a better contact between the transducers and the specimen was achieved by using an appropriate coupling paste provided by the equipment supplier. The calibration of the transducers was checked before each measurement and the transit time was recorded for each specimen as the average of three independent readings.

### 4.2.2 *Schmidt Hammer*

The testing device consists of a spring-loaded piston of a steel mass. When the hammer is constrained against a testing surface, the steel mass is automatically released onto the plunger and the rebound is recorded in a graduate scale by means of a sliding pointer. The principle of the testing equipment is based on the potential energy stored by the spring during the loading that is further released as kinetic energy of the piston that connects to the plunger. It is the absorbed energy in the spring that leads to the actual rebound of the hammer. The distance

covered by the steel mass that is expressed as a percentage of the initial extension of the spring is called as the rebound number (Yilmaz and Sendir, 2002).

Due to the limited dimension of the tensile and compressive test specimens, the Schmidt hammer testing was performed only in the cubic dry specimens, where ultrasonic pulse velocity was also measured. According to the ASTM D5873 (1995) recommendations, a mesh of five points was marked in each specimen at both opposite surfaces so that its location was sufficiently far from the edges and spaced by at least the diameter of the plunger. A total of 10 readings was recorded resulting from a single impact at each point. ISRM (1981e) indicates that 20 rebound values from single impact should be recorded at the surface testing. Before each test sequence, the hammer was calibrated by means of a calibration anvil. If the readings in the anvil deviated from the manufacturer's rebound value, a correction factor should be calculated and applied to the readings obtained on the surface of the granites. The specimens were clamped in a threedimensional frame by means of a vertical pre-load so that movements or vibrations could be prevented, see Figure 4.4.

Figure 4.4 – Equipment and setup of the Schmidt hammer testing

Since the specimens were cut by means of a saw machine, the influence of the roughness of the surface in the test was minimum. All measurements were carried out with the Schmidt hammer type NR (impact energy of 2.207N.m) in the direction perpendicular to the vertical surface.

## 4.3 Experimental results

### 4.3.1 *Ultrasonic pulse velocity*

The mean values of the ultrasonic pulse velocity were obtained by averaging the three measurements of the transit time, $t$, recorded during the test. After measuring the path length, $L$, the values of the velocity, $v$, were calculated as follows:

$$v = \frac{L}{t} \tag{4.5}$$

The mean values of the ultrasonic pulse velocity measured in the cubic specimens and the corresponding coefficient of variation are shown in Table 4.1. The results include the values obtained for different moisture contents, dry and saturated conditions, and for two distinct frequencies of the transducers. Further information regarding the values obtained in the

compressive and tensile specimens is given in appendix E. It should be mentioned that the results obtained in the cubic specimens are considered as the reference, given the reduced dimensions of the compressive and tensile specimens.

Table 4.1 – Mean values of the ultrasonic pulse velocity obtained in cubic specimens. Coefficient of variation is indicated inside brackets (%)

| Granite | Dry specimens | | Saturated specimens | |
|---|---|---|---|---|
| | $UPV_{54}$ (m/s) | $UPV_{150}$ (m/s) | $UPV_{54}$ (m/s) | $UPV_{150}$ (m/s) |
| BA | 4804 (1.5) | 4776 (1.7) | 5527 (1.0) | 5457 (1.1) |
| GA | 4593 (1.0) | 4556 (1.2) | 5423 (1.4) | 5359 (1.5) |
| GA* | 3244 (2.1) | 3203 (2.4) | 4598 (0.97) | 4505 (1.4) |
| RM | 4104 (4.0) | 4037 (4.1) | 5369 (1.3) | 5266 (1.9) |
| MC | 4083 (1.1) | 3986 (0.85) | 5489 (0.89) | 5361 (1.1) |
| AF ⊥ foliation plan | 2256 (4.4) | 2186 (6.0) | 4276 (2.0) | 4163 (1.8) |
| AF // foliation | 2572 (3.7) | 2523 (4.0) | 4410 (4.7) | 4310 (4.8) |
| MDB ⊥ foliation | 2488 (1.5) | 2426 (1.8) | 4041 (1.5) | 3888 (2.1) |
| MDB // foliation | 2241 (2.7) | 2181 (2.8) | 3994 (4.2) | 3805 (5.7) |
| MDB* ⊥ foliation | 2340 (1.6) | 2273 (2.1) | 4025 (1.5) | 3933 (3.1) |
| MDB* // foliation | 2341 (0.76) | 2301 (0.80) | 4029 (2.4) | 3894 (2.5) |
| PTA ⊥ foliation | 3278 (0.53) | 3210 (0.26) | 4723 (2.4) | 4576 (2.8) |
| PTA // foliation | 3585 (0.35) | 3567 (0.5) | 4873 (2.0) | 4779 (2.4) |
| PTA* ⊥ rift plan | 1956 (17.8) | 1899 (18.5) | 4024 (7.2) | 3874 (9.0) |
| PTA* // rift plan | 2545 (12.5) | 2495 (12.2) | 4032 (5.4) | 3907 (7.0) |
| PLA ⊥ rift plan | 2743 (1.8) | 2626 (2.2) | 4706 (5.1) | 4602 (5.0) |
| PLA // rift plan | 4162 (2.1) | 4037 (1.9) | 5421 (2.9) | 5268 (2.3) |
| PLA* ⊥ rift plan | 2650 (2.6) | 2543 (3.1) | 4522 (5.5) | 4294 (6.2) |
| PLA* // rift plan | 3720 (2.3) | 3595 (2.2) | 4981 (2.7) | 4851 (2.9) |

It can be observed that the values of the ultrasonic pulse velocity obtained for frequencies of 54 and 150kHz differs slightly. If a linear correlation is fitted to the experimental data, the velocity obtained with 150kHz transducers could be obtained from the velocity attained with the transducers of natural frequency of 54kHz by the expression $v_{150} = 0.98v_{54}$ ($r^2 = 1.00$). For practical purposes, this means that both transducers yield the same results. As regards the ultrasonic pulse velocity obtained when frequencies of 54kHz are considered, the values range from 1956m/s for the granite PTA* to 4805m/s for granite BA. The latter value is close to the typical values reported for fresh granites (Kahraman, 2002). In case of saturated specimens, the values are between 3994m/s and 5527m/s, which means that a narrow range of values is observed for this moisture condition. The scattering found reflects the heterogeneity of the material that belongs to the same block. Its low value confirms the reliability of the ultrasonic pulse velocity testing.

By comparing the average values of ultrasonic pulse velocity obtained in the specimens with distinct shape and size, all granites exhibit higher values in the cubic specimens with respect to the tensile specimens, see Figure 4.5. Nevertheless, the differences are only significant in case of granite PTA*. In this case, the velocity in the cubic specimens reaches values of 10% and 17.5% higher (direction perpendicular and parallel to the foliation) than the ones obtained in tensile prismatic specimens. In the remaining granites differences lower than 6.5% were recorded. No significant deviations were found with respect to the cylindrical compressive

specimens, being always lower than 6%. This means that the distinct size and shape of the specimens used in the mechanical tests leads to values of the ultrasonic pulse velocity close enough to the reference results. Therefore, statistical correlations between the UPV and the mechanical parameters measured in each specimen can be proposed.

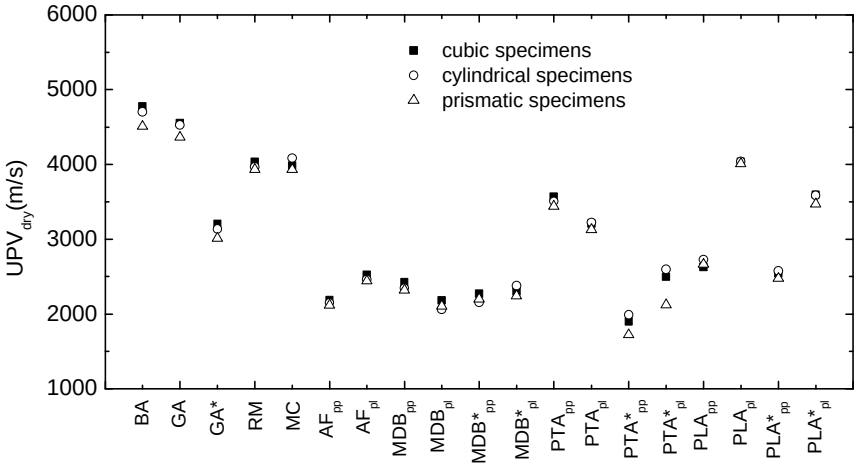


Figure 4.5 – Comparison of the $UPV_{dry}$ among the specimens with distinct size and shape

### 4.3.2 *Analysis of the variation of UPV*

Aiming at obtaining a better insight into the main factors that contribute to the range of variation of the ultrasonic pulse velocity among the granites under study, internal microstructural aspects related to the planar anisotropy, weathering state and moisture content were analyzed.

#### 4.3.2.1 Weathering state and planar anisotropy

The comparison between the values of the ultrasonic pulse velocity measured in fresh and weathered granites is shown in Figure 4.6.

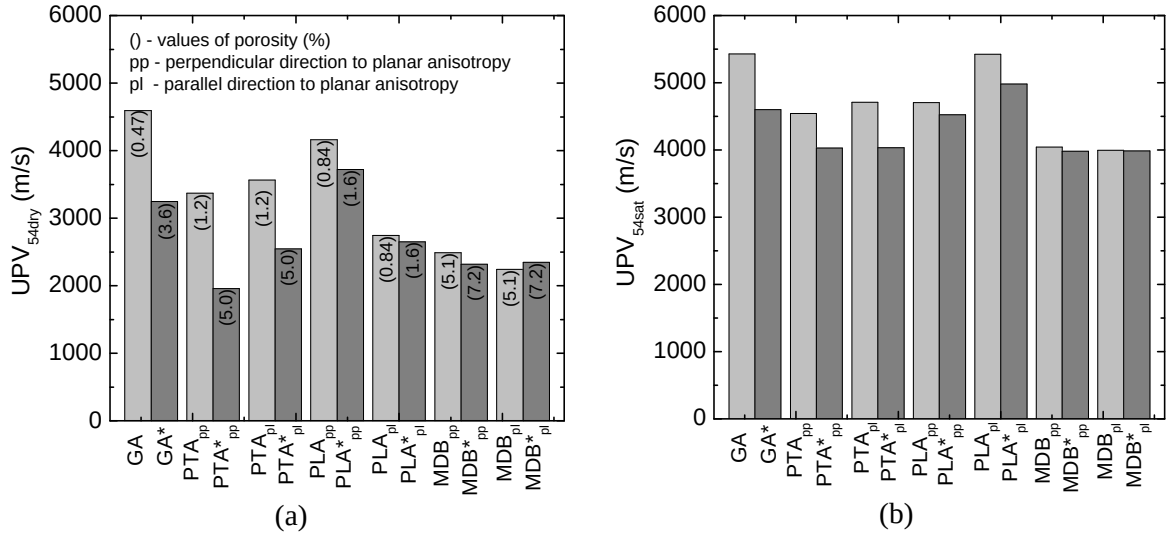


Figure 4.6 – Comparison of the ultrasonic pulse velocity between fresh and weathered granites using 54kHz transducers; (a) dry cubic specimens; (b) saturated cubic specimens

From the test results, one can observe that the weathering state influences the velocity of propagation of the ultrasonic waves through the elastic matrix of the material, both for dry and saturated conditions. Apart from the granite MDB and MDB* in the direction parallel to the foliation, higher values of the ultrasonic velocity were obtained in less weathered granites considering dry conditions. Among these, more remarkable differences were recorded in case of granites PLA and PTA. This behavior can be related to the degree of alteration that can be evaluated through the increase in the porosity. In fact, as shown in the previous Chapters, the increase in the porosity from fresh to weathered granites means a reduction of the stiffness and strength of the granites. This can be associated to the degradation of the rock forming minerals strength and of the grain boundaries stiffness. The higher amount of voids, pores and unavoidable microfissures reflects the slower propagation of the elastic waves. Gupta and Rao (1998) found progressively decreasing values of the ultrasonic pulse velocity as the degree of weathering increases. This difference is less significant in case of saturated specimens since pores and voids, as well as microfissures are filled with water.

Assuming that the ultrasonic pulse velocity is highly affected by the microfissuring of the material, it can be a simple and economic tool to evaluate the degree of weathering of granites. In particular, Goodman (1989) refers it as an index of the degree of fissuring. The theoretical value of the ultrasonic pulse velocity of granite can be calculated from the modal composition and from the knowledge of the velocity of rock forming minerals. A comparison of the theoretical value with the effective measured value of the ultrasonic pulse velocity represents a measure of the rock quality. This comparison can also be an important technique to detect microfracturing in materials subjected to compressive or tensile loading. Meglis *et al*. (1995) and Chow *et al*. (1995) reported the decreasing of the ultrasonic pulse velocity as the damage due to the stress induced cracking grows. During compression tests in granites, anisotropic decreasing on the velocity was recorded, which is associated to the significant decrease of the velocity measured at high angle to the loading direction.

This behavior is also confirmed by the results of uniaxial compression tests conducted on granite PLA* shown in Figure 4.7, where the evolution of the velocity with the increasing compressive stress for the directions parallel and perpendicular to the loading axis is presented.

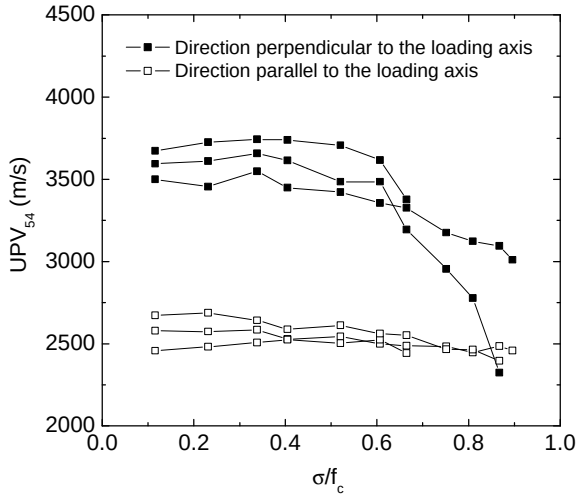


Figure 4.7 – Evolution of the ultrasonic pulse velocity for granite PLA* under increasing uniaxial compressive stress

It was observed a larger lowering of the ultrasonic pulse velocity in the direction perpendicular to the loading. The anisotropic decreasing means that material discontinuities resulting from microcracking developed predominantly in plans oriented in the parallel or subparallel direction to axial loading. Using the results of Chapter 3, it is possible to verify that the lowering on the UPV is particularly noticeable from the stress level corresponding to the crack damage stress, $f_{cd}$, which was found to be approximately $0.5f_c$. Still in this scope, Meglis *et al*. (2005) illustrated the ability of the ultrasonic pulse velocity associated to tomography to identify crack damaged regions on a tunnel excavation.

Under free stress conditions, the velocity anisotropy reflects the internal structure of the material related to the preferential alignment of minerals or cracks (Han *et al*., 2004). The effect of the structural arrangement of the grains on the velocity of propagation of the ultrasonic waves concerning the planar anisotropy (foliation and quarry planes), can be observed in Figure 4.8. The analysis of the results stresses the role of the foliation and rift planes in the velocity of propagation of the ultrasonic waves, mainly in the following granites: AF, PTA, PTA*, PLA and PLA*. The velocity of propagation of the ultrasonic pulse velocity is always higher in the direction parallel to the foliation or rift planes. No significant differences were found in granites MDB and MDB*, as expected.

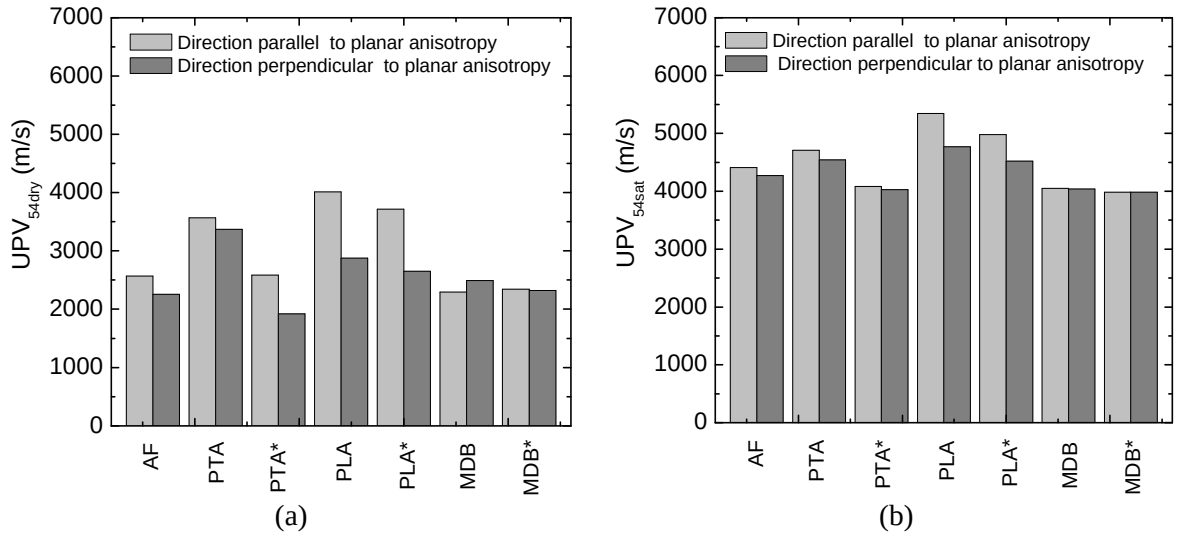


Figure 4.8 – Evaluation of the influence of planar anisotropies on the ultrasonic pulse velocity; (a) dry cubic specimens; (b) saturated cubic specimens

The global information about the values of anisotropy, calculated as the ratio between the UPV measured in the direction parallel and perpendicular to the planar anisotropy, is summarized in Table 4.2. As expected, no significant differences were found between the values of the anisotropy determined with transducers with distinct frequencies. The UPV anisotropy exhibits low to medium values in granites AF, PTA and MDB and medium to high values in granite PLA, PLA* and PTA*. Similarly to what was referred about the weathering effect, also the anisotropy resulting from the internal structure is lowered by water saturation. Granite MDB* can be considered to have isotropic behavior, as far as the ultrasonic pulse velocity is concerned.

Table 4.2 – Degree of anisotropy concerning the UPV measured in dry and saturated cubic specimens relatively to transducers with distinct natural frequency

| Granite | $UPV_{54dry}$ | $UPV_{150dry}$ | $UPV_{54sat}$ | $UPV_{150sat}$ |
|---|---|---|---|---|
| AF // foliation<br>AF ⊥ foliation | 1.14 | 1.15 | 1.03 | 1.04 |
| MDB // foliation<br>MDB ⊥ foliation | 0.92 | 0.92 | 1.00 | 0.99 |
| MDB* // foliation<br>MDB* ⊥ foliation | 1.01 | 1.00 | 1.00 | 1.00 |
| PTA // foliation<br>PTA ⊥ foliation | 1.06 | 1.05 | 1.04 | 1.05 |
| PTA* // rift plane<br>PTA* ⊥ rift plane | 1.35 | 1.37 | 1.01 | 1.02 |
| PLA // rift plane<br>PLA ⊥ rift plane | 1.40 | 1.41 | 1.12 | 1.11 |
| PLA* // rift plane<br>PLA* ⊥ rift plane | 1.40 | 1.41 | 1.10 | 1.13 |

#### 4.3.2.2 Influence of the moisture content

As reported by Wang *et al*. (1990), the compressional wave velocities exhibit distinct values according to the different pore fluid present in the rock. Liquid saturation of rocks increases its compressional velocities. Winkler and Murphy (1995) indicate from Biot's theory that acoustic waves create relative motion between the fluid and the solid skeleton due to inertial effects. When the matrix is accelerated, the fluid lags behind, from which results viscous dissipation of acoustic energy. The effect of the pore fluid saturation on the velocity is however dependent on the frequency of the signal. At higher frequencies, the viscous wavelength is very small and the fluid and solid are essentially decoupled, resulting in maximum velocity. On the contrary, the velocity is minimal at low frequencies, when both fluid and solid are moving in phase.

In this work the effect of the water saturation is investigated by comparing the values of the UPV found in dry and saturated specimens. This analysis shows that moisture content has a remarkable influence on the velocity of propagation of the ultrasonic waves. The results indicate a clear tendency for dry specimens to exhibit considerable lower values of the ultrasonic pulse velocity ($UPV_{dry}$) regarding the ones obtained in saturated specimens ($UPV_{sat}$). Similar tendency was found by Gupta and Rao (1998) also for granites, as well as for basalts. From Figure 4.9a, it can be observed that the values of the ultrasonic pulse velocity obtained in saturated and dry specimens are well correlated. This means that the values of the ultrasonic pulse velocity in saturated specimens can be obtained with reasonable accuracy ($r^2$ =0.88) from the values recorded in dry specimens by the expression resulting from the linear fitting to the experimental data. In spite of the large scatter, the difference of the UPV for both moisture conditions appears to be related to the porosity of the granites, see Figure 4.9b. The increase of the UPV from dry to saturated conditions increases as the porosity increases. Note, however, that for moderate and high porosities there are large variations of the $UPV_{dry}$ to $UPV_{sat}$ ratio, which, to certain extent, can be explained by the attenuation of the anisotropy under saturated conditions.

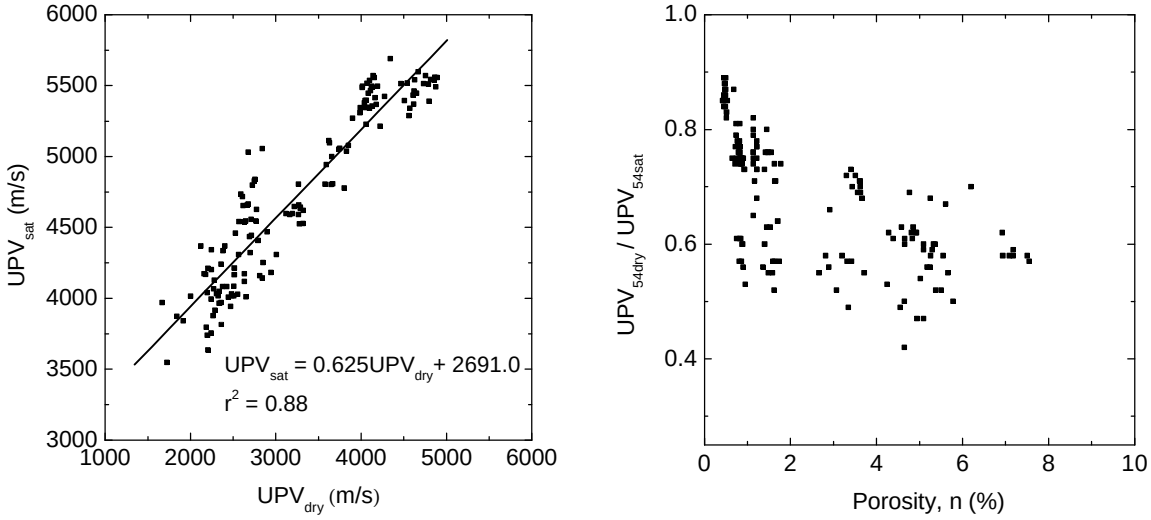


Figure 4.9 – Influence of the moisture state on the ultrasonic pulse velocity; (a) $UPV_{dry}$ vs. $UPV_{sat}$ (b) porosity vs. $UPV_{dry}/UPV_{sat}$ ratio

Figure 4.10 shows the increase of the ultrasonic pulse velocity measured on saturated specimens with respect to dry specimens defined by the following expression:

$$\Delta UPV_{sat} = \frac{UPV_{sat} - UPV_{dry}}{UPV_{dry}} \tag{4.6}$$

In low porosity granites like BA and GA, the difference on the ultrasonic pulse velocity measured in dry and saturated specimens is of 14.1 and 17.4%, whereas in granite RM and MC, the saturated specimens exhibit 30.5 and 35.0% larger values than dry specimens, see Figure 4.10. Reduction of approximately 30% of the dry velocity was recorded in granite PTA. A lowering of the ultrasonic pulse velocity in dry specimens relatively to saturated specimens of about 20-30% was also reported by Todd and Simmons (1972) in low porosity rocks.

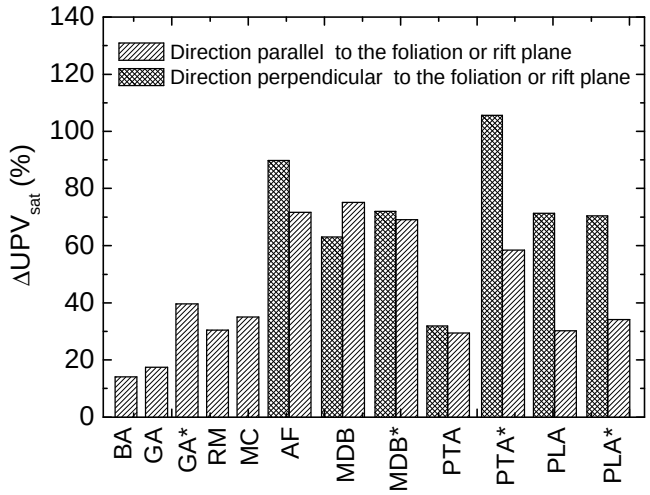


Figure 4.10 – Increase of the UPV in saturated specimens with respect to the dry specimens

Nevertheless, higher deviations were found in high porosity granites such as granites AF, PTA*, MDB and MDB*, where an increase of the ultrasonic pulse velocity in saturated

specimens attains a maximum of 105% in granite PTA* in the direction perpendicular to the rift plane. The increasing on the velocity in saturated specimens depends on the direction of measurement. With the exception of granite MDB the remaining granites exhibit an increase of the ultrasonic pulse velocity in saturated specimens more noticeable in the direction perpendicular to the foliation or rift planes. This characteristic is especially evident in granites PTA*, PLA, PLA*, and AF. As shown in the previous section, the direct consequence of this behavior is the reduction of the anisotropy of granites under saturated conditions, which seems to be related to the loss of sensitivity for the ultrasonic pulse velocity test to detect the major discontinuity in continuum medium associated to pre-existing microfissures aligned in the direction parallel to the rift plane (PLA, PLA*, PTA*) or to foliation plane (AF). Therefore, the ultrasonic pulse velocity appears to be able to capture fissures aligned in the direction perpendicular to the wave propagation in dry specimens. This also justifies the deviation found between the values obtained for the $UPV_{dry}$ in directions parallel and perpendicular to the rift plane in case of granites PLA and PLA*. This is in agreement with the findings of Meglis *et al*. (2005) regarding the lowest values of the ultrasonic pulse velocity of waves propagating at a high angle to the preferred direction of microcracks developed in granites. The preferential alignment of the feldspar megacrystals has been pointed out in Chapters 2 and 3 as the main source of anisotropy in granites PLA and PLA*. However, the results of the UPV obtained under extreme moisture conditions suggest that anisotropy should be related to the preferential orientation of the pre-existing microcracks.

### 4.3.3 *Schmidt hammer*

The Schmidt hammer rebound number is obtained according to the ASTM D5873 standard. From the ten single measurements that were recorded at each point, the average value was calculated and the readings differing from the average by more than seven units were excluded. When necessary, a new average value of the hammer rebound was calculated based on the remaining data. No correction factor had to be applied to the average value since every calibration readings fall within the range provided by the manufacturer (79 ± 2). For each granite, the Schmidt hammer rebound mean value is obtained by averaging the four specimens that were considered in the testing program.

The Schmidt hammer rebound mean values and the corresponding coefficient of variation (CV) are summarized in Table 4.3. In general, the coefficient of variation exhibits remarkable low values. The range of variation is relatively narrow and is between 62.5 for granite MDM and 71.6 for granite MC and PLA. These values are close to values reported in literature for granites. The Schmidt hammer rebound obtained for granite MDM is close to the value of 62.3 pointed out by Kahraman *et al*. (2002), also for granite. The higher values approach the value of 73.4 indicated by Katz *et al*. (2000). The Schmidt hammer rebound appears to be a simple nondestructive method able to evaluate the weathering of the granites under study. In effect, by comparing the values between fresh and weathered granites, it is possible to observe that a lower Schmidt hammer rebound was recorded in weathered granites. The decrease is about 7.1% in granite GA, 4.8% in granite MDB, 8.9% in granite PTA and 3.7% in case of granite PLA. In the two latter granites, the decreasing value represents the mean calculated for the two planes of anisotropy. The ability for the Schmidt hammer test to detect the weathering state of rocks was also referred by Karpuz and Pasamehmetoglu (1997) that pointed out a linear correlation between Schmidt hammer rebound and the degree of weathering. Gupta and Rao (1998) stated the dependence of the Schmidt hammer rebound

number on the weathering state of different rocks, including granites. The Schmidt hammer rebound number was found to decrease significantly as the weathering degree increases (Ekasi and Jiang, 1999; Jiang and Ekasi, 2002). As concerns the detection of planar anisotropy, the Schmidt hammer rebound is not effective since only minor differences were found between the direction parallel and perpendicular to the planar anisotropy in granites AF, PTA, PTA* and PLA*.

Table 4.3 – Average values of the Schmidt hammer rebound value obtained in cubic specimens and the corresponding coefficient of variation, CV (%)

| | N type Schmidt hammer rebound value | |
|---|---|---|
| Granite | *N* | CV (%) |
| BA | 71.4 | 0.5 |
| GA | 71.4 | 0.7 |
| GA* | 66.3 | 0.7 |
| RM | 70.8 | 1.3 |
| MC | 71.6 | 0.9 |
| AF ⊥ foliation plan | 67.5 | 0.9 |
| AF // foliation | 68.6 | 0.8 |
| MDB ⊥ foliation | 65.5 | 2.4 |
| MDB // foliation | 65.6 | 0.6 |
| MDB* ⊥ foliation | 62.6 | 2.2 |
| MDB* // foliation | 62.5 | 1.8 |
| PTA ⊥ foliation | 68.9 | 1.6 |
| PTA // foliation | 69.9 | 1.7 |
| PTA* ⊥ rift plan | 64.3 | 1.4 |
| PTA* // rift plan | 63.2 | 0.8 |
| PLA ⊥ rift plan | 71.4 | 1.7 |
| PLA // rift plan | 71.6 | 0.8 |
| PLA* ⊥ rift plan | 69.6 | 1.1 |
| PLA* // rift plan | 68.3 | 1.3 |

## 4.4 Correlations between NDT results and physical and mechanical properties

Even if limitations are present in the ultrasonic pulse velocity testing, it can effectively be used as a non destructive technique that allows the definition of the elastic properties such as the modulus of elasticity, Poisson's ratio and the shear modulus through the determination of propagation velocities of the compression and shear waves across isotropic or slightly anisotropic rocks. Such elastic properties can be used further in the evaluation of the performance of built structures (Hassan *et al.*, 1995). This non destructive technique is also commonly used in the estimation of the strength of concrete. The procedure implies the definition of a calibration curve that is applied to materials of identical composition, which are fabricated, cured and tested under similar conditions (Komloš *et al*., 1996). Concerning the assessment of the rock properties by means of simple non destructive techniques, various results revealed the dependence of the mechanical properties, namely the modulus of elasticity and compressive strength, on the ultrasonic pulse velocity (Christaras *et al*., 1994; Tugrul and Zarif, 1999; Kahraman, 2001).

The present section aims at the attainment of statistical correlations that enable a first estimation of the granite mechanical properties from the easy and economical non destructive

techniques described. The experimental data collected in the present testing program includes the ultrasonic pulse velocity measurements carried out in the cubic, tensile and compressive specimens, as well as the values of the Schmidt hammer rebound obtained in the cubic specimens.

The relationships between the velocity of the longitudinal ultrasonic waves and the tensile strength and compressive strength are displayed in Figure 4.11a and Figure 4.11b, respectively. A reasonable nonlinear correlation was found between the tensile strength and ultrasonic velocity ($r^2$ = 0.89), meaning that ultrasonic pulse velocity can provide a reliable preliminary estimation of the tensile strength. High strength granites have associated high values of velocity. On the other hand, the compressive strength can only be roughly estimated by the linear expression shown in Figure 4.11b, since the coefficient of correlation corresponding to the linear function found for both variables is lowered by the remarkable scattering ($r^2$ = 0.72).

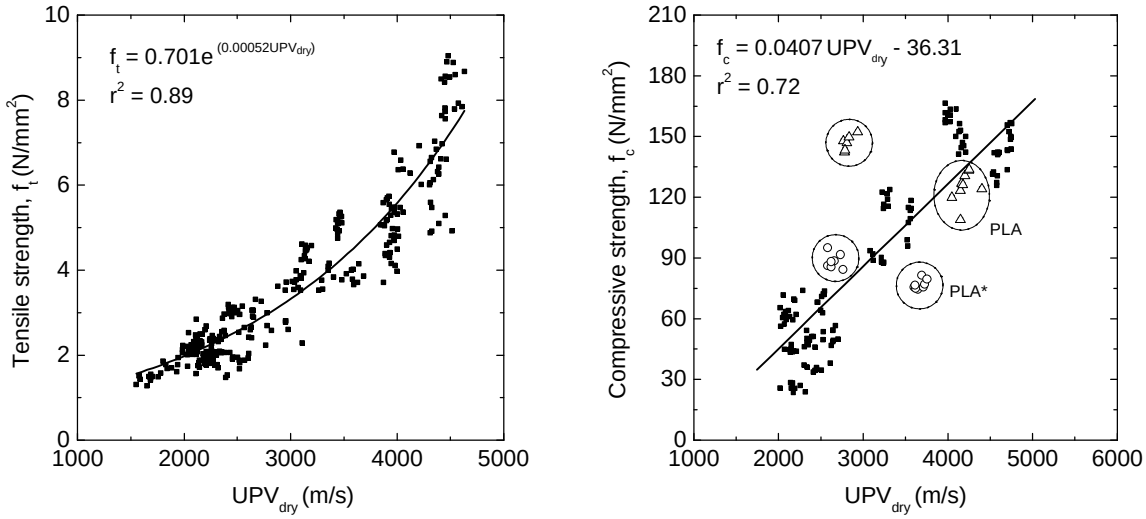


Figure 4.11 – Relationship between ultrasonic pulse velocity and the granite strength; (a) $UPV_{dry}$ vs. tensile strength; (b) $UPV_{dry}$ vs. compressive strength

This statistical correlation is, to great extent, affected by the anisotropy of the granites, particularly, of granites PLA and PLA*. As discussed in Chapter 3, on one hand, the application of compressive loads in the direction parallel or subparallel to the rift plane (which is believed to be governed by the preferential alignment of feldspar megacrystals and the preferential alignment of the microfissures) leads to tensile stress concentrations at the tips of the potential microfissures resulting in the reduction of the compressive strength. On the other hand, the ultrasonic pulse velocity presents noticeable high values in this direction, since it is in the perpendicular direction to the foliation that the pre-existing microfractures planes (discontinuities) are detected. If the values concerning the granites PLA and PLA* were excluded from the experimental data, a linear function $f_c = 0.0446UPV_{dry} - 46.70$ would be found for the relationship between the compressive strength and the ultrasonic pulse velocity with a remarkable higher coefficient of determination ($r^2$ = 0.85). This indicates that improved correlations shall be attained in case of more isotropic granites. Linear correlations between the compressive strength and the UPV were also pointed out by Tugrul and Zarif (1999) for granites and by Kahraman (2001) and and Erdogan (2004) for distinct types of rocks.

The relation between the ultrasonic pulse velocity and the elastic parameters, modulus of elasticity and Poisson's ratio is displayed in Figure 4.12. The significant linear correlation achieved between the modulus of elasticity and the UPV ($r^2$= 0.84) confirms the expected relation between both properties. It should be noticed that, theoretically, the propagation velocity depends on the dynamic modulus of elasticity of the continuum medium. Although no clear correlation was found between the UPV and the Poisson's ratio, there seems to be a tendency for a Poisson's ratio decrease as UPV increases. Despite the influence of the longitudinal velocity on the Poisson's ratio, this property should be essentially controlled by the shear waves.

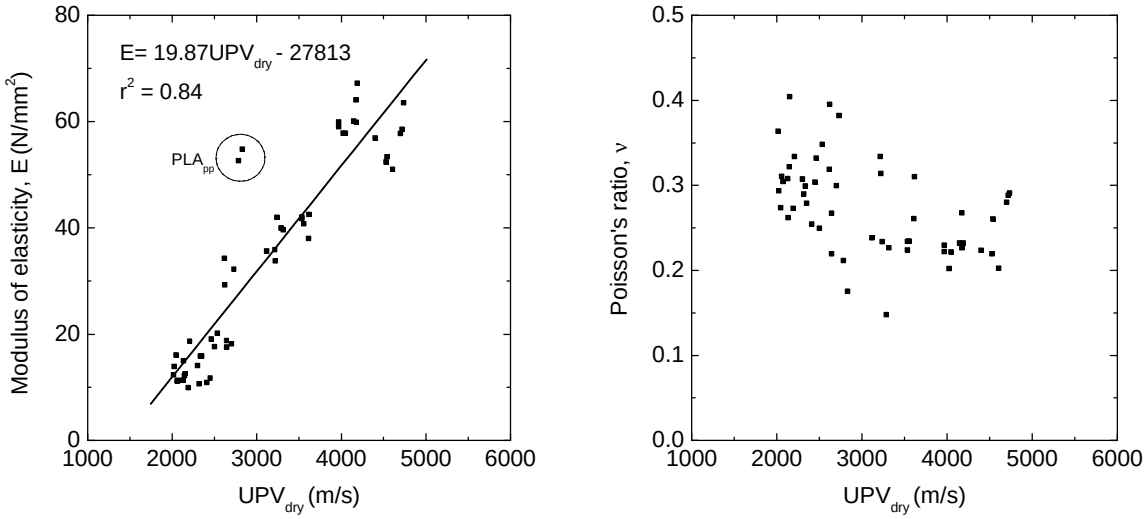


Figure 4.12 – Relationship between ultrasonic pulse velocity and the elastic parameters; (a) $UPV_{dry}$ vs. modulus of elasticity; (b) $UPV_{dry}$ vs. Poisson's ratio

In addition to the previous analyses, relations between the UPV and compressive and tensile fracture properties are also investigated. Regarding the compressive loading, linear fittings of the experimental data composed by the ultrasonic pulse velocity and the stress markers that characterize the pre-peak fracture process are proposed, see Figure 4.13.

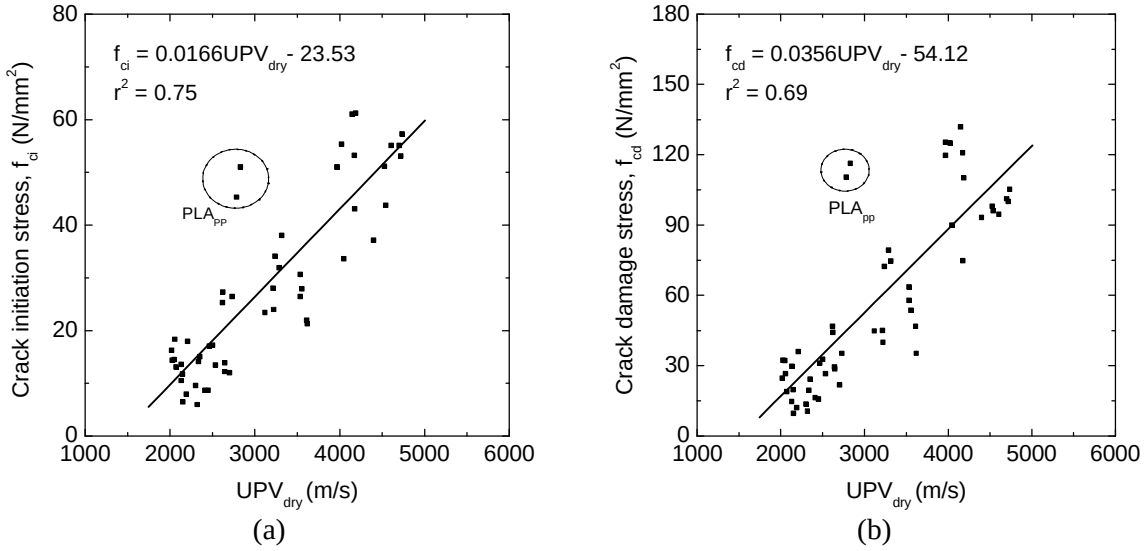


Figure 4.13 – Relationship between ultrasonic pulse velocity and compressive stress levels; (a) $UPV_{dry}$ vs. crack initiation stress; (b) $UPV_{dry}$ vs. crack damage stress

The linear functions show that rough estimations of the crack initiation and crack damage stress levels, $f_{ci}$ and $f_{cd}$, can be obtained from the ultrasonic pulse velocity. The coefficient of correlation would increase considerably if the values concerning the granite PLA (perpendicular direction to rift plane) were excluded from the data.

Regarding the pre and post-peak fracture energy, nonlinear correlations were found between these parameters and the ultrasonic pulse velocity. As shown in Figure 4.14, granites with high values of velocity exhibit compressive brittle behavior, both in the pre and post-peak regimes. Concerning the experimental data of saturated specimens, no correlations were found between $UPV_{sat}$ and the compressive fracture properties. The same result is extended to the relation between $UPV_{sat}$ and the compressive strength obtained in saturated specimens. Note that only a reduced number of saturated specimens were tested under uniaxial compression loading comparatively to tests conducted under dry conditions. Additional experimental data is required in order to obtain a better insight on this issue.

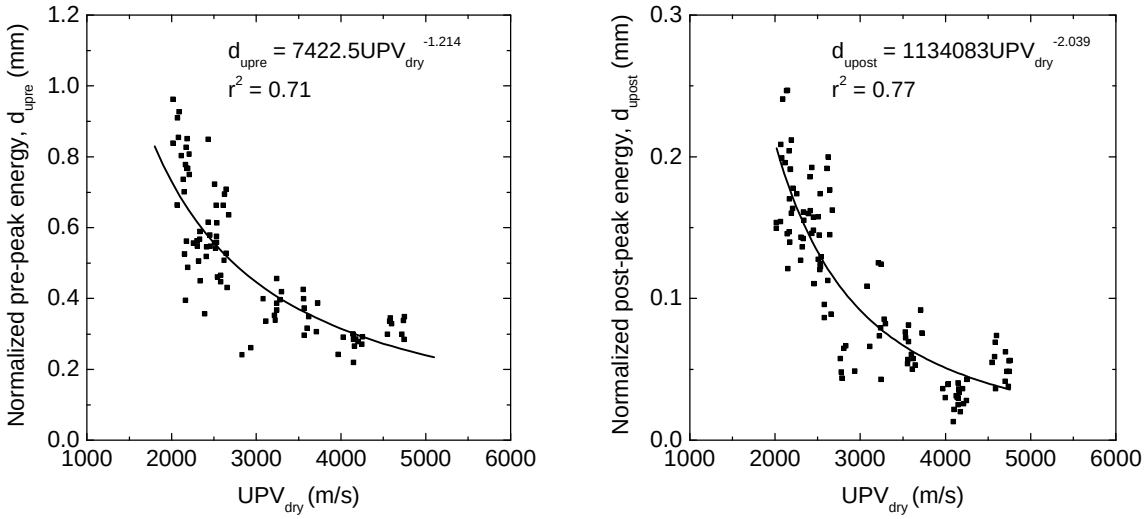


Figure 4.14 – Relationship between ultrasonic pulse velocity and compressive fracture parameters; (a) $UPV_{dry}$ vs. normalized pre-peak fracture energy, $d_{upre}$; (b) $UPV_{dry}$ vs. normalized post-peak fracture energy, $d_{upost}$

Reasonable nonlinear correlations were found between ultrasonic pulse velocity and the parameters that characterize the ductility behavior of granites under tensile loading, namely the ductility index, $d_u$, and the critical crack opening, $w_c$. In spite of the scattered data, there seems to be a clear tendency for the ultrasonic pulse velocity to exhibit high values in case of brittle materials. As can be seen in Figure 4.15, lower values of ductility index and critical crack opening are associated to larger values of the velocity.

The reasonable relations obtained between UPV and tensile and compressive fracture parameters can be, to certain extent, explained by the good correlations achieved between the compressive and tensile fracture properties with the corresponding peak stress. The compressive and tensile strengths are effectively measures of the brittleness of the granites under study. As a main conclusion, it is important to stress the possibility of evaluating the compressive and tensile fracture behavior of granites through the necessarily rough estimations of the fracture parameters by simply measurement of the pulse velocity.

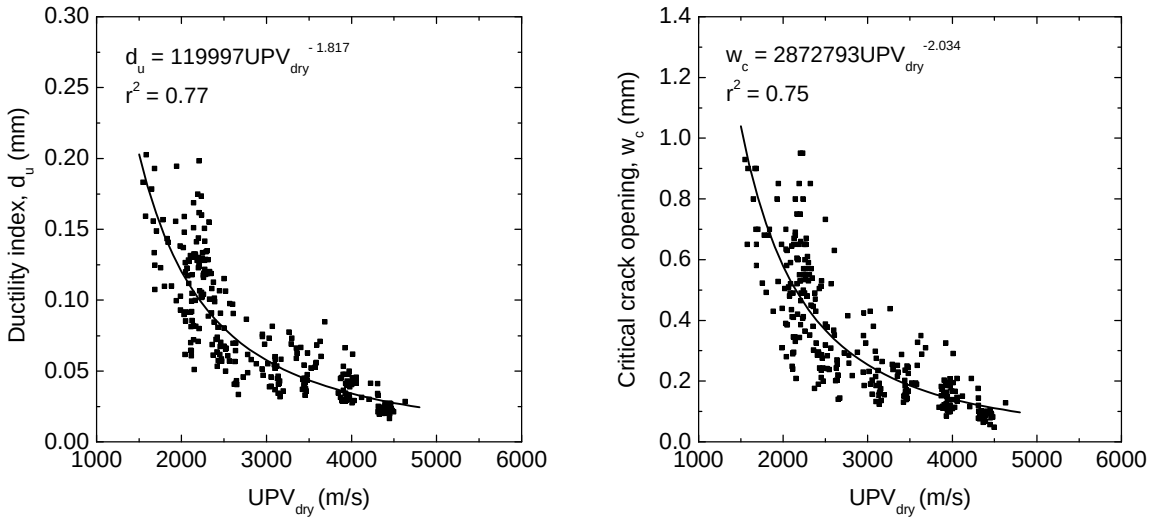


(a) (b)

Figure 4.15 – Relationship between ultrasonic pulse velocity and tensile fracture parameters; (a) $UPV_{dry}$ vs. ductility index; (b) $UPV_{dry}$ vs. critical crack opening

The relations between the ultrasonic velocity and the physical parameters, porosity and density, are displayed in Figure 4.16. Both correlations are characterized by large scatter of the data, which to a certain extent is associated to the anisotropy of some granites. A reasonable nonlinear correlation was found between the ultrasonic pulse velocity and the porosity ($r^2$ = 0.74). If one considers the values of the ultrasonic pulse velocity in saturated conditions, it will be calculated from the porosity through the expression $UPV_{sat} = 5004n^{-0.123}$ ($r^2$ = 0.78). Note that the scatter is particularly remarkable from porosities higher than 1%, which should be the result of the larger heterogeneity of the granites. In spite of the large scatter, there is still a positive trend between the velocity and dry density of the granites.

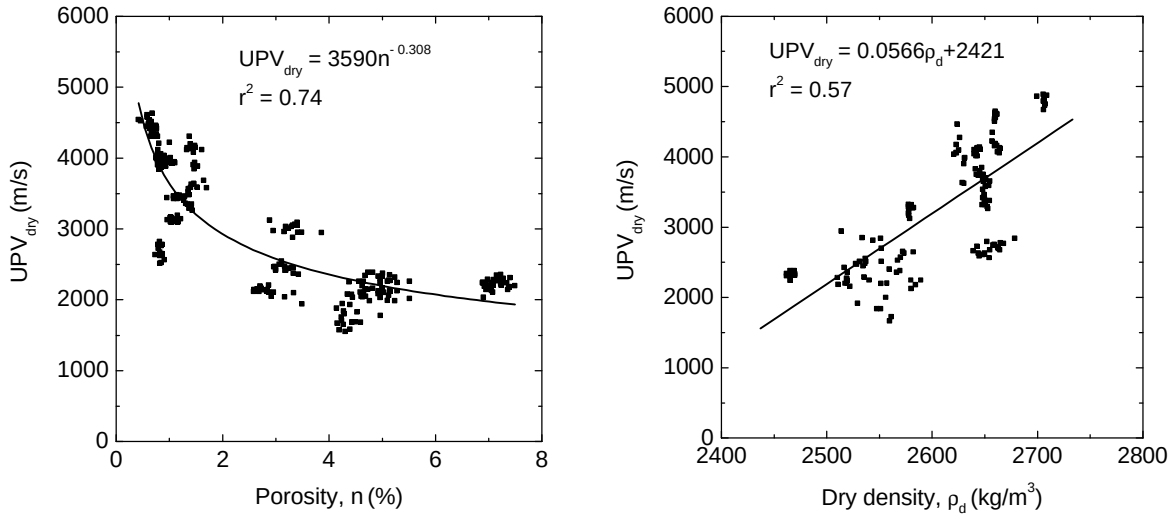


(a) (b)

Figure 4.16 – Relationship between ultrasonic pulse velocity and physical parameters; (a) porosity vs. $UPV_{dry}$; (b) dry density vs. $UPV_{dry}$

The linear correlation between both parameters that is presented in Figure 4.16b is somewhat weak, considering the theoretical assumption that the propagation of the ultrasonic waves in the continuum media is directly connected with its density. Note that the variation on density is, to great extent, related to the variation on the porosity. The statistical correlations of the

mechanical properties, namely, compressive and tensile strengths and modulus of elasticity with the Schmidt hammer rebound number are defined in terms of the average values. The mean values of the mechanical properties are referred to the tensile and compressive specimens, whereas the Schmidt hammer rebound number was obtained in the cubic specimens.

The statistical correlations that were achieved between Schmidt hammer rebound number and the strength and elastic properties can be seen in Figure 4.17a and Figure 4.17b, respectively. It is stressed the significant relations that were found between the rebound number and the compressive strength and modulus of elasticity, from which a coefficient of correlation of $r^2$ = 0.83 was obtained. The compressive strength increases linearly with Schmidt hammer rebound number and the modulus of elasticity can be obtained from the exponential function displayed in Figure 4.17b. In this scope, several other studies have pointed out reliable correlations between the mechanical properties (compressive strength and modulus of elasticity) and the Schmidt hammer rebound number for different types of rocks (Katz *et al*., 2000; Kahraman, 2001; Yilmaz and Sendir, 2002; Dinçer *et al*., 2004). It should be underlined that ultrasonic testing and the Schmidt hammer rebound have been used as nondestructive techniques of preliminary evaluation of the rock strength in stone building structures (Uchida *et al*., 1999).

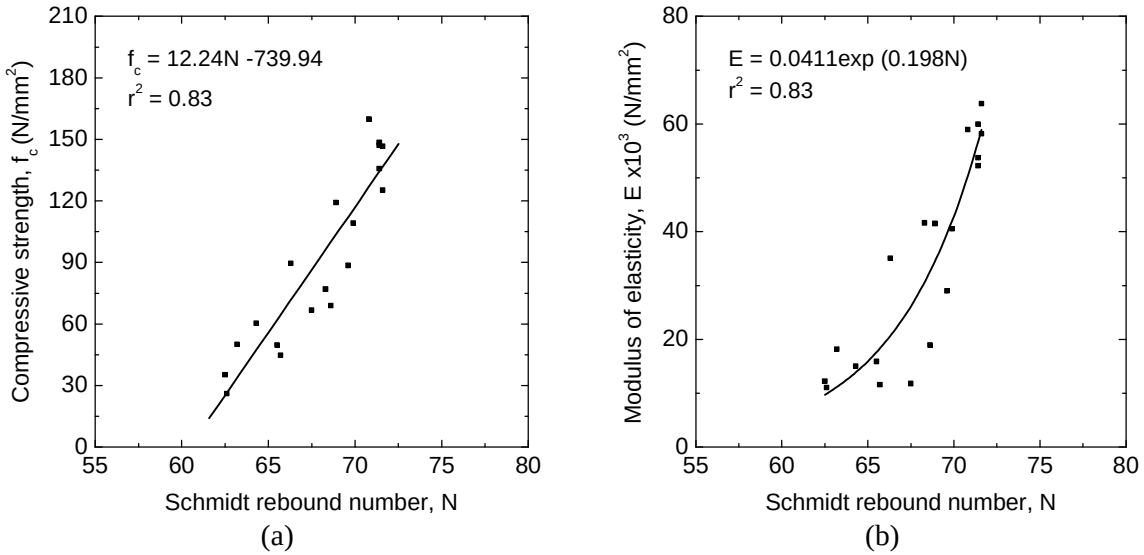


Figure 4.17 – Relationship between Schmidt hammer rebound number and mechanical properties; (a) Schmidt rebound number vs. compressive strength; (b) Schmidt rebound number vs. modulus of elasticity

The tensile strength, on the other hand, can only be obtained in a roughly way from the Schmidt hammer rebound number, since a weak nonlinear correlation was found between both properties, see Figure 4.18a. This can be attributed to the fact that Schmidt hammer rebound is not sensitive to the planar anisotropy. The relationship between the Schmidt hammer rebound number and the ultrasonic pulse velocity obtained in dry conditions is shown in Figure 4.18b. In spite of the large scatter ($r^2$ = 0.53), the tendency for the ultrasonic pulse velocity to increase as the Schmidt rebound number increases is revealed by the nonlinear positive correlation between both parameters. The higher scatter found for this correlation is also affected by the considerable anisotropy of the granites. A positive trend between both parameters was also proposed by Qasrawi (2000) in concrete.

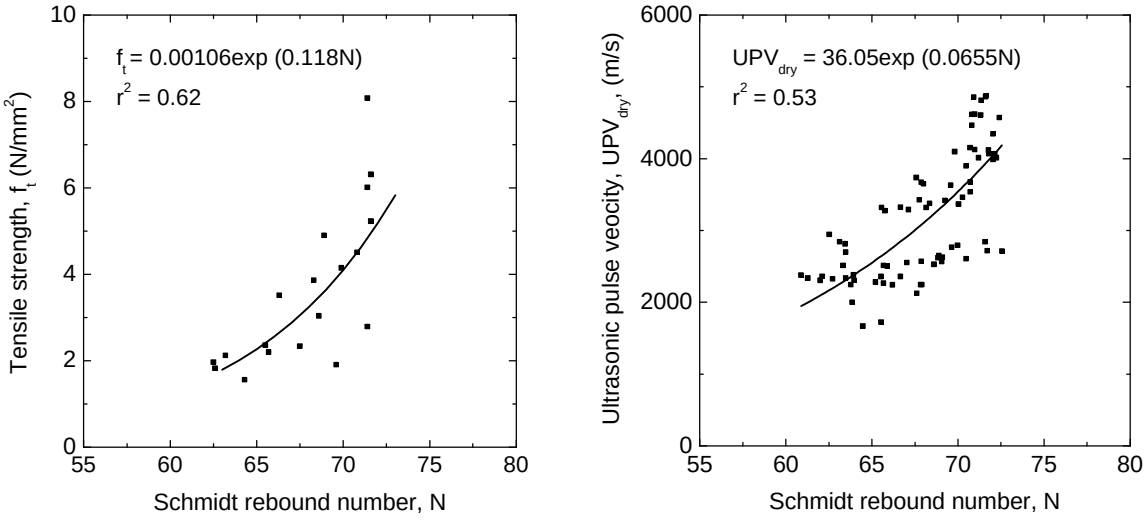


Figure 4.18 – Relationship between Schmidt hammer rebound number and mechanical and physical properties; (a) Schmidt rebound number vs. tensile strength; (b) Schmidt rebound number vs. ultrasonic pulse velocity

The linear correlations shown in Figure 4.19 indicate a reasonable degree of correlation between the Schmidt rebound and the physical properties, porosity and dry density. Low values of the Schmidt rebound were found in high porosity granites. A negative linear correlation between Schmidt rebound and porosity was also pointed out by Yasar and Erdogan (2004b). On the other hand, the dense granites are associated to higher values of the Schmidt rebound. These trends can be pointed out as the main reasons by which a clear decreasing of the Schmidt rebound was found between fresh and weathered granites aforementioned.

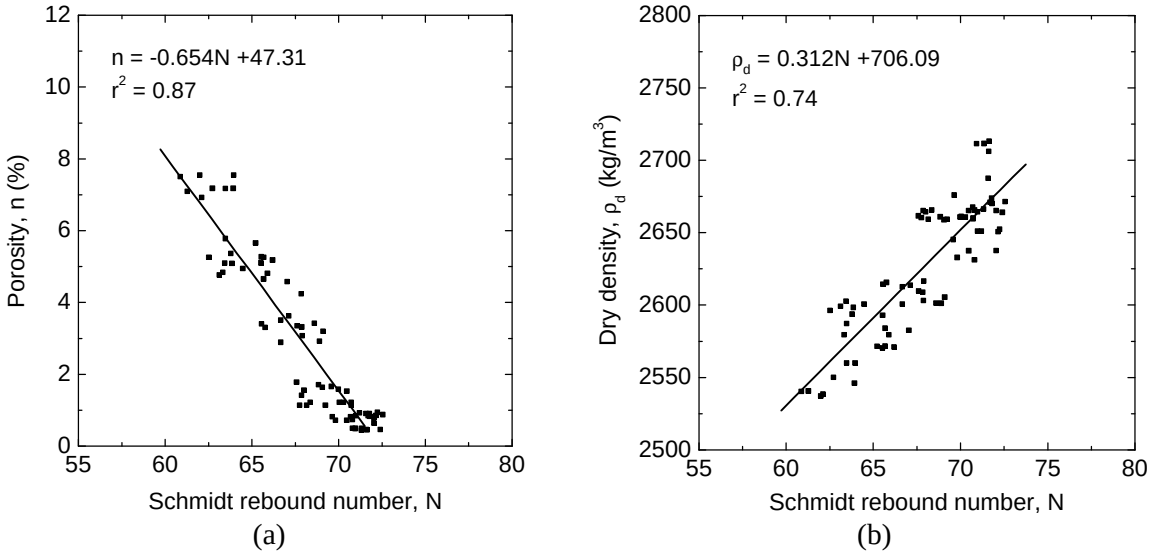


Figure 4.19 – Relationship between Schmidt hammer rebound number and physical properties; (a) Schmidt rebound number vs. porosity; (b) Schmidt rebound number vs. dry density

## 4.5 Concluding remarks

In order to obtain a better insight about the adequacy of using simple and economical nondestructive techniques to predict the elastic and strength properties of granite, a set of

ultrasonic pulse velocity and Schmidt hammer tests was carried out. Cubic specimens, tensile and compressive specimens with distinct shape and size were considered under different moisture conditions, namely, oven dried and saturated. In case of ultrasonic testing distinct natural resonance frequencies of the transducers were considered. From the results, it was observed that although no significant differences were obtained between both frequency transducers, ultrasonic pulse velocity measured with frequency of 150kHz exhibit always lower values than 54kHz transducers. In addition, specimens of reduced size (tensile specimens) present slightly lower values of the ultrasonic velocity.

Factors like weathering state and moisture content were found to affect remarkably the values of ultrasonic pulse velocity and the Schmidt hammer rebound number. The weathered granites exhibit lower values either for UPV or Schmidt hammer rebound number. Besides, the internal microstructure related to the planar foliation or rift plane leads to remarkable anisotropy of the ultrasonic pulse velocity. Higher values of velocity were recorded in the direction parallel to the foliation or rift planes. However, the anisotropy can be to great extent hidden by water saturation of the specimens. This moisture condition leads to the systematic increase of the velocity and to the loss of sensitivity for the UPV testing to detect internal free stress microcracking that induce anisotropy. The ultrasonic pulse velocity appears, in this way, to be a simple nondestructive technique of evaluating the internal anisotropy of dry granites.

The significant statistical correlations that were established between the ultrasonic pulse velocity and the mechanical properties like compressive strength and modulus of elasticity, indicate that these parameters can be reasonably estimated by means of this nondestructive method. Similarly, Schmidt hammer rebound number can also be used in the early prediction of the elastic and strength properties as well in the easy and fast evaluation of the weathering state of the granites. It should be underlined that the statistical correlations obtained between UPV and compressive and tensile fracture parameters can be used also for a preliminary evaluation of the fracture behavior of granites.

Both UPV and Schmidt rebound number are affected by the physical properties, porosity and density. The rebound number increases linearly as the porosity decreases and present larger values for higher density. Analogous increasing linear trend was found between UPV and density. Ultrasonic velocity was also found to exhibit lower values in low porosity granites.

# 5. MECHANICAL CHARACTERIZATION OF MATERIALS FROM MASONRY WALLS

## 5.1 Introduction

Ancient masonry is a non homogeneous material, composed by units and mortar, which can be of different types, with distinct mechanical properties. Concerning ancient constructions existing in Northern Portugal, bricks have taken a significant role in the construction of vaults while stone is the main material used in the construction of walls.

As reported in literature (Hamid and Drysdale, 1980; Samarasinghe and Hendry, 1980), the orientation of the mortar joints to the applied stresses takes a major role in the ultimate strength and failure modes of masonry under in-plane stress state. The influence of mortar joints acting as a plan of weakness on the composite behavior of masonry is even more relevant in case of strong unit-weak mortar joint combinations, which are characteristic of ancient stone masonry. Two basic failure modes can occur at the level of the unit-mortar interface: tensile failure (mode I) associated to stresses acting normal to joints and leading to the separation of the interface, and shear failure (mode II) corresponding to a sliding mechanism of the units or shear failure of the mortar joint. In terms of the composite behavior of masonry, failure modes related to the crushing of the units (compressive failure) or tensile splitting of the units and mortar need to be taken into account. The preponderance of one failure mode over another or the combination of various failure modes is essentially related to the orientation of the bed joints with respect to the principal stresses and to the ratio between the principal stresses.

In addition to the knowledge of the mechanical properties from masonry components, namely units and mortar, the analysis of masonry behavior under in-plane loading is only possible if information about the local composite behavior and the interaction between units and mortar is available.

Therefore, the present Chapter deals with the mechanical characterization of units and mortar, as well as with the shear behavior of dry and mortar masonry joints (cohesion, friction angle and dilatancy) and evaluation of the compressive properties of the masonry composite (compressive strength and modulus of elasticity). In order to attain such goal, an experimental program was defined, including direct shear tests conducted on dry and mortar masonry joints and uniaxial compression tests carried out on a set of stone masonry prisms. The materials selected will be later used in the construction of masonry shear walls, to be tested under cyclic loading. Besides ensuring mechanical properties for numerical simulations of the in-plane behavior of stone masonry wall structures, the adopted testing program provides also the fundamental parameters for its seismic assessment based on simplified analytical models.

## 5.2 Characterization of the materials – units and mortar

The granite that will be later used in the construction of masonry shear walls is a medium-grained two-mica granite. The adoption of this type of granite was based on its similarity with typical granites of ancient buildings. The characterization of the mechanical behavior of the granite used was carried out taking into account the geometry, test setup and procedures described in the previous Chapters 2 and 3. Seven and nine specimens were used in compressive and tensile tests, respectively. With regard to the determination of the Young's

modulus, three vertical strain gauges were attached to three specimens at a maximum angle of 120º apart. The typical complete stress-axial strain diagrams for uniaxial compression and stress-displacement diagrams for direct tension are displayed in Figure 5.1. The average values of the compressive strength, $f_c$, modulus of elasticity, $E$, tensile strength, $f_t$, and mode I fracture energy, $G_f$, are summarized in Table 5.1. Considerable scatter was found in the post-peak regime for both tensile and compressive specimens, which can be confirmed by the large coefficient of variation in the values of the mode I fracture energy. Significantly lower values of the coefficient of variation are found for the compressive and tensile strengths as well as for the modulus of elasticity.

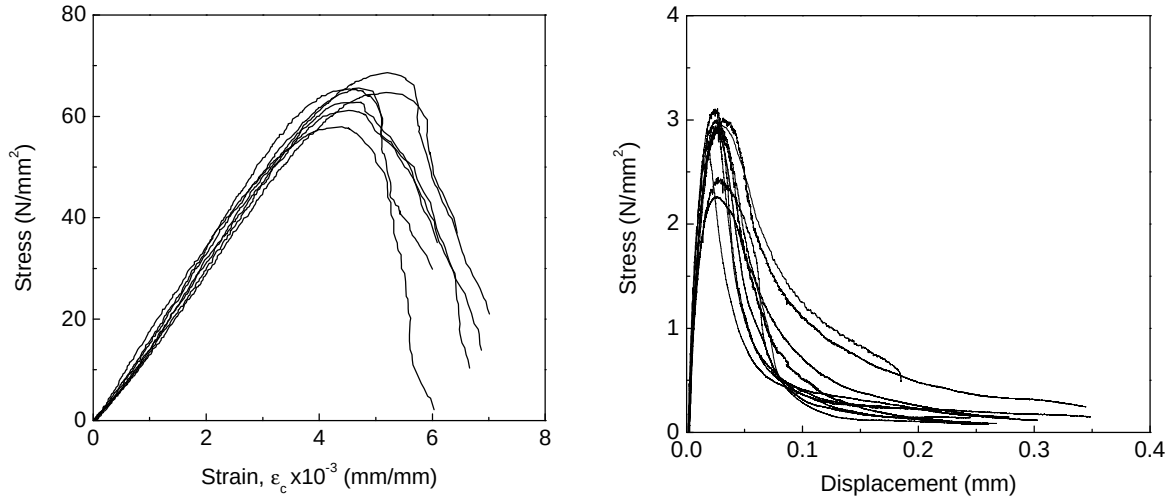


(a) (b)

Figure 5.1 – Behavior of the granitic units; (a) stress-strain diagrams for uniaxial compressive loading (b) stress-displacement diagrams for uniaxial tensile loading

Comparing the values of the average mechanical properties obtained for this material with mechanical properties given in Chapter 2 and Chapter 3 for different types of granites, it is observed that this granite is a medium strength granite. Furthermore, the ratio between the tensile and compressive strengths and the ratio between compressive strength and modulus of elasticity fit well the values indicated in Chapter 3.

Table 5.1 – Mean values of the elastic properties and the compressive strength for the units. Coefficient of variation is indicated inside brackets (%)

| $f_c$ (N/mm$^2$) | $E$ (N/mm$^2$) | $f_t$ (N/mm$^2$) | $G_f$ (N/mm) |
|---|---|---|---|
| 69.2 (5.1) | 20200 (6.6) | 2.8 (10.3) | 0.186 (41.7) |

The mortar that will be used in the construction of the walls is the ready mix "Albaria structturale" type supplied by Bettor-MBT Company. The mortar is mostly composed by natural hydrated lime and natural aggregates with granulometry between 0.1 and 0.2mm. According to the technical information, the mortar compressive strength at seven days would be 3.0N/mm$^2$, which seemed appropriate to simulate low strength mortar, characteristic of ancient constructions. Compressive tests on the mortar specimens were carried out according to the EN 1015-11(1999) standard. The tests were conducted under force control at a rate of 50N/s in a servo controlled machine using the test setup shown in Figure 5.2. Precautions were taken to keep the quantity of added water to the ready mix mortar constant. In order to

simulate the curing conditions of the walls, the mortar specimens were kept under the laboratory conditions. The compression tests were carried out at the age of seven days.

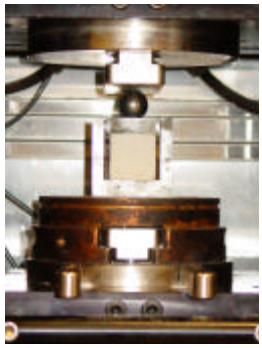

Figure 5.2 – Test setup for compression tests on mortar

The values of compressive strength indicated in Table 5.2 refer to the mortar specimens taken from the compressive masonry prisms and shear assemblages to be analyzed later (Section 5.4). Each value represents the average of the compressive strength recorded in six mortar specimens that were collected from masonry prisms built at distinct phases. PR_SM designates mortar masonry prisms with sawn cut units and PR_IM designates mortar masonry prisms with irregular granitic units. Two series were considered for sawn cut unit prisms, whereas the irregular masonry prisms were built in three series. It should be mentioned that in spite of the supplier indicates values of the compressive strength at seven days of about 3.0N/mm$^2$, larger values were found in the tested specimens. It is also noticed that narrow scatter is associated to the mortar specimens of the same series but considerable scatter is found between the different series of specimens.

Table 5.2 – Mean values of the compressive strength of mortar. Coefficient of variation is indicated inside brackets (%)

| Prism | Number of prisms | Number of mortar specimens | $f_c$ (N/mm$^2$) |
|---|---|---|---|
| PR_SM | 2 | 6 | 6.80 (3.2) |
| PR_SM | 4 | 6 | 5.69 (2.4) |
| PR_IM | 1 | 6 | 5.76 (3.3) |
| PR_IM | 2 | 6 | 4.78 (4.6) |
| PR_IM | 4 | 6 | 4.35 (2.2) |
| | Average | | 5.48 (15.6) |

## 5.3 Shear behavior of stone masonry joints

Although several experimental studies have been carried out in the characterization of the bond shear strength of unit-mortar interfaces (Atkinson *et al.*, 1989; Amadio and Rajgelj, 1991; Binda *et al.*, 1997), lesser research is available on the shear behavior of dry stacked masonry joints, even if recent studies have been carried out on the behavior of dry masonry joints submitted to cyclic loading (Ramos, 2001; Lourenço and Ramos, 2004). On the other hand, the features of rock joints under shear behavior can be partly extended to dry masonry joints. The shear behavior of rock joints has been played an important role in the scope of

rock mechanics research. In particular, several experimental and numerical studies pointed out the role of the surface roughness on the cyclic shear behavior of natural rock joints (Lee *et al*., 2001; Huang *et al*., 2002).

The relation between normal and shear stresses has a major role in the shear behavior of masonry joints, governing its failure mode (Hamid and Drysdale, 1980). For pre-compression stresses above a certain level, the shear strength decreases and a combined shear-splitting failure or splitting of the units occur. In case of shear failure along the joint by slipping of the units along the joint, an increase of the compression normal to bed joint leads to an increase of the shear strength. As has been widely reported (Atkinson *et al*., 1989; Riddington and Ghazali, 1990), the shear strength of masonry under moderate normal stresses, for which the nonlinear behavior of mortar is negligible and the friction resistance takes the central role, can be given by the Coulomb criterion:

$$t = c + ms \tag{5.1}$$

where $c$ is the shear strength at zero vertical load stress (usually denoted by cohesion) and $m$ is the friction coefficient. For dry joints the cohesion is assumed to be zero. It should be kept in mind that the failure envelop given by equation (5.1) describes only a local failure and can not be directly related to the shear failure of masonry walls submitted to in-plane horizontal loads (Mann and Müller, 1982; Atkinson *et al*., 1989; Calvi *et al*., 1996).

Another important issue regarding shear tests is the dilatant behavior of masonry joints. The dilatancy represents the difference between the normal displacements of the upper and the lower unit, *Dv*, as a result of the shear displacement, *Du*, see Figure 5.3. The opening of the joint is associated to positive dilation, whereas negative values of dilatancy represent the compaction of the joint. According to Goodman (1989), the dilatancy of rock joints is mostly controlled by the joint roughness. In conjunction with the cohesion and the friction angle, the dilatancy is also required as a parameter for micro-modeling of masonry. As pointed out by Lourenço (1996), dilatancy in masonry wall structures leads to a significant increase of the shear strength in case of confinement.

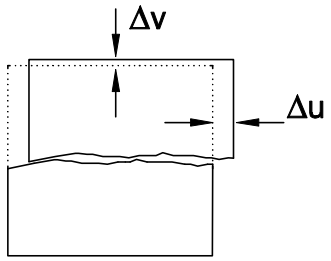


Figure 5.3 – Illustration of the dilatancy associated with the ratio *Dv*/*Du*

A main issue related to the experimental characterization of joint shear behavior concerns the testing setup. Although distinct loading arrangements have been used, it is not possible to provide fully uniform shear and normal stresses along the joint so that failure occurs simultaneously at all points of the joint (Jukes and Riddington, 1997). According to Calvi *et al.* (1996), the cohesion, *c*, is the most sensitive parameter to the uneven normal stress distribution. Figure 5.4 shows some of the most known specimen types and the corresponding loading arrangements.

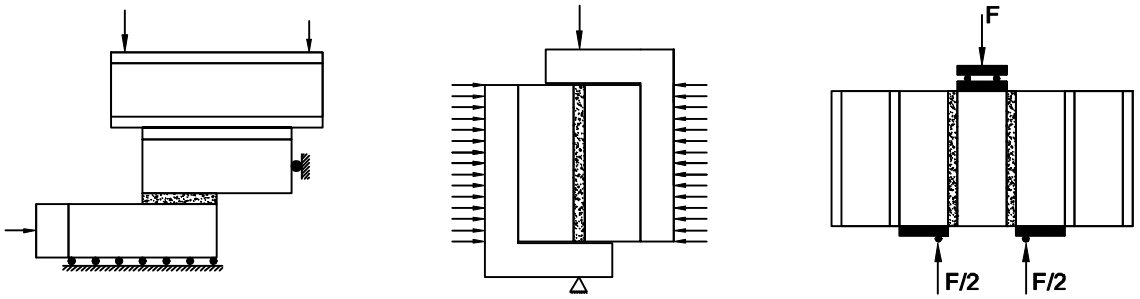


(a) (b) (c)

Figure 5.4 – Different types of shear tests; (a) Hoffmann/Stöckl test; (b) Pluijm test; (c) Triplet test (CEN)

The comparative finite element analysis carried out by Stöckl *et al*. (1990) revealed that the couplet specimen of Hofmann/Stöckl leads to more uniform normal and shear stress distribution along joint than other tests. However, the complexity of the testing setup prevents its adoption as a standard test method. The numerical analysis on the Pluijm (1999) test performed by Riddington *et al*. (1997) pointed out an almost uniform shear stress even if an appreciable uneven normal stress distribution occurs at the joint. Concerning the triplet specimens, the shear strength can also be affected by the non-uniform stress distribution, and a reliable measure of the shear strength is only attained if the bending applied to the specimens is minimized (Bouzeghoub *et al*., 1995). This is achieved by reducing the eccentricity of the reactions that may develop as close as possible of the unit-mortar interface. This situation is foreseen by the loading arrangement corresponding to the CEN triplet test, indicated as the standard shear test method (EN1052-3, 2002), see Figure 5.4c.

As the main goal here is the characterization of the shear behavior of representative joints of the masonry walls to be presented, both dry and mortar joints were tested. Besides the shear strength properties of both types of joints, a description of the whole monotonic shear behavior based on shear stress-shear displacement diagrams is also pointed out. Furthermore, additional insight is provided on the cyclic behavior of dry masonry joints from results obtained in a set of shear cyclic tests.

### 5.3.1 *Specimens, test setup and test procedure*

Although triplet tests have been adopted as the European standard method (EN1052-3, 2002) to perform shear tests in mortar joints, the shear strength properties of dry and mortar joints were obtained by means of direct shear tests conducted on couplet specimens, see Figure 5.5. In fact, in the triplet test, the two joints do not fail at the same time and the analysis of the experimental results is rather complex, Lourenço *et al*. (2004).

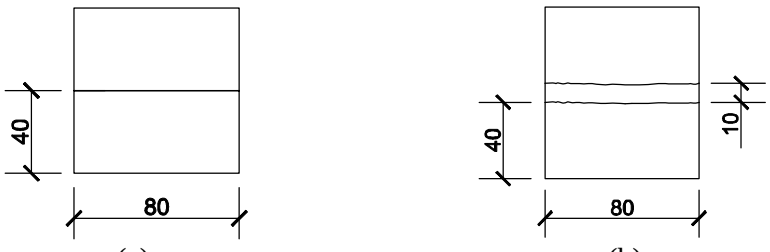


(a) (b)

Figure 5.5 – Test specimens; (a) dry joint; (b) mortar joints (units in millimeters)

The CS7400S servo-controlled universal testing machine described in Chapter 2 for direct tensile tests on the granites was also used in the shear tests. This equipment is composed by two independent hydraulic actuators used to transmit normal and shear loads, able to operate under force or displacement control. The features of the testing equipment and the existing loading platens imply that the most suitable testing sample is composed by two units with geometry and dimensions indicated in Figure 5.5 and a single dry or mortar joint, similarly to Pluijm (1999) and Hansen *et al*. (1998). The surface of the dry masonry units adopted here is smooth resulting from sawing the specimens, whereas the joint surface of the units of the mortar assemblages presents enough roughness to achieve appropriate adherence conditions and thus more realistic masonry can be simulated. For the units and joints, the materials described previously in Section 5.2 were used. The specimens were placed between two thick steel plates and attached to the steel platens by steel bolts, so that shear force could be transmitted, see Figure 5.6. Thin steel sheets were attached to the steel plates to concentrate the shear load as close as possible in the bed joint, aiming at preventing bending moments and provide a more uniform shear stress distribution, see Figure 5.6.

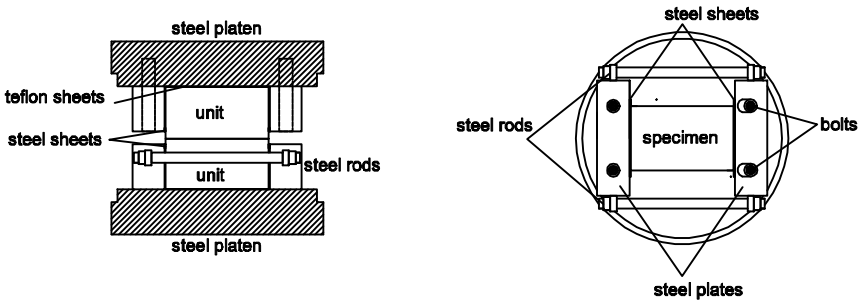


Elevation view Plan view

Figure 5.6 – Test setup used in the shear tests

In addition, two thin sheets of Teflon were interlayered between the steel platens and the specimens to minimize bending effects. In order to guarantee right angle surfaces, the specimens were suitably ground using a rectifying machine. The same procedure was used in the contact surfaces between both units of the specimens to ensure the maximum contact area in case of dry joints. In fact, according to Hansen (1999), the uneven stress distribution can also be attributed to the non-uniform distribution of the material along bed joints. In both types of specimens, when necessary, a thin layer of glue was placed at the surface in contact with the steel platens in order to provide perfectly leveled surfaces. This material was always set above the Teflon sheets in order to prevent monolithic connection between the specimen and steel platens. The confinement of the specimens was improved for load reversal by means of a couple of steel rods fixed to the steel plates through metallic bolts, see Figure 5.6. This arrangement is particularly useful in the cyclic tests but was also used in case of monotonic tests. The numerical assessment of the effectiveness of the test setup was performed by Lourenço and Ramos (2004) based on a finite element model. It was concluded that although a deviation on the stresses occurs in the zone adjacent to the steel plates, an almost uniform normal and shear stress distribution is achieved in 63% of the extent of the bed joint.

In order to simulate the usual range of normal stresses existing in ancient masonry structures three distinct pre-compression stress levels were applied under force control, $\sigma = 0.5 N/mm^2$, $\sigma = 0.75 N/mm^2$ and $\sigma = 1.0 N/mm^2$ corresponding to vertical loads of 2000N, 3000N and

4000N, respectively, in dry joints under monotonic and cyclic loading. An additional pre-compression stress level corresponding to $\sigma$ = 1.25N/mm$^2$ (5000N) was considered for the monotonic tests carried out on unit-mortar assemblages. Three specimens were tested for each level of pre-compression for both types of masonry joints. The possible influence of the moisture content on the shear response of dry masonry joins was investigated by considering dry and saturated conditions. The total number of direct shear tests is summarized in Table 5.3.

Table 5.3 – Number of direct shear tests

| Shear stress, *s* (N/mm$^2$) | 0.5 | 0.75 | 1.0 | 1.25 |
|---|---|---|---|---|
| Dry joints (monotonic) | 3 + 3* | 3 + 3* | 3 + 3* | - |
| Mortar joints (cyclic) | 3 + 3* | 3 + 3* | 3 + 3* | - |
| Mortar joints (monotonic) | 3 | 3 | 3 | 3 |

* dry and saturated specimens

Although the horizontal actuator is servo-controlled, the control was made using the horizontal LVDT adjacent to bed joint because a more stable response was found. The disposition of the LVDTs for measuring the horizontal and vertical displacements of the joint is depicted in Figure 5.7. The relative horizontal displacement of the joint was measured by the horizontal LVDTs placed at each side of the specimen. Although the LVDTs were fixed to the unit through the supports that were glued to it, the influence of the shear deformation of the units should be marginal in the measured final deformation (Hansen, 1999; Ramos, 2001). The vertical displacements of the joint were measured by the LVDTs placed at the opposite corners of the specimen, see Figure 5.7. The relative vertical displacements were monitored in case of dry joints for assessing the possible dilatant behavior of the joints. Nevertheless, technical problems did not allow to measure relative vertical displacements in mortar joints, as tests were conducted in a subsequent phase. Both shear and normal stresses were measured and recorded by the horizontal and vertical load cells of 22kN capacity.

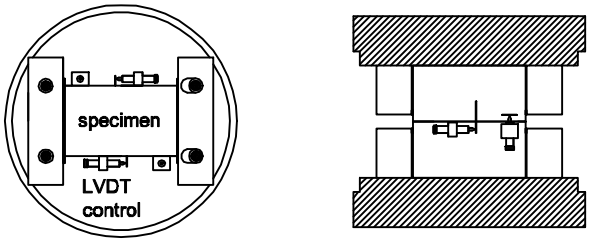


Plan view Elevation view

Figure 5.7 – Arrangement of the LVDTs for measuring of the relative horizontal and vertical displacements

After applying the pre-compression load, the shear tests were carried out under displacement control by imposing increasing static monotonic displacements at a rate of 2μm/s. In case of cyclic tests conducted in dry joints, the reversal displacement history considered is given in Figure 5.8.

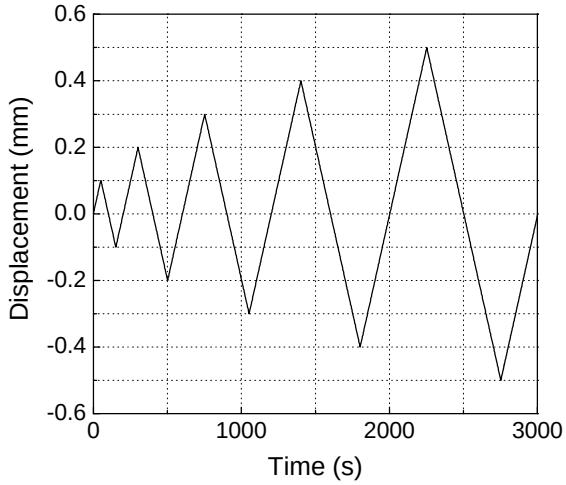


Figure 5.8 – Displacement history for cyclic shear tests on dry masonry joints

### 5.3.2 *Results of the shear tests on dry masonry joints*

The shear load-shear displacement diagrams for distinct pre-compression stress levels resulting from the monotonic tests conducted on dry and saturated specimens are displayed in Figure 5.9a,b respectively. The shear displacement is the result of averaging the measurements recorded by both LVDTs placed at each side of the specimen. The shear stress is calculated by the following expression:

$$t = \frac{H}{A} \tag{5.2}$$

where $H$ is the load in the horizontal actuator and $A$ is the cross area of the joint section. The normal stress is also calculated from the normal pre-compression load, $N$, and is also based on the total area of the cross section as:

$$s = \frac{N}{A} \tag{5.3}$$

From the responses in Figure 5.9, no significant differences were detected between dry and saturated specimens and the peak shear strength was found to increase as the normal stresses increase. By comparing the peak shear stresses, lower values were obtained in case of saturated specimens and higher scatter was found when the maximum pre-compression level ($s_0 = 1.0\text{N/mm}^2$) was applied.

Four stages can be identified in the shear stress-shear displacement diagrams. The pre-peak behavior is characterized by a linear extent for low levels of shear stress, associated to the contact of the joint interface, and by a clear non-linear stretch until peak shear is reached. These features can be confirmed from Figure 5.9, where the pre-peak part is highlighted. A plateau is found at peak stress, as the shear behavior of dry masonry joints under monotonic loading exhibits considerable plastic deformations associated to the inelastic sliding. Similarly to what has been reported in literature (Misra, 2002; Huang *et al*., 2002) no shear softening was recorded after peak stress for smooth surfaces, unlike rough rock joints that exhibit remarkable lowering of the shear resistance as the plastic shear displacement increases due to the roughness fracture.

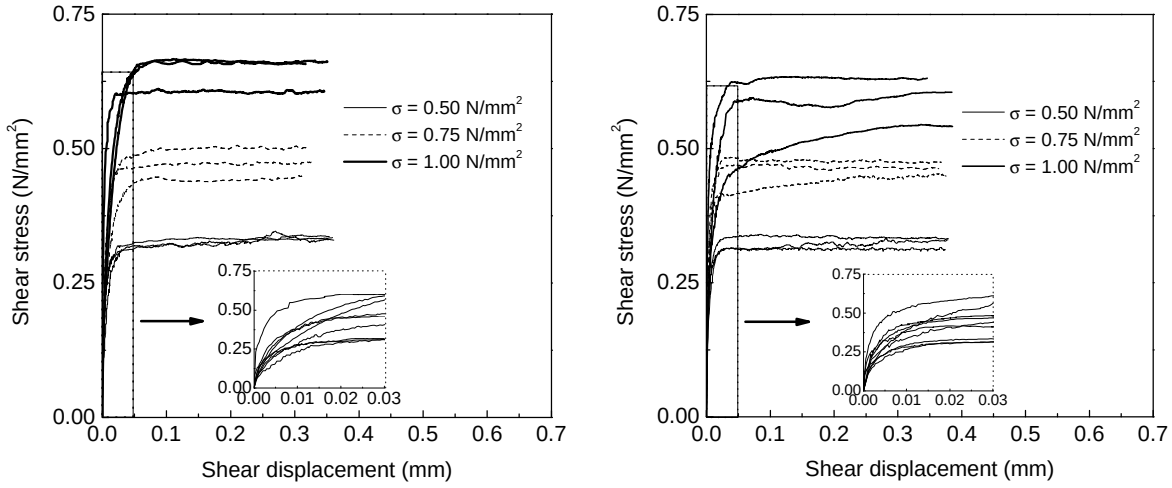


Figure 5.9 – Monotonic shear behavior of dry joints for distinct levels of pre-compression; (a) dry specimens; (b) saturated specimens

The diagram indicated in Figure 5.10, where the evolution of the relative horizontal displacements recorded by the LVDTs with time is shown, enables to conclude that only a rather small in-plane rotation occurs. This result confirms the suitability of the test setup used in the direct shear tests.

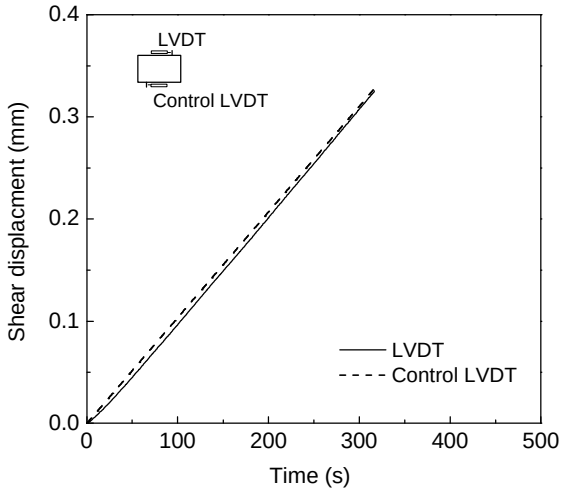


Figure 5.10 – Evolution of the displacements measured by the LVDTs placed at each side of the specimen

The typical shear stress-shear displacement diagrams obtained in direct cyclic shear tests conducted in masonry joints of dry and saturated specimens are displayed from Figure 5.11 to Figure 5.13 for the distinct levels of pre-compression ($\sigma$ = 0.5N/mm$^2$, $\sigma$ = 0.75N/mm$^2$ and $\sigma$ = 1.0N/mm$^2$). An overview of the remaining diagrams is given in Appendix F.

The shear behavior of dry joints during the first cycle agrees with the monotonic diagrams exhibiting nonlinearity in the pre-peak regime and post-peak plastic deformations. Apart from the distinct values of the peak shear stress, no significant differences in the shape of the diagrams can be found in the range of the tested normal stresses, which is valid for both dry and saturated specimens.

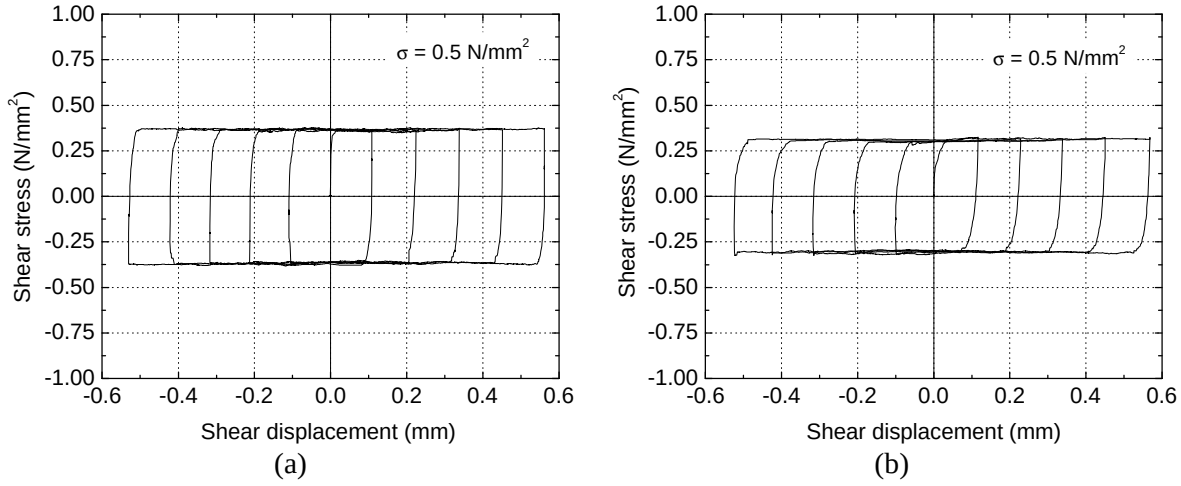


Figure 5.11 – Shear stress-shear displacement diagrams under cyclic loading ($\sigma$ = 0.50N/mm$^2$); (a) dry specimens; (b) saturated specimens

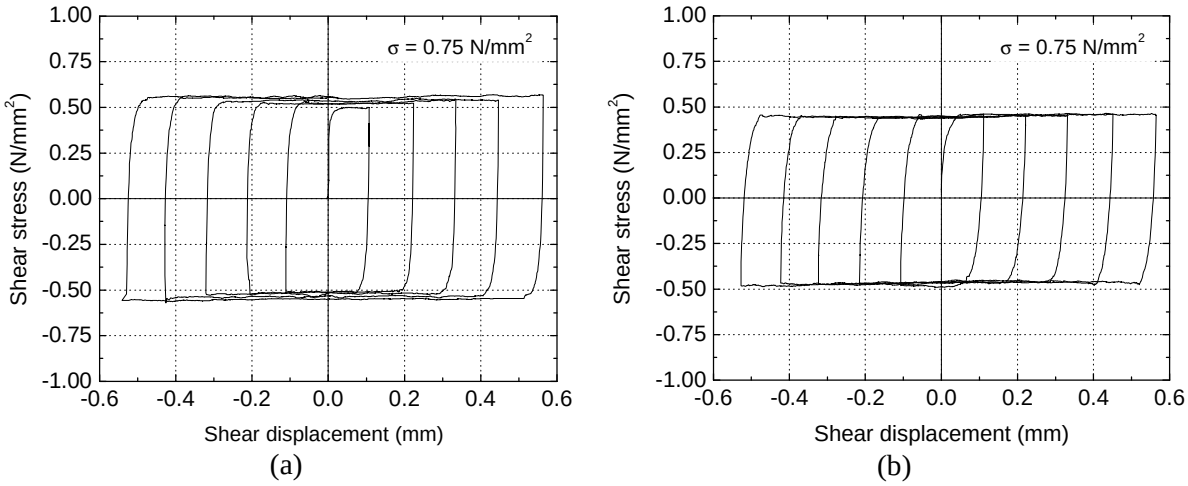


Figure 5.12 – Shear stress-shear displacement diagrams under cyclic loading ($\sigma$ = 0.75N/mm$^2$); (a) dry specimens; (b) saturated specimens

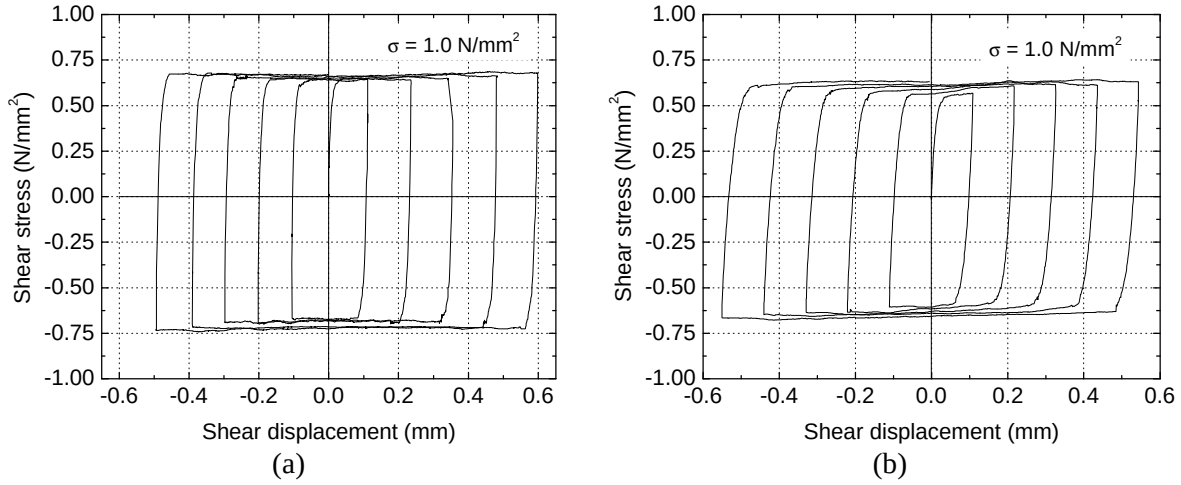


Figure 5.13 – Shear stress-shear displacement diagrams under cyclic loading ($\sigma$ = 1.0 N/mm$^2$); (a) dry specimens; (b) saturated specimens

Figure 5.14a shows the shear stress-shear displacement diagrams for the first and last cycles of loading corresponding to distinct levels of pre-compression. Although minor differences are found in the shear strength during the reversal cycles among the distinct pre-compression levels, there seems to be a more systematic tendency for a slight increase between the first and the last cycles as the vertical pre-compression takes higher values. This effect is more clear in dry specimens. Note that from the monotonic shear stress-shear displacement diagrams, it is observed that for a shear displacement of 0.1mm, the maximum shear forces were already reached. This result is also in agreement with the findings reported by Lee *et al*. (2001) concerning direct shear tests conducted on smooth joints of granite, which referred that the preferential degradation of quartz grains against other rock-forming minerals could provide the stick-slip on the surface of granite. When an analysis of the normal displacement-shear displacement diagrams is carried out, it is possible to observe a more visible tendency for compaction associated to the wearing of the joint surface, see Figure 5.14b.

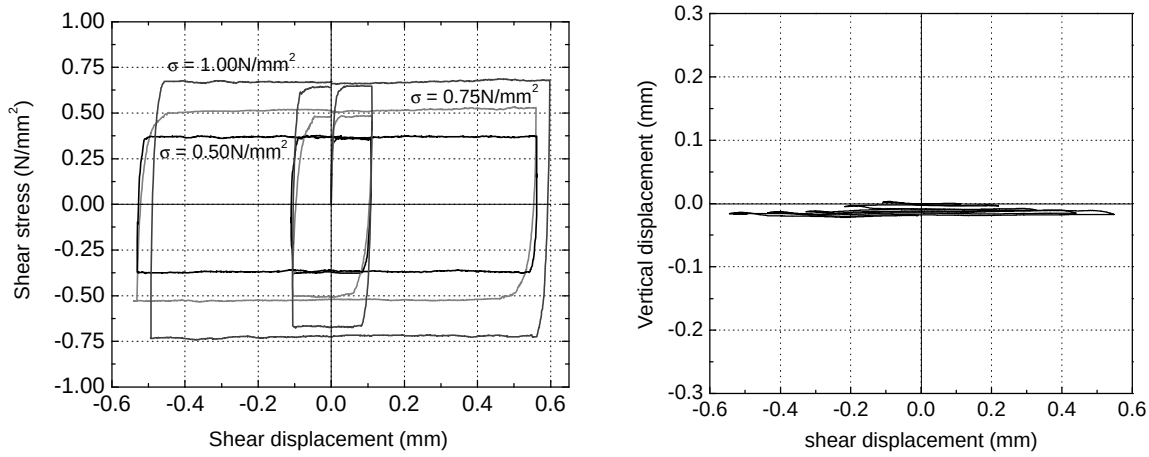


(a) (b)

Figure 5.14 – Characteristic aspects of the shear behavior of dry joints; (a) evolution of the shear stress-shear displacement diagrams between the first and the last cycle of reversal loading; (b) compaction due to the wearing of the joint surface

From the normal-shear displacement diagrams, it is possible to conclude that the values of dilation/compaction are not greater than ±0.06mm, which shows good agreement with the values reported by Ramos (2001) for dilation obtained on sandstone smooth dry joints and with the results pointed out by Homand *et al*. (2001) for hammered granitic joints. In both cases, the degradation mechanism is dominant over the phenomenon of dilatancy. Therefore, it is reasonable to assume that this type of smooth rock joints is non-dilatant. This result is also enlarged to the shear behavior of saturated specimens. In fact, it is well known that the dilatant behavior of rock joints is highly dependent on both roughness of the joint surface and the level of vertical pre-compression (Amadei *et al*., 1998; Chen *et al*., 2000; Huang *et al*., 2002; Misra, 2002). As referred by these authors, in rough joints lower dilation is obtained at high normal stresses and for increasing shear displacements dilatancy tends to exhibit decreasing values.

Based on the shear stress-shear displacement diagrams, it is observed that the shear behavior of dry joints is characterized by an approximately constant stiffness followed by marked nonlinearity close to the peak load in the loading branches. On the other hand, the stiffness of the unloading branches exhibits always considerable high values when compared with the

stiffness obtained in the loading and reloading cycles. The corrected displacement of the dry joint can be obtained by removing the elastic deformation of the unit reading:

$$u_{joint} = u_{meas} - \frac{t}{k_u} \tag{5.4}$$

where $u_{meas}$ is the shear displacement given by the horizontal LVDTs, $t$ is the shear stress for a given displacement and $k_u$ is the stiffness calculated in the unloading branches. Figure 5.15 shows examples of the correction of the shear displacement for both dry and saturated conditions. It is possible to confirm that the elastic deformation of the units has a minor role in the total shear displacement of dry joints.

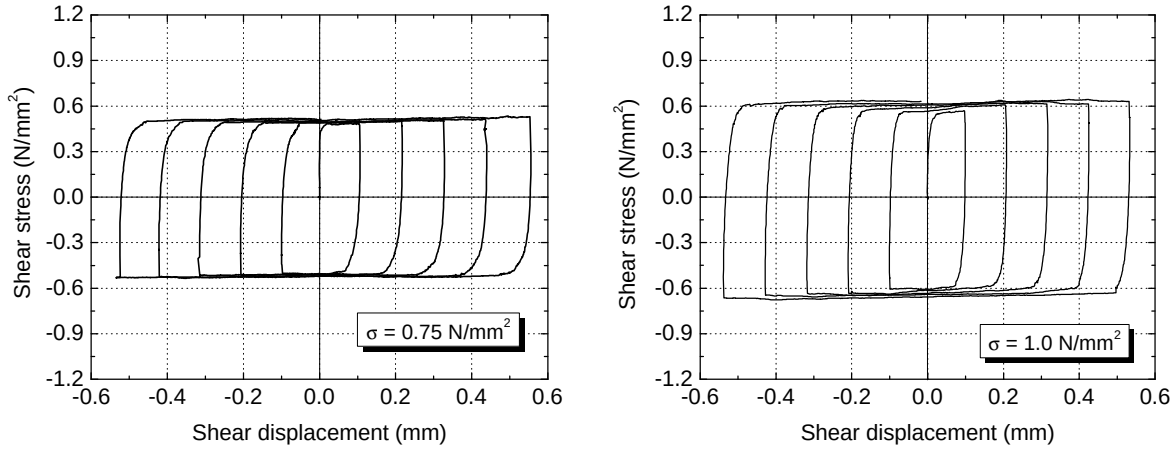


Figure 5.15 – Correction of the measured shear displacement; (a) dry specimens; (b) saturated specimens

The shear behavior of dry joints is thus characterized by significant non-linear deformations in the pre-peak stage and perfect plastic deformations after peak stress resulting from the characteristic sliding failure mode. The former characteristic of the shear behavior of dry joints was already pointed out by Lourenço and Ramos (2004). Apart from the nonlinearity in the pre-peak regime, the envelop of the diagrams is also in good agreement with the shape of the shear stress-shear displacement diagrams indicated by Lee *et al*. (2001), also for smooth sawn-cut granitic joints.

Figure 5.16 shows the relationships between the values of the shear strength obtained in the monotonic tests and in the first cycle of the cyclic tests for dry and saturated conditions as a function of the normal stress. For both specimens, an expressive linear correlation was attained between normal and shear stress, which confirms the initial assumption that the shear strength is well described by Coulomb's friction law.

The slight decrease on the shear strength obtained on saturated specimens is here reflected by the lower value of the friction coefficient, being 0.65 and 0.60 the values that were achieved for dry and saturated specimens, respectively, corresponding to a lowering of the friction coefficient of approximately 10%. The influence of the moisture content on the shear strength of rock joints was also investigated by Geertsema (2002) that pointed out a decrease on the friction coefficient on saturated specimens ranging between 10º and 22.4º for mudstone. The results are obviously not comparable because the materials are considerable different.

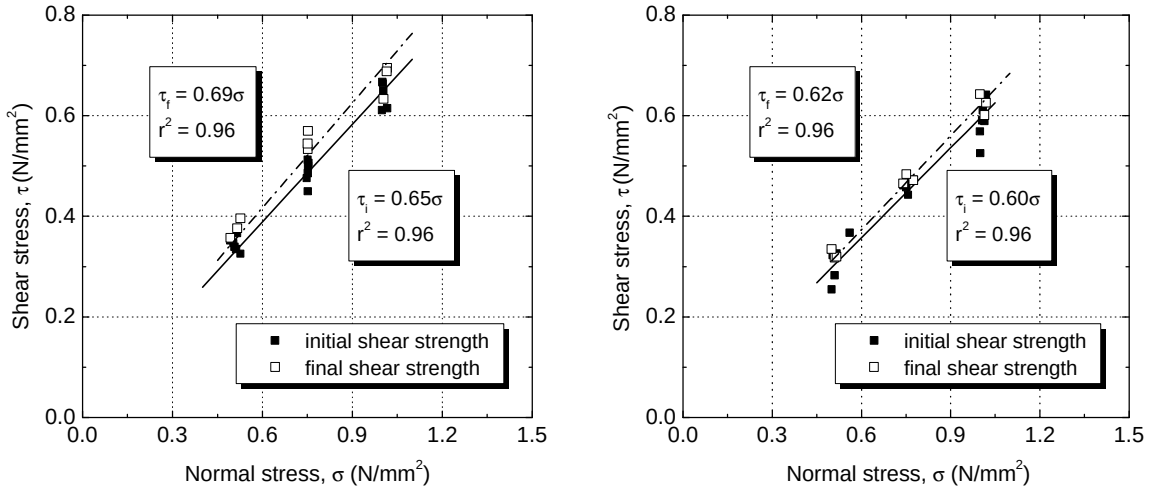


Figure 5.16 – Relationship between normal and shear stress; (a) dry specimens; (b) saturated specimens

The friction angle corresponding to dry joints is slightly larger than the value pointed out by Ramos (2001) for specimens composed by sandstone sawn units tested under dry conditions ($m$ = 0.63) and somewhat lower than the value indicated by Lee *et al*. (2001) for sawn-cut granitic joints ($m$ = 0.69). The narrow range of values for the friction angle seems to indicate that no significant differences for this property should be expected among distinct types of natural stone under similar roughness surface conditions. For the range of vertical stresses considered, the shear strength should be more sensitive to the roughness characteristics of the bed joint surface than to the material properties or even mineralogical composition.

By comparing the values of the initial and final frictional resistance, it can be seen that there is a small increase of the frictional resistance in the last cycle, being the difference more expressive in case of dry specimens. This result confirms the tendency for the slight slipping of the shear stress-shear displacement diagrams previously referred, which can be the result of the wearing of the granitic surface. It is believed that this effect is highlighted due to the considerable porosity of this type of granite.

It should be stressed that in spite of the use of sawn-cut units to characterize the mechanical shear behavior of dry joints of masonry walls discussed later, the experimental investigation on the shear behavior of random rough dry joints, including the definition of the characteristic diagrams, failure criteria and dilatant behavior, would characterize more realistically the mortarless masonry joints existing in ancient masonry construction.

### 5.3.3 *Results of monotonic tests on mortar masonry joints*

The shear stress-shear displacement diagrams of mortar joints with respect to all levels of pre-compression are shown in Figure 5.17a. The horizontal displacement is considered as the average of the displacements recorded by the two horizontal LVDTs located at each side of the specimen and the shear stress is calculated according to equation (5.2). The general shape of the shear stress-shear displacement is characterized by a sharp initial linear stretch. The peak load is rapidly attained for very small shear displacements. Similarly to what was reported for dry masonry joints, non-linear deformations develop in the pre-peak regime, see Figure 5.17b. After peak load is attained there is a softening branch corresponding to

progressive reduction of the cohesion, until reaching a constant dry-friction value. This stabilization is followed by the development of large plastic deformations.

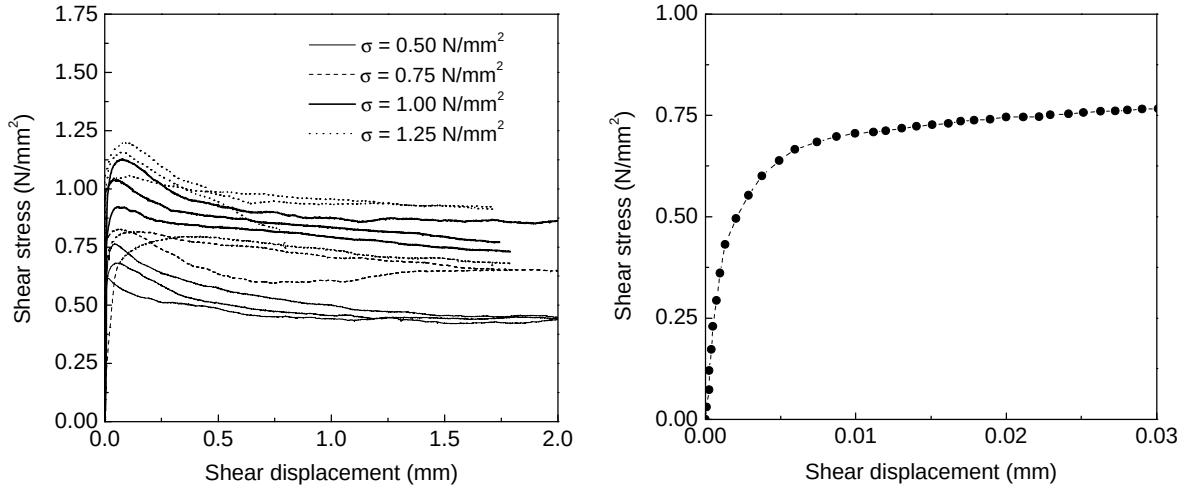


Figure 5.17 – Shear behavior of mortar joints; (a) shear stress-shear displacement diagram; (b) pre-peak nonlinearity

As required, the shear tests were carried out without significant fluctuations of vertical load (less than 2%), which can be confirmed by the evolution of the vertical load with time as shown in Figure 5.18. Note that the shear tests are conducted under horizontal displacement control. This further assesses the validation of the test setup.

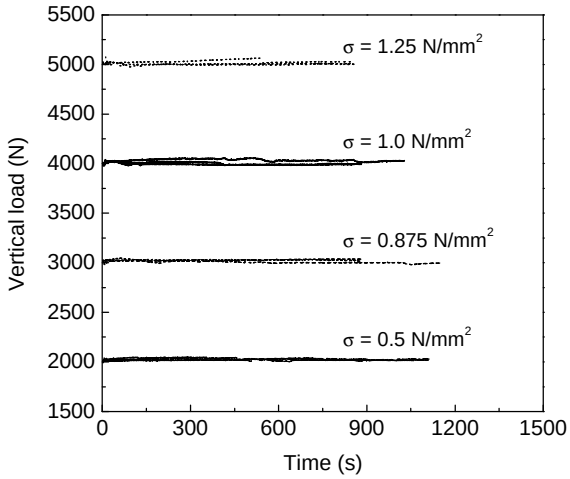


Figure 5.18 – Evolution of the vertical load with time

The relation between the peak and residual shear stress with the normal stress is displayed in Figure 5.19. Significant correlation coefficients were obtained by fitting linear functions to the experimental data composed by peak and residual shear strength, with coefficients of correlation of $r^2 = 0.88$, and $r^2 = 0.80$, respectively. This means that for the range of pre-compression levels tested, the peak and residual shear strength of the bed joint can be reasonably described by means of the Coulomb's friction law given by equation (5.1). Therefore, the linear approach provides shear strength characteristics of the mortar joint, cohesion, $c$, and friction coefficient, $\mu$. A value of cohesion about 0.36 N/mm$^2$ and the tangent of the friction angle, $tan f$, equal to 0.63, corresponding to a friction angle of 32.2º, were

attained for the peak strength. The residual shear strength can be calculated with reasonable accuracy from a friction coefficient of 0.78. This value can be used for evaluation of the shear sliding resistance of walls or piers submitted to seismic action failing along horizontal sliding joints (Calvi *et al*., 1996).

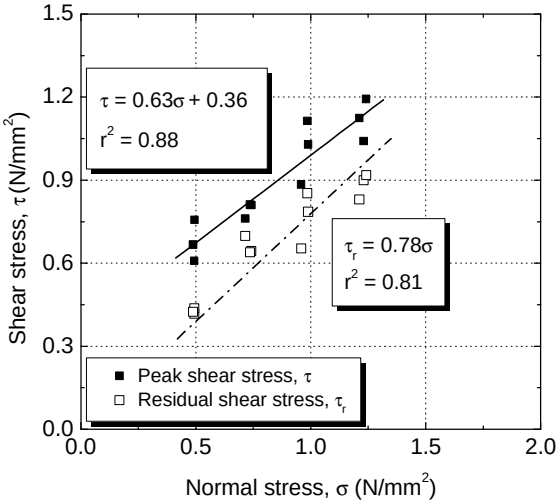


Figure 5.19 – Relation between peak and residual shear stresses with normal stress

The strength values, particularly the bond strength, are greatly dependent on the moisture content and porosity of the units and on the strength and composition of mortar as well as on the nature of the interface (Amadio and Rajgelj, 1990). Binda *et al*. (1994) pointed out that when strong mortar is considered, the strength of the units can also regulate the shear behavior of the joints. This yields that a wide range of shear strength values have been pointed out for various combinations of units and mortar. Mann and Muller (1982) indicated a mean friction coefficient of approximately 0.65 on brick-mortar assemblages and a cohesion ranging from 0.15 up to 0.25, depending on the mortar grade. From the results of direct shear tests carried out by Pluijm (1999), the coefficient of internal friction ranges between 0.61 and 1.17, whereas cohesion varies from 0.28 up to 4.76, depending on different types of units and mortar. Table 5.4 summarizes other results published in literature referring to the shear strength properties for different combinations of materials.

Table 5.4 – Shear strength properties for different unit-mortar assemblages

| Source | units | mortar | $c$ (N/mm$^2$) | $m$ |
|---|---|---|---|---|
| Atkinson (1989) | Old clay units | 1:2:9 (13) | 0.127 | 0.695 |
| | Old clay units | 1:2:9 (7) | 0.213 | 0.640 |
| | New clay units | 1:1.5:4.5 | 0.811 | 0.745 |
| Amadio and Rajgeli (1990) | Solid bricks | Cement mortar<br>Lime-cement mortar | 0.65 | 0.723 |
| Magenes (1992) | Solid bricks | Hydraulic lime mortar | 0.206 | 0.813 |
| | | Lime mortar | 0.081 | 0.652 |
| Binda *et al*. (1994) | Sandstone | Hydraulic lime mortar | 0.33 | 0.74 |
| | Calcareous stone | Hydraulic lime mortar | 0.58 | 0.58 |
| Roberti *et al*. (1997) | Bricks | Hydraulic lime mortar | 0.23 | 0.57 |
| Lourenço *et al*. (2004) | Hollow bricks | Micro-concrete | 1.39 | 1.03 |
| This study | Granitic units | Lime mortar | 0.359 | 0.630 |

It can be observed that the values of the cohesion and friction coefficient found for the granitic unit-lime mortar assemblages are within the range of variation of the shear strength properties suggested by other authors.

In spite of the fact that the relative local vertical displacements of the joint could not be measured due to technical problems with the LVDTs, the total vertical displacement was recorded by the internal LVDT located inside the vertical actuator. The evolution of this displacement with the shear displacement is displayed in Figure 5.20, where in the greater number of the tests two distinct phases can usually be distinguished. Firstly, the uplift of the joint is expressed by increasing positive vertical displacements, which is particularly remarkable for low normal stresses. The nonlinear evolution of the displacements provides variable dilatancy assuming decreasing values as the shear displacement increases. This behavior is connected to the changes on the interfaces due to surface wearing. By comparing the diagrams of Figure 5.17a and Figure 5.20, it can be observed that the shear displacement associated to the maximum value of the vertical displacement is close to the horizontal displacement corresponding to the stabilization of the shear stress. During the regime of pure friction the vertical displacement remains constant or progressively decreases, which is more significant as the level of pre-compression increases, exhibiting even negative values in some specimens submitted to pre-compression levels of $\sigma = 0.75 N/mm^2$ and $\sigma = 1.00 N/mm^2$. This seems to indicate that as the pure shear develops, the wearing of the surface joints leads to compaction in the case of the porous lime mortar used. For the larger pre-compression level ($\sigma = 1.25 N/mm^2$), only compaction of the specimen was recorded, which is revealed by the negative values of the total vertical displacements, resulting from the higher level of degradation of the mortar joint associated to the continuous friction.

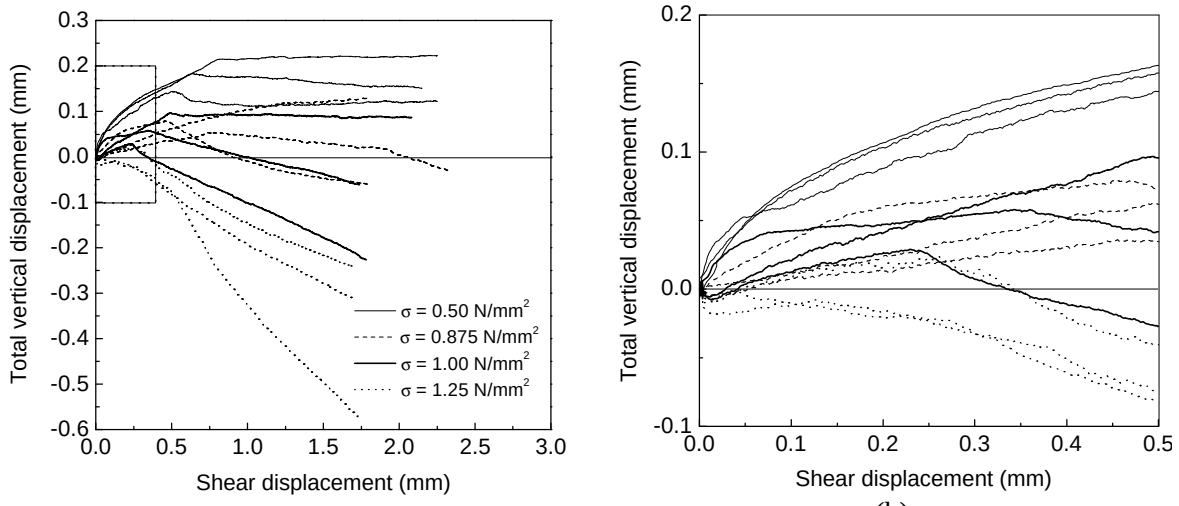


Figure 5.20 – Relation between total vertical displacement and shear displacement; (a) during shear test; (b) zoom of the initial dilatant behavior

The dilatant behavior reflects, to great extent, the distinct shear failure modes obtained in the specimens submitted to different normal stresses. In fact, for low levels of pre-compression, shear failure occurs at the unit-mortar interface along one unit face or, more frequently, divided between two unit faces, see Figure 5.21a. For the larger normal stress level ($\sigma = 1.25 N/mm^2$), the failure is only localized in the mortar and a larger amount of small

mortar particles were found to be detached, see Figure 5.21b. No damage was visible in the stone units in all cases.

(a) (b)

Figure 5.21 – Typical shear failure modes; (a) specimen submitted to normal stress of 0.5N/mm$^2$; (b) specimen submitted to normal stress of 1.25N/mm$^2$

Finally, it should be noted that the described behavior is in agreement with findings reported by other authors concerning the dependency of the dilatancy on the level of the confining stress for mortar joints, and its inexistence for medium to high values (Atkinson *et al*., 1989; Pluijm, 1999). Given the dependence of the dilatancy on the shear displacement and on the vertical stress, the usual procedure generally used for masonry joints is to assume the dilatancy with zero value (Lourenço, 1996).

## 5.4 Masonry in compression

With respect to the compressive behavior of masonry, several experimental, numerical and simplified analytical studies have been carried out in order to enlarge the knowledge about this composite material (Atkinson *et al*., 1985; Naguib and Sutter, 1991; Vermeltfoort, 1994). Being masonry composed by units and mortar, it has been largely accepted that the failure mechanism is governed by the interaction between both materials and by their distinct elastic properties.

The experimental characterization of masonry under compression requires panels representative of its in-situ construction. Recommendations about the geometry and dimensions of the specimens are described in the European Standard EN1052-1(1999), where it is stated that masonry specimens may be wallets, including at least one head joint in the central course centrally placed. Due to high strength of granite, technical limitations related to the maximum capacity of the actuators available at the laboratory were found. Thus, the compressive features of granitic masonry had to be obtained by considering stacked prisms. According to Page and Shrive (1988), although the wallets yield more representative results, the prisms are reasonable masonry assemblages that include simultaneously the effect of bedding type, unit-mortar interaction and workmanship.

The present experimental program aims at obtaining the mechanical compressive data for dry and low strength mortar masonry, which is of use for the assessment of the masonry shear walls detailed in Chapter 6. In addition, the tests aims also at providing insight of the influence of the surface roughness and distinct interlayer materials of the joints on the compressive strength and deformation characteristics of masonry. Table 5.5 summarizes the type of masonry prisms adopted as a function of the stone unit and the type of interlayer material. As regards dry masonry, both sawn (PR_S) and rough surface (PR_SR) joints are taken into consideration. The rough surface is obtained by sand-blasting. Two types of

interlayer material are adopted, namely low strength lime mortar (Albaria structturale) described in section 5.2 and clay (granitic soil). The latter material is common to be found in traditional ancient constructions in North of Portugal. In order to obtain the compressive strength of irregular masonry, specimens combining hand cut units and low strength mortar are also considered.

Table 5.5 – Types of masonry prisms and number of specimens. The number of specimens tested under monotonic loading is indicated inside brackets

| Masonry prism | Units | Interlayer material | Samples |
|---|---|---|---|
| PR_S | Sawn | None | 10 (3) |
| PR_SR | Sawn/sand-blasted | None | 7 (2) |
| PR_SM | Sawn | Mortar | 7 (2) |
| PR_SS | Sawn | Granitic soil | 7 (2) |
| PR_IM | Hand cut | Mortar | 7 (3) |

### 5.4.1 *Specimens, equipment, test setup and procedure*

The compressive strength of masonry prisms is known to be affected by several factors, such as size, height and end conditions (Page and Shrive, 1988; Kingsley *et al*., 1989; Khalaf *et al*., 1994). In order to prevent some kind of end restraint, a height to length ratio of 3 was adopted according to ASTM E447 (1992) standard. Therefore, the masonry prisms were made with three cubic stone units of 150mm and two bed joint courses, as shown in Figure 5.22. The thickness of mortar or granitic soil placed in the bed joints was close to 10mm and the units were oven-dried. The dry stacked masonry prisms, PR_S and PR_SR, were constructed at the testing location by simply laying the second and third unit from the bottom unit in order to obtain vertical alignment of the specimen. The dry bed joints were properly selected so that maximum contact area between units could be attained. When mortar bed joints were considered, the stone units were carefully cleaned and wet to provide enough adhesion between units and mortar. In case of irregular stone units, the masonry prisms, PR_IM, were capped using the same type of mortar as the bed joints. No capping material was used in specimens PR_SM given the smooth sawn surface. Similarly to the masonry walls to be tested, the mortared specimens were cured for seven days at the laboratory environment.

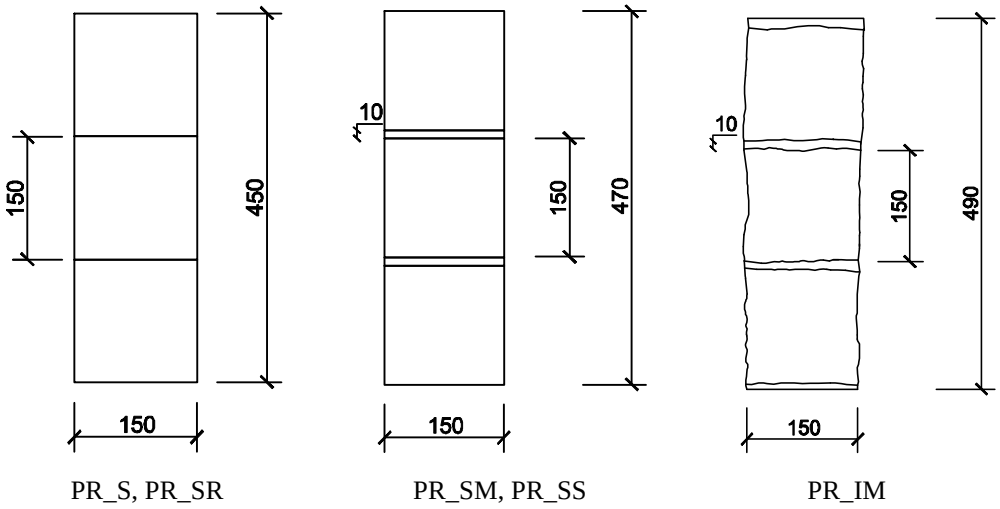


Figure 5.22 – Geometry of the specimens

The testing equipment consisted of the three-dimensional steel frame already mentioned in Chapter 3 for the compressive tests. Besides the large load capacity of the actuator, its remarkable stiffness is useful when stable displacement controlled failure is required. In order to induce uniform load distribution, a thick steel platen was located at the top of the specimen and was connected to a thick spherical seat, see Figure 5.23a.

The deformation of the specimen during the test was acquired by means of four LVDTs located between steel platens at each side of the specimen, as it can be seen in Figure 5.23b. The vertical displacement of masonry prisms is defined by the average of the displacements measured by these LVDTs. Apart from the masonry prisms PR_S, seven specimens of the other types were tested, see Table 5.5. Firstly, two monotonic tests were carried out in order to obtain a value of the compressive strength. In the remaining specimens two loading-unloading cycles were performed at 25%, 50% and 75% of the average compressive strength obtained in monotonic tests under loading control. After this point, the control was switched to vertical displacement control at a velocity of 3μm/s. The adoption of this low velocity was an attempt to obtain a stable failure process and, hence, the recording of the compressive softening behavior of masonry. This procedure is also useful in the prevention of abrupt and explosive failures.

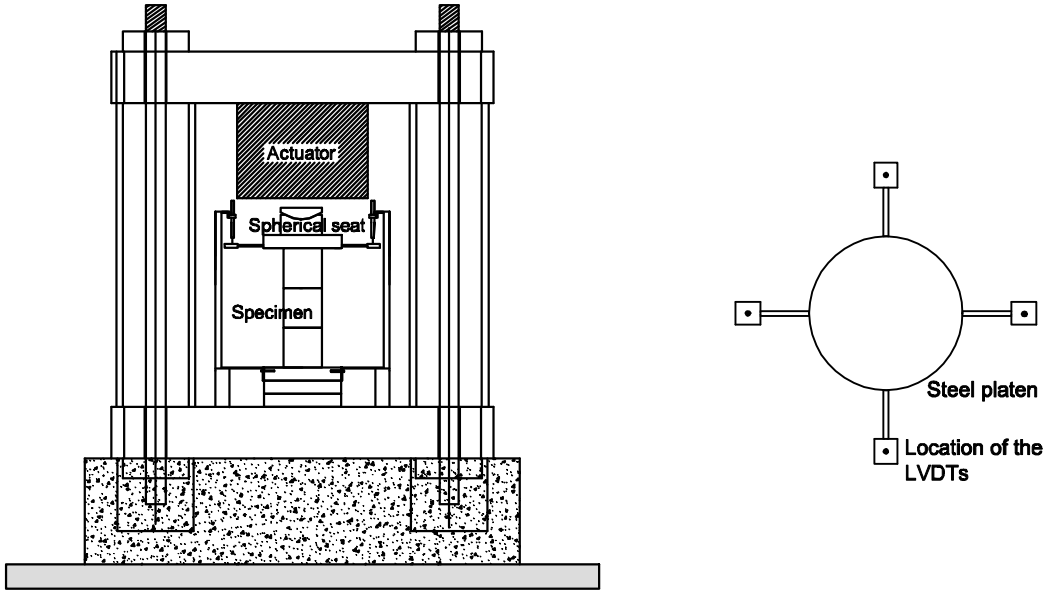


(a) (b)

Figure 5.23 – Test setup and location of the LVDTs; (a) elevation view; (b) top view

## 5.4.2 *Test results*

### 5.4.2.1 Stress-strain diagrams

For each specimen the corresponding value of the compressive stress was obtained by dividing the compressive load by the average cross section calculated from three measures taken at the bottom and top edges and at the middle of the specimen. The deformation at a given stress level, ***e***, was calculated by dividing the vertical displacement by the height of the specimen, since the vertical displacement was taken as the average of the displacements recorded by the four vertical LVDTs.

For a comparative analysis, all stress-strain diagrams obtained under monotonic loading are depicted in Figure 5.24.

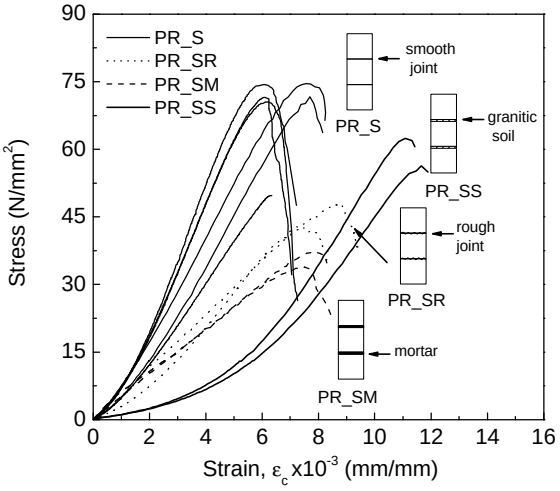


Figure 5.24 – Stress-strain diagrams for monotonic tests

The shape of the stress-strain diagrams of prisms PR_S is similar to the one obtained for the compressive behavior of the granite unit. For low stress levels, the diagram exhibits a upward concavity. Although sawn surfaces are rather smooth and quite good adjustment of the stones was almost always achieved during the construction of this type of masonry prism, this feature was mostly due to the initial settlement that occurs at the bed joints. After the full contact of the bed joints for higher levels of compressive stress, the compressive behavior of masonry prisms is more dependent on the behavior of the material that constitutes the units. All prisms exhibit reasonable linear behavior until values of the compressive stress close the peak strength. After the peak load is reached, it is still possible to record a considerable stretch of the descending branch of the diagrams in some specimens. In spite of this, most of them fail in a brittle manner, which makes the analysis of the final failure pattern impossible, as discussed later.

The stress-strain diagrams concerning dry masonry prisms with rough joint surface, PR_SR, differ from the diagrams obtained for dry masonry sawn prisms. The stress-strain diagrams show also upward concavity for low stress level but this occurs over a larger extension. This behavior leads to higher levels of deformation at peak load. As the compressive load increases, the higher roughness of the contact surface tends to break leading progressively to the leveling of the bed joint and to the improvement of the surface contact. Since the stone units are all of the same material, the total deformation must be the result of the deformation of the units (lower in this case because the peak stress is lower) and the local deformation that occurs at the bed joints level (higher in this case because the surface is rougher).

Unlike the previous results related to the shape of the stress-strain diagrams of the prisms PR_S and PR_SR, the stress-strain diagrams of prisms PR_SM with sawn units and lime mortar bed joints exhibit an initial stretch with downward concavity. This seems to be the result of both component materials, units and mortar, acting as a composite since early stages of loading due to the bonded interface. The lowering on the compressive strength regarding the reference dry masonry specimens (PR_S) is still more significant when mortar bed joints are considered. Similar decreasing tendency is followed by the stiffness.

The significance of the role assumed by deformation properties of the material of the bed joint on the deformational behavior of the masonry prism can be seen from the stress-strain diagrams obtained for the specimens PR_SS. These diagrams are characterized by a large extent with upward concavity from low to medium stress levels. The large initial deformation is essentially related to the compaction of the granitic clay at the bed joint. In fact, after failure of the masonry prism, it was possible to confirm this effect by analyzing the bed joint at the final state of the compressive test. As it can be observed in Figure 5.25, the bed joint with a thickness of nearly 10mm is now a thin layer of compacted soil. Therefore, the clear distinct shape of the stress-strain diagrams is related to the deformational characteristics of both materials. From the stress-strain diagrams obtained for the prisms PR_SS, it is also observed that the compressive strength exhibit considerable higher values than the prisms PR_SR (dry masonry prisms with rough joints) and PR_SM (masonry mortar specimens) and is rather close to the values concerning dry masonry prisms (PR_S). Also for the modulus of elasticity higher values are expected relatively to the ones referring to prisms PR_SR and PR_SM.

Figure 5.25 – Final state of the granitic soil at the bed joints when failure occurs

The stress-strain diagrams with loading-unloading cycles in the pre-peak regime for sawn-cut unit prisms, PR_S, and rough bed joint surface prisms, PR_SR, are displayed in Figure 5.26a, and Figure 5.26b respectively. Note that for the pre-peak cyclic tests, only the result of one specimen is shown so that a clear analysis can be performed. Further details of the stress-strain diagrams can be found in Appendix F. From the analysis the loading-reloading branches during the pre-peak behavior, it is seen that significant higher values of stiffness were recorded comparatively to the stiffness of the virgin stretch, either for prisms PR_S or PR_SR. This feature can be attributed essentially to the fact that the stiffness of the unloading-reloading branches involves permanent deformations corresponding to a given stress level. Considerable differences were also found in the loading-reloading deformations between specimens PR_S and PR_SR. Significant larger amount of recoverable deformation is associated to smooth dry specimens relatively to rough dry specimens. Besides, in the specimens PR_SR the permanent deformations are cumulative for the two cycles of loading-reloading, unlike the specimens PR_S. This distinct behavior is based on the continuous wearing of the higher asperities during the loading process.

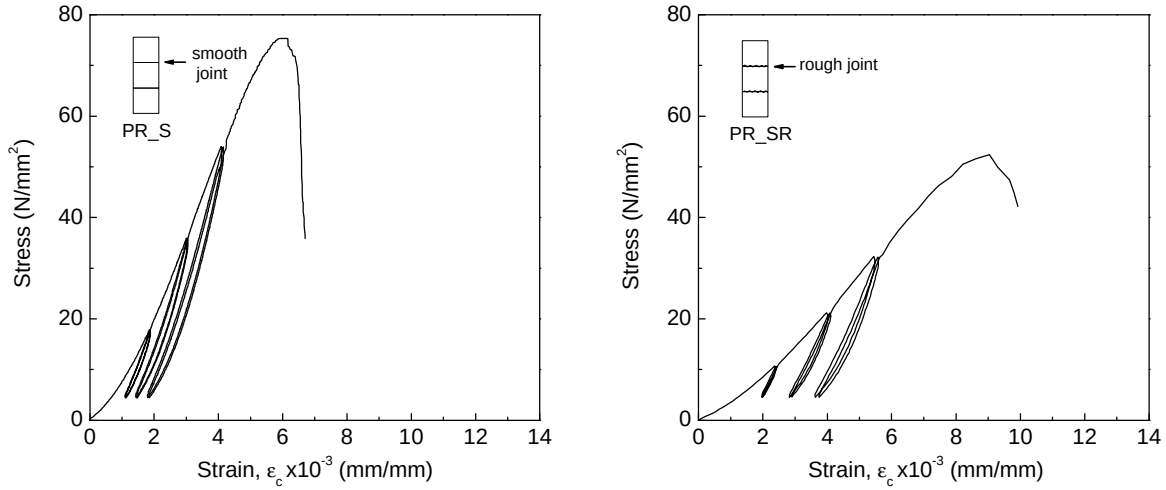


(a) (b)

Figure 5.26 – Stress-strain diagrams for cyclic tests; (a) specimen PR_S10; (b) specimen PR_SR7

For mortar prisms PR_SM, unrecoverable deformations corresponding to the unloading-reloading are even more remarkable than deformations of specimens PR_SR, which should be attributed to the mortar deformability, see Figure 5.27a. Unlike dry masonry prisms, significant permanent deformations were recorded in the pre-peak unloading-reloading cycles in prisms PR_SS, resulting directly from the compaction nature of the interlayer material, even if some part of the deformation could be recoverable, see Figure 5.27b. Significant higher stiffness is associated to the unloading-reloading branches relatively to the virgin branch for both prisms.

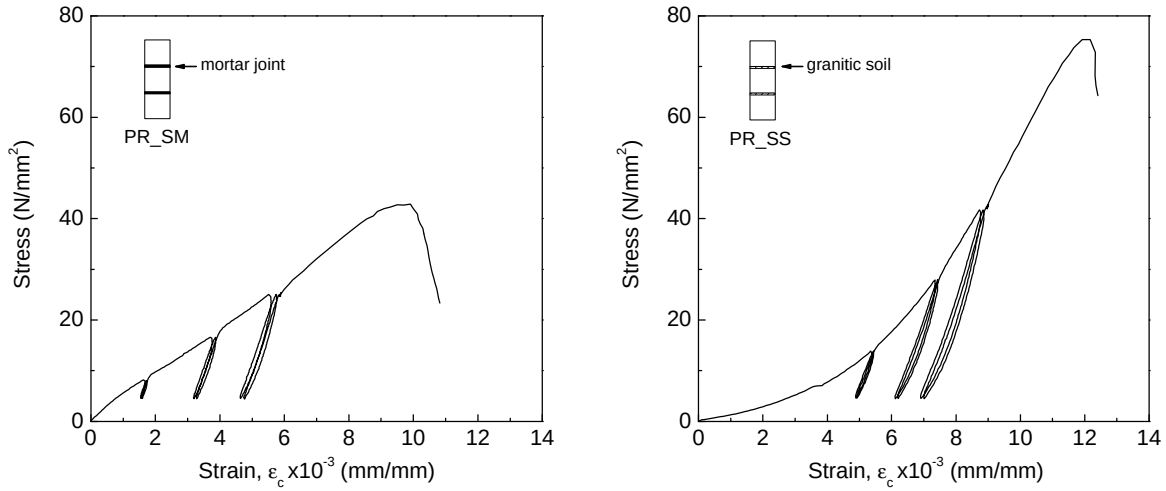


(a) (b)

Figure 5.27 – Stress-strain diagrams for cyclic tests; (a) specimen PR_SM7; (b) specimen PR_SS3

The characteristic compressive behavior of irregular masonry prisms, PR_IM, is displayed in Figure 5.28. The stress-stain diagrams obtained in monotonic tests are compared with the stress-strain diagrams corresponding to mortar masonry prisms with sawn granitic units, PR_SM. As can be observed, a reduction in the compressive strength of approximately 50% was recorded in prisms PR_IM relatively to the specimens PR_SM. The deformational behavior also presents remarkable changes. The deformation at peak stress increases approximately 40% with respect to the deformation exhibited by the specimens PR_SM,

which is to great extent related to the significant decrease of the modulus elasticity. The differences found in the shape of the stress-strain diagrams between both types of masonry prisms are mostly addressed to the distinct assemblage. A higher level of scatter in the pre-peak behavior was found. In spite of these prisms having been built by the same worker, the scatter should also be related to the variability of the workmanship. To a minor extent, the decreasing on the compressive strength can also reflect the lower values of the compressive strength of the mortar achieved for these prisms as presented in Section 5.2. If the same scale is considered in the evaluation of the pre-peak behavior, no differences between the specimens are recorded in the slope of the unloading-reloading branches. Consequently, larger difference between the slope of the unloading-reloading and the virgin branches are found for irregular masonry prisms. Moreover, another important issue refers to the post-peak behavior. Unlike mortar masonry prisms with sawn cut units PR_SM, a controlled fracture process developed in irregular masonry prisms after peak load was reached, which enabled the obtainment of the descending branch of the stress-strain diagrams. The quite smooth shape of softening branch reflects the continuous and progressive growth of the cracks opening. The fracture process is thus associated to large ultimate deformations. These features show that clear distinct characteristics of ductility are addressed to specimens PR_IM and PR_SM.

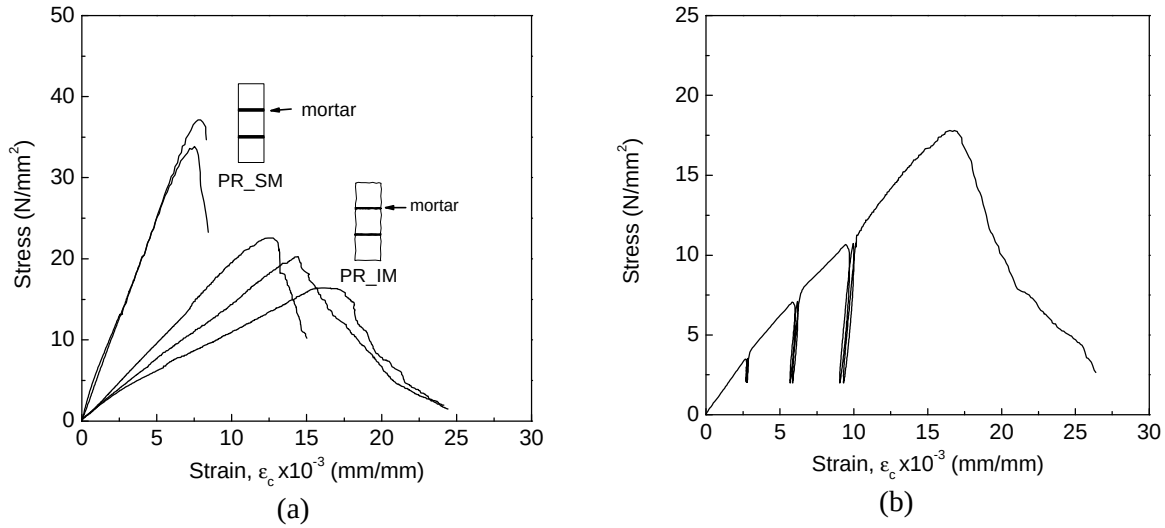


Figure 5.28 – Stress-strain diagrams for the PR_IM masonry prism series; (a) comparison with monotonic results of PR_SM prisms; (b) cyclic tests – specimen PR_IM5

5.4.2.2 Mechanical properties

The mechanical properties were derived directly from the stress-strain diagrams presented in the previous section. The compressive strength, $f_c$, was calculated by dividing the maximum axial load by the average cross section of the prisms. The deformation at the peak stress, $e_c$, was calculated by dividing the vertical displacement corresponding to the peak stress by the initial height of the specimen. Similarly to what was indicated by Binda *et al*. (1997), the Young's modulus, $E_c$, was determined as the secant modulus in the range of 30 and 60% of the ultimate compressive strength calculated in the ascending branch of the stress-strain diagram. For each masonry prism series, the mean value is obtained by averaging the values recorded for all specimens of the series. The mechanical properties that characterize the compressive response of the masonry prisms, namely the compressive strength, $f_c$, modulus of

elasticity, $E_c$, and deformation at peak stress, $e_c$, are displayed in Table 5.6. As can be seen, dry masonry prisms exhibit the larger compressive strength and Young's modulus and the minor deformation at peak stress. The value of the compressive strength is of the same order of the compressive strength of the units. According to Hendry (1998), stone masonry built from accurately shaped blocks with thin joints would be close to stone strength, irrespectively of the mortar strength. The modulus of elasticity measured in dry masonry prisms is 27% lower than the modulus of elasticity of the stone unit. Note that, even if the modulus of elasticity of the granite is calculated at 50% of the peak strength, the differences should be mostly attributed to the discontinuities of the masonry prisms associated to bed joints. As referred in the previous section, the total vertical displacements include also the deformations at the bed joints.

Table 5.6 – Mean values of the mechanical compressive properties of masonry prisms. Coefficient of variation is indicated inside brackets (%)

| Masonry prism | $f_c$ (N/mm$^2$) | $e_c$ (mm/m) | $E_c$ (N/mm$^2$) |
|---|---|---|---|
| PR_S | 73.0 (9.1) | 6.3 (13.2) | 14722 (19.0) |
| PR_SR | 51.9 (16.2) | 8.0 (20.5) | 7934 (37.1) |
| PR_SM | 37.0 (11.8) | 9.1 (9.8) | 4629 (17.5) |
| PR_SS | 64.2 (13.5) | 11.7 (10.3) | 8920 (12.6) |
| PR_IM | 18.4 (8.9) | 14.9 (7.3) | 1248 (27.6) |

Lower values of the compressive strength and significant reduced ascending slope were found in dry masonry prisms with rough bed joints (PR_SR) comparatively to the dry sawn masonry prisms (PR_S). The compressive strength undergoes a reduction of approximately 29%, whereas, the modulus of elasticity is 46% lower when the dry bed joint is rough. These differences reflect the role of rough bed joints in the compressive behavior of the masonry prism. In fact, the rough surfaces have associated a lower contact area (effective area), which provides an increase of the effective stresses (ratio between the compressive stress and the effective area) resulting in the lowering of the compressive stresses measured in the full specimen area. Similar results were given by Marzahn (1999). Since the units are of the same granite of specimen PR_S, the increase of vertical strain at peak stress (approximately 27%) is directly connected to the lower stiffness of the bed joint, which leads to lower values of the stiffness of the masonry prisms. The higher scatter found in masonry prisms PR_SR corresponding to the mechanical properties should be mostly attributed to the variability of the distribution of the roughness at the bed joint surfaces, as a similar scatter occurs in the material of the units.

The lowering on the compressive mechanical properties regarding the reference masonry specimens (PR_S) is still more significant when mortar bed joints are considered (PR_SM), with a reduction of nearly 50% and 70% in the compressive strength and in the modulus of elasticity, respectively. On the other hand, the deformation capacity significantly increases (44%) by the introduction of mortar in the bed joint. As has been widely pointed out in literature (McNary and Abrams, 1985; Atkinson *et al.*, 1985), the compressive behavior of the masonry prisms is dependent on the performance of the materials, units and mortar, and mainly on its composite behavior. Inclusively, the deformation of the mortar appears to take the major role in the deformation characteristics of the masonry prisms, since comparatively to the granitic units the low strength mortar is much less stiff. The reduction of the

compressive strength can be attributed to the compression-lateral tension state of the units induced by the shear stresses at the unit-mortar interface as the result of the restraint to the mortar lateral deformation conferred by the units. The mortar is then submitted to a triaxial compression state, whereas the stone units are laterally in biaxial tensile state. This effect is, thus, the result of the distinct deformational properties of material components, mortar and units, and is more significant as the mortar strength and stiffness decreases.

The effect of material type of the bed joints can be also evaluated through the response of the masonry prisms PR_SS resulting from the addition of granitic soil to the joints. In average, the total strain of the prisms PR_SS is 85% higher than the deformation recorded in dry masonry prisms PR_S. The modulus of elasticity presents a reduction of approximately 40% and the compressive strength is 12% lower. The introduction of granitic soil instead mortar in the bed joint represents an increase of 73% on the compressive strength and an increase of 92% on the modulus of elasticity. This behavior is attributed to the trend for compaction of the granitic soil and a trend for dilation of the mortar. It is believed that negligible shear stresses occurs at bed joint when granitic soil is used and much lower values of splitting tensile stresses develops in the granitic unit.

Considerable lower values of the compressive strength and Young's modulus were found in irregular masonry prisms (PR_IM). A reduction of 75% on the compressive strength and 90% on the Young's modulus is attained relatively to dry masonry prisms. With respect to mortar masonry prisms with sawn cut units, a reduction of about 50% on the compressive strength and a reduction of 73% on the Young's modulus are recorded. On the other hand, the deformation at peak stress addressed to prisms PR_IM is 64% higher than deformation of prisms PR_SM.

Finally, by analyzing the modulus of elasticity and compressive strength obtained in all series of specimens, it is observed that a nonlinear relationship was found to exist between both variables, with rather significant coefficient of correlation ($r^2$ = 0.96), see Figure 5.29. If a linear fit was adopted, the relation between both variables would be given by $E = 240f_c - 3937$ with a coefficient of correlation $r^2 = 0.88$. Note that this expression is far from the empirical relation given by EC6 ($E = 1000f_c$).

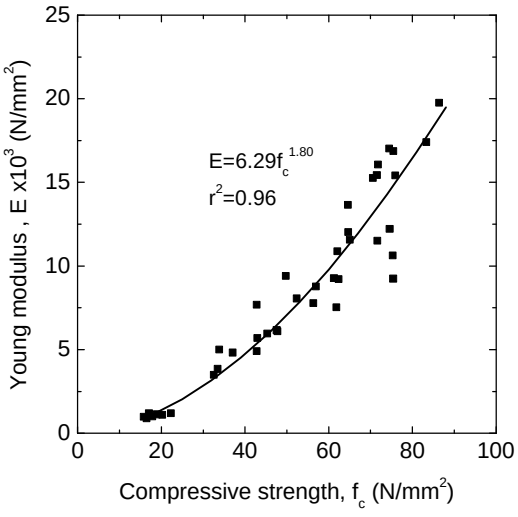


Figure 5.29 – Compressive strength vs. modulus of elasticity for masonry

5.4.2.3 Failure modes

The failure pattern of dry masonry prisms was quite difficult to follow due to the protection placed around the specimens in order to avoid injuries resulting from the projection of stone pieces. Given its brittle behavior, most of the failures of specimens PR_S and were abrupt and explosive, see Figure 5.30a, where the typical final failure of this type of specimens is highlighted. No signs of microcracks were recorded in the pre-peak regime. Micro-cracks become visible only after peak load has been reached. For dry masonry specimens, it is usual that failure cracks develop along shear bands. Although the slenderness of the specimens is about 3, some specimens exhibit even double shear cracks. The failure patterns composed by shear cracks were also referred in Chapter 3 as characteristic of failure of this type of granite under compressive loading. This suggests that after the initial adjustment of dry bed joints, the dry masonry prism behavior is homogeneous and appears to be mostly determined by the compressive behavior of the granitic units. No differences were introduced in the failure modes by increasing the roughness of the bed joint surface. Abrupt failure as indicated for smooth dry prisms in Figure 5.30a occur in two specimens of rough dry masonry prisms. For the remaining five specimens, typical failures as exhibited in Figure 5.30b,c occur. This indicates that roughness provides continuity of the specimen and a mechanism of load transfer between the units is similar to the smooth dry joints.

(a) (b) (c)

Figure 5.30 – Characteristic failure patterns of dry masonry prisms; (a) specimen PR_S6; (b) specimen PR_SR5; (c) specimen PR_SR4

The failure of mortar masonry prisms is characterized by lateral splitting cracks appearing firstly in the central unit that extend to the other stones as the compressive stress increases, see Figure 5.31a,b. This failure mode is the outcome of the lateral tensile stresses of the granitic units induced by the composite behavior of units and mortar with different elastic properties. Similar results have been reported by several authors (Andreaus and Ceradini, 1992). On the other hand, the failure of the specimens PR_SS with granitic soil in the bed joints is more similar to the crack patterns exhibited by the dry masonry specimens, see Figure 5.31c. This can be explained by the peculiar trend for compaction exhibited by the granitic soil joints in contrast with the expansion of mortar.

(a) (b) (c)

Figure 5.31 – Characteristic failure patterns of masonry prisms; (a) and (b) specimens PR_SM; (c) specimens PR_SS

As is shown in Figure 5.32, the failure of prisms PR_IM is also characterized by vertical splitting cracks. The dilatant behavior of the mortar joint can be observed for low stress levels by the detachment of the lateral mortar finishing at the bed joints, as is shown in Figure 5.32a. Visible thin vertical cracks were found to develop until peak load, mainly in the central stone unit, see Figure 5.32b. After this stress level, the cracks extend to the other units. Crack openings grow progressively and attain considerable values, Figure 5.32c,d. This controlled fracture process is reflected by the descending branch of the stress-strain diagrams pointed out in Section 5.4.2.1.

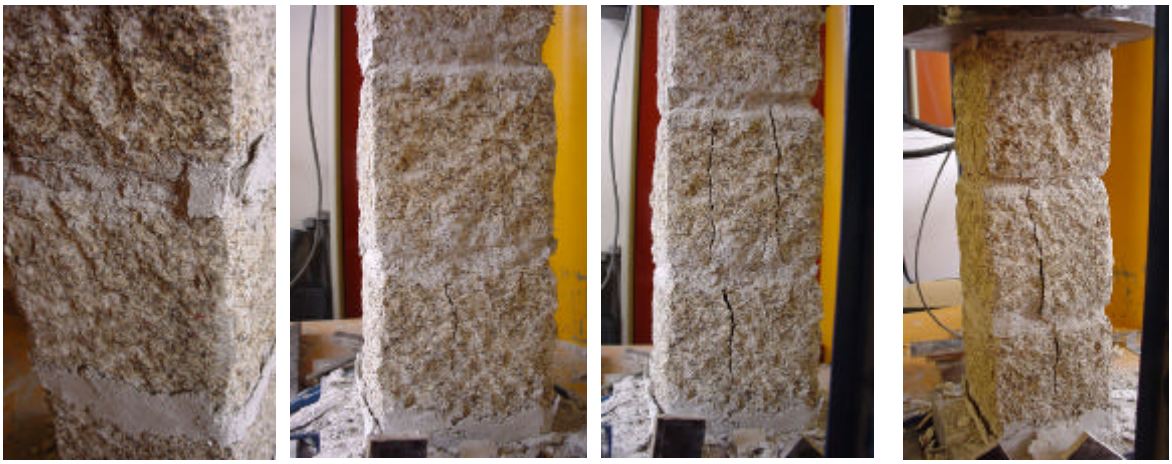

Figure 5.32 – Characteristic failure patterns of irregular mortar masonry prisms

## 5.5 Concluding Remarks

The experimental characterization of masonry assemblages and masonry components used in the shear walls discussed in Chapter 6 is addressed, focusing on the strength properties of dry masonry joints and the unit-mortar interface, as well as on the compressive properties of the masonry.

A set of direct shear tests was conducted on couplet specimens, either considering dry or mortar joints. From these tests it was possible to derive the shear strength properties, namely

cohesion and friction coefficient. Besides, the complete shear stress-shear displacement diagrams enabled a better insight into the shear behavior of these assemblages. An elastic perfectly plastic diagram was found to characterize the monotonic and the cyclic envelope of shear tests conducted in dry masonry joints. No significant differences in the frictional behavior of dry joints under distinct moisture contents were found. A reduction of nearly 5% was recorded on the friction coefficient changing the moisture condition from dry to saturated. Low differences were found between the peak and residual friction angle for dry masonry joints under distinct moisture conditions. No dilatancy was found to characterize the shear behavior of dry masonry joints.

Similarly, an extended plastic branch characterizes the residual post-peak shear behavior of mortar masonry joints. After a reduction of approximately 25% of the peak strength, the shear stress stabilizes with considerable level of plastic deformations. The measured total vertical displacement revealed a tendency for the mortar joint dilation to decrease as the normal stress increases. Only for a pre-compression of $0.5N/mm^2$ a systematic expansive trend was verified up to peak stress. For this case, it was found that dilatancy decreases significantly as the shear displacement increases.

The mechanical characterization of masonry under compression was carried out by means of uniaxial compression tests on small masonry prisms. Besides the compressive strength parameter, an overview of the results obtained on masonry prisms with distinct types of bed joints was presented. The compressive behavior of dry masonry stone prisms appears to be highly dependent on the roughness of surfaces of bed joints, being both compressive strength and modulus of elasticity remarkably lowered by the roughness of the bed joint. The influence of the bed joint material on the compressive behavior is highlighted by considering distinct interlayer materials. The comparison of the performance of masonry prisms with granitic soil and with low strength mortar bed joints revealed that the mechanical compressive behavior of masonry is considerably affected the by deformability properties of the bed joint material.

# 6. IN-PLANE CYCLIC SHEAR BEHAVIOR OF GRANITIC MASONRY WALLS

## 6.1 Introduction

Although traditional masonry walls can be viewed as unsuitable structures to undergo seismic actions, they, in fact, exist and frequently represent the most important structural elements of ancient buildings. In fact, unreinforced stone masonry walls were, in the past, widely used in the construction of monumental and traditional buildings in the Northern region of Portugal. These structural elements play a major role on the seismic response of the whole structure since they represent the basic resisting elements to horizontal seismic actions. Post-earthquake research and experimental investigation revealed that if out-of-plane failure is prevented, the resistant mechanism of the unreinforced masonry building under seismic action is assured by in-plane behavior of masonry walls. As shown in see Figure 6.1, the structural behavior of a building subjected to horizontal loading depends on the connections between the walls and between the walls and the floor. Figure 6.1a shows the response of a building with flexible wooden floors. Without reliable connection between the walls, they behave independently. The failure is associated with the separation of the transversal walls from the intersection vertical line resulting from the effect of the transversal acceleration of the walls plane. The out-of-plane behavior of the transversal walls can also prevail in case of suitable connection between the walls but still with a flexible wooden floor, see Figure 6.1b. When the connection between the walls and rigid floors is provided, the building behaves in a monolithic manner and the out-of-plane failure of the walls is prevented, see Figure 6.1c. In this case, the prevailing mechanism of resistance is associated with the in-plane behavior of the shear walls.

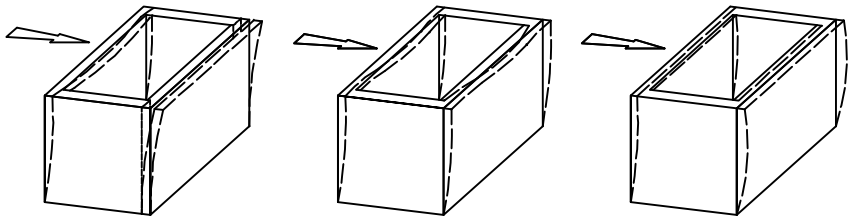

(a) (b) (c)

Figure 6.1 – Seismic behavior of a masonry building - influence of ties and diaphragms; (a) building with wooden floors and without ties; (b) building with wooden floors and tied walls; (c) building with rigid floors and tie-beams (Tomaževic, 1999)

Although the Northern region of Portugal has been classified as low to moderate seismicity zone, the assessment of the resisting and deformation conditions of the existing typical structural elements becomes of relevance due to the need of rehabilitation and retrofitting of ancient structures. On the other hand, the understanding of the seismic behavior of masonry stone walls represents an additional advantage in the perspective of new masonry structures design

Another reason that motivated the present research on stone masonry walls is related to the scarce experimental information on their in-plane behavior. In fact, most research programs in the scope of the seismic behavior focused on unreinforced brick masonry walls either from

experimental or numerical points of view (Hamid and Dreysdale, 1980; Page *et al*., 1980; Samarasinghe *et al*., 1981; Mann and Müller, 1982; Lourenço and Rots, 1994; Anthoine *et al*., 1995). Only few experimental analyses are available on the seismic features of stone masonry walls (Chiostrini and Vignoli, 1992; Beolchini and Grillo, 1992). Some works on the strengthening and improvement of the seismic performance of masonry stone walls were reported by Tomaževic (1999). More recently, Corradi *et al*. (2003) carried out an experimental study on the strength properties of double-leaf roughly cut stone walls by means of in-situ diagonal compression and shear-compression tests. Also, monotonic shear-compression tests were conducted on dry-stacked stone masonry panels by Oliveira (2003).

In the scope of seismic experimental research, distinct testing approaches have been used for unreinforced masonry structures, namely quasi-static monotonic or cyclic tests, dynamic shaking table tests and pseudo-dynamic tests. According to Calvi *et al*. (1996) despite dynamic tests simulate with more accuracy the seismic action, cyclic quasi-static tests enable more accurate measurements of forces and displacements and the record of damage evolution becomes easier. Besides, the facilities required in dynamic testing are not available in most laboratories. In terms of results, differences on strength, stiffness, damage propagation and energy dissipation are known to exist between both testing procedures. The quasi-static tests are more conservative than dynamic tests because lead to lower lateral strength and to more extensive damage. With respect to dynamic tests, it is more common to test complete (scaled) unreinforced masonry structure, composed by masonry shear walls with or without openings, piers and diaphragms. This procedure enables the analysis of the nonlinear interaction between the distinct structural elements. An analysis of the effect of different diaphragms on the dynamic behavior of stone masonry buildings was performed by Tomaževic *et al*. (1993). Four 1:4 scale simplified models of two story unreinforced stone masonry buildings were tested in an one-dimensional shaking table. The shear walls were placed in the direction of the simulated ground motion and the out-of-plane walls were considered to have window and door openings. Four distinct types of wooden floors were taken in the experimental investigation. Abrams (2000) reported results of dynamic shaking table tests carried out using two reduced scale unreinforced clay-unit masonry buildings. Each structure was two stories tall and included a pair of shear walls in the direction parallel to the uniaxial base excitation. Distinct number of opening and dimensions leads to variable pier sizes and aspect ratios. Some important issues to be solved in this type of tests when individual masonry walls are considered concern the high stiffness and the corresponding amplification of the base seismic excitation and the simulation of inertial forces by addition of external masses. Moghaddam *et al*. (1990) carried out a series of shaking table tests on scaled unreinforced brick masonry walls in order to establish a simple physical model to estimate the dynamic shear strength for a given base acceleration. Recently, an extensive experimental program was performed by Elgawady *et al*. (2004) in the scope of retrofitting unreinforced masonry walls. The comparative analysis of results between dynamic and static cyclic tests conducted on the same type of masonry walls revealed similar failure modes and lower lateral resistance under dynamic conditions.

The quasi-static tests can also be performed on building structure to enable the analysis of the nonlinear interaction between the distinct elements under reversal loads as in case of the full-size two-story block building tested by Abrams (1986). Another example is the full scale unreinforced masonry building tested under quasi-static conditions reported by Calvi *et al*. (1996), which is upscaled from the small model tested on a shaking table reported by Abrams

(2000). However, this type of tests is mostly conducted in a single panel submitted to a constant axial load by imposing increasing monotonic or reversal lateral displacements. Typical fixed-fixed or fixed-free cantilever walls are adopted. Although they are not real boundary conditions, they render the interpretation of results and testing setup easier. The typical configuration for quasi-static tests is shown in Figure 6.2. This testing configuration was also suggested by Atkinson *et al*. (1989) as appropriate to simulate the response of walls subjected to in-plane loads. According to Bosiljkov *et al*. (2003), this testing arrangement in conjunction with cyclic loading provides vital information (modes of failure and damage evolution, shape of hysteresis loop and energy dissipation) for the assessment of the seismic performance of masonry shear walls. An extensive research project on the behavior of masonry walls with and without openings under in-plane monotonic loads was carried out by Vermeltfoort and Raijmakers (1992). A comprehensive analysis of the in-plane cyclic behavior of shear walls was provided by Magenes (1992) through quasi-static tests on old brick masonry walls with distinct height to length aspect ratio. Another recent enlarged study of the in-plane cyclic behavior was conducted by Bosiljkov *et al*. (2003), where brick masonry panels with distinct types of mortar joints were analyzed.

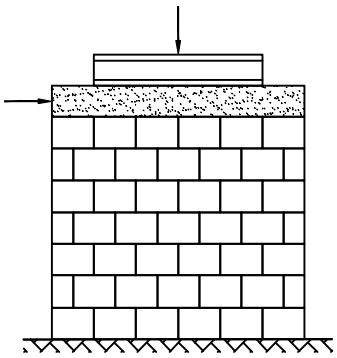

Figure 6.2 – Typical shear test configuration of masonry shear walls

The present work aims at obtaining a better insight on the cyclic behavior of stone masonry walls using quasi-static tests. Distinct typologies corresponding to different masonry bond were adopted. In a first step, the experimental characterization focuses on the definition of the failure modes and force-lateral displacement hysteresis diagrams as they constitute the basic information in the analysis of the test results. In a second step, an evaluation of the seismic performance of the walls and a comparative analysis of the distinct masonry bond based on the ductility factor and on the energy dissipation capacity is performed. Moreover, the nonlinear deformation of the walls is evaluated in the scope of performance based concepts. For this purpose, the nonlinear deformation was converted to lateral drifts corresponding to distinct levels of performance associated with specific levels of structural damage.

Finally, the possibility to use simplified models for the calculation of the shear strength was investigated. Besides, a recent approach based on a strut model (Roca, 2004) was also used to estimate the ultimate load capacity of masonry walls and further comparison with the experimental results was carried out.

The major significance of the present research is the contribution to enlarge the knowledge in the area of in-plane cyclic behavior of stone masonry shear walls, which assume an important

role in the preservation or retrofitting of cultural heritage structures but have been scarcely studied in the past.

## 6.2 Experimental program

As mentioned before, the main objective of this work consists in the evaluation of the seismic performance of the stone masonry shear walls found in the ancient masonry buildings. In order to attain this goal, an experimental program composed by a set of quasi-static cyclic tests on small testing specimens was defined.

Several experimental and theoretical works revealed that the axial load and the aspect ratio are the main parameters influencing the behavior of masonry walls under in-plane cyclic loading. High aspect ratio tends to lead flexural failure (rocking), whereas low aspect ratio induces shear type failures (Samarasinghe *et al*., 1981; Anthoine *et al.*, 1995; Schultz *et al*., 1998). Similarly, low levels of axial load promote the development of flexural response, while high levels of axial load are generally associated to diagonal shear failure (Zhuge *et al*., 1996; Bosiljkov *et al*. 2003). Nevertheless, no experimental results are available about the influence of the textural arrangement (bond) on the cyclic performance of stone masonry walls. Therefore, simultaneously with the variation of the axial load, the present experimental program includes in-plane horizontal cyclic tests on walls with three distinct textural typologies. This aspect should have received more attention given the large diversity of masonry bonds used for walls pertaining to ancient constructions. Fixed-free cantilever walls are considered and the aspect ratio was kept constant due to budget and time constraints.

### 6.2.1 *Typology and construction of test specimens*

The stone used in the construction of the walls is a two mica, medium-coarsed granite, which is considered representative of the material of ancient structures existing in the Northern region of Portugal. The mechanical characterization of the granitic stone is available in Chapter 5. The mortar used is the ready-mix “Albaria Structturale” type supplied by Bettor-MBT Company. The mortar is basically composed of natural hydrated lime and natural aggregates with granulometry between 0.1 and 0.2mm. According to technical specifications, by addition required quantity of water, the mortar compressive strength at seven days is 3.0N/mm$^2$, which is considered to be close to the strength mortar found in ancient buildings.

As is shown in Figure 6.3, three distinct granitic textural typologies were adopted. Walls WS are composed of units with regular shape and dimensions and dry joints. This type of walls allows to increase the knowledge about the mechanics of dry masonry walls under cyclic loading. The walls can be representative of historical masonry constructions where no bonding material between stone units is present or where the major part of the bonding material with low strength properties vanished due to weathering effects. Walls WI consist of the assembly of irregular hand-cut units with similar shape but variable dimensions with low strength mortar filling in the head and bed joints. Rubble masonry walls WR are composed by units with variable shape and dimensions randomly assembled with low strength mortar. Walls WI and WR are mainly characteristic of traditional ancient structures that belong to vernacular and monumental architecture.

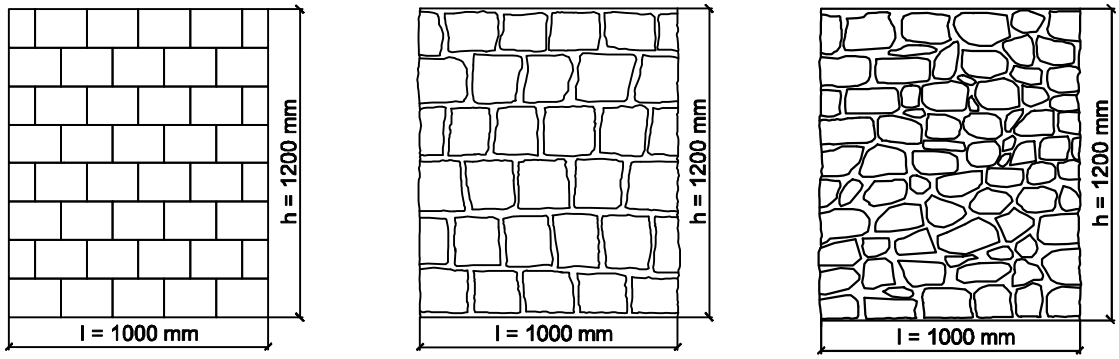


(a) (b) (c)

Figure 6.3 – Geometry and bond details of the walls; (a) sawn stone units walls, WS; (b) irregular walls, WI; (c) rubble walls, WR

The dimensions of the test walls were selected so that they can be successfully tested with the available facilities in the Structural Laboratory of University of Minho. The capacity of the traction-compression horizontal actuator is limited to ±100kN. Therefore, masonry wall panels of 1200mm height and 1000mm width, corresponding to a height to length ratio of 1.2, were adopted. The wall thickness is 200 mm. The adopted dimensions for the walls and stone units are about 1:3 scale for single leaf walls found in the northern region of Portugal.

The walls were built directly on top of a steel profile and tested at the same place. This procedure was advisable so that no local damage of the wall structure occurs during the transportation from casting to the test place. A first course of stone was fixed to the top and to the bottom steel profiles so that the top and bottom extreme wall interfaces are representative of masonry.

The construction of the dry masonry walls (WS) was quite easier. After the first course, the stone units were laid in vertical position and carefully aligned during the construction. This task was straight forward due to the perfection of the stone cutting. Walls WI and WR were built according to traditional execution rules by the same experienced mason, see Figure 6.4. The mortar was prepared simply by adding the required water mentioned in the technical specifications of the supplier. In order to attain a mortar compressive strength of approximately 3.0N/mm$^2$, the tests on walls WI and WR were carried out seven days after the construction. More details about the mechanical characterization of mortar can be found in Chapter 5. The mean compressive strength of six mortar control specimens is presented in Section 6.4.1. The granitic units were suitably moisten before laying in order to reduce shrinkage effects and excessive absorption. Similarly to walls WS, special care was taken in the alignment of walls in both vertical and horizontal directions in order to ensure alignment with the horizontal actuator.

As mentioned previously, the cyclic tests were carried out with different axial load. Taking into account that masonry walls are submitted to low vertical stresses, the reference level of pre-compression corresponding to the average normal stress $s$ = 0.5N/mm$^2$ was considered. In order to evaluate the influence of the axial load on behavior of the walls, two additional higher pre-compression levels were also adopted, $s$ = 0.875N/mm$^2$ and $s$ = 1.25N/mm$^2$. The average normal stress, $s$, is calculated from:

$$s = \frac{N}{A} \tag{6.1}$$

where $N$ is the axial load and $A$ is the cross section of the wall.

Figure 6.4 – Construction of the walls WR at different stages

The notation used for the distinct types of walls as a function of the three vertical pre-compression levels is shown in Table 6.1. The number of specimens is indicated inside brackets. Three specimens were considered for the dry masonry walls and two specimens were considered for the mortared masonry walls. The lower number of specimens for the mortared walls was due to the cost involved in the construction of the walls and to the need to save time required for curing before testing. However, one additional dry masonry wall specimen and two additional mortared masonry wall specimens (WI.175 and WR.250) were considered. In case of the dry masonry walls, it was a preliminary test to verify the test setup, which performed as expected. In the case of the mortared walls WI, the specimen that presented extensive shrinkage was repeated, in order to reduce a bias introduced by this cracking. After analysis of results, it was decided to test one more masonry panel WR.250 in order to dissipate doubts about the brittle behavior.

Table 6.1 – Designation of the walls and number of specimens (total of 24 walls)

| Wall | Vertical load (kN) | Normal stress ($N/mm^2$) |
|---|---|---|
| WS.100 (4), WI.100(2), WR.100(2) | 100 | 0.50 |
| WS.175 (3), WI.175(3), WR.175(2) | 175 | 0.875 |
| WS.250 (3), WI.250 (2), WR.250 (3) | 250 | 1.25 |

### 6.2.2 *Experimental setup and test procedure*

The static cyclic tests were carried out for three distinct pre-compression levels by using the typical test setup shown in Figure 6.5. In order to prevent horizontal displacements at the base, the cantilever wall was fixed to a steel profile using a small steel beam with two adjustable clamping angles. In turn, the steel profile was connected to the strong floor through a couple of steel rods. The pre-compression loading was applied by using a vertical actuator with a maximum capacity of 250kN as shown in Figure 6.5a. The vertical steel cables provide the connection to the strong floor. A stiff beam was used for the distribution of the vertical loading from the actuator and a set of steel rollers were placed to allow relative displacement of the wall with regard to the vertical actuator. The horizontal load is transmitted to the wall by means of a top steel beam that is appropriately strengthened with internal ribs. The

horizontal force is recorded in the horizontal actuator that is linked to the reaction wall by means of a two-dimensional hinge. This feature allows vertical displacements at the top of the wall and corresponding rotation. A set of steel tubes connected to vertical steel rollers is used to prevent any possible out-of-plane movements of the wall, see Figure 6.5b. It was found that a minimal distance between the steel roller and the steel beam is required to minimize friction with the top beam and thus to guarantee the free horizontal movement of the wall.

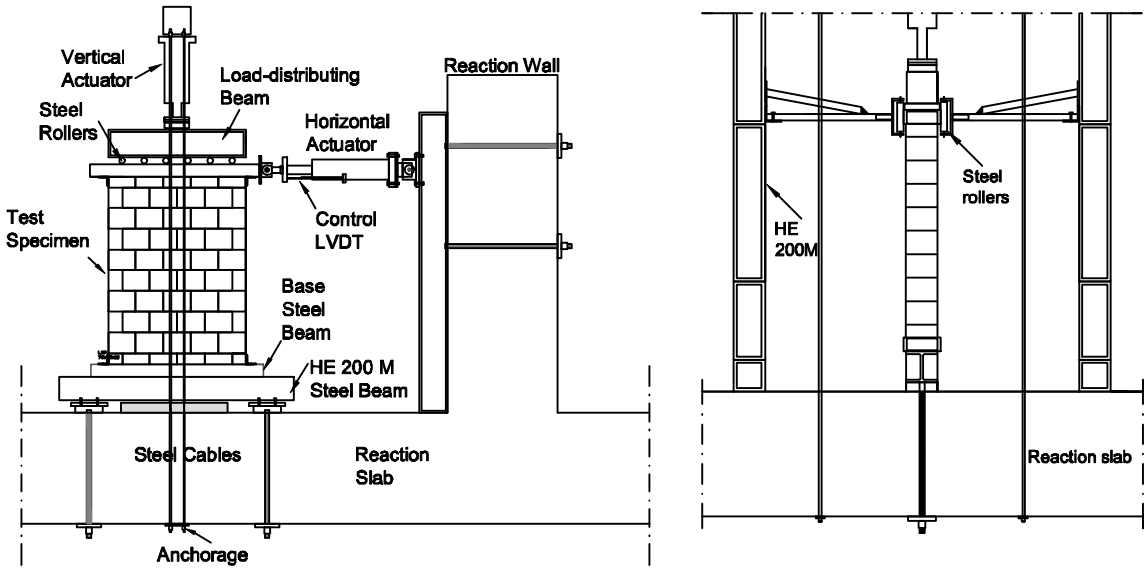


(a) (b)

Figure 6.5 – Test setup; (a) front view; (b) side view

The cyclic tests were conducted under displacement control by means of the horizontal LVDT connected to the actuator, see Figure 6.5a. As has been reported, the selection of the displacement history to simulate the seismic action has some relevance on the results, particularly in the post-peak region, where strength and stiffness degradation occurs (Calvi *et al*., 1996; Tomaževic *et al*., 1996). For this reason, the same displacement history shown in Figure 6.6 was used as an input seismic action for walls WI and WR. For dry masonry walls, the displacement increment of 5mm was defined from the prescribed displacement of 10mm. A rate of 100μm/s displacement was adopted.

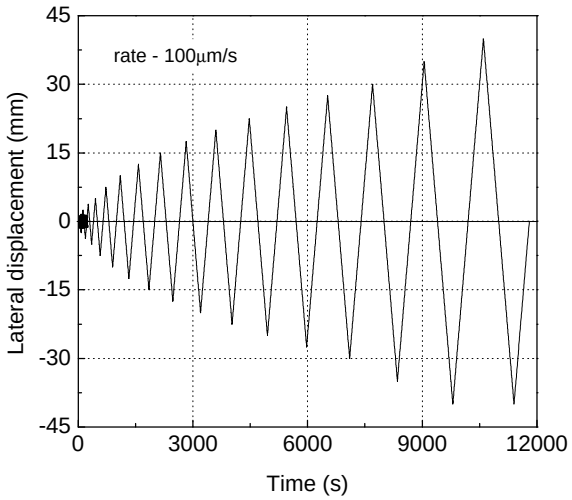


Figure 6.6 – Displacement-time history

In order to evaluate the shear behavior of dry masonry walls, to further compare the results with cyclic behavior and to validate the test setup in the framework of monotonic/cyclic testing, a set of four monotonic tests were carried out for distinct pre-compression levels. The monotonic tests were conducted by imposing increasing lateral displacement at a similar rate of cyclic tests. The tests with dry masonry walls allow to re-use the stone units, being therefore particularly fast and inexpensive to use in multiple testing.

The displacements of the wall under cyclic loading were measured through a set of LVDTs indicated in Figure 6.7a. The vertical displacement of the top steel beam was measured by the LVDTs nº2. From these displacements, it is possible to calculate the rotation of the upper part of the wall. Besides, these displacements are indicators of the potential rocking mechanism of the wall and also any possible seating of the joint due to reverse loading. The possible slippage between the wall and the stones that constitute the boundaries is monitored by LVDTs nº3. The potential toe crushing is measured by LVDTs nº4 and the horizontal displacement of the wall is recorded by the LVDT nº1. The disposition of the LVDTs nº5 shown in Figure 6.7b is used to evaluate the modulus of elasticity of the wall. The same arrangement of the LVDTs was made on both faces of the wall.

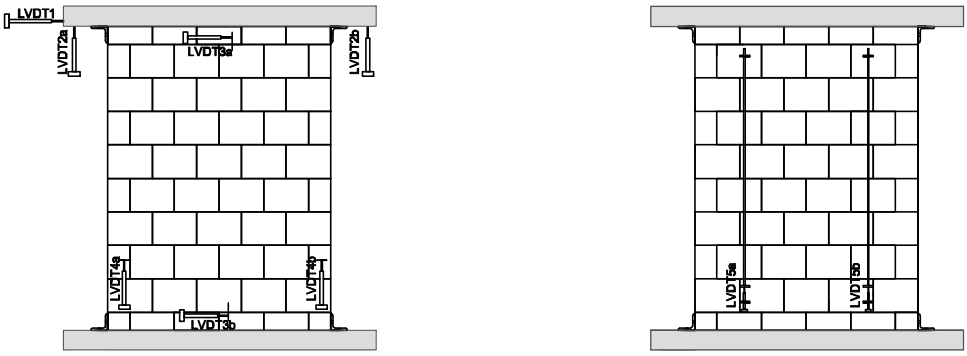


(a) (b)

Figure 6.7 – Instrumentation of the wall by means of LVDTs; (a) during cyclic tests; (b) during vertical loading (measuring modulus of elasticity)

The tests on each specimen were carried out in two phases. In a first phase, aiming at estimating the modulus of elasticity of the wall, a set of five loading-unloading cycles for each pre-compression level was established, see also Faella *et al*. (1993). During this phase, the vertical displacements were recorded by the LVDTs nº5 fixed to the wall according to the arrangement indicated in Figure 6.7b. The second phase refers to the cyclic tests. Firstly, the pre-compression was applied until the maximum value was reached and after its stabilization, the cyclic tests started under displacement control according to the displacement history shown in Figure 6.6.

## 6.3 Results of the monotonic tests on dry masonry walls

In spite of static monotonic tests are not the main objective of the present experimental program, the results obtained in these tests are useful for further comparison with shear resistance obtained in the cyclic tests. Another aspect to be discussed regarding the failure patterns obtained in monotonic and cyclic tests concerns the out-of plane movements of the units. The monotonic tests were conducted for four distinct pre-compression levels:

$\sigma = 0.2N/mm^2$ (corresponding to a vertical force of 40kN), $\sigma = 0.5N/mm^2$, $\sigma = 0.875N/mm^2$, $\sigma = 1.25N/mm^2$. One specimen was tested for each level of pre-compression.

The shear behavior of dry masonry walls under monotonic loading is similar for the distinct pre-compression levels. The typical failure patterns are shown in Figure 6.8. For low levels of lateral displacement, the cracking pattern is characterized by the opening of flexural stepped cracks. For higher levels of lateral displacement, the shear resistance of the bed joints is exceeded and a diagonal stepped crack along bed and head joints opens. After that, the upper part of the wall tends to rotate around the lower corner (rocking mechanism) where the shear stress is still transferred. If the compressive stress of the stone unit is exceeded, the collapse occurs in a brittle manner by toe crushing, see Figure 6.8b. This failure pattern occurred only for pre-compression level of $\sigma = 0.875N/mm^2$. In the remaining cases, when the lateral displacement is reversed up to the origin, the walls recover its original shape, see Figure 6.8c.

(a) (b) (c)

Figure 6.8 – Failure patterns of dry masonry walls under monotonic loading; (a) cracking pattern of the wall WS.100; (b) collapse mode of wall WS.175; (c) final configuration of the wall WS.100 after removing the imposed lateral displacements

The lateral force-lateral displacement diagrams that describe the behavior of dry masonry walls under monotonic loading are given in Figure 6.9. Here, the plus (+) sign in the Figure indicates the positive direction of loading and displacement.

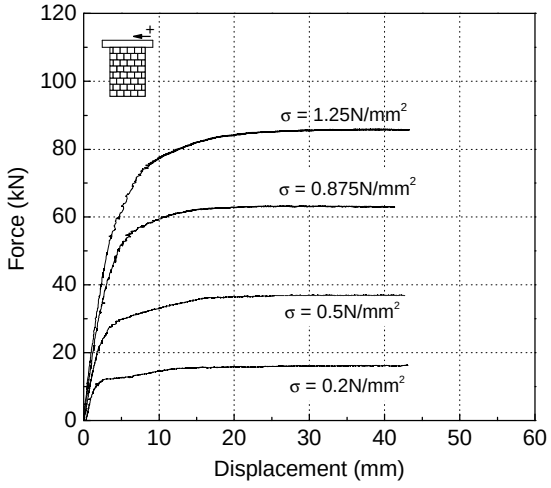


Figure 6.9 – Typical monotonic force-displacement diagrams of walls WS under distinct pre-compression levels

After an initial linear elastic branch, nonlinear behavior develops until the maximum lateral force is attained, from which plastic behavior occurs. A considerable lateral displacement can be sustained by these walls, which is directly connected to rocking mechanism. As can be observed from Table 6.2, both lateral force and lateral stiffness increase with the pre-compression level, as expected. The initial stiffness was obtained by the best linear fit obtained from the origin up to 30% of the maximum lateral force.

Table 6.2 – Values of lateral force, *H*, and initial stiffness, *K*

| Walls | $H^+$ (kN) | $K^+$ (kN/mm) |
|---|---|---|
| WS.40 | 16.2 | 10.0 |
| WS.100 | 36.9 | 13.1 |
| WS.175 | 63.1 | 14.9 |
| WS.250 | 85.6 | 18.6 |

Although with a reduced data, significant indicative linear correlation between the axial stress, $\sigma$, and the shear stress, $t$, is achieved, ($t = 0.35s$, $r^2 = 0.99$). The shear strength corresponding to the maximum lateral force is calculated as follows:

$$t = \frac{H}{A}, \tag{6.2}$$

where $A$ is the cross section of the wall and $H$ is the maximum lateral resistance measured by the load cell connected to the horizontal actuator.

By comparing the friction coefficient obtained from monotonic tests with the value achieved in direct shear tests of one single joint given in Chapter 5, it is observed that a much lower value is found for monotonic tests (the friction coefficient $m$ is equal to 0.65 for the dry joints joint and equal to 0.35 for the walls). This is well known as the monotonic tests conducted in the wall reflect its structural behavior and not the microstructural behavior of the individual joints (Atkinson *et al*., 1989).

## 6.4 Results of the cyclic tests

The failure modes and lateral force-lateral displacement hysteresis diagrams obtained from cyclic tests are the required data for the evaluation of the seismic performance of masonry stone walls. From the force-lateral displacement diagrams, experimental envelop diagrams are derived and the values of the lateral strength and stiffness are calculated. In addition, particular values of the lateral forces and deformations corresponding to certain performance levels are analyzed. A comparative analysis of the capacity to dissipate energy for the different types of walls is also carried out. Finally, the seismic performance in terms of nonlinear deformation capacity is evaluated based on the ultimate ductility factors and lateral drifts.

Before addressing the issues of seismic performance, two introductory sections are provided with information about the mortar strength and the modulus of elasticity of each wall type (WS, WI and WR). This is useful information for a future numerical analysis of the walls and for the better understanding of the wall behavior.

### 6.4.1 *Compressive strength of the mortar*

During the construction of the walls, the right quantity of water prescribed by the supplier was used to reach a compressive strength of about 3.0N/mm$^2$ at the time of testing. Usually, three mortar samples were taken at two random distinct stages of the construction of each wall. Although far from the real curing conditions of the mortar inside the masonry, the mortar specimens were placed at the laboratory environment. Compressive tests of the mortar specimens were carried out according the prEN1015 standard mentioned in Chapter 5. The compression tests were carried out at the same time of testing the walls, i.e. seven days after the construction. The results obtained for the irregular walls, WI and WR, are presented in Table 6.3. It can be seen that the compressive strength is, in general, larger than the value given in the technical specifications provided by the supplier. The differences can be partly attributed to the fact that hand mixing was used for the mortar preparation. Despite the small number of mortar specimens, for the mortar used in each wall, the coefficient of variation ranges from low to moderate.

Table 6.3 – Mean values of the compressive strength of mortar, $f_c$, for walls WI and WR. The coefficient of variation is indicated inside brackets (%)

| Walls WI | $f_c$ (N/mm$^2$) | Walls WR | $f_c$ (N/mm$^2$) |
|---|---|---|---|
| WI1.100 | 3.8 (9.3) | WR1.100 | 3.2 (2.5) |
| WI2.100 | 3.7 (8.4) | WR2.100 | 3.4 (15.8) |
| WI1.175 | - | WR1.175 | 3.2 (6.9) |
| WI2.175 | 4.6 (13.1) | WR2.175 | 4.0 (13.8) |
| WI3.175 | 5.1 (2.7) | WR1.250 | 3.8 (10.2) |
| WI1.250 | 4.5 (13.3) | WR2.250 | 3.6 (11.3) |
| WI2.250 | 4.4 (4.3) | WR3.250 | 3.3 (7.8) |

### 6.4.2 *Modulus of elasticity of the walls*

The values of the modulus of elasticity result from averaging the vertical displacements measured by the four LVDTs located at both sides of the wall. The stress-strain diagram was defined from the average normal stress and the strain calculated by dividing the average vertical displacement by the corresponding measured length. For each wall, the value of the modulus of elasticity is calculated by averaging five cycles of loading-reloading. It was observed that the values associated to the successive cycles were rather close. The average values of the modulus of elasticity for the distinct types of walls are presented in Table 6.4. For dry masonry walls, a clear tendency for the elastic modulus to increase as the pre-compression levels increases was recorded. This behavior is in good agreement with the results obtained by Oliveira (2003) on dry sandstone masonry walls. The simple linear regression for the modulus of elasticity provide the relation $E = 2352+1913s$. The difference between the maximum and minimum elastic modulus is 44%. This tendency is followed, on average, by irregular and rubble masonry walls but the evolution is much less significant. The difference between the maximum and minimum modulus of elasticity is 2% and 7% for walls WI and WR respectively. For practical and analysis purposes, and giving the scatter in the analysis, the modulus of elasticity for these mortared walls can be assumed as independent of the pre-compression level.

The lowest value of the modulus of elasticity was found for the rubble masonry walls, which appears to be the outcome of the random textural arrangement and the larger quantity of mortar employed. If the dry stone walls are compared with the irregular walls, WI, lower modulus of elasticity is found for low pre-compression levels but higher modulus of elasticity is found once the pre-compression level increases. In spite of the large coefficient of variation that is usually addressed to masonry walls composed by natural stone, low to medium coefficients of variation were found for the walls under analysis. It is stressed that these values are considerably lower than the modulus of elasticity obtained in the prism tests presented in Chapter 5, as expected (Lourenço, 1996). The values obtained in the masonry walls should be considered as more realistic given the size of the specimens.

Table 6.4 – Values of the modulus of elasticity of the walls. Coefficient of variation is indicated inside brackets (%)

| Walls | $\sigma$ = 0.5 (N/mm$^2$) | $\sigma$ = 0.875 (N/mm$^2$) | $\sigma$ = 1.25 (N/mm$^2$) |
|---|---|---|---|
| WS | 3287.5 (18.7) | 4068.9 (20.7) | 4722.0 (19.6) |
| WI | 3840.8 (15.3) | 3863.9 (15.1) | 3911.9 (17.5) |
| WR | 2329.4 (9.1) | 2393.6 (6.7) | 2496.1 (7.9) |

### 6.4.3 *Failure modes*

Besides the evaluation of the differences in terms of crack patterns and deformation of distinct types of walls under analysis, the information about the failure modes is of great value so that particular load stages can be associated to a certain damage level.

#### 6.4.3.1 Dry masonry shear walls - WS

The deformation patterns that characterize the cyclic behavior of dry stone masonry walls were found to be quite similar for the distinct pre-compression levels, meaning that the compressive strength of the stone is too high and plays no role in the response. Similarly to the monotonic tests, the behavior under cyclic reversal loading is governed by flexural response up to the maximum lateral force is reached. This behavior is characterized by the opening of stepped cracks that are identified with numbers 1 and 2 in Figure 6.10a.

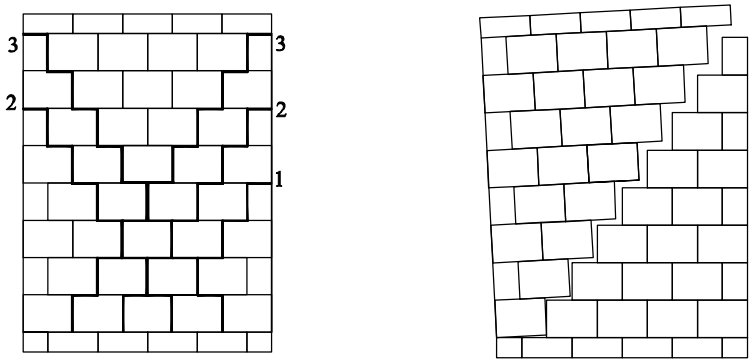


(a) (b)

Figure 6.10 – Deformation patterns of dry stone masonry walls; (a) location and opening of flexural cracks by order; (b) diagonal crack and final rocking mechanism

These cracks opens with low values of imposed lateral displacement ranging between 2.5mm and 7.5mm depending on the vertical level of pre-compression. For high prescribed lateral displacements and close to the maximum lateral load, a diagonal stepped crack as it is shown in Figure 6.10a with the number 3 opens and a rocking mechanism about the lower corner develops, see Figure 6.10b.

The displacement at which the final stepped diagonal crack opens depends on the pre-compression level. The average values of lateral displacement corresponding to the opening of the diagonal crack are about 5.8mm, 7.6mm and 10.3mm for the pre-compression levels of $s = 0.5\text{N/mm}^2$, $s = 0.75\text{N/mm}^2$ and $s = 1.25\text{N/mm}^2$ respectively. As the lateral displacement increases and rocking mechanism develops, the effective cross section resisting the compressive stresses is reduced and stress concentration takes place. When compression stress level exceeds the compressive strength of the masonry, toe crushing occurs suddenly in a brittle manner. Although this type of failure was verified for intermediate levels of pre-compression, it is particularly characteristic of dry masonry walls subjected to the highest level of pre-compression, $s = 1.25\text{N/mm}^2$. Again, toe crushing was found to occur for very large imposed lateral displacements, meaning that the response in only affected by compressive damage at the end of the test. Toe crushing led to very brittle failure and the test was immediately stopped.

It should be underlined that when solely rocking mechanism is present, global collapse of the structure does not occur. In fact, the application of the lateral reversal loads leads to the successive opening and closing of the diagonal cracks as a result of restoring the initial shape and no damage on the stone units was observed. However, residual inelastic horizontal displacements appeared due to sliding along bed joints of the units adjacent to the stepped flexural and diagonal cracks. Figure 6.11 illustrates typical failure patterns of dry masonry walls at the end of the tests including residual horizontal displacements of the units only, toe crushing, wedge formation and out-of-plane movements.


(a) (b) (c)

Figure 6.11 – Typical failure patterns of dry masonry walls at the end testing; (a) horizontal residual displacements in wall WS1.175; (b) toe crushing and wedge formation in the wall WS2.250; (c) out-of-plane displacement of units in wall WS4.100

The latter aspect is particularly relevant because it was insignificant in the monotonic loading tests. This failure indicates that, even in the absence of out-of-plane solicitation, large out-of-plane movements can be found in the units adjacent to the stepped cracks due to the irregularities of the stones and to the fact they become almost loose during testing. In a real

earthquake simulation, the effect can be amplified because in-plane and out-of-plane acts together. Thus, the vulnerability of low interlocking stone units due to inadequate stone arrangements or inadequate shapes (e.g. round units), as well as dry or strongly deteriorated mortar joints need further studies. According to the author's experience, this type of displacements can also be significant in shaking table tests.

Table 6.5 presents an overview of the failure modes exhibited by all dry masonry walls. A particular remark should be made with respect the wall WS2.100. In fact, its distinct failure mode relatively to the ones obtained with similar pre-compression level can possibly be attributed to unexpected low values of the compressive strength of the units located in the toes. Note that stone units with visible damage were not used in the wall construction.

Table 6.5 – Summary of failure modes of dry masonry walls

| Wall | Failure mode | Wall | Failure mode | Wall | Failure mode |
|---|---|---|---|---|---|
| WS1.100 | Rocking | WS1.175 | Rocking | WS1.250 | Rocking and toe crushing |
| WS2.100 | Rocking and toe crushing | WS2.175 | Rocking and toe crushing | WS2.250 | Rocking and toe crushing |
| WS3.100 | Rocking | WS3.175 | Rocking | WS3.250 | Rocking and toe crushing |
| WS4.100 | Rocking | - | - | WS4.250 | Rocking and toe crushing |

### 6.4.3.2 Irregular masonry shear walls - WI

The irregular walls that are subjected to low levels of pre-compression ($s$ = 0.5N/mm$^2$) are essentially governed by flexural response. Horizontal cracks develop since early stages of displacement at the base of the wall and progressively spread along its height, see Figure 6.12a,b.

(a) (b) (c)

Figure 6.12 – Failure mode and collapse of the walls WI.100; (a) bed joint cracks at the base of the wall WI2.100; (b) long bed joint crack of the wall WI2.100; (c) final failure pattern of the wall WI1.100

As the lateral displacement increases, flexural cracks evolve from the sides of the walls. Flexural cracking leads to the reduction of the resistant cross section and, therefore, thin

stepped cracks develop at the stone unit-mortar interfaces towards the opposite lower corner as the result of the redistribution of stresses. Progressive damage was detected by spreading and increasing number of cracks opening. In both tested specimens, diagonal stepped cracks develop due to the failure of the bed joint of the upper corners. As can be observed from Figure 6.12c, after opening of the final diagonal cracks, a rocking-type mechanism takes place about the lower corners. It should be mentioned that no visible damage in the stones was observed and the behavior was similar to the dry masonry walls.

Concerning the intermediate pre-compression level $s$ = 0.875N/mm$^2$, distinct failure patterns were observed for the first specimen and the remaining two specimens. In the first specimen, a net of vertical, shrinkage cracks in the stone-unit mortar interface was clearly visible before testing. Stepped subvertical cracks developed from the shrinkage cracks at early stages of deformation, roughly about a peak displacement of 5mm, see Figure 6.13a. From the shrinkage cracks other branches propagated as the lateral load increases. These cracks are combined with flexural cracks developed along bed joints in the second and fourth courses on the right side the masonry wall. It was noticed that the major crack damage was centralized in the lower left corner, see Figure 6.13b. The local failure of the upper corners occurred from the shear failure of the mortar joint for high lateral displacements after which the wall tends to rock. The collapse of the wall was attained by crushing of the left lower corner, as can be seen in Figure 6.13c. It should be underlined that the collapse of the wall is followed by considerable large crack openings. The result is rather interesting as it indicates that the response can be severely determined by existing damage, which is clearly the case of ancient structures.

(a) (b) (c)

Figure 6.13 – Crack patterns and collapse mode of the wall WI1.175; (a) shrinkage cracks before testing; (b) propagation of cracks towards the lower left corner; (c) collapse of the wall

The crack pattern corresponding to the wall WI2.175 is characterized by minor damage at low levels of lateral displacement. Thin stepped cracks along the unit stone-mortar interface developed at the middle of the wall towards the right bottom corner, which seem to be associated to the shear failure of the unit-mortar interface. The increasing lateral displacements induce spreading of flexural cracks through the height of the specimen from the right side of the wall. A stepped unit-mortar interface crack opened during the cycle loading corresponding to a prescribed lateral displacement of ±17.5mm from the right top corner. The final failure pattern was defined by X stepped cracks and rocking mechanism of

the wall about the toes for reversal loads. This was the result of the failure of mortar bed joint at the upper corners of the specimen, see Figure 6.14a. No visible cracking of the stones was observed. The cyclic response of the wall WI3.175 is also predominantly influenced by flexure. The onset and growth of flexural cracks along mortar bed joints involved different courses, see Figure 6.14b. This crack pattern leads to minor damage up to considerable lateral prescribed displacements, since the lateral displacement is mostly recoverable. As can be seen in Figure 6.14c, a diagonal stepped crack started from the upper right corner as the consequence of the failure of the mortar joint and a subsequent rocking mechanism developed. The failure of the wall was attributed to the toe crushing, see Figure 6.14c.

(a) (b) (c)

Figure 6.14 – Failure mode and collapse of the walls WI.175; (a) collapse of the wall WI2.175; (b) flexural behavior of the wall WI3.175; (c) failure pattern of the wall WI3.175

Even if the flexural behavior prevails in the cyclic behavior of irregular walls submitted to the highest level of pre-compression ($s$ = 1.25N/mm$^2$), rocking mechanism takes a minor role in the global lateral response. The crack pattern of wall WI1.250 is composed by stepped cracks that developed at both sides of the wall, see Figure 6.15a.

(a) (b) (c)

Figure 6.15 – Failure mode and collapse of the walls WI.250; (a) collapse of the wall WI2.250; (b) crack patterns of wall WI2.250; (c) failure pattern of the wall WI3.250

As the lateral displacements increased, other stepped cracks developed towards the lower corners. These cracks are particularly noticeable in the lower right corner. Failure of the upper corner induces large opening on existing cracks and a tendency for rocking. The collapse of the wall occurred by crushing of the lower left corner. In the wall WI2.250, rocking mechanism also takes a minor role in the global response. Diagonal stepped cracks as indicated in Figure 6.15b were observed for rather low levels of imposed lateral displacement. As can be seen in Figure 6.15c, a high level of deformation and a large amount of damage developed in the middle of walls as the consequence of the opening of several stepped diagonal cracks. The final collapse of the wall is related to the progressive damage of the left lower corner that led to the rotation and subsequent separation of the left part of the wall, see Figure 6.15c. A summary of the failure modes is provided in the next section, together with rubble masonry walls results.

#### 6.4.3.3 Rubble masonry shear walls WR

In rubble masonry walls, failure patterns are clearly dependent on the level of pre-compression. Besides, they revealed sensitive to the individual textural arrangement of the granitic stones. This aspect takes particular relevance in case of walls WR.100 and WR.250. In fact, the failure patterns observed for walls WR.100 differ considerably from each specimen, see Figure 6.16. The crack pattern of wall WR1.100 is composed by flexural cracks at the base of the wall for small lateral displacements. The onset of two thin inclined cracks in the stone unit-mortar interface was also observed at early stages of loading. As the lateral force increases, the opening of these cracks reaches larger values. The extension of the diagonal crack connecting the upper left and the lower right corners occurred for a lateral displacement of approximately 12mm during the load cycle corresponding to a prescribed peak displacement of 17.5mm, which is followed by some damage in the stones. Afterwards, progressive damage localized at the middle of the wall. The typical flexural behavior (rocking) of the wall WR2.100 is displayed in Figure 6.16b,c.

(a) (b) (c)

Figure 6.16 – Failure mode and collapse of the walls WR.100; (a) crack pattern of the wall WR1.100; (b) and (c) crack pattern of the wall WR2.100

Inclined and horizontal cracks in the stone unit-mortar interfaces developed from both sides of the wall. The opening of this type of cracks is clearly associated to rocking mechanism. As

in flexural response the damage is mostly localized in the unit-mortar interfaces, when the cyclic loading ceased the cracks closed and almost no damage was observed. It can be observed that flexural response prevails for wall WR2.100, whereas wall WR1.100 fails predominantly in shear.

Apart from small and thin flexural cracks, no substantial damage was observed in wall WR1.175 up to a thick and rough diagonal shear crack propagated from the upper left to the lower right corner at the load cycle with displacement of ±12.5mm. A diagonal crack connecting the upper right and the lower left corners appeared for the load cycle with displacement of ±15.0mm, see Figure 6.17a. Damage evolution was characterized by large opening of the diagonal cracks and the softening of the lower corners of the wall by a progressive and soft crushing of the stones. Damage of the stones along the diagonal crack was also visible, see Figure 6.17b. Similarly, the crack pattern of the wall WR2.175 was characterized by rough diagonal cracks between the upper and lower corners following the stone unit-mortar interface, see Figure 6.17c. With the failure of the stone at the upper right corner, the wall tends to rock about the lower left toe leading to crushing of the units. Progressive damage growth occurred inside the wall due to additional rough cracks that developed essentially at the stone-mortar interfaces and extended up to the diagonal cracks when the load reversed.

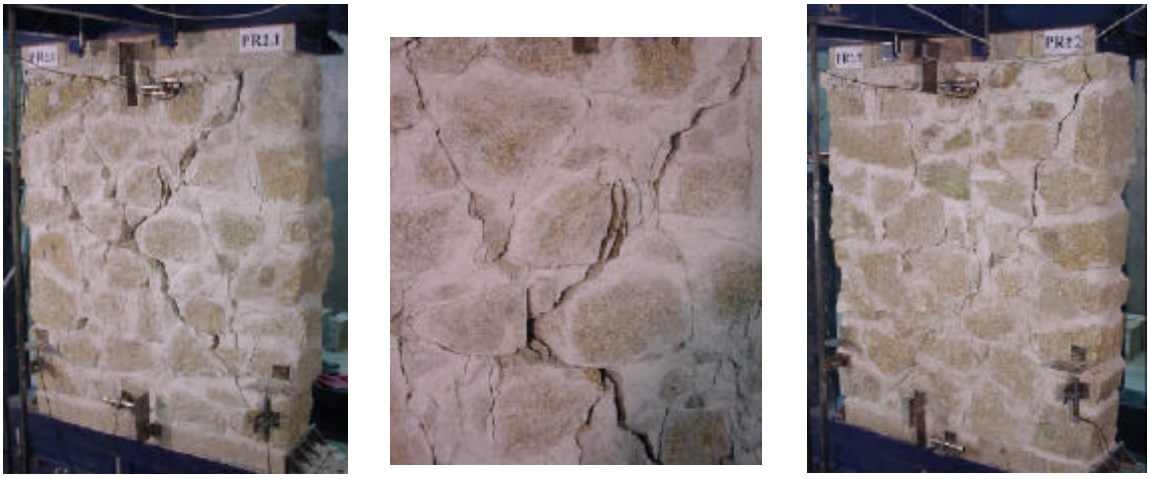

(a) (b) (c)

Figure 6.17 – Failure mode and collapse of the walls WR.175; (a) collapse of the wall WR1.175; (b) detail of the stone cracking along diagonal crack of wall WR1.175; (c) failure pattern of the wall WR2.175

Rubble masonry shear walls WR2.250 and WR3.250 are characterized by a similar failure pattern, see Figure 6.18a,b . In both specimens a main shear crack developed in the middle of the wall and propagates towards the upper left and the bottom right corners. Crack damage in the stones was found along the shear crack, and crushing of the upper and bottom corners occurred. It should be mentioned that the little pieces of stone introduced in the mortar joints also crushed. Subvertical cracks developed through the stone-mortar interfaces when loading was applied in the opposite direction. With respect to wall WR1.250, a series of subvertical cracks developed mainly in the middle of the wall since early stages of deformation, see Figure 6.18c. Some of these cracks passed even through stone units.

(a) (b) (c)

Figure 6.18 – Failure modes of walls WR.250; (a) failure of the wall WR3.250; (b) failure of the wall WR2.250; (c) failure of the wall WR1.250

A summary of the failure modes observed in irregular and rubble masonry walls is given in Table 6.6 for later reference.

Table 6.6 – Summary of the failure modes of irregular and rubble masonry walls

| Wall | Failure mode | Wall | Failure mode |
|---|---|---|---|
| WI1.100 | Flexural/rocking | WR1.100 | Flexural/shear |
| WI2.100 | Flexural/rocking | WR2.100 | Flexural/rocking |
| WI1.175 | Flexural/toe crushing | WR1.175 | Shear |
| WI2.175 | Flexural/shear/rocking | WR2.175 | Flexural/shear |
| WI3.175 | Flexural/toe crushing | WR1.250 | Shear |
| WI1.250 | Flexural/toe crushing | WR2.250 | Shear |
| WI2.250 | Flexural/shear/toe crushing | WR3.250 | Shear |

As a final statement for irregular and rubble masonry, it should be noticed that the variability on the arrangement of the stones can lead to unsymmetry of cracking distribution as certain crack patterns develop from the weakest links related to the stone unit-mortar interfaces, and not necessarily follows the most unfavorable stress fields. In this scope, the crack distribution between the walls WR.100 is particularly different, although both walls are submitted to the same stress state. Besides, it is worth to note the differences in the crack patterns and failure modes of the different types of walls. Typical shear cracks developed for moderate to high level of pre-compression in rubble masonry walls, whereas clear flexural response governs the in-plane behavior of irregular masonry walls, with rocking mechanism to prevail in case of moderate vertical stress levels. Different failure modes were also found for distinct levels of pre-compression, which is in agreement with other experimental results obtained in unreinforced brick masonry walls reported in the literature (Mann and Müller, 1982; Zhuge *et al*., 1996; Bosiljkov *et al*., 2003). Apart from the rubble walls submitted to the highest level of pre-compression, which failed for relatively low levels of lateral displacement, low to moderate damage was observed for low levels of displacement. However, in cases of walls WI.175, WI.250 and WR.175 significant damage is gathered before collapse.

### 6.4.4 *Hysteresis diagrams*

In addition to the crack patterns and failure modes, the lateral load-lateral displacement diagrams provide valuable information on the lateral in-plane behavior needed to evaluate the seismic performance. In this section, a qualitative discussion on particular features of typical diagrams is undertaken. Relevant values (force, displacement) of the force-displacement diagrams, associated to particular load or damage levels, are defined. The state corresponding to the maximum lateral resistance is identified with the set of values ($H_{max}$, $d_{Hmax}$) and the first shear crack is associated to the set ($H_s$, $d_s$). The definition of the latter values results from the visual information gathered during cyclic loading.

#### 6.4.4.1 Dry masonry walls, WS

Typical load-displacement hysteresis diagrams describing the in-plane response of dry masonry walls are given in Figure 6.19 and Figure 6.20. More detailed information about the hysteresis diagrams for distinct walls is given in Appendix G.

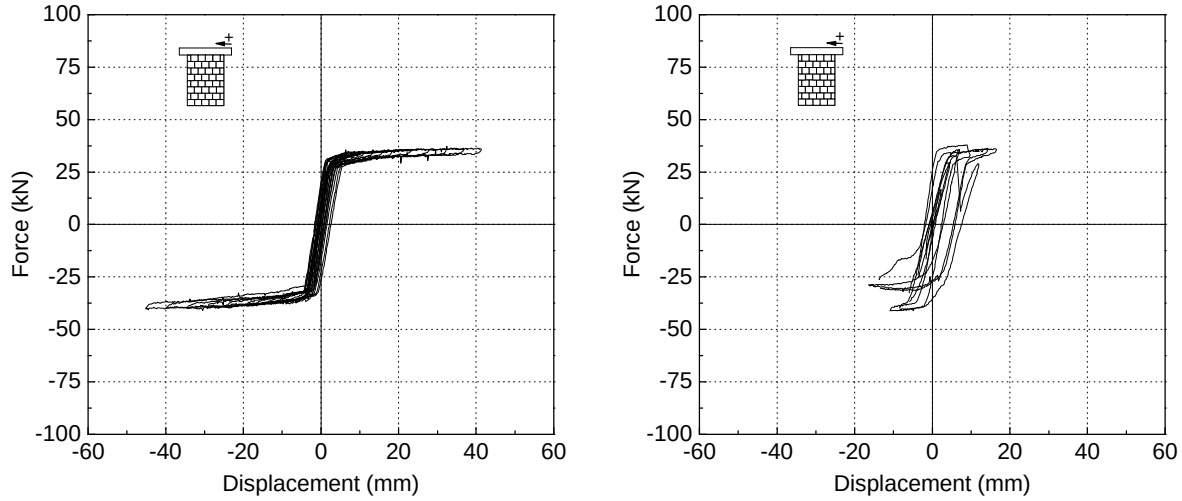


(a) (b)

Figure 6.19 – Force-displacement diagrams for dry masonry walls WS.100; (a) wall WS4.100; (b) wall WS2.100

As can be observed, the shape of these diagrams reflects, to great extent, the deformation patterns and failure modes discussed in the previous section. In fact, the remarkable S shape of the hysteresis loops found for dry stacked masonry walls reveals the rocking mechanism that characterizes the deformation response of these walls under cyclic loading. Apart from the different maximum values of the lateral resistance and lateral displacement, all walls exhibit significant nonlinear response with almost no strength or stiffness degradation, which confirms that no damage occurs in the stone units. Although a large amount of lateral displacements is recovered, all walls exhibit inelastic displacements that accumulate during the load reversal attributed to the bed joint sliding of the stones adjacent to the flexural and diagonal stair stepped cracks. In spite of the large nonlinear lateral displacements, a low capacity to dissipate energy is associated to these walls.

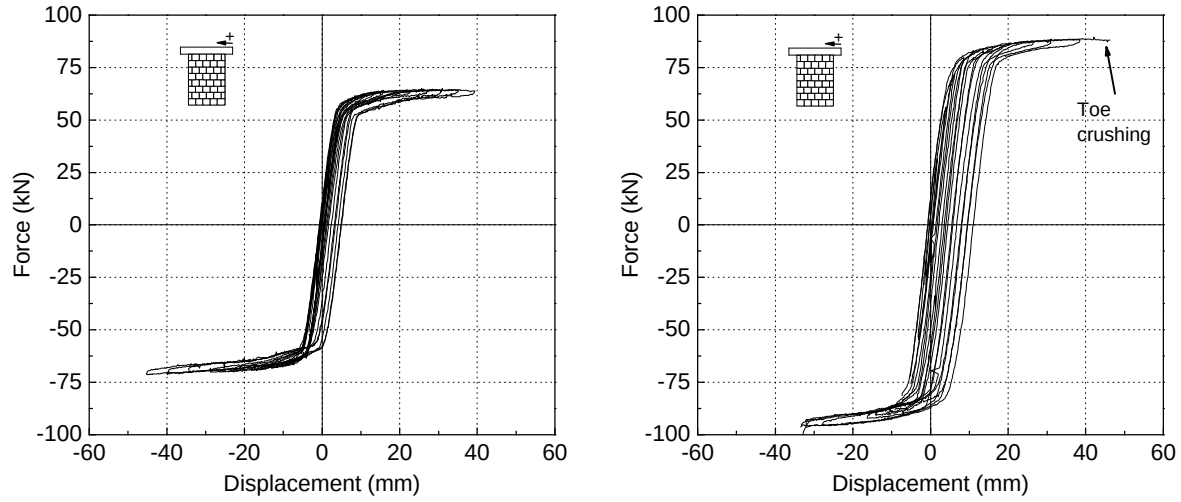


Figure 6.20 – Force-displacement diagrams for dry masonry walls WS; (a) wall WS3.175; (b) wall WS1.250

The rocking mechanism that characterizes the lateral response of dry masonry walls is well described by the evolution of the vertical displacements of the top steel beam with the lateral displacement of the walls as shown in Figure 6.21.

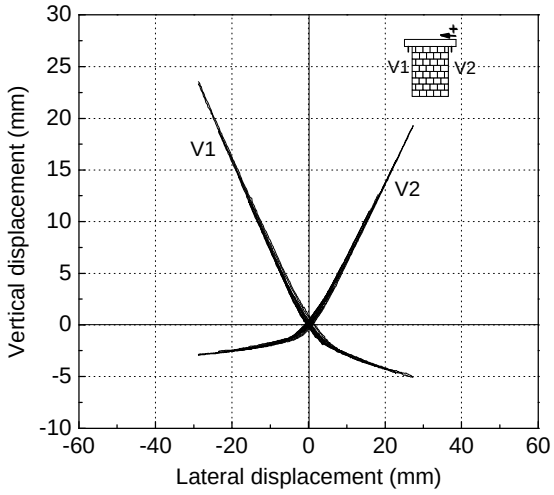


Figure 6.21 – Typical diagram that relates the vertical displacements with the lateral displacements of dry walls - wall WS3.175

Considerable vertical displacements were measured implying that remarkable rotation is experienced by the walls. Note that the asymmetry of the diagram is related to the maximum close of the bed joints.

A note should be made concerning the specimen WS2.100, whose force-lateral displacement is depicted in Figure 6.19b. Although flexural response governs its initial lateral behavior, possible microcracking in the stones (in the bottom course of the wall) leads to the premature collapse of the wall controlled by a significant reduction of its deformation capacity. This indicates that material properties can indeed regulate the structural behavior of these walls. However, as can be seen in Table 6.7, where the relevant values of the force-displacement diagrams are shown, the lateral strength is of the same order of the lateral resistance obtained

for the remaining walls submitted to the same pre-compression level. The values indicated for the points ($H_s$, $d_s$) are corresponding to the opening of the diagonal stair stepped crack. It is observed that some increase on the lateral strength occurs after diagonal crack opening.

Table 6.7 – Relevant values of force-displacement diagrams - dry masonry walls, WS

| State | *First diagonal crack* (kN, mm) | | | | *Lateral strength* (kN, mm) | | | |
|---|---|---|---|---|---|---|---|---|
| Wall | $H^+_s$ | $d^+_s$ | $H^-_s$ | $d^-_s$ | $H^+_{max}$ | $d^+_{Hmax}$ | $H^-_{max}$ | $d^-_{Hmax}$ |
| WS1.100 | 32.2 | 6.1 | -37.1 | -5.1 | 38.8 | 12.8 | -42.1 | -18.7 |
| WS2.100 | 33.4 | 6.4 | -37.3 | -5.6 | 37.6 | 9.0 | -40.3 | -8.3 |
| WS3.100 | 33.3 | 5.8 | -37.1 | -6.0 | 36.5 | 16.3 | -41.1 | -19.3 |
| WS4.100 | 33.1 | 6.2 | -35.8 | -4.3 | 35.5 | 24.08 | -39.4 | -24.8 |
| average | 33.0 | 6.1 | -36.8 | -5.2 | 36.9 | 12.8 | -40.7 | -17.8 |
| WS1.175 | 56.4 | 7.2 | -62.7 | -7.9 | 61.7 | 20.5 | -67.4 | -24.4 |
| WS2.175 | 57.0 | 7.8 | -60.9 | -8.0 | 63.2 | 21.7 | -68.1 | -23.8 |
| WS3.175 | 60.0 | 7.4 | -66.0 | 7.4 | 63.5 | 15.9 | -67.8 | -19.3 |
| average | 57.8 | 7.5 | -63.2 | 7.8 | 62.8 | 22.6 | -67.8 | -22.5 |
| WS1.250 | 81.4 | 9.5 | -87.9 | 9.5 | 88.1 | 33.2 | -95.3 | -24.2 |
| WS2.250 | 80.4 | 10.0 | -86.9 | 8.9 | 85.1 | 18.4 | -92.2 | -16.4 |
| WS3.250 | 81.2 | 11.8 | -87.2 | 11.9 | 85.6 | 21.2 | -91.6 | -22.1 |
| average | 81.0 | 10.4 | -87.3 | 10.1 | 86.3 | 24.3 | -93.0 | -20.9 |

Similarly to what was pointed out for dry masonry walls subjected to monotonic loading, also under cyclic loading, a dependency of the lateral resistance on the level of pre-compression was observed. By comparing the values obtained in monotonic and cyclic tests, one can conclude that similar values of the lateral resistance characterize the shear behavior of dry masonry walls, being the behavior of dry masonry walls independent on the displacement history, for the given failure modes. Note that the values of the lateral resistance obtained for the different specimens subjected to the same axial load are rather close, which is necessarily associated to the common failure pattern. When toe crushing occurs, the lateral resistance has already been developed confirming the low influence on the compressive failure in the global response. Although not very significant, some differences exist between the lateral resistance in the positive and negative directions of the wall, which can be possibly attributed to the test setup.

#### 6.4.4.2 Irregular masonry walls, WI

The force-displacement diagrams obtained for the irregular walls WI1.175 and WI2.175 submitted to intermediate levels of pre-compression are exhibited in Figure 6.22a and Figure 6.22b respectively. As can be noticed, a clear distinct shape is addressed to each specimen. As was mentioned before, the initial shrinkage cracking of the wall WI1.175, seems to be the reason for the asymmetric response in terms of the lateral resistant load and softening post-peak behavior. The smooth strength and stiffness degradation, if attributed to the continuous weakness of the stone skeleton of the left side of the wall, disable the efficient carrying of the internal forces up to the base. On the other hand, the global response in flexure and, particularly, the rocking mechanism that develops in wall WI2.175 after failure of the upper

corners is associated to the S shape of the force-displacement diagram. Even if slight strength degradation is exhibited by right side of the wall after opening of stepped cracks in the unit-mortar interface, the local failure of the left upper corner activated the rocking mechanism, which leads to the stabilization of the lateral strength, see Figure 6.22b. The S shape characterizes also the force-displacement evolution of the wall WI3.175, see Appendix G. In comparison with dry masonry walls, irregular masonry walls show significantly higher hysteresis and, thus, significant dissipation of energy. Note that the large residual deformation at zero horizontal force level indicates the large opening of the diagonal crack.

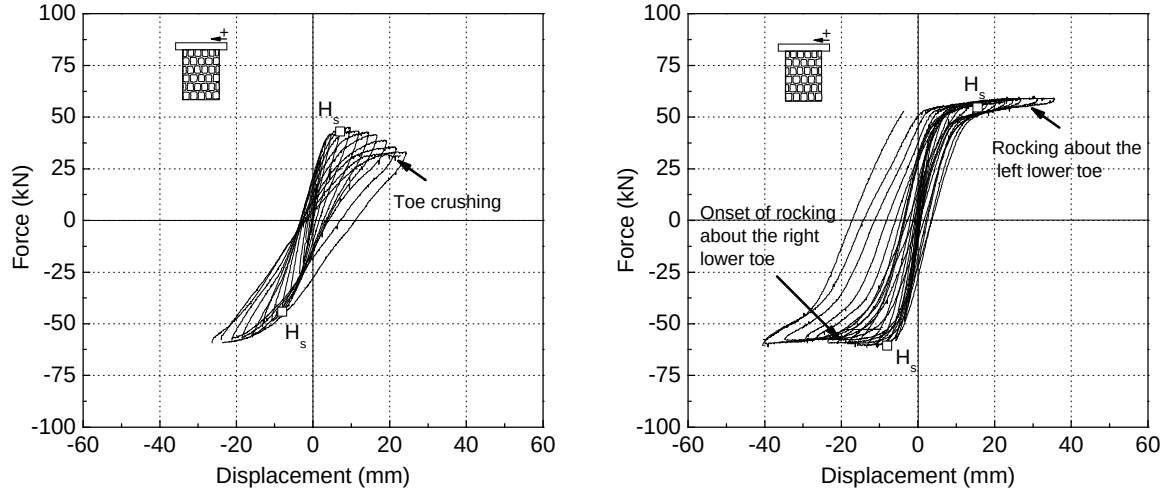


Figure 6.22 – Force-displacement diagrams for irregular masonry walls WI.175; (a) wall WI1.175; (b) wall WI2.175

The rocking mechanism that was found to rule the behavior of irregular walls subjected to the low level of pre-compression is well correlated with the S shape exhibited by the force-lateral displacement diagram for the wall WI1.100 shown in Figure 6.23a. This is also the case of wall WI2.100, Figure 6.23b.

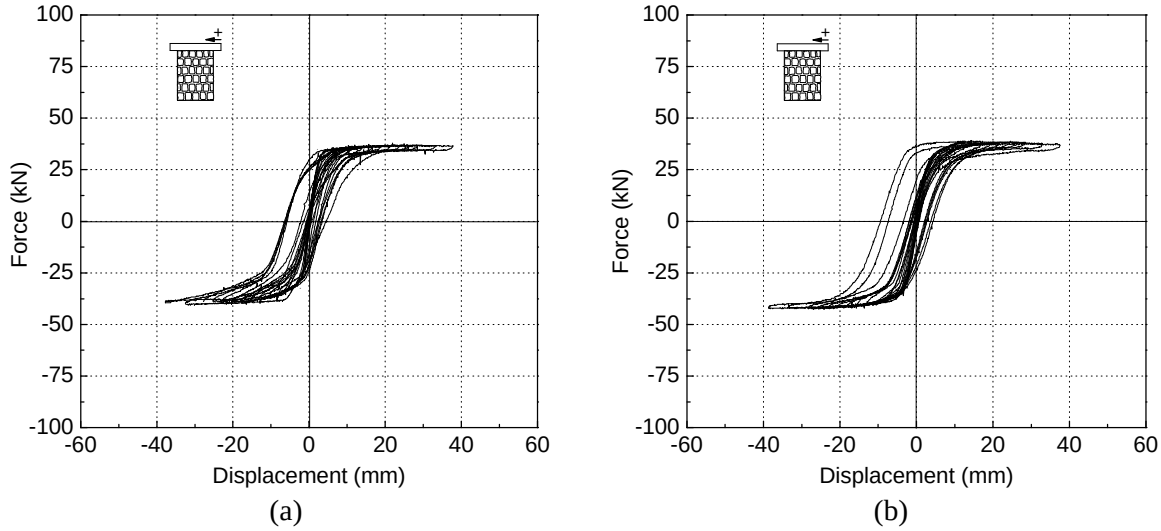


Figure 6.23 – Force-displacement diagrams for irregular masonry walls WI.100; (a) wall WI1.100; (b) wall WI2.100

The nonlinear deformation capacity of irregular masonry walls, when submitted to low to moderate levels of pre-compression, is remarkable. Similarly to walls WI.175, the walls submitted to low levels of pre-compression also show higher energy dissipation capacity than WS walls. Nevertheless, no significant stiffness degradation was observed because the prevailing rocking mechanism contributes to the low levels of damage accumulation.

The shape of the force-displacement diagrams obtained for the walls submitted to the highest level of pre-compression differs significantly from the other walls, see Figure 6.24. Since moderate deformation levels, the hysteresis loops indicates some dissipation of energy, which becomes particularly significant after peak load is reached in case of walls WI2.250 and to minor extent in case of walls WI1.250. This is directly related to the strength and stiffness degradation beyond the peak load and results from the progressive degradation of the lower toes of the wall. Although wall WI2.250 fails due toe crushing, the failure was not explosive, which enabled to capture the post-peak regime as well. In turn, the toe crushing of the wall WI1.250 is followed by a significant reduction of the lateral resistance and a remarkable loss of lateral stiffness. It is noted that, in comparison to the other stress levels, a reduction in deformation capacity was found for the walls under high normal stress level.

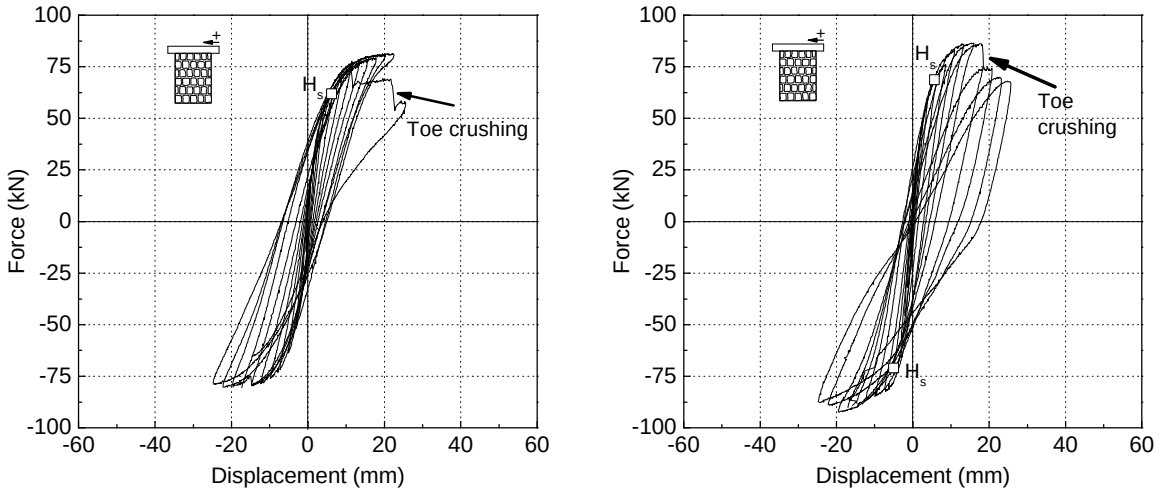


Figure 6.24 – Force-displacement diagrams for irregular masonry walls WI.250; (a) wall WI1.250; (b) wall WI2.250

The relation between the vertical displacements measured by the LVDTs located in the upper steel beam and the lateral displacement of the walls WI1.100 and WI2.250 is displayed in Figure 6.25. Similarly to dry masonry walls, for the wall WI1.100, the vertical displacements measured in the LVDTs increase with increasing lateral displacements, attain remarkable values and present almost symmetric positive values. This confirms that significant rotation of the wall occurs as the outcome of the prevailing rocking mechanism. The wall WI2.250 exhibits very small and almost symmetric vertical displacements for low levels of lateral displacement. From the load cycle with a peak prescribed displacement of ±7.5mm, corresponding to the first stepped shear crack, the growth rate differs clearly from the initial evolution. Given a certain lateral displacement, the corresponding vertical displacement presents distinct and decreasing values for reversal loads. Beyond the peak lateral load, both vertical displacements progressively decrease for the subsequent load cycles.

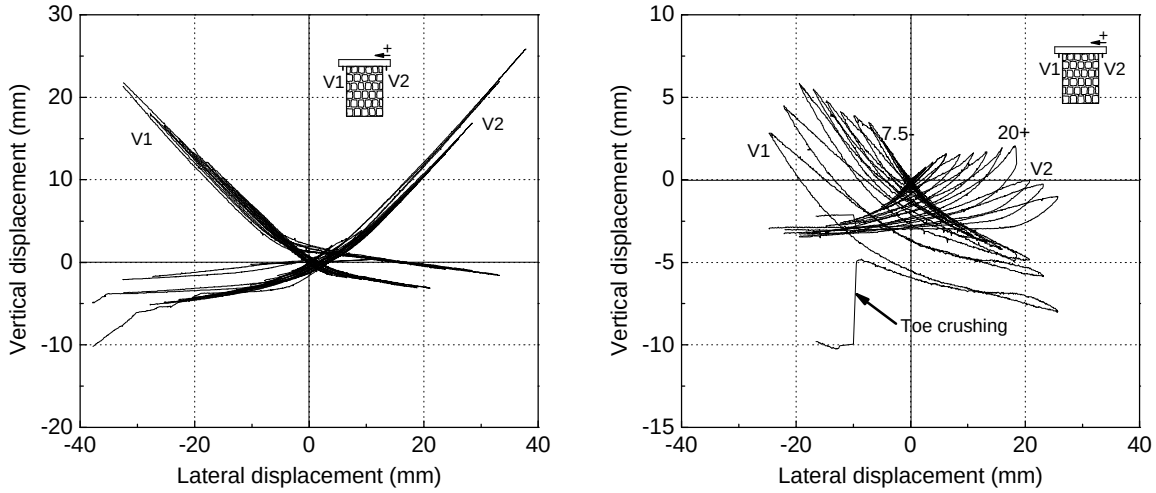


Figure 6.25 – Lateral displacement vs. vertical displacement; (a) wall WI1.100; (b) wall WI2.250

The evolution of the vertical displacement shows that, globally, there is a tendency for compaction that should be ascribed to the increasing damage of the wall. Figure 6.26 shows the local displacement measured by the LVDT located at left lower corner. As can be observed, the displacement was already negative before the first shear crack but increases significantly from this point. This illustrates to certain extent the evolution of damage at the lower toe of the wall.

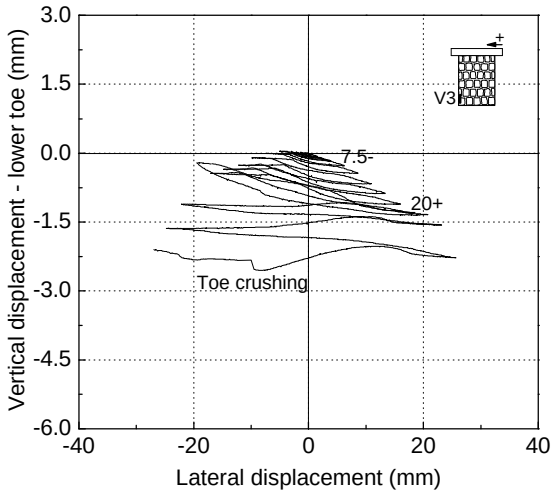


Figure 6.26 – Vertical displacement at the lower toe of the wall WI2.250

The relevant couple of values describing singular states of the force-displacement diagrams are presented in Table 6.8. The values of lateral force corresponding to opening of subvertical shear cracks in walls WI1.175 are indicated with an asterisk, since they originate from previous cracks developed by shrinkage. The maximum values of the lateral resistance attained by the irregular walls are quite close to the ones obtained for the dry masonry walls for low levels of pre-compression, which is explained by the common failure mechanism associated with flexural response. Apart from the specimen WI1.175, whose lateral resistance appears to be influenced by pre-existing microfissures originated by shrinkage, no significant differences are recorded for the walls WS.175. A tendency for a slight decrease on the values of the lateral strength was observed for walls WI.250 compared to the walls WS.250, which

can be attributed to the lower compressive strength. Higher difference is found in the maximum lateral deformation, being approximately 30% lower in case of walls WI.250. It is noted that in comparison with dry masonry walls, higher scatter in the results is achieved due to variability on the textural arrangement. It should be underlined that shear cracks seem not to control the mechanism of lateral resistance since they coexist with flexural cracks. Besides, its typical pattern, following the head and bed mortar joints, provides the formation of a flexural mechanism after failure of the upper corners.

Table 6.8 – Characteristic values of the hysteretic envelops - irregular masonry walls, WI

| State | *First diagonal crack* (kN, mm) | | | | *Lateral strength* (kN, mm) | | | |
|---|---|---|---|---|---|---|---|---|
| Wall | $H^+_s$ | $d^+_s$ | $H^-_s$ | $d^-_s$ | $H^+_{max}$ | $d^+_{Hmax}$ | $H^-_{max}$ | $d^-_{Hmax}$ |
| WI1.100 | - | - | - | - | 36.7 | 15.7 | -39.1 | -17.7 |
| WI2.100 | - | - | - | - | 38.5 | 13.1 | -40.9 | -18.0 |
| average | - | - | - | - | 37.6 | 14.4 | 40.0 | 17.9 |
| WI1.175 | 43.0* | 7.13* | -44.2* | -8.0* | 44.8 | 9.8 | -58.8 | -22.2 |
| WI2.175 | 54.6 | 15.6 | -59.7 | -8.0 | 57.9 | 24.8 | -60.6 | -10.8 |
| WI3.175 | 63.4 | 15.1 | - | - | 63.9 | 27.6 | 68.7 | 20.5 |
| average | - | - | - | - | 55.7 | 19.8 | 62.7 | 17.8 |
| WI1.250 | 61.8 | 6.2 | - | - | 80.3 | 18.2 | -79.1 | -14.6 |
| WI2.250 | 68.7 | 5.7 | -71.0 | -5.0 | 86.0 | 16.0 | -91.0 | -16.9 |
| average | 66.0 | 6.6 | - | - | 83.2 | 17.1 | 85.0 | 15.8 |

### 6.4.4.3 Rubble masonry walls, WR

In case of rubble masonry walls, the role taken by the textural variability on the lateral response is well evidenced in Figure 6.27, where the force-lateral displacement diagrams for the walls WR.100 are displayed.

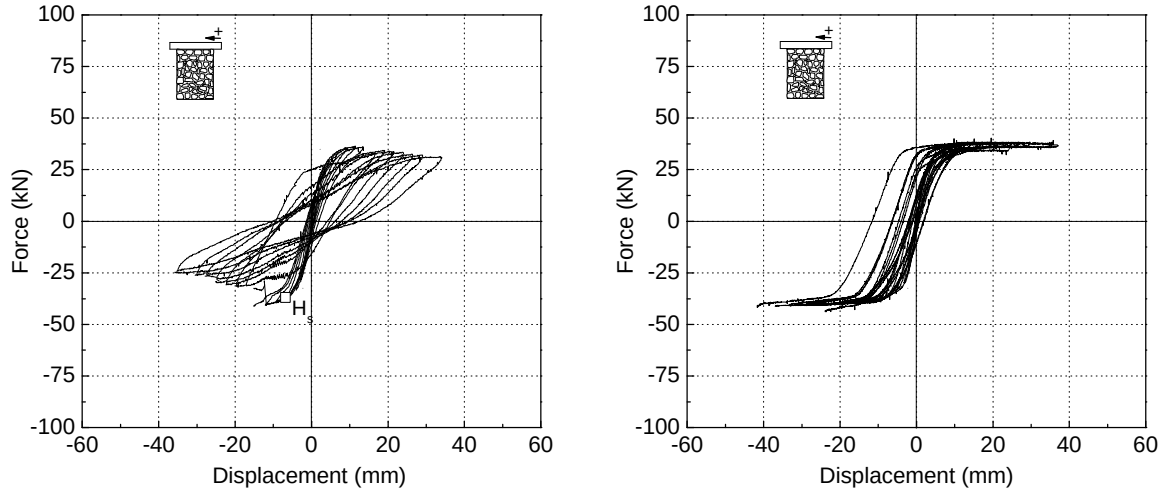


Figure 6.27 – Force-displacement diagrams for rubble masonry walls WR.100; (a) wall WR1.100; (b) wall WR2.100

As discussed earlier, in the Section 6.4.3, the lateral response of the wall WR2.100 is governed by a rocking mechanism and is well described by an expressive S of the hysteresis loops. Reduced stiffness degradation is observed due to the low level of damage induced by rocking response. Concerning wall WR1.100, two phases can be distinguished in the force-displacement diagram. Firstly, the mixed deformation mode composed of flexural and shear cracking at early stages of prescribed displacement is associated to the diagram with moderate hysteresis. After the propagation of the diagonal crack up to the right lower corner, which took place for a peak prescribed displacement of 15mm, a sudden drop in the load bearing capacity occurs. Subsequently, damage manifestations include strength and stiffness degradation followed by remarkable nonlinear deformations. For the two specimens, the differences in the maximum lateral strength are minimal but the differences found in the post-peak regime include clear distinct characteristics in terms of dissipation of energy.

The force-displacement diagrams obtained for rubble masonry walls subjected to intermediate levels of pre-compression reveal a significant decrease on its deformation capacity, see Figure 6.28. Although walls WR.175 exhibit rather similar values in terms of maximum lateral resistance, the hysteresis loops are somewhat asymmetric, which to certain extent can be related to the textural scatter that is intrinsic to the construction of these walls. It in noticed that the lateral load corresponding to the opening of shear cracking, $H_s$, is close to the lateral resistance. Both specimens tested under intermediate pre-compression levels show stable cycles displacement beyond the maximum lateral resistance with significant but progressive strength and stiffness degradation associated to potential ability to dissipate energy, see Figure 6.28.

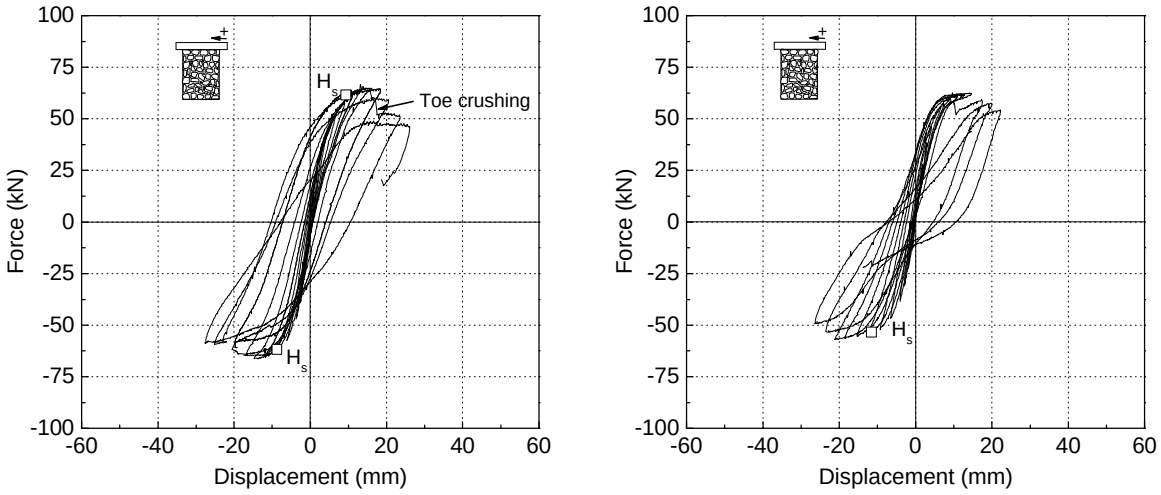


Figure 6.28 – Force-displacement diagrams for rubble masonry walls WR.175; (a) wall WR1.175; (b) wall WR2.175

The reduced deformation capacity of rubble masonry walls subjected to high levels of pre-compression becomes clear from the analysis of the force-displacement diagrams for the walls WR1.250 and WR2.250 displayed in Figure 6.29. The brittle behavior of these walls is also verified from the fact that failure occurs practically for the maximum lateral resistance, and almost no post-peak response develop. Diagonal or smeared subvertical shear cracks opened for lateral forces rather close or coincident with the lateral resistance.

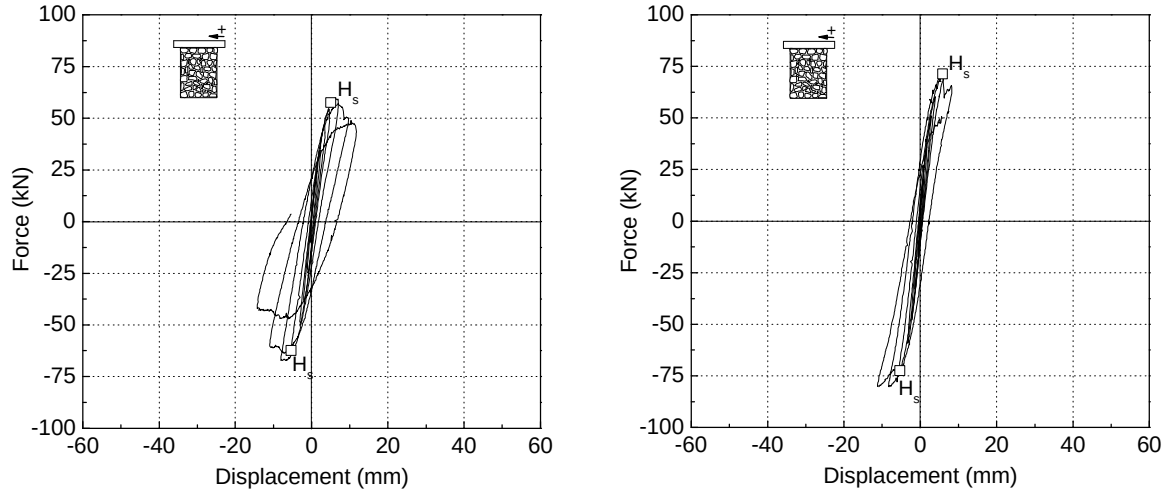


Figure 6.29 – Force-displacement diagrams for rubble masonry walls WR.250; (a) wall WR1.250; (b) wall WR2.250

The evolution of the vertical displacements with the lateral displacement for the walls WR1.100 and WR2.250 is presented in Figure 6.30. With respect the wall WR1.100, two phases can be distinguished. The first phase is characterized by moderate almost reversed vertical displacements, meaning that flexural mechanism takes an important role. After opening of the diagonal crack, which is indicated by the sudden drop of the displacement in Figure 6.30a, the vertical displacements progressively decrease. The diagram of the wall WR2.250 indicates that only slight rotation of the walls develops, Figure 6.30b. A clear tendency for compaction of the wall is recorded after shear cracking.

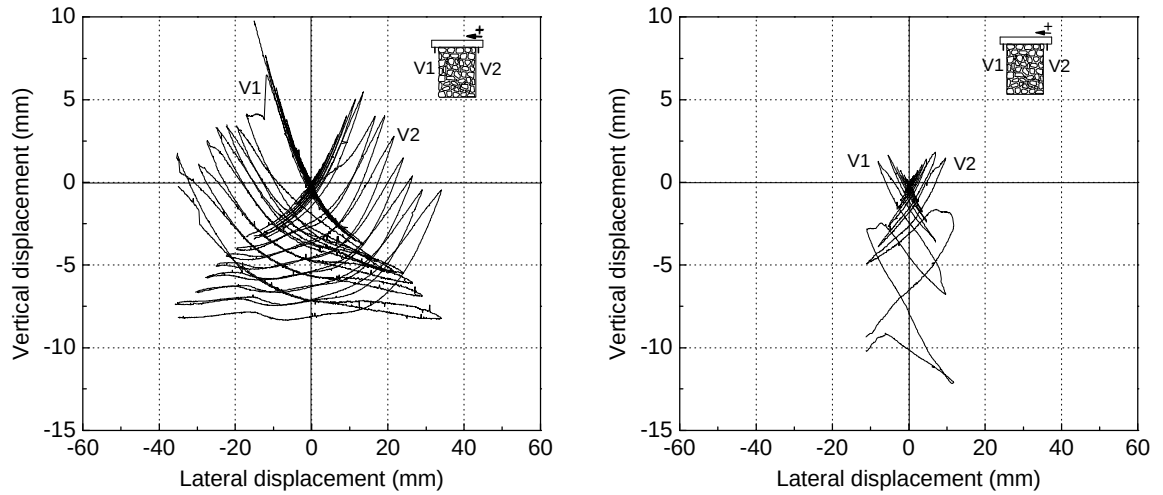


Figure 6.30 – Lateral displacement vs. vertical displacement; (a) wall WR1.100; (b) wall WR2.250

Concerning the relevant couple of values of the force-displacement diagrams shown in Table 6.9, some aspects should be pointed out. The walls WR.100 exhibit similar lateral resistance relatively to the walls WS.100 and WI.100. In spite of the wall WR1.100 failing in shear, the maximum lateral resistance is similar to the one obtained for the wall WR2.100 whose lateral response in governed by rocking. For intermediate levels of pre-compression, also a similarity of the lateral strength is observed between rubble masonry walls and dry and irregular walls

submitted to the same axial load. In turn, a noticeable strength decrease is recorded in the walls WR.250. The shear crack resistance is practically coincident with the values of the maximum lateral strength, meaning that the opening of the shear cracks results in the failure of the walls. This result is in agreement with the statements of Magenes and Calvi (1997) indicating diagonal shear cracking can be considered as a limit state since it occurs for lateral loads ranging between 90 and 100% of the maximum resistance.

Table 6.9 – Relevant values of the hysteretic envelops - rubble masonry walls, WR

| State | *First diagonal crack* (kN, mm) | | | | *Lateral strength* (kN, mm) | | | |
|---|---|---|---|---|---|---|---|---|
| Wall | $H^+_s$ | $d^+_s$ | $H^-_s$ | $d^-_s$ | $H^+_{max}$ | $d^+_{Hmax}$ | $H^+_{max}$ | $d^+_{Hmax}$ |
| WR1.100 | - | - | -37.3 | -6.8 | 36.4 | 11.5 | -40.6 | -11.8 |
| WR2.100 | - | - | - | - | 37.3 | 14.3 | -40.1 | -15.6 |
| average | - | - | | | 36.9 | 12.9 | -40.4 | -13.7 |
| WR1.175 | 61.5 | 9.3 | -61.8 | -8.8 | 64.5 | 14.9 | -64.8 | -11.6 |
| WR2.175 | - | - | -53.4 | -11.5 | 62.8 | 12.8 | -56.1 | -15.2 |
| average | | | -57.6 | -10.2 | 63.6 | 13.8 | -60.4 | -13.4 |
| WR1.250 | 57.5 | 5.0 | -62.4 | -5.4 | 59.4 | 6.4 | -65.4 | -8.0 |
| WR2.250 | 72.5 | 6.1 | -71.3 | -5.8 | 72.5 | 6.1 | -78.5 | -8.3 |
| WR3.250 | 65.4 | 8.8 | -64.8 | -5.6 | 65.7 | 8.8 | -71.0 | -8.6 |
| average | 65.2 | 6.6 | -66.2 | -5.6 | 65.9 | 7.1 | -71.6 | -8.3 |

## 6.5 Evaluation of the cyclic performance

This section deals with the evaluation of the seismic performance of unreinforced stone masonry shear walls, which is, herein, carried out in terms of performance indices, including the ductility and energy dissipation capacity. This analysis is also addressing the novel performance based design concepts. In this scope, lateral drifts associated to certain performance levels (limit states) are defined as a measure of the nonlinear deformation capacity of the masonry walls. This goal is reached combining the experimental data composed by the force-displacement diagrams and the information about the crack damage patterns.

### 6.5.1 *Bilinear idealization of the experimental envelops*

The most common approach used for the evaluation of the in-plane seismic performance in terms of nonlinear deformability is the definition of an idealized bilinear envelop of the force-lateral displacement diagrams. This procedure has been widely reported in the literature as a simplified method of evaluating the stiffness, strength and deformation capacity expressed in terms of the ductility factor of masonry walls under cyclic loading (Shing *et al.*, 1989; Magenes and Calvi, 1997; Bosiljkov *et al.*, 2003; Mohamed and Barakat, 2003). The idealized bilinear diagram is also defined in the scope of performance based concepts (Abrams, 2001; Abrams, 2004).

The experimental envelopes were defined here by considering the force-displacement points of the hysteresis loops for which the displacement exceeds the previous maximum displacement (Schultz *et al.*, 1998). For this purpose, the positive direction of the wall was

selected. Examples of experimental cyclic envelopes are given in Figure 6.31 for walls WI and WR, which reveal qualitative information on the post-peak behavior of the walls. The envelope corresponding to the wall WR2.250 is characteristic of a structure that behaves in a brittle manner due to its inability to deform beyond the peak lateral load. On the other hand, the wall WI2.250 exhibit considerable nonlinear deformations in the post peak-regime and, thus, better cyclic performance is expected.

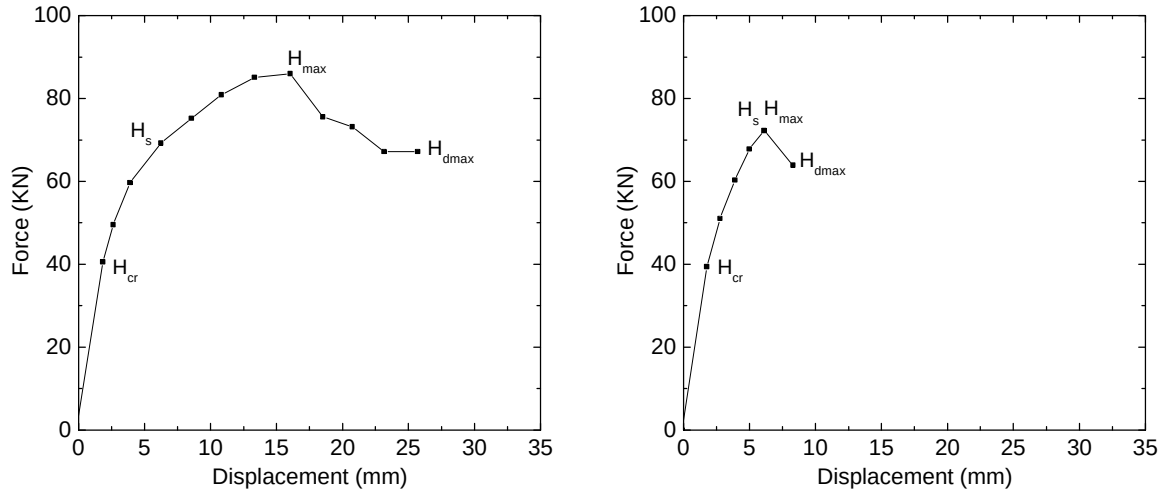


Figure 6.31 – Examples of experimental envelopes; (a) wall WI2.250; (b) wall WR2.250

According to Tomaževic (1999) three limit states need to be defined in order to idealize the experimental envelope, see Figure 6.32. The limit states attained by the walls during the cyclic loading are identified with three characteristic points of the experimental envelope based on the force-displacement diagrams. The crack limit state is defined with the point ($H_{cr}$, $d_{cr}$) corresponding to the formation of the first significant cracks and, generally, is associated to the change of the slope of the experimental envelope. The maximum resistance is identified by the couple ($H_{max}$, $d_{Hmax}$) and the ultimate state is related to the maximum displacement attained during the cyclic test and is associated to the point ($H_{dmax}$, $d_{max}$).

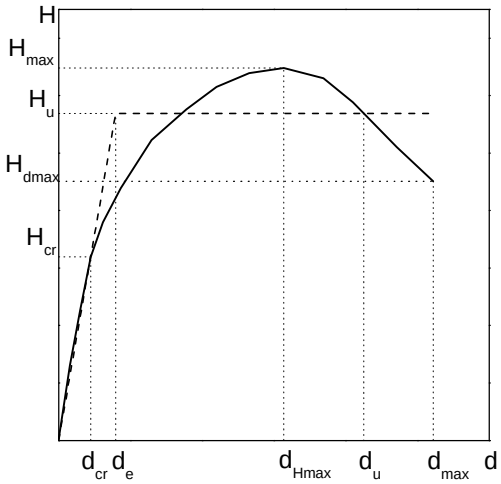


Figure 6.32 – Hysteresis envelope and the equivalent bilinear idealization

The initial slope in the elastic-plastic diagram, also called secant stiffness at the formation of flexural cracks, is calculated as the ratio between the lateral force, $H_{cr}$, and lateral deformation, $d_{cr}$, at the crack limit state defined by the following expression:

$$K_e = \frac{H_{cr}}{d_{cr}} \tag{6.3}$$

The value of the ultimate resistance of the elastic-plastic diagram, $H_u$, is obtained by ensuring equal energy dissipation of the idealized diagram and the cyclic experimental envelope, meaning that the areas below both diagrams should be equal, see Figure 6.32. Once the elastic stiffness, $k_e$, and area under the experimental envelope, $A_{env}$, are calculated, the ultimate resistance can be calculated from (Tomaževic, 1999):

$$H_u = K_e \left( d_{\max} - \sqrt{d^2{}_{\max} - \frac{2A_{env}}{K_e}} \right) \tag{6.4}$$

The corresponding displacement at the idealized elastic limit is obtained from:

$$d_e = \frac{H_u}{K_e} \tag{6.5}$$

The ultimate idealized displacement, $d_u$, is defined as the intersection of the idealized bilinear diagram with the softening branch of the experimental cyclic envelope (Tomaževic, 2003).

The evaluation of the seismic performance of unreinforced stone masonry shear walls is carried out based on the values of ductility. After defining the ideal bilinear envelope, the value of ductility is obtained by dividing the ultimate horizontal displacement by the elastic displacement:

$$m = \frac{d_u}{d_e} \tag{6.6}$$

Note that in-plane cyclic behavior of dry stone masonry walls is characterized by flexural rocking response. In fact, no ultimate state can be attributed to this type of walls since no strength degradation occurs. If premature toe crushing does not occur, the ultimate displacement is only attained through second order (P-Δ) effects associated with overturning (Magenes and Calvi, 1997). However, as seen previously, these masonry walls exhibit remarkable nonlinear behavior to cyclic horizontal reversal loads. Therefore, idealized bilinear diagrams were also considered for this type of walls and the ductility factor is calculated from the maximum displacement, $d_{max}$. This appears to be a reasonable procedure for a comparative analysis about the nonlinear deformability among the distinct types of walls.

The characteristic values of the hysteretic envelopes and of the corresponding bilinear idealization defining each limit state of the shear walls WS, WI and WR, are respectively summarized in Table 6.10, 6.11 and 6.12. The couple of values defining the maximum resistance state ($H_{max}$, $d_{Hmax}$) are repeated here so that immediate comparison with the ultimate is possible. A detailed discussion about the ductility will be presented in the next section. In case of dry masonry walls and as expected, the values of the ultimate resistance of the bilinear idealization are remarkably close to the maximum lateral resistance. In spite of the pre-peak

nonlinearity, the experimental envelopes obtained for the dry masonry walls are almost elastic-perfectly plastic. Concerning the values of the secant lateral stiffness, it is observed that it depends on the level of pre-compression. A positive linear correlation between stiffness and the pre-compression was achieved by statistical fitting to the experimental data ($k_e$ = 0.036$N$+10.57, $r^2$ = 0.87).

Table 6.10 – Characteristic values of the hysteretic envelopes - dry masonry walls, WS

| Wall | $H_{cr}$ (kN) | $d_{cr}$ (mm) | $K_e$ (kN/mm) | $d_e$ (mm) | $H_u$ (kN) | $H_{max}$ (kN) | $d_{Hmax}$ (mm) | $d_{max}$ (mm) | $\mu$ |
|---|---|---|---|---|---|---|---|---|---|
| WS1.100 | 18.81 | 1.45 | 12.97 | 2.80 | 36.32 | 38.81 | 12.80 | 36.32 | 12.99 |
| WS2.100 | 18.21 | 1.99 | 9.15 | 3.53 | 32.30 | 35.82 | 9.01 | 16.53 | 4.68 |
| WS3.100 | 18.51 | 1.28 | 14.46 | 2.50 | 36.19 | 37.61 | 16.35 | 36.53 | 14.60 |
| WS4.100 | 16.41 | 1.21 | 13.56 | 2.57 | 34.91 | 35.52 | 13.41 | 41.36 | 16.07 |
| average | 17.99 | 1.48 | 12.54 | 2.87 | 34.93 | 36.94 | 12.89 | 32.70 | 12.08 |
| WS1.175 | 27.16 | 1.56 | 17.41 | 3.39 | 59.09 | 61.79 | 30.33 | 30.33 | 8.94 |
| WS2.175 | 25.40 | 1.38 | 18.38 | 3.31 | 60.98 | 63.28 | 21.71 | 39.37 | 11.87 |
| WS2.175 | 25.37 | 1.42 | 17.87 | 3.36 | 60.01 | 63.58 | 15.93 | 27.24 | 8.11 |
| average | 25.97 | 1.45 | 17.89 | 3.36 | 60.03 | 62.88 | 22.65 | 32.31 | 9.64 |
| WS1.250 | 35.55 | 1.84 | 19.32 | 4.40 | 85.01 | 88.14 | 33.27 | 46.18 | 10.50 |
| WS2.250 | 33.16 | 1.77 | 18.73 | 40.23 | 79.29 | 85.10 | 18.41 | 18.41 | 4.35 |
| WS3.250 | 31.97 | 1.67 | 19.14 | 4.24 | 81.10 | 85.69 | 21.21 | 32.34 | 7.63 |
| average | 33.96 | 1.76 | 19.07 | 4.29 | 81.80 | 86.31 | 24.30 | 32.31 | 7.49 |

For irregular masonry walls, the mean values of the ultimate resistance, $F_u$, are between 0.97$F_{max}$, for the WI.100, 0.93$F_{max}$ for WI.175 and 0.90$F_{max}$ for walls WI.250, see Table 6.11. These differences reflect the distinct failure modes found in the walls submitted to low and high pre-compression levels. The flexural rocking mechanism prevails in the lateral response of walls WI.100 and a mixed flexural/shear/toe crushing mode rules the lateral behavior of the walls under higher level of vertical stresses. The values for the lateral stiffness in irregular masonry walls are rather similar to the values obtained in dry masonry walls. This seems to be in agreement with the values of the modulus of elasticity measured previously.

Table 6.11 – Characteristic values of the hysteretic envelopes - irregular masonry walls, WI

| Wall | $H_{cr}$ (kN) | $d_{cr}$ (mm) | $K_e$ (kN/mm) | $d_e$ (mm) | $H_u$ (kN) | $H_{max}$ (kN) | $d_{Hmax}$ (mm) | $d_{max}$ (mm) | $\mu$ |
|---|---|---|---|---|---|---|---|---|---|
| WI1.100 | 20.90 | 1.49 | 14.03 | 2.59 | 36.39 | 36.72 | 15.68 | 37.31 | 14.38 |
| WI2.100 | 20.60 | 1.70 | 12.12 | 3.07 | 37.26 | 38.51 | 11.95 | 37.49 | 12.19 |
| average | 20.75 | 1.60 | 13.07 | 2.83 | 36.83 | 37.62 | 13.82 | 37.40 | 13.29 |
| WI1.175 | 27.76 | 1.80 | 15.42 | 2.63 | 40.64 | 44.78 | 9.75 | 24.26 | 9.21 |
| WI2.175 | 28.96 | 1.74 | 16.64 | 3.34 | 55.58 | 58.81 | 21.81 | 35.65 | 10.68 |
| WI2.175 | 29.55 | 1.95 | 15.15 | 3.90 | 59.04 | 63.58 | 27.69 | 27.69 | 7.11 |
| average | 28.76 | 1.83 | 15.74 | 3.29 | 51.75 | 55.72 | 19.75 | 29.2 | 9.90 |
| WI1.250 | 38.21 | 1.99 | 19.20 | 3.75 | 72.09 | 80.60 | 20.15 | 25.61 | 6.82 |
| WI2.250 | 40.60 | 1.84 | 22.07 | 3.42 | 75.41 | 85.37 | 13.83 | 25.71 | 7.52 |
| average | 39.41 | 1.92 | 20.63 | 3.59 | 73.75 | 82.98 | 16.99 | 25.66 | 7.17 |

With respect to the values of the ultimate lateral resistance of walls WR, see Table 6.12, only the value of the wall WR2.100 is approximately $0.95H_{max}$. A relation of $H_u = 0.9H_{max}$ was found for the other walls. This finding is in agreement with the value reported by Tomaževic (1999) as the average value of the idealized ultimate resistance obtained from more than 60 tests on walls failing in shear. The reduction on the elastic lateral stiffness relatively to dry masonry walls is for low pre-compression about 8.9%, 17.1% for intermediate pre-compression level and 9.1% for the highest level of pre-compression. However, the differences are less significant when compared to irregular masonry walls.

Table 6.12 – Characteristic values of the hysteretic envelopes - rubble masonry walls, WR

| Wall | $H_{cr}$ (kN) | $d_{cr}$ (mm) | $K_e$ (kN/mm) | $d_e$ (mm) | $H_u$ (kN) | $H_{max}$ (kN) | $d_{Hmax}$ (mm) | $d_{max}$ (mm) | $\mu$ |
|---|---|---|---|---|---|---|---|---|---|
| WR1.100 | 17.56 | 1.56 | 11.26 | 2.71 | 32.94 | 36.42 | 11.49 | 33.97 | 12.54 |
| WR2.100 | 16.72 | 1.42 | 11.77 | 3.06 | 35.98 | 37.61 | 16.95 | 35.65 | 11.65 |
| average | 17.14 | 1.49 | 11.52 | 2.89 | 34.46 | 37.01 | 14.22 | 34.81 | 12.09 |
| WR1.175 | 27.16 | 1.84 | 14.76 | 3.97 | 56.74 | 64.78 | 15.68 | 26.09 | 6.57 |
| WR2.175 | 27.50 | 1.74 | 15.80 | 3.64 | 57.49 | 62.79 | 12.77 | 22.22 | 6.10 |
| average | 27.33 | 1.79 | 15.28 | 3.81 | 57.12 | 63.78 | 14.22 | 24.15 | 6.34 |
| WR1.250 | 31.04 | 1.74 | 17.84 | 2.93 | 52.62 | 60.01 | 6.28 | 11.74 | 4.01 |
| WR2.250 | 39.40 | 1.77 | 22.26 | 2.96 | 65.95 | 72.24 | 6.10 | 8.23 | 2.78 |
| WR3.250 | 28.96 | 1.74 | 16.64 | 2.93 | 58.04 | 65.67 | 8.58 | 10.89 | 3.72 |
| average | 33.13 | 1.75 | 18.91 | 2.94 | 58.87 | 65.97 | 6.99 | 10.28 | 3.50 |

In all walls the secant stiffness is clearly dependent on the level of pre-compression. By fitting a linear function to the experimental data composed by the secant stiffness and the pre-compression level, *N*, for all walls, a reasonable linear relation was found between both properties, see Figure 6.33. The secant stiffness increases with increasing axial load. The existent scatter is related to the variation on the masonry bond.

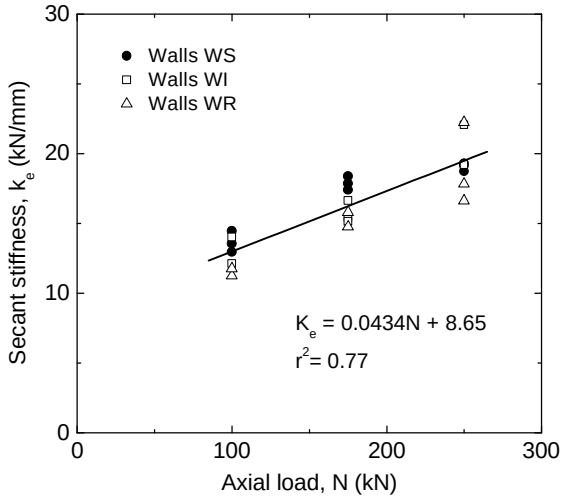


Figure 6.33 – Relation between pre-compression level and the secant stiffness for all walls

### 6.5.2 *Evaluation of the ductility*

As was aforementioned, the capacity of shear walls to deform nonlinearly beyond the peak strength without pronounced strength loss or stiffness degradation is evaluated by means of the ductility factor. The ductility is a useful measure that makes possible the reduction of elastic seismic design actions by means of a behavior factor, since it gives an indication of the ability of the structure to dissipate energy (Tomaževic, 2003). In terms of performance based concepts, the ductility is usually assumed as the force reduction factor that reduces expected elastic levels of the base shear strength to acceptable design levels (Priestley, 2000; Abrams, 2001; Abrams, 2004).

The evaluation of the ductility of the stone masonry walls is carried out from the values indicated in the previous section and the average values are summarized in Figure 6.34a.

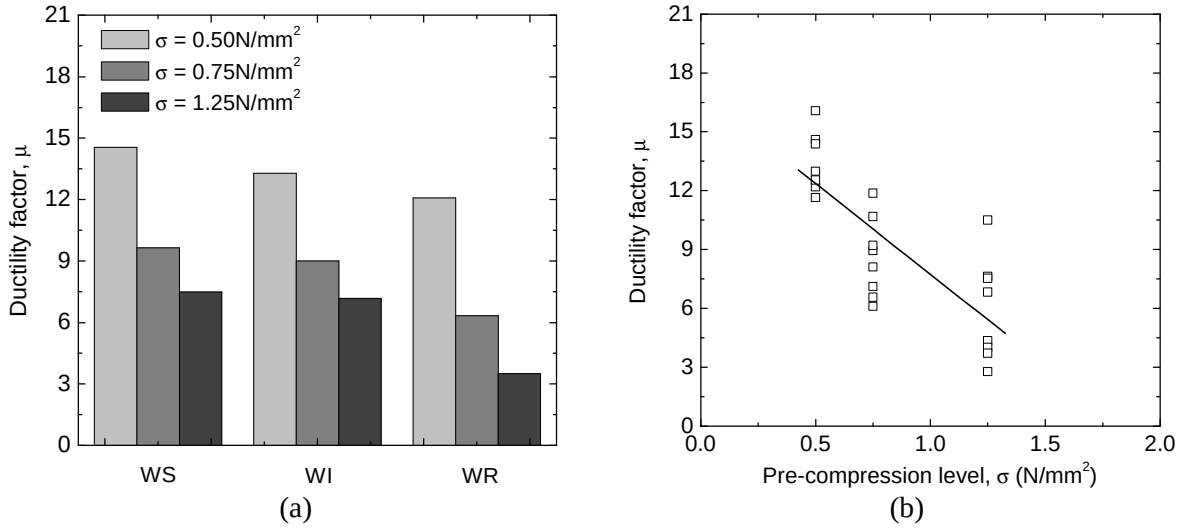


Figure 6.34 – Evaluation of the ductility factor; (a) average values of ductility for walls with different masonry bond and distinct level of pre-compression; (b) relationship between pre-compression level and ductility factor

A clear tendency for the ultimate ductility factor to decrease as the irregularity of the textural arrangement is more significant was observed. The reduction from walls WS to walls WI and WR is quite moderate in case of low pre-compression levels, because similar failure modes governed by the flexural rocking mechanism were found. The reduction of the ductility factor is also low in case of walls WI.175, when compared with walls WS.175. Higher reduction was recorded from walls WS.175 to walls WR.175, which is directly related to the changing of failure mode from rocking to a mixed mode of flexural/shear failure. The reduction is even more significant when walls submitted to the highest level of pre-compression are compared. In fact, a much more brittle failure should be expect to occur in case of walls WR.250 failing in shear. The difference found between walls WS.250 and WI.250 is minimal since toe crushing rules the maximum lateral resistance of both walls, only after extensive flexural damage.

From Figure 6.34b, where the values of ductility factor for all walls are shown, the dependence of the ductility on the level of pre-compression is clear. In spite of the scatter, a clear tendency for the ultimate ductility to decrease as the pre-compression level increases was found. This tendency is the outcome of the influence of the level of vertical stresses on the lateral response of the distinct types of walls. In case of walls WS, the reduction of the

ductility factor can be attributed essentially to the failure pattern associated to the toe crushing that prevails for moderate to high levels of pre-compression. The same behavior is followed by irregular walls, where toe crushing predominates in walls WI.250, which is agreement with the results reported by Shing *et al*. (1989). In case of walls WR, the relatively low values of the ductility factor for moderate levels of pre-compression and, particularly, for the walls WR.250, are the result of the cyclic response being governed by shear patterns. Similar results were pointed out by Bosiljkov *et al*. (2003). The dependence of the ductility capacity on the axial load was also reported by Priestley (2000).

A note should be made concerning the scattering on the results of the ductility factor. On one hand, it was only possible to carry out a reduced number of specimens on walls WI and WR. On the other hand, the scatter is highly influenced by the dispersion of failure modes. If rocking failure pattern is associated with toe crushing, as in case of walls WS, the values of maximum deformation will be significantly reduced and, hence, higher scattering is achieved.

If on one hand, a higher level of pre-compression leads to higher values of the lateral resistance under cyclic loads, on the other hand, it yields more brittle responses and, thus, lower capacity to deform nonlinearly. In the scope of repair and rehabilitation of ancient masonry structures, efforts are often related to enhancement the performance under seismic loading by improving the nonlinear capacity of deformation of masonry structures and, hence, to obtain higher levels of ductility.

### 6.5.3 *Performance levels based on lateral drifts*

In this section, a discussion of the nonlinear deformation capacity of unreinforced stone masonry walls in the scope of the concepts of performance based design is carried out. According to the new concepts, a new or rehabilitated structural system should be designed to achieve a particular level of performance during an earthquake event (Abrams, 2001). The so-called performance levels are directly connected to certain levels of structural damage induced by the lateral deformations to individual structural components. In general, three performance levels are considered: Immediate Occupancy (IO), Life Safety (LS) and Collapse Prevention (CP) (Abrams, 2004). Here it is noted that monumental and residential masonry structures might have different performance levels, but this discussion is outside the scope of the present work.

At Immediate Occupancy level (IO), damage is relatively limited, and the structure remains with significant amount of its original stiffness and strength. This performance level is associated to the onset of shear cracking. For the stone masonry walls under analysis, this performance level is represented by the point ($H_s$, $d_s$) of the force-lateral displacement diagram. The corresponding level of deformation is defined by the lateral drift calculated as $d_s/h$ (%), where $h$ is the wall height. At the Life Safety level (LS), the structure presents considerable damage and has lost significant amount of its original stiffness. Although in theory a substantial margin could remain for additional deformation before collapse would occur, in case of the structure behaving in a brittle manner, see Figure 6.35 as an example, a low margin can exist between the three performance levels. The life safety level is represented by the point ($H_{max}$, $d_{Hmax}$). The corresponding lateral drift is calculated as $d_{Hmax}/h$ (%). At the Collapse Prevention level (CP), the structure has experienced extreme damage and additional lateral deformation beyond the point ($H_{dmax}$, $d_{max}$), which characterizes this performance level, means the instability and collapse of the structure. The corresponding

lateral drift is calculated as $d_{max}/h$ (%). Here, similarly to what was proposed by Bosiljkov *et al*. (2003), an additional performance level corresponding to the onset of the first flexural crack is taken into account. This First Cracking level (FC) is represented by the point ($H_{cr}$, $d_{cr}$) and the corresponding lateral drift is calculated as $d_{cr}/h$ (%).

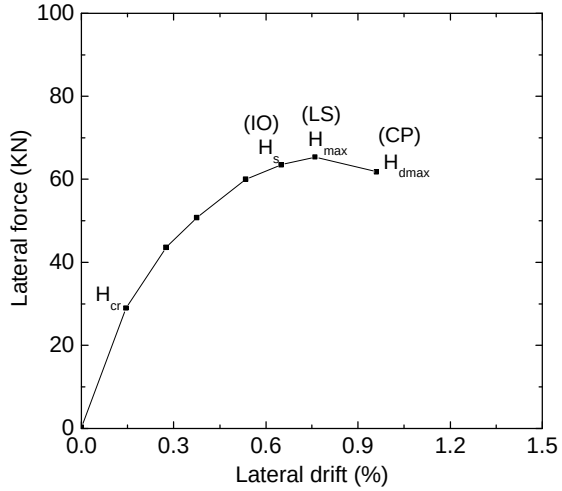


Figure 6.35 – Performance levels for the wall WR2.250

Besides the ultimate ductility factor, the capacity of nonlinear deformation is here also evaluated from the lateral drifts connected to each performance level previously considered. The average values of the lateral drifts corresponding to distinct levels of performance are displayed in Table 6.13. The values of the lateral drift corresponding to First Cracking level (FC) are close to the values reported by Bosiljkov *et al*. (2003) for brick masonry walls. Note that considerable values of lateral drifts are associated to minor extent of damage corresponding to the Immediate Occupancy level (IO). Apart from the walls WR.250, remarkable lateral deformation capacity was found for all types of walls and for distinct levels of pre-compression. As expected, the higher values are associated to rocking failure patterns, which occurs in a pronounced manner in walls WS, and to low levels of pre-compression. Maximum lateral drifts of approximately 2.5% were also reported by Abrams (2001) in unreinforced masonry piers, whose response under lateral cyclic loads was governed by rocking. The ultimate lateral displacements obtained in dry masonry walls are also well correlated with the results reported by Oliveira (2003) with respect to in-plane monotonic behavior of dry masonry walls. Maximum lateral drifts ranging between 2.25 and 3.0% were recorded by this author. Similar levels of maximum lateral drift were found for walls WS, WI and WR subjected to a low level of pre-compression ($s$ = 0.5N/mm$^2$), which is necessarily related to the common prevailing failure mechanism of rocking. Decreasing, but still rather high, values of the lateral drift were obtained for walls subjected to moderate levels of pre-compression ($s$ = 0.875N/mm$^2$), including the walls WR.175. Exception to this trend is the behavior of the walls WR subjected to high level of pre-compression of $s$ = 1.25N/mm$^2$. These walls exhibit maximum lateral drifts close the ones indicated by Magenes and Calvi (1997) for masonry brick walls failing in shear. A lateral drift corresponding to Collapse Prevention of about 0.8% was reported by Abrams (2004) for a typical masonry building system. It should be stressed that, with the exception of walls WR.250, a large difference of lateral deformation exist between the Life Safety and the Collapse Prevention performance

levels, which confirms the ductile character of stone masonry walls under in-plane cyclic loading exhibiting similar failure modes to ones obtained in the present work.

Table 6.13 – Performance index for masonry stone walls

| Wall | FC | IO | LS | CP |
|---|---|---|---|---|
| WS.100 | 0.12% | - | 1.07% | 2.72% |
| WS.175 | 0.12% | - | 1.89% | 2.69% |
| WS.250 | 0.15% | - | 2.02% | 2.69% |
| WI.100 | 0.13% | - | 1.15% | 3.12% |
| WI.175 | 0.15% | 0.66% | 1.65% | 2.43% |
| WI.250 | 0.16% | 0.41% | 1.42% | 2.14% |
| WR.100 | 0.12% | 0.57% | 1.19% | 2.90% |
| WR.175 | 0.15% | 0.85% | 1.19% | 2.01% |
| WR.250 | 0.15% | 0.47% | 0.58% | 0.86% |

In the scope of new performance based concepts for masonry structures it seems even advisable that walls and piers are designed to fail in rocking or bed joint sliding (Abrams, 2001). Rocking behavior is poor in energy dissipation but it is highly nonlinear elastic, and in general, associated to large nonlinear deformation capacity, without relevant damage. On the other hand, bed joint sliding possesses large capacity of nonlinear inelastic deformation and it is able to dissipate high amount of energy (Abrams, 2000). In performance based concepts, both types of failure patterns are displacement controlled actions corresponding to large nonlinear deformation and to minimum strength and stiffness degradation (Abrams, 2001). In contrast, diagonal tension and toe crushing are force controlled since they occur when a certain stress is attained, causing sudden and substantial strength deterioration. In fact, this new design concept is in opposition to the classic ultimate state design. Note that, according to section 6.5.2 and the force-displacement hysteresis diagrams, high level of inelastic deformation was found in walls WI and WR due to flexural rocking mechanism and, simultaneously higher energy dissipation capacity was found in comparison with walls WS.

### 6.5.4 *Energy dissipation and stiffness degradation*

Besides ductility, the energy dissipation capacity is an important factor in the evaluation of the seismic response of a structure. A dissipative structure can mean the reduction of the seismic response and, consequently, the reduction of the ductility demand (Shing *et al*., 1989). Despite the force-displacement diagrams provide qualitative information about the ability to dissipate energy, a quantitative and comparative analysis for the different types of walls is carried out in this section.

The energy that is dissipated at each loading cycle, $E_{diss}$, is obtained by integrating numerically the force-displacement hysteresis loop as shown in Figure 6.36a. The energy needed to deform the wall up to an imposed lateral displacement is called input energy, $E_{inp}$, and is calculated as the sum of areas under the positive and negative branches of the hysteresis loop, see Figure 6.36b.

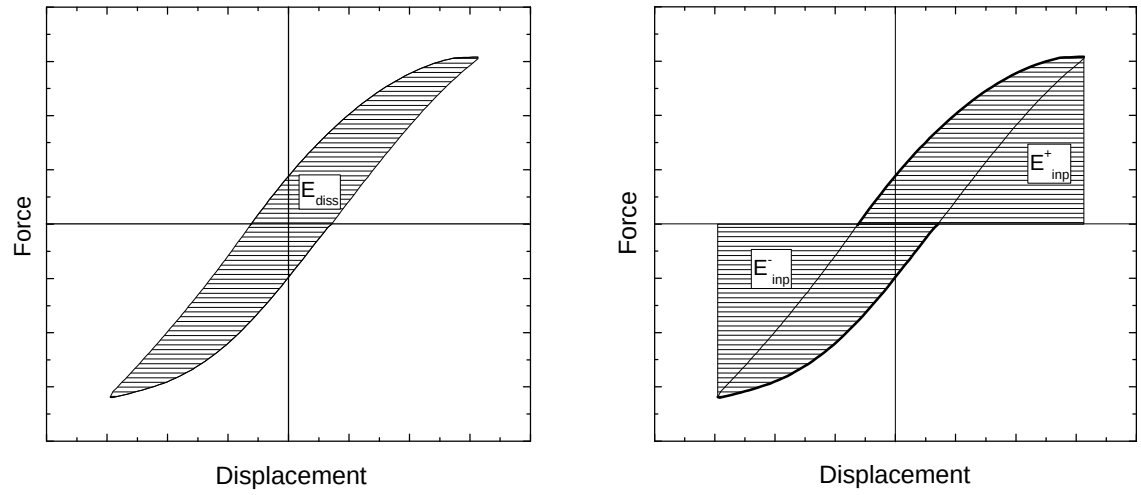


Figure 6.36 – Evaluation of energy in one loading cycle; (a) dissipated energy; (b) input energy

The evolution of the dissipated energy corresponding to each loading cycle obtained for the walls WI and WR is indicated in Figure 6.37. The presentation of the dissipated energy by loading cycle enables the identification of critical points corresponding to particular events in the cyclic response of the walls.

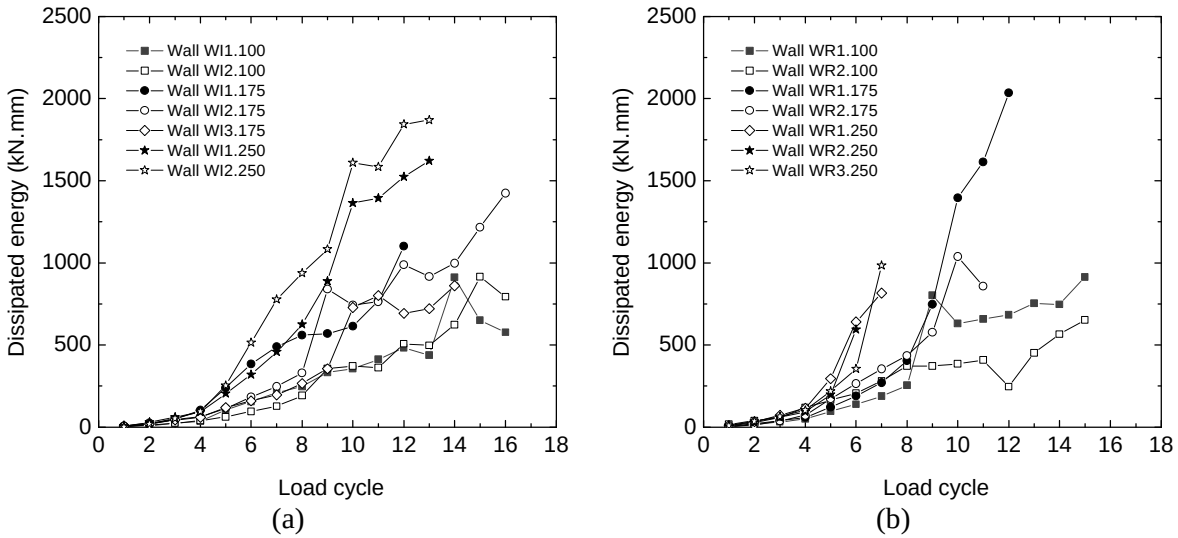


Figure 6.37 – Evolution of dissipated energy for each cyclic loop in mortared walls; (a) walls WI; (b) walls WR

As can be observed, the dissipation of energy found for both types of wall tends to increase with larger lateral displacements. This is necessarily associated with the damage growth and thus with the development of nonlinear displacements. In fact, by its definition, large dissipation of energy is equivalent to high energy inside the hysteresis loop, which is achieved if permanent nonlinear displacements develop. However, it is noticed that the evolution of dissipated energy is not directly proportional to the lateral displacements. The sudden increase of the dissipated energy is almost always associated to the full opening of diagonal cracks, such as in wall WR1.100 for a lateral drift of 1.45% (load cycle nº9) or in wall WR1.175 for a lateral drift of 1.45% and 1.67% (load cycles nº9 and nº10). In walls submitted to a normal stress of 1.25N/mm$^2$, the most significant energy rise occurs for a lateral drift of 0.83% (load

cycle nº6) in walls WR1.250 and wall WR2.250 and for a lateral drift of 1.04% (load cycle nº6) in wall WR3.250, in correspondence with the opening and growth of diagonal cracks. Nevertheless, an energy jump appears also in wall WI1.100 as the result of the failure of the upper right corner, leading to considerable increase on nonlinear displacements in the positive direction of the wall. Similar occurrence is recorded in wall WI2.175 with the opening of a stepped unit-mortar interface crack in the positive direction for a lateral drift of 1.45% (load cycle nº9) and in the wall WI3.175 for a lateral drift of 1.67% (load cycle nº10). For the walls WI1.250 and WI2.250, the dissipated energy undergoes a sharp increase when the thickness of stepped diagonal cracks previously opened suffers a sudden increase.

As is shown in Figure 6.38, the energy dissipated by dry masonry walls is rather low, when compared to the other walls. Similarly to irregular and rubble masonry walls, the dissipated energy increases with lateral displacement, but a much more regular increase rate is found. This feature is in agreement with the prevailing rocking failure mechanism that governs the cyclic in-plane lateral response of dry masonry walls.

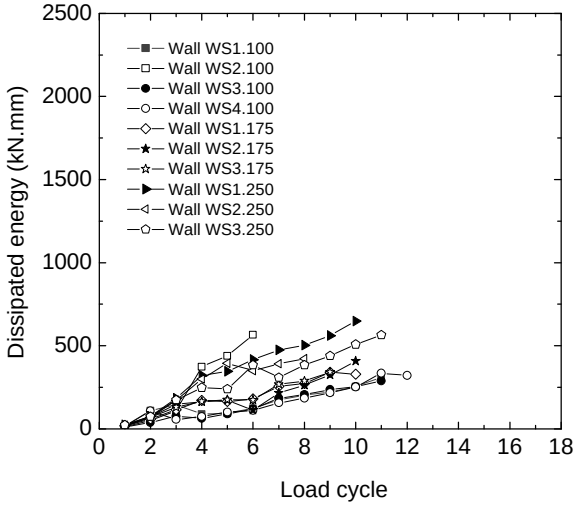


(a)

Figure 6.38 – Evolution of dissipated energy for each cyclic loop in dry masonry walls

Furthermore, from the three distinct types of walls, it is clear that the total dissipated energy depends on the level of pre-compression. Although the differences are not significant for low levels of lateral displacement, for increasing lateral displacements, there is a tendency for the walls submitted to higher levels of pre-compression to exhibit a larger amount of dissipated energy. This feature can also be confirmed through Figure 6.39, where the ratio between the total dissipated energy (cumulative dissipated energy) and the total input energy (cumulative input energy), $E_{diss}/E_{inp,}$ is shown.

As seen in section 6.5.3, the walls submitted to higher normal stresses also have larger values of lateral strength, which can influence the global evaluation of the dissipative features of the walls, provided that the computations are based on the force-lateral displacement diagrams. Therefore, a more objective measure of the dissipated energy is required. For example, it can be adopted the energy dissipation normalized by the elastic energy absorption of the equivalent elastic-plastic model (Shing *et al*., 1989). Thus, for a given lateral drift associated to a certain damage state, the normalized cumulative dissipated energy, $E_N$, is defined as:

$$E_N = \frac{1}{H_u d_e} \sum_{i=1}^{n} E_{i\,diss} \tag{6.7}$$

where $n$ is the load cycle corresponding to a certain lateral drift. $H_u$ and $d_e$ are, respectively, the ultimate lateral load and the elastic displacement of the equivalent elastic-plastic model as defined in section 6.5.1.

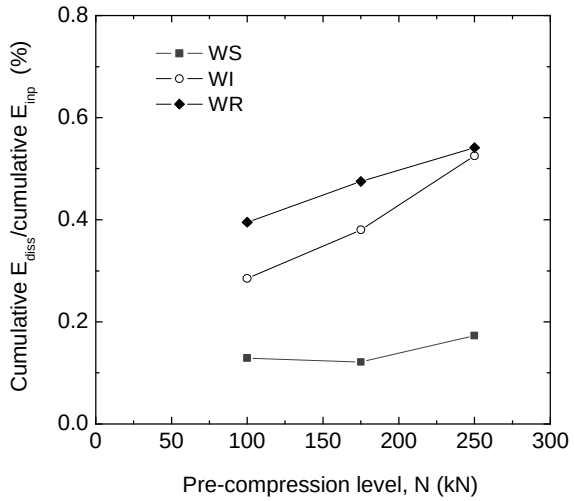


Figure 6.39 – Relation between pre-compression level and the cumulative $E_{diss}$/cumulative $E_{inp}$ ratio

Concerning the evolution of cumulative normalized dissipated energy as a function of the lateral drift, which is shown in Figure 6.40a for all walls, some relevant aspects should be pointed out. It is possible to define two groups corresponding to distinct evolutions of the normalized dissipated energy. The first includes the walls WI and WR and the second refers to the dry masonry walls. The increase rate of cumulative normalized dissipated energy is notably larger in case of irregular or rubble masonry walls compared to dry masonry walls. The cumulative normalized dissipated energy exhibits low to moderate values for lateral drifts ranging between 1.04% and 1.45%, generally associated to the attainment of the maximum lateral resistance (Life Safety performance level, LS). This seems to confirm that low to moderate damage develops before the maximum lateral force is reached. In fact, the major damage growth occurs after the peak lateral strength in correspondence with the increase of the cumulative dissipated energy. A similar trend was reported by Alcocer and Zepeda (1999) for the seismic behavior of multi-perforated clay brick walls. It is also possible to point out a tendency for walls WR and WI submitted to higher levels of pre-compression to exhibit larger values of cumulative dissipated energy than the walls submitted to low levels of pre-compression. This reveals that the dissipated energy is related to the prevailing failure pattern, which is further confirmed by the distinct evolution of the normalized dissipated energy found for walls WR.100. In spite of both walls being submitted to the same pre-compression level, the cumulative normalized dissipated energy is remarkably larger in case of wall WR1.100 that fails in shear. On the contrary, dry masonry walls WS submitted to the lowest level of pre-compression exhibit the larger cumulative dissipated energy. Note that the failure mechanism is common for all pre-compression levels but walls WS.250 are more brittle. This seems to be related to the higher probability of these walls to fail by toe crushing. A similar finding was pointed out by Shing *et al.* (1990) for flexural specimens failing by toe crushing. Another particular feature of the lateral behavior of dry masonry walls governed by a rocking

mechanism is associated to the progressive decrease on the ratio between the dissipated energy and the input energy, see Figure 6.40b. Again, exception should be made for wall WS2.100 whose lateral behavior is not governed by rocking.

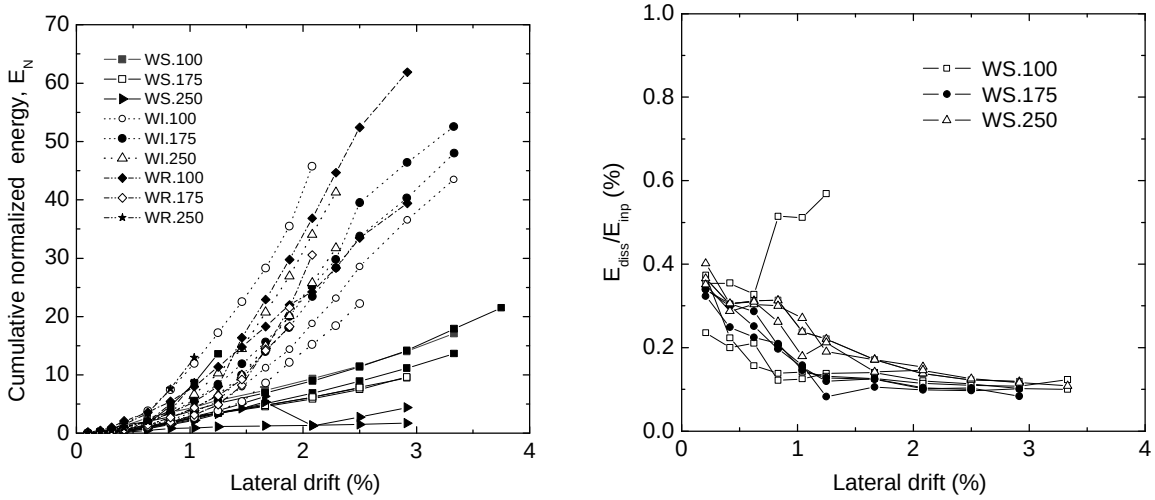


(a) (b)

Figure 6.40 – Features of energy dissipation; (a) evolution of the cumulative normalized dissipated energy as a function of the lateral drift (all walls); (b) relationship between the lateral drift and the ratio between dissipated energy and the input energy (dry masonry walls)

Specimens with lateral cyclic behavior predominantly characterized by a rocking mechanism do not show considerable stiffness degradation, as is the case of dry masonry walls and the specimens of walls WI and WR subjected to low to moderate levels of pre-compression. However, opposite behavior is found in walls, in which other failure modes prevail. The degradation of the lateral stiffness was assessed by calculating a secant stiffness for each loading cycle as the slope of the straight line that connects the maximum and minimum lateral strength obtained from the force-displacement diagrams (Zepeda *et al.*, 2000). As can be observed from Figure 6.41, for the walls WI1.175, WI.250, WR1.100, WR.175 and WR.250, a pronounced decreasing on the values of lateral stiffness takes place as the lateral drift increases. Besides, a similar exponential shape seems to represent well the stiffness deterioration function for all the analyzed walls.

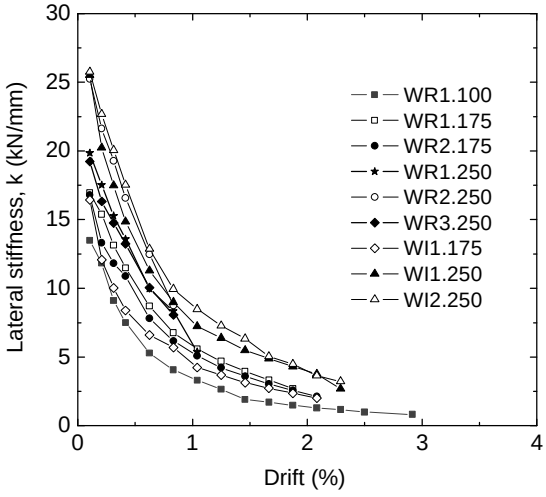


Figure 6.41 – Degradation of the lateral stiffness for selected walls

## 6.6 Failure criteria for masonry

During the last few decades several failure criteria have been proposed to describe the in-plane static strength of masonry walls (Yokel and Fattal, 1976; Turnsek and Sheppard, 1980; Samarasinghe and Hendry, 1980; Mann and Muller, 1982; Drysdale and Hamid, 1984; Dialer, 1991; Dhanasekar *et al*., 1985; Ganz, 1989; Andreaus, 1996). Given the anisotropic nature of masonry, consisting of units, vertical and horizontal mortar joints, failure cannot be associated only to a single unfavorable condition. Thus, failure criteria include distinct expressions that define a particular stress state associated with a possible failure mode. Despite masonry shear walls being typically submitted to a biaxial stress state, the failure criteria cannot be defined simply from the principal stresses, as it is common in isotropic materials, see Figure 6.42. Most contributions for the development of a consistent failure criterion are phenomenological, meaning that they are based on the interpretation of data from the experimental tests.

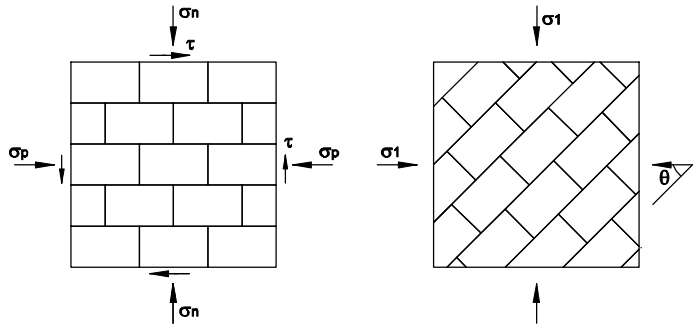


Figure 6.42 – Possible representations of the stress components; (a) stress components using the material axis reference; (b) principal stresses and rotation angle, with respect to material axis

Here, the experimental results of the current testing program are analyzed in the light of selected failure criteria. In order to allow a straight forward comparison of the criteria, the weight of the walls and steel profiles is neglected. For information, the total weight of the actuator and steel profiles is about 2.2kN.

### 6.6.1 *Simplified formulations for the shear strength prediction*

The prediction of the in-plane behavior of masonry walls by means of complex numerical methods assumed a central role in the research effort in the scope of masonry structures. However, for design purposes, it is often required to use simplified assumptions that enable a simplified analysis. This section aims at introducing the most used simplified analytical methods to obtain the lateral resistance, which are associated to distinct failure patterns consisting of different limit states occurring in masonry walls under in-plane loading. As widely reported in the literature, when subjected to a combination of horizontal and vertical loads, masonry walls can fail in flexural, shear mode (diagonal shear cracking) or a combination of both, see Figure 6.43a. To the different failure mechanisms contribute not only the boundary conditions and geometry, but also the mechanical properties of the masonry materials (shear strength of unit-mortar interface and tensile and compressive strength of masonry). An increase in the aspect ratio leads to rocking failure, whereas a decrease is associated to shear type failures. As confirmed by the present research, walls

subjected to low compressive stresses behaves predominantly in flexure (rocking), while increasing vertical stress enhances combined flexural/shear responses or even shear failures. The present research indicates that failure modes are also affected by the masonry bond.

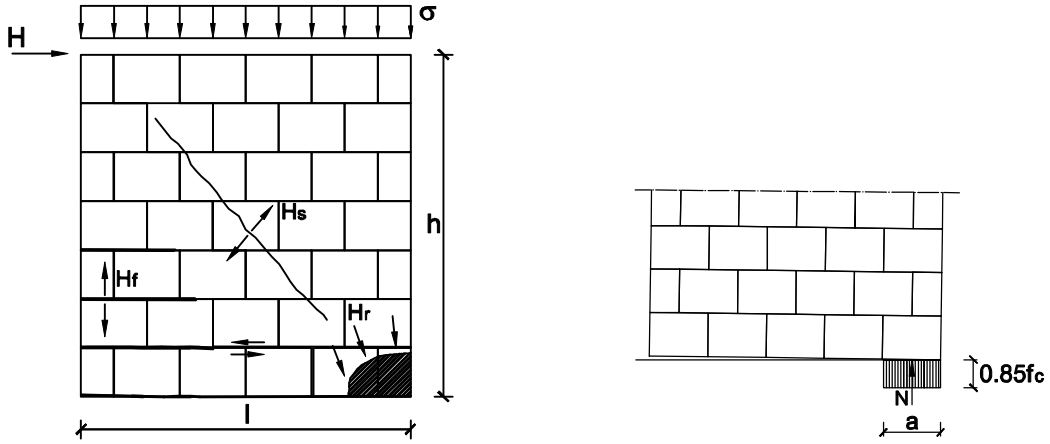


(a) (b)

Figure 6.43 – Simplified approaches; (a) failure modes of unreinforced masonry shear wall; (b) flexural failure at compressed toe (rocking)

Flexural response is ruled by the opening of horizontal or inclined cracks by breaking the tensile bond between units and mortar. Although no failure state is associated to flexural cracking, it generally entails a reduction of stiffness and leads to the onset of the nonlinear behavior of the walls. Assuming a linear distribution of normal stresses, the force corresponding to flexural cracking of a rectangular section with tensile strength capacity is given by the expression:

$$H_f = \frac{s l^2 t}{6h} + \frac{f_{jt} l^2 t}{6h} \tag{6.8}$$

where $h$, $l$ and $t$ are, respectively the height, width and the thickness of the wall, $f_{jt}$ is the tensile bond strength of the bed joint and $s$ is the medium vertical stress (positive sign assumed). The flexural cracking is, thus, a linear function of the applied pre-compression level. Here, in case of dry masonry walls, the tensile bond strength of the bed joint is zero.

After flexural cracking and subsequent reduction of the resistant section of the wall, vertical compressive loading migrates towards the compressive toe. If compressive stresses at the toe exceed the bearing compressive strength of masonry, the limit state is reached by toe crushing. Assuming a rectangular stress block at the base of the wall, as illustrated in Figure 6.43b, the lateral strength associated to flexural response is given by the expression:

$$H_r = s \frac{l^2 t}{2h}\left(1 - \frac{s}{0.85 f_c}\right) \tag{6.9}$$

where $f_c$ is the compressive strength of the masonry and a value of 0.85 is assumed for the reduction of the compressive strength.

The shear response of masonry walls subjected to combined vertical and horizontal loads can be associated to different cracking typology, which depends essentially on the material

properties. Shear stepped cracks following vertical and horizontal joints occurs when the shear strength of the joint is considerable lower than the tensile strength of the units. Another possibility is that diagonal cracks also intercept the masonry units, which reach their tensile strength. Note that the typical shear cracks of the stone walls under study occur in the (mortar) joints as the result of the difference between the low shear strength of the joints and the high strength of the granite used for the units.

Two main simplified criteria have been used to describe the shear failure of panel walls. The first approach consists in a Mohr-Coulomb type criterion, being the ultimate shear strength, $t$, given by the expression:

$$t = c + ms \tag{6.10}$$

where $c$ and $m$ are considered as global strength parameters. This expression is similar to the criteria used to describe the local shear failure at the joint level, but the coefficients $c$ and $m$ presents generally lower values since the local stress state of the joint differs from the stress field of the wall, considered as homogeneous material. Therefore, global strength parameters cannot be directly related to the local shear strength of the bed joints. Two different possibilities can be adopted in the evaluation of the shear strength: using the horizontal section of the wall ($l$x$t$) or considering cracking due to flexure and taking an effective uncracked length (Magenes and Calvi, 1997).

The other approach for the shear resistance is based on the Turnšek and Sheppard (1980) criterion, which is based on the assumption that diagonal cracking takes place when the maximum principal stress at the center of the wall reaches the tensile strength of masonry. Similarly to what was pointed out in section 6.4.1, and to what was reported by other authors (Calvi *et al.*, 1996), diagonal shear cracking can be related to distinct crack patterns, being a single wide isolated crack or diffused cracking, as a combination of joint failure or brick shear-tension splitting.

The stress state is calculated by assuming that masonry is an isotropic and homogeneous material, which is not corresponding to its actual behavior, since tensile strength is dependent on the orientation of the principal stress with respect the bed joints. The tensile principal stress can be calculated as (Turnšek and Cacovic, 1971):

$$s_t = \sqrt{\left(\frac{s}{2}\right)^2 + t^2_{\max}} - \frac{s}{2} \tag{6.11}$$

being the vertical stress, $s$, calculated as $N/tl$, the horizontal stress is negligible and $t_{max}$ is the maximum shear stress. Considering that the shear stress, $t$, assumes a parabolic distribution, the horizontal shear force corresponding to the opening of shear cracks, $H_s$, reads Turnšek and Cacovic (1971):

$$H_s = \frac{f_t \; lt}{b}\sqrt{1+\frac{s}{f_t}} \tag{6.12}$$

where $f_t$ is taken as the tensile strength of masonry. The variable $b$ assumes the value of 1.5 for walls with height to width ratios larger than 1.5. In case of height to width ratios ($h/l$) ranging between 1.0 and 1.5, the shear stress distribution deviates from the parabolic shape

and the horizontal normal stress becomes different from zero. Thus, the shear strength is calculated by considering a value for *b* equal to the height to width ratio. As reported by Magenes and Calvi (1997), the load corresponding to shear cracking is usually higher than $0.85H_{max}$, and, thus, can be assumed an ultimate state.

It should be underlined that the major advantage of the above simplified approaches is the scarce information needed. Apart from the geometrical features of the walls and the average normal stress, only compressive and tensile strength of masonry are required.

#### 6.6.1.1 Assessment of the experimental lateral strength

The simplified criteria given above are now used for assessing the values of the shear strength resulting from the present experimental work. For this purpose, the available data on the material properties obtained in the Chapter 5 with respect to compressive strength of masonry and shear strength properties of the unit-mortar interface are summarized in Table 6.14.

Table 6.14 – Material properties of dry and irregular walls

| Property | $c$ (N/mm$^2$) | $\mu$ | $f_c$ (N/mm$^2$) |
|---|---|---|---|
| Walls WS | 0.0 | 0.65 | 73.0 |
| Walls WI | 0.36 | 0.63 | 18.4 |

The tensile strength of masonry is usually obtained by means of diagonal compression tests. However, in the absence of such information, as indicated by Magenes (1992), the value of tensile strength can be calculated from the shear-compression tests assuming that the first shear cracking occurs when the maximum principal stress at the middle of the walls reaches the value given by equation 6.12. Thus, an average value of 0.11N/mm$^2$ for this property was obtained from the recorded experimental values of the horizontal force corresponding to shear cracking by using this procedure, see Table 6.15. The value of the tensile strength of walls WI is calculated from the force corresponding to shear cracking, recorded in wall WI2_250. For a horizontal force of 68.7kN the tensile strength is 0.12N/mm$^2$. These values are close to the tensile strength obtained from in-situ shear-compression tests conducted on ancient stone masonry walls (Chiostrini and Vignoli, 1992).

Table 6.15 – Average tensile strength of masonry - rubble masonry walls, WR

| Wall | $F_s$ (kN) | $f_t$ (N/mm$^2$) |
|---|---|---|
| WR1.100 | 37.31 | 0.0856 |
| WR1.175 | 61.79 | 0.136 |
| WR2.175 | 53.41 | 0.105 |
| WR1.250 | 57.51 | 0.0892 |
| WR2.250 | 71.31 | 0.132 |
| WR3.250 | 64.78 | 0.111 |
| Average | | 0.110 |
| CV(%) | | 19.2 |

The evaluation of the theoretical lateral force corresponding to the flexural cracking is calculated assuming a zero value for the bond strength, $f_{jt}$. If this is true in case of dry masonry walls, for the walls WR and WI this procedure is only an approximation. The

comparison between the experimental results of the first crack lateral stress, $t_{cr}$, and the flexural predicted values is displayed in Figure 6.44. It can be observed that the lateral force corresponding to flexural cracking increases as the normal stress increases. The differences between experimental and theoretical values can be viewed as acceptable for dry walls. For irregular walls, WI, the flexural cracking envelope underestimates the cracking lateral force for all levels of pre-compression, which is explained by assumption of zero bond tensile strength. The same tendency is also followed for low to moderate levels of pre-compression applied on walls WR. However, in average, a reasonable prediction of flexural cracking load is also obtained for rubble masonry walls.

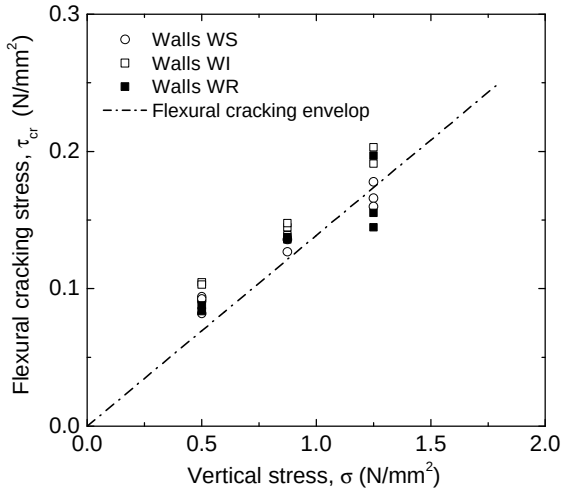


Figure 6.44 – Evaluation of the experimental lateral stress corresponding to flexural cracking

The comparison of the analytical flexural and shear strength envelopes with experimental lateral resistance obtained from the shear tests is displayed in Figure 6.46a for the walls WS. The lateral resistance obtained in shear tests is remarkably close to the flexural resistance calculated for a compressive strength of $f_c$ = 73.0N/mm$^2$. However, flexural response appears to be an upper bound of the lateral resistance, possibly due to the very high compressive strength found in the prism tests, which are hardly representative of the masonry condition and state of stress in the compressed toe. If a statistical regression is fitted to the experimental data, an expressive coefficient of determination ($r^2$ = 0.97) is found to exist for the linear relation between the lateral resistance and the vertical pre-compression: $t = 0.382\,s$. This means that the behavior of dry masonry walls is also well described by the shear failure criterion based on the Coulomb's friction formulation. Similarly to what was reported in the literature (Magenes, 1992), the friction coefficient obtained in shear walls ($m$ = 0.382) is remarkable lower than the local friction coefficient found for dry bed joints ($m$ = 0.65). A friction coefficient of $m$ = 0.33 is obtained by using the simplified model of Mann and Müller (1982). Figure 6.45b shows that a good agreement is obtained between experimental values corresponding to the opening of the diagonal crack, defined in Section 6.4.4, and the failure envelope associated to shear sliding of the bed joints. This means that the characteristic failure of dry walls is, in fact, inside the friction failure of the bed joints and rather far of the failure domain describing the cracking of the bricks, which is the result of the large tensile strength of the granitic units $f_{bt}$ = 2.8N/mm$^2$.

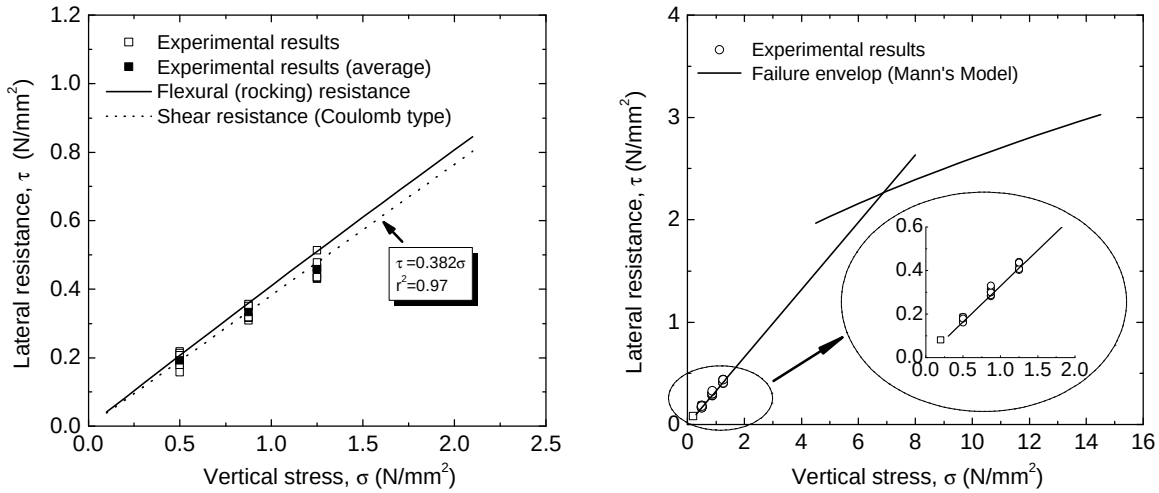


Figure 6.45 – Comparison between the experimental and theoretical lateral resistance: walls WS

The assessment of the experimental shear strength of walls WI and WR by the simplified models is based on the results displayed in Figure 6.46. Although with acceptable values, it is observed that the experimental lateral resistance of irregular walls is overestimated by flexural resistance envelope corresponding to a compressive strength $f_c$ = 18.4N/mm$^2$ for the intermediate and mainly for the highest level of vertical pre-compression. In terms of average lateral strength, the difference for the flexural envelope is, respectively, 10.8% and 13.8%. Again, a better prediction would be attained if low values of compressive strength were considered. This can be indicative that the value of the compressive strength normal to bed joints obtained in the masonry prisms can be a rough estimation and can not be a reliable representative value of the actual compressive strength of irregular masonry. In fact, neither the irregular arrangement of the stones nor the vertical joints are taken into account in the prism assemblages. Note that the flexural envelope is not very sensitive to the compressive strength for the range of vertical pre-compression levels under analysis, particularly for low to moderate values. Although flexural typical failure characterizes the in-plane behavior of this type of walls, a significant approximation to the lateral strength of this type of walls is also attained with the Coulomb failure. A linear relation was found to exist between the lateral and the vertical strength, ($t$ = 0.051 + 0.297$\sigma$, $r^2$ = 0.95), as the result of the statistical fitting to the experimental data. Note that the value of the lateral strength obtained in the first wall WI1.175 was excluded from the data. Similarly to dry walls, the shear strength is calculated by considering the gross horizontal section of the wall. Also in this case, a significant reduction in the global strength parameters ($c$ = 0.051N/mm$^2$, $m$ = 0.297) is achieved relatively to the shear strength parameters obtained for the mortar bed joints ($c$ = 0.36N/mm$^2$, $m$ = 0.63). The Turnsek's envelope based on the assumption that diagonal cracks arises for a certain stress state at the middle of the panel, deviates clearly from the experimental lateral resistance. The shear cracks that develop predominantly in the unit mortar interfaces appears to be more the result of the friction failure unit-mortar interface than the outcome of the critical stress state at the middle of the panel.

With respect to rubble masonry walls, apart from the specimens submitted to the lower level of pre-compression, the flexural envelope obtained using the compressive strength found for irregular walls ($f_c$ = 18.4N/mm$^2$) deviates clearly from the average lateral for the highest level of pre-compression, see Figure 6.46b. The flexural resistance would be better adjusted if a lower compressive strength ($f_c$ = 5.0N/mm$^2$) was adopted. In the absence of an experimental

value for the compressive strength, this value seems to be suitable and realistic in order to approximate the lateral resistance of this type of walls, even if the strength of the walls subjected to higher pre-compression levels is not well reproduced. This is due to the different failure mechanism triggered in this case. The Coulomb type friction law ($t = 0.112 + 0.193\sigma$, $r^2 = 0.81$) resulting from the linear fitting to the experimental results shows that with respect to the irregular walls, a considerable lower value of the coefficient of determination is achieved. The higher scatter is, to great extent, influenced by the lower values of the lateral strength obtained for the higher levels of pre-compression. In spite of the heterogeneity, the shear envelope based on the simplified Turnšek's model gives a reasonable prediction of the average lateral resistance exhibited by the rubble masonry. For the highest level of pre-compression the difference for the average shear strength in only about 6%. It provides also a reasonable prediction of the average shear strength for walls submitted to intermediate pre-compression levels (difference of about 11%). This is the result of the failure being governed by mixed flexural/shear and shear modes of failure obtained, respectively for moderate and high levels of pre-compression. Note that the experimental results obtained in rubble masonry walls possibly suggest the need of a failure criterion composed by different envelope functions, as proposed by Mann and Muller, (1982) to better describe distinct failure modes occurring for different shear/compression ratios.

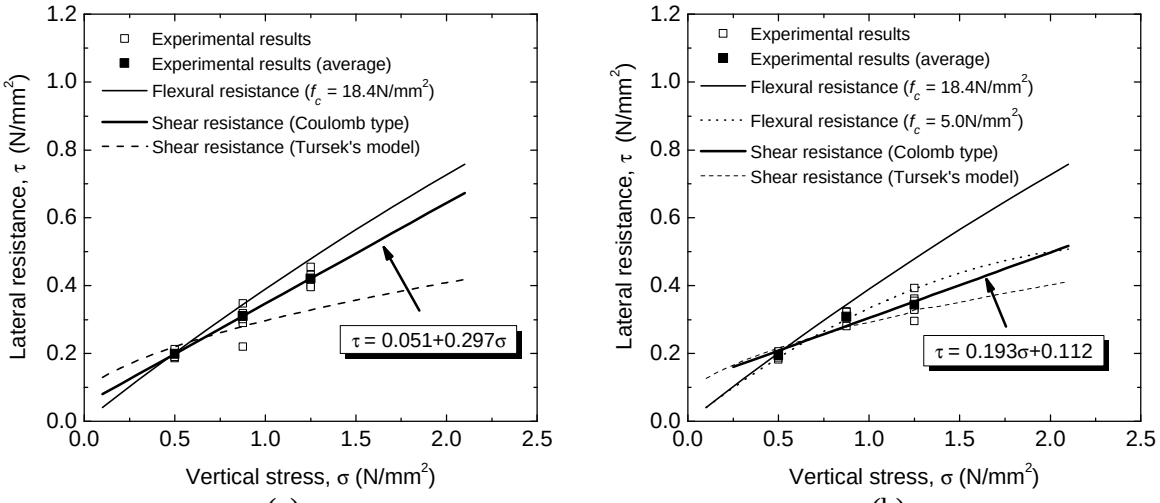


Figure 6.46 – Comparison between the experimental and theoretical lateral resistance; (a) walls WI; (b) walls WR

Despite the known key role of the geometry of the walls in the shear response of walls, the results obtained in the present work show that vertical normal stresses and masonry bond are also quite relevant. The shear strength is almost insensitive to the arrangement of the stones for low to moderate normal stress states but this observation does not hold for the highest level of pre-compression under consideration. Thus, the shear strength was found to decrease as the randomness of the masonry bond increases, particularly for the highest level of normal stresses, which is associated to typical diagonal shear failure. Moreover, it has been shown that a single simplified failure criterion can be difficult to obtain. Therefore, a recent approach based in a strut-and-tie model is investigated in the next section.

### 6.6.2 *Assessment of the shear strength by a simplified equilibrium model*

Although equilibrium models based on struts and ties have been widely accepted by modern concrete codes for design and assessment purposes, almost no information is available on its applicability in the scope of masonry structures. The main reason of this is related to the brittle nature of the masonry material and its reduced ability to conduct tensile stresses. However, some developments arose recently from a simple equilibrium model for assessment of the shear strength of masonry shear walls proposed by Roca (2004). The model is based on the lower bound theorem of plasticity and its applicability can be justified by plastic mechanisms associated to the limit sate of the wall: friction in joints and compression failure of masonry. This means that ultimate mechanisms must be governed by the maximum friction in the joints or maximum compression at the nodes.

In case of shear walls submitted to uniformly distributed loads, a model composed by smeared struts arranged according to a parallel or fan distribution is shown in Figure 6.47. In the fan model indicated in Figure 6.47a, the slope of the struts varies gradually to make the stress paths consistent with the geometry, with $\beta_m$ being defined as the average slope the struts. The model shown in Figure 6.47b consists of a modified fan model that complies with the limitation on the maximum slope of the struts. It becomes equivalent to the fan model in case of very compressed or narrow walls, when the width of the minimum contact surface required to transfer the vertical load, *N*, in plastic regime, *m*, follows the expression:

$$m \geq l - h\tan\alpha \qquad m = \frac{N}{tf_c} \tag{6.13}$$

where $l$ and $h$ are, respectively, the width and the height of the wall, and $\alpha$ is the maximum slope of the struts. Depending on the type of bed joints, the maximum slope of the struts is given by the expressions:

$$\begin{aligned} &\tan\alpha = m && \text{Dry bed joints} \\ &\tan\alpha = m + \frac{c}{s} && \text{Cohesive bed joints} \end{aligned} \tag{6.14}$$

where $m$ is the tangent of the friction angle of the dry joint or unit-mortar interface, $c$ is the cohesion and $s$ is the vertical compression. Thus, the slope of the parallel struts, $\beta_p$, and the average slope of the struts with variable inclination, $\beta_f$, are defined as follows:

$$\begin{aligned} &\tan\beta_p = \tan\alpha \\ &\tan\beta_f = \frac{\tan\alpha}{2} \end{aligned} \tag{6.15}$$

Thus, for the models shown in Figure 6.47b, c or d, the horizontal load is given as follows (Roca, 2004):

$$H = N\tan\beta_m = N\frac{l-m}{2h} \qquad \text{if} \qquad m \geq l - h\tan\alpha \tag{6.16}$$

and by:

$$H = N\tan a\left[1-\frac{h}{2l}\tan a\left(\frac{1}{1-n}\right)\right] \qquad \text{if} \qquad m \le l - h\tan a \tag{6.17}$$

being $n$ given by:

$$n = \frac{m}{l} \quad = \frac{V}{tlf_c} \tag{6.18}$$

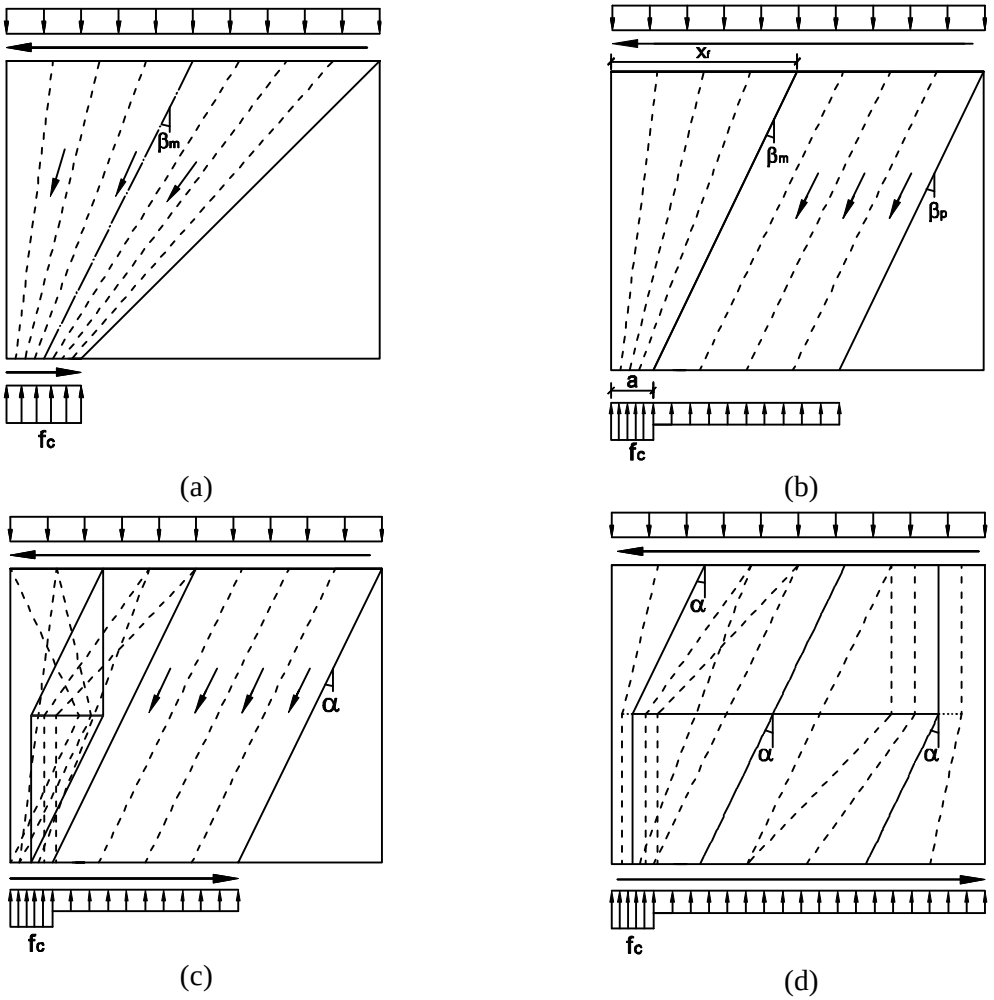


Figure 6.47 – Models proposed for walls submitted to uniform load, Roca (2004)

These models were used to predict the horizontal shear resistance of the cyclic tests of the walls submitted to uniform distributed vertical load from the monotonic and cyclic tests described in Section 6.4.2. This assumption is valid since the rotation of the upper steel beam is free.

In case of dry masonry walls, the model shown in Figure 6.47b is possible to develop for any of the pre-compression levels considered ($m<l-htana$), and the horizontal shear load, $H$, is obtained by expression 6.17. As is shown in Figure 6.48, good agreement was found between the experimental and the predicted values of the maximum horizontal load. Note that for the high compressive strength of masonry considered, $f_c$ = 73N/mm$^2$, the failure envelope defined by equation 6.17 is practically linear. This model is thus practically independent on the compressive strength of the wall. This also means that in the attainment of the ultimate load,

sliding failure mechanism takes an important role in the shear response. If a linear regression was obtained by fitting the predicted shear load for distinct levels of pre-compression, a ratio of approximately 0.4 ($H = 0.393N$, $r^2 = 1$) would be found between lateral resistance and vertical pre-compression level. This value is also indicated by EC6 (2001) as the friction coefficient of the Coulomb type criteria defining the shear strength of masonry walls.

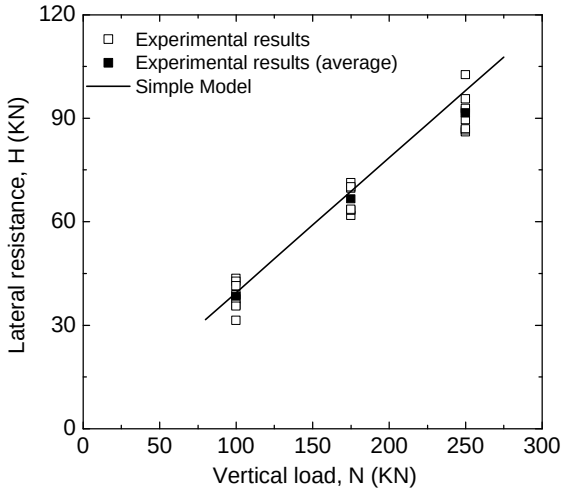


Figure 6.48 – Comparison between the experimental and predicted lateral resistance given by the simple model for dry masonry walls

The evaluation of the usage of the simple models to predict the maximum horizontal load of cohesive walls is performed by means of the results displayed in Figure 6.49. The values of the predicted shear strength are obtained through the expression 6.16. Using the value of compressive strength obtained by testing irregular masonry prisms, $f_c$ = 18.4MPa, it can be observed that predictions deviate from the experimental strength for the higher level of pre-compression. The error obtained for the average lateral strength (~15.2%) can be, to great extent, attributed to cracking of stones in the diagonal crack before the maximum lateral force is attained verified in wall WI2.250. Besides, as previously discussed, it seems reasonable to admit that compressive strength of masonry could exhibit a lower value. According to Roca (2004), due to the anisotropy of masonry, the compressive strength of masonry walls may be significantly dependent on the angle of the struts and the resulting stress state. In fact, a much better prediction would be attained for a compressive strength $f_c = 7.0\text{N/mm}^2$. It is noticed that the failure envelope obtained with equation 6.16 is rather similar to the flexural failure criteria pointed out in section 6.7.1. In fact, both approaches are based on the same plastic mechanism associated to yielding of the masonry in compression.

Concerning rubble masonry walls, a good agreement between experimental results and the shear prediction through the simplified model for low and moderate levels of pre-compression would be achieved if a the compressive strength ($f_c = 5.0\text{N/mm}^2$) was considered, see Figure 6.49b. Nevertheless, also this model deviates definitely from the experimental lateral strength obtained for the highest level of pre-compression, which is associated to the fact that ultimate state is ruled by diagonal tension cracking that develops before maximum lateral resistance is mobilized. This simplified model also suggests a failure criteria composed by different envelope functions for this type of masonry walls.

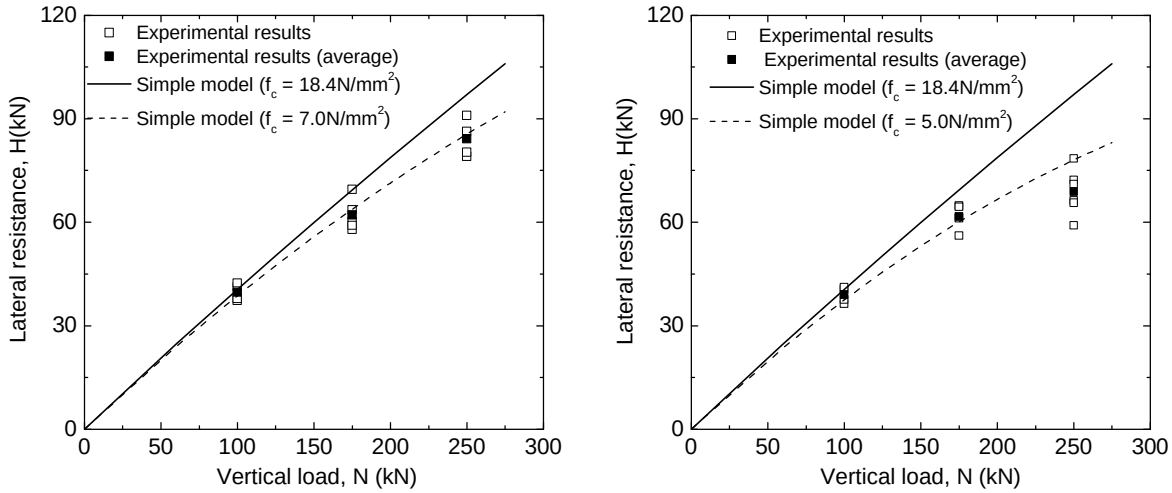


Figure 6.49 – Comparison between the experimental and predicted lateral resistance given by the simple model; (a) irregular masonry walls, WI; (b) rubble masonry walls, WR

## 6.7 Concluding remarks

In order to evaluate the seismic performance of stone masonry walls an experimental program composed by in-plane static cyclic tests was carried out. Different textural arrangements and axial load levels were adopted in order to simulate distinct types of walls existing in ancient buildings and variable normal stresses. The height towidth ratio was kept constant and equal to 1.2.

For the selected height/width ratio, it was observed that failure modes depend clearly on the level of axial load and on the textural arrangement. For low to moderate axial loads, the flexural/rocking mechanism prevails, whereas, for high levels of pre-compression, the lateral response is either characterized by mixed flexural/shear/toe crushing or by shear failure. Rubble masonry walls fail in shear for moderate and high levels of axial load. Nevertheless, they are very sensitive to the textural arrangement and can fail in shear for low levels of pre-compression.

The information provided by lateral force-lateral displacement diagrams enables the assessment of the seismic performance in terms of energy dissipation capacity and nonlinear deformation, defined from the ductility. Moreover, the nonlinear deformation of the walls was evaluated in the scope of performance based concepts. Apart from rubble masonry walls submitted to high levels of pre-compression that exhibit a brittle failure, it was verified that masonry stone walls exhibit large nonlinear deformation up to the collapse state. The ductility factor was found to decrease as the irregularity of the masonry bond increases and, particularly, as the axial load level increases. Considerable lateral drifts were recorded at the maximum lateral resistance, without considerable damage. It is after the maximum lateral resistance is attained that higher amount of energy is dissipated, which reflect the progressive increase of damage. In spite of the high nonlinear deformation capacity of dry masonry walls, they are not able to dissipate energy due to the rocking mechanism obtained. Considerable high amount of energy is dissipated by irregular and rubble masonry walls, for the same geometry. In these walls, higher level of energy dissipation is associated to moderate and high levels of pre-compression, which reflects the distinct failure modes that govern the lateral response.

The prediction of the lateral resistance though simplified analytical methods appears to agree reasonably well with the experimental results, even if it seems difficult to obtain a single failure criterion, mainly as rubble masonry walls is concerned. Moreover, the suitability of an equilibrium approach based on strut-and-tie model to predict the lateral strength was reasonably confirmed in case of lateral response is mobilized by plastic mechanisms, namely flexural and shear sliding response.

# 7. CONCLUSIONS AND FUTURE WORK

The need of structural rehabilitation and strengthening of ancient masonry structures has been resulting in a progressively increasing interest from the research community in this area. In spite of recent efforts, both in the numerical and experimental techniques applied to masonry structures, the structural behavior of stone masonry walls subjected to seismic actions received only moderate attention from the research community. This thesis focuses mostly on the experimental field and represents a step forward in the understanding of materials and the mechanics of ancient masonry with comprehensive mechanical characterization of stone masonry.

## 7.1 Experimental investigation on the stone masonry

The mechanical characterization of typical masonry units, considered to be representative of ancient constructions, involved an extensive experimental program composed by direct tensile and compressive tests on a set of different types of granites aiming at characterizing different types of granite from Portugal. Besides, the possibility of estimating the mechanical properties of granites from simple and economical non-destructive techniques was also addressed. Finally, the shear and compressive composite behavior of granitic masonry assemblages was investigated.

*Mechanical characterization of granites*

The tensile and compressive testing programs enabled the definition of the elastic, tensile and compressive strength properties of distinct types of granites, which appear as fundamental input data for advanced numerical analysis, but also in the design of remedial measures. The major significance of the tensile and compressive mechanical characterization carried out in this work deals with the obtainment of the fracture properties of different types of granites, practically non-existent up to date. This was achieved by considering appropriate control testing techniques.

The pre-peak compressive behavior of granites was successfully characterized by adopting stress markers defining distinct levels of damage. The Poisson's ratio appeared to be an additional property that enables the evaluation of the pre-peak fracture process. It was shown that compressive microcracking in the pre-peak regime is predominantly governed by tensile mechanisms since a reasonable correlation was found between pre-peak normalized compressive fracture energy and the normalized mode I fracture energy. The analysis of the pre-peak tensile and compressive test results revealed that granites behave nonlinearly since early stages of deformation. The tensile and compressive strength are effective measures of the brittleness of granites as good correlations were found between these properties and the normalized mode I ductility.

A wide range of tensile/compressive strengths and elastic properties were found among the distinct types of granites under study. This variation is explained by the internal microstructure of the granites, weathering state and, to minor extent, by the mineralogy. The weathering state of granites is reflected by a remarkable reduction on the tensile/compressive loading bearing capacity. The modulus of elasticity decreases in weathered granites, whereas the Poisson's ratio exhibits higher values. In general, weathered granites exhibit a smoother

softening post-peak tensile/compressive behavior, which is reflected by its higher ductility (normalized fracture energy). This behavior is explained by the alteration of the internal structure of the granites. The weathering of granites leads to the increase of the heterogeneity by the higher number of voids and cracks due to the degradation of the bond mineral interfaces. This behavior is reflected by the reasonable correlation between compressive strength and porosity. The correlation between tensile strength and porosity is less evident, given the high anisotropy exhibited by granites under tensile loading. In fact, planar anisotropy associated to foliation or rift planes represents a particular weak plane when load is applied perpendicularly to such weakness. This leads to lower values of the tensile strength when tensile loading is perpendicular to foliation or rift planes and to lower values of the compressive strength when compressive load is parallel to the planar anisotropy. To this behavior contributes also the compressive crack patterns composed by axial or subaxial failures. The anisotropic behavior is also reflected in the elastic properties, being a higher modulus of elasticity obtained in the direction of foliation or rift planes. The anisotropy is also the main reason by which only a rough correlation between the tensile and compressive strength was found. However, good correlations were found between the tensile/compressive strength and the modulus of elasticity. Although in a minor scale, the mineralogy is also a factor that explains the variation of the mechanical properties. Biotite granites exhibit both larger strength and elastic properties than two mica granites. The moisture content was found to take an important role in the deformability and strength properties of granites under tension and compression. The granites are considerably weakened by the addition of water and a remarkable reduction in compressive deformability was found.

The characterization of the relief of the fractures surfaces obtained under tensile loading was made by considering texture profiles acquired by a 3D topographic inspection system in two perpendicular directions. For each profile, the microroughness was set apart from the macroroughness (waviness) by a suitable filtering procedure and a linear correlation was found between mode I fracture energy and the microroughness. Rougher surfaces are associated to a higher consumption of energy. The planar anisotropy can significantly affect the roughness of the fracture surfaces. This is particularly remarkable when feldspar phenocrystals flow structures are present. Rather smooth fracture surfaces are obtained when tensile load is perpendicular to this planar anisotropy.

*NDT - non-destructive techniques applied to granites*

Simple and economical non-destructive techniques as such ultrasonic pulse velocity and Schmidt hammer revealed themselves as potential tools able to predict the strength and elastic properties of granites. Significant novel statistical correlations were proposed between the ultrasonic pulse velocity (*UPV*) and mechanical properties like tensile/compressive strength and modulus of elasticity. Similarly, Schmidt hammer rebound number can also be used in the preliminary prediction of the elastic and strength properties. Moreover, an indication of the weathering state of the granites is possible. Given the good correlations between *UPV* and fracture properties, this technique appears to be a simple tool to evaluate also the brittleness of granites. It is stressed that ultrasonic pulse velocity can give good indications about the crack damage growth in compressive tests. It was found that the lowering of the *UPV* is remarkable after interaction of initiated microcracks. The *UPV* is also able to detect planar anisotropy. Planar anisotropy associated to the foliation or to the rift plane yields remarkable anisotropy of the ultrasonic pulse velocity. Higher values of velocity were recorded in the

direction parallel to the foliation or rift planes. Both *UPV* and Schmidt rebound number are affected by the physical properties, namely porosity and density, meaning that they can provide indications about the physical properties of the granites.

It should be mentioned that the proposed correlations may be affected by the moisture content since it was found that water saturation led to a significant increase of the ultrasonic velocity. Besides, it was shown that water saturation can hide the planar anisotropy exhibited by granites. This means that further research is needed to clarify the effect of the moisture content, which can be achieved if several moisture contents are considered.

*Shear and compressive behavior of masonry*

These tests aimed at providing needed data to use in the analysis of the shear behavior of masonry walls. However, interesting conclusions can be highlighted from the direct shear tests conducted on dry and mortar joints, as well as from the compressive tests carried out on masonry prisms.

The Coulomb's type failure criterion was found to describe the shear behavior of dry and mortar joints. An elastic perfectly plastic diagram was found to characterize the monotonic and the cyclic envelope of shear tests conducted in dry masonry joints. No significant differences in the frictional behavior of dry joints under extreme moisture contents (oven dry and saturated) were recorded. It was found that dry joints can be considered as non-dilatant. Mortar joints exhibit post-peak softening behavior up to a certain load level from which frictional mechanisms govern the shear behavior of this type of joints, with the attainment of considerable plastic deformations. Only for low levels of pre-compression, a systematic expansive trend was verified up to peak stress. For this case, it was found that dilatancy decreases significantly as the shear displacement increases.

Concerning the compressive behavior of masonry prisms, it was found that the compressive behavior of dry masonry stone prisms appears to be highly dependent on the roughness of surfaces of the joints. Compressive strength and elastic modulus are remarkably lowered by the roughness of the joint. The influence of the material of the joints on the compressive behavior is highlighted by considering distinct interlayer materials. The comparison of the performance of masonry prisms with granitic soil and low strength mortar joints revealed that the mechanical compressive behavior of masonry is considerably affected by the deformability properties of the bed joint material.

## 7.2 Experimental investigation on the cyclic shear walls behavior

The evaluation of the seismic performance of stone (granitic) masonry walls was achieved by an extensive experimental program composed by in-plane static cyclic tests. Different masonry bonds and axial load levels were adopted in order to simulate distinct types of walls existing in ancient buildings and variable normal stresses, being constant the height to width ratio.

The dependence of the failure modes on the level of axial load and on the textural arrangement was shown. For low to moderate axial loads, the flexural/rocking mechanisms govern the cyclic response of the shear masonry walls, while mixed flexural/shear/toe crushing or shear failure prevails for high levels of pre-compression. It is stressed that rubble masonry walls fail in a mixed flexural/shear mode and shear mode, for moderate and high

levels of axial load respectively. Additionally, it is stressed that the rubble masonry walls are very sensitive to the textural arrangement and can also fail in shear for low levels of pre-compression.

Apart from rubble masonry walls submitted to high levels of pre-compression that exhibit a brittle failure, it was verified that masonry stone walls exhibit large nonlinear deformation up to the collapse state. This feature is mostly associated to the typical flexural rocking response. In spite of this characteristic behavior, the ductility factor was defined as the ratio between the maximum displacement and the elastic displacement of the equivalent elastic-plastic model. It was found that ductility decreases as the irregularity of the masonry bond increases and, particularly, as the axial load level increases. Besides, considerable lateral drifts were recorded at the maximum lateral resistance, without considerable damage. However, it is stressed that ductility of dry masonry walls is attributed to higher nonlinear displacements and not as a measure of the ability to dissipate energy. In fact, it was found that this type of walls has a low capacity to dissipate energy. On the contrary, high amount of energy is dissipated by irregular and rubble masonry walls. In these walls, a higher level of energy dissipation is associated to moderate and high levels of pre-compression when compared to the lower pre-compression level, which reflects the distinct failure modes that govern the lateral response. The cumulative dissipated energy indicates that the most dissipation takes place after maximum lateral load is attained, which is followed by progressive increase of the damage.

The existent simplified models originally developed for brick masonry walls appear to predict reasonably well the lateral resistance of stone masonry walls. However, a better agreement would be possibly attained if the compressive strength was obtained more realistically. The suitability of an equilibrium approach based on a strut-and-tie model to predict the lateral strength was reasonably confirmed in case that the lateral response is mobilized by plastic mechanisms, namely flexural and shear sliding response.

## 7.3 Future work

### 7.3.1 *Materials*

In the scope of mechanical characterization of masonry materials some aspects that deserve further attention are highlighted:

- Evaluation of the role taken by the mineralogy in the mechanical properties of the granites by means of modal mineralogical composition of the granites

- Numerical simulation of the fracture process of granites under tensile and compressive loading. In this scope, specific analysis of the evaluation of the effect of the microstructure, (planar anisotropy) is to be considered. This goal could be accomplished by using two and three-dimensional lattice models.

- Investigation of the fractal nature of the fracture surfaces and possible further correlations with fracture properties.

- Further investigation should be considered in the assessment of the role taken by the surface roughness in the shear cyclic behavior of dry masonry joints, mainly concerning the shear strength and shear stiffness/strength degradation.

- Finally, additional investigation should be made to validate the proposed correlations between nondestructive indexes, *UPV* and Schmidt hammer rebound number, and the mechanical properties. This includes laboratorial testing in other types of granites with variable moisture content and an enlarged measurement on site. The latter is of high significance since it can provide the degree of relevance of the empirical correlations.

### 7.3.2 *Stone masonry walls*

In the scope of stone masonry walls, further research in the following aspects particularly of relevance:

- Evaluation of the cyclic behavior of masonry stone walls with similar bonds but with different height to length ratios and further comparison with the results presented herein.

- Investigation of the possible strengthening techniques to be applied in order to improve the seismic performance of stone masonry shear walls in terms of energy dissipation.

- Experimental characterization of the out-of-plane behavior of stone masonry walls.

- Numerical simulation of the cyclic behavior of stone masonry walls based on micro and macro-modeling strategies and comparison with experimental results. The macro-modeling takes the major role in practical applications related to irregular or rubble masonry walls, whereas micro-models and limit analysis seem to be more suitable for dry masonry walls.

# REFERENCES


Abrams, D.P. – Lateral *resistance of a two-story block building, ASCE Structures Congress*, New Orleans, USA, 41-57, 1986.

Abrams, D.P. – *Performance-based engineering concepts for unreinforced masonry building structures*, Journal of Progress in Structural Engineering and Materials, 48-56, 2001.

Abrams, D.P. – *Seismic assessment and rehabilitation of unreinforced masonry buildings in USA*, International Workshop on Masonry Walls and Earthquakes, University of Minho, Guimarães, 71-80, 2004.

Abrams, D.P. – *Seismic response patterns for URM buildings*, TMS Journal, 71-78, 2000.

Adam, J.P. – *La construcción Romana, materiales y técnicas*, Editorial de los Oficios, Polígono Industrial de León, 1996. ISBN 84-87469-95-7.

Addison, P.S., Mckenzie, W.M.C., Ndumu, A.S., Dougan, L.T., Runter, R. – *Fractal cracking of concrete: parameterization of spatial diffusion*, Journal of Engineering Mechanics, 125 (6), 622-629, 1999.

Åkesson, U., Stigh, J., Lindqvist, J.E., Göransson, M. – *The influence of foliation on the fragility of granitic rocks, image analysis and quantitative microscopy*, Engineering Geology, 68, 275-288, 2003.

Akita, H., Koide, H., Tomon, M., Sohn, D. – *A practical method for uniaxial tension test of concrete, Materials and Structures*, 36, 365-371, 2003.

Akkaya, Y., Voigt, T., Subramaniam, K.V., Shah, S.P. – *Nondestructive measurement of concrete strength gain by an ultrasonic wave reflection method*, Materials and Structures, 36, 507-514, 2003.

Alcocer, S.M., Zepeda, J.A. – *Behavior of multi-perforated clay brick walls under earthquake-type loadings*, 8th North American Masonry Conference, Austin, Texas, 235-246, 1999.

Amadei, B., Wibowo, J., Sture, S., Price, R.H. – *Applicability of existing models to predict the behavior of replicas of natural fractures of welded tuff under different boundary conditions*, Geotechnical and Geological Engineering, 16, 79-128, 1998.

Amadio, C., Rajgelj, S. – *Shear behavior of brick-mortar joints*, Masonry International, 5 (1), 19-22, 1991.

Andreaus, U. – *Failure criteria for masonry panels under in-plane loading*, Journal of Structural Engineering, 122 (1), 37-45, 1996.

Andreaus, U., Ceradini, G. – *Failure modes of solid brick masonry under in-plane loading*, Masonry International, 6 (1), 1-8, 1992.

Anthoine, A., Magonette, G., Magenes, G. – *Shear-compression testing and analysis of brick masonry walls*, 10th European Conference on Earthquake Engineering, Balkema, Rotterdam, 1657-1662, 1995.

ASTM D2845 – *Standard test method for laboratory determination of pulse velocities and ultrasonic elastic constants of rock*, American Society for Testing Materials, 1995.

ASTM D2936 – *Standard test method for direct tensile of intact rock core specimens*, American Society for Testing Materials, 1995.

ASTM D2938 – *Standard test method for unconfined compressive strength of rock core specimens*, American Society for Testing Materials, 1986.

ASTM D5873 – *Standard test method for determination of rock hardness by rebound hammer method*, American Society for Testing Materials, 1995.

ASTM E447 – Standard test method for compressive strength of masonry prisms, American Society for Testing Materials, 1992.

Atkinson, R.H., Amadei, B.P., Saeb, S., Sture, S. – *Response of masonry bed joints in direct shear*, Journal of Structural Engineering, 115 (9), 2277-2296, 1989.

Atkinson, R.H., Noland, J.L., Abrams, D.P. – *A deformation failure theory for stack-bond brick masonry prisms in compression*, Proc. 3rd NAMC, paper 18, Eds. J.H. Mathys and J.G. Borchelt, Arlington, Texas, 1985.

Avdelidis, N.P., Delegou, E.T., Almond, D.P., Moropoulou, A. – *Surface roughness evaluation of marble by 3D laser profilometry and pulsed thermography*, NDT&E international, 37 (7), 571-575, 2004.

Bascoul, A. – *State of the art report - part 2: mechanical micro-cracking of concrete*, Materials and Structures, 29, 67-78, 1996.

Bažant, P.Z. – *Concrete fracture models: testing and practice*, Engineering Fracture Mechanics, 69 (2), 165-205, 2002.

Bazant, Z.P. – *Size effect in blunt fracture: concrete, rock metal analysis*, Journal of Engineering Mechanics, 110 (4), 518-535, 1984.

Bazant, Z.P., Xiang, Y. – *Size effect in compression fracture: splitting crack band propagation*, Journal of Engineering Mechanics, 123 (2), 163-172, 1997.

Bentz, D.P, Schlangen, E., Edward, J. – *Computer simulation of interfacial zone microstructure and its effects on the properties of cement-based composites*, Materials Science of Concrete IV, J.P. Skalny and S. Mindell, Editors, American Ceramic Society, 155-199, 1995.

Beolchini G.C., Grillo, F. – *In situ tests of stone masonry panels*, Proceedings of International Workshop on Effectiveness of Injection Techniques for Retrofitting of Brick and Stone Masonry Walls in Seismic Areas, 197-205, 1992.

Bésuelle, P., Desrues, J., Raynaud, S. – *Experimental characterization of the localization phenomenon inside a Vosges sandstone in triaxial cell*, International Journal of Rock Mechanics and Mining Sciences, 37 (8), 1223-1237, 2000.

Binda, L., Fontana, A., Mirabella, G. – *Mechanical behavior and stress distribution in multiple-leaf stone walls*, 10th International Brick Block Masonry Conference, Calgary, Canada, 51-59, 1994.

Binda, L., Lensi, G., Saisi, A. – *NDE of masonry structures: use of radar tests for the characterization of stone masonries*, NDT&E International, 31 (6), 411-419, 1998.

Binda, L., Tiraboschi, C., Abbaneo, S. – *Experimental research to characterize masonry materials*, Masonry International, 10 (3), 592-101, 1997.

Bobet, A., Einstein, H.H. – *Fracture coalescence in rock-type materials under uniaxial and biaxial compression*, International Journal of Rock Mechanics and Mining Sciences, 36 (7), 863-888, 1998.

Bobji, M.S., Shivakumar, K., Alehossein, H., Venkateshwarlu, V., Biswas, S.K. – *Influence of surface roughness on the scatter in hardness measurements – a numerical study*, International Journal of Rock Mechanics and Mining Sciences, 36, 399-404, 1999.

Bosiljkov, V., Page, A., Bokan-bosiljkov, V., Žarnic, R. – Performance based studies of in-plane loaded unreinforced masonry walls, Masonry International, 16 (2), 39-50, 2003.

Bouzeghoub, M.C., Jukes, P., Riddington, J.R. – *Influence of the loading arrangement on the initial mode of failure of brick triplet shear specimens*, Computer Methods in Structural Masonry - 3, Eds. J. Middleton and G.N. Pande, Books and Journals International, 97-106, 1995.

Brace, W.F. – *Dependence of fracture strength of rocks on grain size*, Proc. 4th Symp. Rock Mech., Univ. Park, Penn., PA, 99-103, 1961.

BS 1881: Part 203 – *Testing concrete: recommendations for measurement of velocity of ultrasonic pulse in concrete*, 1986.

Calvi, G.M., Kingsley, G.R., Magenes, G. – *Testing masonry structures for seismic assessment*, Earthquake Spectra, Journal of Earthquake Engineering Research Institute, 12 (1), 145-162, 1996.

Carpinteri, A., Chiaia, B. – *Multifractal nature of concrete fracture surfaces and size effects on nominal fracture energy*, Materials and Structures, 28, 435-443, 1995.

Carpinteri, A., Chiaia, B., Cornetti, P. – *A scale invariant cohesive model for quasi-brittle materials*, Engineering Fracture Mechanics, 69 (2), 207-217, 2002.

Carpinteri, A., Chiaia, B., Ferro, G. – *A Size effects on nominal tensile strength of concrete structures: multifractality of material ligaments and dimensional transition from order to disorder*, Materials and Structures, 28, 311-317, 1995.

Carpinteri, A., Chiaia, B., Nemati, K.M. – *Complex energy dissipation in concrete under different loading conditions*, Mechanics of Materials, 26, 93-108, 1997.

Carpinteri, A., Cornetti, P., Barpi, F., Valente, S. – *Cohesive crack model description of ductile to brittle size-scale transition: dimensional analysis vs. renormalization group theory*, Engineering Fracture Mechanics, 70 (14), 1809-1839, 2003.

Carpinteri, A., Ferro, G. – *Size effects on tensile fracture properties: a unified explanation based on disorder and fractality of concrete microstructure*, Materials and Structures, 27, 563-571, 1994.

Carpinteri, A., Scavia, C., Yang, G.P. – *Microcrack propagation, coalescence and size effects in compression*, Engineering Fracture Mechanics, 54 (3), 335-347, 1996.

CEN-prEN 1996-1-1: EUROCODE 6, Design of masonry structures - Part 1-1: General rules for buildings - rules for reinforced and unreinforced masonry, 2001.

Chen, Y., Nishiyama, T., Kusuda, H., Kita, H., Sato, T. – *Correlation between microcrack distribution patterns and the granitic rock splitting planes*, International Journal of Rock Mechanics and Mining Sciences, 36 (4), 535-541, 1999.

Chen, Z., Narayan, S.P., Yang, Z., Rahman, S.S. – *An experimental investigation of hydraulic behavior of fractures and joints in granitic rock*, International Journal of Rock Mechanics and Mining Sciences, 37 (7), 1061-1071, 2000.

Chen, Z.H., Tham, L.G., Yeung, M.R., Tsui, Y., Lee, P.K.K. – *A study on the peak strength of brittle rocks*, Rock Mechanics and Rock Engineering, 35 (4), 255-270, 2002.

Chiaia B., Van Mier, J.G.M., Vervuurt, A. – *Crack growth mechanisms in four different concretes: microscopic observations and fractal analysis*, Cement and Concrete Research, 28 (2), 103-114, 1998.

Chiaia, B., Vervuurt, A., Van Mier, J.G.M. – *Lattice model evaluation of progressive failure in disordered particle composites*, Engineering Fracture Mechanics, 57 (2-3), 301-318, 1997.

Chiostrini, S., Vignoli, A. – *In-situ determination of the strength properties of masonry walls through destructive shear and compression tests*, Proceedings of International Workshop on Effectiveness of Injection Techniques for Retrofitting of Brick and Stone Masonry Walls in Seismic Areas, 253-282, 1992.

Choi, S., Shah, S.P. – *Fracture mechanism in cement-based materials subjected to compression*, Journal of Engineering Mechanics, 124 (1), 94-102, 1998.

Chow, T.M., Meglis, I.L., Young, R.P. – *Progressive microcracking development in tests on Lac du Bonnet granite*, International Journal of Rock Mechanics and Mining Sciences, 32 (8), 751-761, 1995.

Christaras, B., Auger, F., Mosse, E. – *Determination of the moduli of elasticity of rocks. Comparison of the ultrasonic velocity and mechanical resonance frequency methods with direct static methods*, Materials and Structures, 27, 222-228, 1994.

Corradi, M., Borri, A., Vignoli, A. – *Experimental study on the determination of strength of masonry walls*, Construction and Building Materials, 17 (3), 325-337, 2003.

Costa, M.F.M. – *Surface Inspection by an optical triangulation method*, Optical Engineering 35 (9), 2743-2747, 1996.

Costa, M.F.M., Pinho, V. – *Microtopographic inspection of thermoplastic rubber shoe's sole. The influence of surface roughness on the sole to leather gluing*, NDT&E international, 34 (1), 11-16, 2001.

Cunningham, E. – *Digital Filtering: An Introduction*, Houghton Mifflin Company, USA, 1994. ISBN 0-395-53989-7.

Dhanasekar, M., Page, A.W., Kleeman, P.W. – *The failure of brick masonry under biaxial stress*, Proc. Instn. Civ. Engrs., Part 2, 295-313, 1985.

Dialer, C. – *Some remarks on the strength and deformation behavior of shear stressed masonry panels under static monotonic loadings*, Proceedings of the 9th International Brick Block Masonry Conference, 276-283, 1991.

Dias, P. – *A arquitectura Gótica portuguesa*, Editorial Estampa, 1994. ISBN 972-33-0984-X.

Dinçer, I., Acar, A., Çobanoglu, I., Uras, Y. – *Correlation between hardness, uniaxial compressive strength and Young's modulus for andesites, basalts and tuffs*, Bulletin Engineering Geology and Environment, 63, 141-148, 2004.

Drysdale, R.G., Hamid, A.A. – *Tension failure criteria for plain concrete masonry*, Journal of Structural Engineering, 110 (2), 228-244, 1984.

Eberhardt, E., Stead, D., Stimpson, B., Lajtai, E.Z. – *The effect of neighbouring cracks on elliptical crack initiation and propagation in uniaxial and triaxial stress fields*, Engineering Fracture Mechanics, 59 (2), 103-105, 1998.

Eberhardt, E., Stead, D., Stimpson, B. – *Quantifying progressive pre-peak brittle fracture damage in rock during uniaxial compression*, International Journal of Rock Mechanics and Mining Sciences, 36 (3), 361-380, 1999a.

Eberhardt, E., Stimpson, B., Stead, D. – *Effects of grain size on the initiation and propagation thresholds of stress-induced brittle fractures*, Rock Mechanics and Rock Engineering, 32 (2), 81-99, 1999b.

Elgawady, M., Lestuzzi, P., Badoux, M. – *Dynamic versus static cyclic tests of masonry walls before and after retrofitting with FRP*, 13th World Conference on Earthquake Engineering, Vancouver, Canada, paper nº 2913, 2004.

Elices, M., Guinea, G.V., Gómez, J., Planas, J. – *The cohesive model: advantages, limitations and challenges*, Engineering Fracture Mechanics, 69 (2), 137-163, 2002.

EN 1015-11, Methods of test for mortar for masonry - part 11*: determination of flexural and compressive strength of hardened mortar*, 1999.

EN 1052-1, Methods of test for masonry: part 1 - determination of compressive strength, 1999.

EN 1052-3, Methods of test for masonry: part 3 - determination of initial shear strength, 2002.

Esaki, T., Jiang, K. – *Comprehensive study of the weathered condition of welded tuff from a historic stone bridge in Kagoshima, Japan*, Engineering Geology, 55, 121-130, 1999.

Faella, G., Manfredi, G., Realfonzo, R. – *Stress-strain relationships for tuff masonry: experimental results and analytical formulations*, Masonry International, 7 (2), 55-61, 1993.

Fairhurst, C.E., Hudson, J.A. – *Draft ISRM suggested method for the complete stress-strain curve for intact rock in uniaxial compression*, International Journal of Rock Mechanics and Mining Sciences, 36, 279-289, 1999.

Fardin, N., Feng, Q., Stephansson, O. – *Application of a new in situ 3D laser scanner to study the scale effect on the rock joint surface roughness*, International Journal of Rock Mechanics and Mining Sciences, 41 (2), 329-335, 2004.

Farmer, I.W. – *Engineering Behavior of Rocks*, 2nd Edition, Chapman and Hall, 1983. ISBN 0-412-13980-4.

Feng, X.T., Chen, S., Li, S. – *Effects of water chemistry on microcracking and compressive strength of granite*, International Journal of Rock Mechanics and Mining Sciences, 38 (4), 557-568, 2001.

Fitchen, J. – *The construction of Gothic cathedrals: a study of medieval vault erection*, University of Chicago Edition, 1981. ISBN 0-226-25203-5.

Froidevaux, Y.M. – *Techniques de l'archiecture ancienne, Construction et Restauration*, 3nd edition, Pierre Mardaga, Liège, 1985. ISBN 2-87009-256-3.

Ganz, H.-R. – *Failure criteria for masonry*, 5th Canadian Masonry Symposium, Vancouver, Canada, 65-77, 1989.

Geertsema, A.J. – *The shear strength of planar joints in mudstone*, International Journal of Rock Mechanics and Mining Sciences, 39 (8), 1045-1049, 2002. (Technical note)

Goodman, R. – *Introduction to rock mechanics*, 2nd edition, John Wiley & Sons, Inc., New York, 1989. ISBN 0-471-61718-0.

Griffith, A.A. – *The phenomena of rupture and flow in solids*. Philos. Trans. Roy. Soc. London, series A, 221, 163-198, 1920.

Grinzato, E., Marinetti, S., Bison, P.G., Concas, M., Fais, S. – *Comparison of ultrasonic velocity and IR thermography for the characterization of stones*, Infrared Physics & Technology, 46, 63-68, 2004.

Guinea, G.V. – *Modelling the fracture of concrete: the cohesive crack*, Materials and Structures, 28, 187-194, 1995.

Guinea, G.V., El-Sayed, K., Rocco, C.G., Elices, M., Planas, J. – *The effect of the bond between the matrix and the aggregates on the cracking mechanism and fracture parameters of concrete*, Cement and Concrete Research, 32 (12), 1961-1970, 2002.

Gupta, A.S., Rao, K.S. – *Index properties of weathered rocks: inter-relationships and applicability*, Bulletin Engineering Geology and Environment, 57, 161-172, 1998.

Gupta, A.S., Rao, K.S. – *Weathering effects on the strength and deformational behavior of crystalline rocks under uniaxial compression state*, Engineering Geology, 56, 257-2574, 2000.

Haied, A., Kondo, D., Henry, J.P. – *Strain localization in Fontainebleau sandstone*, Mechanics of Cohesive-Frictional Materials, 5, 239-253, 2003.

Hamid, A.A., Drysdale, R.G. – *Behavior of brick masonry under combined shear and compression loading*, Proc. 2nd Canadian Masonry Conference, 57-64, 1980.

Hamid, A.A., Drysdale, R.G. – Concrete masonry under combined shear and compression along the mortar joints, ACI Journal, 77 (5), 314-320, 1980.

Hansen, K.F. – *Bending and shear tests with masonry*, SBI Bulletin 123, Danish Building Research Institute, pp.36, 1999.

Hansen, K.F., Nykänen, E., Gottfredsen, F.R. – *Shear behavior of bed joints at different levels of precompression*, Masonry International, 12 (2), 70-78, 1998.

Hassan, M., Burdet, O., Favre, R. – *Ultrasonic measurements and static load tests in bridge evaluation*, NDT&E International, 28 (6), 331-337, 1995.

Hatzor, Y.H., Palchick, V. – *The influence of the grain size and porosity on the crack initiation stress and critical flaw length in dolomites*, International Journal of Rock Mechanics and Mining Sciences, 34 (5) 805-816, 1997.

Hawkes, I., Mellor, M. – *Uniaxial testing in rock mechanics laboratories*, Engineering Geology, 4 (3), 177-285, 1970.

Hawkins, A.B. – *Aspects of rock strength*, Bulletin of Engineering Geology and Environment, 57, 17-30, 1998.

Hendry, A.W. – *Structural masonry*, 2nd edition, MacMillian Press LDT, 1998. ISBN 0-333-73309-6.

Heyman, J. – *El esqueleto de piedra: mecánica de la arquitectura de fábrica*, Instituto Juan de Herrera, 1999. ISBN 84-89977-73-9.

Hillergorg, A., Modéer, M., Petersson, P.E. – *Analysis of crack formation and crack growth in concrete by means of fracture mechanics and finite elements*, Cement and Concrete Research, 6, 773-782, 1976.

Holzhausen, G.R., Johnson, A.M. – *Analyses of longitudinal splitting of uniaxially compressed rock cylinders*, International Journal of Rock Mechanics and Mining Sciences, 16, 163-177, 1979.

Homand, F., Belem, T., Souley, M. – *Friction and degradation of rock joint surfaces under shear loads*, International Journal for Numerical and Analytical Methods in Geomechanics, 25, 973-999, 2001.

Huang, T.H., Chang, C.S., Chao, C.Y. – *Experimental and mathematical modeling for fracture of rock joint with regular asperities*, Engineering Fracture Mechanics, 69 (17), 1977-1996, 2002.

Hudson, J.A., Harrison, J.P.H. – *Engineering rock mechanics, an introduction to the principles*, 1st edition, Pergamon, 1998. ISBN 0-08-041912-7.

ISO 13565 – *Geometrical Product Specifications (GPS) - Surface texture: Profile method; Surfaces having stratified functional properties - Part 1: Filtering and general measurement conditions*, 1994.

ISRM Suggested Methods, *Suggested methods for determining water content, porosity, density, absorption and related properties and swelling and slake-durability index properties*, In: Brown E.T., ISRM Suggested Methods. Pergamon, Oxford, 1981a.

ISRM Suggested Methods, *Suggested method for determining tensile strength of rock materials*, In: Brown E.T., ISRM Suggested Methods. Pergamon, Oxford, 1981b.

ISRM Suggested Methods, *Suggested method for determining uniaxial compressive strength and deformability of rock materials*, In: Brown E.T., ISRM Suggested Methods. Pergamon, Oxford, 1981c.

ISRM Suggested Methods, *Suggested method for determining sound velocity*, In: Brown E.T., ISRM Suggested Methods. Pergamon, Oxford, 1981d.

ISRM Suggested Methods, *Suggested method for determining of Schmidt rebound hardness*, In: Brown E.T., ISRM Suggested Methods. Pergamon, Oxford, 1981e.

Issa, M.A., Issa, M.A., Islam, Md.S., Chudnovsky, A. – *Fractal dimension - a measure of fracture roughness and toughness of concrete*, Engineering Fracture Mechanics,70 (1), 125-137, 2003.

Jansen, D.C., Shah, S. – *Effect of length on compressive strain softening of concrete,* Journal of Engineering Mechanics, 123 (1), 25-35, 1997.

Jansen, D.C., Shah, S.P., Rossow, E.C. – *Stress-strain results of concrete from circumferential strain feedback control testing,* ACI Materials Journal, 92 (4), 419-428, 1995.

Jiang, K., Esaki, T. – *Quantitative evaluation of stability changes in historical stone bridges in Kagoshima, Japan, by weathering,* Engineering Geology, 63, 83-91, 2002.

Jukes, P., Riddington, J.R. – *A review of masonry joint shear strength tests methods,* Masonry International, 11 (2), 37-43, 1997.

Kahraman, S. – *Evaluation of simple methods for assessing the uniaxial compressive strength of rock,* International Journal of Rock Mechanics and Mining Sciences, 38 (7), 981-994, 2001.

Kahraman, S. – *Estimating the direct P-wave velocity value of intact rock from indirect laboratory measurements,* International Journal of Rock Mechanics and Mining Sciences, 39 (1), 101-104, 2002. (Technical Note).

Kahraman, S., Fener, M., Gunaydin, O. – *Predicting the Schmidt hammer values of in-situ intact rock from core samples values,* International Journal of Rock Mechanics and Mining Sciences, 39 (3), 395-399, 2002. (Technical Note).

Karpuz, C., Pasamehmetoglu, A.G. – *Field characterization of weathered Ankara andesites,* Engineering Geology, 46, 1-17, 1997.

Katz, O., Reches, Z., Roegiers, J.-C. – *Evaluation of mechanical rock properties using a Schmidt hammer,* International Journal of Rock Mechanics and Mining Sciences, 37 (4), 723-728, 2000. (Technical Note).

Khalaf, F.M., Hendry, A.W., Fairbairn, D.R. – *Study of the compressive strength of blockwork masonry,* ACI Structural Journal, 91 (4), 367-374, 1994.

Kingsley, G.R., Atkinson, R.H., Noland, J.L., Hart, G.C. – *The effect of height on stress-strain measurements on grouted concrete masonry prisms,* 5th Canadian Masonry Symposium, Vancouver, Canada, 587-695, 1989.

Kolluru, V.S., Mohsen, J.P., Shaw, C.K., Shah, S.P. – *Ultrasonic technique for monitoring concrete strength gain at early age,* ACI Materials Journal, 99 (2), 458-462, 2002.

Komloš, K., Popovics, S., Nürnbergerová, T., Babál, B., Popovics, J.S. – *Ultrasonic pulse velocity test of concrete properties as specified in various standards,* Cement and Concrete Composites, 18 (5), 357-364, 1996.

Korinets, A., Alehossein, H. – *On the initial non-linearity of compressive stress-strain curves for intact rock,* Rock Mechanics and Rock Engineering, 35 (4), 319-328, 2002.

Kotsovos, M.D. – *Effects of testing techniques on the post-ultimate behavior of concrete in compression,* Materials and Structures, 16, 1-12, 1983.

Kranz, R.L. – *Crack-crack and crack-pore interactions in stressed granite,* International Journal of Rock Mechanics and Mining Sciences, 16, 37-47, 1979.

Lajtai, E.Z. – *Microscopic fracture process in a granite*, Rock Mechanics and Rock Engineering, 31 (4), 237-250, 1998.

Lajtai, E.Z., Carter, B.J., Ayari, M.L. – *Criteria for brittle fracture in compression*, Engineering Fracture Mechanics, 37 (1), 59-74, 1990.

Leal Gomes, M.J. – *A Hierarquização da heterogeneidade e o efeito de escala em maciços rochosos*, Geotecnia, 89, 91-97, 2000.

Lee, H.S., Park, Y.J., Cho, T.F., You, K.H. – *Influence of asperity degradation on the mechanical behavior of rough rock joints under cyclic shear loading*, International Journal of Rock Mechanics and Mining Sciences, 38 (7), 967-980, 2001.

Lee, Y-H., William, K. – *Mechanical properties of concrete in uniaxial compression*, ACI Materials Journal, 94 (6), 457-471, 1997.

Li, C., Prikryl, R., Nordlund, E. – *The stress-strain behavior of rock material to fracture under compression*, Engineering Geoloy, 49, 293-302, 1998.

Li, S., Lajtai, E.Z. – *Modeling the stress-strain diagram for brittle rock loaded in compression*, Mechanics of Materials, 30, 243-251, 1998.

Lin, Y., Lay, C.-P., Yen, T. – *Prediction of ultrasonic pulse velocity (UPV) in concrete*, ACI Materials Journal, 100 (1), 21-28, 2003.

Lourenço, P.B. – *Computational strategies for masonry structures*, PhD Thesis, Delft University of technology, Delft, The Netherlands, 1996. ISBN 90-407-1221-2. Available from www.civil.uminho.pt/masonry.

Lourenço, P.B., Barros, J.O., Oliveira, J.T. – *Shear testing of stack bonded masonry*, Construction and Building Materials, 18 (2), 125-132, 2004.

Lourenço, P.B., Ramos, L.F. – *Characterization of cyclic behavior of dry masonry joints*, Journal of Structural Engineering, 130 (5), 779-786, 2004.

Lourenço, P.B., Rots, J.G. – *Understanding the behavior of shear walls: a numerical review*, 10th International Brick Block Masonry Conference, 5-7 July, Calgary, Canada, 11-20, 1994.

Magenes, G. – *Seismic behavior of brick masonry: strength and failure mechanisms*, PhD Thesis, Department of Structural Mechanics, University of Pavia, 1992 (in Italian).

Magenes, G., Calvi, G.M. – *In-plane seismic response of brick masonry walls*, Earthquake Engineering and Structural Dynamics, 26, 1091-112, 1997.

Malhotra, V.M., Carino, N.J. – *CRC handbook on nondestructive testing of concrete*, editors V.M. Malhotra and N.J. Carino, Boca Raton: CRC Press, 1991. ISBN 0-8493-2984-1.

Mann, W., Müller, H. – *Failure shear-stressed masonry – an enlarged theory, tests and application to shear walls*, Proc. British Ceramic Society, 30, 223-235, 1982.

Mark, R. – *Architectural technology up to scientific revolution*, 2nd edition, The MIT Press, Massachusets Institute of Technology, Cambridge, Massachusets, 1995. ISBN 0-262-63157-1.

Markeset, G., Hillerborg, A. – *Softening of concrete in compression – localization and size effect*, Cement and Concrete Research, 25 (4), 702-708, 1995.

Marzahn, G. – *Investigation on the initial settlement of dry-stacked masonry under compression*, LACER (4), University of Leipzig, 1999.

McNary, W.S., Abrams, D.P. – *Mechanics of masonry compression*, Journal of Structural Engineering, 111 (4), 857-870, 1985.

Meda, A. – *Tensile behavior in natural building stone: Serena sandstone*, Materials and Structures, 36, 553-559, 2003.

Meglis, I.L., Chow, T., Martin, C.D., Young, R.P. – *Assessing in situ microcrack damage using ultrasonic velocity tomography*, International Journal of Rock Mechanics and Mining Sciences, 42 (1), 25-34, 2005.

Meglis, I.L., Chow, T., Young, R.P. – *Progressive microcracking development in tests on Lac du Bonnet granite – I. Acoustic emission source location and velocity measurements*, International Journal of Rock Mechanics and Mining Sciences, 32 (8), 741-750, 1995.

Mendes, F.M. et al. – *The use of modal analysis in the mechanical characterization of rock masses*, Proc. 1st Int. Cong. Rock Mech., volume I, 217-223, 1966.

Mirmiram, A., Wei, Y. – *Damage assessment of FRP-encased concrete using ultrasonic pulse velocity*, Journal of Engineering Mechanics, 127 (2), 126-135, 2001.

Misra, A. – *Effect of the asperity damage on shear behavior of single fracture*, Engineering Fracture Mechanics, 69 (17), 1997-2014, 2002.

Moghaddam, H.A., Chinwah, J.G., Hargreaves, A.C. – *Dynamic response of brick shear wall to strong ground motion*, Masonry International, 3 (3), 115-120, 1990.

Mohamed, A.H. A.-H., Barakat, S.A. – *Cyclic performance of concrete-backed stone masonry walls*, Journal of Structural Engineering, 129 (5), 596-605, 2003.

Moore, D.E., Lockner, D.A. – *The role of microcracking in shear-fracture propagation in granites*, Journal of Structural Geology, 17 (1), 95-114, 1995.

Naguib, E.M.F., Suter, G.T. – *Stresses in a running bond brick masonry 3-D finite element model under axial compression*, Masonry International, 5 (2), 48-54, 1991.

Oliveira, D. – *Experimental and numerical analysis of block masonry structures under cyclic loading*, PhD Thesis, University of Minho, Portugal, 2003. Available from www.civil.uminho.pt/masonry.

Page, A., Samarasinghe, W., Hendry, A.W. – *The failure of masonry shear walls*, International Journal of Masonry Construction, 1 (2), 52-57, 1980.

Page, A.W., Shrive, N.G. – *A critical assessment of compression tests for hollow block masonry*, Masonry International, 5 (2), 64-70, 1988.

Palchik, V. – *Influence of the porosity and elastic modulus on uniaxial compressive strength in soft brittle porous sandstones*, Rock Mechanics and Rock Engineering, 32 (4), 303-309, 1999.

Palchick, V., Hatzor, Y.H. – *Crack damage stress as a composite function of porosity and elastic stiffness in dolomites and limestones*, Engineering Geology, 63, 233-245, 2002.

Palchick, V., Hatzor, Y.H. – *The influence of porosity on tensile and compressive strength of porous chalks*, Rock Mechanics and Rock engineering, 37 (4), 331-341, 2004.

Pan, Y., Wang, X., Li, Z. – *Analysis of the strain softening size effect for rock specimens based on shear strain gradient plasticity theory*, International Journal of Rock Mechanics and Mining Sciences, 39 (6), 801-805, 2002.

Pettitt, W.S., King, M.S. – *Acoustic emission and velocities associated with the formation of sets of parallel fractures in sandstones*, SINOROCK2004 Symposium, Paper1A 25, CD-ROM, 2004.

Pluijm, R.V.D. – *Out-of-Plane bending of masonry, behavior and strength*, PhD Thesis, Eindhoven University of Technology, 1999. ISBN 90-6814-099-X.

Popovics, J. S. – *NDE techniques for concrete and masonry structures*, Progress in Structural Engineering and Materials, 5 (2), 49-59, 2003.

Prado, E.P., Van Mier, J.G.M. – *Effect of particle structure on mode I fracture process of concrete*, Engineering Fracture Mechanics, 70 (14), 1793-1807, 2003.

Priestley, M.J.N. – *Performance based seismic design*, 12th World Conference on Earthquake Engineering, 2831-2852, 2000.

Prikryl, R. – *Some microstructural aspects of strength variation in rocks*, International Journal of Rock Mechanics and Mining Sciences, 38, 671-682, 2001.

Prikryl, R., Lokajícek, T., Rudajev, V. – *Acoustic emission characteristics and failure of uniaxially stressed granitic rocks: the effect of rock fabric*, Rock Mechanics and Rock Engineering, 36 (4), 255-270, 2003.

Qasrawi, H.Y. – *Concrete strength by combined nondestructive methods simply and reliable predicted*, Cement and Concrete Research, 30 (5), 739-746, 2000.

Ramos, L.F. – *Experimental and numerical analysis of historical masonry structures*, Msc Thesis, University of Minho, 2001 (in Portuguese). Available from www.civil.uminho.pt/masonry.

Rao, G.A., Prasad, B.K.R. – *Fracture energy and softening behavior of high-strength concrete*, Cement and Concrete Research, 32 (2), 247-252, 2002.

Reinhardt, H.-W., Groβe, C., Herb, A. – *Ultrasonic monitoring of setting and hardening of cement mortar*, Materials and Structures, 33, 580-583, 2000.

Riddington, J.R., Fong, K.H., Jukes, P. – *Numerical study of failure initiation in different joint shear tests*, Masonry International, 11 (2), 44-50, 1997.

Riddington, J.R., Ghazali, M.Z. – *Hypothesis for shear failure in masonry joints*, Proc. Instn. Civ. Engrs, 89, 89-102, 1990.

Roberti, G.M., Binda. L., Cardani, G. – *Numerical modeling of shear bond tests on small brick-masonry assemblages*, Computer Methods in Structural Masonry - 4, Florence, Italy, 145-152, 1997.

Roca, P. – *Simplified methods for assessment of masonry shear-walls*, International Workshop on Masonry Walls and Earthquakes, Guimarães, 101-118, 2004.

Rodrigues, J.D. – *Laboratory study of thermally-fissured rocks*, 4th International Congress on Deterioration and preservation of stones objects, Louisville, 1982.

Sabir, B.B., Wild, S., Asili, M. – *On the tortuosity of the fracture surface in concrete*, Cement and Concrete Research, 27 (5), 785-795, 1997.

Sack, D.A., Olson, L.D. – *Advanced NDT methods for evaluating concrete bridges and other structures*, NDT&E International, 28 (6), 349-357, 1995.

Saka, M., Uchikawa, T. – *Simplified NDE of a closed vertical crack using electronics*, NDT&E International, 28 (5), 289-296, 1995.

Samarasinghe, W., Hendry, A.W. – *The tensile of brickwork under biaxial tensile and compressive stress*, Proc. 7th International Symposium on Load Bearing Brickwork, London, 129-139, 1980.

Samarasinghe, W., Page, A.W., Hendry, A.W. – *Behavior of brick masonry shear walls*, The Structural Engineer, 59B (3), 42-48, 1981.

Santos, S.F., Rodrigues, J.A. – *Correlation between fracture toughness, work of fracture and fractal dimensions of alumina-mullite-zirconia composites*, Materials Research, 6 (2), 1961-1970, 2003.

Saouma, V.E., Barton, C.C. – *Fractals, fractures, and size effects in concrete*, Journal of Engineering Mechanics, 120 (4), 835-854, 1994.

Schuller, M., Berra, M., Atkinson, R., Binda, L. – *Acoustic tomography for evaluation of unreinforced masonry*, Construction and Building Materials, 11 (3), 199-204, 1997.

Schultz. A.E., Hutchinson, R.S., Cheok, G.C. – *Seismic performance of masonry walls with bed joint reinforcement*, paper T119-4, Elsevier Science Ltd., 1998. ISBN 0-08-042845-2.

Seo, Y.S., Jeong, G.C., Kim, J.S., Ichikawa, Y. – *Microscopic observation and contact stress analysis of granite under compression*, Engineering Geology, 63, 259-275, 2002.

Shah, S.P., Sankar, R. – *Internal cracking and strain softening in concrete under uniaxial compression*, ACI Materials Journal, 84 (3), 200-212, 1987.

Shing, P.B., Noland, J.L., Klamerus, E., Spaeh, H. – *Inelastic behavior of concrete masonry shear walls*, Journal of Structural Engineering, 115 (9), 2204-2225, 1989.

Shing, P.B., Schuller, M., Hoskere, V.S. – *In-plane resistance of reinforced masonry shear walls*, Journal of Structural Engineering, 116 (3), 619-640, 1990.

Stöckl, S., Hofmann, P., Mainz, J. – *A comparative finite element evaluation of mortar joint shear tests*, Masonry International, 3 (3), 101-104, 1990.

Tadesmir, M.A., Tadesmir, N.M., Mills, N., Barr, B.I.G., Lydin, F.D. – *Combined effects of silica fume, aggregate type, and size on the postpeak response on concrete in bending*, ACI Materials Journal, 96 (1), 55-63, 1999.

Takemura, T., Golshani, A., Oda, M., Suzuki, K. – *Preferred orientations of open microcracks in granite and their relation with anisotropic elasticity*, International Journal of Rock Mechanics and Mining Sciences, 40 (4), 443-454, 2003.

Tang, C.A., Kou, S.Q. – *Crack propagation and crack coalescence in brittle materials under compression*, Engineering Fracture Mechanics, 61 (3-4), 311-324, 1998.

Tang, C.A., Liu, H., Lee, P.K.K., Tsui, Y., Tham, L.G. – *Numerical tests on micro-macro relationship of rock failure under uniaxial compression – part I: effect of heterogeneity*, International Journal of Rock Mechanics and Mining Sciences, 37 (4), 555-569, 2000a.

Tang, C.A., Tham, L.G., Lee, P.K.K., Tsui, Y., Liu, H. – *Numerical studies of the influence of microstructure on rock in uniaxial compression – part II: constraints, slenderness and size effect*, International Journal of Rock Mechanics and Mining Sciences, 37 (4), 571-583, 2000b.

Todd, T., Simmons, G. – *Effect of the pore pressure on the velocity of compressional waves in low-porosity rock*s, Journal of Geophysical Research, 10, 3731-3743, 1972.

Tomaževic, M. – *Design of earthquake resistant masonry structures*, Architectural and Structural Design of Masonry, Dresden University of Technology, December 7-18, 2003.

Tomaževic, M. – *Earthquake-resistant design of masonry buildings*, Imperial College Press, London, 1999. ISBN 1-86094-066-8.

Tomaževic, M., Lutamn, M., Petkovic, L. – *Seismic behavior of masonry walls: experimental simulation*, Journal of Structural Engineering, 122 (9), 1040-1047, 1996.

Tomaževic, M., Lutman, M., Weiss, P. – *The seismic resistance of historical urban buildings and the interventions in their floor systems: an experimental study*, The Masonry Soc. Journal, 12 (1), 77-86, 1993

Torrenti, J.M., Benaija, E.H., Boulay, C. – *Influence of boundary conditions on strain softening in concrete compression test*, Journal of Engineering Mechanics, 119 (2), 2369-2383, 1993.

Tugrul, A. – *The effect of the weathering on pore geometry and compressive strength of selected rock types from Turkey*, Engineering Geology, 72, 215-227, 2004.

Tugrul, A., Zarif, I.H. – *Correlation of mineralogical and textural characteristics with engineering properties of selected granitic rocks from Turkey*, Engineering Geology, 51, 303-317, 1999.

Turnšek, V., Cacovic, F. – *Some experimental results on the strength of brick masonry walls*, SIBMAC Proceedings, 149-156, 1971.

Turnšek, V., Sheppard, P. – The shear and flexural resistance of masonry walls, *International Research Conference on Earthquake Engineering*, Sophie, 1980.

Twiss, R.J., Moores, E.M. – *Structural Geology*, W. H. Freeman and Company, New York, 1992. ISBN 0-7167-2252-6.

Uchida, E., Ogawa, Y., Maeda, N., Nakagawa, T. – *Deterioration of stone materials in the Angkor monuments, Cambodia*, Engineering Geology, 55, 101-112, 1999.

Van Mier, J.G.M. – *Strain-softening of concrete under multiaxial loading conditions*, PhD Thesis, Eindhoven, University of Technology, The Netherlands, 1984.

Van Mier, J.G.M., Shah, S.P., Arnaud, M. – *Rilem TC148-SSC: Strain softening of concrete - test methods for compressive softening*, Materials and Structures, 33, 347-351, 2000.

Van Mier, J.G.M., Shah, S.P., Arnaud, M. – *Rilem TC148-SSC: Test methods for the strain-softening response of concrete*, Materials and Structures, 30, 195-209, 1997.

Van Mier, J.G.M., Schlangen, E., Vervuurt, A. – *Tensile cracking in concrete and sandstone: part 2 – effect of boundary conditions*, Materials and Structures, 29, 87-96, 1996.

Van Mier, J.G.M., Shi., C. – *Stability issues in uniaxial tensile tests on brittle disordered materials*, International Journal of Solids and Structures 39, 3359-3372, 2002.

Van Mier, J.G.M., Van Vliet, M.R.A. – *Uniaxial tension test for the determination of fracture parameters of concrete: state of the art*, Engineering Fracture Mechanics, 69 (2), 235-247, 2002.

Van Mier, J.G.M., VanVliet, M.R.A – *Influence of microstructure of concrete on size/scale effects in tensile fracture* , Engineering Fracture Mechanics, 70 (16), 2281-2306, 2003.

Van Vliet, M.R.A – *Size effect In Tensile Fracture of Concrete and Rock*, PhD Thesis, Delft University of Technology, 2000. ISBN 90-407-1994-2.

Van Vliet, M.R.A, Van Mier, J.G.M. – *Effect of strain gradients on the size effect of concrete in uniaxial tension*, International Journal of Fracture, 95, 195-219, 1999.

Van Vliet, M.R.A, Van Mier, J.G.M. – *Experimental investigation of size effects in concrete and sandstone under uniaxial tension*, Engineering Fracture Mechanics, 65 (2-3), 165-88, 2000.

Vasarhelyi, V. – *Some observations regarding the strength and deformability of sandstones in dry and saturated conditions*, Bull Eng Geol Env, 62, 245-249, 2003.

Vermeltfoort, A.Th. – *Compression properties of masonry and its components*, 10$^{tt}$ International Brick Block Masonry Conference, Calgary, Canada, 1433-1442, 1994.

Vermeltfoort, A.Th., Raijmakers, T.M.J. – *Deformation controlled tests in masonry shear walls*, part2. Report TUE/BKO/93.08, Eindhoven University of Technology, Eindhoven, The Netherlands.

Vervuurt, A., Schlangen, E., Van Mier, J.M.G. – *Cracking in concrete and Sandstone: part 1 - basic instruments*, Materials and Structures, 29, 9-18, 1996.

Viollet-Le-Duc, E. – *La construcción medieval*, Instituto Juan de Herrera, CEHOPU – Centro de Estudios Históricos de Obras Públicas y Urbanismo, 1996. ISBN 84-920297-3-0.

Villalba, A.C. – *Historia de la construcción arquitectónica*, 2$^{nd}$ edition, Edicions UPC, Universitat Politècnica de Catalunya, 1996. ISBN 84-7653-559-7.

Vonk, R.A. – *A micromechanical investigation of softening of concrete loaded in compression*, Heron, 38 (3), pp.94, 1993.

Wang, E.Z., Shrive, N.G. – *Brittle fracture in compression: mechanisms, models and criteria*, Engineering Fracture Mechanics, 52 (6), 1107-1126, 1995.

Wang, Y., Diamond, S. – *Fractal study of the fracture surfaces of cement pastes and mortars using a stereoscopic SEM method*, Cement and Concrete Research, 31 (10), 1385-1392, 2001.

Wang, Z., Battle, M.L., Nur, A. – *Effect of different pore fluids on seismic velocities in rocks*, Canadian Journal of Exploration Geophysics, 26, 104-112, 1990.

Watanabe, K., Niwa, J., Iwanami, M., Iokota, H. – *Localized failure of concrete in compression identified by AE method*, Construction and Building Materials, 18 (3), 189-196, 2004.

Whitehouse, D.J. – *Handbook of Surface Metrology*, IOP Publishing Lta, London, 1994. ISBN 0-7503-0039-6.

Winkler, K.W., Murphy III, W.F. – *Acoustic velocity and attenuation in porous rocks*, Rock Physics and Phase Relations, American Geophysical Union, 20-34, 1995.

Wittmann, F.H., Slowik, V., Alvaredo, A. M. – *Probabilistic aspects of fracture energy of concrete*, Materials and Structures, 27, 499-504, 1994.

Yan, A., Wu, Ke-Ru, Zhang, D., Yao, W. – *Effect of the fracture path on the fracture energy of high-strength concrete*, Cement and Concrete Research, 31 (11), 1601-1606, 2001.

Yasar, E., Erdogan, Y. – *Correlating sound velocity with density, compressive strength and Young modulus of carbonate rocks*, International Journal of Rock Mechanics and Mining Sciences, 41 (5), 871-875, 2004a. (Technical Note)

Yasar, E., Erdogan, Y. – *Estimation of rock physicomechanical properties using hardness methods*, Engineering Geology, 71, 281-288, 2004b.

Yilmaz, I., Sendir, H. – *Correlation of Schmidt hardness with unconfined compressive strength and Young's modulus in gypsum from Sivas (Turkey)*, Engineering Geology, 66, 211-219, 2002.

Yokel, F.Y., Fattal, S.G. – *Failure hypothesis for masonry shear walls*, Journal of Structural Division, 102 (ST3), 515-531, 1976.

Yuan, S.C., Harrison, J.P. – *An empirical dilatancy index for the dilatant deformation of rock*, International Journal of Rock Mechanics and Mining Sciences, 41 (4), 679-686, 2004.

Zepeda, J.A., Alcocer, S.M., Flores, L.E. – *Earthquake-resistant construction with multi-perforated clay brick walls*, 12th World Conference on Earthquake Engineering, 1541-1548, 2000.

Zhang, Z.X. – *An empirical relation between mode I fracture toughness and the tensile strength of rock*, International Journal of Rock Mechanics and Mining Sciences, 39 (3), 401-406, 2002.

Zhuge, Y., Corderoy, J., Thambiratnam, D. – *Behavior of unreinforced brick masonry under lateral (cyclic) loading*, TMS Journal, 14 (2), 55-62, 1996.

Zisopoulus, P.M., Kotsovos, M.D., Pavlovic, M.N. – *Deformational behavior of concrete specimens in uniaxial compression under different boundary conditions*, Cement and Concrete Research, 30 (1), 153-159, 2000.

# APPENDIX A

## Stress-displacement diagrams for direct tensile tests

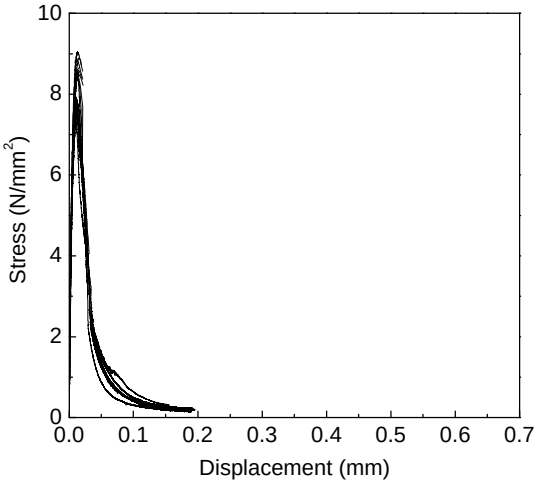


Figure A.1 – Stress-displacement diagrams for granite BA

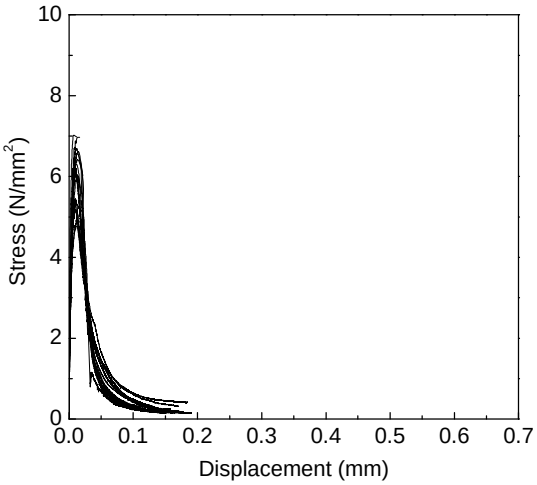


Figure A.2 – Stress-displacement diagrams for granite GA

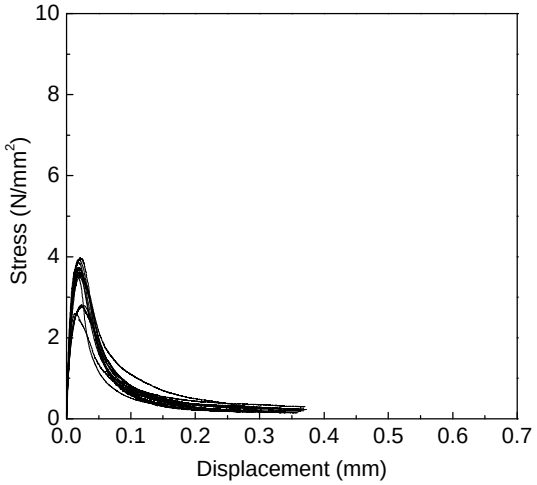


Figure A.3 – Stress-displacement diagrams for granite GA*

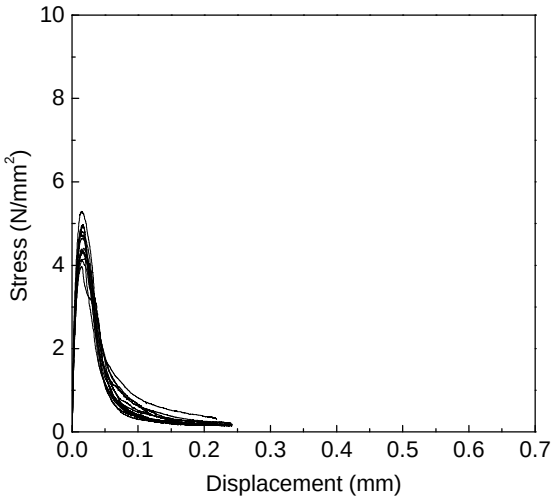


Figure A.4 – Stress-displacement diagrams for granite RM

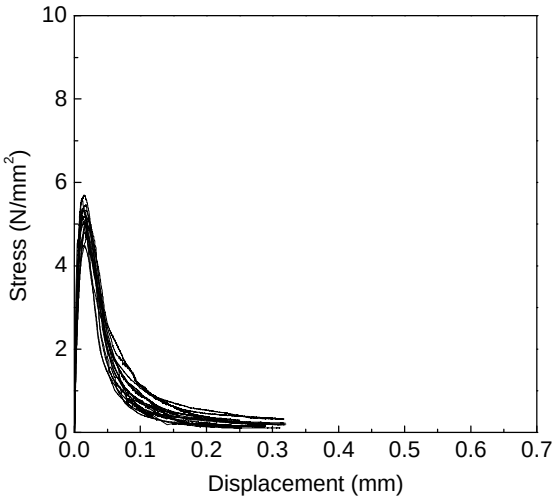


Figure A.5 – Stress-displacement diagrams for granite MC

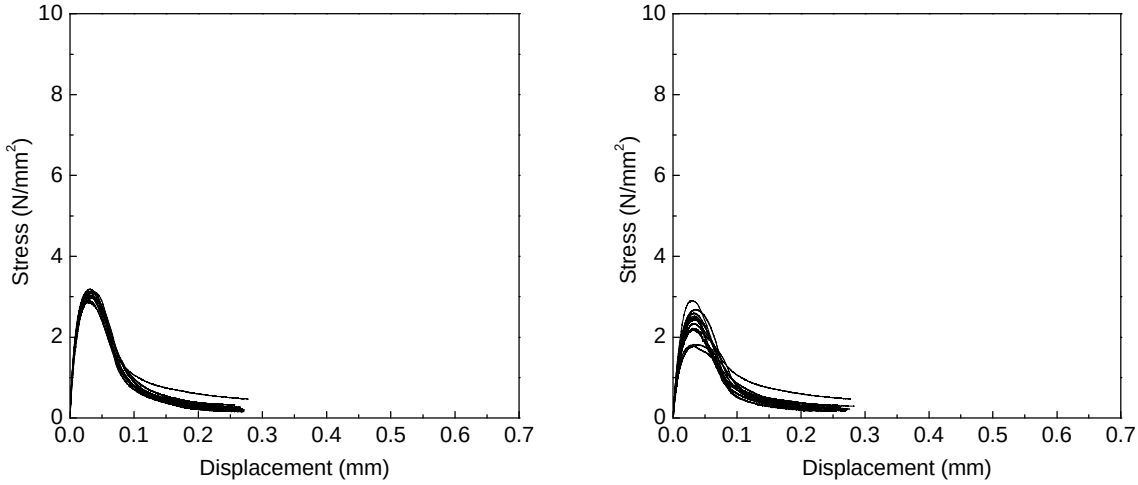


Figure A.6 – Stress-displacement diagrams for granite AF; (a) direction parallel to foliation plane; (b) direction perpendicular to foliation plane

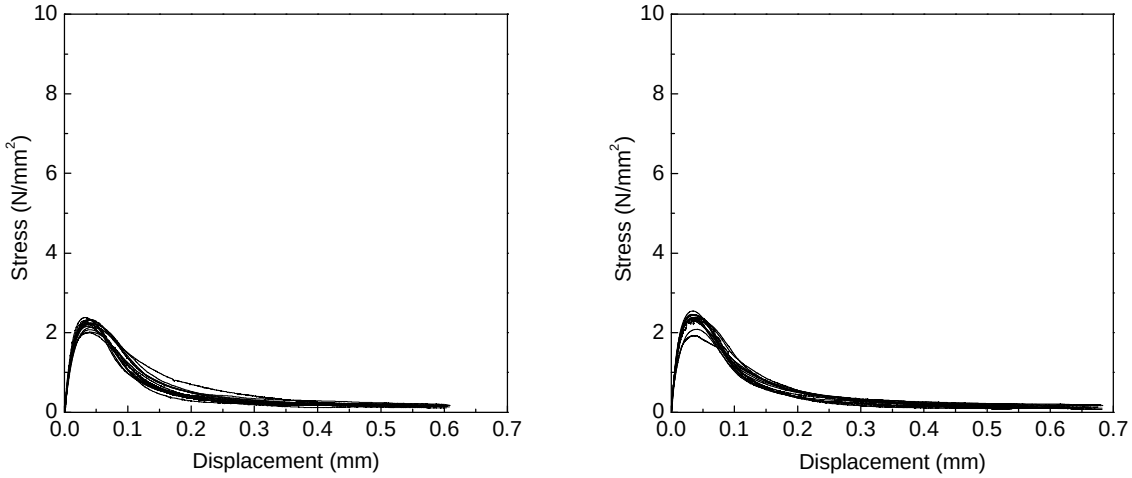


(a) (b)

Figure A.7 – Stress-displacement diagrams for granite MDB; (a) direction parallel to the foliation plane; (b) direction perpendicular to the foliation plane

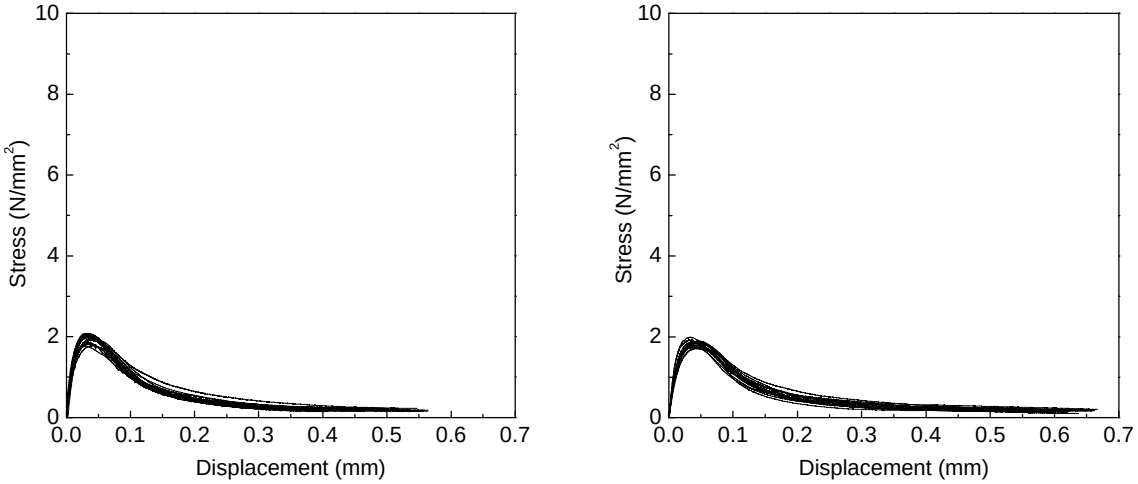


(a) (b)

Figure A.8 – Stress-displacement diagrams for granite MDB*; (a) direction parallel to the foliation plane; (b) direction perpendicular to the foliation plane

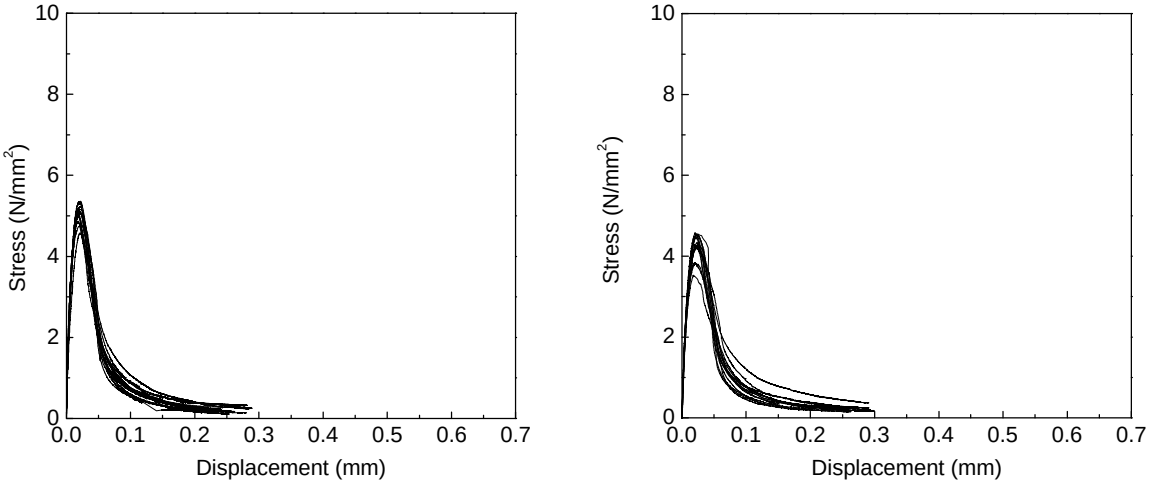


(a) (b)

Figure A.9 – Stress-displacement diagrams for granite PTA; (a) direction parallel to the foliation plane; (b) direction perpendicular to foliation plane

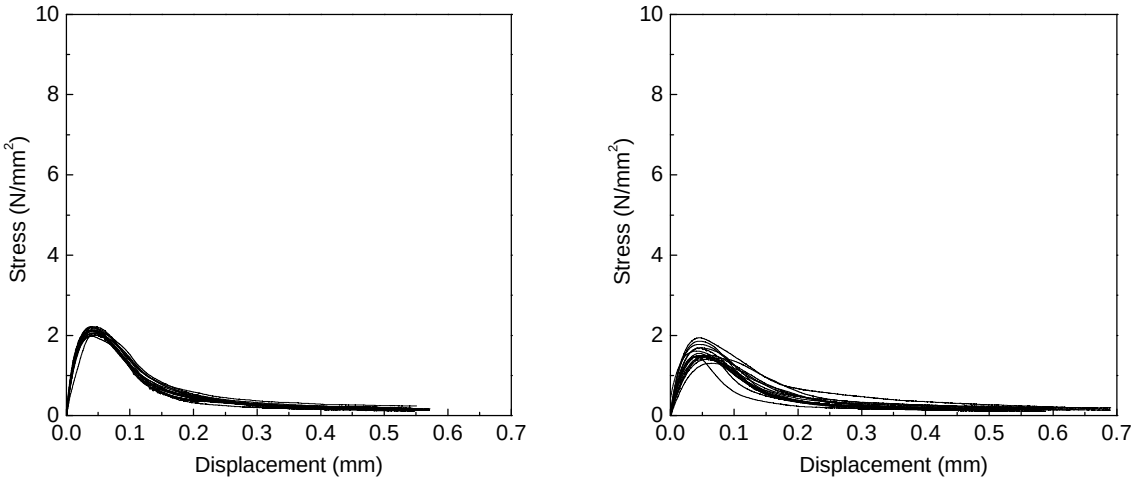


(a) (b)

Figure A.10 – Stress-displacement diagrams for granite PTA*; (a) direction parallel to the rift plane; (b) direction perpendicular to the rift plane

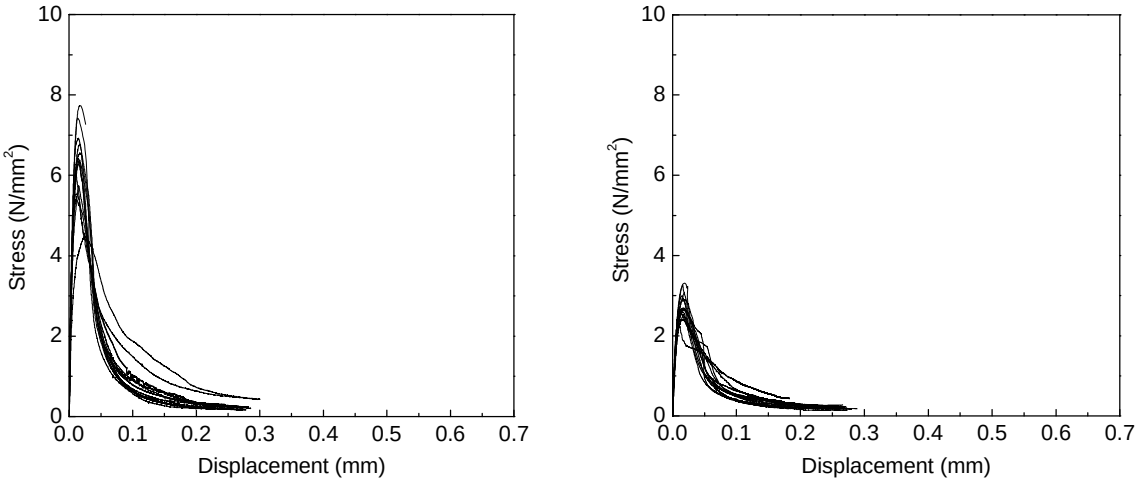


(a) (b)

Figure A.11 – Stress-displacement diagrams for granite PLA; (a) direction parallel to the rift plane; (b) direction perpendicular to the rift plane

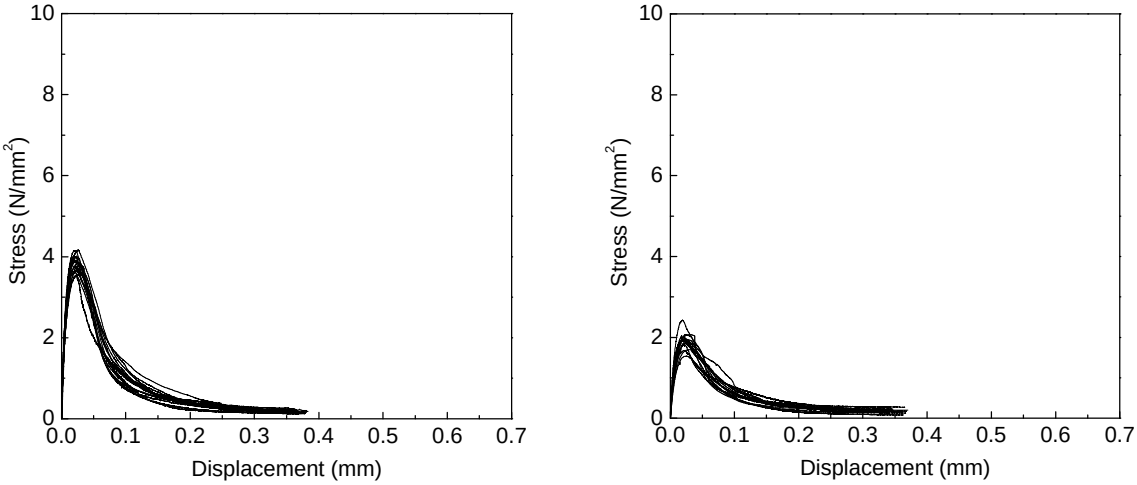


(a) (b)

Figure A.12 – Stress-displacement diagrams for granite PLA*; (a) direction parallel to the rift plane; (b) direction perpendicular to the rift plane

# APPENDIX B

## Filtering of the texture profile

Filtering is a procedure used to separate certain frequency components of the surface profile. The best way to filter a given surface profile is to use digital filters. Generally, digital filtering involves the adoption of a weighting function to be convolved with the raw data, *z(x)*. A simplistic way of understanding this idea of convolution is to think of it as a sliding multiplication and integration. If a weighting function, *h(x)*, with a finite shape is centered in a particular point of the profile, the multiplication of the weighting function by the profile and consequent integration results on a point of the new convolved profile (in this case "filtered"), see Figure B.1

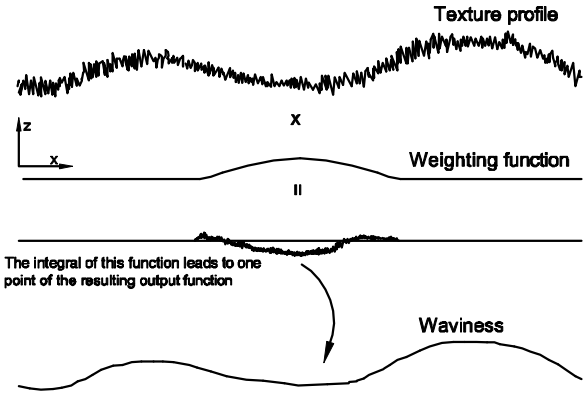


Figure B.1 – General procedure of digital filtering

The waviness, *w(x)*, is thus a weighting or a convolution of the texture profile, see eq. (B.1).

$$w(x) = z(x) \otimes h(x) = \int_{-\infty}^{\infty} z(x')h(x-x')dx' \tag{B.1}$$

The shape of the weighting function, *h(x)*, should be chosen according to the international ISO standards, in particular ISO13565(1994), which defines a Gaussian form for *h(x)*:

$$h(x) = \sqrt{\frac{a}{p}} e^{-ax^2} \tag{B.2}$$

If the Fourier domain is considered, the Fourier transform of the weighting function, *H(k)*, and of the profile, *Z(k)*, ($k = 2p/l$), can be calculated and the filtered profile, in frequency domain, is simply the result of the multiplication of the transformed functions:

$$w(k) = H(k)Z(k) \tag{B.3}$$

If the filter is defined in the frequency domain in terms of its magnitude response, depending on the frequency range that it either passes or attenuates it, generally falls into one of the four categories:

- lowpass - passes low frequencies components below $l_c$
- highpass - passes high frequencies above $l_c$

- bandpass - passes a certain band of frequencies between $l_{c1}$ and $l_{c2}$
- bandstop - cuts a certain band of frequencies between $l_{c1}$ and $l_{c2}$

The ideal frequency response of these filters is shown in Figure B.2. As can be seen, lowpass filter passes all frequencies below $l_c$, whereas the highpass filter passes all frequencies above $l_c$. The bandpass filter passes all frequencies between $l_{c1}$ and $l_{c2}$, while the bandstop filter attenuates all frequencies between $l_{c1}$ and $l_{c2.}$

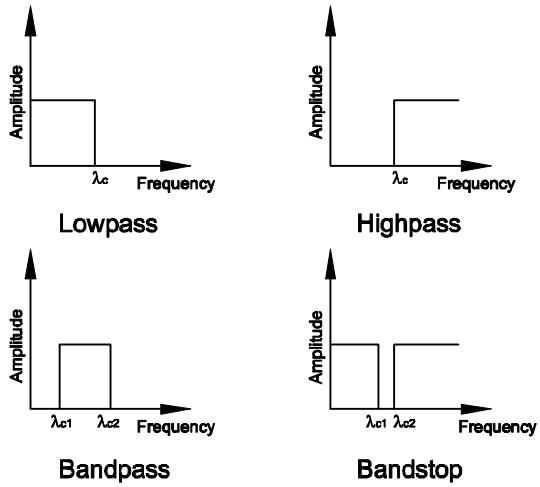


Figure B.2 – Ideal filters

The characteristic frequencies for which these ideal filters are defined are the cutoff frequencies. The selection of the appropriate cutoff frequency in order to obtain the waviness profile is performed based on the frequency domain content in terms of the magnitude, which is given by means of the Fast Fourier Transform (FFT) of the surface texture profile. Referring to Figure B.3, in this particular case, from the analysis of the frequency content of the texture profile, it can be observed that to obtain the waviness profile from the original texture profile, the frequency of 0.10Hz can be selected as input for the lowpass filter, which means that all frequencies above this value will be cut.

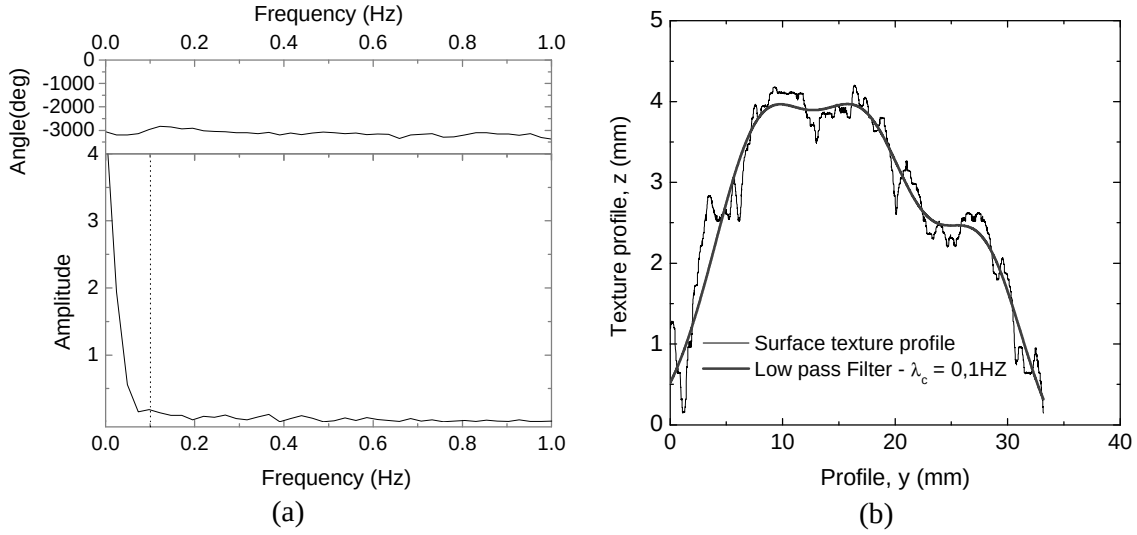


Figure B.3 – Digital filtering procedure; (a) Fast Fourier Transform (FFT) of the surface texture profile; (b) obtainment of the waviness profile by application of FFT lowpass filter

By its simplicity of implementation, in this work, the filter used for separating the waviness and the roughness regimes was a basic finite impulse response filter (FIR), the moving average filter, accordingly defined by eq.(B.4), (Cunningham, 1994):

$$x'_k = \frac{1}{m}\sum_{i=-r}^{r} x_{k-i}\ , \qquad r+1 \le k \le N-r, \tag{B.4}$$

where $N$ is the length of the sequence data and $m$ ($m = 2r+1$) is the number of subsequences of length lower than $N$.

It should be referred that $2r$ points are lost, since that it is not possible to apply the eq. (B.4) for $r$ points of the profile located at the beginning and at end of the profile, see Figure B.4.

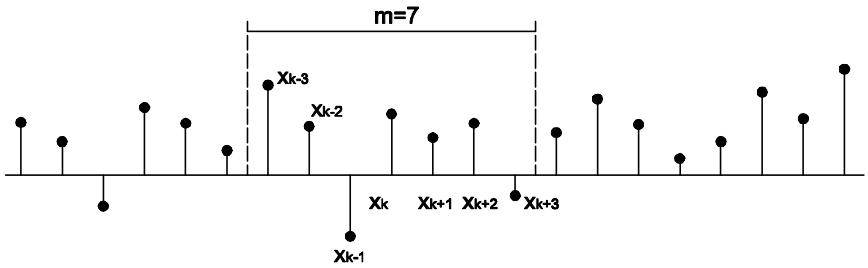


Figure B.4 – Moving average filter procedure (Cunningham, 1994)

In the scope of digital filtering it is important to enhance the meaning of the cutoff spatial lengths. International standards define the cutoff length in order to evaluate the filter length for waviness and roughness. This procedure specifies the range of spatial wavelengths or spatial frequencies in the waviness and roughness data. According to the values obtained for the total surface texture profile (unfiltered roughness data), there are five standard cutoff lengths, see Table B.1

Table B.1 – Standard spatial cutoff filter

| Roughness Range (*m*m) | Cutoff, $l_c$ (mm) | Scan length $L = 5\,l_c$ |
|---|---|---|
| < 0.002 | 0.08 | 0.4 |
| 0.002-0.1 | 0.25 | 1.25 |
| 0.1-2.0 | 0.8 | 4.0 |
| 2.0-10.0 | 2.5 | 12.5 |
| >10 | 8.0 | 40.0 |

By physical limitations imposed by the size of the samples (sometimes slightly smaller than 40mm wide), the surface texture profiles acquired at the fracture surfaces have a total length of about 35mm. The total sequence length ($N$) is of 3500 points. As the values of the unfiltered roughness present considerable higher values than the roughness range indicated in Table B.1 and following the standard recommendations, a spatial length cutoff of 8.0mm can be adopted. However, in order to minimize the points lost at the ends of the profile when the moving average filter was applied, a cutoff of seven was adopted. In this way, sub-sequences, $m$, of 501 points with $r = 250$ were considered. The range of points $k$ of the texture profile to which the moving average filter was applied falls in the interval $251 < k < 3250$.

The influence of the spatial cutoff on the waviness profiles is clarified by the results shown in Figure B.5, where different nonstandard cutoffs ($m$ = 501 and $m$ = 151) were used in the filtering of the total surface texture profile. In effect, depending on the cutoff lengths, the resulting waviness profiles present distinct characteristics. For higher cutoff spatial lengths, only the larger wavelengths are captured by the waviness. If the cutoff is reduced, higher number of shorter wavelengths and consequently small features of the original profile are present in the waviness profile. The differences between the waviness profiles corresponding to different cutoff spatial lengths are obviously more significant when the small features of the profile are more relevant.

It is essential to note that with respect to the evaluation of the fracture surface profiles, the filtering of all of them was carried out by considering the same spatial cutoff length (all samples have high $R_a >> 10m$m), which facilitates the global analysis of the results.

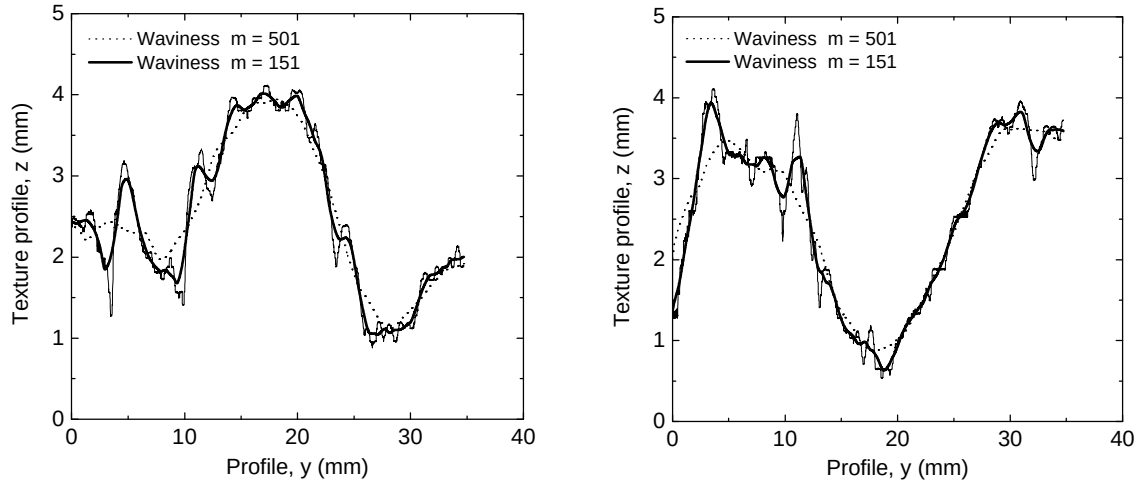


Figure B.5 – Examples of the influence of the spatial cutoff length on the waviness profiles; (a) granite MDB in the direction parallel to the foliation; (b) granite PLA* in the direction parallel to the rift plane

In order to show the validity of the moving average filter, a comparison of the waviness profile obtained from two distinct digital filtering techniques was carried out. Figure B.6 shows the waviness profiles for two surface texture profiles resulting from the application of the moving average filter and the Fast Fourier Transform (FFT) lowpass filter.

The comparison of both profiles allows to conclude that apart from the ends, the values are rather close and, therefore, the waviness profile seems to be calculated with good accuracy using the moving average filter. In the diagram of Figure B.6b, the moving average filter seems to work reasonably well while the cutoff frequency of the Fourier filter appears no to be adequate.

The roughness profile is the result of subtracting the waviness profile obtained according to the procedure described to the total surface texture profile. The statistical parameters of roughness, $R_a$, $R_q$ and waviness, $W_a$, $W_q$, are calculated from the corresponding roughness and waviness profiles.

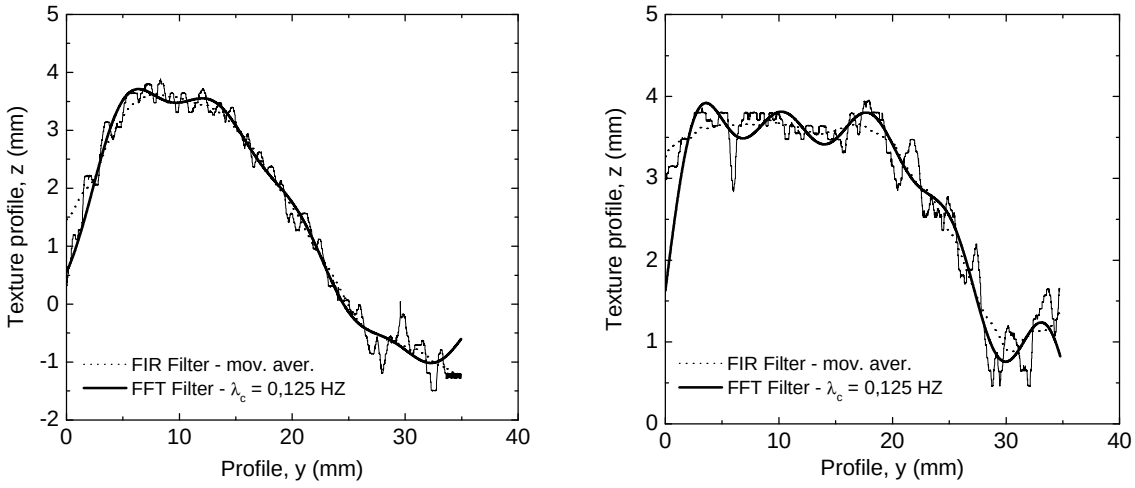


Figure B.6 – Comparison between distinct filtering procedure; (a) granite BA; (b) granite GA

# APPENDIX C

## Evaluation of the texture surface features

With respect to the characterization of the texture surfaces, it is reasonable to assume that both waviness and roughness regimes are originated from different sources. The roughness regime seems to be mostly related to the microstructure of the granites. Its variation can be explained based on the material microstructure such as the size of the grains, internal texture (fabric) or weathering state (different levels of porosity). This dependence is confirmed, to certain extent, from the statistical correlation found between the fracture energy and the roughness parameter, $R_a$. The waviness regime seems to be essentially associated to the macrocracking progress that is determined by the material microstructure features and additionally by the testing structural effects such as boundary conditions, as well as, by the geometry of the specimens, particularly if notches are used.

As referred previously in the literature (Van Mier *et al*., 1996; Van Vliet, 2000), when direct tensile tests are carried out under fixed boundary ends it is usual that fracture surfaces present an S shape. The S configuration of the texture surface results from the fact that fracture surface develops from different sides through the specimen and not only from one side. This S shape of the fracture surfaces can be confirmed by visual inspection of several tested specimens from different granites, see Figure C.1.

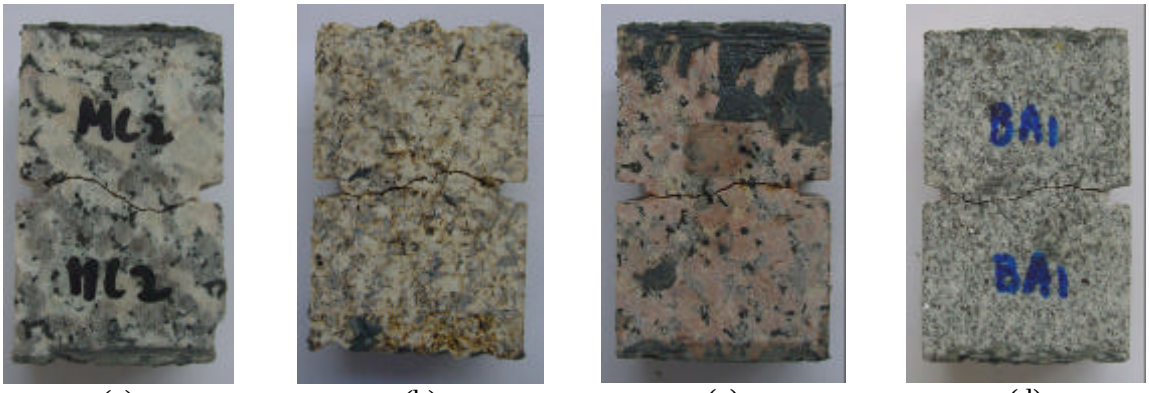


(a) (b) (c) (d)

Figure C.1 – Typical examples of the S shape of the fracture surfaces; (a) granite MC; (b) granite MDB*; (c) granite RM; (d) granite BA

The analysis of the texture profiles of the S shape fracture surfaces indicates that the long wave components play the major role in the description of their topography. As shown in Figure C.2, the global form of these characteristic texture profiles is not flat and is essentially ruled by the waviness regime.

This type of relief can be the outcome of the discontinuity of the fracture surface induced by the additional bending moments that appear during the direct tensile tests due to the fixed boundaries. As reported in the literature Van Vliet (2000), this setup leads also the development of larger crack densities. Apart from the abnormally high values of the waviness parameter in granites MC and PLA in the parallel direction to the rift plane and in spite of the large scatter, a trend for the fracture energy increase with the waviness parameter increase was verified in Chapter 2. In fact, the waviness appears to contribute to the increase of the

energy needed to the fracture growth. Therefore, it can be concluded that the increase on the fracture energy, when fixed boundaries are used in direct tensile tests, is partly associated with the high tortuosity of the fracture path dominated by the waviness regime.

Another typical shape that occurs in some specimens of all types of granites consists in the curved crack pattern that is displayed in Figure C.3, characterized by wrinkled peaks or valleys. The three-dimensional character of the fracture process already pointed out by Vervuurt *et al.* (1996), Van Mier and Van Vliet (2002), is well represented by this characteristic topographic surfaces where the waviness also represent the main component and clearly determines the global shape of the fracture surface.

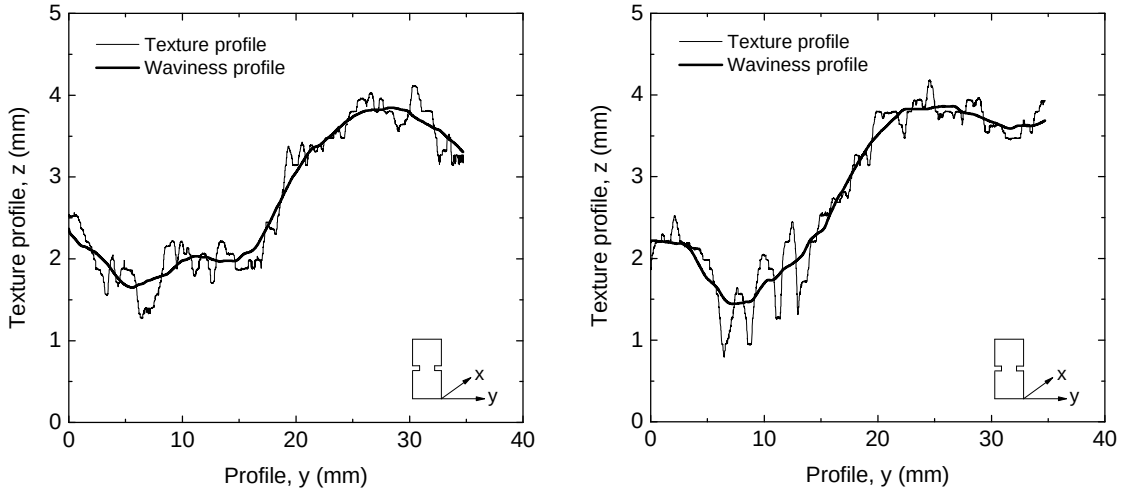


Figure C.2 – Typical examples of inspected S shape of the surface texture profile; (a) granite MDB; (b) granite PTA*

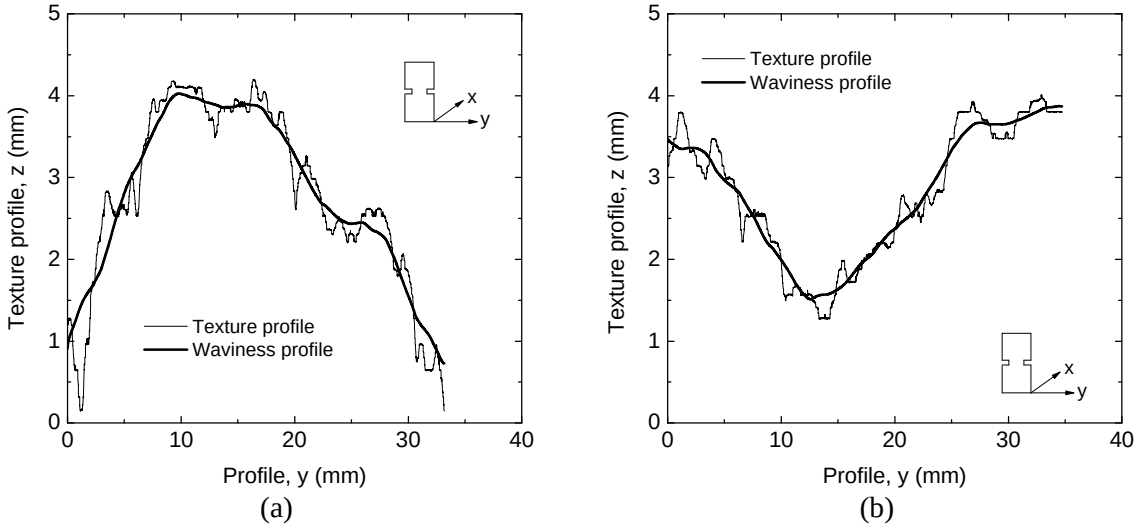


Figure C.3 – Typical examples of curved peak or valley shape of the fracture surfaces; (a) granite BA; (b) granite GA

The S shape of the fracture surface is mainly significant in case of brittle granites, like BA, GA and PLA. This indicates that the effect of non-rotating ends is more relevant when the tensile strength is high or the heterogeneity of the material is large.

It should be also noticed that the S shape of the fracture surface appears predominantly on the direction of the notches. Next, the average values of the texture parameters are calculated for both directions separately, namely the direction of the notches and the perpendicular direction. The relationships found between the roughness and waviness obtained for both directions are displayed in Figure C.4. It was possible to verify that both roughness and waviness parameters exhibit lower values for the direction perpendicular to the notches, which demonstrate that the notches influence the texture of the fracture surface. Regarding the waviness, in particular, the higher values reflect directly the form of the texture profile.

Despite the fact that fracture surface exhibits remarkable three-dimensional geometry, the difference achieved for the parameters regarding both directions of analysis suggests that the direction of the notches represents a preferential direction of cracking growth. This aspect is confirmed by the evolution of the displacements that are measured by the LVDTs located on the sides with notches, which, in general, present higher values than the LVDTs located on the perpendicular sides.

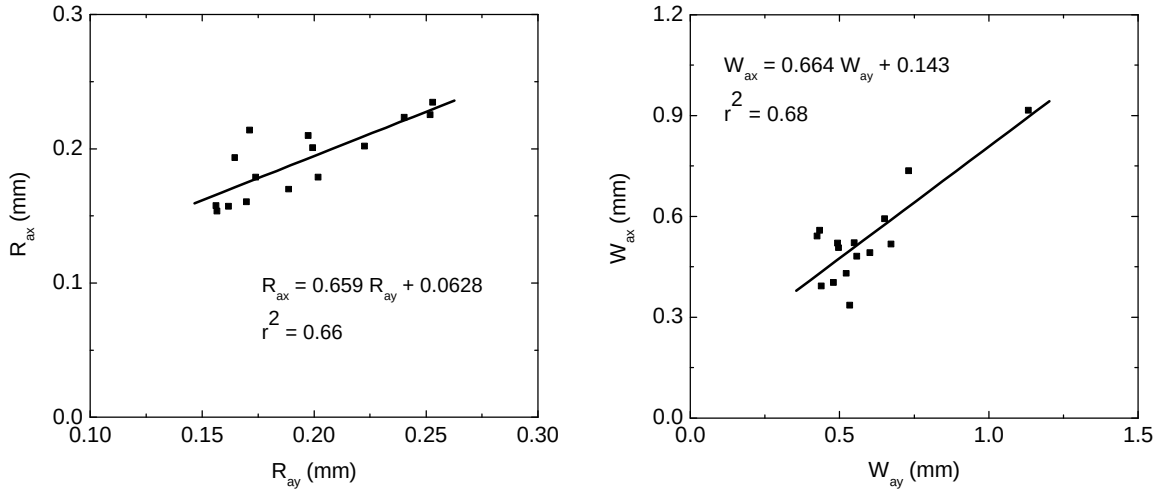


Figure C.4 – Relation between texture parameters; (a) mean roughness in the notched direction, $R_{ay}$, vs. mean roughness in the direction perpendicular to the notch direction, $R_{ax}$; (b) waviness in the notched direction, $W_{ay}$, vs. waviness in the direction perpendicular to the notch, $W_{ax}$

Another relevant issue is related to the difference obtained between the lateral and central profile parameters measured on the specimens. Through Figure C.5 it is possible to verify that, in the direction perpendicular to the notches, there is a tendency for the texture parameters to exhibit higher values on the lateral profiles comparatively to the central profiles. This fact is demonstrated by the analysis of the slope of the linear correlation found between the parameters calculated for the central and the lateral profiles, which indicates that the boundary effect also has some influence on the results.

In the notched direction, only central and lateral roughness parameters are linearly correlated, see Figure C.6. Also in this case, the roughness is higher in the lateral profiles. However, no correlation was found for the waviness parameter, see Figure C.6b. Regarding the unnotched direction, the high values found for the lateral surface texture parameters may possibly be attributed to the strain and stress-gradients that appear in the proximity of the notches. This behavior can be based on the distinct response of the material microstructure under

remarkable strain rates. The pre-peak high stress levels and the corresponding deformations can locally induce different mechanisms for the cracking process. It is possible that higher deformation rates leads to the premature failure of the interface mineral bonds and consequently to more tortuous path is achieved in the lateral profile, in the case of an unnotched direction.

Another reason that justifies rougher lateral profiles is the discontinuity of the material in the lateral boundaries of the specimens. This zone is characterized by the weakness of the binding forces field between the minerals, which facilitates the crack growth through grain boundaries.

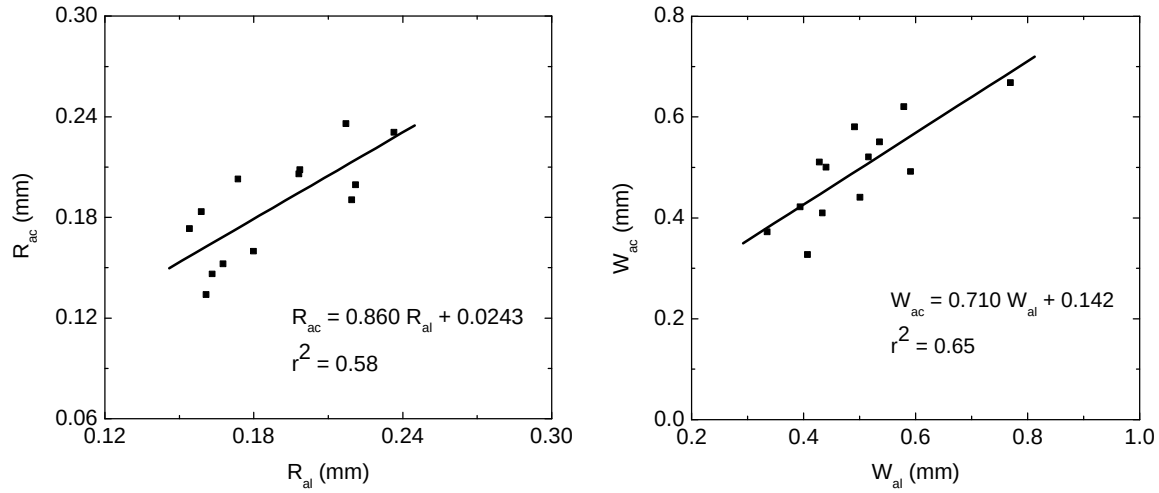


Figure C.5 – Relation between texture parameters for lateral and central texture parameters profiles in the direction perpendicular to the notches; (a) mean lateral roughness, $R_{al}$, vs. mean central roughness, $R_{ac}$; (b) lateral waviness, $W_{al}$, vs. central waviness, $W_{ac}$

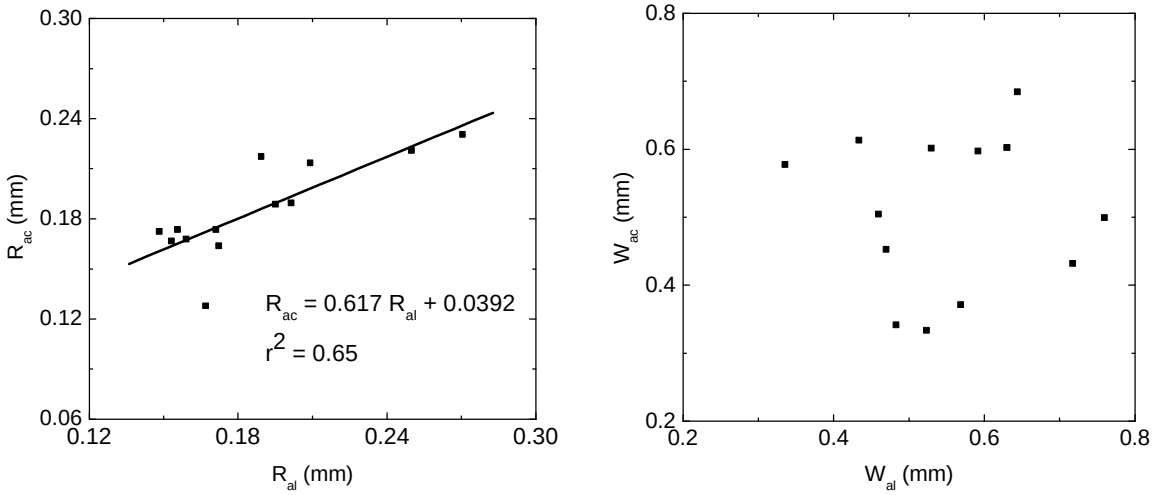


Figure C.6 – Relation between texture parameters for lateral and central texture parameters profiles in the direction of the notches; (a) mean lateral roughness, $R_{al}$, vs. mean central roughness, $R_{ac}$; (b) lateral waviness, $W_{al}$, vs. central waviness, $W_{ac}$

# APPENDIX D

## D.1 Stress-strain diagrams for uniaxial compression tests

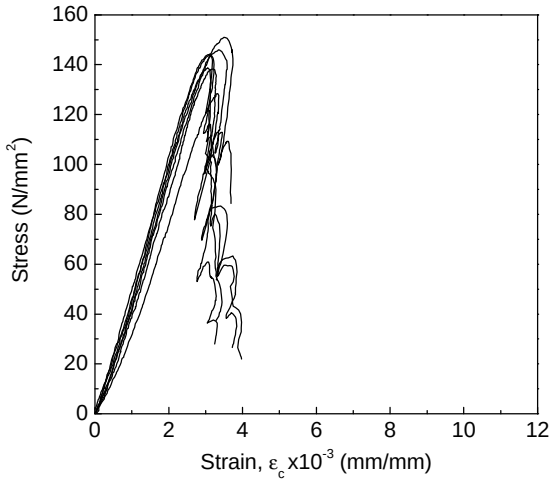


Figure D.1– Stress-strain diagrams for granite BA

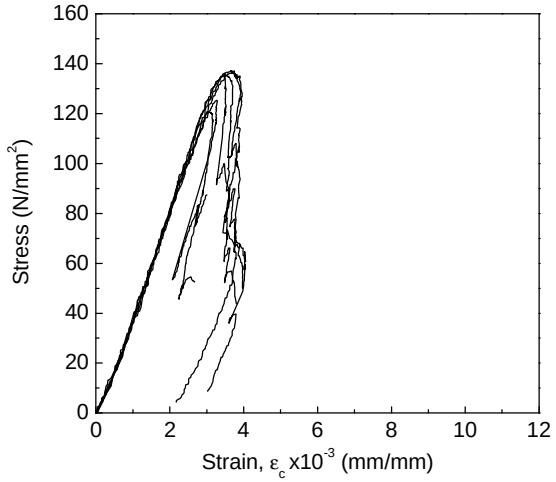


Figure D.2 – Stress-strain diagrams for granite GA

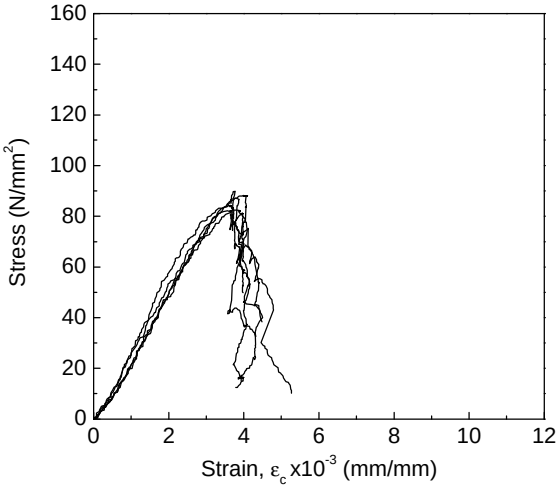


Figure D.3 – Stress-strain diagrams for granite GA*

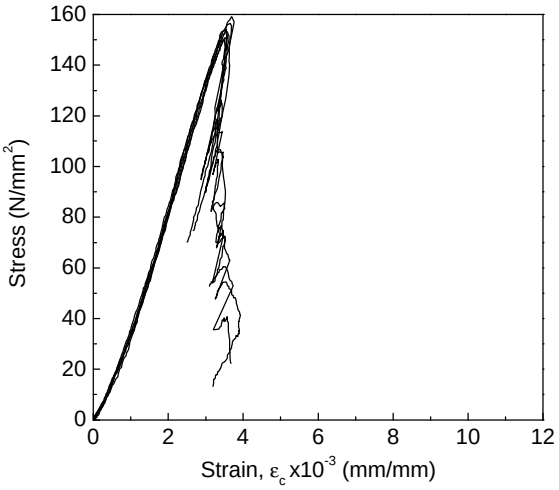


Figure D.4 – Stress-strain diagrams for granite RM

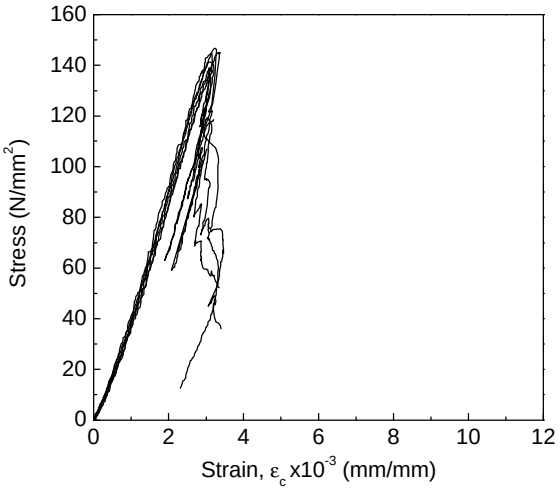


Figure D.5 – Stress-strain diagrams for granite MC

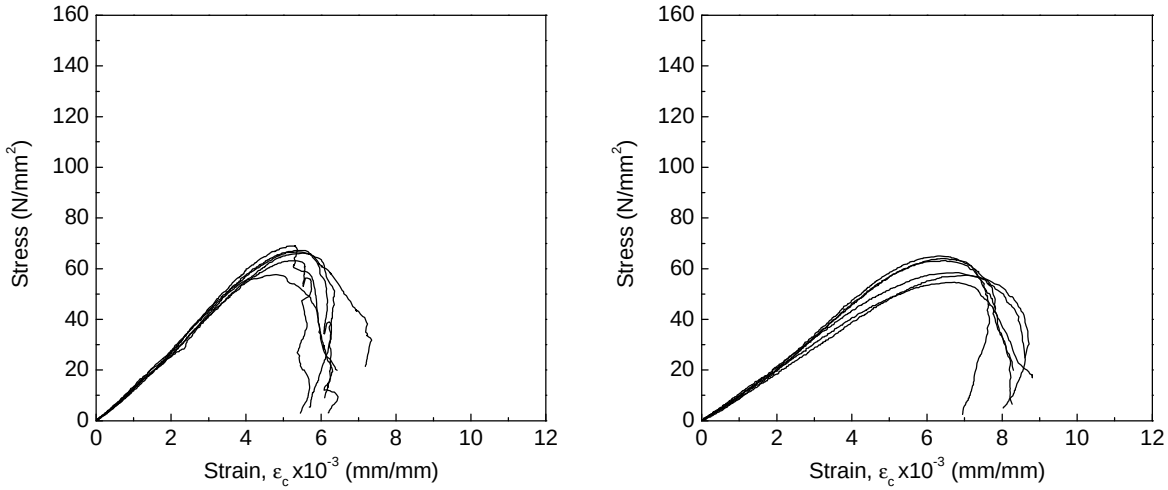


(a) (b)

Figure D.6 – Stress-strain diagrams for granite AF; (a) direction parallel to the foliation plane; (b) direction perpendicular to the foliation plane

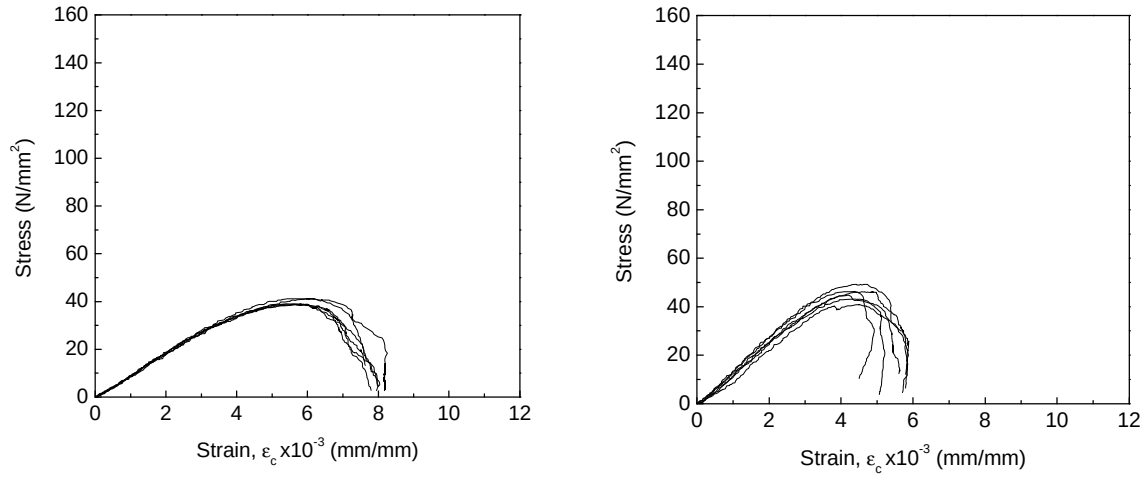


Figure D.7 – Stress-strain diagrams for granite MDB; (a) direction parallel to the foliation plane (b) direction perpendicular to the foliation plane

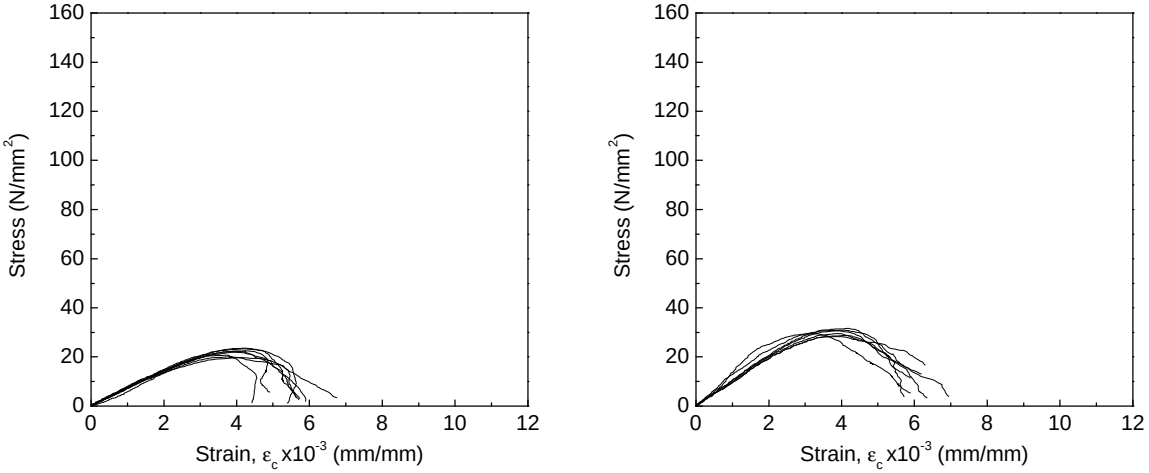


Figure D.8 – Stress-strain diagrams for granite MDB*; (a) direction parallel to the foliation plane (b) direction perpendicular to the foliation plane

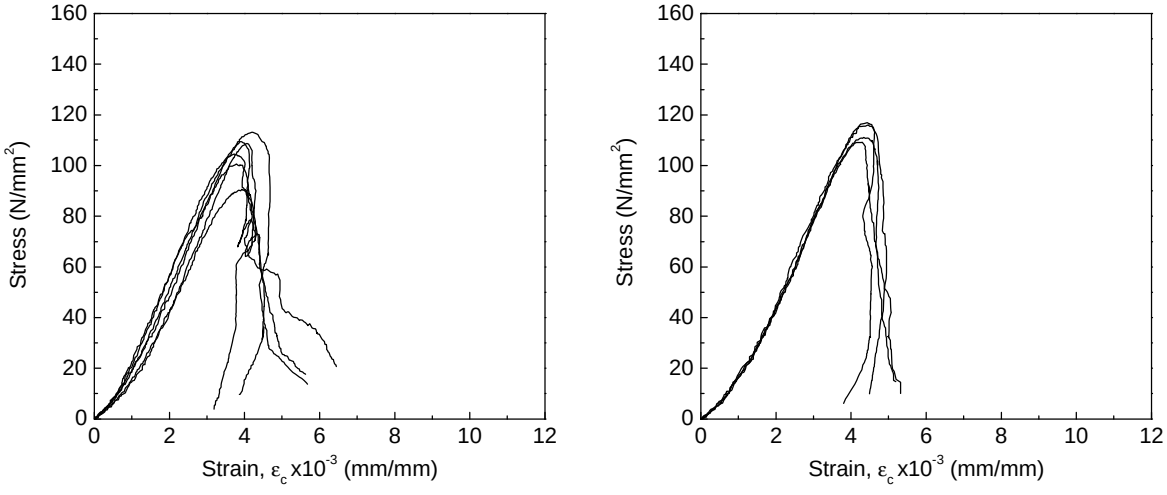


Figure D.9 – Stress-strain diagrams for granite PTA; (a) direction parallel to the foliation plane; (b) direction perpendicular to the foliation plane

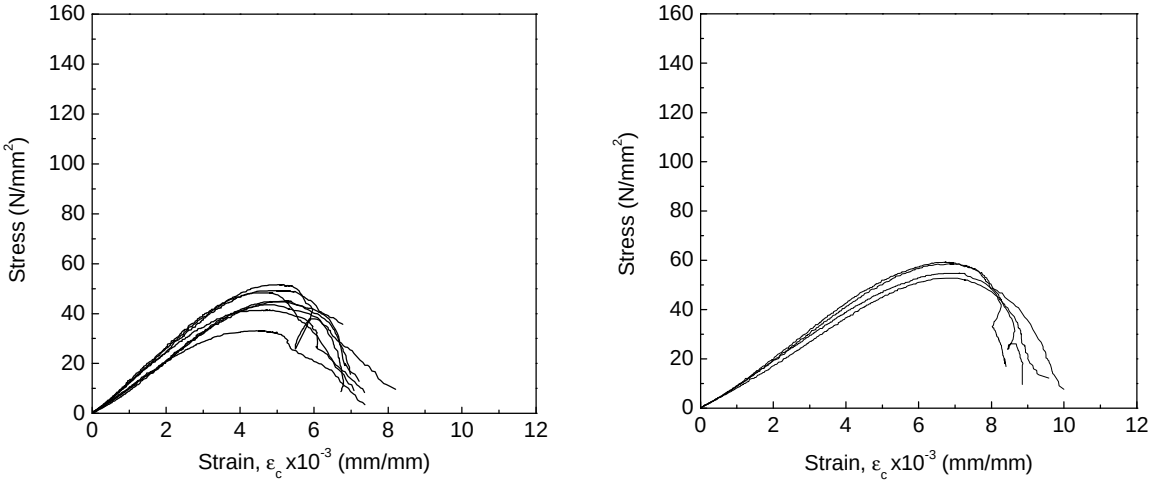


Figure D.10 – Stress-strain diagrams for granite PTA*; (a) direction parallel to the rift plane; (b) direction perpendicular to the rift plane

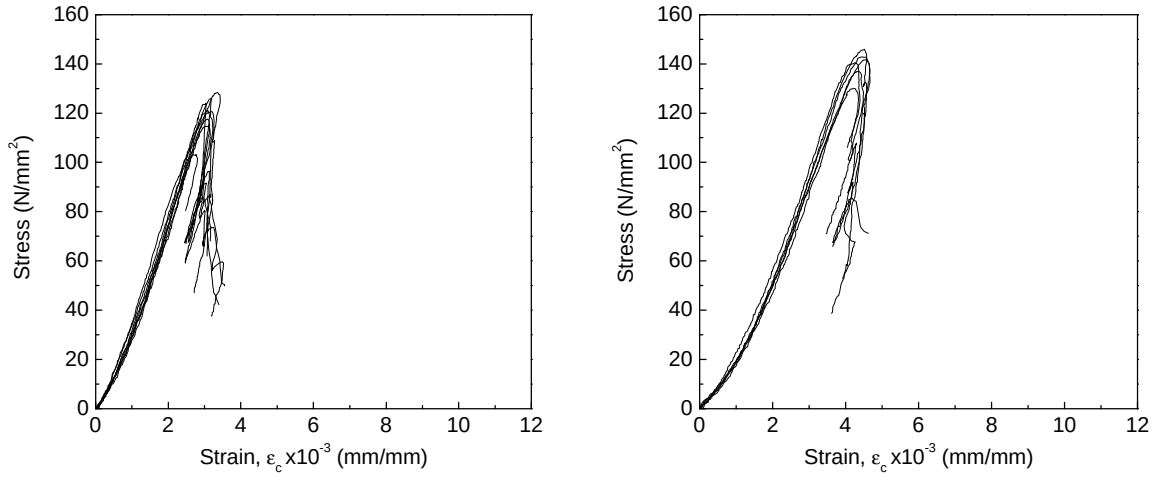


Figure D.11 – Stress-strain diagrams for granite PLA; (a) direction parallel to the rift plane; (b) direction perpendicular to the rift plane

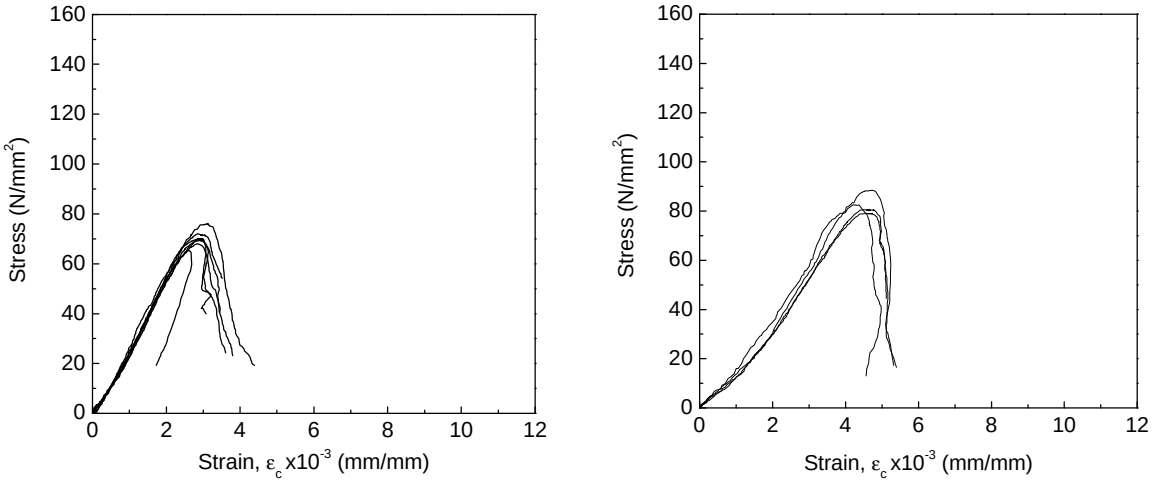


Figure D.12 – Stress-strain diagrams for granite PLA*; (a) direction parallel to the rift plane; (b) direction perpendicular to the rift plane

## D.2 Stress-displacement diagrams for compressions tests – saturated specimens

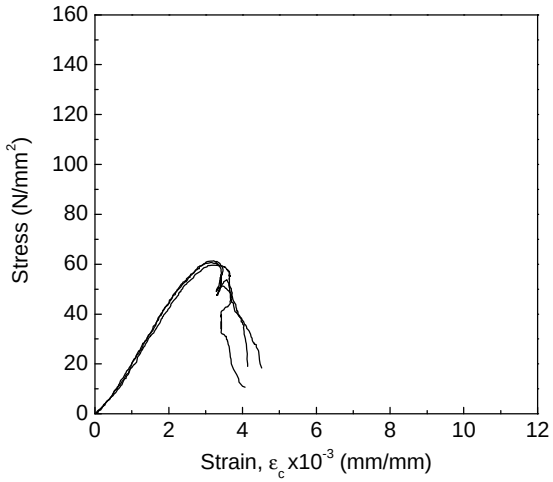


Figure D.13 – Stress-strain diagram for granite GA*

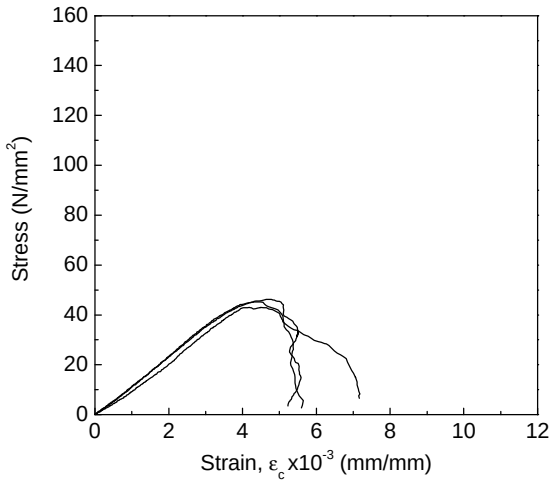


Figure D.14 – Stress-strain diagram for granite AF in the direction parallel to the foliation

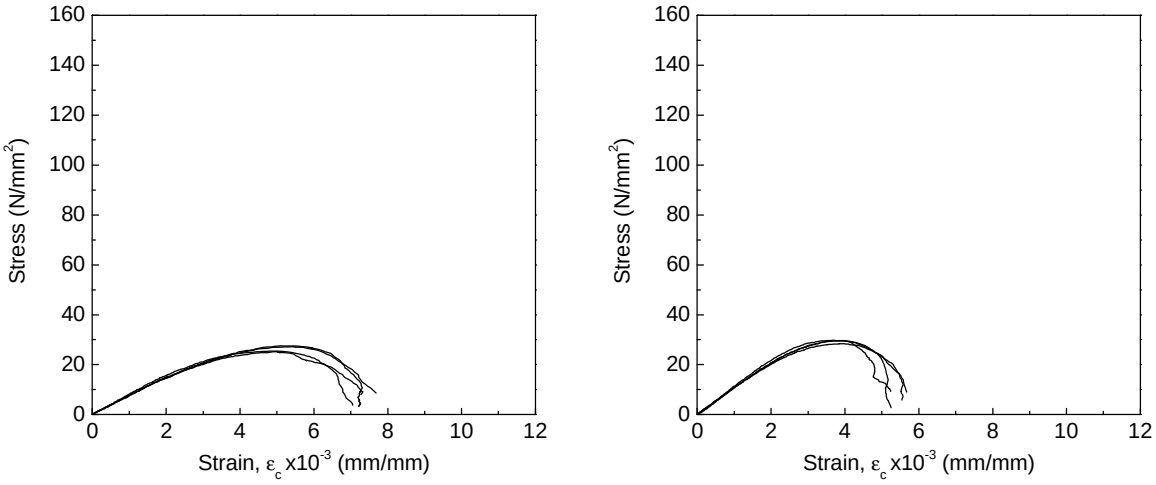


(a) (b)

Figure D.15 – Stress-strain diagram for granite MDB; (a) perpendicular direction to the foliation plane; (b) parallel direction to the foliation plane

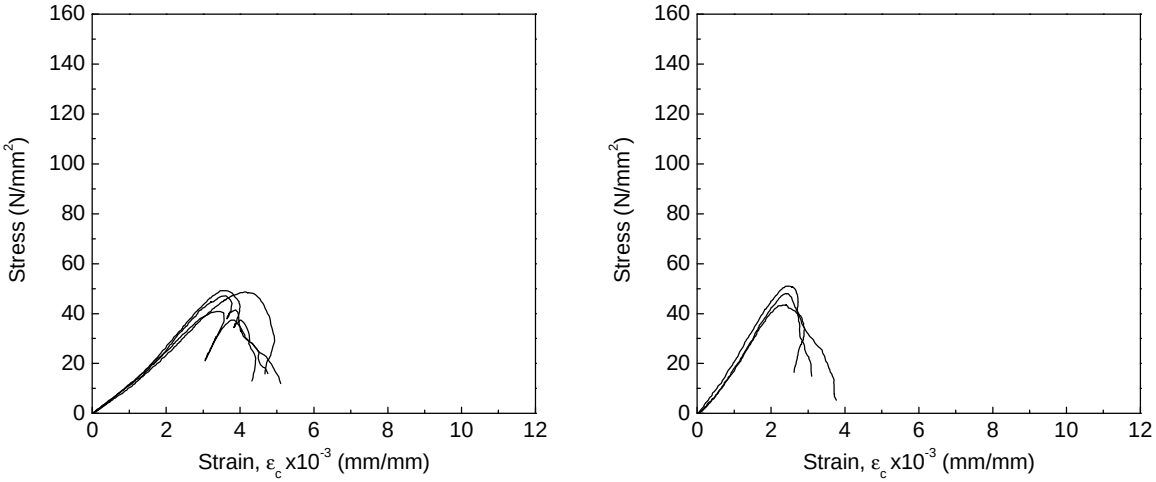


Figure D.16 – Stress-strain diagram for granite PLA*; (a) direction perpendicular to rift the plane; (b) direction parallel to the rift plane

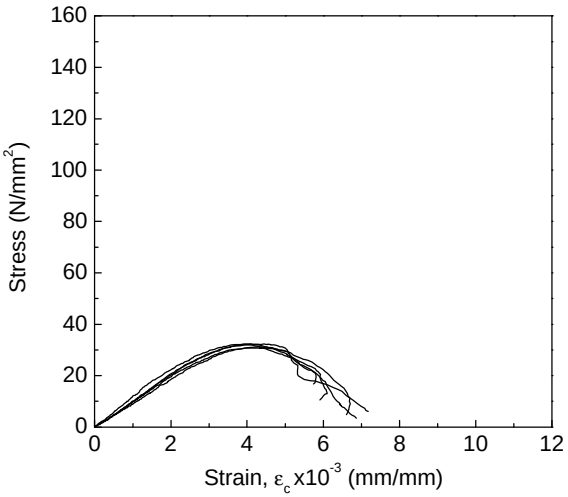


Figure D.17 – Stress-strain diagram for granite PTA* in the direction parallel to the rift plane

# APPENDIX E

## E.1 Ultrasonic pulse velocity - tensile and compressive specimens

Table E.1 – Average values of the ultrasonic pulse velocity - compressive specimens. Coefficient of variation is indicated inside brackets (%)

| Granite | Dry specimens | | Saturated specimens | |
|---|---|---|---|---|
| | $UPV_{54}$ (m/s) | $UPV_{150}$ (m/s) | $UPV_{54}$ (m/s) | $UPV_{150}$ (m/s) |
| BA | 4728 (0.45) | 4703 (0.71) | 5540 (0.31) | 5468 (0.46) |
| GA | 4575 (0.55) | 4526 (0.61) | 4574 (0.55) | 4526 (0.61) |
| GA* | 3174 (2.1) | 3137 (2.2) | 4442 (1.2) | 4345 (1.3) |
| RM | 4030 (1.6) | 3965 (1.6) | 4163 (0.88) | 4085 (1.1) |
| MC | 4163 (0.88) | 4084 (1.1) | 4030 (1.6) | 3965 (1.6) |
| AF ⊥ foliation plan | 2148 (4.2) | 2148 (4.2) | 3391 (5.8) | 3271 (5.8) |
| AF // foliation | 2495 (2.3) | 2460 (2.6) | 3721 (2.4) | 3620 (2.5) |
| MDB ⊥ foliation | 2370 (1.7) | 2347 (1.9) | 4118 (3.4) | 3982 (3.9) |
| MDB // foliation | 2134 (1.8) | 2060 (2.7) | 3895 (2.5) | 3711 (3.5) |
| MDB* ⊥ foliation | 2204 (5.3) | 2156 (5.2) | 3918 (2.0) | 3723 (2.8) |
| MDB* // foliation | 2437 (3.4) | 2378 (3.3) | 3992 (2.1) | 3839 (2.3) |
| PTA ⊥ foliation | 3272 (1.0) | 3224 (1.5) | 4523 (1.3) | 4399 (1.8) |
| PTA // foliation | 3546 (0.52) | 3505 (0.62) | 4528 (1.4) | 4404 (1.9) |
| PTA* ⊥ rift plan | 2079 (1.5) | 1987 (1.6) | 3386 (15.5) | 3289 (15.4) |
| PTA* // rift plan | 2640 (3.6) | 2597 (5.3) | 3865 (4.5) | 3723 (3.9) |
| PLA ⊥ rift plan | 2680 (2.6) | 2727 (2.6) | 3719 (3.2) | 3443 (4.0) |
| PLA // rift plan | 3646 (1.9) | 4040 (2.8) | 4736 (1.7) | 4568 (2.5) |
| PLA* ⊥ rift plan | 2823 (2.3) | 2574 (2.8) | 4240 (1.8) | 4056 (2.9) |
| PLA* // rift plan | 4192 (2.3) | 3586 (2.3) | 5228 (2.3) | 5072 (3.0) |

Table E.2 – Average values of the ultrasonic pulse velocity - tensile specimens. Coefficient of variation is indicated inside brackets (%)

| Granite | Dry specimens | | Saturated specimens | |
|---|---|---|---|---|
| | $UPV_{54}$ (m/s) | $UPV_{150}$ (m/s) | $UPV_{54}$ (m/s) | $UPV_{150}$ (m/s) |
| BA | - | 4511 (1.6) | - | 5268 (0.86) |
| GA | - | 4364 (1.1) | - | 5227 (2.0) |
| GA* | - | 3014 (2.0) | - | 4287 (4.1) |
| RM | - | 3935 (0.89) | - | 5056 (3.6) |
| MC | - | 3931 (1.5) | - | 5184 (2.4) |
| AF ⊥ foliation plan | - | 2117 (2.7) | - | 3682 (13.4) |
| AF // foliation | - | 2442 (1.6) | - | 4216 (3.6) |
| MDB ⊥ foliation | - | 2320 (2.0) | - | 3554 (3.0) |
| MDB // foliation | - | 2106 (2.6) | - | 3150 (3.6) |
| MDB* ⊥ foliation | - | 2198 (2.5) | - | 3707 (1.4) |
| MDB* // foliation | - | 2242 (2.3) | - | 3813 (2.2) |
| PTA ⊥ foliation | - | 3442 (0.82) | - | 4301 (1.7) |
| PTA // foliation | - | 3127 (0.93) | - | 3853 (3.0) |
| PTA* ⊥ rift plan | - | 1723 (6.0) | - | 2729 (6.4) |
| PTA* // rift plan | - | 2123 (3.8) | - | 3010 (2.8) |
| PLA ⊥ rift plan | - | 2665 (3.0) | - | 4108 (3.4) |
| PLA // rift plan | - | 4010 (2.9) | - | 4311 (2.4) |
| PLA* ⊥ rift plan | - | 2476 (3.0) | - | 4017 (3.6) |
| PLA* // rift plan | - | 4511 (1.6) | - | 5268 (0.86) |

# APPENDIX F

## Details of the experimental tests - masonry materials

### F.1 Shear load-shear displacement diagrams for cyclic tests on dry masonry joints

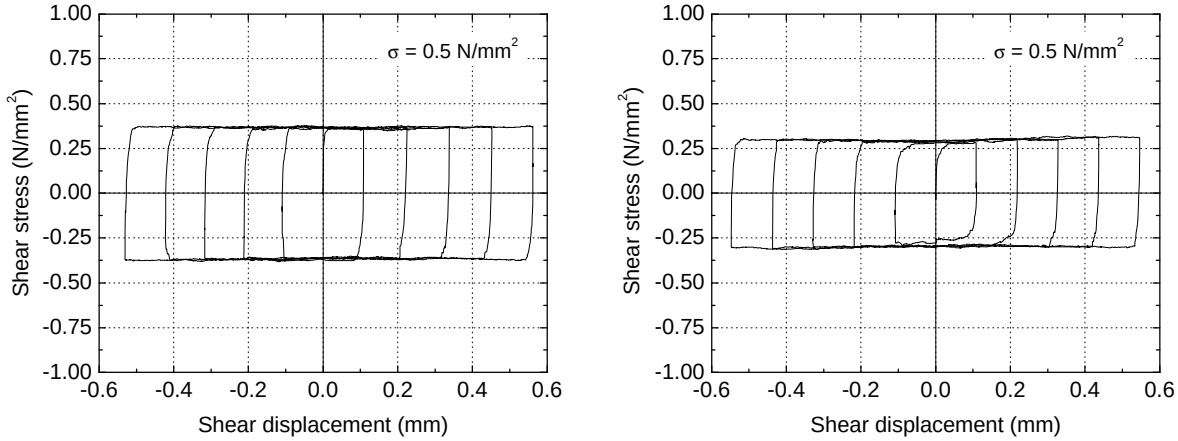


(a) (b)

Figure F.1 – Shear stress-shear displacement diagrams on sawn dry masonry joints under cyclic loading; (a) dry specimen; (b) saturated specimen

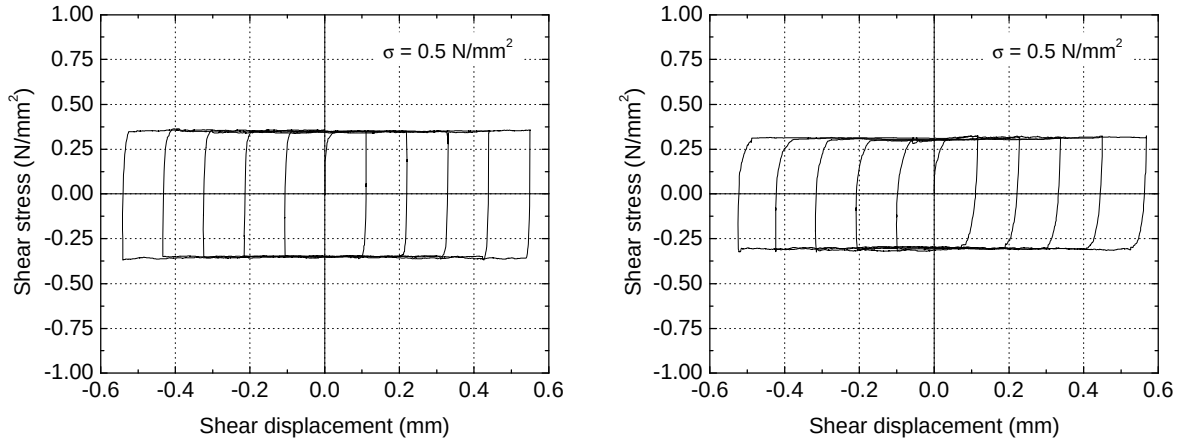


(a) (b)

Figure F.2 – Shear stress-shear displacement diagrams on sawn dry masonry joints under cyclic loading; (a) dry specimen; (b) saturated specimen

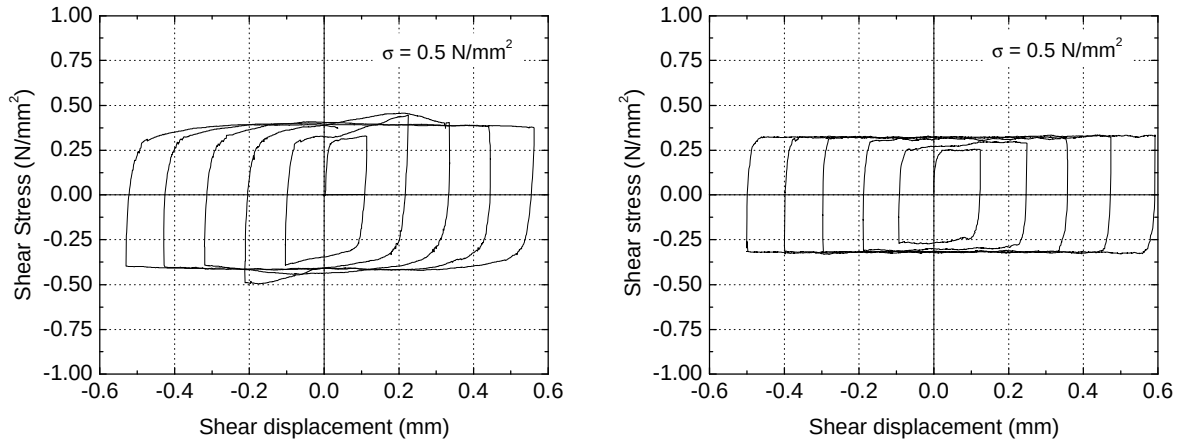


Figure F.3 – Shear stress-shear displacement diagrams on sawn dry masonry joints under cyclic loading; (a) dry specimen; (b) saturated specimen

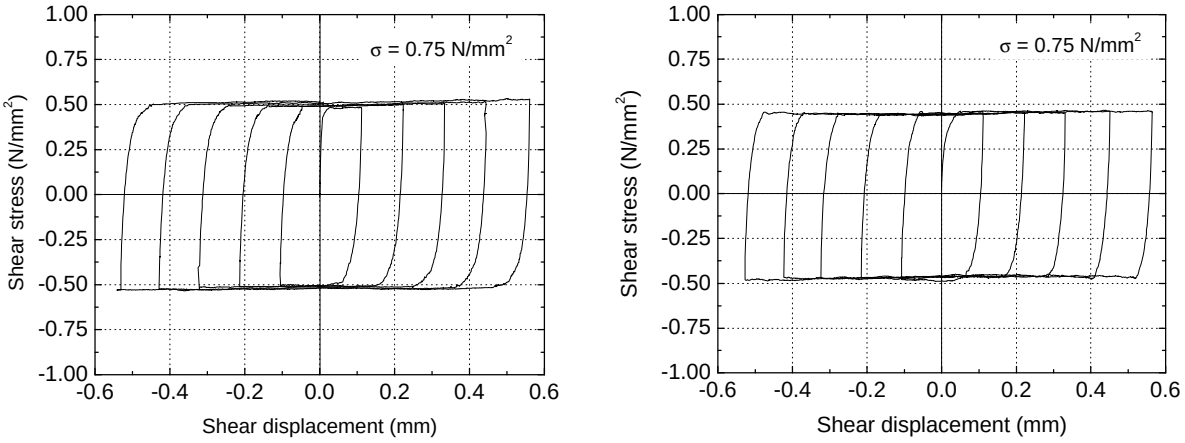


Figure F.4 – Shear stress-shear displacement diagrams on sawn dry masonry joints under cyclic loading; (a) dry specimen; (b) saturated specimen

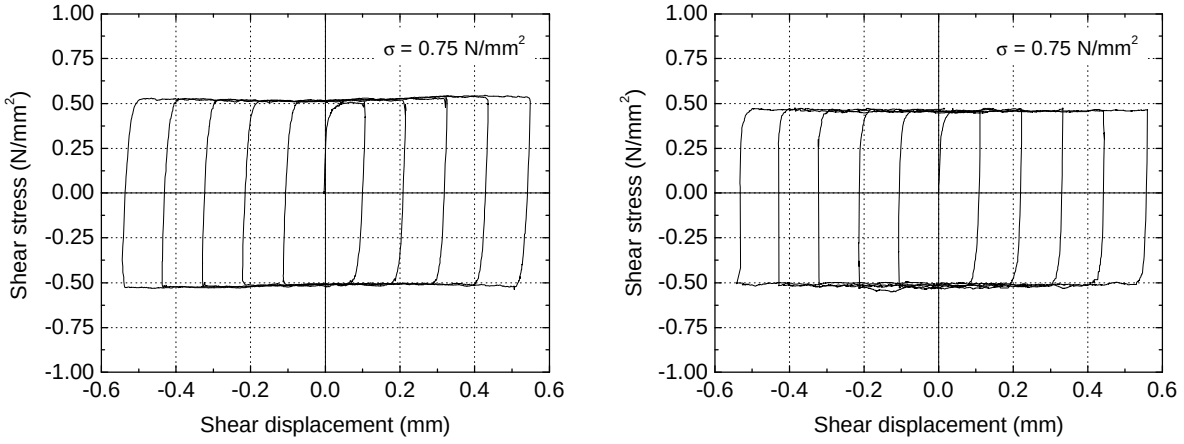


Figure F.5 – Shear stress-shear displacement diagrams on sawn dry masonry joints under cyclic loading; (a) dry specimen; (b) saturated specimen

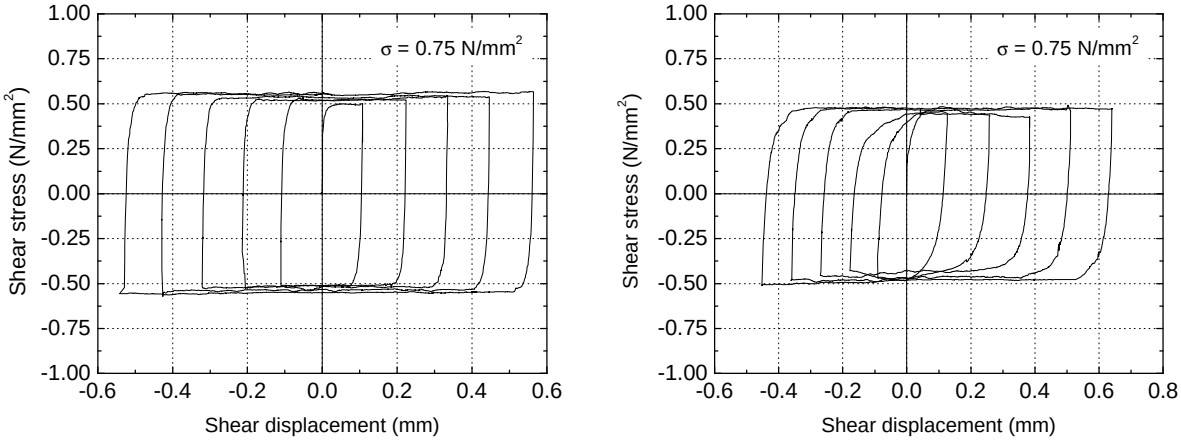


(a) (b)

Figure F.6 – Shear stress-shear displacement diagrams on sawn dry masonry joints under cyclic loading; (a) dry specimen; (b) saturated specimen

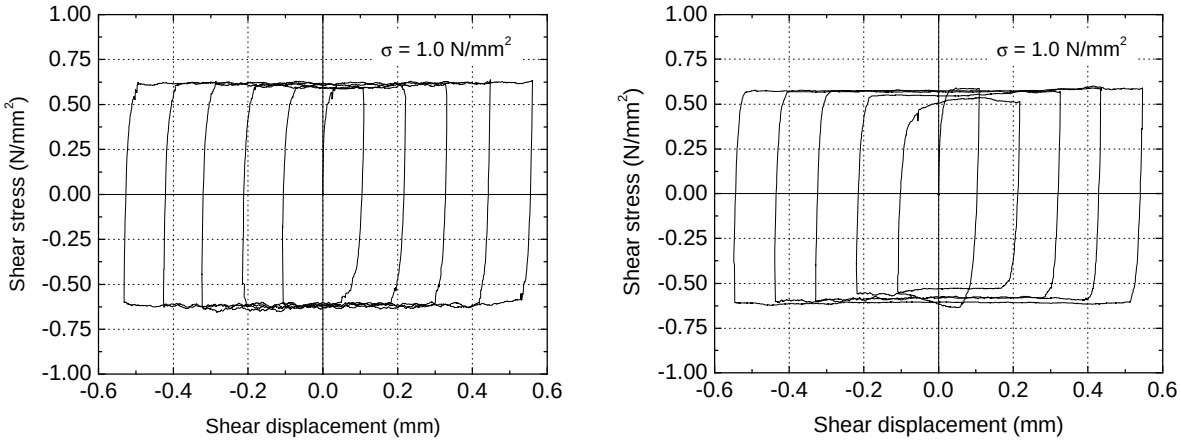


(a) (b)

Figure F.7 – Shear stress-shear displacement diagrams on sawn dry masonry joints under cyclic loading; (a) dry specimen; (b) saturated specimen

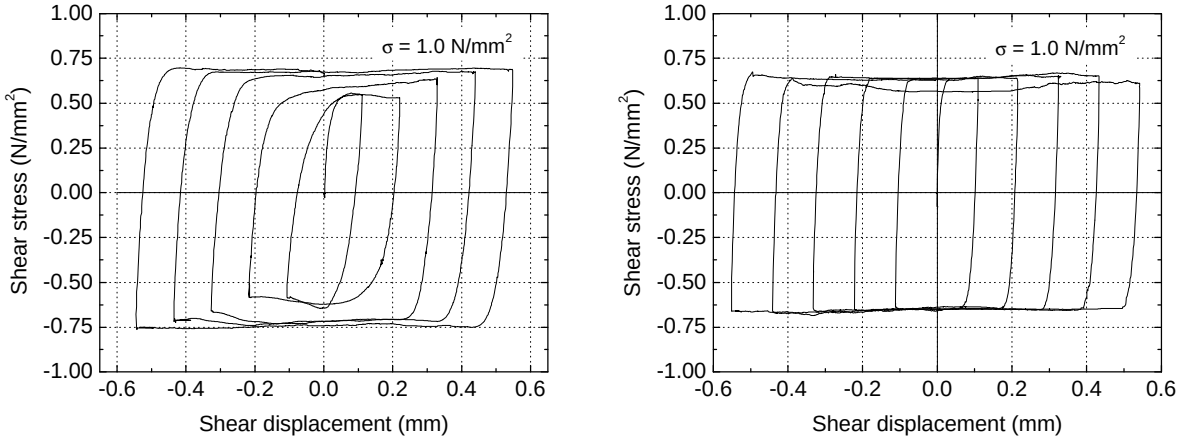


(a) (b)

Figure F.8 – Shear stress-shear displacement diagrams on sawn dry masonry joints under cyclic loading; (a) dry specimen; (b) saturated specimen

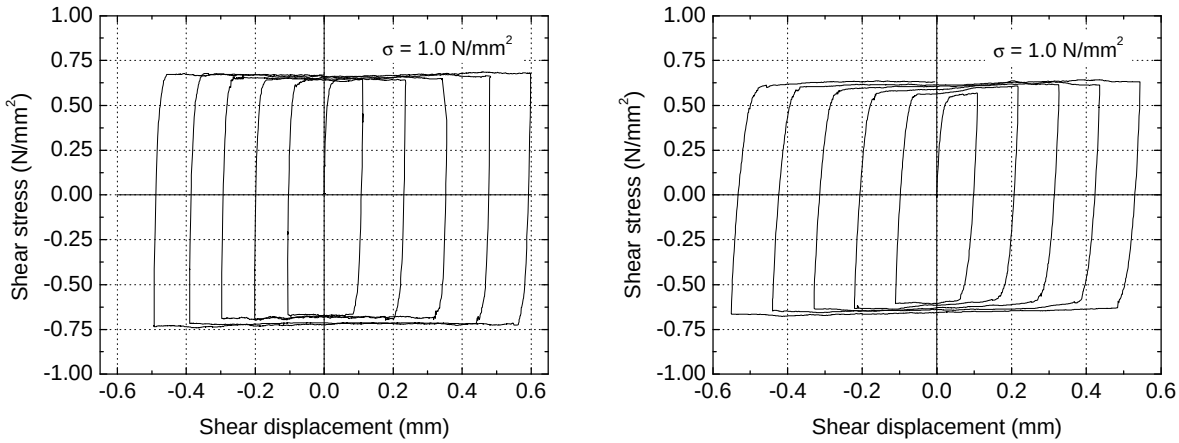


(a) (b)

Figure F.9 – Shear stress-shear displacement diagrams on sawn dry masonry joints under cyclic loading; (a) dry specimen; (b) saturated specimen

## F.2 Force-displacement diagrams for masonry prisms

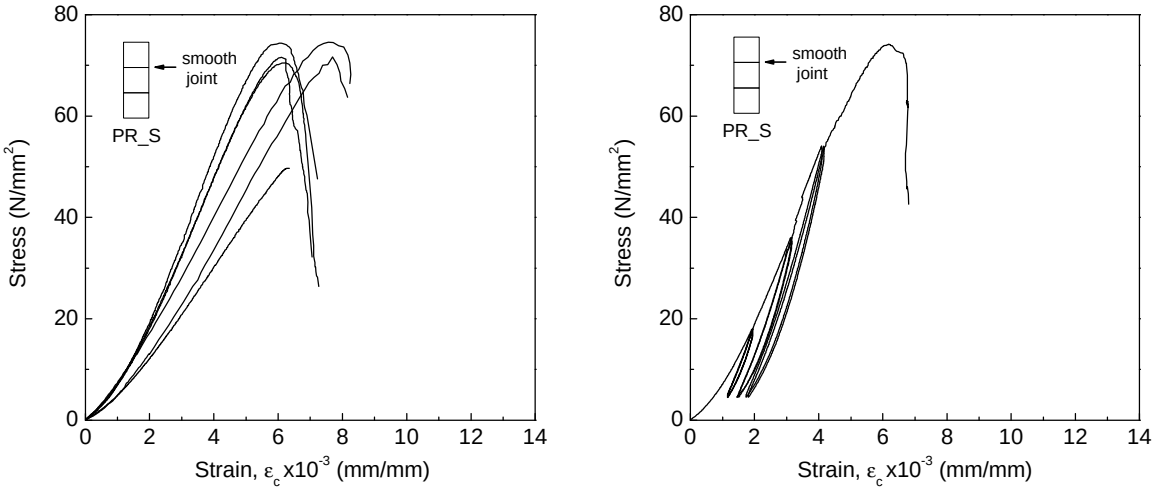


(a) (b)

Figure F.10 – Stress-strain diagrams for dry masonry prisms (PR_S); (a) monotonic tests; (b) cyclic tests - specimen PR_S7

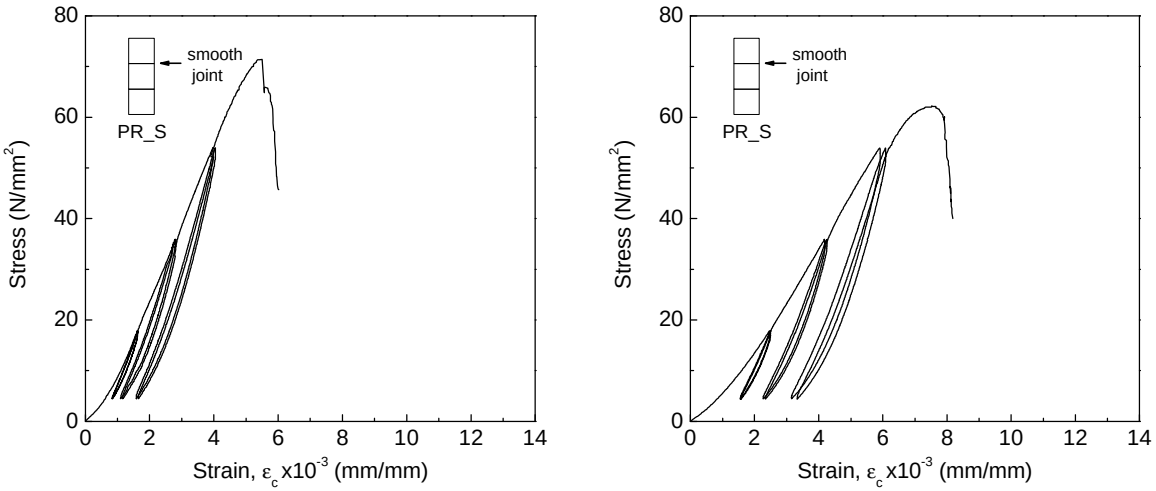


(a) (b)

Figure F.11 – Stress-strain diagrams for cyclic tests; (a) specimen PR_S8; (b) specimen PR_S9

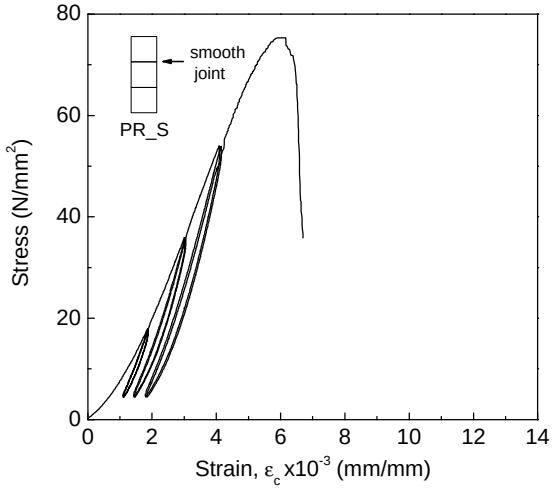


Figure F.12 – Stress-strain diagrams for cyclic tests: specimen PR_S10

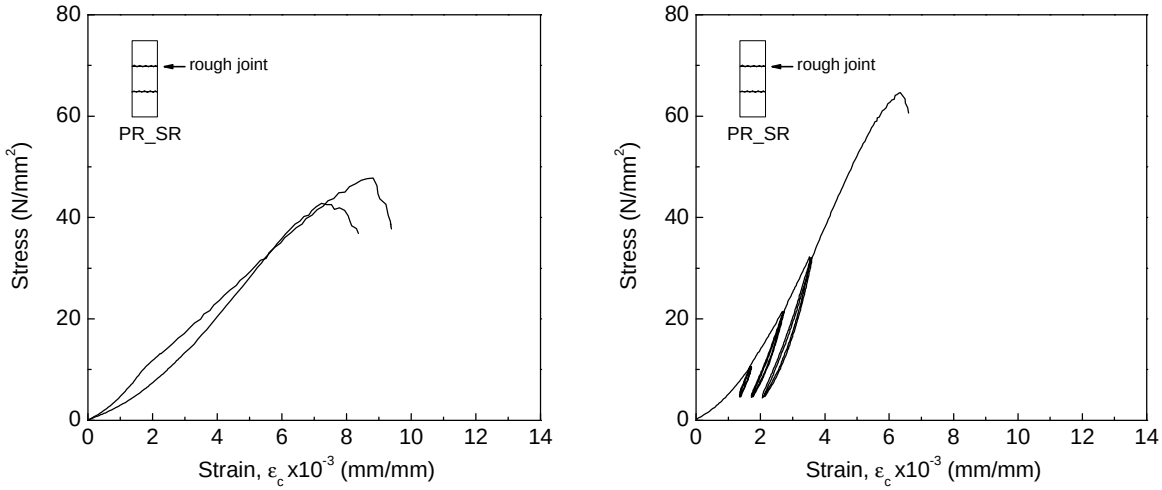


Figure F.13 – Stress-strain diagrams for rough bed joint specimens (PR_SR); (a) monotonic tests; (b) cyclic tests - specimen PR_SR3

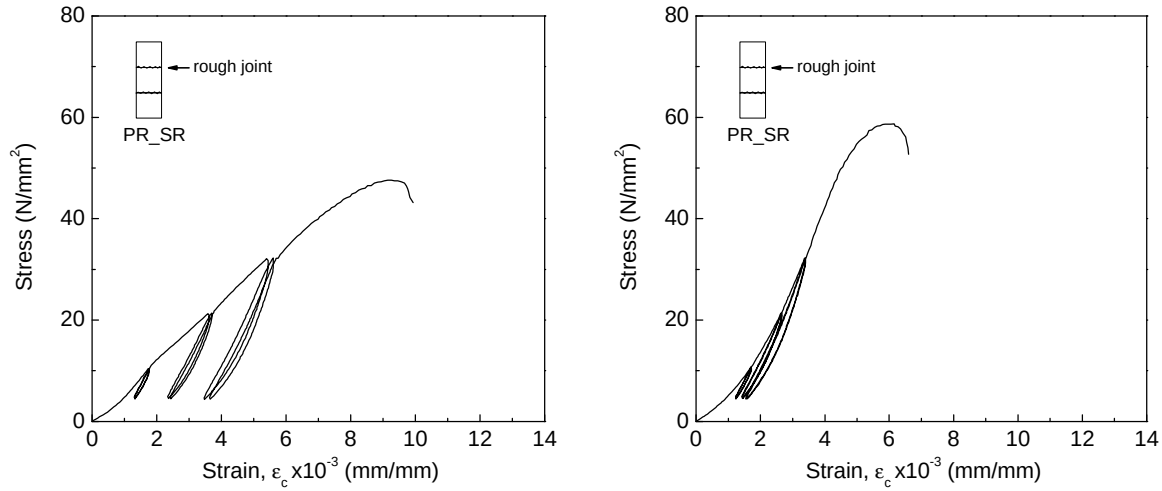


Figure F.14 – Stress-strain diagrams for cyclic tests; (a) specimen PR_SR4; (b) specimen PR_SR5

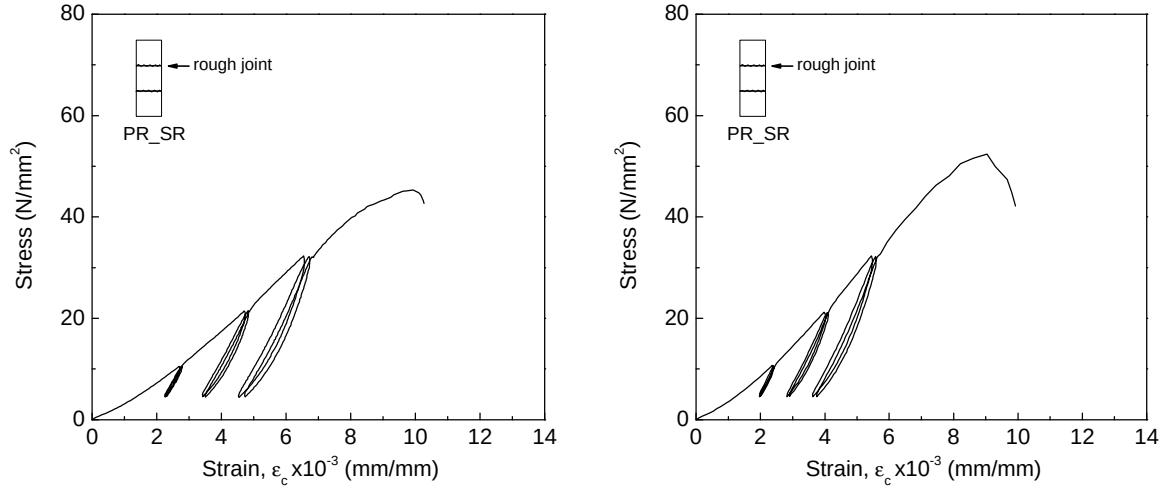


Figure F.15 – Stress-strain diagrams for cyclic tests; (a) specimen PR_SR6; (b) specimen PR_SR7

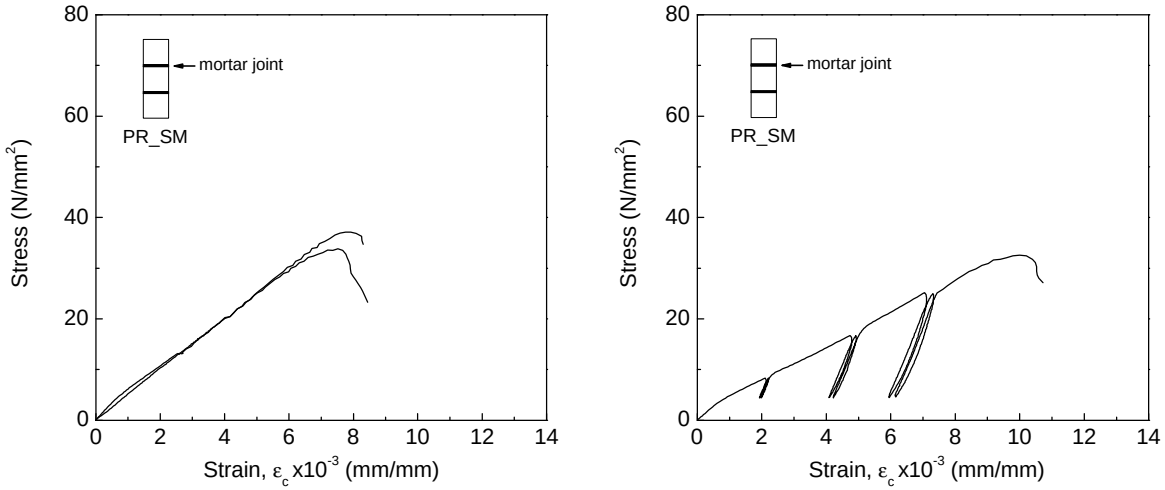


(a) (b)

Figure F.16 – Stress-strain diagrams for mortar masonry prisms (PR_SM); (a) monotonic tests; (b) cyclic tests - specimen PR_SM3

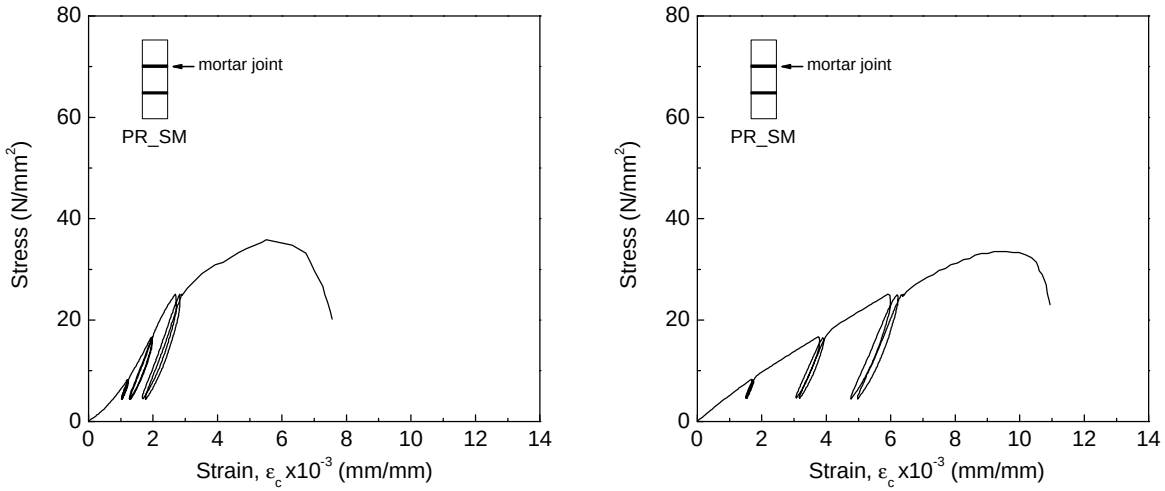


(a) (b)

Figure F.17 – Stress-strain diagrams for cyclic tests; (a) specimen PR_SM4; (b) specimen PR_SM5

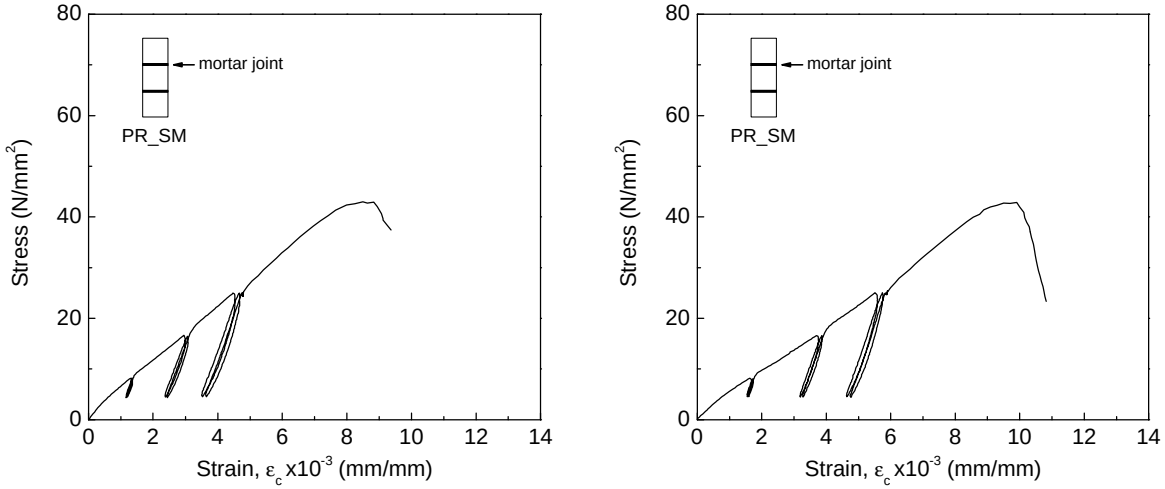


(a) (b)

Figure F.18 – Stress-strain diagrams for cyclic tests; (a) specimen PR_SM6; (b) specimen PR_SM7

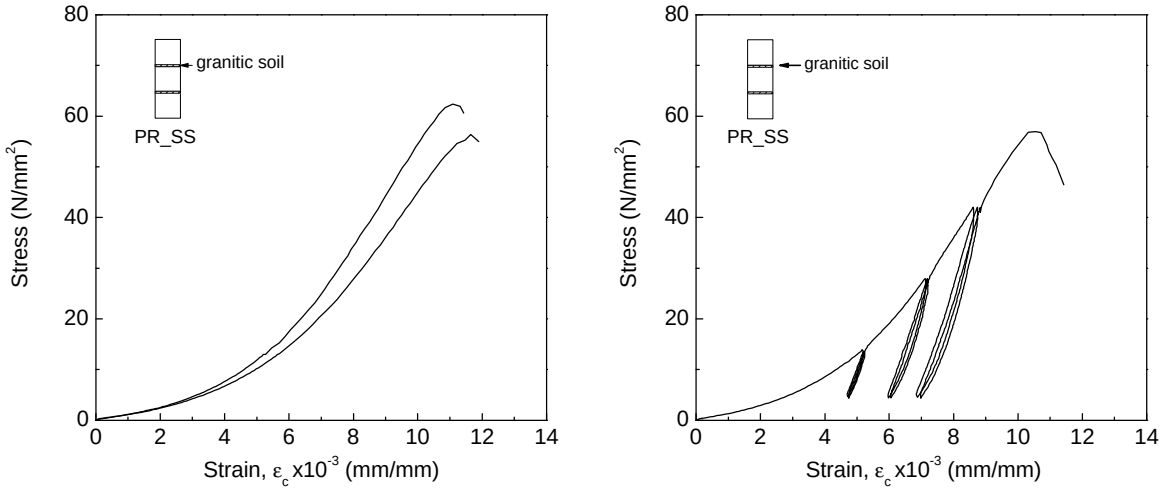


Figure F.19 – Stress-strain diagrams for granitic soil masonry prisms (PR_SS); (a) monotonic tests; (b) cyclic tests - specimen PR_SS3

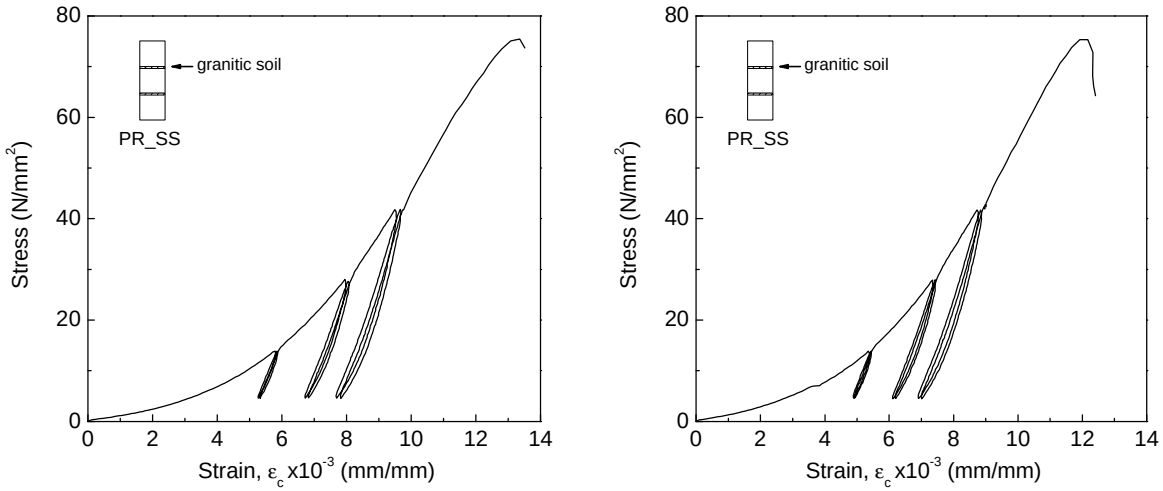


Figure F.20 – Stress-strain diagrams for cyclic tests; (a) specimen PR_SS4; (b) specimen PR_SS5

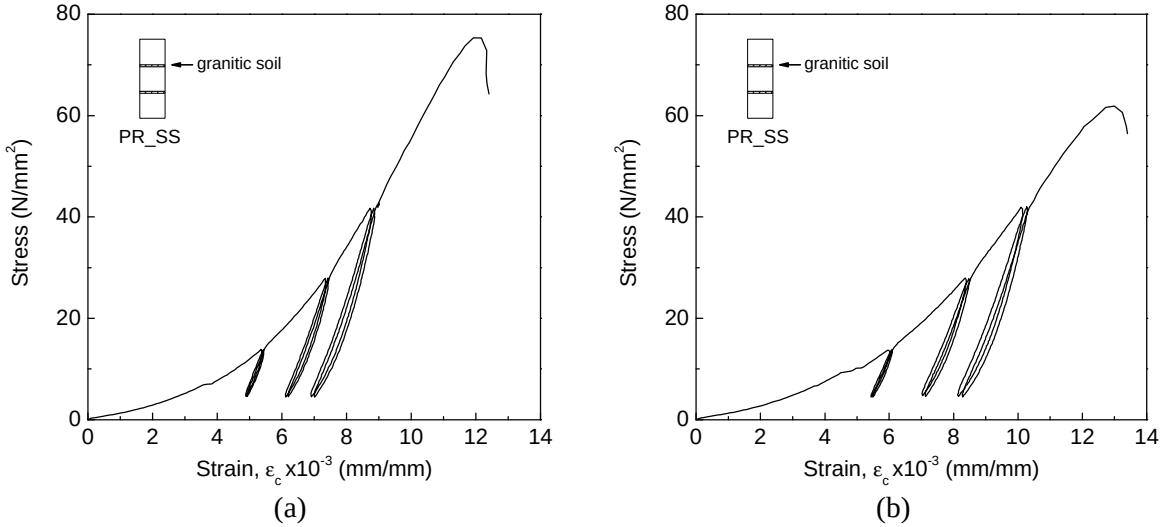


Figure F.21 – Stress-strain diagrams for cyclic tests; (a) specimen PR_SS6; (b) specimen PR_SS7

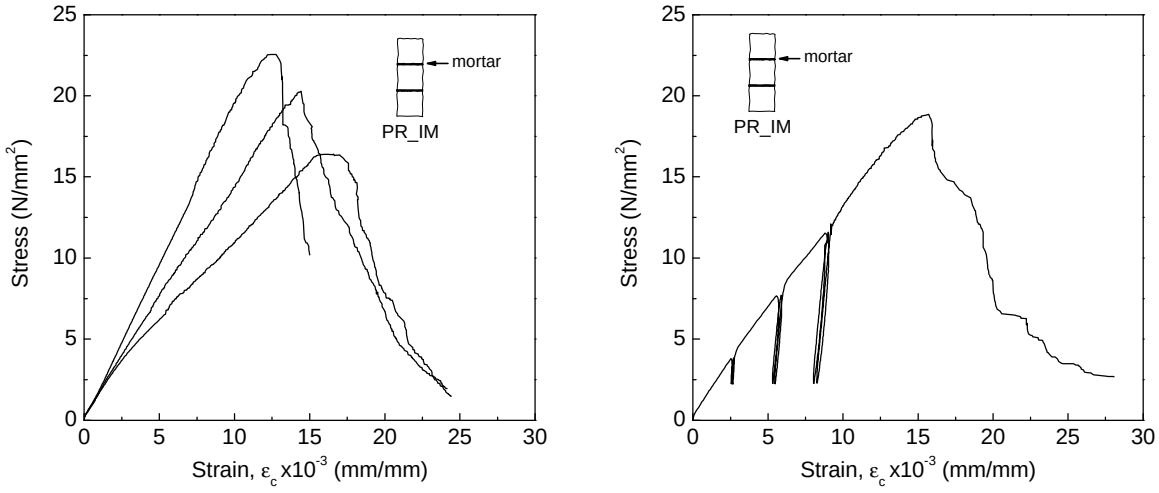


Figure F.22 – Stress-strain diagrams for irregular hand cut masonry prisms; (a) monotonic tests; (b) cyclic tests - specimen PR_IM4

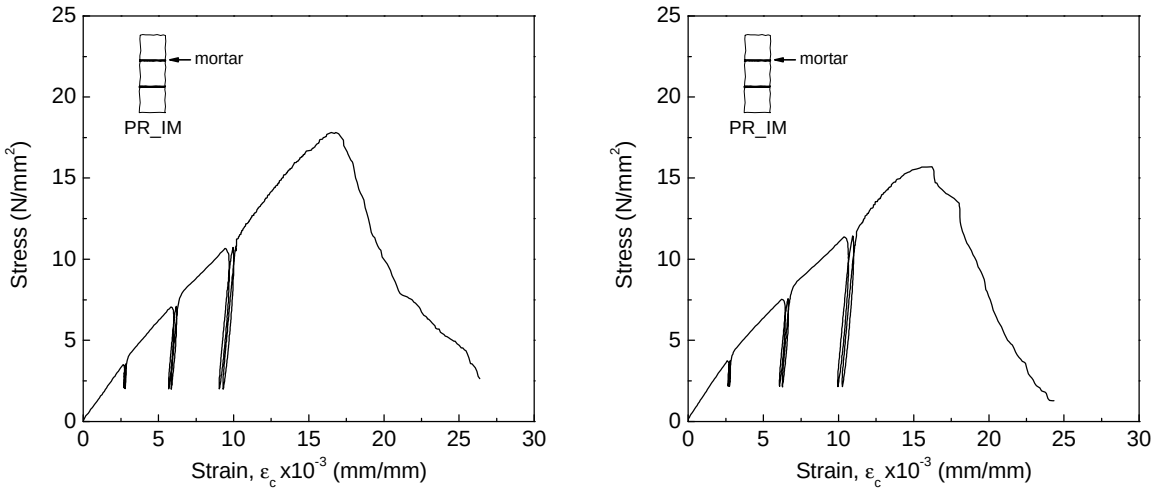


Figure F.23 – Stress-strain diagrams for cyclic tests; (a) specimen PR_IM5; (b) specimen PR_IM6

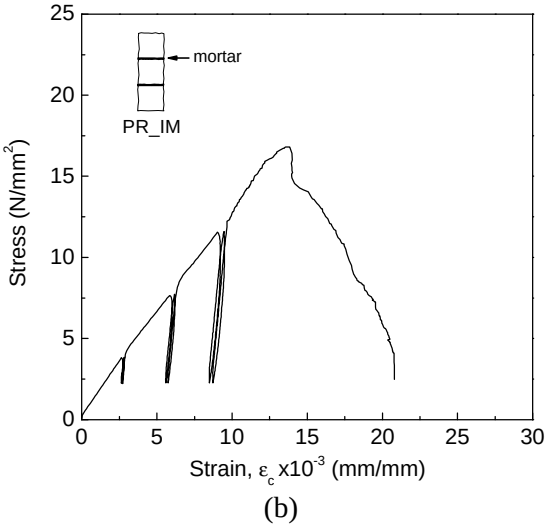


Figure F.24 – Stress-strain diagrams for cyclic tests - specimen PR_IM7

# APPENDIX G

## Force-displacement diagrams for granitic masonry walls - in-plane cyclic shear behavior

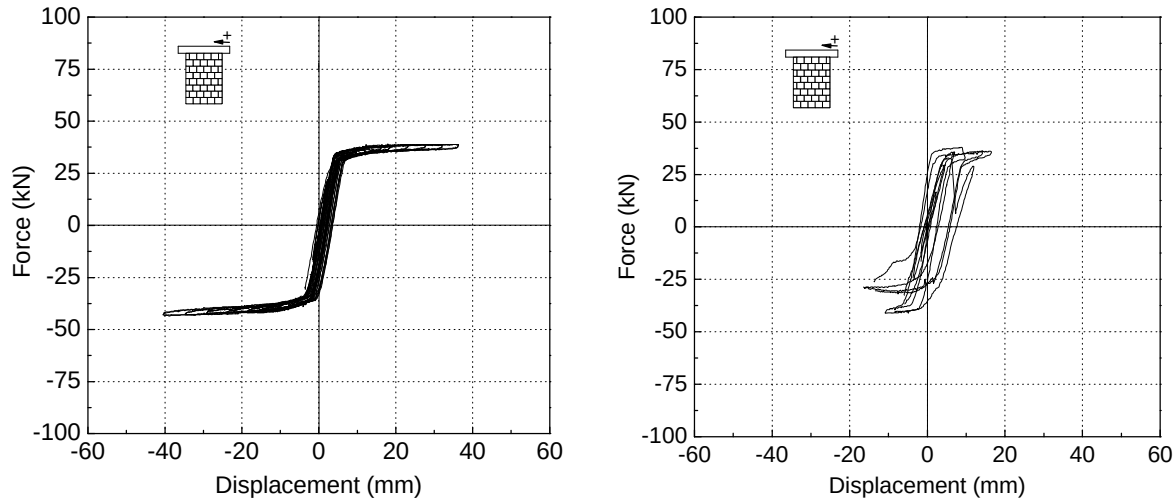


(a) (b)

Figure G.1 – Force-displacement diagrams for dry masonry walls WS.100; (a) wall WS1.100; (b) wall WS2.100

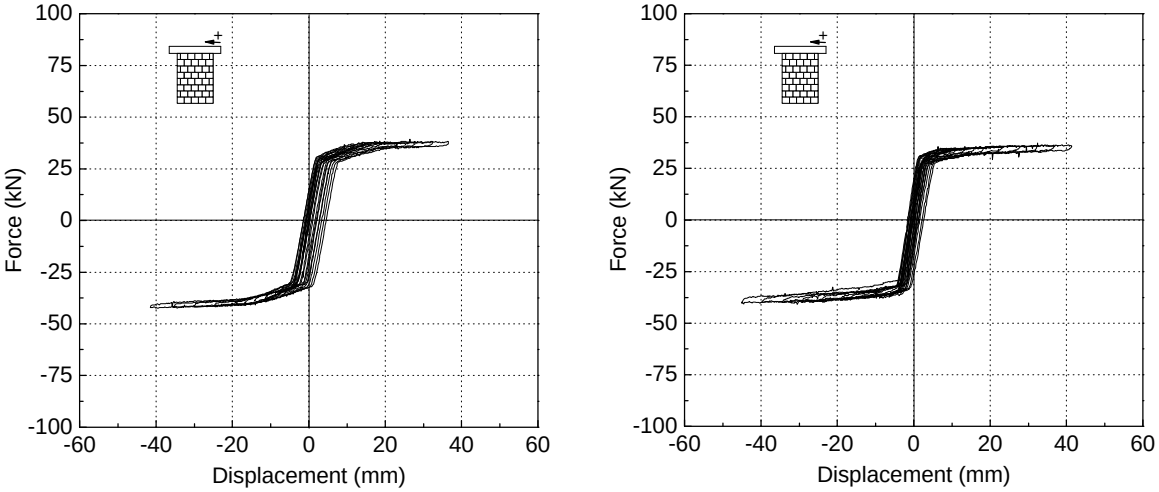


Figure G.2 – Force-displacement diagrams for dry masonry walls WS.100; (a) wall WS3.100; (b) wall WS4.100

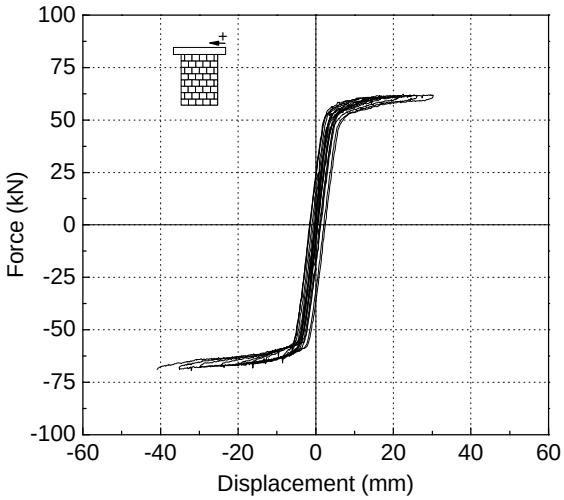


Figure G.3 – Force-displacement diagram for dry masonry wall WS1.175

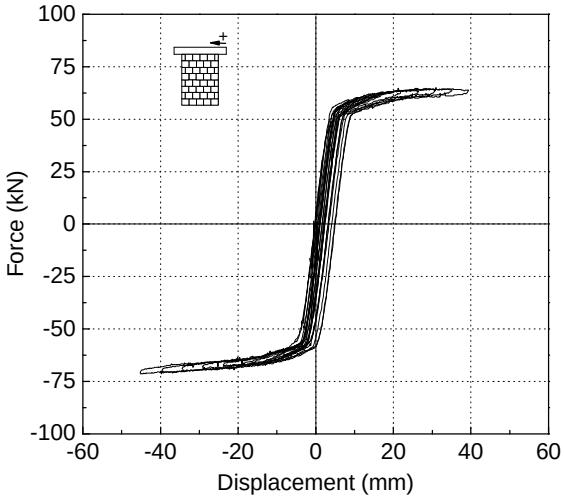


Figure G.4 – Force-displacement diagram for dry masonry wall WS2.175

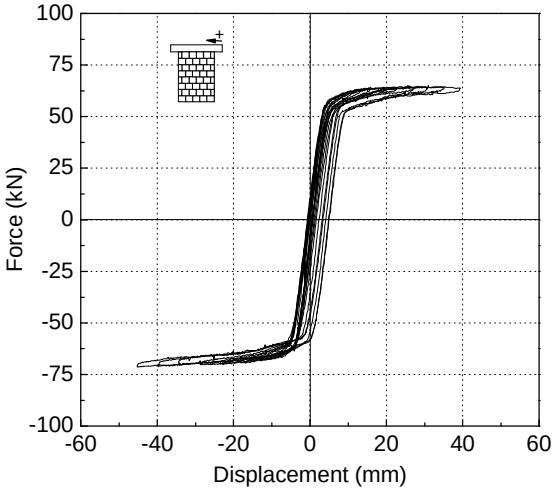


Figure G.5 – Force-displacement diagram for dry masonry wall WS3.175

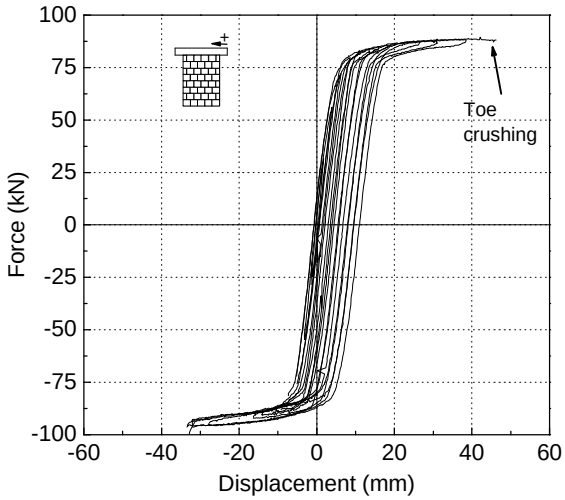


(a)

Figure G.6 – Force-displacement diagram for dry masonry wall WS1.250

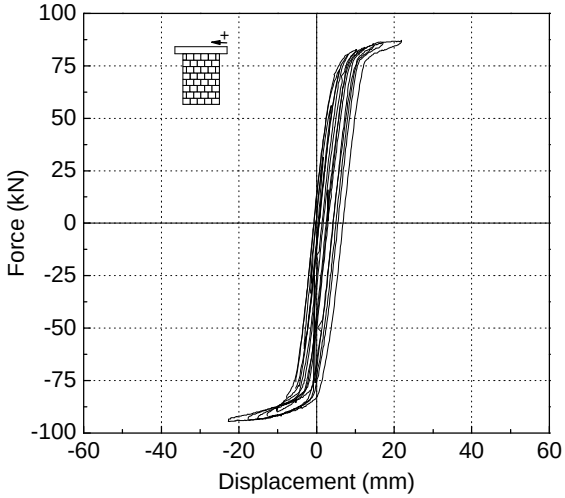


Figure G.7 – Force-displacement diagram for dry masonry wall WS2.250

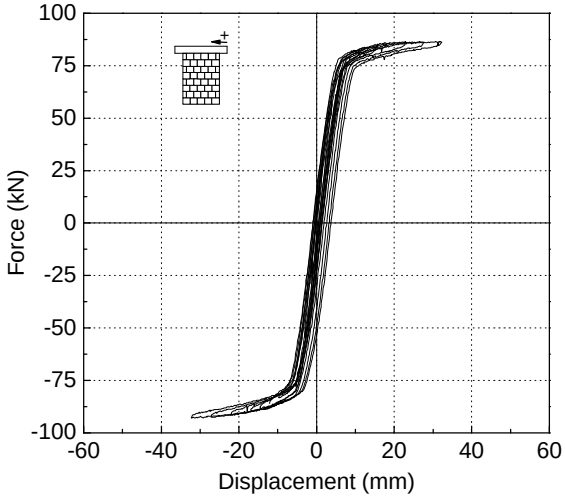


Figure G.8 – Force-displacement diagram for dry masonry wall WS3.250

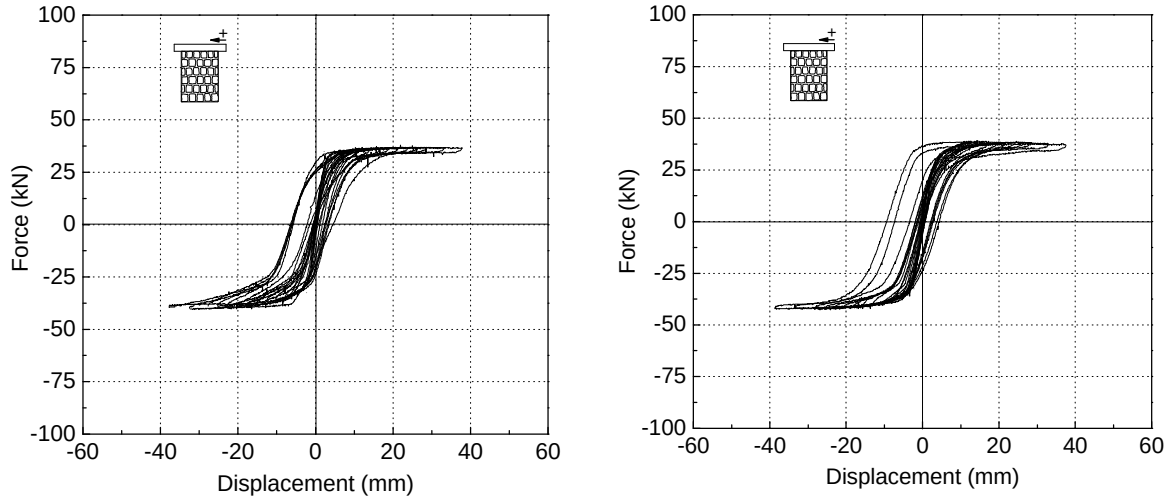


(a) (b)

Figure G.9 – Force-displacement diagrams for irregular masonry walls WI.100; (a) wall WI1.100; (b) wall WI2.100

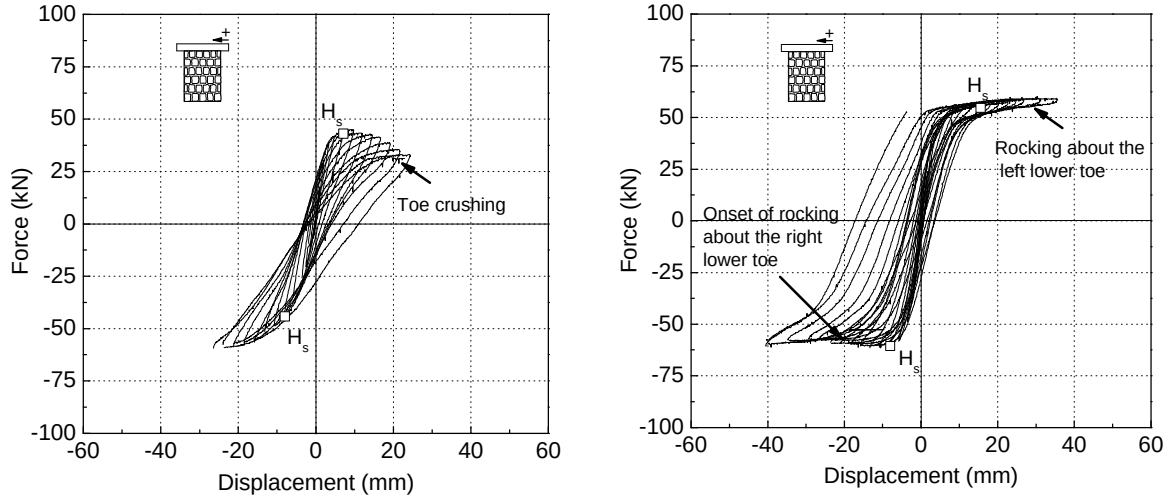


(a) (b)

Figure G.10 – Force-displacement diagrams for irregular masonry walls WI.175; (a) wall WI1.175; (b) wall WI2.175

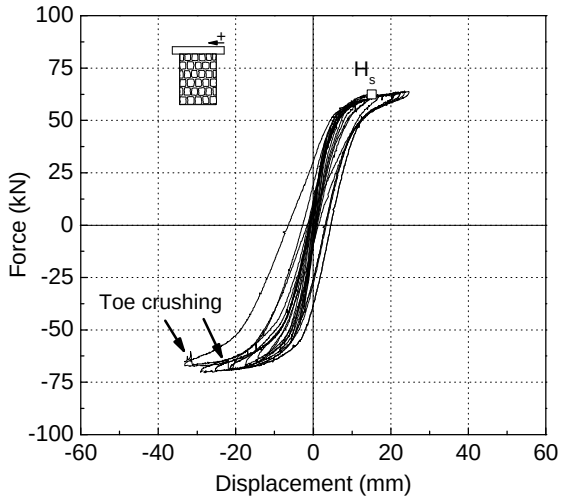


Figure G.11 – Force-displacement diagram for irregular masonry wall WI3.175

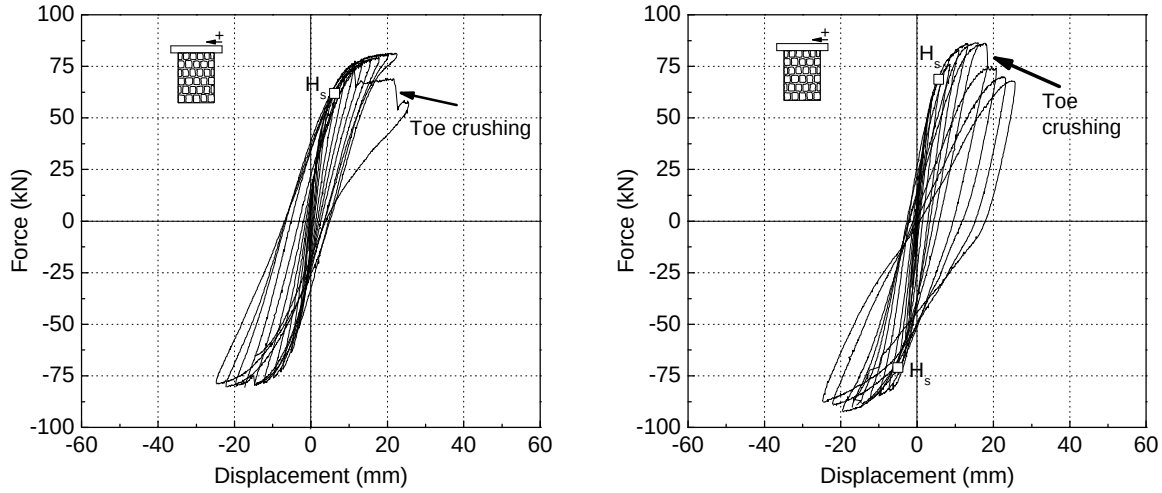


(a) (b)

Figure G.12 – Force-displacement diagrams for irregular masonry walls WI.250; (a) wall WI1.250; (b) wall WI2.250

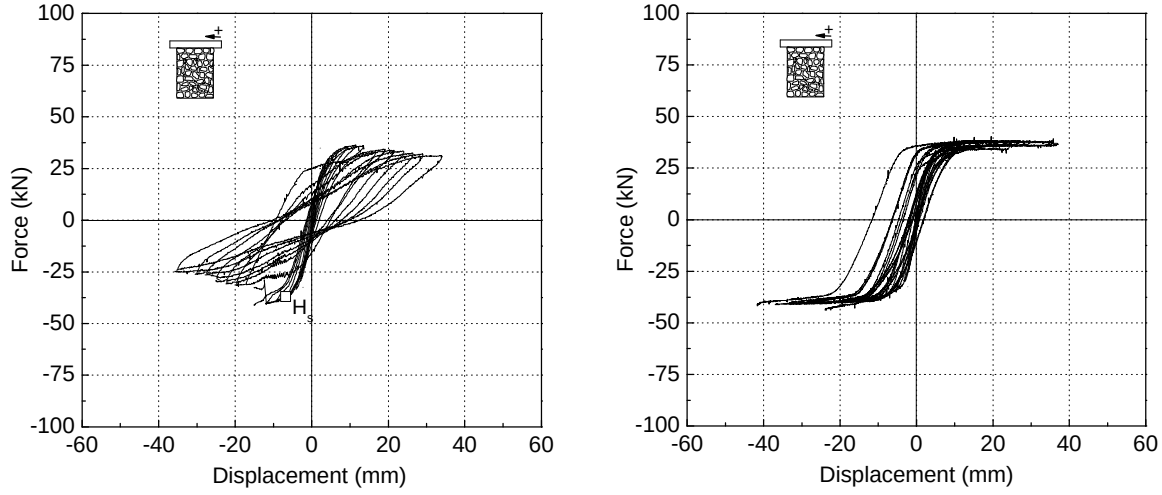


(a) (b)

Figure G.13 – Force-displacement diagrams for rubble masonry walls WR.100; (a) wall WR1.100; (b) wall WR2.100

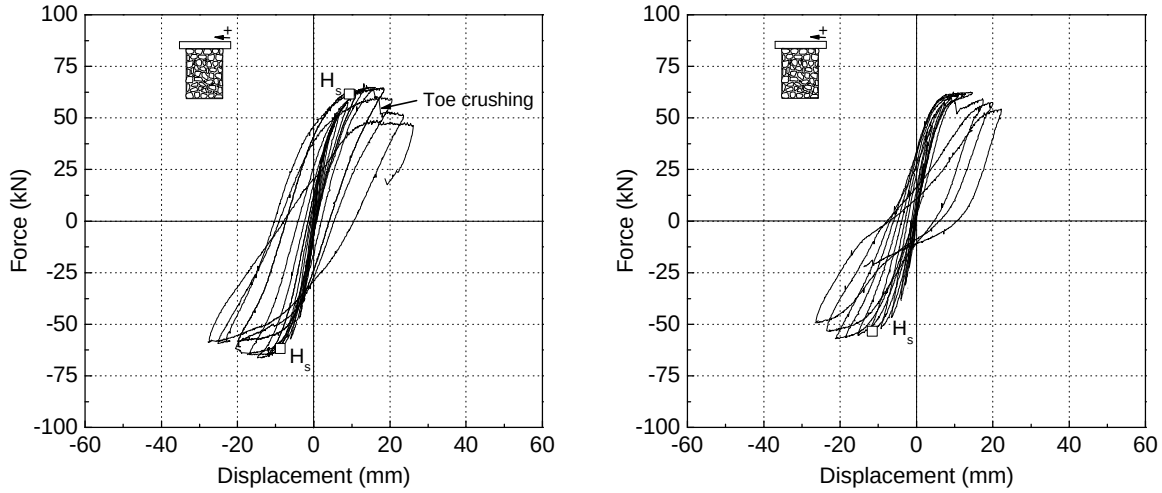


(a) (b)

Figure G.14 – Force-displacement diagrams for rubble masonry walls WR.175; (a) wall WR1.175; (b) wall WR2.175

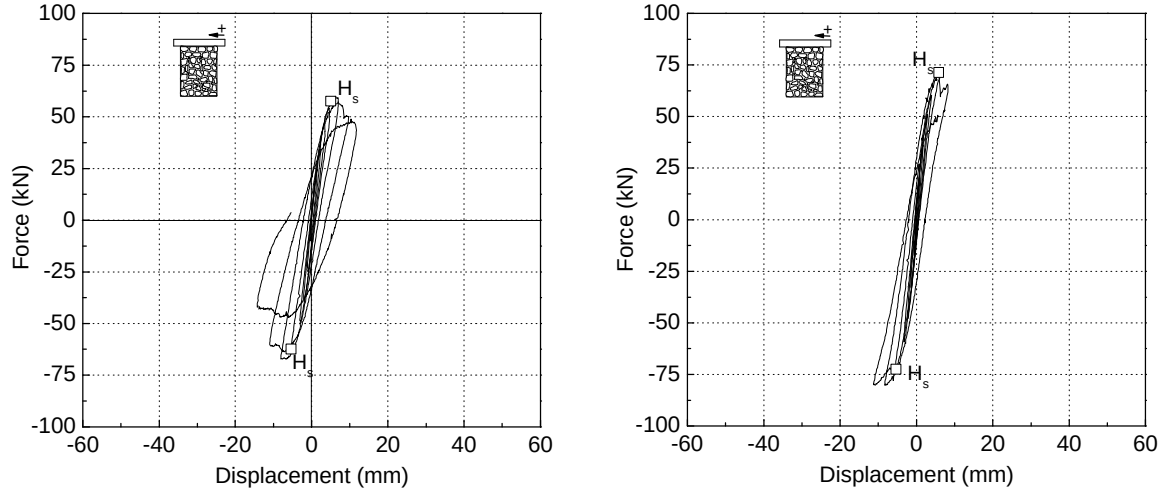


(a) (b)

Figure G.15 – Force-displacement diagrams for rubble masonry walls WR.250; (a) wall WR1.250; (b) wall WR2.250

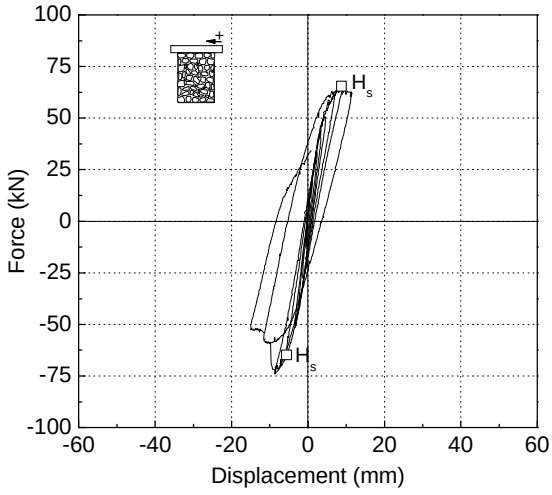


Figure G.16 – Force-displacement diagram for rubble masonry wall WR3.250